

**Department of AERONAUTICS and ASTRONAUTICS
STANFORD UNIVERSITY**

**THREE STUDIES IN AEROELASTICITY
AND
UNSTEADY AERODYNAMICS**

(NASA-CR-170138) THREE STUDIES IN
AEROELASTICITY AND UNSTEADY AERODYNAMICS
(Stanford Univ.) 227 p

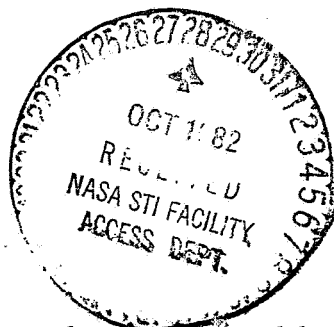
N83-75071
THRU
N83-75074
Unclas

00/01 31281

by

**Larry L. Lehman
James K. Natham
Holt Ashley**

SUDAAR NO. 529



LIBRARY COPY

OCT 24 1982

LANGLEY RESEARCH CENTER
LIBRARY, NASA
HAMPTON, VIRGINIA

This research was supported by the Air Force Office of Scientific Research under Contracts Nos. AFOSR-79-0061, AFOSR-74-2712A, AFOSR-77-3263 and by National Aeronautics and Space Administration under Grant No. ~~NASA-243~~.

31281

Department of Aeronautics and Astronautics
Stanford University
Stanford, California

THREE STUDIES IN AEROELASTICITY

AND

UNSTEADY AERODYNAMICS

By

Larry L. Lehman

James K. Nathman

Holt Ashley

SUDAAR NO. 529

This research was supported by the Air Force Office of Scientific Research under Contracts Nos. AFOSR-79-0061, AFOSR-74-2712A, AFOSR-77-3263 and by National Aeronautics and Space Administration under ~~Grant No. NASA 243.~~ *Q*

GENERAL TABLE OF CONTENTS

General Preface	iii
The Constructive Uses of Aeroelasticity	A-1
Hybrid State Vector Methods for Structural Dynamic and Aeroelastic Boundary Value Problems	B-1
Unsteady Aerodynamic Propulsion	C-1

GENERAL PREFACE

The "constructive uses of aeroelasticity," as a subject for serious research, has been a dream of mine for almost thirty years. It was, therefore, a matter of considerable pleasure when two of the finest doctoral students with whom I have ever been associated — J. K. Nathman and L. L. Lehman — both chose dissertation topics closely related to that subject. By coincidence their studies were completed within a few weeks near the end of Summer 1981. At AIAA's invitation, they and I had also collaborated a year earlier on a survey and general-interest paper for the 1980 International Meeting and Technical Display in Baltimore. The resulting opportunity of combining these three neighborly documents into a single large SUDAAR seems to provide an efficient and economical means of distribution. It is worth mentioning that our survey paper has been submitted for publication in a special issue of a Polish journal, honoring the 70th birthday of Professor Wladyslaw Fiszdon, but has not yet appeared there.

The two dissertations speak so well for themselves that no summary need be provided. Mr. Lehman's had its origins in his fascination with the possibilities of filamentary composite materials as a means of modifying aeroelastic behavior. Although a focus of the final product is on an extremely effective scheme of solving one-dimensional boundary value problems, yet many of the examples involve such composites. Mr. Nathman's grew, among other roots, from an interest

in the propulsion of birds, fish and variable-geometry aircraft. One of its highlights is accurate measurement of the aerodynamic force components which have special significance for this kind of flight.

Except for minor proof corrections, the two dissertations are reproduced without change as parts B and C of this report. They therefore differ in format, notation, organization and style. Quite properly they are the individualistic products of their signed authors. The curious scheme of page numbering is another consequence of the combination, and no apology need be made.

One message appears repeatedly in this report: our expression of appreciation for the continued, enlightened research support that we receive from AFOSR and NASA. Without their involvement, neither these contributions to knowledge nor the education achieved during their creation would have been possible.

Holt Ashley

D,

THE CONSTRUCTIVE USES OF AEROELASTICITY

by

Holt Ashley,^{*} Larry L. Lehman,[†] and James K. Nathman^{†*}

Stanford University
Stanford, CA 94305, USA

ABSTRACT

Historical, previously-published and new material is illustrated and discussed in support of the proposition that static or dynamic structural deformations of aerospace vehicles can often be used for constructive purposes. Examples are presented chronologically in categories related to the intended function. Efficient control of flight is attainable, as by the Wrights' wing warping. Constraints can be relaxed on the performance of high-speed aircraft, fixed-pitch propellers and rotors. Accelerations and loads in rough air are diminished. Aeroelastic deformations furnish a means for primary propulsion. Prospects for the future are examined, notably the "complete aeroelastic CCV."

Based on Paper No. 80-0877, presented at AIAA International Annual Meeting and Technical Display, Baltimore, MD, USA, May 6-11, 1980. Submitted in January 1981.

^{*} Professor, Aeronautics/Astronautics and Mechanical Engineering.

[†] Research Scientist, Nielsen Engineering & Research, Inc.

^{†*} Research Scientist, Analytical Methods, Inc.

Introduction

Because all structural materials exhibit finite elasticity, no artifact of engineering behaves under load in a completely rigid fashion. As a rule, elastic or plastic deformation is regarded as an undesirable by-product of design, and it must be limited in some appropriate way. Thus construction codes typically constrain the deflections of such civil structures as bridges or building floors, and elongated compression members must be protected against buckling instability. It is equally obvious, however, that (reversible) flexibility can often be put to good use. Instances may be found in such tiny, homely objects as paperclips or the bistable keys of an electronic calculator. But they also include springs of all sizes, shock absorbers, arresting or landing gear, and a host of other devices that will occur to the thoughtful reader.

Static and dynamic structural deformation plays a peculiarly significant role in aeronautics, where the imperative of light weight invariably comes into conflict with requirements involving stiffness and stability. When such design conditions relate to members which sustain the heavy aerodynamic pressures of flight, the associated phenomena are called "aeroelastic." First identified during World War I, their treatment gave birth to a specialized discipline* that remains active today, although it is gradually being absorbed into the mainstream of atmospheric vehicle design.

Despite fascinating challenges the career of the aeroelastician has many frustrations, for he is usually cast as a "policeman." The analyses and tests which he performs, in the course of avoiding dangerous instabilities like wing flutter or excessive structural loads, are seen as penalizing flight speeds or creating unwanted and perhaps unnecessary weight increases. This is a justifiable, but sometimes inappropriate view.

* Representative early books which summarized the state of the aeroelastic art were those by Fiszdon,¹ Fung,² and Bisplinghoff, Ashley and Halfman.³ Among numerous other citations that might be made, consider the recent text by Dowell et al.⁴ and Collar's historical survey.⁵

By no means universally recognized is that aeroelastic behavior can be constructively employed toward improving the performance, controllability, efficiency and comfort of airplanes and related aerodynamic machines. With the aim of demonstrating this proposition — and perhaps of enhancing the "image" of aeroelasticity in an entertaining way — the authors have assembled numerous illustrative examples. Some are from the earlier history of aeronautics, others current or purely conceptual. With certain arbitrariness, a selection of these examples has been categorized in accordance with the titles of sections which follow. Each is summarized as succinctly as possible, with carefully chosen pictures, graphs and references. They encompass quite different devices, a wide range of operating speeds, and varying degrees of sophistication. One hopes that unity is achieved on the theme of "constructiveness."

Improved Control and Static Stability

In his appreciation of the engineering achievements of Wilbur and Orville Wright, Coombs⁶ identifies about half a dozen which he judges especially original and important. One of these was really effective control about the airplane's roll axis — something they accomplished with the aeroelastic technique of "wing warping."

The outlines of this scheme are depicted in Fig. 1 by means of two phantom views of the 1903 Wright "Flyer" wing taken from Culick's excellent article.⁷ In the upper sketch one sees that the diagonal bracing wires which stiffen the fore and aft truss structures between the wings are omitted from the two outer aft bays nearest each wingtip. Thus the outboard trailing edges are made more flexible, so that they can be twisted antisymmetrically up and down by the control wires shown in the lower sketch. Lying prone in the "cradle," the pilot could move his hips sideways toward the wing which he wished to depress. From all reports, versions of this system employed on all the later Wright gliders and airplanes made it a simple matter either to keep the wings level or to bank for turning, as necessary, in proper coordination with rudder control. Only with the 1909 adoption of the aileron by Farman⁸ was wing torsion supplanted as the best way to do the job.

Wing warping made its appearance again in a very modern context as part of the lateral-directional control system for the successful man-powered aircraft, "Gossamer Condor" and "Gossamer Albatross." The functioning of this system is explained by Lissaman,⁹ and its mechanical realization is detailed in Burke's excellent summary¹⁰ of the Condor designs. Figure 2 is a closeup photograph of the Albatross in flight. Barely visible are some of the bracing wires which run diagonally from the base of the vertical king post out to various stations along the wingspan. These wires are part of primary structure, but one pair of them was cleverly arranged to twist the tips antisymmetrically in response to the pilot's stick actuation.

A remarkable feature of the Condor system is that, by intent, a given wing twist leads to opposite turning from what occurred on the Wright Flyer. This is because the very light, wide Condor lifting surface carried with it in roll a huge virtual mass of air, which makes it very unresponsive to bank commands. On the other hand, the increased induced drag of the wing whose trailing edge is warped downward — say, the right — causes that wing to swing backward and to build up both a yawing velocity and a sideslip toward the left. Some rightward tilting of the canard surface assists in producing this motion. Three related effects then cause the right wing to drop⁹: loss of lift due to its reduced airspeed, the tip-down rolling due to the positive yawing velocity, and later the rolling moment due to sideslip. When the desired angle of bank is developed, the pilot reduces the warping and uses opposite lateral displacement of the canard to trim to zero sideslip and achieve a coordinated turn. Reversal of these steps will then bring the bank angle back to zero. Although great insight was needed to discover this procedure, it proved fairly easy to learn and execute in flight.

Airplanes with sweptback wings of large aspect ratio can benefit from an aeroelastic phenomenon which — at least initially — was not anticipated by their designers. Basically it involves spanwise shifting of the center of additional lift caused by bending and twisting of the structure. Although of negligible importance when the sweep angle Λ is small, wingtip-upward bending due to a positive lift increment when $\Lambda > 15$ or 20 degrees can reduce effective angles of attack near the tips, thus moving the lift center

inboard and forward by a distance which depends strongly on flight dynamic pressure q . One consequence is a forward shift of the vehicle's aerodynamic center (A.C.) relative to where it would be if the wing were rigid. Taken from a classic paper by Brown, Holtby and Martin,¹¹ Fig. 3 illustrates this effect in terms of the stability derivative dC_M/dC_L as it might vary with q on an airplane like the B-47.

Figure 3 actually shows what one would measure on an elastically-scaled model, mounted in a wind tunnel and subjected to changes in fuselage incidence only. Fortunately for the B-47 and similar configurations of the 1940's and 1950's there are other consequences when incidence is changed in flight, as during a pull-up, entry into a turn, etc. The increased lift also causes a positive normal acceleration, whose inertia forces bend the wingtips back downward and tend to compensate for the aeroelastic A.C. shift. It is said that this cancellation was almost perfect on the B-47 and thus produced an airplane whose longitudinal dynamics and control were not substantially different from what might have occurred with a rigid wing.

Incidentally, there are numerous by-products of aeroelasticity in the presence of sweep. On the one hand, the loss of outboard aileron control at high q (cf. the discussion in Perkins¹²) is undesirable and definitely requires correction. On the other, divergence instability is avoided completely when Λ is large enough. One interesting example is the "aero-isoclinic" scheme of Hill,¹³ whereby a proper mixture of sweep angle, bending and torsional rigidity produces exactly infinite divergence speed with a consequent disappearance of the aeroelastic influence on A.C. location.

Variable sweep angle confers significant performance advantages on airplanes like the F-111, F-14, B-1 and early Boeing SST designs. But care must be taken to understand the role of wing flexibility, especially in cases of large span and structural aspect ratio. These vehicles must operate at both subsonic and supersonic speeds, and to a degree they are subject to the familiar rearward A.C. shift and greater static margin that go with transition from the former to the latter. The accompanying increase in Λ would seem to exacerbate this shift. It turns out, however, that designers have been able

to adapt the aeroelastic effect of Fig. 3 so as to keep the "open-loop" A.C. migration within acceptable bounds; C.G. control by fuel transfer may also be required.¹² Published data are hard to find on these features of variable-sweep aircraft. Relative to the F-111, however, R. Peloubet of General Dynamics Corporation kindly furnished a report by Jones,¹⁴ and the present authors have attempted some rough analyses which suggest very favorable behavior. For instance, study of pitching moment curves near the maximum-q flight limits¹⁴ show roughly complete cancellation of A.C. shifts. Going from Mach number 0.9 at 16° sweep to 1.5 at 72.5° causes a rigid-wing aft A.C. displacement of about 0.5 of the mean aerodynamic chord, but the forward displacement due to wing deformation is 0.4. Since the inertia-elastic influence on A.C. in flight is very small, there is thus an 80% compensation between the two effects. It is recognized that the F-111 would not fly at Mach 0.9 with wings full forward, but this calculation is done for fixed altitude, and similar compensation occurs also at intermediate Λ 's.

A more recent case where aeroelasticity improves pitching-moment characteristics is furnished by the AD-1. This experimental vehicle is intended to prove in flight the oblique-wing concept proposed by Jones.¹⁵ In 1977, Hopkins and Yee¹⁶ carried out wind-tunnel measurements on an elastically-scaled aluminum model (Fig. 4) resembling the AD-1. Figure 5 presents typical plots* of the pitching-moment curves for this model at $\Lambda = 45^\circ$. It and other data in Ref. 16 fully substantiate their conclusion that "an oblique wing designed with the proper amount of flexibility can 'self relieve' itself of asymmetric spanwise stalling and the associated nonlinear moment curves." As discussed in a subsequent section here, it is believed that the use of filamentary composite structural skins might be even more effective in producing such results.

Better Performance of Propellers and Rotors

In the past five years there has been renewed attention to the aeroelasticity of propellers, stimulated by the development of large wind turbines and of high-speed, high-efficiency turboprop aircraft designs. Notably the

* The two higher dynamic pressures on Fig. 5 simulate cruising and high-speed operation.

work by Hamilton Standard Division on advanced propellers with composite blades (cf. Black et al.¹⁷) has rekindled interest in tailoring stiffness properties so as to increase efficiency. From a brief look into the past, however, one discovers that using flexibility to advantage in propellers was an old idea.

The "Flex-O-Prop"

The first such practical application of aeroelasticity was by Max Munk in his patented wooden "Flex-O-Prop".¹⁸ Munk's propeller employed laminated wood to produce elastic coupling between bending and twisting in such a manner that a highly loaded blade would assume a shallower pitch setting as it bent forward, thereby providing for more efficient operation at the high-thrust, low-speed takeoff condition. Since thrust is diminished somewhat in cruising flight, the blades would naturally return to the larger pitch settings desirable for efficient high speed operation at reduced engine rpm.

The idea (Fig. 6) for utilizing coupling between bending and twist was arrived at after making the observation that the blade tip path of test propellers moved forward and backward under different throttle settings. The final design, which resulted from several years of trial-and-error testing in collaboration with engineer Eli Amanuel, employed diagonally-oriented outer laminations at approximately 45° to the spanwise axis combined with inner laminations which were radially disposed. The result was a propeller which counteracted normal undesirable twisting tendencies and produced, on a somewhat limited scale, the effects of a variable-pitch propeller.

Flight tests comparing the Flex-O-Prop with an identical standard wooden propeller were performed using a Model 'E' Ercoupe with an 85 hp Continental engine (Hoadley¹⁹). Results included a 16% decrease in takeoff distance, a rate-of-climb increase of 13%, a maximum static thrust boost of 5%, and a speed increase of 14% at fixed cruise power setting for the Flex-O-Prop. An additional benefit noticed during flight testing was a slight decrease in vibration level, which was attributed to the 'dampening' action of the diagonal laminations.

Advanced Composite Propellers

A recent theoretical study (Rogers²⁰) examines the aeroelastic benefits to be derived from applying advanced filamentary composite material technology to propeller design. It was demonstrated that, for a fixed-pitch "tailored" propeller, an increase in efficiency of 5% at the design point and as much as 20% at off-design points can be achieved over that of a rigid design (Fig. 7). At the same time, there was shown to be a significant extension to the range of advance ratios over which efficient operation is possible. Controllable-pitch propellers with composite blades were also shown to have approximately a 5% increase in maximum efficiency over rigid controllable blades.

The "Plastomatic" Propeller

Recent research on controllable, composite light-airplane propellers suitable to the general aviation market has been carried out by Larrabee at MIT.^{21,22} His efforts produced a conceptual design for a "Plastomatic" propeller, which would use fiber reinforced plastics in a modern version of the Koppers 'Aeromatic' propeller of the 1950's. In this design, the feathering axis bearings are freed of centrifugal loads by introducing a tensionally strong but torsionally flexible tension tie member and thus allowing the blades to balance their loads against each other while equalizing the blade pitch angles. By having the locus of aerodynamic centers offset from the blade feathering axis, the equilibrium of aerodynamic, inertial, and torsional moments causes a blade angle change with airspeed such that the propeller absorbs its rated horsepower.

In fact, the propeller can be designed to have two equilibrium blade angle settings; one equilibrium corresponds to a low-air-speed, high-thrust condition, and a second to a cruise-speed, cruise-thrust condition. It also exhibits approximate constant-speed characteristics about a specified design rpm but is equipped with a cruise setting override to allow efficient operation at a lower rpm as well.

Performance calculations comparing a Plastomatic design suitable for installation on a Grumman-American AA-1 airplane with a standard McCauley 7157

fixed-pitch metal propeller (71-inch diameter, 57-inch pitch) revealed a takeoff-run reduction of 28% and an increased rate of climb of 39% for the Plastomatic. Another advantage of the Plastomatic stems from its estimated weight of 10 lbs compared with 20 lbs for the solid aluminum fixed-pitch propeller.

Helicopter Rotors

As a helicopter increases its forward speed the aerodynamic conditions experienced by each rotor blade begin to vary more severely with azimuthal position. The result, for a conventional blade, is a buildup of cyclic loads and vibrating hub forces. These forces cannot be effectively controlled throughout the flight envelope with the usual design parameters of twist, airfoil shape, planform and 1/rev cyclic pitch changes. Manufacturers have looked to vibration absorbers mounted on the pylon or hub to achieve acceptable ride quality in the presence of these forces. Multicyclic pitch changes and controllable-twist rotors²³ are another promising means of amelioration.

By careful choice of the aerodynamic and elastic properties of the blade, it is possible to reduce the loads passively. Such a design is referred to as the "aeroelastically conformable" (or adaptive) rotor. Blackwell and Merkley²⁴ found that the most important design parameters were: (1) tip sweep, (2) camber, (3) aerodynamic center, elastic axis and airfoil c.g. positions, (4) torsional stiffness and (5) twist.

A helicopter blade's large negative twist, which distributes the lift efficiently in hover, is detrimental in high-speed forward flight where it produces a positively loaded root and negatively loaded tip on the advancing blade. It would be advantageous if in this condition the blade could be untwisted. By sweeping the blade at the tip (see Fig. 8, designs nos. 2 and 3, from Ref. 24), a predominantly once-per-revolution (1P) twisting moment is exerted on the blade by the airloads. An aft sweep coupled with the download on the tip of the advancing blade produces a nose-up moment, which will tend to untwist the blade and reduce the negative load at the tip. This action is exactly analogous to the gust alleviation characteristics of a swept-back wing. The rotor must, of course, be suitably flexible in torsion, which makes filamentary composite blades nearly ideal.

The effect of airfoil camber is somewhat similar to that of tip sweep. By choosing a section with non-zero pitching moment C_{mo} , a moment (and therefore twist) dependent on the dynamic pressure can be applied to the blade. Negative camber (positive C_{mo}) is favorable, again because it tends to untwist the advancing blade. Wind-tunnel testing (cf. Fig. 9 from Ref. 25) has shown that 1P and 2P flap bending is thereby reduced by about 40% and speed stability is improved with little decrease in rotor efficiency. The efficiency in hover can actually be improved by increasing the static twist of the blade.²⁵ The effect of having the aerodynamic center forward of the elastic axis is similar to that of negative camber.

The Vertical-Axis Wind Turbine

Two schemes have been analyzed and tested for realizing the simplicity and high efficiency promised by the Darrieus wind turbine (VAWT). The first (Fig. 10) curves the blades into a shape which minimizes structural loads due to rotation. The second, whose straight, vertical blades are parallel to the axis of rotation, may require a heavier structure but offers certain other advantages. For example, the power-producing angle-of-attack oscillations which take place as the airfoil revolves in a wind-stream (see Fig. 11) can be conveniently amplified. By imagining the blade in the figure to move around a circle and studying the variation of the forward, chordwise component of the lift force L , one sees that higher average torque can be achieved by varying $\Delta\alpha$ in proportion to $\cos\theta = \cos\Omega t$, where Ω is the angular velocity of rotation.

In the "Giromill" design,²⁶ power is thus augmented by attaching the blade ends to cam supports with adjustable amplitude. An even simpler approach — one which does not require active cam control based on sensing the wind direction — would seem to involve the use of torsion springs at the points of attachment. If the effective spring elastic axis (E.A., as in Fig. 11) were placed behind the aerodynamic center of wind-induced lift, one sees how that force itself can produce the torque needed for blade-angle cycling. The system parameters would, of course, have to be adjusted to avoid resonance and to keep $\Delta\alpha$ in phase with L .

By means of quasi-two-dimensional aerodynamic theory like that proposed in Ref. 27, one can predict the influence of cycling amplitude $\Delta\bar{\alpha}$ on the power coefficient

$$C_p = \frac{\text{Power Output}}{\frac{1}{2} \rho A V_w^3}$$

as it depends on advance ratio $\Omega r/V_w$. (ρ is air density and A frontal area swept by the machine; other symbols are defined in Fig. 11.) For a design with solidity typical of modern VAWT's, Fig. 12 presents some results. Cycling at ± 0.1 radian ($\pm 5.70^\circ$) appears quite practical and avoids airfoil stalling in the optimum range of $\Omega r/V_w$; yet the theoretical increase of output approaches 20%.

It is, incidentally, not unreasonable to suggest for a straight- or curved-bladed VAWT that its torsional properties might be adjusted in such a way that power augmentation occurs without any need for special blade supports. If feasible, this scheme would represent an extremely simple constructive use of aeroelasticity.

Increased Safe Speeds, Turning Performance and Energy Maneuverability Through Use of Composites or Active Control

Among the most pernicious of aeroelastic manifestations are divergence and flutter — critical flight conditions above which a lifting surface or complete air vehicle experiences often-destructive static or dynamic instability due to structural deformations interacting with the airstream. It has long been a dream that active means might be found to ameliorate or eliminate these instabilities, but only in the past decade has there been practical progress toward the goal. Since it is achieved through modifying or controlling elasticity, the results fall within the purview of this paper.

Divergence

A dramatic instance of passive "divergence control" is furnished by the skillful use of composites in the skins of sweptforward wings. Although these wings offer performance gains for certain aircraft types, when constructed

in conventional materials their bending-torsion coupling usually leads to such low divergence* speed V_D that designers have been loath to adopt them. In the 1980's, however, fighters similar to the Rockwell International "SabreBat" (Fig. 13) will soon be flying. They owe their success to research like the simplified analyses published by Weisshaar.^{28,29}

Figure 14, adapted from Ref. 28, shows clearly what the possibilities are. It relates to a cantilever of constant chord and sweep Λ , whose coupling between bending and twist is controlled by orienting the unidirectional fibers in its uniform, reinforced-plastic skins. The fiber angle, θ , is measured from a reference normal to the elastic axis; therefore, favorable values around $\theta = 100^\circ$ correspond to reinforcement parallel to a direction 10° ahead of this axis. For an unswept and two sweptforward cases, the figure shows θ 's influence on V_D — as referred to the speed V_{D0} that would be observed on a wing of similar configuration at zero Λ and θ . One sees how, even up to 60° of forward sweep, the divergence boundary can be made equal or superior to that of an acceptable reference design. On an actual airplane, other considerations obviously require that some skin plies be oriented in other than the optimum direction. It is significant, however, that about 70% of these plies run very close to $\theta = 100^\circ$ on the wing illustrated (in mockup) by Fig. 13.

Tailoring

The study in Refs. 28 and 29 represents a rather unsophisticated example of what has become known as "aeroelastic tailoring." Although more complex interactions may be employed, this concept typically involves intentional coupling between bending and twist of a lifting surface to accomplish one or more desirable effects — not unlike some of those already discussed in the preceding section. References 30 and 31 are samples from many recent documents on tailoring.

One common objective is to control the spanwise distribution of aerodynamic incidence over a wide range of maneuvering load factors. On an air-superiority fighter, the result can be a substantial decrease of induced drag

* It is remarked that the worst instability may sometimes be a low-frequency flutter.

in rapid turns. The consequent increase in "energy maneuverability" or "specific excess power" could mean the difference between defeat and victory during air-to-air combat. Taken from Vol. I of Ref. 31, Fig. 15 demonstrates how (theoretical) modifications to the YF-16 wing affect its drag polar for flight at Mach 0.9 and 10,000-ft altitude. Graphite-epoxy composite skins are particularly effective; in a typical high-g turn near $C_L = 0.7$ the C_D reduction approximates 26% compared to the original.

Flutter

In principle, one can devise dozens of techniques for actively or passively raising an airplane's flutter speed and thereby avoiding the associated performance limitations. The passive approach, which was the only recourse until 1973, nearly always carries with it some sort of penalty: increased weight to enhance stiffness or to massbalance a movable surface, increased complexity for a hingeline damper, reduced range from a restriction on wing fuel distribution, or whatever. One possible counter-example, however, may be the "decoupler pylon" of Reed (see Reed et al.³²; the use of nonlinearity to prevent excessive static deflection is discussed by Desmarais and Reed³³). This clever device proposes to overcome the usual flutter-speed reduction due to an auxiliary tank or weapon mounted near a fighter's wingtip by placing a relatively soft torsional spring between primary structure and the supporting pylon. Although it has not yet been adopted operationally, the decoupler shows promise of solving a serious problem for aircraft types which must carry a variety of heavy objects beneath their wings.

Active flutter control came into its own on August 2, 1973, when U.S. Air Force NB-52E No. 56-632 flew at 21,000-ft altitude 10 kts faster than its measured "open-loop" flutter speed. The flutter mode involved was symmetrical, with the relatively low frequency 2.4 Hz. It had been driven artificially unstable within the flight envelope by means of lead ballast attached to the noses of two large wingtip fuel tanks. Nevertheless, the design and practical realization of the B-52 FMCS (Flutter Mode Control System) presages the ultimate use of this sort of reliable electronic technology on many other aircraft. The development of FMCS is summarized by Hodges.³⁴ Flight tests are reported in Ref. 35. Space limitations prohibit

a detailed description of the system, but it was based on rather conventional analog processing applied to signals from two pairs of wing-mounted accelerometers. The effectors consisted of symmetrically-deflected outboard ailerons and "flaperons."

The NB-52E was, in fact, a thoroughly-instrumented research airplane intended to demonstrate several potential benefits of aeroelastic control. In addition to the FMCS, it carried four other partially-independent systems. Their purposes are quite well defined by their names: Ride Control, Maneuver Load Control, Augmented Stability and Fatigue Reduction (the reference is to fatigue damage in primary structural material). As space permits, certain of these projects will be discussed in the next section.

Numerous theoretical and experimental programs involving the active modification of aircraft flutter characteristics had been completed or were in progress at the time of writing. One of the most comprehensive is NASA's "Drones for Aerodynamic and Structural Testing" (DAST), of which a comprehensive summary is given in Murrow and Eckstrom.³⁶ DAST is aimed at providing research data, from the wind tunnel and unmanned flight tests, on active controls for wings with supercritical airfoils operating through the transonic speed range. The first model wing resembles that of a transport designed for cruise around Mach 0.98. Its "flutter suppressor" activates small ailerons in response to signals from a pair of wingtip accelerometers, and two or more control algorithms are being tried.

Figure 16 contains a photograph of a simplified, full-scale version of half the DAST aeroelastic research wing (ARW-1), mounted from one wall of the Transonic Dynamics Tunnel, NASA Langley Research Center. The trace at the bottom of the figure reproduces the accelerometer signal from a test wherein the dynamic pressure was raised to above the uncontrolled V_F . The system (design reported by Abel, Newsom and Dunn³⁷) is then activated, and one observes the immediate return to a stable condition where the wing is responding only to flow turbulence. One of the control syntheses investigated on this model demonstrated a 20% increase in the dynamic pressure of the flutter boundary at Mach 0.95.

Several experiments on the DAST ARW-1, carried by the modified Firebee II target drone, have subsequently been conducted at NASA's Dryden Flight Research Center. Although the vehicle and wing were partly destroyed by an accident in Summer 1980, the program is expected to continue and will involve different wing configurations. A fund of knowledge can be anticipated, which will assist in bringing constructive interaction between aeroelastic modes and active control to a routine status.

Ride Improvement and Alleviation of Cyclic Loading

The comfort of passengers and crew during the unavoidable encounters which occur with atmospheric turbulence is a significant consideration on any aircraft and a paramount one for civil transports. The need to minimize the associated fuselage accelerations and vibration is reinforced by the fact that successful measures will often simultaneously extend the fatigue life of many structural elements. In the context of favorable aeroelasticity, it is therefore very interesting that large-aspect-ratio sweptback wings appeared in the 1940's and 1950's primarily because they enable efficient cruising at much higher speeds. Yet they also provided aviation with a "gust-alleviation" device which could have hardly been improved had that been the principal design condition.

Starting with the B-47, B-52 and first-generation turbojet airliners, sweepback has enhanced the "ride" of almost every large jet airplane. Although the literature is full of comparative data to demonstrate this point, a single example will be cited here which emphasizes that the effect is due mainly to the aforementioned angle-of-attack relief from bending deformation. Codik, Lin and Pian³⁸ published one of the first analyses of wing-flexibility effects on the response of such an airplane to discrete gust encounters. Figure 17 is their Fig. 5.1. It relates to a vehicle with E.A. swept 34° and aspect ratio 9.43 (see the reference for other data), which encounters a "one-minus cosine" gust of half wavelength equal to 15 times the midspan semichord. Abscissa s_0 denotes distance traveled from response initiation, again measured in semichords. Ordinate K is the fuselage acceleration, referred to what this quantity would have been in an encounter with a "sharp-edged" gust of the same amplitude, without relief due to bending or unsteady aerodynamics.

Two kinds of alleviation can be inferred from the maximum values of K . The drop below unity of the "rigid-wing" peak is because of the delayed buildup of wing lift and gradual penetration of the gust front due to sweep-back. As for flexibility, the solid curve is the more accurate and shows a second 30% reduction from $K = 0.75$ to about 0.52, which is wholly attributable to aeroelasticity.

The introduction of active control, of course, provided the designer with much more versatility and freedom to choose his objectives than did the natural properties of swept wings. Extended structural life under cyclic loading — a goal by no means incompatible with increased flutter speed or ride improvement — has been the benefit sought from most systems implemented during the 1960's and 1970's. Such airplanes as the U-2, C-5A, F-4, F-16, and the Boeing 747 and SST concept can be cited as American examples of where the technology was employed in various ways — not all of them primarily aeroelastic. In the cases to be summarized here, however, structural deflections play a key part.

The first is the Aircraft Load Alleviation and Mode Stabilization (LAMS — cf. Burris and Bender³⁹) system, first demonstrated on the B-52. Both the flight-test airplane and the concepts employed were, incidentally, direct precursors of the Control Configured Vehicle (CCV) described in connection with flutter stabilization (Refs. 34 and 35). LAMS was developed and tested in the 1965-69 period. Although existing lateral and longitudinal movable surfaces were employed, the system modified the vehicle by adding hydraulic actuators, "fly-by-wire," various acceleration sensors, and analog computers to implement the transfer functions required for active control. Three discrete flight conditions were accounted for, chosen from a hypothetical B-52E mission profile.

Figure 18, adapted from Fig. 1 of Ref. 39, summarizes better than any other results what was proven in flight for LAMS. Assumed are 575 hours of idealized "usage" at the three combinations of vehicle weight, airspeed and altitude. Six structural analysis stations are represented, with their location numbers given in inches from a reference origin of coordinates.

According to standard methods of fatigue damage estimation due to cyclic loading by a realistic model of turbulence, the three bars compare the experience of the unaugmented B-52E with those predicted when the standard Stability Augmentation System (SAS) and the LAMS are activated. The very favorable contributions of LAMS to structural life are evident for all stations except the horizontal-stabilizer main spar, which does not in any event constitute fatigue-critical structure.

The B-1 (Fig. 19) is a bomber intended for penetration at such low altitudes that its crew and structure experience considerable cyclic loading from turbulence rising off the ground — not to speak of rapid maneuver loads and other sources of fatigue. Among other objectives of its active control system is to ensure an acceptable work environment in the crew cockpit. This is achieved by implementing a "Structural Mode Control System" (SMCS). SMCS is a classical realization of the ILAF (Identically-Located Accelerometer and Force) approach to motion control. Its sensors are longitudinal and lateral accelerometers mounted in the cockpit vicinity. Effectors are the vanes labelled in Fig. 19, which are installed with 30° of anhedral so that symmetric and antisymmetric rotations can generate, respectively, pure vertical and side forces at a point close to the pilot's seat. Figures 20 and 21* involve two different low-level flight conditions, comparing B-1 response with and without SMCS operative. (Details are furnished on the figures and their captions. SCAS is the normal B-1 stability augmentation system.)

The effectiveness of this simple ILAF mechanization is depicted especially well by its tremendous reduction of the peak near 3 Hz in the power spectral density of vertical-acceleration response at the cockpit. In effect, the system endows the airplane with a "damper connected to an inertial reference," which is able to bring the vibratory environment at a chosen location well within acceptable norms. Since the B-1 fuselage is a complicated — but quite compliant — beam, one observes how the property of flexibility must be present in order for such a scheme to work.

* Data supplied by courtesy of J. H. Wykes, B-1 Division, Rockwell International.

The Use of Structural Deformation for Propulsion

Historical Developments

Persistent attempts at sustained flight in aircraft propelled by oscillating wings have been made since the early days of aviation and have continued to the present. Long before the Wrights, Otto Lilienthal⁴⁰ conducted tests on a full-scale machine whose wings were made of multiple slats which "feathered" on the upstroke and closed to form a solid wing on the downstroke, but this proved much too inefficient. Fitz Patrick⁴¹ mentions no less than 20 other inventors who have built model or full-scale aircraft; some of these are illustrated in his paper. Vasil'ev⁴² refers to an even greater number of Soviet inventors, who flew their models at national contests in 1949, 1950, 1951, and other years.

An elegantly simple propulsion scheme, presented in Fig. 22, is a motor whose shaft is parallel to the span which rotates an unbalanced mass. In reaction to this, the airplane oscillates up and down to produce thrust. This idea was recently again put forward by Wolf⁴³ to propel ultralight man-carrying aircraft, except that it is the pilot who is the vibrating mass.

The annual meeting of the Experimental Aircraft Association at Oshkosh, Wisconsin, is the gathering point for present-day inventors interested in ornithopters. Among them are P. H. Spencer of Santa Monica, who has flown gas-driven models. Another is J. L. G. Fitz Patrick of Staten Island Community College, who has designed and built several prototypes of a man-carrying ornithopter. These vehicles are intended to test his unique empirical theory,⁴⁴ based on much personal observation of flying and swimming creatures. In fact, the patented⁴⁵ flapping mechanism of the wings is a "bird-bat analog" with the names of the parts taken from bird physiology. A picture of a 330-lb version of Patrick's ornithopter is presented in Fig. 23. Captive tests have so far met expected thrust levels, but no free flights have been made.

Fitz Patrick has also compiled an extensive bibliography⁴⁶ on the subject of natural flight and its relation to unsteady aerodynamic propulsion. In the

content of the present paper, it is observed that the majority of these devices rely on structural flexibility to effect the geometry variations required for combined sustentation and propulsion. The true man-carrying ornithopter remains a hope for the future. Nevertheless, both improvements in the associated lightweight mechanisms and recent gains in understanding the unsteady aerodynamics permit optimism regarding its attainment.

Aerodynamic Propulsion for Natural Flight

This section is completed with some words and citations on aerodynamics. One remarks that unsteady airload prediction for oscillating lifting surfaces was carried out originally in response to the needs of the aeroelastician. Its extension to the area of natural flight builds on that aeroelastic tradition, as well as the long history of observation and speculation about animal motion through the air and water (cf. Ref. 44, Lighthill⁴⁷, and also Ref. 48).

The key problem involves a two- or three-dimensional wing which simultaneously executes pitching and plunging motions, represented by the quantities α and h as functions of time. When α lags h (positive downward) by about 90° and is of the right magnitude, the instantaneous angle of attack is minimal. It also resembles what is usually seen in nature, that is, animal propulsion is observed to have a phase angle of -90° . At that angle the thrust-coefficient amplitude is near minimum. But birds and fish rightly prefer to flap their wings and tails in this way because the propulsive efficiency is markedly higher than at other phase angles. According to two-dimensional theory, in fact, it can approach 100%. To compensate for the relatively small thrust, animals operate with large amplitudes. Further, one finds that the leading-edge suction is a minimum in the natural flight region. There is some doubt that the theoretical values of suction are realized in flight. Thus, propulsive motion depending mostly on leading-edge suction will suffer in practice.

Garrick⁴⁹ is believed to have written the first highly-mathematical study of chordwise forces on oscillating wings. For airfoils he estimated the average thrust due to plunging and pitching, showed its dependence on the square

of the amplitude, and gave theoretical results that presage other publications more than 25 years later. Obye,⁵⁰ among others, conducted wind-tunnel experiments that validated the early theory. Important recent contributions to this difficult subject include the papers of Wu,⁵¹⁻⁵³ Chopra,^{54,55} Tuck⁵⁶ and Jones.⁵⁷ The forthcoming dissertation by Nathman⁵⁸ contains a critical and quantitative summary of this literature, along with additional airfoil measurements and an assessment of aeroelasticity's potentially constructive role for man-made machines.

Concluding Remarks: The Future

Albeith many were at first unintentional and a few quite unexpected, the examples of the preceding sections, when taken together, are believed to prove the assertions made in the Introduction. They are felt, however, to provide more than merely a career justification for the aeroelastic specialist. Especially those which relate to dynamic coupling between the airframe and the vehicle's automatic controls permit one, with some assurance, to forecast the appearance of "complete CCV's" — that is, aircraft which are designed ab initio in anticipation of favorable interactions among a wholly-reliable control system, rigid-body degrees of freedom and important modes of elastic deformation.

Surely the LAMS B-52³⁹ and, more comprehensively, the program reported in Refs. 34 and 35 have demonstrated the technology itself. Military aircraft are in the development stages with active flutter suppression and gust-load alleviation. Flying operationally are devices like the F-16 longitudinal stability augmentation system,⁵⁹ whose failure would cause unacceptable flying-qualities degradation yet whose record of performance contains no disastrous malfunctions whatever.* Within the state-of-the-art are small, high-powered and fast-acting hydraulic actuators. They ensure that electrical signals in the feedback path are convertible to forces and torques at structural vibration frequencies typical not only of large airplanes but of fighters as well.

*This statement was written in mid-1980.

It is likely that the most significant impediment to the introduction of constructive aeroelastic and "servoelastic" technology during the 1980's will be the human factor. Within the civil aviation field both the certifying authorities and conservative management of industry, concerned about the losses that may result from overoptimism, stand in the way. As in the case of several other structural and aerodynamic innovations, however, there is no doubt about potential CCV benefits in such areas as performance, efficiency and passenger comfort. The question which remains is not whether but when their promise will be fulfilled.

* * *

Acknowledgments

This research was supported by the Air Force Wright Aeronautical Laboratories and Office of Scientific Research under Grant Nos. AFOSR 77-9263 and AFOSR 79-0061. Mr. Wayne Rogers, undergraduate student of engineering at Stanford, assisted with early phases. The authors are appreciative of valuable discussions and of information furnished by colleagues far too numerous to name. The following deserve special mention: R. Peloubet, E. E. Larrabee, J. H. Wykes, J. W. Edwards, P. B. S. Lissaman, W. H. Reed, III, K. Roger and E. Amanuel. Ms. Sydney Koenig prepared the manuscript.

A special apology is due to worthy contributors to the subject of this paper whose work is not referenced. A complete listing would have been impossible, and unintentional oversights are unavoidable.

REFERENCES

1. Fiszdon, W., Fundamentals of Aeroelasticity, (P.W.N.) Polish Scientific Publications, Warsaw, 1951. (In Polish.)
2. Fung, Y.C., An Introduction to the Theory of Aeroelasticity, John Wiley and Sons, New York, 1955.
3. Bisplinghoff, R. L., Ashley, H., and Halfman, R.L., Aeroelasticity, Addison-Wesley Publishing Company, Reading, MA, 1955.
4. Dowell, E.H., Curtiss, Jr., H.C., Scanlan, R.H., and Sisto, F., A Modern Course in Aeroelasticity, Sijthoff and Noordhoff, The Netherlands, 1978.
5. Collar, A. R., "The First Fifty Years of Aeroelasticity," Aerospace, Vol. 5, No. 2, February 1978, pp. 12-20.
6. Coombs, H., with Caidin, M., Kill Devil Hill, Houghton Mifflin Company, Boston, 1979, pp. 61, 69-72.
7. Culick, F.E.C., "The Origins of the First Powered, Man-Carrying Airplane," Scientific American, Vol. 241, No. 1, July 1979, pp. 86-100.
8. See, for example, Anderson, J.D., Jr., Introduction to Flight, McGraw-Hill Book Company, New York, 1978, pp. 293-294.
9. Lissaman, P.B.S., "Wings for Human-Power Flight," The Evolution of Aircraft Wing Design, pp. 49-56. Proc. of a Conference sponsored by AIAA, Air Force Museum, Dayton, OH, March 1980.
10. Burke, J.D., "The Gossamer Condor and Albatross: A Case Study in Aircraft Design," Report No. AV-R-80/540, AeroVironment, Inc., Pasadena, CA, June 1980 (prepared for AIAA Professional Study Series, "Five Case Studies in Aircraft Design").

REFERENCES (Contd.)

11. Brown, R.B., Holtby, K.F., and Martin, H.C., "A Supersposition Method for Calculating the Aeroelastic Behavior of Swept Wings," J. Aero. Sci., Vol. 18, No. 8, August 1951, pp. 531-542.
12. Perkins, C.D., "Development of Airplane Stability and Control Technology," J. Aircraft, Vol. 7, No. 4, July-August 1970, pp. 290-301.
13. Keith-Lucas, D., "The Shape of Wings to Come," Flight, Vol. LXIV, No. 2279, 26 September 1952, pp. 408-410. (See Also Flight, Vol. LXIV, No. 2334, p. 535, and Vol. LXIV, No. 2339, pp. 680-681.)
14. Jones, B.E., "Preliminary Quasi-Steady Aeroelastic Analysis of the F-111 Airplane," Ft. Worth Division, General Dynamics Corp., Report FZS-12-176, July 1966.
15. Jones, R.T., "Reduction of Wave Drag by Antisymmetric Arrangement of Wings and Bodies," AIAA J., Vol. 10, No. 12, February 1972, pp. 171-176.
16. Hopkins, E.J., and Yee, S.C., "Effect of Wing Flexibility on the Experimental Aerodynamic Characteristics of an Oblique Wing," NASA TMX-3460, March 1977.
17. Black, D.M., Menthe, R.W., and Wainauski, H.S., "Aerodynamic Design and Performance Testing of an Advanced 30 Degree Swept, Eight-Bladed Propeller at Mach Numbers from 0.2 to 0.85," NASA CR-3047, September 1978.
18. Munk, M.M., "Propeller Containing Diagonally Disposed Fibrous Material," U.S. Patent No. 2,484,308, October 11, 1949 (filed August 25, 1947).
19. Hoadley, E., "A New Twist in Props," Flying, July 1951.
20. Rogers, J.B., "Aeroelastically Tailored Propellers," Master's Thesis, The University of Texas at Austin, May 1976.

REFERENCES (Contd.)

21. Larrabee, E.E., "Design of Propellers for Motorsoarers," Intl. Symposium of the Aerodynamics of Low Speed and Motorless Flight, NASA Conference Publication 2085, Part I, 1978.
22. Ibid., "Composite Material Propellers," Summary report for NASA Langley Research Center, April 1977.
23. McCloud, J.L., III, and Weisbrich, A.L., "Wind-Tunnel Test Results of a Full-Scale Multicyclic Controllable Twist Rotor," Preprint No. 78-60, Annual National Forum, American Helicopter Society, Washington, May 1978.
24. Blackwell, R.H., and Merkley, D.J., "The Aeroelastically Conformable Rotor Concept," Preprint No. 78-59, *ibid.*
25. Doman, G.S., Tarzanin, F.J., and Shaw, J., Jr., "Investigation of Aeroelastically Adaptive Rotor Systems," Proc. American Helicopter Society Mideast Region Symposium on Rotor Technology, Washington, August 1976.
26. Brulle, R.V., and Larsen, H.C., "Giromill (Cyclogiro-Windmill) Investigation for Generation of Electric Power," Proceedings, Second Workshop of Wind Energy Conversion Systems, Mitre Corp, Washington, MTR-6970, September 1975, pp. 452-460.
27. Ashley, H., "Some Contributions to Aerodynamic Theory for Vertical-Axis Wind Turbines," J. Energy, Vol. 2, No. 2, March/April, 1978, pp. 113-119.
28. Weisshaar, T.A., "Aeroelastic Stability and Performance Characteristics of Aircraft with Advanced Composite Sweptforward Wing Structures," AFFDL-TR-78-116, U.S. Air Force Flight Dynamics Lab, September 1978.
29. Weisshaar, T.A., "Forward Swept Wing Aeroelasticity," AFFDL-TR-79-3087, U.S. Air Force Flight Dynamics Lab, June 1979.

REFERENCES (Contd.)

30. Williams, J.G., "Analysis/Theory of Controlled Configured Structures," AFFDL-TR-74-137, U.S. Air Force Flight Dynamics Lab, December 1974.
31. Lynch, R.W., Rogers, W.A., and Braymen, W.W., "Aeroelastic Tailoring of Advanced Composite Structures for Military Aircraft," Vol. I (General Study) and Vol. II (Wing Preliminary Design), AFFDL-TR-76-100, *ibid.*, April 1977.
32. Reed, W.H., III, Foughner, J.T., Jr., and Runyan, H.L., Jr., "Decoupler Pylon: A Simple, Effective Wing/Store Flutter Suppressor," J. Aircraft, Vol. 17, No. 3, March 1980, pp. 206-211.
33. Desmarais, R.N., and Reed, W.H., III, "Wing/Store Flutter with Nonlinear Pylon Stiffness," Proceedings, AIAA/ASME/ASCE/AHS 21st Structures, Structural Dynamics and Materials Conference, Seattle, WA, May 1980, pp. 748-753.
34. Hodges, G.E., "Active Flutter Suppression — B-52 Controls Configured Vehicle," Paper No. 73-322, Proceedings, AIAA Dynamics Specialists Conf., Williamsburg, VA, March 1973.
35. Roger, K.L., Hodges, G.E., and Felt, L., "Active-Flutter Suppression — A Flight Test Demonstration," Paper No. 74-402, Proceedings, AIAA/ASME/SAE 15th Structures, Structural Dynamics and Materials Conf., Las Vegas, NV, April 1974. (See also papers in this same volume by Redd, Gilman, Cooley and Severt; by Sandford, Abel and Gray; and by Cwach and Stearman.)
36. Murrow, H.N., and Eckstrom, C.V., "Drones for Aerodynamic and Structural Testing (DAST) — A Status Report," J. Aircraft, Vol. 16, No. 8, August 1979, pp. 521-526.
37. Abel, I., Newsom, J.R., and Dunn, H.J., "Application of Two Synthesis Methods for Active Flutter Suppression on an Aeroelastic Wind Tunnel Model," AIAA Paper No. 79-1633, 1979.

REFERENCES (Contd.)

38. Codik, A., Lin, H., and Pian, T.H.H., "Effect of Structural Flexibility on Aircraft Loading," Part XII — "The Gust Response of a Sweptback Tapered Wing Including Bending Flexibility," A.F. Technical Report No. 6358, October 1953.
39. Burris, P.M., and Bender, M.A., "Aircraft Load Alleviation and Mode Stabilization (LAMS)," AFFDL-TR-68-158, U.S. Air Force Flight Dynamics Lab, April 1969.
40. Lilienthal, O., Birdflight: The Basis of Aviation, Longmans, Green & Co., New York, 1911.
41. Patrick, J.L.G.F., "Design and Construction of a Full Scale Ornithopter," Report of Staten Island Community College, 1960.
42. Vasil'ev, G.S., Principles of Flight of Models with Flapping Wings, E.B. Mikirtumov, Ed., published by G.I.O.D., Moscow, 1953 (translation by Air Technical Intelligence Center, OH; available from Defense Documentation Center as AD-167 173).
43. Wolf, J., "The Technological Prospects for Oscillating Wing Propulsion of Ultralight Gliders," Proceedings, 2nd Intl. Symposium on the Technology and Science of Low-Speed and Motorless Flight, Cambridge, MA, September 1974.
44. Patrick, J.L.G.F., "Natural Flight and Related Aeronautics, 1969 Report on Beating Wings and Fins," The College of Staten Island, NY, 1969.
45. Ibid., U.S. Patent No. 2,783,955, March 5, 1975.
46. Ibid., "Natural Flight and Related Aeronautics," Paper No. FF-7, Inst. of Aeronautical Sciences, NY, 1952.
47. Lighthill, M.J., Mathematical Biofluidynamics, Soc. Industrial and Applied Mathematics, Philadelphia, 1975.

REFERENCES (Contd.)

48. Many authors, Swimming and Flying in Nature, Vols. 1 and 2, Plenum Press, NY, 1975.
49. Garrick, I.E., "Propulsion of a Flapping and Oscillating Airfoil," NACA Report 557, 1936.
50. Obye, R.C., "Experimental Measurement of Lift and Thrust on an Airfoil Undergoing Large Amplitude Motion," M.S. Thesis, Dept. of Aerophysics and Aerospace Engineering, Mississippi State University, State College, MS, December 1972.
51. Wu, T.Y.-T., "Swimming of a Waving Plate," J. Fluid Mech., Vol. 10, Part 3 (1961), pp. 321-344.
52. Ibid., "Hydrodynamics of Swimming Propulsion: Parts 1, 2 and 3," J. Fluid Mech., Vol. 46, Part 1 (1971), pp. 337-355; Part 3 (1971), pp. 521-544; Part 3 (1971), pp. 544-568.
53. Ibid., "Extraction of Flow Energy by a Wing Oscillating in Waves," J. Ship Research, Vol. 14, No. 1, 1972, pp. 66-78.
54. Chopra, M.G., "Large-Amplitude Lunate-Tail Theory of Fish Locomotion," J. Fluid Mech., Vol. 74, Part 1 (1976), pp. 161-182.
55. Ibid., "Hydromechanics of Lunate-Tail Swimming Propulsion," J. Fluid Mech. Vol. 64, Part 2 (1974), pp. 375-391.
56. Tuck, E.O., "The Effect of Spanwise Variations in Amplitude on the Thrust-Generating Performance of a Flapping Thin Wing," Swimming and Flying in Nature, Vol. 2, Plenum Press, NY, 1975, pp. 953-973.
57. Jones, R.T., "Wing Flapping with Minimum Energy," NASA TM 81174, January 1980.

REFERENCES (Contd.)

58. Nathman, J.K., "Unsteady Aerodynamic Propulsion," Ph.D. Dissertation, Stanford University, Stanford, CA, 1981.
59. Ostgaard, M.A., and Swortzel, F.R., "CCV's — Active Control Technology Creating New Military Aircraft Design Potential," Astronautics and Aeronautics, Vol. 15, No. 2, February 1977, pp. 42-51.

FIGURE CAPTIONS

- Fig. 1: Two simplified sketches of Wright Flyer wing boxes. Lower picture shows rigging from prone pilot's hip cradle to warp the wingtips. (From Ref. 7.)
- Fig. 2: Photograph of the "Gossamer Albatross" in flight.
- Fig. 3: Influence of flight dynamic pressure q on slope of the curve of pitching moment vs. lift, as it might be measured on wind-tunnel models of rigid and flexible sweptback wings (Ref. 11).
- Fig. 4: Flexible wind-tunnel model resembling wing and fuselage of the variable-sweep AD-1. (From Ref. 16; length dimensions are in cm.)
- Fig. 5: Curves of pitching moment coefficient vs. lift coefficient for model of Fig. 4 at 45° sweep. There are four indicated values of dynamic pressure q (Ref. 16).
- Fig. 6: Sketch and title of Patent No. 2,484,308, by Munk (Ref. 18).
- Fig. 7: Theoretical curves of efficiency ($\eta = \text{Thrust HP}/\text{Engine BHP}$) vs. advance ratio for four propeller designs (Ref. 20). V is flight speeds, N and D the rpm and diameter of the propeller.
- Fig. 8: Three configurations illustrating tip sweepback and reduced torsional stiffness for the "conformable" helicopter rotor of Blackwell and Merkley (Ref. 24).
- Fig. 9: Plots of amplitudes of root bending moment vs. advance ratio, experienced at once and twice per revolution, for "aeroelastically adaptive" rotors designs of Doman et al. (Ref. 25).
- Fig. 10: Two-bladed Darrieus VAWT with zero-bending-moment shape; note small Savonius rotors used for starting. (Courtesy National Aeronautical Laboratory, Bangalore, India.)

FIGURE CAPTIONS (Contd.)

- Fig. 11: Horizontal cross-section of straight, rotating blade of VAWT, showing instantaneous relative wind V_w . Also pictured is the incremental angle of attack $\Delta\alpha$ that might occur on a torsionally-suspended blade due to moment of lift L acting through the aerodynamic center A.C.
- Fig. 12: Power-coefficient curves for straight-bladed VAWT, calculated by the method of Ref. 27 for four values of amplitude $\bar{\Delta\alpha}$ of cyclic angle of attack. In the definition of "solidity," N , c and $C_{L\alpha}$ are number of blades, blade chord and lift-curve slope, respectively.
- Fig. 13: Photograph of mockup of Rockwell International's "SabreBat," forward-swept-wing fighter design.
- Fig. 14: Influence of orientation θ of composite skin plies on divergence speed of three uniform, swept cantilever wings. Note that negative Λ means forward sweep (Ref. 28).
- Fig. 15: Curves of trimmed airplane lift coefficient vs. drag coefficient for "rigid" YF-16 and two flexible-wing designs of different materials and aspect ratios AR (Ref. 31).
- Fig. 16: Photograph of DAST model in Transonic Dynamics Tunnel, with accelerometer trace showing flutter suppression by active control. (Courtesy of W. H. Reed, III, NASA Langley Research Center.)
- Fig. 17: Dimensionless fuselage acceleration vs. chordlengths traveled after encounter with a "one-minus-cosine" gust, plotted for three idealizations of a swept-wing airplane. (From Ref. 38; see text for definitions.)
- Fig. 18: Fatigue-damage rates at six stations on B-52E bomber, estimated for the unaugmented airplane and with the SAS and LAMS systems active (Burris and Bender³⁹).

FIGURE CAPTIONS (Contd.)

- Fig. 19: Three-view drawing of B-1 bomber, showing location of vanes used by Structural Mode Control System (SMCS).
- Fig. 20: Typical plots vs. time of the indicated quantities for B-1 with and without SMCS activated. (Courtesy of J. H. Wykes, Rockwell International.)
- Fig. 21: Measured power spectral density of cockpit acceleration, per unit mean-square value of gust-induced angle of attack, plotted vs. frequency for the B-1 in random turbulence at the indicated flight condition. Solid and dashed curves are for SMCS off and on, respectively. (Courtesy of J. H. Wykes, Rockwell International.)
- Fig. 22: Miturich's model airplane which flaps because of an unbalanced flywheel. The wings twist about the leading edge as it flaps.
- Fig. 23: Photograph of model ornithopter, designed, built and tested by J. L. G. Fitz Patrick (courtesy of the inventor).

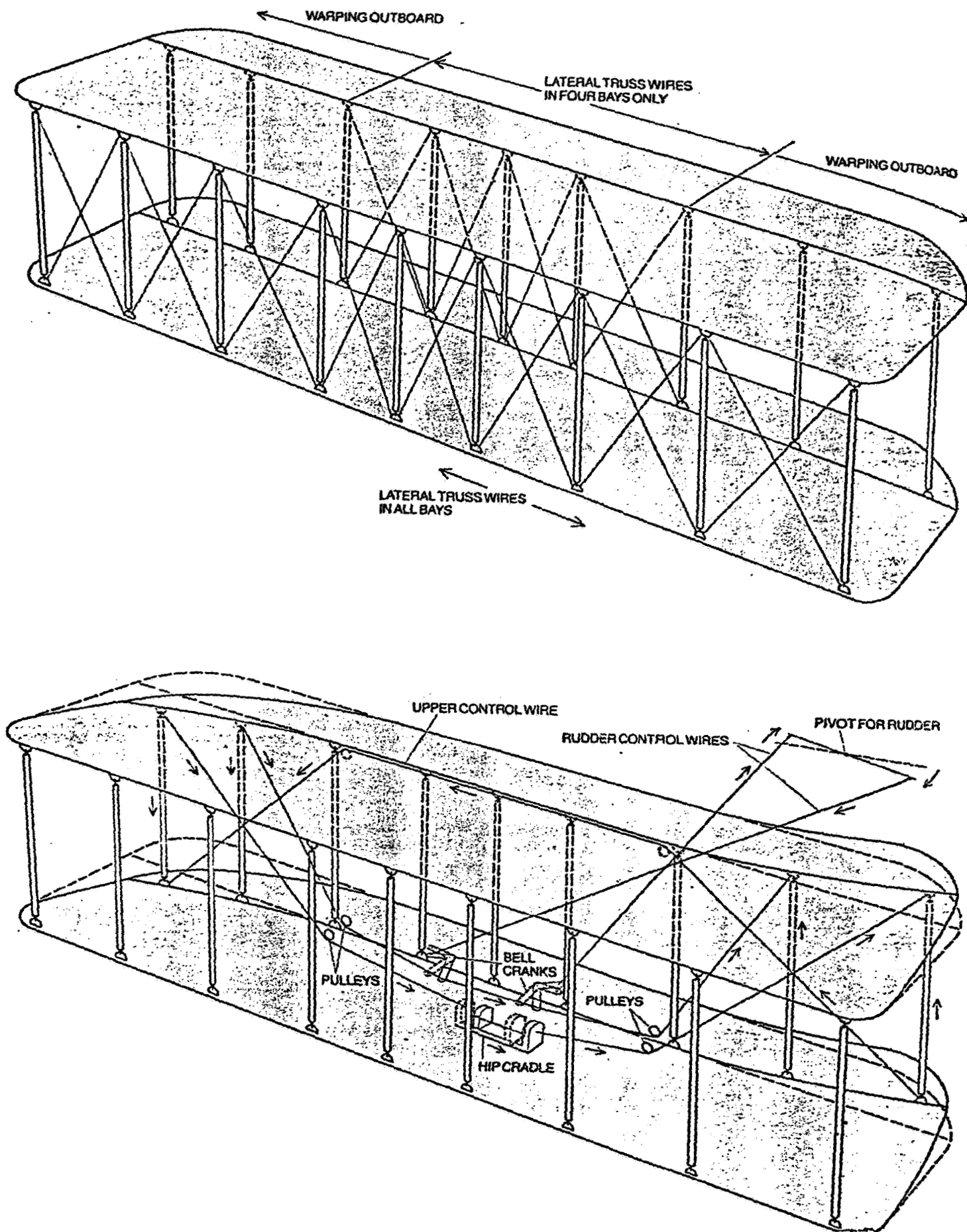


Figure 1

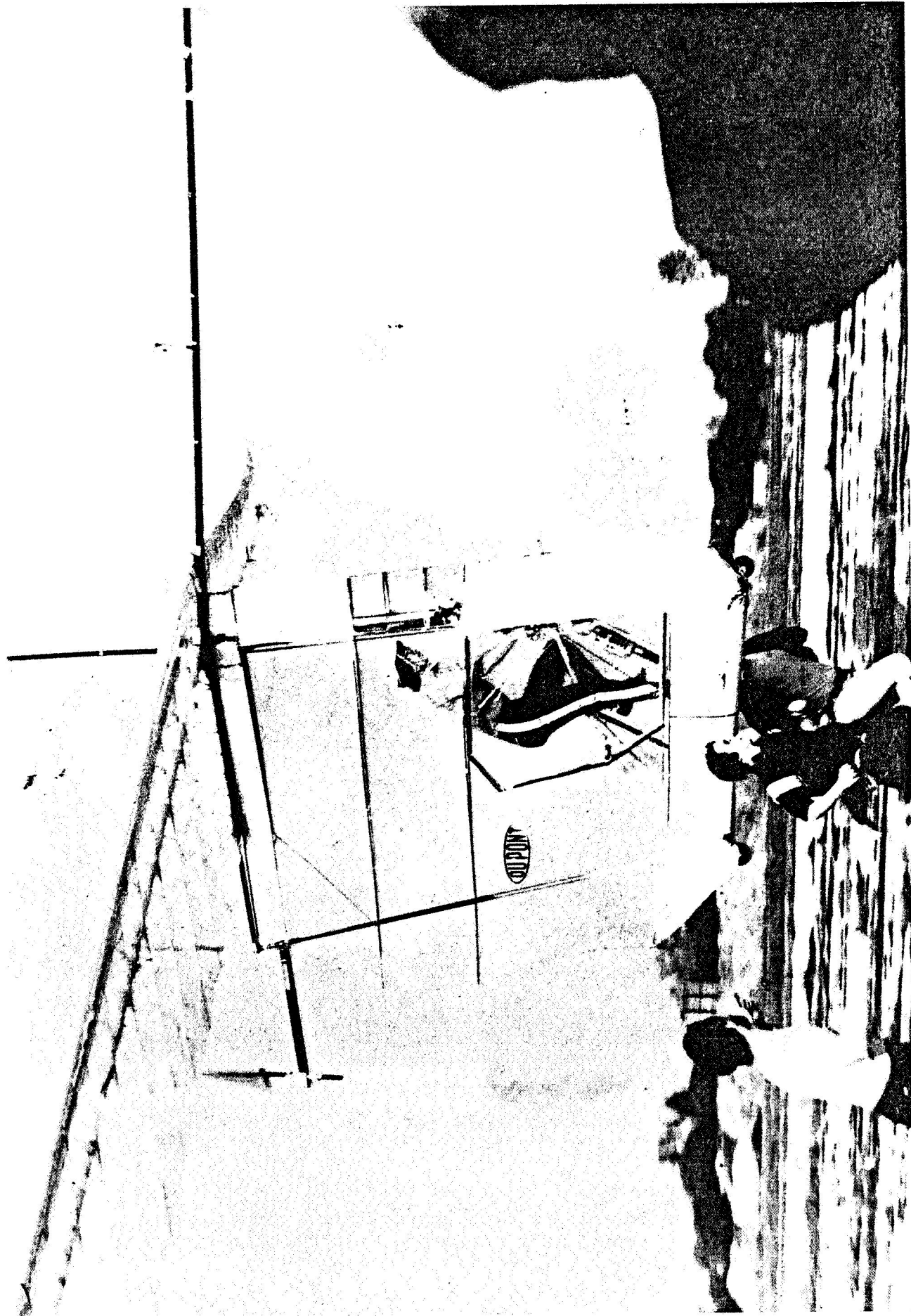


Figure 2

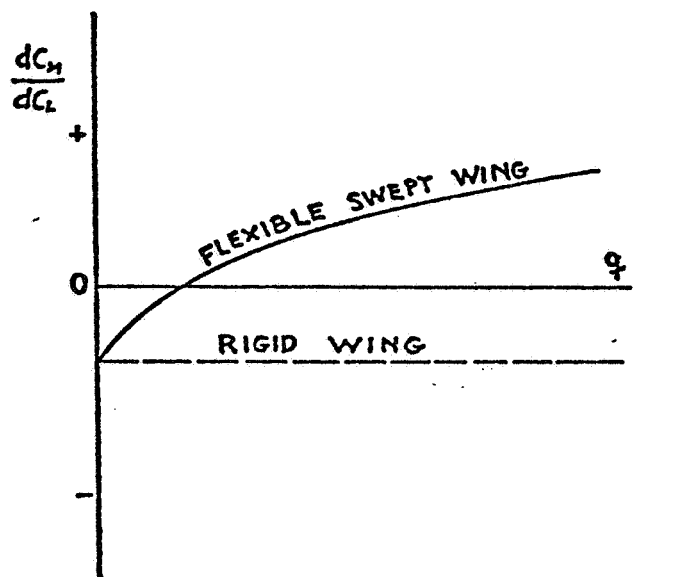


Figure 3

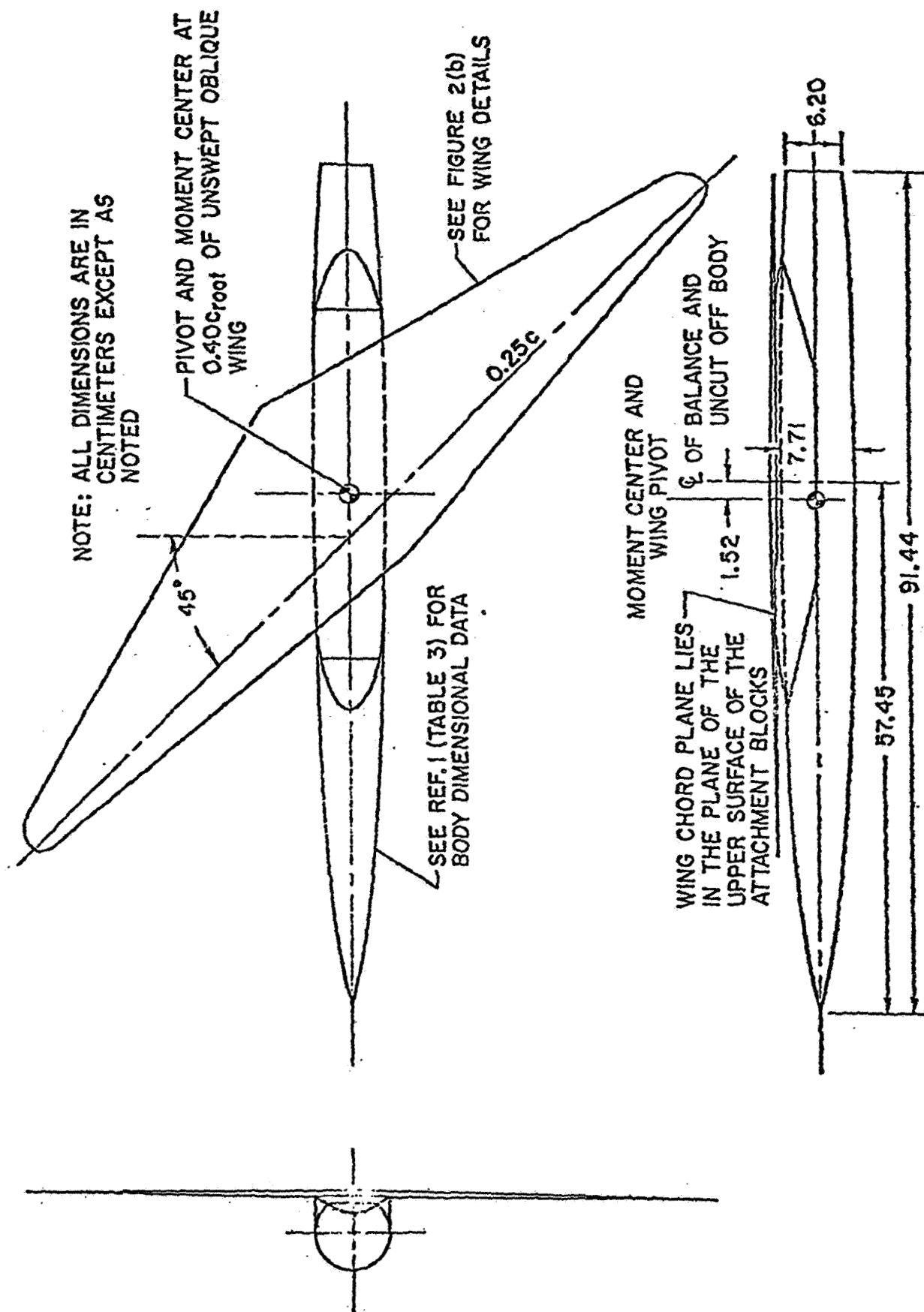
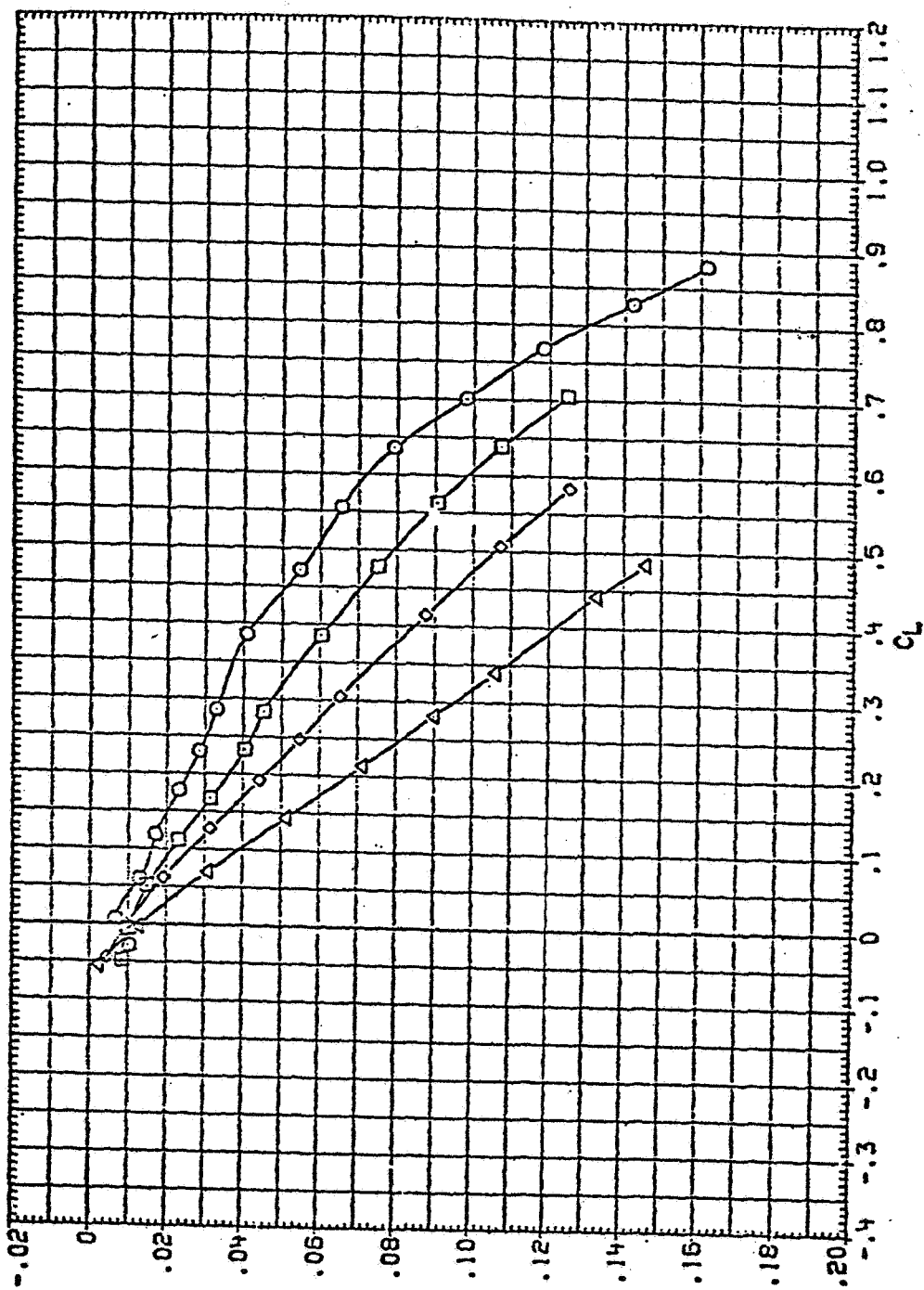


Figure 4



$\Lambda = 45^\circ$
 z (p.s.f.)

- 204
- 288
- ◇ 388
- △ 524

Figure 5

Oct. 11, 1949.

M. M. MUNK
PROPELLER CONTAINING DIAGONALLY
DISPOSED FIBROUS MATERIAL
Filed Aug. 25, 1947

2,484,308

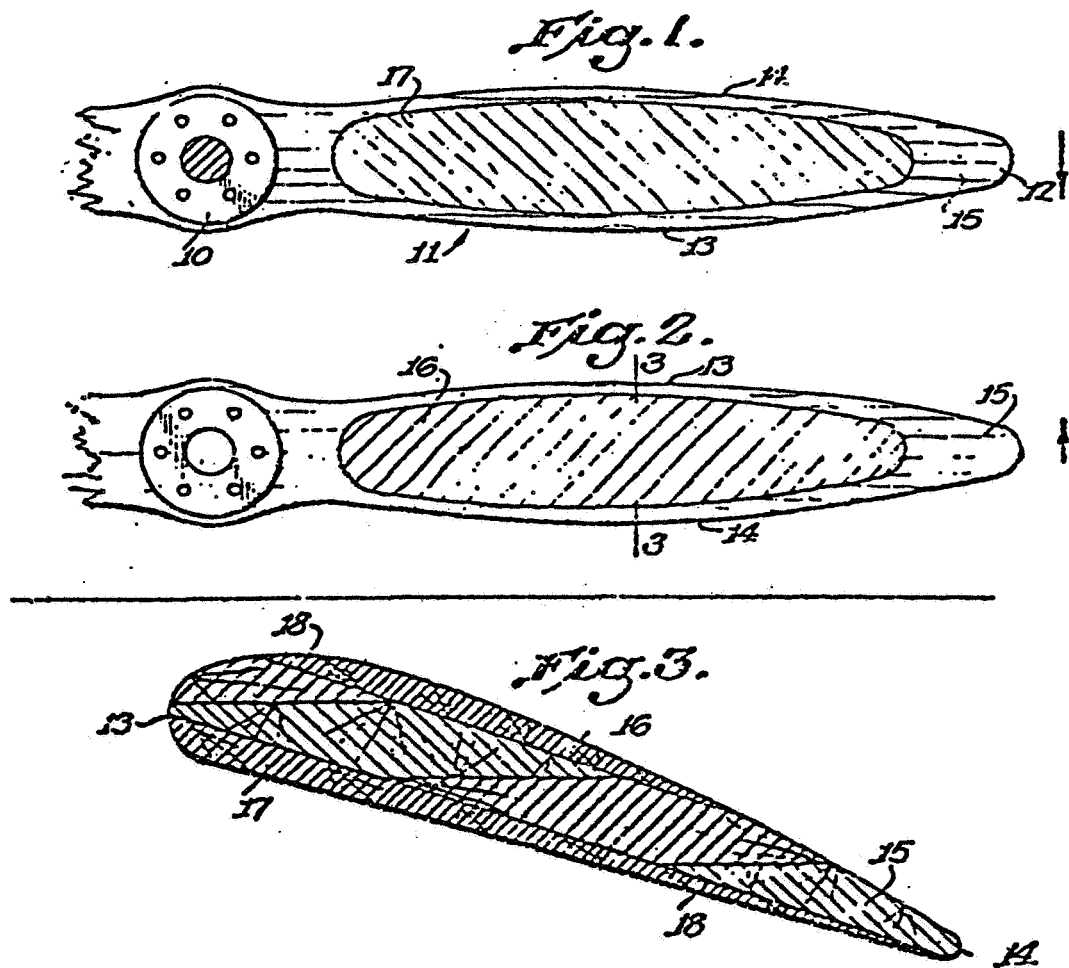


Figure 6

I: Controllable Propeller-Composite Blades

II: Controllable Propeller-Rigid Blades

III: Composite Propeller

IV: Rigid Propeller

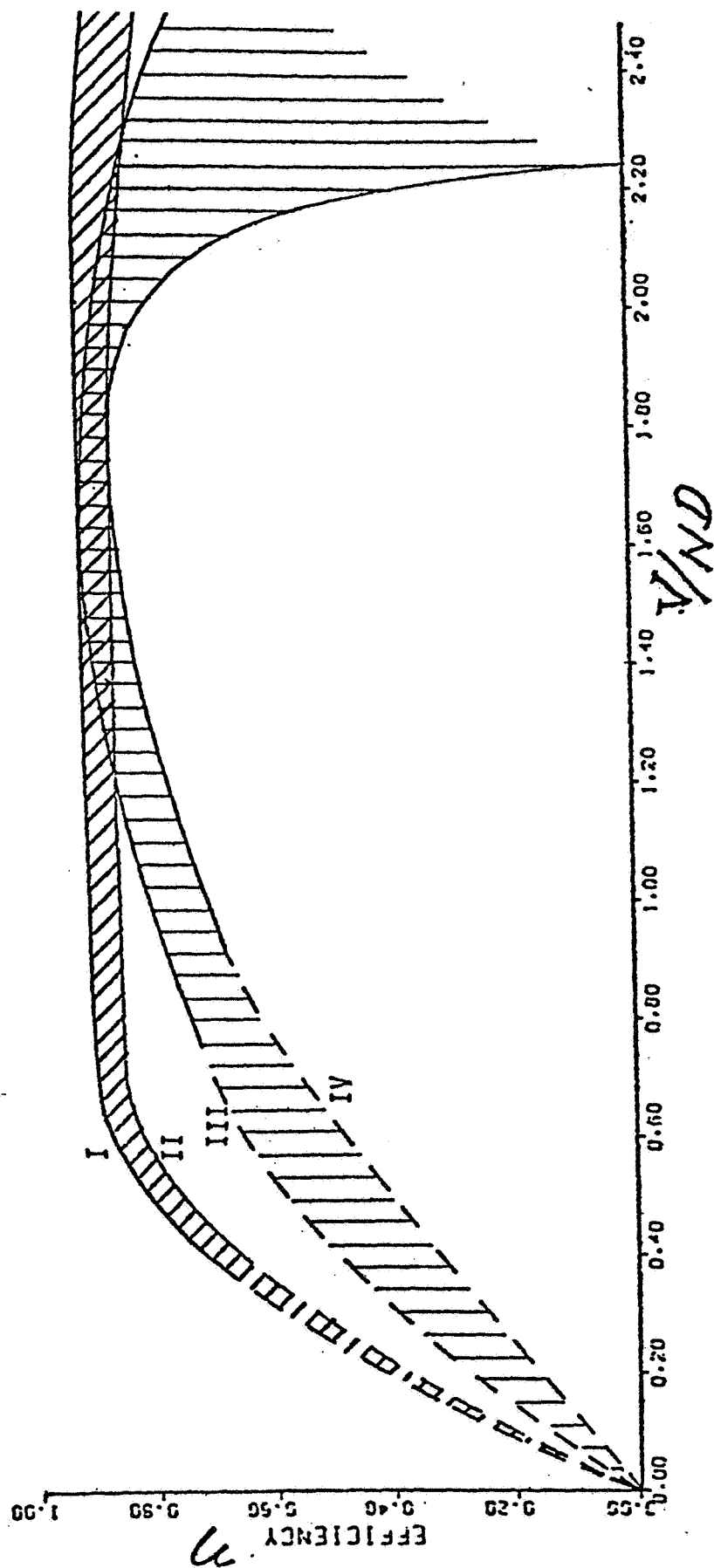


Figure 7

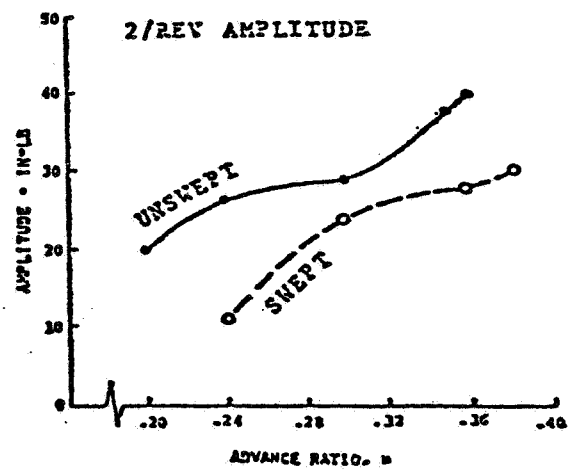
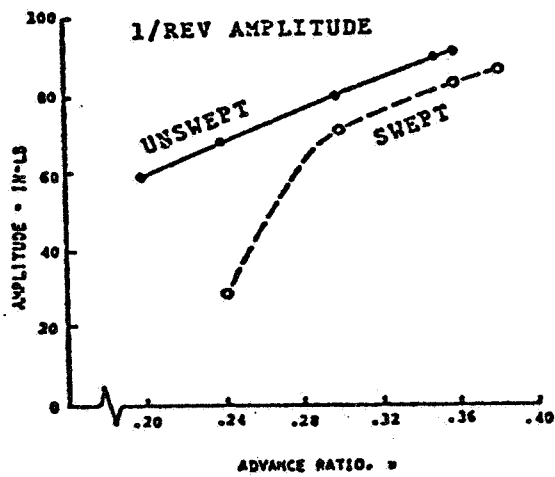


Figure 8

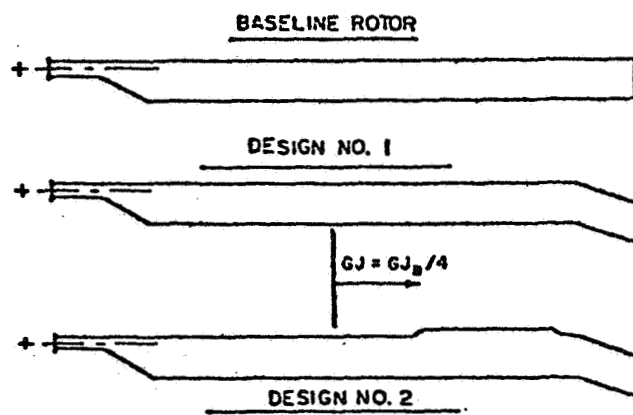


Figure 9

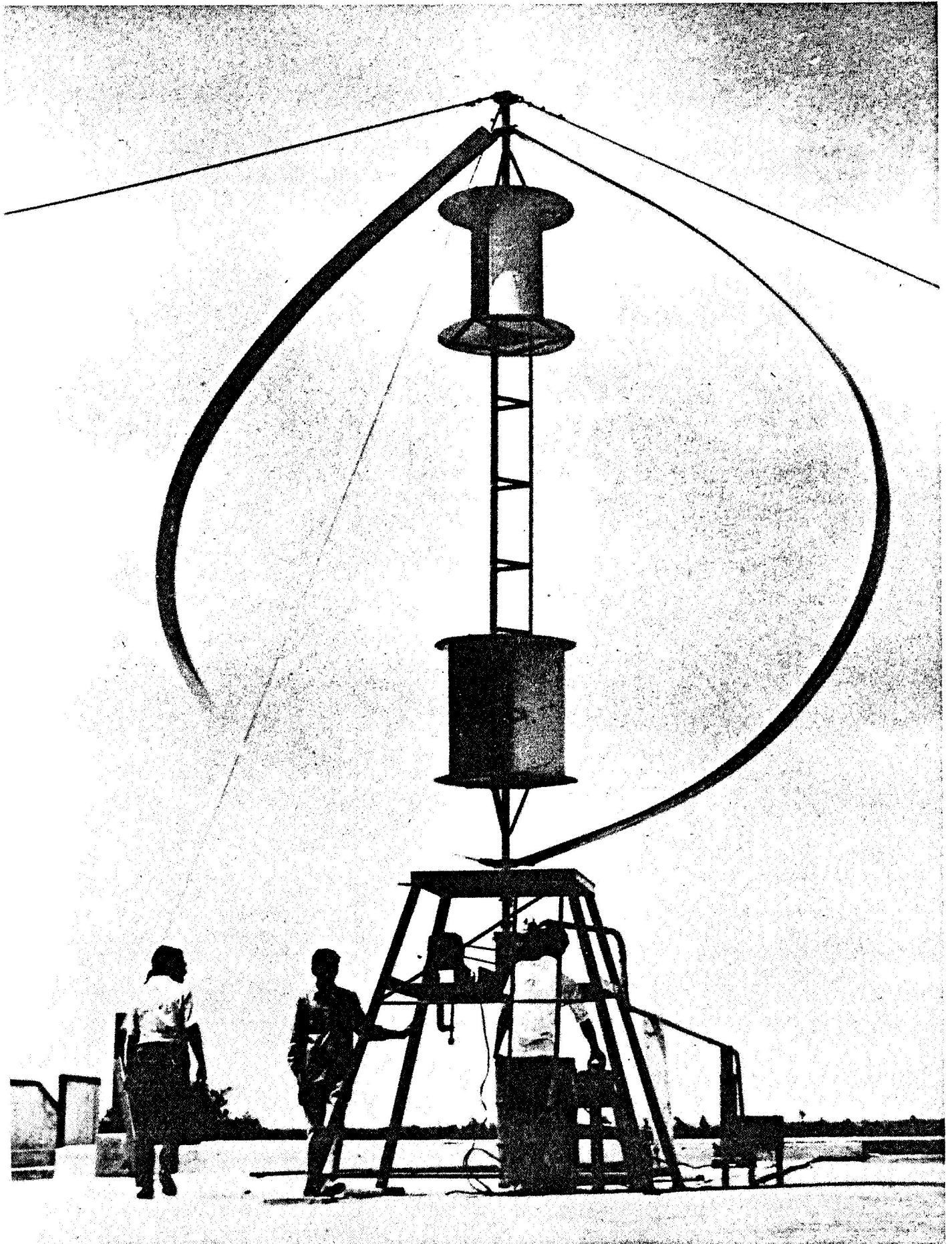


Figure 10

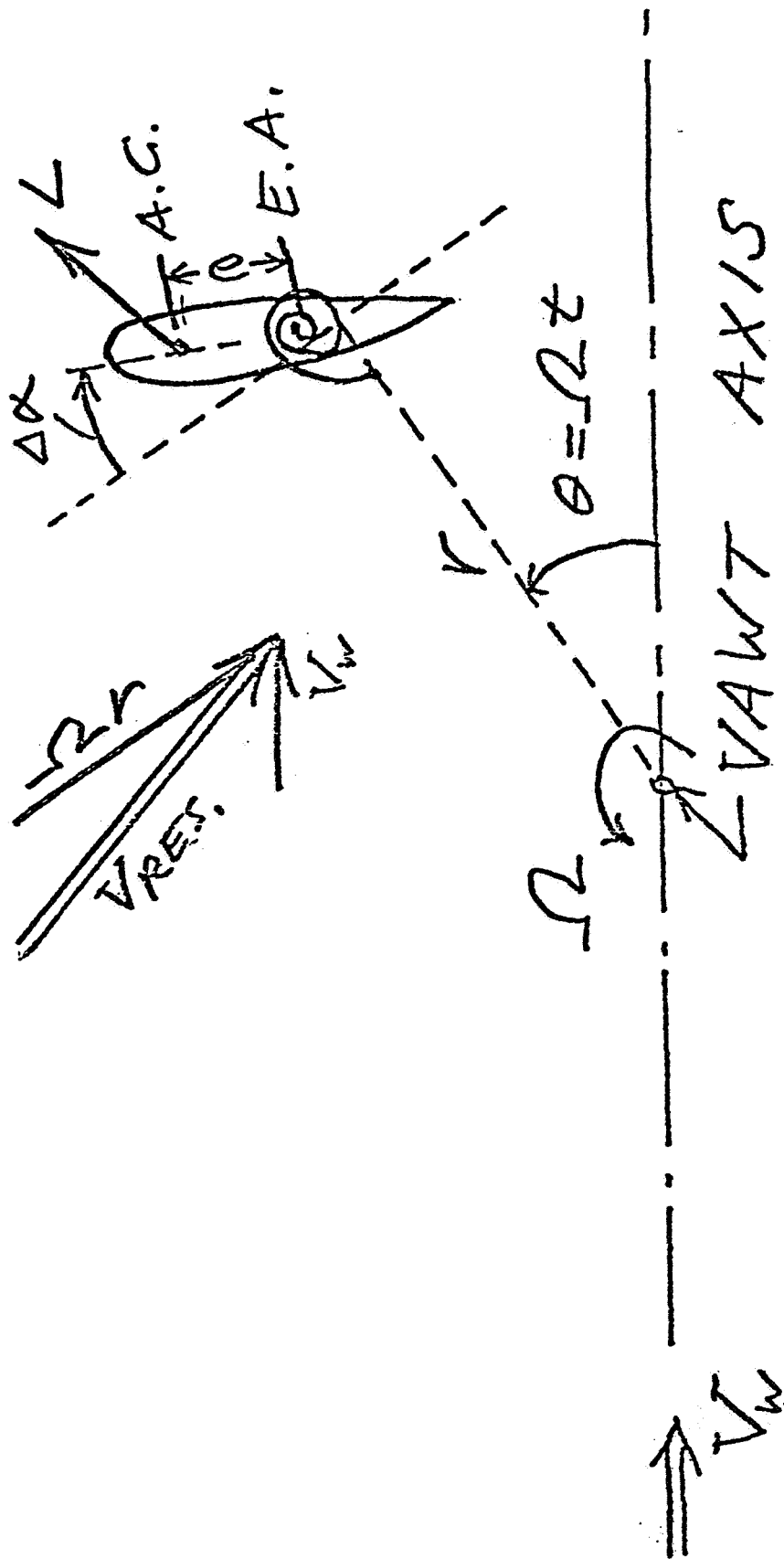


Figure 11

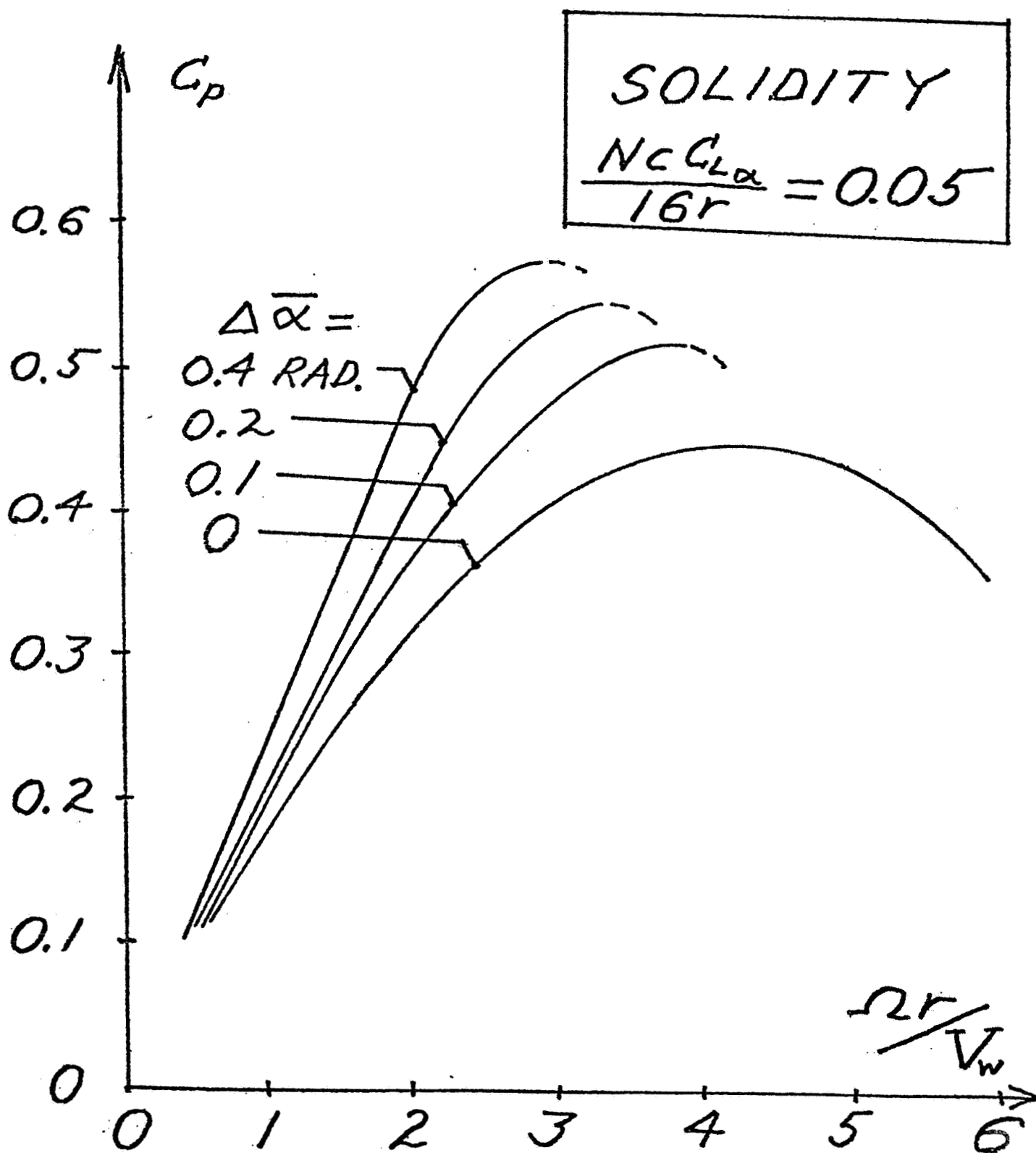


Figure 12

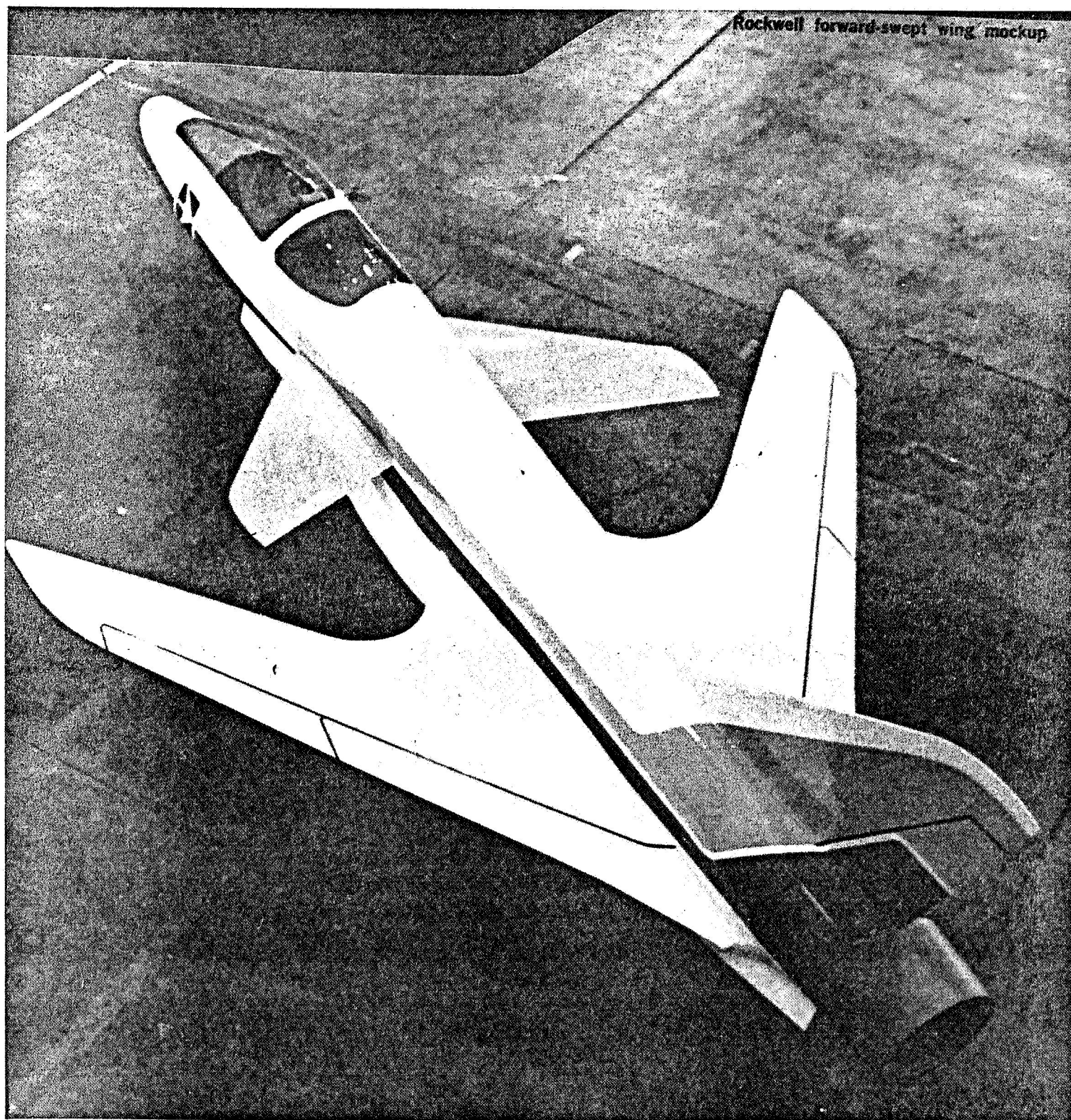


Figure 13

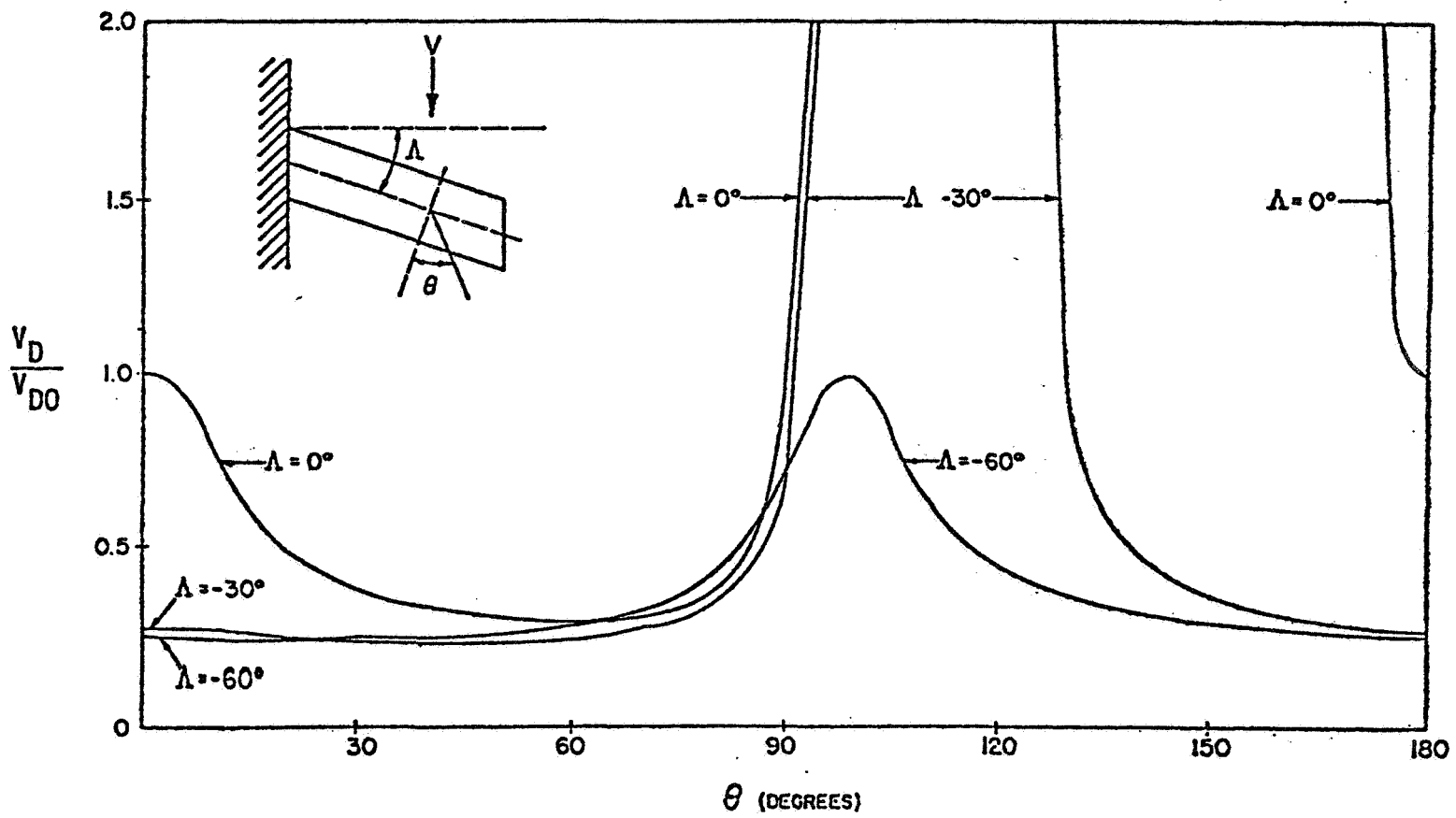


Figure 14

$h = 10,000 \text{ ft.}$

YF-16

$M = 0.9$

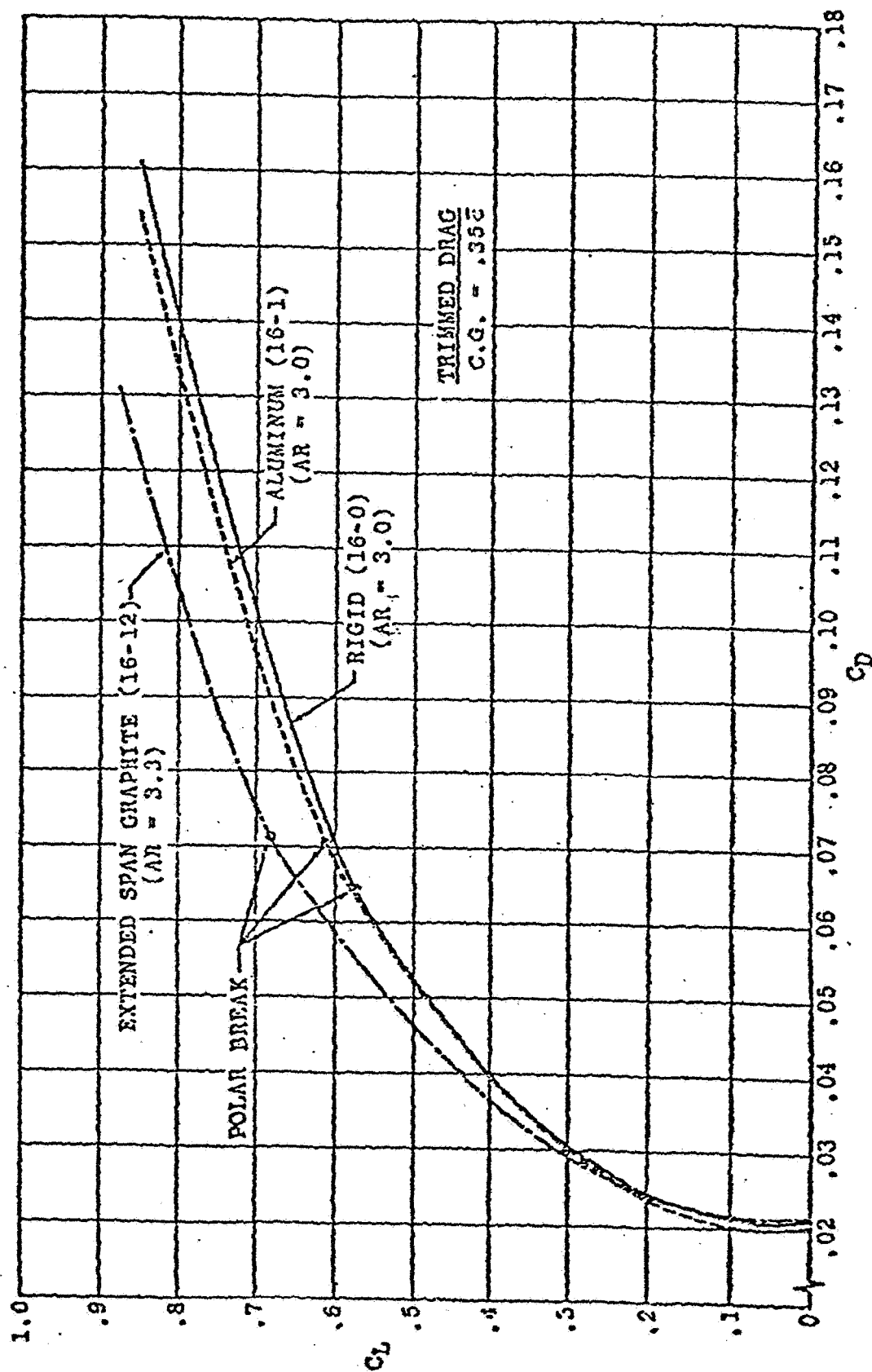


Figure 15

DAST WING FLUTTER SUPPRESSION SYSTEM SHOWN EFFECTIVE IN TDT TESTS

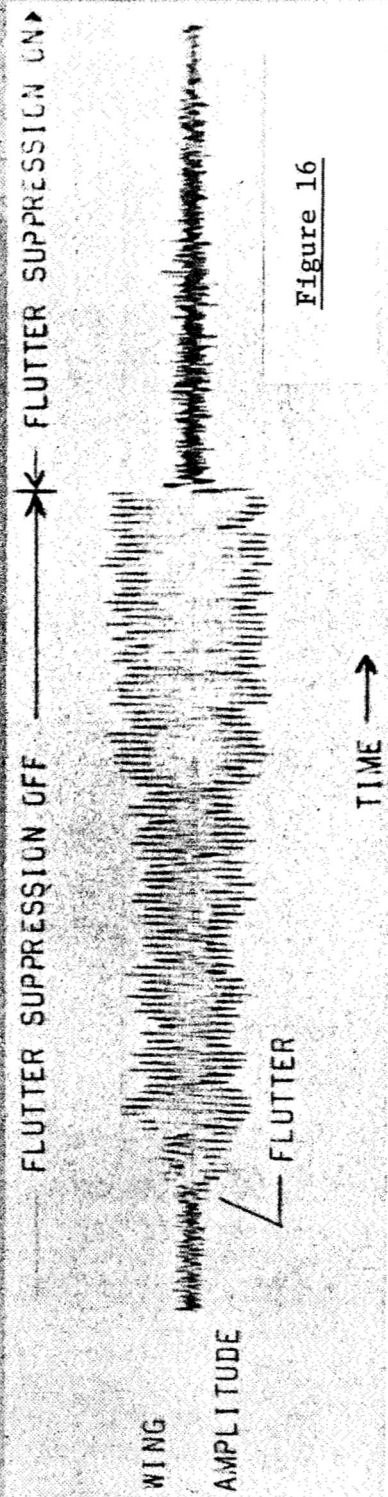
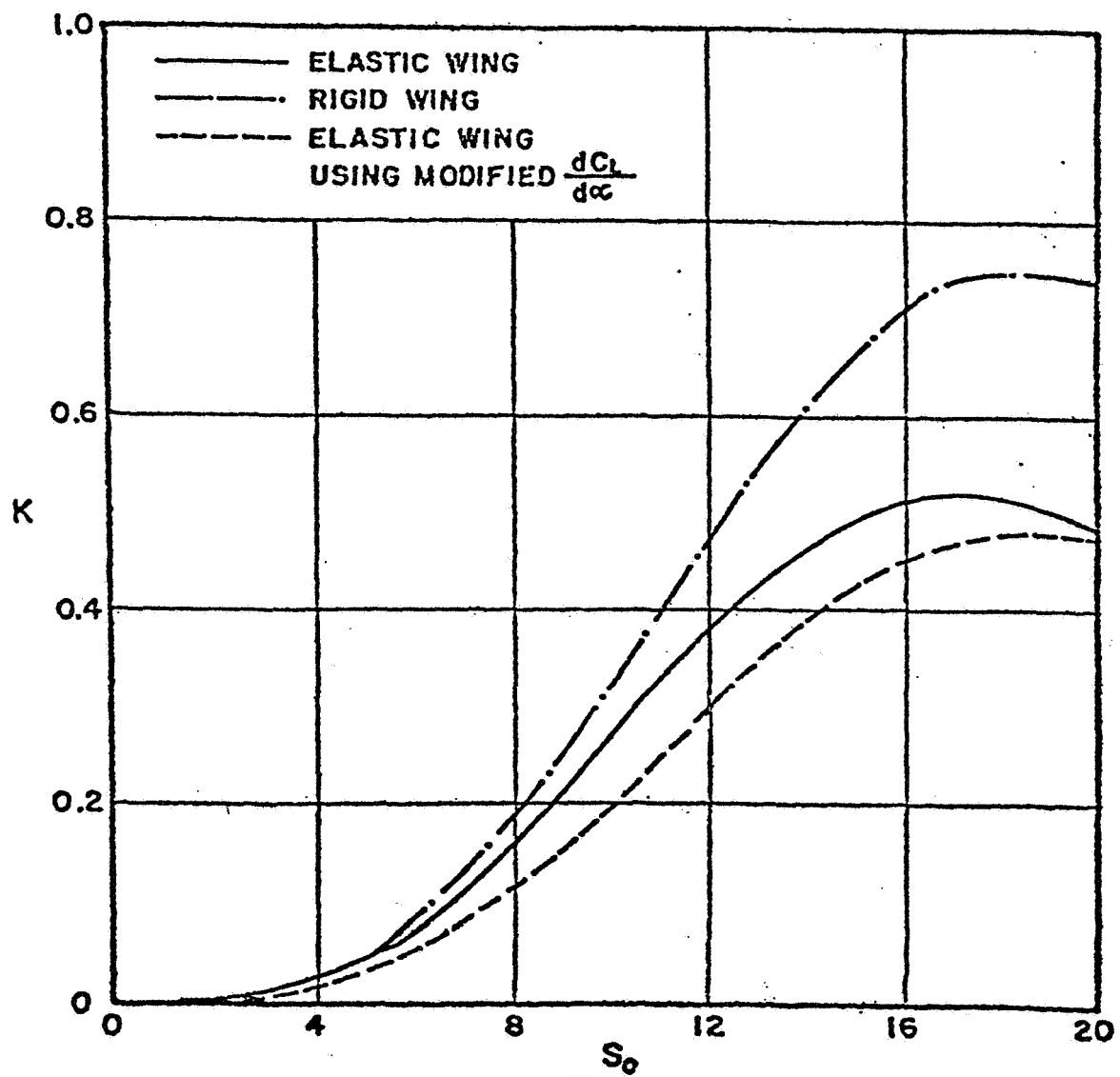
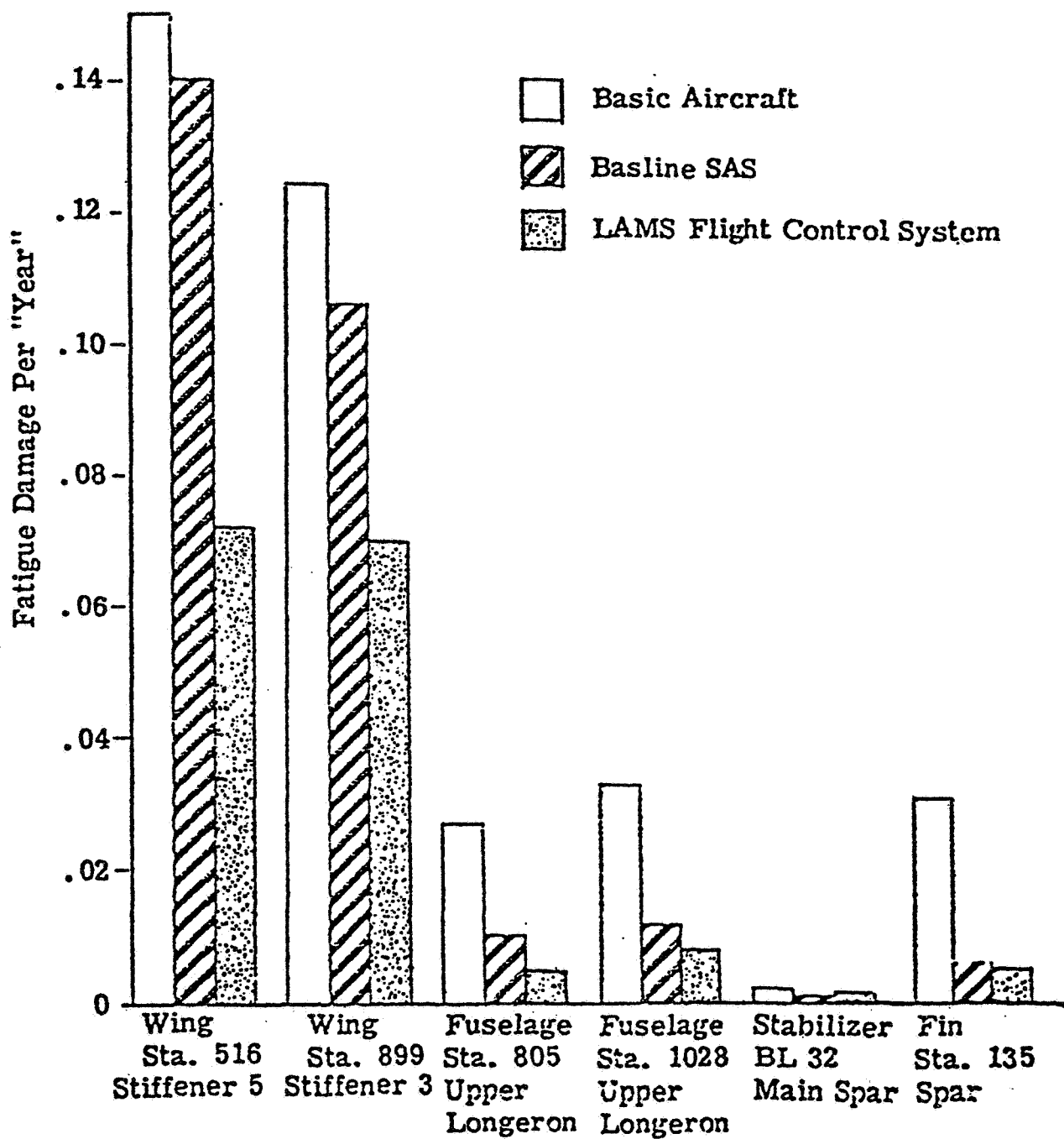


Figure 16



VARIATION OF FUSELAGE ACCELERATION RATIO

Figure 17



LAMS B-52 PREDICTED FATIGUE DAMAGE RATES

Figure 18

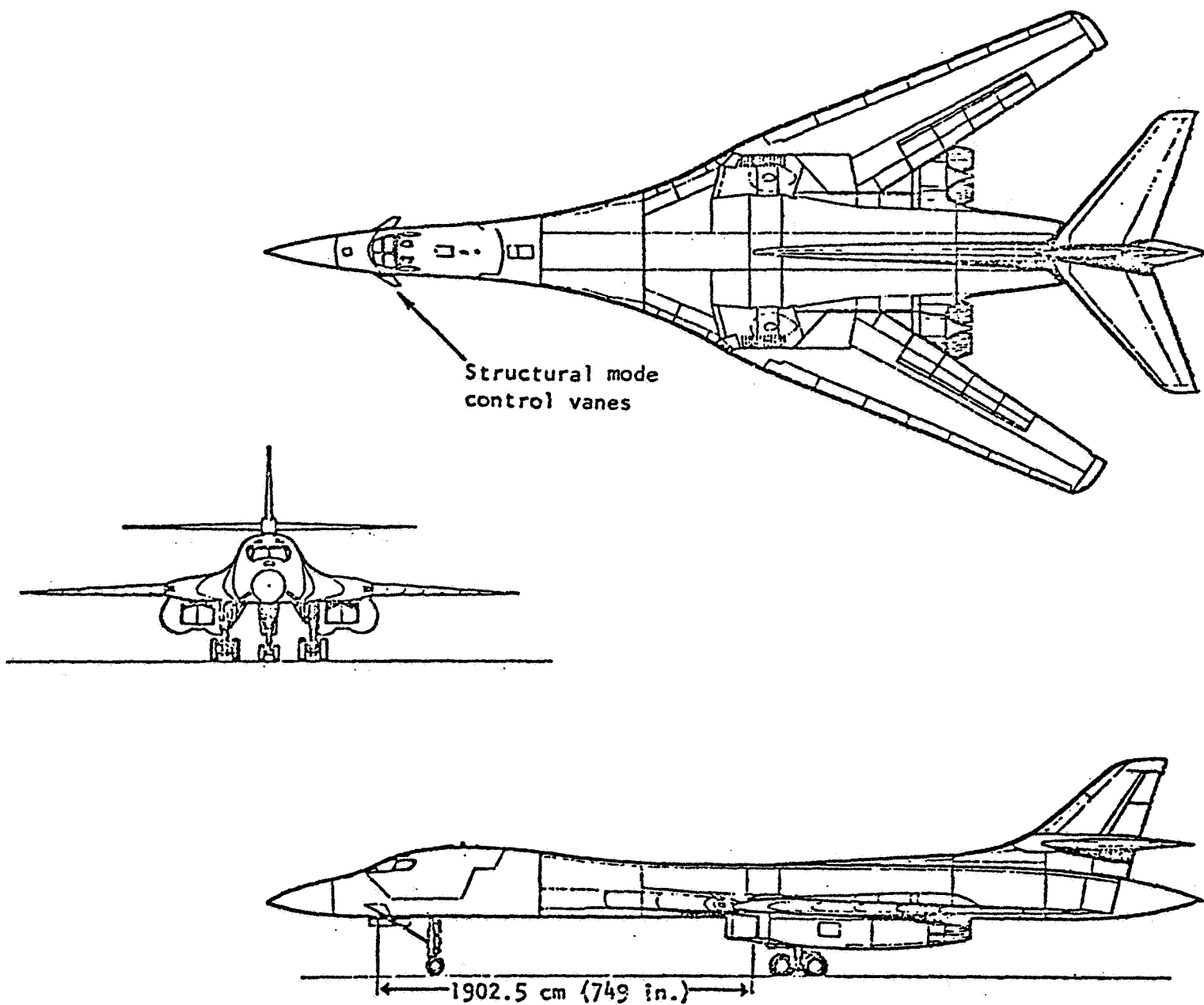
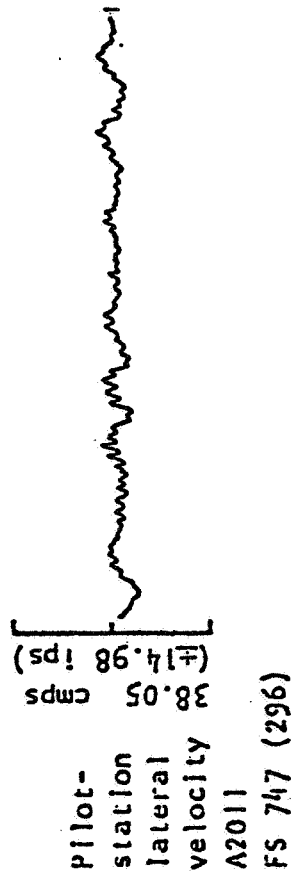
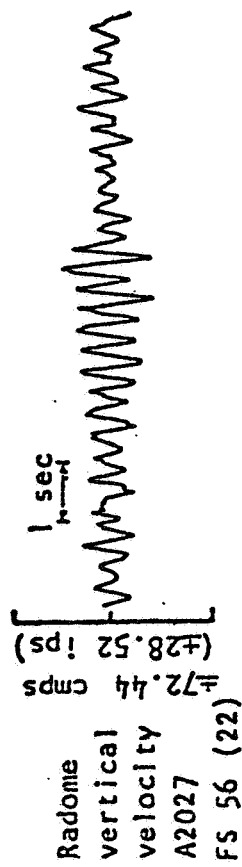


Figure 19

SMCS PERFORMANCE IN TURBULENCE

$\Lambda = 65^\circ$, $M = .70$, $ALT = 10000 FT$

SMCS OFF



SMCS ON

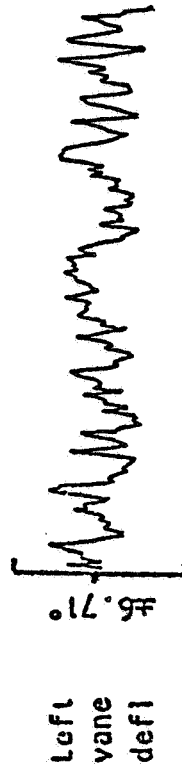
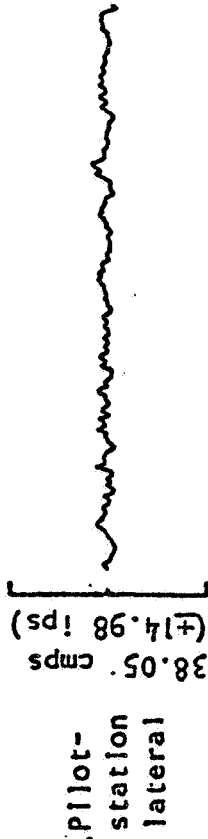
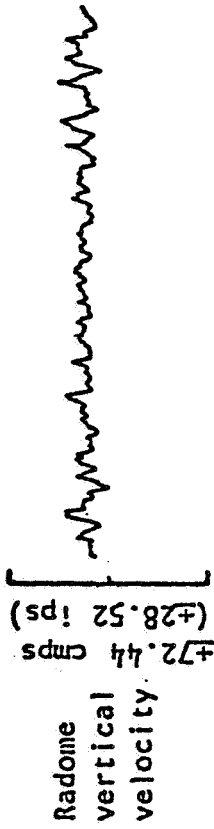


Figure 20

VERTICAL SMCS PERFORMANCE IN TURBULENCE

$\Lambda = 65^\circ$, $M = .85$, ALT. = 500 FT., WT. = 276,000 LBS.

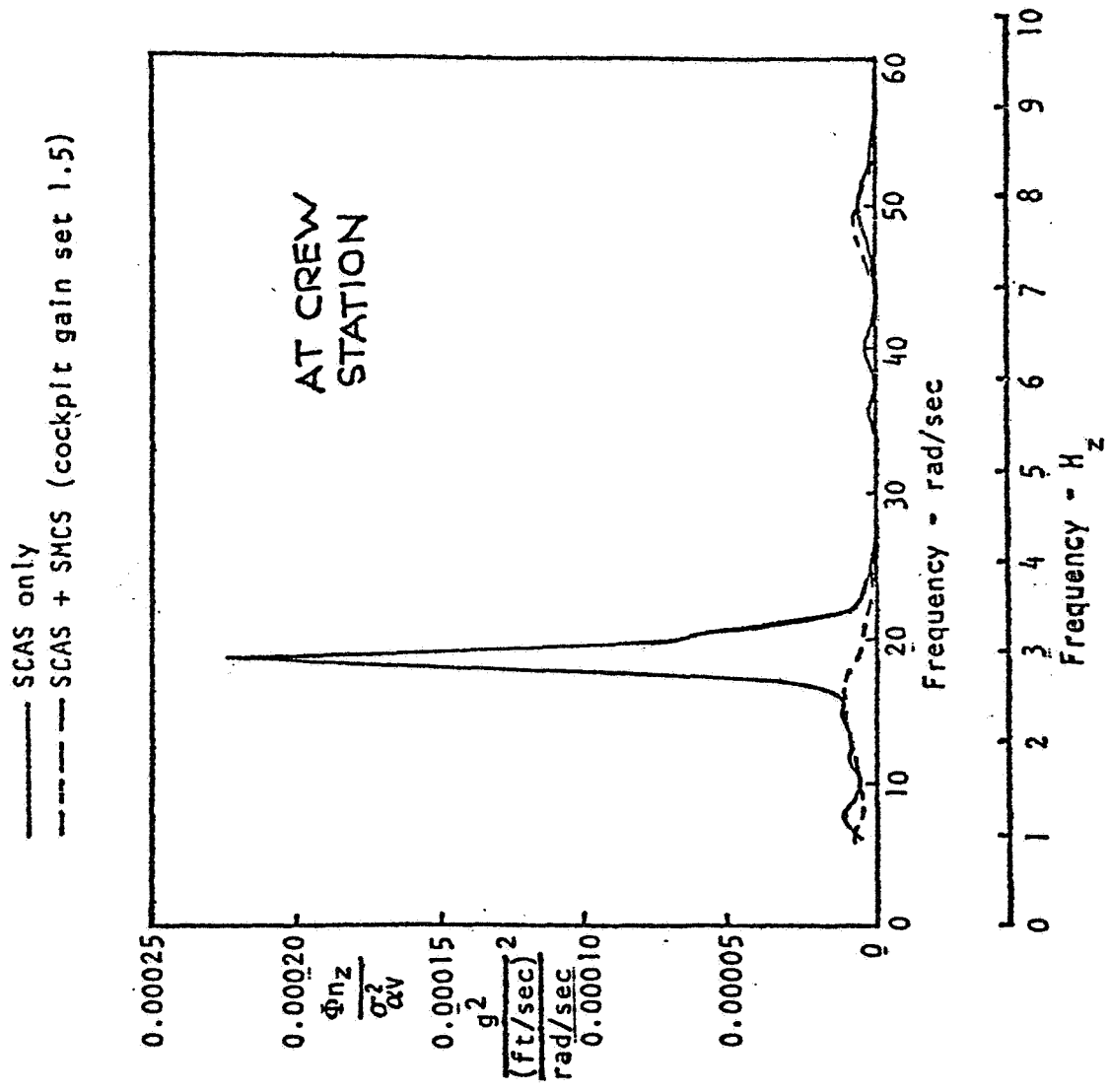


Figure 21

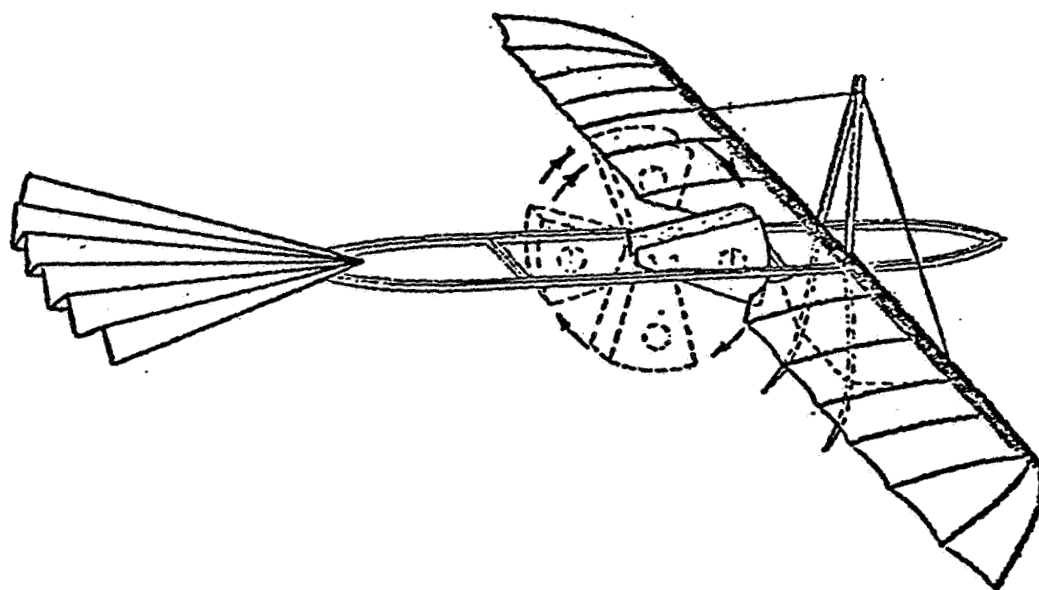


Figure 22

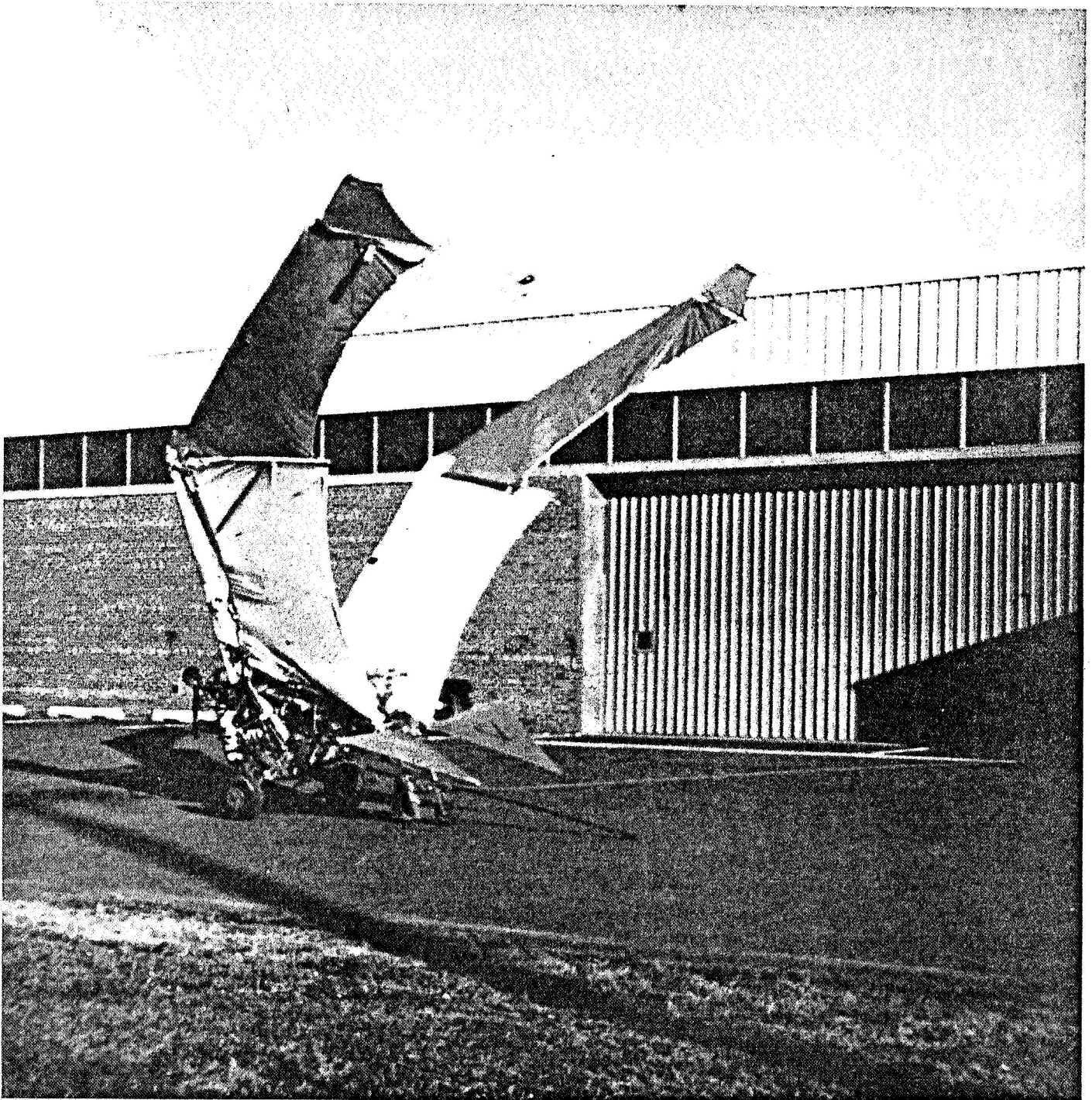


Figure 23

D2
STARTS ON
P. B-1

**HYBRID STATE VECTOR METHODS FOR STRUCTURAL DYNAMIC
AND AEROELASTIC BOUNDARY VALUE PROBLEMS**

**A DISSERTATION SUBMITTED TO
THE DEPARTMENT OF AERONAUTICS AND ASTRONAUTICS
AND THE COMMITTEE ON GRADUATE STUDIES
OF STANFORD UNIVERSITY
IN PARTIAL FULFILLMENT OF THE REQUIREMENTS
FOR THE DEGREE OF
DOCTOR OF PHILOSOPHY**

**By
Larry Lee Lehman
February 1982**

Acknowledgments

I wish to express my deepest gratitude to my advisor, Professor Holt Ashley, for his expert advice and guidance throughout the course of this research. I also wish to thank Professor Jean Mayers for his excellent instruction in both composite materials and variational methods. Special thanks are also due Professor Charles R. Steele, whose unique structural solution methods motivated much of this research.

My special appreciation is extended to the many friends who unreservedly gave of their time and assistance.

A note of thanks is also extended to CONTEXT and the Text Network Program Office for open access to their newly forming system for preparing technical text.

The author would like to express his appreciation to the National Aeronautics and Space Administration, who provided support for this research under Grant NGL-05-020-243, and to the Air Force Office of Scientific Research who provided additional support under Grant No. AFOSR 77-3263.

And most of all, I wish to express my undying gratitude to my parents, who gave me the opportunity and the encouragement to seek a higher education.

Abstract

A computational technique is developed that is suitable for performing preliminary design aeroelastic and structural dynamic analyses of large aspect ratio lifting surfaces. The method proves to be quite general and can be adapted to solving various two-point boundary value problems.

The solution method, which is applicable to both fixed and rotating wing configurations, is based upon a formulation of the structural equilibrium equations in terms of a hybrid state vector containing generalized force and displacement variables. A mixed variational formulation is presented that conveniently yields a useful form for these state vector differential equations. Solutions to these equations are obtained by employing an integrating matrix method. The application of an integrating matrix provides a discretization of the differential equations that only requires solutions of standard linear matrix systems. It is demonstrated that matrix partitioning can be used to reduce the order of the required solutions. Results are presented for several example problems in structural dynamics and aeroelasticity to verify the technique and to demonstrate its use. These problems examine various types of loading and boundary conditions and include aeroelastic analyses of lifting surfaces constructed from anisotropic composite materials.

Integrating matrices, which provide a powerful tool for solving differential equations, are discussed in detail, and methods are given for their calculation. A derivation and calculation procedure is presented for a new type of maximum accuracy integrating matrix based upon orthogonal polynomials.

Contents

	Page
Acknowledgments	iii
Abstract	v
Tables	ix
Figures.	xi
Nomenclature.	xiii
Chapter 1 Introduction	1
Chapter 2 Hybrid State Vector Equations	7
2.1 Variational Formulation of State Vector Equations.	9
2.2 Aeroelastic and Structural Dynamic Equations	16
2.3 Anisotropic Beam Equations	18
Chapter 3 Integrating and Differentiating Matrices	25
3.1 Integrating Matrices for Continuous Integrands	27
3.2 Integrating Matrices for Discontinuous Integrands	38
3.3 Differentiating Matrices.	43
Chapter 4 Integrating Matrix Solution of State Vector Equations	45
4.1 Discretized State Vector Equations	47
4.2 State Vector Equation Reduction	52
Chapter 5 Solutions for Isotropic Beams and Rods	59
5.1 Axial Vibration of Cantilevered Rods.	59
5.1.1 Rods with Continuous Mass and Stiffness	61
5.1.2 Rods with Discontinuous Mass and Stiffness	69
5.1.3 Rods with Elastic Restraint.	73
5.1.4 Rods with Concentrated Mass	77
5.2 Bending Vibration of Beams	80
5.2.1 Cantilevered Beam	82
5.2.2 Simply Supported Beam.	83
5.2.3 Hinged-Free Beam	85
5.2.4 Free-Free Beam	87
5.3 Buckling of a Rotating Beam	89
5.4 Deflection of Beams	91

Chapter 6	Divergence and Aeroelastic Lift of Composite Wings	101
6.1	Divergence of a Forward Swept Composite Wing	102
6.2	Aeroelastic Lift of a Forward Swept Composite Wing	110
Chapter 7	Flutter of Isotropic and Composite Wings	115
7.1	Flutter Equations	116
7.2	Flutter of an Isotropic Wing	119
7.3	Flutter of a Composite Wing	120
Chapter 8	Summary and Recommendations	127
Appendix A.	Weighting Matrices and Shape Functions for Jacobi Polynomials. .	131
Appendix B.	Tables of Integrating Matrices	143
Appendix C.	Composite Laminate Constitutive Equations	151
Appendix D.	Modified Strip Theory Aerodynamics.	159
Appendix E.	Solutions for Problems with Concentrated Loads.	163
Appendix F.	Constraint Equations	167
Appendix G.	Calculation of Transition and Influence Matrices	169
References.	175

Tables

	Page
Table 1: Nondimensional frequencies, $\lambda^{1/2}$, for the axial modes of a uniform cantilevered rod with N collocation intervals. ($\lambda = \omega^2 m_R \ell^2 / (EA)_R$).	94
Table 2: Axial vibration mode shapes, $\{u\}$, for a uniform cantilevered rod (Numerical solutions obtained with five collocation intervals).	94
Table 3: Nondimensional frequencies, $\lambda^{1/2}$, for the axial modes of a linearly tapered cantilevered rod with N collocation intervals. ($\beta_t = 0.5$; $\lambda = \omega^2 m_R \ell^2 / (EA)_R$)	95
Table 4: Nondimensional frequencies, $\lambda^{1/2}$, for the axial modes of a three segment cantilevered rod with discontinuous stiffness and mass. There are N collocation intervals per segment. ($\lambda = \omega^2 m_R \ell^2 / (EA)_R$; $\gamma = 10$, $\delta = 100$; Error based on six significant figures).	96
Table 5: Nondimensional frequencies, $\lambda^{1/2}$, for the axial modes of a uniform cantilevered rod with variable stiffness elastic restraint at the free end. Results were obtained with a Jacobi integrating matrix using six collocation points. ($\bar{k}_e = k / (EA)_R$; $\lambda = \omega^2 m_R \ell^2 / (EA)_R$)	97
Table 6: Nondimensional frequencies, $\lambda^{1/2}$, for the axial modes of a uniform cantilevered rod with tip mass. Results were obtained with a Jacobi integrating matrix using six collocation points. ($m_n^+ = m_n / m_R \ell$; $\lambda = \omega^2 m_R \ell^2 / (EA)_R$)	97
Table 7: Nondimensional bending frequencies, $\lambda^{1/2}$, of a uniform cantilever beam for a Jacobi integrating matrix solution using five collocation intervals. ($\lambda = \omega^2 m_R \ell^4 / (EI)_R$).	98
Table 8: Lateral bending mode shapes, $\{w\}$, of a uniform cantilever beam (Jacobi integrating matrix solution using five collocation intervals)	98
Table 9: Nondimensional bending frequencies, $\lambda^{1/2}$, of a uniform, simply supported beam with N collocation intervals; ($\lambda = \omega^2 m_R \ell^4 / (EI)_R$)	99

Table 10:	Nondimensional bending frequencies, $\lambda^{1/2}$, of a uniform, hinged-free beam with N collocation intervals.	99
Table 11:	Nondimensional bending frequencies, $\lambda^{1/2}$, of a uniform, free-free beam with N collocation intervals	100
Table 12:	Nondimensional buckling speeds, Ω , of a uniform, inward-oriented, rotating beam. Jacobi integrating matrix solutions with N collocation intervals. ($\Omega = \alpha_e^2 \sqrt{\lambda_e}$).	100
Table 13:	Geometric, aerodynamic, and structural parameters for a uniform composite wing.	105
Table 14:	Flutter velocities for an unswept, uniform, isotropic wing . . .	119
Table 15:	Inertia parameters for the uniform composite wing of Table 13	120

Figures

	Page
Fig. 1: Lifting Surface Model	20
Fig. 2: Typical integration regions for a discontinuous function	39
Fig. 3: Typical regions for piecewise integration of a continuous function	41
Fig. 4: Error in computed frequencies, compared to exact solutions, for the first three axial modes of a uniform cantilevered rod. The error for both Jacobi and Newton integrating matrix solutions is plotted vs. the number of collocation intervals N	66
Fig. 5: Error in computed frequencies, compared to exact solutions, for the first three axial modes of a linearly tapered cantilevered rod with a taper ratio of one half ($\beta_t = 0.5$). The error for both Jacobi and Newton integrating matrix solutions is plotted vs. the number of collocation intervals N	68
Fig. 6: Error in computed frequencies, compared to exact solutions, for the first three axial modes of a cantilevered rod with discontinuous stiffness and mass ($\bar{\gamma} = 10$; $\bar{\theta} = 100$). The rod has three uniform segments between the points $x = 0, .25, .75, 1$. The error for the integrating matrix solutions is plotted vs. the number of collocation intervals per segment N	72
Fig. 7: A cantilevered axial rod with a spring restraint boundary condition	74
Fig. 8: Rotating beam geometry	90
Fig. 9: Nondimensional compliances for a symmetric angle-ply laminate with a single layer	107
Fig. 10: Nondimensional divergence velocities of a uniform, cantilevered, composite wing—symmetric angle-ply with 1, 5, and 15 layers. ($\Lambda = -30^\circ$, $\lambda_{REF} = \lambda_{(\Lambda=-30^\circ, \theta=-90^\circ)}$)	108
Fig. 11: Nondimensional divergence velocities of a uniform, cantilevered, composite wing—symmetric angle-ply with 1, 5, and 15 layers. ($\Lambda = -60^\circ$, $\lambda_{REF} = \lambda_{(\Lambda=-30^\circ, \theta=-90^\circ)}$)	109

Fig. 12:	Limiting elastic lift distributions for a uniform composite wing—symmetric angle-ply with a single layer	113
Fig. 13:	Effect of fiber orientation on flutter dynamic pressure for an unswept, uniform composite wing—symmetric angle-ply laminate with 1, 3, 5, and 15 layers. ($\lambda_{REF} = \lambda_{(\theta=-90^\circ)}$)	121
Fig. 14:	Roots loci of aeroelastic modes for a uniform composite wing. (Three layer laminate; $\mu = 10$; $\theta = 10^\circ$)	125
Fig. 15:	Roots loci of aeroelastic modes for a uniform composite wing. (Single layer laminate; $\mu = 64$; $\theta = 45^\circ$)	126
Fig. C-1:	Lamina axis system (1,2,3)	153
Fig. C-2:	Laminate axis system (x, y, z)	153

Nomenclature

a	nondimensional location, in semichords, of structural reference axis with respect to aerodynamic midchord, positive aft of midchord (nondimensionalized by b_R)
a_c	nondimensional location, in semichords, of aerodynamic center with respect to aerodynamic midchord, positive aft of midchord (nondimensionalized by b_R)
a_d	aerodynamic downwash point, (D.6)
a_0	lift curve slope
a_n	leading coefficient of orthonormal polynomial (coefficient of x^n)
$\mathbf{a}, \tilde{\mathbf{a}}$	local, global loads vector (Jp)
$\mathbf{a}_r, \tilde{\mathbf{a}}_r$	local, global vector containing nonhomogeneous load terms
\mathbf{a}_r^+	vector of nonhomogeneous concentrated load terms
A_{ij}, B_{ij}, D_{ij}	composite stiffness terms, $i, j = 1, 2, 3$, (C.15)
$\bar{A}_{ij}^*, \bar{B}_{ij}^*, \bar{D}_{ij}^*$	nondimensional composite plate compliance terms ($i, j = 1, 2, 3$), (2.32)
$\mathbf{A}, \tilde{\mathbf{A}}$	local, global matrix of displacement dependent load terms
$\bar{\mathbf{A}}^+$	matrix of displacement dependent concentrated load terms, (E.6)
$\mathbf{A}^*, \mathbf{B}^*, \mathbf{D}^*$	dimensional composite plate compliance matrices
b, \bar{b}	dimensional, nondimensional aerodynamic semichord, $\bar{b} = b/b_R$
$\mathbf{b}_0, \mathbf{b}_n$	boundary condition vectors defined in (4.7–4.8)
$\beta_{j,k}, \beta_{j,k}^*$	matrix elements defined in (A.25) and (A.49), respectively, for interval j , collocation point k
$\mathbf{B}_0, \mathbf{B}_n$	homogeneous boundary condition matrices, (4.5–4.6)
$\tilde{\mathbf{B}}$	block diagonal global boundary condition matrix (for homogeneous boundary conditions)
$\tilde{\mathbf{B}}_{nh}$	matrix of nonhomogeneous boundary conditions

c	chord length of structural box normal to structural reference axis
$C(\bar{z})$	Theodorsen function
C_{ℓ_e}	elastic lift distribution
C_{ℓ_r}	rigid lift distribution
$\mathbf{C}, \mathbf{C}_{FD}$	damping matrices
d_j	end points of interpolation interval ($j = 1, 2$), (A.13)
\mathbf{D}	constant matrix defined in (2.6)
\mathbf{D}	differentiating matrix, (D.3–D.4)
c_m^n	product defined in (A.11)
EA	axial stiffness
EI	bending stiffness
\bar{EI}	nondimensional isotropic bending compliance, (5.48)
E_1, E_2	Young's modulus
\mathbf{f}	nonhomogeneous loads vector defined in (4.13)
F_t	nondimensional tension parameter, (5.93)
F_u	nondimensional axial force defined in (5.4)
\mathcal{F}	defined in (3.5)
$\overline{\mathcal{F}}$	defined in (3.9)
\mathbf{F}	matrix defined in (4.12) (contains boundary condition modified integrating matrices)
\mathbf{F}^+	matrix defined in (E.11) (contains boundary condition modified summing matrices)
g	function defined in (3.13)
GJ	torsional stiffness
G_{12}	shear modulus
\mathbf{H}	structural matrix defined in (4.11)
\mathbf{H}^*	\mathbf{H}^{-1} , see (4.18)
\mathbf{I}	identity matrix

\mathbf{I}^*	matrix defined in (5.35)
j	$\sqrt{-1}$
\mathbf{J}	antisymmetric matrix with unit elements ($\mathbf{D} - \mathbf{D}^T$)
\bar{k}_s	nondimensional restraint spring stiffness, (5.27)
$\bar{\mathbf{k}}$	constant vector of integration
\mathbf{K}	symmetric matrix containing structural related terms
ℓ	specified length along x -coordinate
L_α, L_γ	nondimensional steady aerodynamic lift terms, (6.2)
\hat{L}_i	nondimensional Laplace transforms of unsteady aerodynamic lifts, $i = w, \alpha, \gamma, \tau$
$\mathbf{L}, \tilde{\mathbf{L}}$	local, global integrating matrix
\mathbf{L}_i^*	integrating matrix modified by boundary conditions (type i)
m, \bar{m}	dimensional, nondimensional running mass distribution, $\bar{m} = m/m_R$
\bar{m}_i	nondimensional mass terms defined in (7.4), $i = ww, w\alpha, \alpha\alpha$
\bar{m}_n^+	nondimensional concentrated tip mass, $m_n/m_R\ell$
\mathbf{m}	dimensional vector of moment resultants (moment/unit length)
M_i, \bar{M}_i	dimensional, nondimensional components of moment resultant vector ($i = x, y, xy$), (2.31)
M_α, L_γ	nondimensional steady aerodynamic moment terms, (6.2)
\hat{M}_i	nondimensional Laplace transform of unsteady aerodynamic moments, $i = w, \alpha, \gamma, \tau$
$\mathbf{M}, \mathbf{M}_{FD}$	mass distribution matrices
\mathbf{n}	dimensional vector of stress resultants (force/unit length)
N	number of collocation intervals
N_i, \bar{N}_i	dimensional, nondimensional components of stress resultant vector ($i = x, y, xy$), (2.31)
\mathcal{N}	interpolation shape functions
n_L	number of layers
\mathbf{NS}	number of states in local state vector

p, \bar{p}	dimensional, nondimensional lateral loading per unit length, (5.99)
p_i, \bar{p}_i	dimensional, nondimensional running external loads ($i = u, \gamma, w, \alpha$), (2.31)
p_i^+	magnitude of concentrated load, (E.1)
$p_n^{(\alpha, \beta)}, P_n^{(\alpha, \beta)}$	normalized, unnormalized Jacobi polynomial
\mathbf{p}	vector of running external loads
q	dynamic pressure
$\mathbf{Q}, \mathbf{Q}_{FD}$	unsteady aerodynamic matrices
r_α	dimensionless radius of gyration of section, $r_\alpha = r_\alpha/b_R$
R	ratio of compressible to incompressible Theodorsen function
s, s^*	dimensional, nondimensional Laplace variable, $s^* = s\ell^2\sqrt{m_R/(EI)_R}$
\bar{s}	nondimensional Laplace variable defined in (D.5)
\bar{S}^*	nondimensional transverse shear compliance, (2.33)
$\mathbf{S}, \tilde{\mathbf{S}}$	local, global lower triangular summing matrix, (3.8)
t	time variable
\mathbf{T}	structural matrix defined in (4.25) (performs the function of a structural flexibility matrix by operating on force distribution terms)
\mathbf{T}^+	structural matrix defined in (E.15)
u, v, w	displacement variables along x, y, z , respectively
$\bar{u}, \bar{v}, \bar{w}$	displacement variables nondimensionalized by ℓ
u_0, v_0, w_0	plate geometric midplane displacements
\mathcal{U}	functional appearing in (2.1)
\mathbf{U}	constraint and coordinate transformation matrix
V	freestream velocity
V^*	velocity normal to structural reference axis, $V \cos \Lambda$
V_x, \bar{V}_x	dimensional, nondimensional transverse shear resultant, (2.31)
\mathcal{W}_n	weighting matrix

x, y, z	spatial coordinates
$\bar{x}, \bar{y}, \bar{z}$	spatial coordinates nondimensionalized by ℓ
$\mathbf{y}, \tilde{\mathbf{y}}$	local, global state vector
$\mathbf{y}_D, \tilde{\mathbf{y}}_D$	local, global generalized displacement components of state vector
$\mathbf{y}_F, \tilde{\mathbf{y}}_F$	local, global generalized force components of state vector
$\hat{\mathbf{y}}$	Laplace transform of state vector (with respect to time)
$\mathbf{Z}, \tilde{\mathbf{Z}}$	local, global coefficient matrix containing structural terms (JK)

Greek Symbols

α	angle of twist (elastic angle of attack for aeroelastic problems)
α_e	effective angle of attack, (6.6)
α_{er}	effective angle of attack for a rigid wing
α_s	nondimensional hub radius, R_0/ℓ
β_s	dimensional shear compliance (often written as μ_s/EA , where μ_s is a cross section shape factor)
β_t	taper parameter in (5.23); taper ratio equals $(1 - \beta_t)$
γ	rotation of the normal to the elastic axis
γ_{xy}	shear strain
$\bar{\gamma}$	axial stiffness ratio defined in (5.24)
Γ	gamma function
Γ_i	selection matrix for i th point, (G.9)
δ	first variation operator
δ_n	square of normalizing factor for P_n
$\delta(x - x_i)$	unit delta function, (E.1)
ϵ^0	vector of plate midplane strains, (C.9)
θ	composite fiber orientation angle (with respect to structural reference axis)
$\bar{\theta}$	mass ratio defined in (5.24)

κ	vector of plate bending curvatures, (C.9)
λ	nondimensional constant parameter (dynamic pressure parameter for aeroelastic problems and eigenvalue for vibration problems)
λ_{D0}	reference divergence dynamic pressure parameter
λ_s	nondimensional spin parameter, (5.95)
Λ	wing sweep angle, positive aft (aerodynamic and structural reference axis sweep angles are assumed equal for a uniform wing)
μ	nondimensional mass ratio parameter, (D.5)
ν_{12}, ν_{21}	Poisson's ratio
\mathbf{E}	selection matrix, (G.2)
Π	product
ρ	air density
σ^*	real part of s^* , $s^* = \sigma^* + j\omega^*$
σ_i	inplane stresses, $i = 1, 2, x, y$
r	nondimensional axial compliance, (5.2)
τ_{12}, τ_{xy}	shear stresses
\mathbf{T}	matrix defined in (G.6–G.7)
Φ	transition matrix, Appendix G
\bar{X}_α	nondimensional location in semichords of section mass center with respect to structural reference axis, positive aft, $\bar{X}_\alpha = X_\alpha/b_R$
ω	natural frequency of vibration
ω^*	imaginary part of s^* , $s^* = \sigma^* + j\omega^*$
ω_s	rotational speed of hub, (5.95)
Ω	nondimensional buckling speed, $\alpha_s^2 \sqrt{\lambda_s}$
ϑ	nonnegative integrable weighting function for Gaussian integration rules, (3.12)

Miscellaneous Symbols

\mathbf{i}	vector of unit elements
--------------	-------------------------

(γ)	$\frac{\partial}{\partial x}$
$(\vec{})$	vector
$\text{'}()$	diagonal matrix
$()^T$	transpose
$()^{-1}$	inverse
$()_F$	force subset
$()_D$	displacement subset
$()_R$	reference value

Chapter 1

Introduction

AN EXPANDED UTILIZATION of laminated composite materials in aircraft structural design has led to a search for new ways to employ these relatively high specific strength and stiffness materials. One result of this search has been the development of the concept of aeroelastic tailoring of a lifting surface, in which the directional characteristics of the composite material are used to synthesize a structure with enhanced aeroelastic performance. But along with the possibility for innovative design with structural composites comes greater complexity in the preliminary design task. This increased complexity arises in part from the anisotropic nature of the composites materials and in part from the increased design freedom allowed by these materials. Because of the additional complexity of the design task, new analysis tools are needed to aid the preliminary designer in efficiently evaluating the sometimes large number of design concepts available to him. Therefore, the primary objective of this research has been to develop a simple and versatile analysis method compatible with the needs of preliminary aeroelastic and structural dynamic design.

The motivation for this research effort stemmed from a desire to investigate the performance enhancements that can be achieved by aeroelastically tailoring large aspect ratio composite lifting surfaces. Essentially, aeroelastic tailoring involves

designing a structure to take advantage of the elastic deformation during loading. For static aeroelastic problems, this means controlling the relative amounts of bending and torsional deflection of a wing or lifting surface. By maintaining a desirable wing deformation shape, or by passively controlling the distribution of aerodynamic loading, it is often possible to enhance aerodynamic performance and to extend the operating envelopes of a lifting surface. For dynamic aeroelastic problems, the coupling between bending and torsion of composite structures provides a way of maximizing the dynamic instability (flutter) speed of a lifting surface. Since the primary objective of this research is to develop a convenient method for analyzing such aeroelastic and dynamic behavior, the above mentioned problems provide some excellent, nontrivial examples for verification of the devised solution method. At the same time, these example solutions hopefully provide a firm foundation for other in-depth studies of the aeroelastic behavior of composite structures, including the investigation of optimized aeroelastic designs.

Historically, most aeroelastic analyses of composite structures have been carried out by very complex computer codes involving finite element structural methods coupled with lifting surface aerodynamics. Unfortunately, these complicated numerical approaches can tend to obscure a basic understanding of the important parameters appearing in the analysis and, owing to cost considerations, often preclude an extensive study involving numerous design variations. Recent developments, such as those of Gimmestad [1], offer a suitable alternative for preliminary design investigations.

A fundamental approach to performing the aeroelastic and dynamic analyses of a structure described by one independent spatial coordinate involves formulating the ordinary differential equations representing the aeroelastic or dynamic response and obtaining analytical solutions to the resulting boundary value problems. Although the coupled bending and torsion equations can be formulated, it is often difficult,

if not impossible, to obtain analytical solutions for the general case in which the coefficients of the equations are variable. Some useful solutions have been obtained, however, for cases in which the coefficients in the linear aeroelastic equations can be written as constants. For instance, solutions to the differential equations for divergence and load distribution have been obtained for isotropic metallic wings by Diederich and Budiansky [2] and Diederich and Foss [3], and more recently, divergence and load distribution solutions for composite swept forward wings have been obtained by Weisshaar [4,5]. But with the application of the hybrid state vector approach discussed herein, approximate solutions to the differential equations can be easily obtained for much more difficult cases involving variable coefficients. The hybrid state vector approach has been utilized by Lehman [6] to obtain a variety of aeroelastic solutions, including flutter of composite wings. This type of solution does not require an explicit calculation of structural influence coefficients and can utilize various forms of aerodynamic influence matrices.

A major requirement for a solution method to be used in preliminary design is that the method be reasonably flexible in allowing solution of different types of problems, and yet easily specialized so that computations can be carried out efficiently. Furthermore, it is desirable to have a numerical solution that is easily programmable and that makes use of standard numerical methods, thus requiring minimal investment in software. It has been found that these requirements are well satisfied by a mixed state vector formulation of the differential equations combined with an integrating matrix solution procedure—hence, one of the reasons for referring to the method as a hybrid approach.

Other investigators (see the introduction to Chapter 3) have provided initial formulations for the concept of the integrating matrix solution in structural mechanics and have applied this concept to solving a variety of problems. Compared to other numerical approaches, such as finite element and finite difference, relatively little

has been done to generalize the integrating matrix method. In order to bring some generality to the integrating matrix method, it has been found useful to incorporate some of the familiar concepts employed in finite element analysis.

Even though the solution method presented here is applied only to two-point boundary value problems arising in aeroelasticity and structural dynamics, the approach is, in fact, quite general and can be applied to initial value problems as well as to multipoint boundary value problems. The method can also be extended to handle systems described by more than one independent variable.

The compact matrix notation used in the development of the hybrid state vector method is intended to aid in the task of programming the solutions, regardless of the programming language employed. Solutions for dynamic flutter instabilities in Chapter 7, which are iterative by nature, operate quite efficiently in languages like *FORTRAN* or *Pascal*. The hybrid state vector solution formulations, however, are especially suited to the matrix oriented programming language *APL*. In fact, the hybrid state vector method presented here, when coupled with *APL*, forms an extremely powerful interactive problem solving tool. It is further anticipated that the hybrid state vector solutions, since they are formulated in terms of simultaneous matrix operations, will be readily adaptable to parallel processing techniques.

In Chapter 2, a mixed variational formulation is presented for obtaining the linear state vector differential equations of structural equilibrium. This formulation is given for structures that can be described by one independent spatial variable. By casting the aerodynamic and inertial loads acting on a structure in terms of the displacement state variables, the state vector equations can be expanded into the equations suitable for aeroelastic and structural dynamic analyses. A detailed form of the state vector equations is then presented to describe an anisotropic plate-beam that is constructed from laminated composite materials. These equations are reserved for later use in the example solutions of Chapters 6 and 7.

Chapter 3 gives a general derivation of integrating matrices and describes how they are applied to the integration of either continuous or discontinuous integrands. Several different types of integrating matrices are discussed, including maximum precision integrating matrices based upon orthogonal polynomial approximations. The concept of a differentiating matrix is also introduced.

Chapter 4 describes how integrating matrices are used to formulate solutions for the discretized versions of the state vector equations derived in Chapter 2. By using matrix partitioning techniques, it is then shown that reduced order matrix equations for the displacement variables can be obtained by eliminating the force variables.

In Chapter 5, sample solutions are presented for simple beam and rod problems. These examples illustrate the application of the hybrid state vector method to the solution of two-point boundary value problems. Continuous and discontinuous parameter problems are demonstrated along with various types of boundary and loading conditions. Numerical results are compared with analytical results to evaluate the accuracy of the integrating matrix solutions.

Chapter 6 presents sample solutions for divergence and elastic lift distribution of composite wings. For the composite wings, solutions are given for the case of forward aerodynamic sweep. Brief comparisons are made with alternate solutions available for these problems.

Chapter 7 demonstrates solutions for flutter instabilities of both isotropic and composite wings. The isotropic wing flutter solutions are compared with known analytical solutions.

A brief summary and recommendations for additional research are given in Chapter 8.

Chapter 2

Hybrid State Vector Equations

A GENERAL FORMULATION of the structural equations will be presented which casts them into a state vector form involving a coupled system of first order differential equations. The state vector that appears in the following derivations will be termed a *hybrid* state vector in the sense that it is derived from a so-called *mixed* formulation involving both stress and displacement variables. Although this formulation is not entirely new to structural mechanics, it has not seen extensive use, nor has it been included among the everyday tools of most engineers working in structures and structural dynamics. However, some very noteworthy developments of improved numerical procedures based on mixed formulations combined with finite-difference solutions have been reported by Noor, Stephens, and Fulton [7]. Additional work presented by Noor and Stephens [8,9] has further demonstrated both the simplicity and high accuracy of such mixed formulation procedures. Results obtained by Stroud and Mayers [10] indicate that a numerical solution based upon direct application of a mixed variational principle also offers superior accuracy and convergence, especially for bending-moment solutions. More recently, investigations by Steele [11], Steele *et al.* [12], and Steele and Barry [13] have indicated that mixed state vector formulations of the differential equations in conjunction with asymptotic solutions can be advantageous for both analytical

investigation and numerical calculation. The present investigation will demonstrate that a simple and highly accurate numerical solution procedure is obtained by combining the mixed state vector formulation of the structural differential equations with an integrating matrix solution approach. It is worth noting that the transfer matrix method of structural solution also employs a mixed state vector similar to the one used in the following formulations.

The derivations to be presented employ a mixed variational formulation that can be consistently applied to a broad class of structural problems. This formulation, which will be discussed in Section 2.1, involves terms that are expressible as a product of generalized stresses and strains in addition to other terms that can be related to the complementary energy. For systems with linear stress-strain behavior, the complementary energy is, of course, the same as the strain energy. Therefore, in the context of linear systems, this formulation is equivalent to the more usual stationary potential energy approach. As will be demonstrated, the mixed variational formulation provides a convenient way of expressing the energy functional and allows a direct determination of the state vector equations in a desirable form.

There are also many classical structural problems for which differential equations already exist. In these instances, it may be convenient to recast these equations into a matrix form directly and dispense with the formality of rederiving them. As many readers are well aware, it is possible to take higher order differential equations and convert them to an equivalent system of first order equations. But this process becomes increasingly difficult as the complexity of the system increases. Regardless of how one chooses to obtain the differential equations describing a structural problem, there is a preferred way to write the state vector equivalent. The preferred state vector form will be shown to arise naturally from a mixed variational formulation. As will be discussed in more detail in later sections, the mixed (hybrid) state vector form of the equations, with fundamental unknowns consisting of both

generalized force and displacement parameters, will possess a natural decomposition that proves quite useful for numerical solutions.

The equation derivations that follow will be presented in matrix notation. The primary advantage of matrix notation is that it allows a consistent treatment of problems with differing size and complexity. Furthermore, it is anticipated that the equation formulation will lead directly to a numerical algorithm that must necessarily deal with the matrix terminology of discretized systems. An additional reason for adhering to matrix notation is that several intermediate points exist at which further analytical formulation and simplification can be put aside in favor of numerical computation. If a matrix formulation is used throughout, it is easy to begin numerical calculations at these intermediate points.

2.1 Variational Formulation of State Vector Equations

A mixed variational formulation is presented here for the hybrid state vector equations that describe structural equilibrium. For the interested reader, some rather general examples of mixed variational statements can be found, for instance, in Nemat-Nasser [14]. Also, brief historical accounts of mixed variational methods in solid mechanics appear in both Nemat-Nasser [15] and Reissner [16]. In these accounts, the work of a number of investigators is cited, including the work of authors such as Hellinger, Reissner, and Washizu. In the literature in general, the mixed variational formulation involving independent variation of both stress and displacement variables is usually referred to as a Reissner (or sometimes Hellinger-Reissner) formulation, whereas the principle involving independent variation of stress, displacement, and strain is often referred to as a Hellinger-Reissner-Washizu formulation. In the work presented here, the development of the mixed state vector equations is based upon the formulation of Reissner [17] in which stress and displacement variables are independently varied to yield the appropriate equations

and boundary conditions. A similar development of mixed state vector equations from the Reissner formulation is given in Ref. [11].

Although the Reissner formulation is applicable to either linear or nonlinear problems, the following presentation will restrict consideration to the solution of linear aeroelastic and structural dynamic equations. From nonlinear equations, it is often feasible to obtain a set of linearized equations by perturbing about an appropriate nonlinear solution. This might be useful, for example, when considering problems with geometric nonlinearities. The linear perturbation equations obtained by such an approach fall within the scope of the following linear analyses. When considering future extensions of the present work to nonlinear analyses, it is anticipated that the Reissner principle should prove valuable for problems with nonlinear material behavior. Some important illustrations of the application of the Reissner principle to problems involving nonlinear material behavior are given by Nimmer and Mayers [18] and Anderson and Mayers [19].

For those problems that can be described by a single spatial variable, x , the mixed variational formulation can be written in general terms as

$$\delta \int_0^{\ell} \mathcal{U}(x, t, \mathbf{y}(x, t), \mathbf{y}'(x, t)) dx = 0 \quad (2.1)$$

where the prime on \mathbf{y} indicates partial differentiation with respect to x only. The Euler-Lagrange equations resulting from variation on x are

$$-\frac{d}{dx} \frac{\partial \mathcal{U}}{\partial \mathbf{y}'} + \frac{\partial \mathcal{U}}{\partial \mathbf{y}} = 0. \quad (2.2)$$

Since the variation is being taken only with respect to the spatial variable, the time variable simply follows along as a parameter. For static problems, time disappears from the previous equations.

The next step in the formulation is to give an appropriate form of the functional appearing in Eqs. (2.1–2.2). When linearity is invoked, it is then possible to express

the functional in the following convenient form:

$$U = \mathbf{y}'^T \mathbf{D} \mathbf{y} - \frac{1}{2} \mathbf{y}^T \mathbf{K} \mathbf{y} + \mathbf{p}^T \mathbf{y} \quad (2.3)$$

where \mathbf{K} is a spatially variable symmetric matrix containing structural relations, \mathbf{p} contains the external loads, and \mathbf{D} is defined such that $(\mathbf{D} - \mathbf{D}^T)$ is a constant skew-symmetric matrix with unit elements.

The state vector, \mathbf{y} , is specified in the form

$$\mathbf{y} = \{\mathbf{y}_F \quad \mathbf{y}_D\}^T \quad (2.4)$$

where \mathbf{y}_F are generalized forces and \mathbf{y}_D are generalized displacements. This form for \mathbf{y} is the same as would appear in a transfer matrix structural solution based upon a "mixed" finite element force-displacement relationship. The precise nature of the matrix terms appearing in the above representation of the functional will be clarified with specific examples.

Next, substituting Eq. (2.3) into Eq. (2.2) and performing the indicated differentiation yields the equilibrium equations

$$-\mathbf{J} \mathbf{y}' - \mathbf{K} \mathbf{y} + \mathbf{p} = 0 \quad (2.5)$$

in which

$$\mathbf{J} = \mathbf{D} - \mathbf{D}^T = \begin{bmatrix} \mathbf{0} & -\mathbf{I} \\ \mathbf{I} & \mathbf{0} \end{bmatrix}. \quad (2.6)$$

Noticing that

$$\mathbf{J}^{-1} = \mathbf{J}^T = -\mathbf{J} \quad \text{and hence} \quad \mathbf{J}^T \mathbf{J} = \mathbf{I}, \quad (2.7)$$

Eq. (2.5) can be rewritten in the standard state vector form

$$\mathbf{y}' = \mathbf{Z} \mathbf{y} - \mathbf{s} \quad (2.8)$$

where

$$\mathbf{Z} = \mathbf{JK} \quad \text{and} \quad \mathbf{a} = \mathbf{Jp}. \quad (2.9)$$

Eq. (2.8) will be the starting point for analyses to be presented in later chapters.

Rather than using the procedure demonstrated above, Eq. (2.5) and corresponding boundary conditions can also be obtained by substituting Eq. (2.3) into Eq. (2.1) and applying integration by parts. The consistent boundary conditions obtained with this approach are one of the key advantages of a variational development. Corresponding to the state vector equations in Eq. (2.8), the boundary conditions are obtained as

$$\mathbf{y}^T \mathbf{D}^T (\delta \mathbf{y}) \Big|_0^L = 0. \quad (2.10)$$

Fortunately, in the state vector formulation, these boundary conditions always remain quite simple. This will prove to be especially advantageous when dealing with anisotropic structures, for which other formulations can yield coupled and considerably more complicated forms of the boundary conditions.

At this point, a simple example describing the lateral bending deflection of a beam will help to clarify the nature of the matrix terms appearing in the foregoing derivation. The example presented here follows an example given by Steele [11] for a Timoshenko beam. In the notation used in this study, the functional in Eq. (2.3) can be written for a Timoshenko beam in the form

$$U = M_x \left(\gamma' - \frac{1}{2} (EI)^{-1} M_x \right) + V_x \left(\gamma + w' - \frac{1}{2} \beta_s V_x \right) - pw \quad (2.11)$$

where the moment resultant is M_x ; the transverse shear resultant is V_x ; the rotation of the normal is γ ; the normal displacement is w ; the shear compliance is β_s ; and the load per unit length is p . Prime, of course, denotes differentiation with respect

to x . In order to obtain a resemblance to the expression in Eq. (2.3), Eq. (2.11) can be rewritten as

$$U = M_x \gamma' + V_x w' - \frac{1}{2} \left((EI)^{-1} M_x^2 + \beta_s V_x^2 - 2V_x \gamma \right) - pw. \quad (2.12)$$

For linear systems, this functional can be constructed by subtracting the complementary energy from the product of stresses and strains, after which a slight rearrangement yields Eq. (2.12). Also note that the nature of U , as used in this presentation, implies that it has been obtained by integrating an energy density functional over the cross section of the beam.

If the state vector is now defined as

$$\mathbf{y} = \{M_x \quad V_x \quad \gamma \quad w\}^T \quad (2.13)$$

then \mathbf{p} , \mathbf{D} , and \mathbf{K} in Eq. (2.3) take on the forms

$$\mathbf{p} = \{0 \quad 0 \quad 0 \quad -p\}^T \quad (2.14)$$

$$\mathbf{D} = \begin{bmatrix} 0 & 0 & 0 & 0 \\ 0 & 0 & 0 & 0 \\ 1 & 0 & 0 & 0 \\ 0 & 1 & 0 & 0 \end{bmatrix} \quad (2.15)$$

$$\mathbf{K} = \begin{bmatrix} (EI)^{-1} & 0 & 0 & 0 \\ 0 & \beta_s & -1 & 0 \\ 0 & -1 & 0 & 0 \\ 0 & 0 & 0 & 0 \end{bmatrix}. \quad (2.16)$$

The procedure for arriving at this form of the matrix equations first involves specifying the state vector, \mathbf{y} , which is taken to be the same vector as would be

obtained in a *mixed*, or *hybrid* force-displacement formulation of the equilibrium equations. Such a formulation is discussed, for example, in Chapter 2 of McGuire and Gallagher [20]. This state vector form is also the same as that used in the *transfer matrix* format of structural analysis. It is assumed here, as shown in Eq. (2.4), that \mathbf{y} will always be partitioned into two sets; one set contains generalized forces and the other contains generalized displacements. Once the state vector is specified in this way, then \mathbf{p} is chosen so that one obtains the proper potential of the external loads.

After choosing the state vector, then \mathbf{D} must be determined such that the derivative terms in the functional are given by the first group on the right hand side of Eq. (2.3). This requirement is met by specifying that \mathbf{D} always be a square matrix having the same form as that given in Eq. (2.15); that is, it should have the same structure as Eq. (2.15) and should always contain only zero and unit terms. One can refer to Eq. (2.6) to see that \mathbf{D} must be specified in this way to insure that \mathbf{J} be an antisymmetric matrix with unit elements. If \mathbf{J} is as shown in Eq. (2.6), then Eq. (2.5) and Eq. (2.8) are said to have a *symplectic* character. The symplectic nature of these equations means that an especially simple relationship will exist between the fundamental solution of the system in Eq. (2.8) and its adjoint (see Eq. (G.17) in Appendix G). For a description of this useful property of symplectic systems, refer to page 157 of Bryson and Ho [21].

Other remaining terms in the functional are now determined by specifying \mathbf{K} , which is restricted to be a symmetric matrix. The elements of \mathbf{K} contain spatially dependent constitutive terms and fixed structural kinematic relationships. It is usually easy to determine the elements of \mathbf{K} by simple observation.

Having determined \mathbf{y} , \mathbf{p} , \mathbf{D} , and \mathbf{K} as just discussed, it is then clear that \mathbf{a} and \mathbf{z} in Eq. (2.9) become

$$\mathbf{a} = \{0 \quad p \quad 0 \quad 0\}^T, \quad (2.17)$$

$$\mathbf{Z} = \begin{bmatrix} 0 & 1 & 0 & 0 \\ 0 & 0 & 0 & 0 \\ (EI)^{-1} & 0 & 0 & 0 \\ 0 & \beta_e & -1 & 0 \end{bmatrix}. \quad (2.18)$$

It should be noted that the right hand side of Eq. (2.18) displays a particular form that will show up again, even for much more complicated problems than the one discussed above. As mentioned in the introduction to this chapter, for many simple problems it is not necessary to follow through the complete equation derivation as just presented. In fact, once one becomes familiar with the matrix formulation given here, it is usually easy to write down Eq. (2.18) directly, at least for relatively simple systems. However, for considerably more complicated situations, the variational approach provides a consistent method for formulating equilibrium equations and boundary conditions. In addition, the mixed variational formulation also demonstrates a "natural" form of the state vector equations. Later, Section 4.2 will show that this natural form, when coupled with an integrating matrix solution procedure, provides significant savings in the numerical solution by allowing convenient analytical simplification. One should also keep in mind that with knowledge of the natural form of the equations it is possible to recast equations derived by other methods. To give one example, the nonlinear equations of an initially bent and twisted rod derived in Chapter 18 of Love [22] and examined by Ojalvo and Newman [23] can be linearized and recast into the desired form. In fact, a similar approach has been followed by Nitzsche [24] to obtain hybrid state vector equations for the aeroelastic analysis of vertical axis wind turbines.

2.2 Aeroelastic and Structural Dynamic Equations

The general equations presented in the previous section can be specialized to both aeroelastic and structural dynamic problems by being more specific about the type of loading. For both aeroelastic and dynamic problems the loading can be related in some way to the displacements of the structure (i.e., the displacement states of the structural state vector). In static aeroelastic problems the airloads are directly determined by the deformed shape of the structure, whereas in dynamic problems, the inertial, aerodynamic, and structural damping loads are related to time rates of change of the structural deformation. The discussion in this section will focus on the way in which these loads appear in the structural equilibrium equations, and the form of the equations to be used in later analyses will be given.

First, static aeroelastic problems will be analyzed by the usual procedure of breaking the total external loads acting on the system into a summation of those loads that act on a rigid structure plus perturbation loads due to elastic deformation. Therefore, the loads vector \mathbf{a} , which first appeared in Eq. (2.8), can be rewritten as

$$\mathbf{a} = q\mathbf{A}\mathbf{y} + \mathbf{a}_r \quad (2.19)$$

where \mathbf{a}_r is a vector of the nonhomogeneous loads acting on a rigid structure, q is the dynamic pressure, and \mathbf{A} is developed from an aerodynamic influence relationship. In fact, for the discrete version of these equations, \mathbf{A} contains terms from an inverse aerodynamic influence matrix. Additionally, if \mathbf{A} is partitioned corresponding to the force and displacement subsets of the state vector, only one of its submatrices contains nonzero elements, namely, that submatrix providing forces due to displacement. Although one can make use of various aerodynamic theories to calculate \mathbf{A} , the analyses of Chapters 5–7 will primarily use aerodynamic strip theory.

The static aeroelastic equations are now obtained by substituting Eq. (2.19) into Eq. (2.8). The result is

$$\mathbf{y}' = \mathbf{Z}\mathbf{y} - q\mathbf{A}\mathbf{y} - \mathbf{a}_r, \quad (2.20)$$

with $\mathbf{y} = \mathbf{y}(x)$. When the dynamic pressure is specified, then Eq. (2.20) is simply a system of equations for \mathbf{y} . On the other hand, if the nonhomogeneous term \mathbf{a}_r is set to zero and the dynamic pressure is left unspecified, then Eq. (2.20) leads to a divergence eigenvalue problem, with q being the divergence dynamic pressure.

Now consider a dynamic aeroelastic system. The airloads still depend in some way on the displacements, but now time has entered the equations. Furthermore, inertia loads, and possibly damping loads, must be included in the analysis; as mentioned earlier these are also related in some way to the displacement. The approach taken here will be to remove the differential time dependence of the dynamic equations by Laplace transformation on time, thereby obtaining equations with an algebraic dependence on the Laplace variable, s . This has an added advantage for unsteady aeroelastic problems since the unsteady aerodynamic terms for general motion are conveniently described in the Laplace domain.

After Laplace transformation, one finds that the homogeneous state vector equations suitable for aeroelastic stability analysis can be written in the form

$$\frac{d}{dx}\hat{\mathbf{y}} = \mathbf{Z}\hat{\mathbf{y}} + s^2\mathbf{M}\hat{\mathbf{y}} + s\mathbf{C}\hat{\mathbf{y}} - \mathbf{Q}(s, q)\hat{\mathbf{y}} \quad (2.21)$$

where $\hat{\mathbf{y}} = \hat{\mathbf{y}}(x, s)$ and the matrices \mathbf{M} , \mathbf{C} , and \mathbf{Q} contain, respectively, the mass, damping, and unsteady aerodynamic terms. (The hat symbol denotes a Laplace transformed variable). As mentioned for the static aeroelastic problem in Eq. (2.20), the matrices expressing any form of displacement dependent loading (here, \mathbf{M} , \mathbf{C} , and \mathbf{Q}) have only one nonzero partition, namely, the partition that multiplies the displacements in the state vector.

In order to specialize Eq. (2.21) to free vibration analysis, neglect the damping and aerodynamic terms, \mathbf{C} and \mathbf{Q} . For undamped vibration, the Laplace variable s is purely imaginary. Therefore, if one takes $s = j\omega$, then the free vibration counterpart of Eq. (2.21) is given by

$$\frac{d}{dx}\hat{\mathbf{y}} = \mathbf{Z}\hat{\mathbf{y}} - \omega^2\mathbf{M}\hat{\mathbf{y}}. \quad (2.22)$$

Clearly, dynamic response problems in the time domain can also be accommodated by including forcing terms on the right hand sides of the time domain versions of Eqs. (2.21) and (2.22).

2.3 Anisotropic Beam Equations

A simplified anisotropic plate-beam model is presented here for which the resulting equations are suitable for analyzing aeroelastic phenomena of large aspect ratio lifting surfaces. The purpose for developing these equations is twofold: first, they will help clarify the application of the foregoing general formulation and second, these equations will later be used in numerical examples of aeroelastic analyses. The assumptions used in developing the equations for the plate-beam model will be discussed briefly here, but it should be noted that they are similar to those employed by Weisshaar [4,5] to describe laminated composite box beam lifting surfaces. As a consequence, the following equations will be specialized somewhat to deal with structures whose anisotropic behavior arises due to laminated composite construction. A summary of composite plate lamination theory is presented in Appendix C; for a more detailed development, however, the reader can refer to Chapter 4 of the text by Jones [25].

With the aid of the cartesian coordinate system presented for the lifting surface model in Fig. 1, the aeroelastic equations will be developed for aerodynamic strip

sections taken normal to the structural reference axis. The structural reference axis is specified to be coincident with the x -axis, also shown in Fig. 1. Primarily for reasons of convenience, it will be assumed that this reference axis coincides with the geometric middle surface of the structural box. Although the reference axis location is arbitrary, this particular choice follows the conventions used for development of the composite plate constitutive relations. For this study, it is assumed that the structural reference axis is a straight line which, of course, will be swept accordingly as the wing aerodynamic sweep angle, Λ , changes. When considering aerodynamic surfaces with structural axis curvature, then the present approach should be adapted to take this curvature into account. It is further assumed that no appreciable chordwise deformation occurs in cross sections normal to the structural reference axis, so that wing deformation is only a function of the spanwise coordinate, x . Applying these assumptions means that the deformation of the plate-beam model can be represented in terms of a bending deflection $w(y)$, positive downward, of the reference axis, plus a rotation $\alpha(y)$, positive nose-up, about this axis. For problems dealing with rotating beams, an additional displacement variable u , along the x -axis, must be added to describe the deformation. In the presentation given here, bending deformation in the x - y plane is neglected. This lead-lag deformation can be easily added, however, in a more detailed analysis.

As the next step, the in-plane strains and curvatures can be written in terms of the foregoing displacement variables by applying the differential relationships that describe strain-displacement for a plate (see Appendix C). But first, an additional remark concerning shearing deformations should be made. Since standard lamination theory assumes no transverse shearing effects, this assumption will be adhered to here, but only for the composite laminate. That is, the shearing deformation of the laminated portion of the structure will be assumed negligible, but the gross shearing behavior of the overall structure can still be included. For instance,

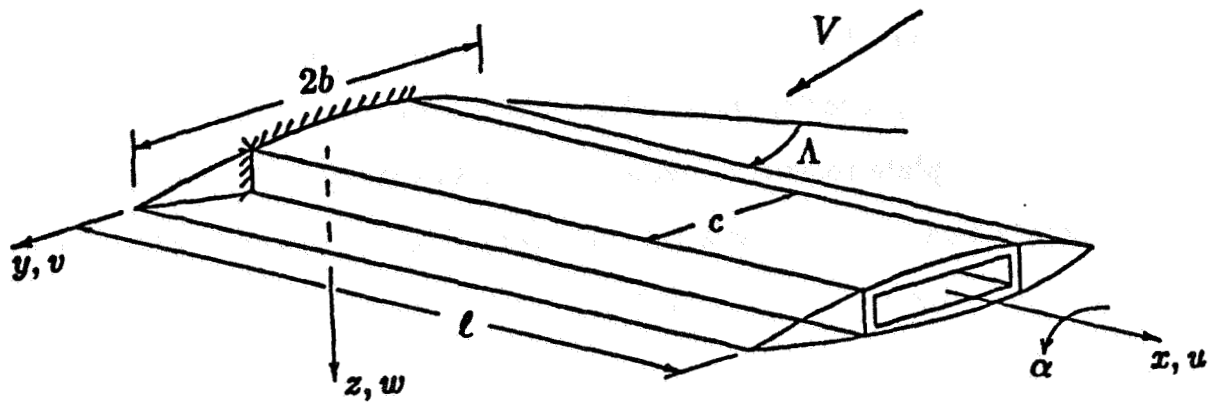


Fig. 1. Lifting Surface Model

standard composite structure fabrication quite often employs thin laminated face sheets placed over shear webs or a thick deformable core material. The transverse shearing effects induced by the webs or the core material can be included by adding a shearing energy to the energy functional. The transverse shear effects included here are assumed to arise in this manner. At the same time, it can reasonably be assumed that the composite cover sheets carry most of the bending stresses (and bending energy) of the structure.

Before introducing the preceding assumptions explicitly, the functional in the form specified by both Eq. (2.1) and Eq. (2.3) can be expressed in general terms for a composite plate as

$$\begin{aligned}
u = \int_{-c/2}^{c/2} & \left[\mathbf{n}^T \boldsymbol{\epsilon}^0 + \mathbf{m}^T \boldsymbol{\kappa} - \frac{1}{2} (\mathbf{n}^T \mathbf{A}^* \mathbf{n} + \mathbf{n}^T \mathbf{B}^* \mathbf{m} + \mathbf{m}^T \mathbf{B}^* \mathbf{n} + \mathbf{m}^T \mathbf{D}^* \mathbf{m} \right. \\
& \left. + \beta_s V_x^2 - 2V_x \gamma) \right] dy - p_u u - p_\gamma \gamma - p_w w - p_\alpha \alpha
\end{aligned} \tag{2.23}$$

where an integration is to be performed over the chord length of the structural box. The composite plate compliance matrices \mathbf{A}^* , \mathbf{B}^* , and \mathbf{D}^* are developed in Appendix C. Also found in the same appendix are descriptions of the resultant stress and moment vectors \mathbf{n} and \mathbf{m} , respectively. Note that the transverse shear, V_x , has been included in Eq. (2.23) along with a transverse shear compliance term, β_s . The variable γ represents rotation of the normal to the neutral axis measured with respect to its initially undeformed position. In the absence of shearing deformation, it is assumed that normals remain normal so that γ is equal in magnitude to the slope of the neutral axis.

By introducing the assumption that the primary stresses are those that occur in the spanwise direction due to bending and axial stretching, the stress and moment resultants can be approximated as

$$\mathbf{n} = \{N_x \quad 0 \quad 0\}^T, \quad \mathbf{m} = \{M_x \quad 0 \quad M_{xy}\}^T. \tag{2.24}$$

Furthermore, considering the deformation assumptions discussed earlier in this section, the midplane strains and bending curvatures can be approximated by

$$\boldsymbol{\epsilon}^0 = \{u'_0 \quad 0 \quad 0\}^T, \quad \boldsymbol{\kappa} = \{(\gamma' + y\alpha'') \quad 0 \quad 2\alpha'\}^T, \tag{2.25}$$

where the prime denotes differentiation with respect to x . All of the variables in Eq. (2.25) are assumed to be functions of x only. Next, substituting Eqs. (2.24–2.25) into Eq. (2.23) and performing the indicated integration yields an expression from which the state vector and other terms appearing in Eq. (2.3) can be readily defined.

The resulting state vector is

$$\mathbf{y} = \{ \underline{N}_x \quad \underline{M}_x \quad \underline{V}_x \quad 2\underline{M}_{xy} \quad u \quad \gamma \quad w \quad \alpha \}^T, \quad (2.26)$$

with

$$\underline{N}_x = cN_x, \quad \underline{M}_x = cM_x, \quad \underline{V}_x = cV_x, \quad \underline{M}_{xy} = cM_{xy}. \quad (2.27)$$

Having defined the state vector in this way, the differential equations can be determined by the approach laid down in Section 2.1.

It is convenient at this point to introduce a nondimensionalized version of the resulting anisotropic beam equations. The nondimensional differential equations, in the form of Eq. (2.8), can be written as

$$\frac{d}{dx} \begin{Bmatrix} \underline{N}_x \\ \underline{M}_x \\ \underline{V}_x \\ 2\underline{M}_{xy} \\ u \\ \gamma \\ w \\ \alpha \end{Bmatrix} = \begin{bmatrix} 0 & 0 & 0 & 0 & 0 & 0 & 0 & 0 \\ 0 & 0 & 1 & 0 & 0 & 0 & 0 & 0 \\ 0 & 0 & 0 & 0 & 0 & 0 & 0 & 0 \\ 0 & 0 & 0 & 0 & 0 & 0 & 0 & 0 \\ \bar{A}_{11}^* & \bar{B}_{11}^* & 0 & \bar{B}_{13}^* & 0 & 0 & 0 & 0 \\ \bar{B}_{11}^* & \bar{D}_{11}^* & 0 & \bar{D}_{13}^* & 0 & 0 & 0 & 0 \\ 0 & 0 & \bar{S}^* & 0 & 0 & -1 & 0 & 0 \\ \bar{B}_{13}^* & \bar{D}_{13}^* & 0 & \bar{D}_{33}^* & 0 & 0 & 0 & 0 \end{bmatrix} \begin{Bmatrix} \underline{N}_x \\ \underline{M}_x \\ \underline{V}_x \\ 2\underline{M}_{xy} \\ u \\ \gamma \\ w \\ \alpha \end{Bmatrix} - \begin{Bmatrix} \bar{p}_u \\ \bar{p}_\gamma \\ \bar{p}_w \\ \bar{p}_\alpha \\ 0 \\ 0 \\ 0 \\ 0 \end{Bmatrix} \quad (2.28)$$

where the nondimensional coordinate and displacement variables are

$$\bar{x} = \frac{x}{\ell}, \quad \bar{u} = \frac{u}{\ell}, \quad \bar{w} = \frac{w}{\ell}. \quad (2.29)$$

It is also convenient to define

$$(EI)_R = c_R D_{11R}, \quad \text{and} \quad (GJ)_R = 4c_R D_{33R}, \quad (2.30)$$

which are the reference values of bending and torsional stiffness in terms of the appropriate composite stiffnesses derived in Appendix C. (The subscript R designates a reference value.) In terms of the reference bending stiffness, other nondimensional parameters appearing in Eq. (2.28) are the force and moment resultants and external loads

$$\begin{aligned} N_x &= \frac{c\ell^2 N_x}{(EI)_R}, & \bar{M}_x &= \frac{c\ell M_x}{(EI)_R}, & V_x &= \frac{c\ell^2 V_x}{(EI)_R}, & \bar{M}_{xy} &= \frac{c\ell M_{xy}}{(EI)_R}, \\ \bar{p}_u &= \frac{\ell^3 p_u}{(EI)_R}, & \bar{p}_\gamma &= \frac{\ell^2 p_\gamma}{(EI)_R}, & \bar{p}_w &= \frac{\ell^3 p_w}{(EI)_R}, & \bar{p}_\alpha &= \frac{\ell^2 p_\alpha}{(EI)_R}, \end{aligned} \quad (2.31)$$

and the nondimensional composite compliances

$$\begin{aligned} \bar{A}_{11}^* &= \frac{(EI)_R A_{11}^*}{c\ell^2}, & \bar{B}_{11}^* &= \frac{(EI)_R B_{11}^*}{c\ell}, & \bar{B}_{13}^* &= \frac{(EI)_R B_{13}^*}{2c\ell}, \\ \bar{D}_{11}^* &= \frac{(EI)_R D_{11}^*}{c}, & \bar{D}_{13}^* &= \frac{(EI)_R D_{13}^*}{2c}, & \bar{D}_{33}^* &= \frac{(EI)_R D_{33}^*}{4c}, \end{aligned} \quad (2.32)$$

and finally, the nondimensional shear compliance

$$\bar{S}^* = \frac{(EI)_R \beta_s}{\ell^2}. \quad (2.33)$$

It should be noted that the state vector equations presented in Eq. (2.28) are easily extended to both static and dynamic aeroelastic analyses by adopting the approach of Section 2.2 in which the load terms (i.e., inertia, damping, and aerodynamic) are expressed in terms of the displacement states of the structural state vector. The nondimensionalization of the load terms remains the same as that given in Eq. (2.31). Further use will be made of Eq. (2.28) when examining

aeroelastic behavior of composite lifting surfaces in Chapters 6 and 7. As a final observation about the anisotropic equations presented here, the equivalent equations representing isotropic structures can be obtained by simply replacing the composite compliance terms by isotropic compliances.

Chapter 3

Integrating and Differentiating Matrices

AN INTEGRATING MATRIX approach will now be developed to solve the state vector equations derived in Chapter 2. The solution of such equations can often be a difficult task since these equations, with their boundary conditions, take the form of two-point boundary value problems. Additional complexity is added for those equations that have nonconstant coefficients. By necessity, one is forced to consider numerical solutions since analytical approaches can be exceedingly difficult, if not impossible, for all but the simplest of cases. The primary objective of this chapter is to discuss the development of integrating matrices, which provide the basis for a simple and efficient concept for numerically solving two-point boundary value problems. Applications of the integrating matrix to the solution of differential equations will be considered in the next chapter. It is hoped that the discussions here will lend some perspective to the integrating matrix concept as a general numerical tool.

In Section 3.1, a general derivation is presented for integrating matrices that are suited to the integration of continuous functions. A new type of maximum precision integrating matrix that is developed from orthogonal polynomials will also be introduced. Some methods are discussed in Section 3.2 for applying continuous integrating matrices to the piecewise integration of discontinuous functions. Finally,

Section 3.3 discusses some of the aspects of a related topic, differentiating matrices.

Although numerical solution by an integrating matrix procedure is not an entirely new idea, this approach has seen relatively little attention and development compared to other well known numerical tools such as finite element and finite difference. In fact, only a handful of investigators have contributed to the integrating matrix method. One of the first applications of the integrating matrix method to problems in structural mechanics was presented in Russia by Vakhitov [26]. In this country, Hunter [27] is credited with much of the initial development of the integrating matrix procedure. As mentioned by Hunter, however, an integrating matrix was also used by Spector [28] to simply evaluate the integrals of an asymptotic "integral series" solution for nonuniform beam vibration. Other major contributions to the application of integrating matrices (including nonlinear problems) have been made by White and Malatino [29] and Kvaternik, White, and Kaza [30,31]. Most of their analyses were for vibration and stability of rotating beams. Vakhitov [32] has also employed integrating matrices for a circular plate analysis, while Levashov [33-35] has used integrating and differentiating matrices in the context of a generalized Ritz method. And recently, Lakin [36] has made useful contributions to the formulation of integrating matrices for arbitrarily spaced grid points.

Despite the fact that most of the applications in this work will be confined to structural mechanics, the developments in this chapter are quite general and can be applied to problems in other areas as well. It is interesting to note that the integrating matrix technique can often be closely related to discretization methods used in other areas of research. To pick a single example out of many, one could reexamine the spline series solutions used by Schneider and Reddy [37] to solve for optimal nonlinear thrust vector controls for guidance of an atmospheric interceptor. This problem can be solved in essentially the same manner with an integrating matrix formulation, where the integrating matrices are developed from the appropriate

spline approximations. Many parallels can also be drawn with the finite element method. In fact, the integrating matrix approach can be considered as a special type of collocation finite element method. The presentation given here, however, will differ from the formalism of the usual finite element approach.

As mentioned by Hunter [27], the integrating matrix also provides a useful tool for initial value calculations. Furthermore, the integrating matrix method is applicable in either linear or nonlinear situations. In the applications to be considered here, the focus will be on linear boundary value problems.

3.1 Integrating Matrices for Continuous Integrands

This section presents the basic development of the integrating matrix. As a preliminary requirement, it is assumed that the functions to be integrated are a continuous function of the spatial variable. More specifically, the integrating matrix development will be based upon integration of continuous polynomials that approximate the functional behavior of the structural state variables. The requirement of continuity, however, does not prove to be a restriction on the solution of more general problems. As will be shown in the next section, integrating matrices can be developed for piecewise continuous functions by extending the results presented here for continuous functions. With piecewise continuous functions, solutions are obtainable for almost any practical problem.

First, a review will be given of the fundamental theory of the integrating matrix. This review will be independent of a specific polynomial approximation. The viewpoint presented here will parallel the presentations given by both Hunter [27] and Lakin [36], in which it is assumed that the function to be integrated can be represented by a polynomial of given degree. Appendix A specializes this fundamental presentation to the case of integrating matrices based upon Jacobi

polynomials.

It should be noted that it is possible to derive many different types of integrating matrices, with each type dependent upon the form of approximation employed. One can easily formulate special purpose integrating matrices intended for a specific application. In this respect, the integrating matrix approach is very similar to finite element procedures that use element types suited to a given problem.

The primary objective of the integrating matrix approach is to develop a numerical procedure for performing indefinite integrations. In contrast with initial value integration schemes, which are commonly used for solving differential equations, the integrating matrix is formulated instead from a numerical quadrature. A quadrature is simply a numerical integration rule for integrating between fixed limits. An integrating matrix developed from such a quadrature rule is especially suited to solving boundary value problems since the region of integration is fixed by the boundaries. As pointed out by Hunter [27], however, the integrating matrix is just as easily applied to initial value problems.

To begin, let $f(x)$ be a continuous function on an interval $[a, b]$. In addition, suppose that a discrete set of $N + 1$ grid points, x_0, x_1, \dots, x_N , has been chosen on this interval such that

$$a = x_0 < x_1 < \dots < x_N = b, \quad (3.1)$$

and let the function values at these points be given by

$$f_i = f(x_i). \quad (3.2)$$

In general, the points x_i can have either equal spacing or unequal spacing; ultimately, this will be determined by the nature of the approximations used for $f(x)$. Furthermore, the number of points chosen is somewhat arbitrary, but for an n th

degree polynomial approximation to $f(x)$ there must be at least $n + 1$ grid points, where $n \leq N$. The $N + 1$ grid points on $[a, b]$ determine N subintervals $[x_i, x_{i+1}]$ ($i = 0, \dots, N - 1$). In general, a consecutive set of $n + 1$ grid points will be designated by the sequence $x_m, x_{m+1}, \dots, x_{m+n}$, where the subscript m denotes the starting grid point for the sequence.

Assuming that $f(x)$ can be approximated by an n th degree polynomial, then an approximation to $f(x)$ on any subinterval $[x_i, x_{i+1}]$ can be obtained in terms of the values $f_i = f(x_i)$ given for a consecutive set of $n + 1$ grid points containing that subinterval. An appropriate approximation to $f(x)$ can be obtained by any of several different approaches, but the most useful methods include interpolation, spline fitting, and least-squares fitting. In the work presented here, only the interpolation method will be discussed in detail. If any type of approximate data is involved, however, a least-squares approximation would be preferable. Lakin [36] presents a nice discussion of the least-squares approach as applied to the determination of integrating matrices.

By integrating the approximation to $f(x)$ over any subinterval and arranging the result as a linear combination of the f_i 's, one obtains a convenient numerical description of the integration. For a typical subinterval on $[a, b]$ this would appear as

$$\int_{x_i}^{x_{i+1}} f(x) dx \approx [w_{im}f_m + w_{im+1}f_{m+1} + \dots + w_{im+n}f_{m+n}] \quad (3.3)$$

where the w 's are weighting terms that arise from integrating the approximation to $f(x)$. An approximation to $\int_a^b f(x) dx$ is now easily obtained by noting that $\int_a^b f(x) dx$ can be written as a sum of the integrations for each of the N subintervals. That is,

$$\int_a^b f(x) dx = \left\{ \int_{x_0}^{x_1} + \int_{x_1}^{x_2} + \dots + \int_{x_{N-1}}^{x_N} \right\} f(x) dx. \quad (3.4)$$

The integrating matrix representation for the approximate integration of $f(x)$ contains the same information as expressed in Eqs. (3.3–3.4), but puts it in a compact matrix notation suitable for matrix manipulation. First, define the column vectors $\{\mathcal{F}\}$ and $\{f\}$ by

$$\{\mathcal{F}\} = \left(0, \int_{x_0}^{x_1} f(x) dx, \int_{x_1}^{x_2} f(x) dx, \dots, \int_{x_{N-1}}^{x_N} f(x) dx \right)^T \quad (3.5)$$

and

$$\{f\} = (f_0, f_1, \dots, f_N)^T. \quad (3.6)$$

With these definitions, the integral in Eq. (3.3) can be expressed for all subintervals in the matrix notation

$$\{\mathcal{F}\} = \mathcal{W}_n \{f\}, \quad (3.7)$$

where the subscript n indicates the degree of the polynomial used to approximate $f(x)$. \mathcal{W}_n is an $(N+1) \times (N+1)$ weighting matrix. Since the first element of $\{\mathcal{F}\}$ is zero, the first row of \mathcal{W} contains only zeros.

A summation of the subinterval integrations can now be formally obtained by premultiplying both sides of Eq. (3.7) by an $(N+1) \times (N+1)$ lower-triangular summing matrix,

$$\mathcal{S} = \begin{bmatrix} 1 & 0 & \dots & 0 \\ 1 & 1 & \dots & 0 \\ \vdots & \vdots & & \vdots \\ 1 & 1 & \dots & 1 \end{bmatrix}, \quad (3.8)$$

for which $S_{ij} = 1$ when $i \geq j$ but $S_{ij} = 0$ if $i < j$. As a result of this summing operation, if $\{\mathcal{F}\}$ is defined to be the the $N+1$ dimensional column vector,

$$\{\mathcal{F}\} = \left(0, \int_{x_0}^{x_1} f(x) dx, \int_{x_0}^{x_2} f(x) dx, \dots, \int_{x_0}^{x_N} f(x) dx \right)^T, \quad (3.9)$$

then the integrating matrix relationship can be written as

$$\{\mathcal{F}\} = \mathbf{L}\{f\} \quad (3.10)$$

where the integrating matrix \mathbf{L} is defined by

$$\mathbf{L} = \mathbf{S}\mathcal{W}_n. \quad (3.11)$$

Incidentally, the summation indicated by \mathbf{S} is most easily carried out in practice by simple summing, rather than by matrix multiplication.

As can be seen from Eq. (3.11), the derivation of the integrating matrix \mathbf{L} relies primarily on the determination of \mathcal{W}_n in Eq. (3.7) because the summing matrix \mathbf{S} is known a priori. It is important to note that the integrating matrix depends on the polynomial approximation employed and on the number and spacing of the grid points, but it does not depend on the function values f_i at the grid points. Therefore, the integrating matrix has a separation of grid dependence and function dependence. Furthermore, the integrating matrix can now be viewed as a linear matrix operator that performs integrations via a simple matrix multiplication.

Although the foregoing discussion has presented the general procedure to be followed in deriving an integrating matrix, it is now worthwhile to focus a bit more closely on integrating matrices that can be derived from orthogonal polynomials. Traditionally, orthogonal polynomials have been used as a foundation for well-conditioned numerical procedures. The motivation for deriving integrating matrices based upon orthogonal polynomials actually stems from the fact that orthogonal polynomials form the basis for high accuracy quadrature rules of the Gaussian type (cf. Section 5.4 of the text by Conte and de Boor [38]). For these Gaussian integration rules, the function to be integrated can be written as a product of a sufficiently smooth function $g(x)$ and a nonnegative integrable weighting function

$\vartheta(x)$. That is, the integral of $f(x)$ over (a, b) is put into the form

$$\int_a^b f(x) dx = \int_a^b g(x) \vartheta(x) dx \quad (3.12)$$

where

$$g(x) = \frac{f(x)}{\vartheta(x)}. \quad (3.13)$$

As shown in Section 5.4 of Conte and de Boor [38] and Section 7.1 of Krylov [39], a quadrature of the highest possible precision for a given number of grid points is obtained when the polynomial approximation to $g(x)$ is orthogonal to the weight function $\vartheta(x)$ over the interval (a, b) . In addition, the nodes (grid points) are specified to be the zeroes of the appropriate orthogonal polynomial. These nodes are nonevenly spaced and are all inside of the end points a and b .

But to be useful for the development of integrating matrices, the concept of an "optimal" quadrature must be extended one step further to allow nodes to be located exactly at the end points of an interval. The requirement for end point nodes becomes obvious when considering boundary value problems; these problems require that boundary conditions be satisfied precisely at the end points of the interval. The basic theory for the development of optimal quadratures having preassigned nodal locations is discussed in detail in Chapter 9 of Krylov [39], therefore, it will not be discussed in depth here. One point worth noting, however, is that fixed nodes at the end points give rise to a special weighting function, $\vartheta(x)$. This natural weighting function is a result of end point terms that appear in the interpolation of $f(x)$.

Because of the form of the weighting function that arises when end points of an interval are included, certain members of the Jacobi polynomial family turn out to be the appropriate orthogonal polynomials to use in deriving optimal quadratures. For this reason, the resulting integrating matrices will be referred to simply as "Jacobi" integrating matrices. Appendix A contains a detailed discussion of the

calculation procedure for Jacobi integrating matrices and Appendix B tabulates the corresponding weighting matrices up to $n + 1 = 10$. To give an idea of the accuracy of the quadrature on which these integrating matrices are based, all polynomials of degree $\leq 2n - 1$ will be integrated exactly.

For convenient use in later calculations, weighting matrices tabulated originally by Hunter [27] are also repeated in Appendix B. The corresponding integrating matrices are referred to as "Newton" integrating matrices since they are developed from Newton forward difference interpolating formulas. Some additional Lagrange and least-squares integrating matrices not listed here are tabulated by Lakin [36].

The Lagrange integrating matrices discussed by Lakin are somewhat related to the Jacobi matrices described above since both originate from Lagrange interpolations, which are valid for unequal grid point intervals. As noted by Lakin, however, the Lagrange integrating matrices are somewhat cumbersome to numerically compute for grid spacings chosen on an ad hoc basis. In contrast, however, the computation of Jacobi matrices is a much simpler numerical task. It turns out that Jacobi integrating matrices can be calculated by a procedure that is in many respects similar to the procedure presented by Lakin for least-squares fitting based on orthogonal polynomials. In fact, if the least-squares fit procedure is applied to the Jacobi grid points for an approximating polynomial of the maximum degree (i.e., the same degree used for an interpolation), then the least-squares procedure yields the Jacobi integrating matrix. A nice feature of the Jacobi integrating matrices is that optimal grid point locations are determined automatically by the underlying quadrature rule.

There are some other features of Jacobi integrating matrices that differ from Newton and Lagrange integrating matrices. The first of these differences arises because of the unequal grid point spacing. In the calculation of Newton matrices

for instance, the interpolations over a subinterval $[x_i, x_{i+1}]$ are performed by roving polynomials. That is, a polynomial of degree n , which makes use of $n+1$ consecutive grid points, can be shifted along the interval of $N+1$ grid points, one point at a time. This is possible, of course, because the Newton matrices are based on equal grid point spacings. For the interpolations required by the Jacobi integrating matrices, however, the unequal subinterval lengths mandate the use of a stationary polynomial. Because of the use of stationary polynomials, the Jacobi integrating matrices are in some respects analogous to high order, polynomial-based finite elements. That is, a Jacobi "element" corresponds to $n+1$ consecutive grid points and has $n-1$ unequally spaced internal nodes. The complete interval $[a, b]$ can be constructed by placing so-called Jacobi "elements" end to end. Experimentation with the Jacobi matrices reveals that the highest numerical efficiency is obtained by using a small number of "elements" of high order. This is in accord with results for finite element and other numerical approximation techniques.

A second aspect of a Jacobi integrating matrix (or any other type of integrating matrix with unequal intervals) is that interpolation may be required if one desires solution results at points other than the grid points. This is a fairly simple process, however, since interpolation shape functions are easily developed for the Jacobi polynomials. These shape functions are presented in Appendix A. Again, these shape functions are analogous to shape functions commonly used in finite element analysis.

Regardless of the type of integrating matrix, some very useful information can be obtained by investigating the quadrature rule on which the integrating matrix is based. The quadrature rule consists of the weighting terms that are applied to the integrand at each of the grid points. To be specific, the quadrature rule for the integral

$$\int_a^b f(x) dx \approx [w_a f_a + \cdots + w_b f_b] \quad (3.14)$$

simply consists of the w 's and the corresponding x_i 's. The w 's, which are the primary values of interest, are contained in the last row of the integrating matrix. These quadrature weights, of course, can also be obtained by summing each of the terms in a column of the weighting matrix W .

An examination of the underlying quadrature can often lead to a better understanding of the nature of a particular integrating matrix. For example, for the Jacobi weighting matrices given in Appendix B, the grid points are arranged symmetrically on the normalized interval $[-1, 1]$ and the quadrature weights (obtained by summing the columns) are all positive numbers that steadily increase in value as one approaches the midpoint of the interval. The values of the weight terms are also symmetric about the midpoint of the interval. But the important revelation is that the quadrature rule associated with Jacobi integrating matrices turns out to be the same as a well known numerical integration method, Lobatto quadrature. In fact, the numerical calculations for the Jacobi weighting matrices in Appendix B were verified by comparing the quadrature weights with those tabulated for Lobatto integration on page 920 of Abramowitz and Stegun [40].

An aspect of Newton integrating matrices that became apparent during this investigation was a possible asymmetry of the underlying quadrature. This phenomenon, which was also noted by Lakin [36], is referred to as "biasing." Biasing only arises when using interpolating polynomials for which the number of interpolation points, $n + 1$, is an odd number. The reason that biasing occurs for odd $n + 1$ is that away from the end points the interpolating polynomials cannot be centered on the subintervals $[x_i, x_{i+1}]$ that are being interpolated. When biasing is present, integrating matrices corresponding to Newton forward difference formulas differ from those derived from backward difference formulas. When $n + 1$ is even, there is

no biasing and both forward difference and backward difference formulations yield identical integrating matrices. When using the Newton integrating matrices, it is generally convenient to employ those matrices that are not biased (i.e., based upon \mathcal{W}_n with $n + 1$ even). It is interesting to note, however, that there is an easy way to symmetrize a biased Newton integrating matrix. Essentially, one develops a weighting matrix from one-half the sum of forward difference and backward difference weighting matrices. This is conveniently illustrated by taking a particular example that considers a quadratic Newton weighting matrix written for five grid points. By expressing the weighting matrix as a sum of forward and backward difference matrices, we have

$$\mathcal{W}_2 = \frac{1}{2}(\mathcal{W}_{2,f} + \mathcal{W}_{2,b}) \quad (3.15)$$

where the subscripts f and b refer, respectively, to forward and backward differencing. Equation (3.15) expands into (see Appendix B)

$$\begin{aligned} \mathcal{W}_2 &= \frac{1}{2} \left(\frac{h}{12} \right) \left\{ \begin{bmatrix} 0 & 0 & 0 & 0 & 0 \\ 5 & 8 & -1 & 0 & 0 \\ 0 & 5 & 8 & -1 & 0 \\ 0 & 0 & 5 & 8 & -1 \\ 0 & 0 & -1 & 8 & 5 \\ \hline 5 & 13 & 11 & 15 & 4 \end{bmatrix} + \begin{bmatrix} 0 & 0 & 0 & 0 & 0 \\ 5 & 8 & -1 & 0 & 0 \\ -1 & 8 & 5 & 0 & 0 \\ 0 & -1 & 8 & 5 & 0 \\ 0 & 0 & -1 & 8 & 5 \\ \hline 4 & 15 & 11 & 13 & 5 \end{bmatrix} \right\} \\ &= \left(\frac{h}{24} \right) \begin{bmatrix} 0 & 0 & 0 & 0 & 0 \\ 10 & 16 & -2 & 0 & 0 \\ -1 & 13 & 13 & -1 & 0 \\ 0 & -1 & 13 & 13 & -1 \\ 0 & 0 & -2 & 16 & 10 \\ \hline 9 & 28 & 22 & 28 & 9 \end{bmatrix} \end{aligned} \quad (3.16)$$

where the values below the horizontal bar in each matrix represent the quadrature weights. As can be seen, the final weighting matrix in Eq. (3.16) yields a symmetric quadrature. An interesting comparison can be made with the equivalent nonbiased

cubic Newton weighting matrix. It appears as

$$w_3 = \left(\frac{h}{24} \right) \begin{bmatrix} 0 & 0 & 0 & 0 & 0 \\ 9 & 19 & -5 & 1 & 0 \\ -1 & 13 & 13 & -1 & 0 \\ 0 & -1 & 13 & 13 & -1 \\ 0 & 1 & -5 & 19 & 9 \\ \hline 8 & 32 & 16 & 32 & 8 \end{bmatrix}. \quad (3.17)$$

The similarity of the interior matrix elements between Eq. (3.17) and the last expression in Eq. (3.16) indicates that the symmetrized, nonbiased quadratic matrix will approach the accuracy of the cubic matrix. Obviously, error cancellation inherent in the summing of forward and backward difference formulations is responsible for the accuracy increase.

Also, rough comparisons between integrating matrices can be made based upon the quadrature rules. For instance, the Newton integrating matrices, in contrast with Jacobi integrating matrices, have quadrature weights that can oscillate considerably as one proceeds along the interval of integration. This oscillation tends to increase somewhat for the higher order Newton integrating matrices. This basic difference between the underlying quadratures for Newton and Jacobi integrating matrices can manifest itself in both accuracy and convergence properties. This will be discussed again in later chapters when comparisons are made between Newton and Jacobi solutions. It should be noted, however, that Newton and Jacobi matrices are identical for the quadratic approximation. For higher order approximations, their properties and relative accuracies differ. Although both types of integrating matrices provide very good solution accuracies, it has been found that Jacobi matrices are capable of offering faster, more predictable convergence and higher accuracy with fewer grid points.

3.2 Integrating Matrices for Discontinuous Integrands

Aided by the developments of the previous section, it is now straight forward to determine appropriate weighting matrices and integrating matrices for systems with discontinuous parameters. Basically, there are two types of discontinuities that occur often in static structural analysis and structural vibration. The first of these discontinuities stems from stepwise changes in coefficient terms of the differential equations. Such stepwise discontinuities could easily be the result of changes in stiffness or mass parameters. Appropriately, these discontinuities are best described by step functions. Methods for handling this type of discontinuity will be considered in this section. The methods discussed here for treating stepwise discontinuous systems are similar in some respects to the methods described by Vakhitov [26].

A second type of discontinuity results from point loading. Point loads can arise from either applied external loads or inertia loads associated with point masses. Point loads are most easily handled by introducing impulse functions. Since impulse functions are to be treated by an approach different from that for step functions, the methods for including concentrated loads in an analysis are taken up in Appendix E rather than this section.

The treatment of a problem with stepwise discontinuities is straightforward. The solution interval is simply divided up into analytic regions by breaking the integration at points of discontinuity. For each of these separate regions a different (or the same) weighting matrix can be used. An integrating matrix for the complete solution interval is then obtained in the normal way by summing the weighting matrix terms for each of the piecewise regions. This summation procedure is identical with the one carried out by the summing matrix S in Eq. (3.11). The only difference in forming the integrating matrix for stepwise discontinuous systems is that the weighting matrix \mathcal{W} for the complete solution interval has a block matrix

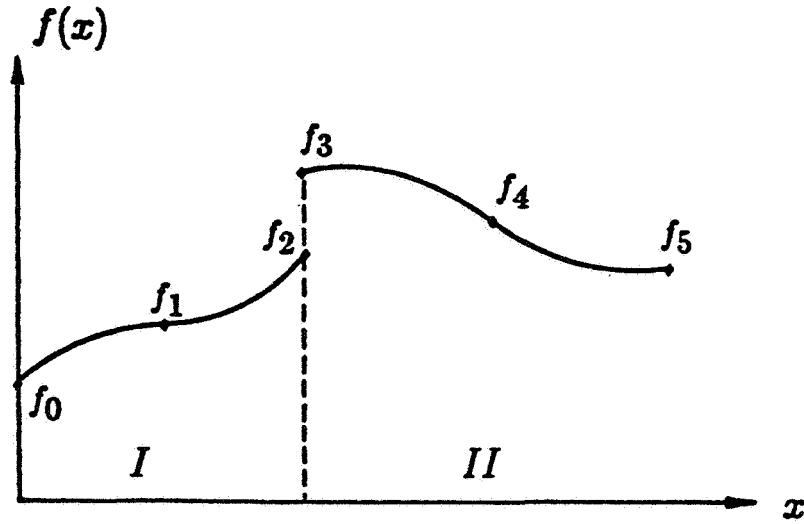


Fig. 2. Typical integration regions for a discontinuous function

structure, where each of the blocks corresponds to a normal weighting matrix written for one of the analytic regions.

Perhaps a simple example best explains the procedure to be applied to discontinuous functions. Consider integrating a function that has a single point of discontinuity, as shown in Fig. 2. The integration of the discontinuous function can clearly be broken into the two distinct integrations indicated by the regions *I* and *II*. For this particular example, which assumes weighting matrices with end point nodes, the equivalent of Eq. (3.7) can be written as

$$\{f\} = \begin{bmatrix} \mathcal{W}_I & 0 \\ 0 & \mathcal{W}_{II} \end{bmatrix} \begin{Bmatrix} f_I \\ f_{II} \end{Bmatrix} = \mathcal{W}_{I+II} f. \quad (3.18)$$

Here, as in Eq. (3.11), the resulting integrating matrix can be calculated from

$$\mathbf{L} = \mathcal{S} \mathcal{W}_{I+II}. \quad (3.19)$$

In Eq. (3.18), it should be noted that the "merged" weighting matrix has no overlap of rows or columns between the individual matrices for each region.

Note in Fig. 2 that two distinct function values have been defined at the discontinuous point, each corresponding to the appropriate function value an infinitesimal distance away from the discontinuity. These identically located points occur for the case in which the weighting matrices on either side of the discontinuity make use of grid points located at the end points of an interval. Strictly speaking, it is not mandatory that one have grid points at the discontinuity, unless, of course, boundary conditions or loads must be applied at such a point. For instance, an interior region of a multiple region integration might make use of weighting matrices based on Gauss-Legendre quadrature, which does not require grid points at the ends of an interval (see Appendix B). Regardless of whether or not grid points are located at discontinuities in the integrand, the continuity of the integration assures that solutions will be continuous.

Another feature that can be accommodated in much the same fashion as a stepwise discontinuity in integration is either a change in step size or a change in integrating matrix type within a solution interval. Grid points are fixed, of course, for weighting matrices based on orthogonal polynomials, but can be variable for constant step size matrices like the Newton integrating matrices. It is quite easy to switch to different types of integrating matrices to satisfy particular solution requirements for portions of a solution interval. The method for handling a discontinuous integration arising from integrating matrix changes or step size changes is very much similar to the method employed for discontinuous system parameters.

When compared to the discontinuous problem in Eq. (3.18), changes in either step size or integrating matrix type lead to a slightly different way of adding the *local* weighting matrices into the *global* weighting matrix. If weighting matrices with different step sizes (or even with the same step sizes) are merged to integrate a larger region, there will be some "overlap" between weighting values for the merged matrices. This is true for weighting matrices that use end point nodes as well as

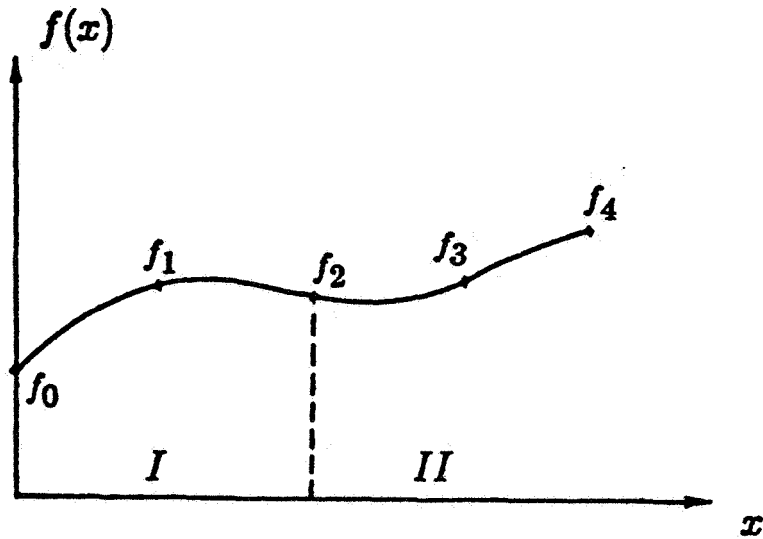


Fig. 3. Typical regions for piecewise integration of a continuous function

those that do not. The "overlap" shows up in the global weighting matrix as an overlapping of some of the rows and columns of adjoining matrix blocks. Again, a specific example easily demonstrates the procedure. Consider the five grid point, two region integration shown in Fig. 3. For the sake of illustration, second degree Newton weighting matrices having equal step sizes will be employed in both regions *I* and *II*. Furthermore, the the step size is conveniently chosen such that the constant step size factor $h/12$ has the value of unity. (See Appendix B.) With these specifications, the equivalent of Eq. (3.7) becomes

$$\{\mathcal{F}\} = \begin{bmatrix} 0 & 0 & 0 & & \\ 5 & 8 & -1 & & \\ -1 & 8 & 5 & 0 & 0 \\ & 5 & 8 & -1 & \\ & -1 & 8 & 5 & \end{bmatrix} \begin{Bmatrix} f_0 \\ f_1 \\ f_2 \\ f_3 \\ f_4 \end{Bmatrix} . \quad (3.20)$$

For this specific example, it can be seen that the region *I* and region *II* submatrices overlap by one row and one column.

In the integrating matrix method, the process of merging weighting matrices is analogous to the merging of stiffness matrices in the finite element method. In fact, by considering the different situations that can arise in connection with discontinuous integrations, it is possible to write down a simple set of rules describing how weighting matrices should be merged. To be able to give a consistent set of rules for weighting matrices with and without end point nodes, one basic requirement must be met. This requirement simply stipulates that weighting matrices without end point nodes must conform to weighting matrices with end point nodes. An example of a conforming Gauss-Legendre weighting matrix is given in Appendix B. It should be noted too that the merging process is carried out by starting at one boundary of the solution interval and proceeding with consecutive piecewise regions in the direction of integration.

The rules for merging weighting matrices at points of continuous or discontinuous system coefficients can be considered separately. First, for discontinuous parameter systems we have the following requirements for merging at a point of discontinuity:

1. If both adjacent matrices have end point nodes, there will be no row or column overlap (e.g., Eq. (3.18)).
2. If one of the adjacent matrices has end point nodes and the other does not, there will be one row and one column of overlap.
3. If neither of the adjacent matrices have end point nodes, there will be one row of overlap and two columns of overlap.

For continuous parameter systems, the following rules for merging apply at any point within the solution interval:

1. If either or both of the adjacent matrices have end point nodes, there will be one row and one column of overlap (e.g., Eq. (3.20)).
2. If neither of the adjacent matrices have end points, there will be two rows and two columns of overlap.

Any of the above merging rules can be easily checked by taking a sample problem and examining the subinterval integrations, as demonstrated, for example, in Eq. (3.20). Since the merged weighting matrices only specify the subinterval integrations, the logical conclusion of the merging process is in the determination of the corresponding integrating matrix from Eq. (3.11). From the standpoint of numerical calculation, the merging rules can be applied during the summing process that forms the integrating matrix from the weighting matrix.

3.3 Differentiating Matrices

Similar to the idea of an integrating matrix, there is also a differentiating matrix. The differentiating matrix expresses the derivative of a function in terms of the function values at a discrete set of points. Usually, a differentiating matrix is determined by differentiating an interpolating polynomial, just as the integrating matrix is determined by integrating that same polynomial. It is also feasible to use simple differencing to calculate a differentiating matrix.

Differentiating matrices, in fact, are quite common in finite element applications. For instance, the strain-displacement relationships in a finite element analysis are usually written in terms of a differentiating matrix determined by differentiating the displacement shape functions. The papers by Levashov [33–35] show how a combination of both differentiating matrix and integrating matrix concepts can be used to solve structural problems by the displacement method. For the integrating matrix approach as presented here, one rarely has to resort to using differentiating matrices. Nonetheless, the differentiating matrix proves to be a useful tool in certain circumstances and is worthy of mention.

With the state vector formulation of the aeroelastic equations given in Chapter 2, it is normally possible to write the structural portion of the equations without

need for a differentiating matrix. To express certain descriptions of the aerodynamic loads, however, higher derivatives of some of the structural state variables may be required. In such a situation, the differentiating matrix provides a convenient way of writing these higher derivatives in terms of existing state variables. A similar situation can exist when writing the "preload" terms for a structure with initial curvature. In this latter case though, it appears that it's usually possible to rewrite the equations in such a way that the use of a differentiating matrix is avoided.

A variety of differentiating matrices can be calculated depending on the type of interpolating polynomial assumed. Methods for calculating differentiating matrices are quite straight forward since one simply determines derivative expressions for the approximating polynomials. Detailed calculations will not be presented here for differentiating matrices; however, some precalculated formulas do exist for derivatives of certain types of interpolations. For example, expressions for the derivatives of Newton forward difference interpolation formulas, which form the basis for the Newton integrating matrices, can be found on page 883 of Abramowitz and Stegun [40]. Also tabulated there are similar expressions for the derivatives of Lagrange's interpolation formula, which is useful for approximating functions with nonuniform grid spacings. And finally, differentiating matrices corresponding to Jacobi integrating matrices can be calculated by differentiating the shape functions presented in Appendix A. The finite series expansion for the Jacobi polynomials presented in that appendix should prove useful in obtaining the proper derivative expressions.

Chapter 4

Integrating Matrix Solution of State Vector Equations

INTEGRATING MATRICES PROVIDE a convenient and efficient method for solving two-point boundary value problems. The prime concern is the solution of the aeroelastic and structural dynamic equations presented in Chapter 2. The major focus of this chapter is on the formulation of discrete solutions for these equations when they are represented in state vector form. Other important issues that are discussed include methods for manipulating and reducing the discrete state vector equations to a suitable form for numerical solution.

A direct approach that does not require the calculation of influence matrices will be presented for formulating linear systems of equations and eigenvalue problems. It also turns out that the integrating matrix solutions to be discussed are closely related to alternate solutions in terms of transition matrices. In fact, the integrating matrix provides one of the easiest means for numerically calculating transition matrices. Furthermore, with the aid of a transition matrix, one can in turn calculate symmetric stiffness influence matrices for the types of problems considered in this chapter. Although the transition matrix approach will not be discussed here, it is presented briefly in Appendix G. Many of the ideas contained in this chapter can be used in connection with transition matrix calculations.

As will be evident to those familiar with approximate solution techniques, the integrating matrix approach belongs to a class of collocation solution methods. Since collocation solutions belong to the more general family of methods known as weighted residual methods, it is possible, in fact, to formalize the integrating matrix approach in much the same way that finite element methods are formalized. For the sake of simplicity, however, the following presentations will employ a more intuitive approach.

Collocation solutions are conveniently classified by Collatz [41] (also, Meirovitch [42]) according to the nature of the approximating functions. Within this classification scheme, the integrating matrix approach presented here falls into the category of a mixed method. That is, the approximating functions initially satisfy neither the differential equations nor the boundary conditions of the problem. (Other categories stipulate that the functions must initially satisfy either the boundary conditions or the differential equations.) Solutions with the mixed method are obtained by insisting that at selected collocation grid points the boundary conditions, or differential equations, as appropriate, are satisfied exactly. From the discussions of chapter 3, it should be clear that the arrangement of collocation grid points, as well as the approximating functions, are specified by the choice of integrating matrix.

A general advantage that collocation methods have over some other methods lies in the ease with which coefficient matrices can be generated for the approximate equations. As will be shown, the integrating matrix approach provides a very simple way of obtaining the matrix equations that describe a particular set of differential equations. In addition, if these differential equations are in state vector form, it is often possible, at least for linear problems, to take advantage of the structure of the state vector equations to further simplify the corresponding matrix equations.

There is, however, a disadvantage to collocation type approaches. Namely, the matrices involved are always nonsymmetric, thereby requiring less efficient

solution routines. But in many instances, this disadvantage is entirely offset by the simplicity of the approach. Furthermore, since the integrating matrix method easily accommodates very high order approximating functions, one often finds a considerable reduction in problem size for a required solution accuracy.

4.1 Discretized State Vector Equations

To obtain a discretized form of the state vector equations, it is convenient to consider a particular example problem. A suitable choice is Eq. (2.20), which can be used to describe aeroelastic response for a one dimensional structure. Although this equation is intended primarily for static aeroelastic response, with appropriate generalization it encompasses other types of equations, including dynamic equations like Eq. (2.21) and Eq. (2.22). To make the results generally applicable, it is assumed that Eq. (2.20) can be expressed in a nondimensional form so that it appears as

$$\mathbf{y}' = \mathbf{Z}\mathbf{y} - \lambda\mathbf{A}\mathbf{y} - \mathbf{a}_r \quad (4.1)$$

where λ represents a nondimensional parameter. For homogeneous problems, which are obtained by dropping the nonhomogeneous term \mathbf{a}_r , the parameter λ is to be taken as an eigenvalue. In the sample problems to be presented later, more precise definitions will be given for the terms appearing in Eq. (4.1), but for now it is convenient to use them simply as generic terms. In what follows, the state vector \mathbf{y} in Eq. (4.1) will be referred to as a *local* state vector.

Since Eq. (4.1) must be valid for any value of the spatial coordinate, it can be written at a discrete set of $N + 1$ points along the desired solution interval. In this discrete form it can be expressed as

$$\tilde{\mathbf{y}}' = \tilde{\mathbf{Z}}\tilde{\mathbf{y}} - \lambda\tilde{\mathbf{A}}\tilde{\mathbf{y}} - \tilde{\mathbf{a}}_r \quad (4.2)$$

The discrete version of the state vector, $\bar{\mathbf{y}}$, will be referred to as a *global* state vector. Note that the dimension of $\bar{\mathbf{y}}$ will be $NS(N + 1)$, where NS refers to the number of states in the local state vector. The ordering of components in the global state vector is actually arbitrary, but it turns out to be very useful in what follows to specify a particular ordering. It will be assumed that the global state vector is ordered such that its structure is the same as that of \mathbf{y} . More precisely, it is partitioned into generalized force and generalized displacement subsets as was done for the local vector \mathbf{y} in Eq. (2.4), and furthermore, the discrete set of values for a particular state variable are grouped together. This will be clearly demonstrated in the sample problems of Chapter 5.

With the aforementioned ordering in mind, a global version of the integrating matrix, $\tilde{\mathbf{L}}$, can now be applied as a matrix operator to both sides of Eq. (4.2). The result is

$$\dot{\bar{\mathbf{y}}} = \tilde{\mathbf{L}}\dot{\bar{\mathbf{z}}}\bar{\mathbf{y}} - \lambda\tilde{\mathbf{L}}\tilde{\mathbf{A}}\bar{\mathbf{y}} - \tilde{\mathbf{L}}\tilde{\mathbf{a}}_r + \tilde{\mathbf{k}} \quad (4.3)$$

where $\tilde{\mathbf{k}}$ is a constant vector of integration to be determined from boundary conditions. Note that the effect of applying the integrating matrix to the isolated derivative term on the left-hand side of Eq. (4.2) was simply to integrate that term and thus remove the derivative. Integrating matrices on the right-hand side of Eq. (4.3) perform their integration function through a matrix multiplication.

The global integrating matrix in Eq. (4.3) is a block diagonal matrix that appears as

$$\tilde{\mathbf{L}} = \begin{bmatrix} \mathbf{L} & & \\ & \ddots & \\ & & \mathbf{L} \end{bmatrix} \quad (4.4)$$

with each block being a standard $(N + 1) \times (N + 1)$ integrating matrix as derived in the previous chapter. The appropriate number of matrix blocks on the diagonal

is determined by the number of state variables, NS, in the local state vector. In essence, the integrating matrix allows one to proceed in much the same manner as solving a simple integrable equation by analytical methods. But with the numerical integration properties of the integrating matrix, it is now possible to deal with otherwise difficult integrations in a very simple manner.

At this point, Eq. (4.3) provides a matrix equation from which one can obtain a solution of the state vector differential equations. The only remaining step is to determine $\tilde{\mathbf{k}}$ from specified boundary conditions. And once $\tilde{\mathbf{k}}$ is known, there remains only a linear systems solution if considering the nonhomogeneous problem, or a matrix eigenvalue solution if considering the related homogeneous problem.

For two-point boundary value problems, it is useful to introduce the boundary condition matrices \mathbf{B}_0 and \mathbf{B}_n . These boundary condition matrices, which relate to homogeneous boundary conditions, will aid in solving for $\tilde{\mathbf{k}}$. \mathbf{B}_0 and \mathbf{B}_n can be written as

$$\mathbf{B}_0 = \tilde{\mathbf{1}}\mathbf{b}_0^T \quad (4.5)$$

and

$$\mathbf{B}_n = \tilde{\mathbf{1}}\mathbf{b}_n^T \quad (4.6)$$

where $\tilde{\mathbf{1}}$ is a column vector containing all unit terms. The vectors \mathbf{b}_0 and \mathbf{b}_n can be expressed as

$$\mathbf{b}_0^T = \{1, 0, \dots, 0\} \quad (4.7)$$

and

$$\mathbf{b}_n^T = \{0, \dots, 0, 1\}. \quad (4.8)$$

The dimensions of \mathbf{B}_0 and \mathbf{B}_n are $(N+1) \times (N+1)$, the same as a normal integrating matrix. Also, since the first row of the integrating matrix contains only zeroes, one has that $\mathbf{B}_0 \mathbf{L} = \mathbf{0}$.

Corresponding to the global block diagonal integrating matrix $\tilde{\mathbf{L}}$, there is a similar block diagonal boundary condition matrix, $\tilde{\mathbf{B}}$. For a two-point boundary value problem, each matrix block on the diagonal of $\tilde{\mathbf{B}}$ is specified by applying either \mathbf{B}_0 or \mathbf{B}_n (or equivalently, \mathbf{b}_0^T or \mathbf{b}_n^T) to the corresponding state variable and solving for its constant vector of integration. This process will be clearly demonstrated in the examples of Chapter 5. Since \mathbf{b}_0^T and \mathbf{b}_n^T contain mostly zero elements, along with a strategically located unit term, their operational effect on a discrete state vector is to select the "degree of freedom" at which a boundary condition is to be applied.

In addition to the homogeneous boundary condition matrix $\tilde{\mathbf{B}}$, one can define $\tilde{\mathbf{B}}_{nh}$ to account for nonhomogeneous boundary conditions that can be written in terms of the state variables. The specific form of $\tilde{\mathbf{B}}_{nh}$ has to be determined for each particular problem, but one should note that for many common problems it is simply zero. When $\tilde{\mathbf{B}}_{nh}$ does need to be determined, it is defined in such a way that when it premultiplies the global state vector, it produces the required nonhomogeneous boundary terms. Similar to the situation for $\tilde{\mathbf{B}}$, $\tilde{\mathbf{B}}_{nh}$ will consist mainly of zeroes, but will have a few strategically located nonzero terms. The nonzero terms in $\tilde{\mathbf{B}}_{nh}$, however, are not usually unit terms as was required for $\tilde{\mathbf{B}}$.

With the foregoing definition of boundary condition matrices, a general expression can be obtained for the solution of $\tilde{\mathbf{k}}$. To obtain this expression, Eq. (4.3) is first multiplied through by $\tilde{\mathbf{B}}$. Since $\tilde{\mathbf{B}}$ has been defined for homogeneous boundary conditions, we have that $\tilde{\mathbf{B}}\tilde{\mathbf{y}} = \mathbf{0}$. Furthermore, the form of $\tilde{\mathbf{k}}$ is specified to be such that $\tilde{\mathbf{B}}\tilde{\mathbf{k}} = \tilde{\mathbf{k}}$. With these two identities, and with the aid of the nonhomogeneous boundary term $\tilde{\mathbf{B}}_{nh}\tilde{\mathbf{y}}$, one obtains from Eq. (4.3) the general result

$$\tilde{\mathbf{k}} = -\tilde{\mathbf{B}}\tilde{\mathbf{L}}(\tilde{\mathbf{Z}}\tilde{\mathbf{y}} - \lambda\tilde{\mathbf{A}}\tilde{\mathbf{y}} - \tilde{\mathbf{a}}_r) - \tilde{\mathbf{B}}_{nh}\tilde{\mathbf{y}} \quad (4.9)$$

where it can be noted that $\tilde{\mathbf{k}}$ consists of both homogeneous and nonhomogeneous components. For nonhomogeneous boundary terms that express displacement dependent loads, it is often possible to rewrite these terms in such a way that they can be included in $\tilde{\mathbf{A}}$ rather than $\tilde{\mathbf{B}}_{nh}$. The advantage in doing this will be discussed in the next section.

Having now determined a general expression for $\tilde{\mathbf{k}}$, the next step is to obtain a suitable matrix equation that can be solved by standard methods. This is easily achieved by substituting the expression for $\tilde{\mathbf{k}}$ from Eq. (4.9) into Eq. (4.3). Grouping similar terms and then rearranging leads to

$$[\mathbf{H} - \lambda\mathbf{F}\tilde{\mathbf{A}}]\tilde{\mathbf{y}} = \mathbf{f} \quad (4.10)$$

where

$$\mathbf{H} = \mathbf{I} + \tilde{\mathbf{B}}_{nh} + \mathbf{F}\tilde{\mathbf{Z}} \quad (4.11)$$

$$\mathbf{F} = [\tilde{\mathbf{B}} - \mathbf{I}]\tilde{\mathbf{L}} \quad (4.12)$$

$$\mathbf{f} = \mathbf{F}\tilde{\mathbf{a}}_r, \quad (4.13)$$

with \mathbf{I} being an identity matrix with appropriate dimensions. It is obvious that Eq. (4.10) represents a system of linear equations when λ is specified and when the nonhomogeneous external load term, \mathbf{f} , is nonzero. If \mathbf{f} is zero, then Eq. (4.10) provides a matrix eigenvalue problem. Furthermore, if one chooses to give different interpretations to $\lambda\tilde{\mathbf{A}}$, then Eq. (4.10) encompasses a broad range of aeroelastic, vibration, and structural problems. For instance, the free vibration and unsteady aeroelastic problems described by Eqs. (2.21–2.22) are manipulated into similar forms after application of the integrating matrix. More precise definitions for several

types of problems will be given in the following sections and in the example solutions of Chapters 5, 6, and 7.

It is possible to stop at this point and numerically solve Eq. (4.10) with standard methods. To do so, however, requires the solution of matrix equations with twice the number of necessary variables. As mentioned previously, the global state vector, $\tilde{\mathbf{y}}$, is partitioned into both force and displacement variables, $\tilde{\mathbf{y}}_F$ and $\tilde{\mathbf{y}}_D$, similar to Eq. (2.4). The next section will show that by applying matrix partitioning techniques one can conveniently reduce the solution of Eq. (4.10) to an equivalent problem written solely in terms of the displacement variables $\tilde{\mathbf{y}}_D$.

4.2 State Vector Equation Reduction

By partitioning the matrices in Eq. (4.10) according to the force and displacement states of the global state vector, it is possible to achieve an analytical reduction of the matrix equations such that only displacement variables are involved in the final solution. As will be shown, the reduction task is greatly simplified due to the structure of the state vector equations developed in Section 2.1.

Writing out the partitioned form of the matrices appearing in Eq. (4.10) reveals that

$$\mathbf{H} = \begin{bmatrix} \mathbf{H}_{FF} & \mathbf{H}_{FD} \\ \mathbf{H}_{DF} & \mathbf{H}_{DD} \end{bmatrix} \quad (4.14)$$

$$\tilde{\mathbf{A}} = \begin{bmatrix} \mathbf{0} & \mathbf{A}_{FD} \\ \mathbf{0} & \mathbf{0} \end{bmatrix} \quad (4.15)$$

$$\mathbf{F} = \begin{bmatrix} \mathbf{F}_{FF} & \mathbf{0} \\ \mathbf{0} & \mathbf{F}_{DD} \end{bmatrix} \quad (4.16)$$

and

$$\mathbf{f} = \begin{Bmatrix} \mathbf{F}_{FF} \tilde{\mathbf{a}}_F \\ \mathbf{0} \end{Bmatrix} \quad (4.17)$$

First of all, it should be noted that the \mathbf{H} matrix contains structural related terms, including elastic restraint boundary terms that arise from $\tilde{\mathbf{B}}_{nh}$. The \mathbf{H}_{FD} submatrix consists of these elastic restraint terms as well as "geometric stiffness" terms for problems involving initial structural curvature and deformation dependent "preloads." As mentioned in connection with nonhomogeneous boundary terms in the previous section, it is often possible to shift terms that appear in \mathbf{H}_{FD} so that instead they can be included in \mathbf{A}_{FD} . This can be easily done, for example, for the centrifugal stiffening term that appears in rotating beam problems. The motivation for rearranging in this way is to zero out the \mathbf{H}_{FD} submatrix. If $\mathbf{H}_{FD} = 0$, the reduction process is considerably simplified, as will be indicated in what follows. For problems without nonhomogeneous boundary terms and without geometric nonlinearities, \mathbf{H}_{FD} is automatically zero.

Other matrices and vectors appearing in Eqs. (4.15–4.17), such as $\tilde{\mathbf{A}}$ and \mathbf{f} , have the indicated forms because of the natural structure of the state vector equations derived in Section 2.1. For instance, since $\tilde{\mathbf{A}}$ contains only displacement dependent load terms, the only nonzero partition is given by \mathbf{A}_{FD} , which is the submatrix that expresses loads in terms of the displacement variables. \mathbf{F} , on the other hand, is a block diagonal matrix simply because the matrices from which it is calculated are also block diagonal.

With the partitioned form of the matrices given by Eqs. (4.14–4.17), it is straight forward to write out the corresponding partitioned equations from Eq. (4.10) and use them to eliminate the the generalized force variables, $\tilde{\mathbf{y}}_F$. This elimination process yields the expressions to be used in solving for the force variables once the displacement variables $\tilde{\mathbf{y}}_D$ are obtained. The method to be used in reducing

the partitioned equations involves multiplying them through by the inverse of the \mathbf{H} matrix, where this inverse is obtained from the partitioned form of \mathbf{H} . Matrix inversion by partitioning is discussed, for example, in Appendix A of the text by Przemieniecki [43]. If the inverse of \mathbf{H} is denoted by

$$\mathbf{H}^{-1} = \begin{bmatrix} \mathbf{H}_{FF}^* & \mathbf{H}_{FD}^* \\ \mathbf{H}_{DF}^* & \mathbf{H}_{DD}^* \end{bmatrix}, \quad (4.18)$$

then the inverted terms that will be needed in the following reductions are

$$\mathbf{H}_{FF}^* = \mathbf{H}_{FF}^{-1} + \mathbf{H}_{FF}^{-1} \mathbf{H}_{FD} (\mathbf{H}_{DD} - \mathbf{H}_{DF} \mathbf{H}_{FF}^{-1} \mathbf{H}_{FD})^{-1} \mathbf{H}_{DF} \mathbf{H}_{FF}^{-1} \quad (4.19)$$

and

$$\mathbf{H}_{DF}^* = -(\mathbf{H}_{DD} - \mathbf{H}_{DF} \mathbf{H}_{FF}^{-1} \mathbf{H}_{FD})^{-1} \mathbf{H}_{DF} \mathbf{H}_{FF}^{-1}. \quad (4.20)$$

The first set of reduced equations to be obtained are those for aeroelastic lift distribution and structural deflection problems. Beginning with the nonhomogeneous linear equations given in Eq. (4.10), their partitioned form appears as

$$\begin{bmatrix} \mathbf{H}_{FF} & \mathbf{H}_{FD} \\ \mathbf{H}_{DF} & \mathbf{H}_{DD} \end{bmatrix} - \lambda \begin{bmatrix} \mathbf{0} & \mathbf{F}_{FF} \mathbf{A}_{FD} \\ \mathbf{0} & \mathbf{0} \end{bmatrix} \begin{Bmatrix} \tilde{\mathbf{y}}_F \\ \tilde{\mathbf{y}}_D \end{Bmatrix} = \begin{Bmatrix} \mathbf{F}_{FF} \tilde{\mathbf{a}}_{r_F} \\ \mathbf{0} \end{Bmatrix}. \quad (4.21)$$

Multiplying Eq. (4.21) through by \mathbf{H}^{-1} then yields

$$\begin{bmatrix} \mathbf{I} & -\lambda \mathbf{H}_{FF}^* \mathbf{F}_{FF} \mathbf{A}_{FD} \\ \mathbf{0} & \mathbf{I} - \lambda \mathbf{H}_{DF}^* \mathbf{F}_{FF} \mathbf{A}_{FD} \end{bmatrix} \begin{Bmatrix} \tilde{\mathbf{y}}_F \\ \tilde{\mathbf{y}}_D \end{Bmatrix} = \begin{Bmatrix} \mathbf{H}_{FF}^* \mathbf{F}_{FF} \tilde{\mathbf{a}}_{r_F} \\ \mathbf{H}_{DF}^* \mathbf{F}_{FF} \tilde{\mathbf{a}}_{r_F} \end{Bmatrix}. \quad (4.22)$$

By applying Eqs. (4.19–4.20), this can be simplified to give the generalized force equation

$$\tilde{\mathbf{y}}_F = -\mathbf{H}_{FF}^{-1} [\mathbf{H}_{FD} - \lambda \mathbf{F}_{FF} \mathbf{A}_{FD}] \tilde{\mathbf{y}}_D + \mathbf{H}_{FF}^{-1} \mathbf{F}_{FF} \tilde{\mathbf{a}}_{r_F} \quad (4.23)$$

and the reduced linear system

$$\left[I - \lambda T A_{FD} - H_{DD}^{-1} H_{DF} H_{FF}^{-1} H_{FD} \right] \tilde{y}_D = T \tilde{a}_{rF} \quad (4.24)$$

where

$$T = -H_{DD}^{-1} H_{DF} H_{FF}^{-1} F_{FF}. \quad (4.25)$$

If $H_{FD} = 0$, then Eq. (4.24) simplifies to

$$[I - \lambda T A_{FD}] \tilde{y}_D = T \tilde{a}_{rF}. \quad (4.26)$$

This simplified result provides the expression to be used in several examples that will be presented in later chapters. Note that λ must be specified before solutions can be obtained from Eqs. (4.24) and (4.26). In the absence of aerodynamic or inertial loading, λ will be equal to zero and Eq. (4.26) directly provides structural deflection solutions.

The next important result concerns the reduced eigenvalue equations for both aeroelastic divergence and free vibration problems. This result is easily reached by first setting the right-hand side of Eq. (4.21) to zero to obtain the homogeneous version of the partitioned equations. Then, by following an approach similar to that given above for the nonhomogeneous case, one obtains the reduced eigenvalue equations

$$[H_{DF}^* F_{FF} A_{FD} - (1/\lambda) I] \tilde{y}_D = 0. \quad (4.27)$$

The corresponding generalized forces, after solving for \tilde{y}_D , are given by

$$\tilde{y}_F = \lambda H_{FF}^* F_{FF} A_{FD} \tilde{y}_D. \quad (4.28)$$

Similar to Eq. (4.26), a useful form of the reduced eigenvalue problem in Eq. (4.27) is obtained by considering $\mathbf{H}_{FD} = 0$, which gives the result

$$[\mathbf{T}\mathbf{A}_{FD} - (1/\lambda)\mathbf{I}]\tilde{\mathbf{y}}_D = 0. \quad (4.29)$$

This form of the eigenvalue problem will be employed in later examples.

To complete the presentation of the reduced equations, it is useful for reference purposes to give the flutter eigenvalue problem that will be discussed in Chapter 7. The flutter equations, which will be written for the Laplace domain, are obtained in a manner similar to Eq. (4.29), except that they derive initially from Eq. (2.21) rather than Eq. (2.20). By taking $\mathbf{H}_{FD} = 0$, these equations can be written in the form

$$\left[\mathbf{I} + \mathbf{T}[\mathbf{M}_{FD}s^{*2} + \mathbf{C}_{FD}s^* - \mathbf{Q}_{FD}(s^*, \lambda)] \right] \hat{\mathbf{y}}_D = 0 \quad (4.30)$$

where \mathbf{M}_{FD} is a mass matrix, \mathbf{C}_{FD} is a damping matrix, and \mathbf{Q}_{FD} is an unsteady aerodynamic matrix. The variables s^* and $\hat{\mathbf{y}}_D$ are, respectively, a nondimensional Laplace variable and a nondimensional complex eigenvector. The terms appearing in Eq. (4.30) will be defined in more detail in Chapter 7.

An important observation about the foregoing reductions is that although the required matrix inversions can be carried out numerically, they can often easily be avoided or simplified. This is possible because of the particularly simple block matrix structure of \mathbf{H} . For example, if $\mathbf{H}_{FD} = 0$, then the inversion of \mathbf{H} is given by

$$\begin{bmatrix} \mathbf{H}_{FF} & \mathbf{0} \\ \mathbf{H}_{DF} & \mathbf{H}_{DD} \end{bmatrix}^{-1} = \begin{bmatrix} \mathbf{H}_{FF}^{-1} & \mathbf{0} \\ -\mathbf{H}_{DD}^{-1}\mathbf{H}_{DF}\mathbf{H}_{FF}^{-1} & \mathbf{H}_{DD}^{-1} \end{bmatrix}. \quad (4.31)$$

Furthermore, as a result of the structure of the hybrid state vector equations, inversions for \mathbf{H}_{DD} and \mathbf{H}_{FF} are trivially obtained. This is due in part to the

sparseness of these matrices. Further clarification of the inversion process will be offered in the examples of Chapter 5. As a final result, however, one will find it possible to write out the simple matrix expressions for the calculation of T and its product with other matrices.

Additional simplification of the reduced equations is possible for situations where constraint equations exist. The equations of constraint that will be applied in later chapters express simple relationships between solution variables. Such relationships between variables can be used to eliminate certain degrees of freedom by writing them in terms of other degrees of freedom. The methods for applying such constraints to the discrete state vector equations are presented in Appendix F.

Chapter 5

Solutions for Isotropic Beams and Rods

INTEGRATING MATRIX SOLUTIONS are most easily demonstrated with the aid of sample problems. This chapter, and the next two, present examples of how integrating matrix solutions can be used to solve a variety of problems in structural dynamics and aeroelasticity. These solutions are presented both to validate the methods discussed in Chapter 4, and to evaluate the accuracy and convergence trends of the integrating matrix solutions. Comparisons are made between the integrating matrix solutions and alternate analytical or numerical calculations. Among the items considered in the following examples are various types of boundary conditions and loading conditions, all of which commonly arise in performing practical vibration studies and aeroelastic analyses.

5.1 Axial Vibration of Cantilevered Rods

Axial vibration of a rod provides a simple example with which to study the integrating matrix solution process. Since axial rod vibration is described by a second order Sturm-Liouville differential equation, analytical solutions are available for comparison with numerical solutions. The integrating matrix solution properties presented for these simple Sturm-Liouville systems carry through to the much more complicated problems to be discussed later. Aeroelastic divergence of unswept

isotropic wings is also described by a similar Sturm-Liouville differential equation. Therefore, the fundamental eigenvalue of the following eigenvalue solutions can alternately be interpreted in terms of divergence dynamic pressure.

A nondimensional form of the second-order Sturm-Liouville problem describing axial rod vibration can be written as

$$\frac{d}{dx} \left(\frac{1}{\tau} \frac{du}{dx} \right) + \lambda m u = 0 \quad (5.1)$$

where

$$\begin{aligned} u(x) &= \frac{u}{\ell}, & x &= \frac{x}{\ell}, & m(x) &= \frac{m}{m_R}, \\ \tau(x) &= \frac{(EA)_R}{EA}, \\ \lambda &= \frac{\omega^2 m_R \ell^2}{(EA)_R}. \end{aligned} \quad (5.2)$$

For this simple differential equation, the dimensionless state vector form can be written down directly, yielding

$$\frac{d}{dx} \begin{Bmatrix} F_u \\ u \end{Bmatrix} = \begin{bmatrix} 0 & 0 \\ \tau & 0 \end{bmatrix} \begin{Bmatrix} F_u \\ u \end{Bmatrix} - \lambda \begin{bmatrix} 0 & m \\ 0 & 0 \end{bmatrix} \begin{Bmatrix} F_u \\ u \end{Bmatrix} \quad (5.3)$$

where

$$F_u(x) = \frac{1}{\tau} \frac{d\bar{u}}{dx}. \quad (5.4)$$

If the rod is considered to be clamped at the end $x = 0$, the cantilever boundary conditions for Eqs. (5.1) and (5.3) can also be specified as

$$u(0) = 0, \quad F_u(1) = 0. \quad (5.5)$$

The differential equations appearing in either Eq. (5.1) or Eq. (5.3) can be readily solved with an integrating matrix, as will be demonstrated next.

5.1.1 Rods with Continuous Mass and Stiffness

The first solution to be presented will consider axial vibration for a cantilevered rod that can have variable mass and stiffness parameters. Because of its simplicity, this problem serves as a good demonstration of the integrating matrix solution procedures. The integrating matrix will be applied first to the hybrid state vector equations given in Eq. (5.3). It is also instructive to demonstrate how the integrating matrix can be utilized to solve the differential equations given in the form of Eq. (5.1). Both types of solutions will be presented in detail to serve as models for other problems discussed in this chapter.

Beginning with the discretized form of the state vector equations in Eq. (5.3), the integrating matrix is applied as an operator to perform the necessary integrations. The next step is the application of boundary conditions to determine the boundary condition matrices $\tilde{\mathbf{B}}$ and $\tilde{\mathbf{B}}_{nh}$. From the boundary condition matrices follow the definitions for the other matrices appearing in Eqs. (4.10–4.13), which have the partitioned forms displayed in Eqs. (4.14–4.17). For example, in a homogeneous vibration problem, for which $\tilde{\mathbf{a}}_r = 0$, the \mathbf{F} matrix is defined in terms of the given boundary condition matrices, followed by the determination of the \mathbf{H} matrix.

For the axial vibration problem, an application of the global integrating matrix to the discretized version of Eq. (5.3) yields

$$\begin{Bmatrix} F_u \\ \bar{u} \end{Bmatrix} = \begin{bmatrix} \mathbf{L} & 0 \\ 0 & \mathbf{L} \end{bmatrix} \left\{ \begin{bmatrix} 0 & 0 \\ \bar{r} & 0 \end{bmatrix} \begin{Bmatrix} F_u \\ \bar{u} \end{Bmatrix} - \lambda \begin{bmatrix} 0 & \bar{m} \\ 0 & 0 \end{bmatrix} \begin{Bmatrix} F_u \\ \bar{u} \end{Bmatrix} \right\} + \begin{Bmatrix} \mathbf{k}_F \\ \mathbf{k}_u \end{Bmatrix}. \quad (5.6)$$

To make it convenient to solve for boundary conditions, Eq. (5.6) is easily expanded into the two sets of equations

$$\{F_u\} = -\lambda \mathbf{L} \bar{m} \{\bar{u}\} + \mathbf{k}_F \quad (5.7)$$

$$\{\bar{u}\} = \mathbf{L} \bar{r} \{F_u\} + \mathbf{k}_u. \quad (5.8)$$

Applying the boundary condition $u(0) = 0$ to Eq. (5.8) gives

$$\mathbf{b}_0^T \{u\} = 0 = k_u \quad (5.9)$$

where use has been made of $\mathbf{b}_0^T \mathbf{L} = 0$ and $\mathbf{b}_0^T \mathbf{k}_u = k_u$. (Note, for example, that $\mathbf{k}_u = \tilde{\mathbf{l}} k_u$, where $\tilde{\mathbf{l}}$ is as defined in Eqs. (4.5) and (4.6).) In a similar manner, the boundary condition $F_u(1) = 0$ can be applied to Eq. (5.7), yielding the scalar solution

$$\mathbf{b}_n^T \{F_u\} = 0 = -\lambda \mathbf{b}_n^T \mathbf{L} \tilde{\mathbf{m}} \{u\} + k_F, \quad (5.10)$$

which can be converted to the vector form

$$\mathbf{k}_F = \lambda \mathbf{B}_n \mathbf{L} \tilde{\mathbf{m}} \{u\}. \quad (5.11)$$

From the results in Eqs. (5.9) and (5.11), the boundary condition matrix $\tilde{\mathbf{B}}$ appearing in Eq. (4.9) can be written as

$$\tilde{\mathbf{B}} = \begin{bmatrix} \mathbf{B}_n & 0 \\ 0 & 0 \end{bmatrix}. \quad (5.12)$$

For this problem, one also has that $\tilde{\mathbf{B}}_{nh} = 0$.

Having obtained expressions for the constant vector of integration, the partitioned matrices in Eqs. (4.14–4.16) are given, via Eqs. (4.10–4.12), as

$$\mathbf{H} = \begin{bmatrix} \mathbf{I} & 0 \\ -\mathbf{L}^T & \mathbf{I} \end{bmatrix} \quad (5.13)$$

$$\tilde{\mathbf{A}} = \begin{bmatrix} 0 & \tilde{\mathbf{m}} \\ 0 & 0 \end{bmatrix} \quad (5.14)$$

$$\mathbf{F} = \begin{bmatrix} (\mathbf{B}_n - \mathbf{I})\mathbf{L} & 0 \\ 0 & -\mathbf{L} \end{bmatrix} = \begin{bmatrix} \mathbf{L}_1^* & 0 \\ 0 & -\mathbf{L} \end{bmatrix} \quad (5.15)$$

where L_1^* can be considered as a special type of integrating matrix. (L_1^* is actually the equivalent of what Vakhitov [26] refers to as a "type two" integrating matrix. To see the significance of this modified integrating matrix, one can write out the type of integration that it performs; namely,

$$B_n L - L = \int_0^\ell - \int_0^x = \int_x^\ell. \quad (5.16)$$

Other such special integrating matrices will be defined for convenience sake in later problems. Each one will be assigned a different subscript that will serve to distinguish it.)

The matrices in Eqs. (5.13-5.15) can be used directly in Eq. (4.25) and Eq. (4.29) to obtain the reduced eigenvalue problem for free vibration. From Eq. (4.25), we obtain the result

$$T = L^* r L_1^*, \quad (5.17)$$

and from Eq. (4.29) the eigenvalue problem is

$$[L^* r L_1^* \bar{m} - (1/\lambda)I]\{u\} = 0. \quad (5.18)$$

This result provides the eigenvalue problem for a cantilevered axial rod with variable stiffness and mass parameters. As can be seen, the eigenvalue problem is formed by specifying the integrating matrix and the corresponding discrete values for the diagonal matrices r and m .

For simple problems, such as the one considered here, an alternate approach that often proves very convenient is to apply the integrating matrix to the form of the equations given in Eq. (5.1), rather than utilizing the state vector form. A discrete form of Eq. (5.1) can be written as

$$\frac{d}{dx}\{F_u\} + \lambda^* \bar{m}\{u\} = 0. \quad (5.19)$$

Applying the integrating matrix to Eq. (5.19) yields

$$\{F_u\} + \lambda L^{\tau} \bar{m}\{u\} = k_F. \quad (5.20)$$

Now multiplying this result through by the diagonal matrix τ to isolate another derivative term gives

$$\frac{d}{dx}\{u\} + \lambda \tau L^{\tau} \bar{m}\{u\} = \tau k_F. \quad (5.21)$$

Another application of the integrating matrix then produces the result

$$\{\bar{u}\} + \lambda L^{\tau} \tau L^{\tau} \bar{m}\{u\} = L^{\tau} \tau k_F + k_u. \quad (5.22)$$

If Eq. (5.22) is multiplied through by b_0^T , then use of the boundary condition $\bar{u}(0) = 0$ gives, as before, $k_u = 0$. Similarly, multiplying Eq. (5.20) by b_n^T and using $F_u(1) = 0$ leads to the result in Eq. (5.11). Substituting these results for the constant vectors into Eq. (5.22) and rearranging gives the eigenvalue problem presented in Eq. (5.18).

From the eigenvalue problem given by Eq. (5.18), results can be obtained for either uniform or variable property rods. For the case of a uniform rod, the matrices τ and \bar{m} are simply identity matrices. The numerical calculation of the eigenvalues and eigenvectors can make use of standard eigenvalue routines. For the examples presented, the computations were carried out on an IBM 3033. The calculations that form the matrix for the eigenvalue problem were performed in single precision arithmetic, and the eigenvalues and eigenvectors of the resulting real, nonsymmetric matrix were calculated with a reliable double precision routine available in the EISPACK eigenvalue package (see Smith [44]). Calculations were performed for both Jacobi and Newton integrating matrices, with the number of discretization intervals N varying from two to five. For each level of discretization, the maximum order integrating matrix was used for the given number of collocation points ($N + 1$).

The numerical solutions for axial vibration of both uniform and linearly tapered rods were compared with analytical solutions. For the uniform rod, analytical solutions for the constant coefficient Sturm-Liouville problem can be found in Section 3.5 of Bisplinghoff, Ashley, and Halfman [45]. For linearly tapered rods, useful analytical solutions for the eigenvalues of the homogeneous differential equation are given in closed form by Hildebrand and Reissner [46]. (These solutions are also repeated in Ref. [45], pp. 432–434.)

In the case of the uniform rod, results for the axial frequencies obtained with both Newton and Jacobi integrating matrices are presented in Table 1 at the end of this chapter. Also presented in Table 1 are the percentage errors between the approximate integrating matrix results and the exact analytical solutions. Fig. 4 gives a display of these percentage errors for the first three vibrational modes. As can be seen by comparing the frequency errors, both Newton and Jacobi solutions provide highly accurate results despite the relatively crude discretization. It is also clear that for those frequencies that are nearing convergence, the Jacobi solutions are more accurate than those provided by the Newton solutions. For the uniform rod, the frequencies given by the Jacobi integrating matrices always converge from above to the exact frequencies, unlike the oscillatory convergence of the Newton solutions. Since all of the available frequencies are displayed for each discretization level, it is useful to note how the higher frequencies behave as the discretization level increases. For the Jacobi solutions, it is apparent that each newly introduced modal frequency is quite high compared to the exact result, but rapidly converges to the correct solution as new discretization intervals are introduced. In comparison, each newly introduced Newton solution frequency is not as high, but the convergence to the correct result tends to be somewhat oscillatory. These convergence trends for uniform parameter systems are also evident in additional solutions to be presented in the following sections. Aside from the finer details of convergence, however, both

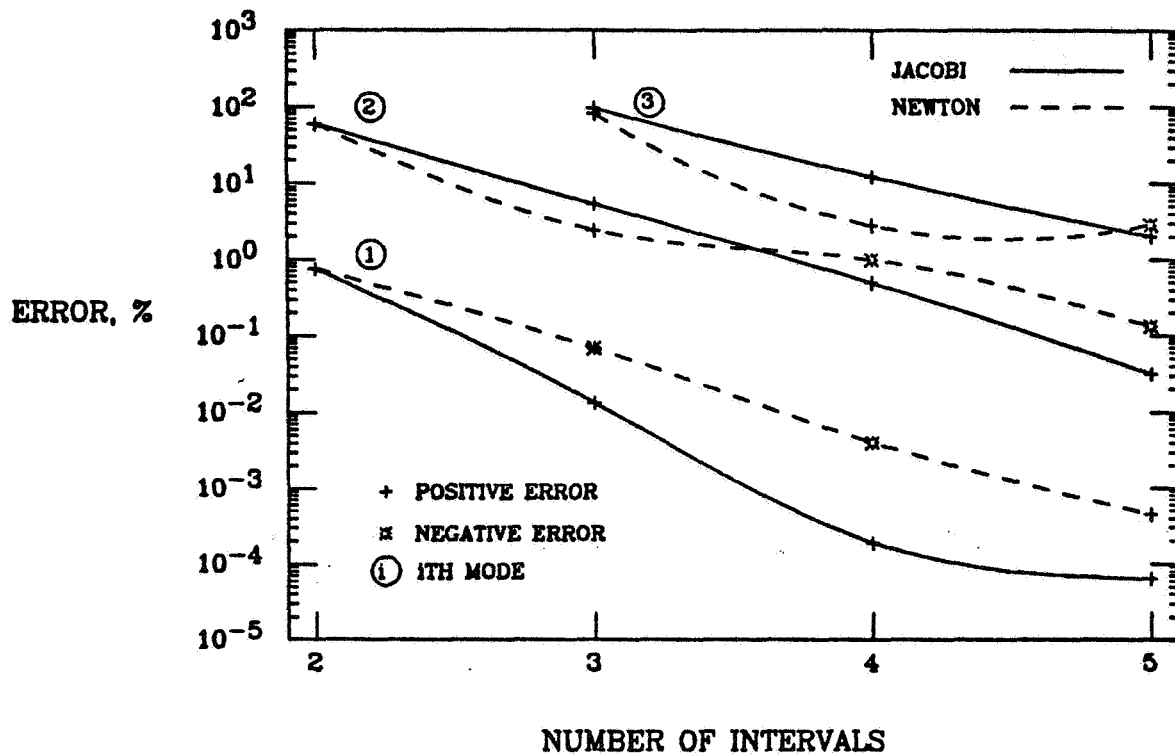


Fig. 4. Error in computed frequencies, compared to exact solutions, for the first three axial modes of a uniform cantilevered rod. The error for both Jacobi and Newton integrating matrix solutions is plotted vs. the number of collocation intervals N .

Newton and Jacobi solutions have the capability to provide accurate results for the lower frequencies without requiring a highly refined mesh of grid points.

For the uniform axial rod vibration just discussed, Table 2 gives the first three axial mode shapes. Results are shown for both Newton and Jacobi integrating matrix solutions based on five collocation intervals. Since the Newton solutions make use of evenly spaced collocation points, the Newton based mode shapes in Table 2 are simply presented for these collocation points without interpolation being required. On the other hand, the Jacobi solutions have been interpolated to these evenly spaced points with the same order Jacobi polynomial used in the solution. The results of performing such an interpolation are less than satisfactory since it appears that the Jacobi mode shapes in Table 2 are less accurate than the Newton results. But in fact, it is easily shown that the Jacobi mode shapes are quite accurate if evaluated at the Jacobi collocation points. This behavior emphasizes an important aspect of interpolation processes in general. Due to the fact that interpolation error is itself an oscillatory function, the highest accuracy for the interpolated displacement solutions can be expected to occur at the collocation points, and the largest error will occur between the collocation points. The same conclusion is reached if the Newton solutions are interpolated to the unevenly spaced Jacobi points. This all seems to suggest, not unexpectedly, that if mode shape results must be interpolated, it is probably better to use a localized least squares procedure based on a slightly lower order polynomial approximation.

Vibration frequencies for a linearly tapered rod can be easily determined from Eq. (5.18) after introducing the following variables to describe the taper. First, the taper ratio of the rod is defined to be $(1 - \beta_t)$, where β_t is the taper parameter. Each dimension in the cross section of the rod varies linearly as $(1 - \beta_t \bar{x})$. For this description of the taper, it follows that the mass and stiffness parameters m and EA appearing in Eq. (5.2) can be written as

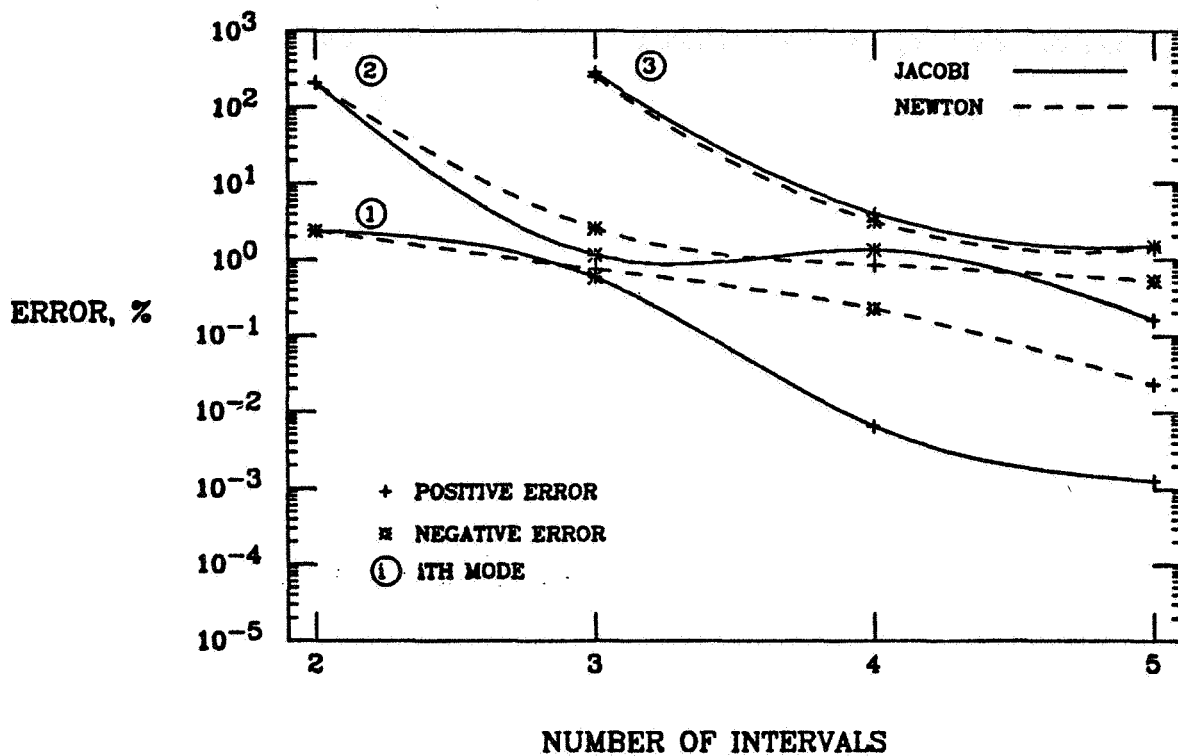


Fig. 5. Error in computed frequencies, compared to exact solutions, for the first three axial modes of a linearly tapered cantilevered rod with a taper ratio of one half ($\beta_t = 0.5$). The error for both Jacobi and Newton integrating matrix solutions is plotted vs. the number of collocation intervals N .

$$\begin{aligned} m &= m_R(1 - \beta_t x)^2, \\ EA &= (EA)_R(1 - \beta_t x)^4. \end{aligned} \tag{5.23}$$

Using these definitions for the mass and stiffness, the frequencies of a linearly tapered rod with $\beta_t = 0.5$ are given in Table 3. The percentage errors between the exact solutions and the integrating matrix solutions are also displayed in Fig. 5 for the first three vibrational modes. As evident from the eigenvalue error results, neither the Jacobi nor the Newton solutions converge quite as rapidly as in the uniform rod case, which is to be expected. For this linearly tapered rod, the Jacobi results do not necessarily converge to the exact frequencies from above as they do for uniform parameter problems. Nonetheless, the convergence of the Jacobi solutions is quite predictable in that all modes, except the first, appear at a high frequency and only very slightly overshoot on the negative side enroute to converging. The Jacobi solutions still provide faster convergence to the lower modes. In contrast, the Newton solutions retain their oscillatory convergence character, with the frequency error changing sign for each added collocation interval. Aside from this oscillatory behavior, the magnitude of the Newton solution errors can be considered quite small. It is well known that one cannot always guarantee convergence from above for eigenvalues obtained from a collocation procedure. The fact that there are sign changes in the error of both Jacobi and Newton frequencies for this nonuniform parameter problem is indicative of the collocation nature of the integrating matrix solutions.

5.1.2 Rods with Discontinuous Mass and Stiffness

Because of the common occurrence of structural elements with parameter discontinuities, it is useful to examine the hybrid state vector technique as applied to axial vibration of rods having stepwise jumps in mass and stiffness. The eigenvalue

problem for a discontinuous rod is still given by Eq. (5.18), which was originally derived for continuous parameter rods. The only difference arises in the proper specification of the integrating matrix and the diagonal coefficient matrices τ and \bar{m} . The methods for specifying the integrating matrix and the corresponding function values for a discontinuous integrand were discussed in Section 3.2.

To allow comparison with alternate solutions, the problem chosen for discontinuous axial rod vibration is the same as a problem discussed by Hodges [47], in which solutions were obtained by a Ritz method. The cantilevered rod, which is normalized to unit length and clamped at $x = 0$, is divided into three segments. The first segment extends from $x = 0$ to $x = 0.25$, the second segment from 0.25 to 0.75, and the third segment from 0.75 to 1.0. Mass and stiffness parameters in the first and third segments are assigned the same values, and within each segment the parameters are assumed constant. The ratios between the parameters of the different segments are given by

$$\tau = \frac{(EA)_2}{(EA)_1} = \frac{\tau_1}{\tau_2}, \quad \bar{\theta} = \frac{\bar{m}_2}{\bar{m}_1}, \quad (5.24)$$

where

$$\begin{aligned} \tau_1 = \tau_3 &= \frac{1 + \tau}{2}, \\ \bar{m}_1 = \bar{m}_3 &= \frac{2}{1 + \bar{\theta}}. \end{aligned} \quad (5.25)$$

Thus, when $\tau = 1$ and $\bar{\theta} = 1$ there is no discontinuity in the parameters.

Integrating matrix solutions are obtained for the discontinuous case by calculating an integrating matrix for the piecewise integration of the three segments. Maximum order weighting matrices are assumed in this calculation. An equal number of collocation intervals are used for each segment; thus, it is appropriate to describe the solution in terms of the number of intervals per segment.

For $\gamma = 10$ and $\bar{\theta} = 100$ the results are presented in Table 4 for the axial frequencies obtained with both Jacobi and Newton integrating matrices. Fig. 6 displays for the first three vibrational modes the percentage error between the exact solutions (Ref. [47]) and the integrating matrix solutions. Similar to the earlier discovery for uniform axial rod vibration, the Jacobi solutions for a piecewise uniform rod offer the advantage of a rapid, monotonic convergence to the exact result from above. From a practical viewpoint, either the Jacobi or the Newton integrating matrix yields highly accurate results without requiring an extremely fine mesh of grid points.

An interesting point to notice in Fig. 6 is that the eigenvalue error for the fundamental mode bottoms out and then begins to rise slightly. The reason for this occurrence is that the numerical precision limit has been reached for the calculation of this eigenvalue. As a consequence, the last digits of the result change rather than remaining exactly at the converged value. This same phenomenon was encountered by Hodges [48] when obtaining similar high accuracy solutions with a variable order Ritz finite element method. The apparent cure for this is to increase the precision level of the computations.

Because integrating matrices with end points were used to solve this problem, one should note that two identically located collocation points are present at each discontinuity. Since the solution values will be identical for each of these points, a constraint is available that can be used to eliminate the solution degrees of freedom at one of the points. The rectangular transformation matrix resulting from this constraint can be applied as discussed in Appendix F. It turns out that this transformation matrix, which consists only of ones and zeroes, produces a diagonal matrix when premultiplied by its transpose. Therefore, the pseudoinverse mentioned in Appendix F can be obtained quite simply. It should be pointed out, however, that for small sized problems it is not necessary, and generally not worth

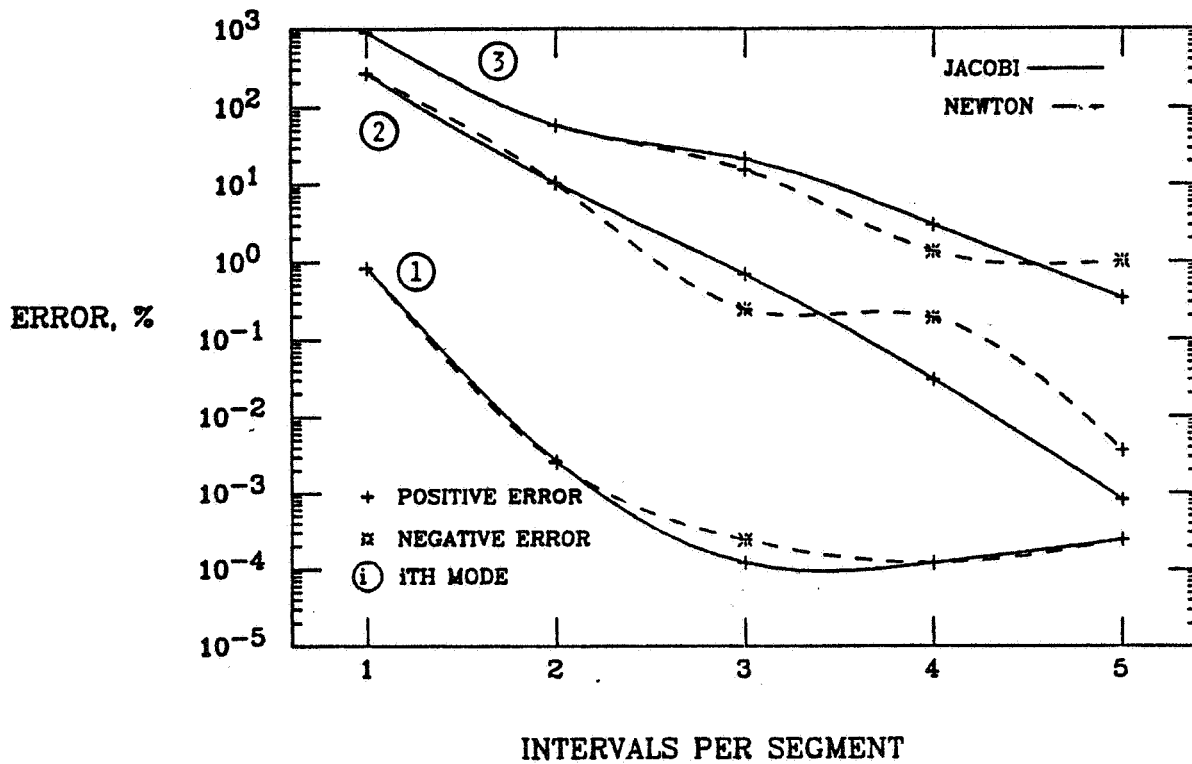


Fig. 6. Error in computed frequencies, compared to exact solutions, for the first three axial modes of a cantilevered rod with discontinuous stiffness and mass ($\bar{\gamma} = 10$; $\bar{\theta} = 100$). The rod has three uniform segments between the points $\bar{x} = 0, .25, .75, 1$. The error for the integrating matrix solutions is plotted vs. the number of collocation intervals per segment N .

the trouble, to apply this constraint. The exception would be a large sized problem. In that case one might expect a significant reduction in the number of degrees of freedom present in the solution.

A final note concerning axial vibration of a discontinuous rod is that solutions were also tried in which the discontinuities were ignored. That is, an integrating matrix was used which allowed the integrations (i.e., the interpolations) to proceed across the discontinuity boundaries. As expected, the eigenvalue solutions approached the exact results when enough collocation points were taken. Although a reasonably accurate solution for the fundamental mode could be obtained without too much effort, matching the accuracies of Table 4 for the higher modes required a somewhat larger number of collocation points. Furthermore, the convergence with this approach was highly oscillatory for some modes and seemed unpredictable for anything but the fundamental mode.

5.1.3 Rods with Elastic Restraint

A type of boundary condition that occurs quite often is that of elastic restraint. Methods for handling this type of boundary condition are easily demonstrated for a uniform axial rod. It will be assumed that the axial modes of vibration are to be found for a rod that is cantilevered at one end and has an axial spring restraint at the opposite end. Fig. 7 illustrates a rod with these boundary conditions. Since the axial restraining spring applies a force to the rod that is proportional to the displacement at the end of the rod, the boundary condition can be included as a displacement dependent loading in the A_{FD} submatrix of Eq. (4.15). In the present example, however, the restraint will be introduced instead through the nonhomogeneous boundary condition matrix \tilde{B}_{nh} .

The nondimensional equations describing the rod are given by Eqs. (5.3–5.4)

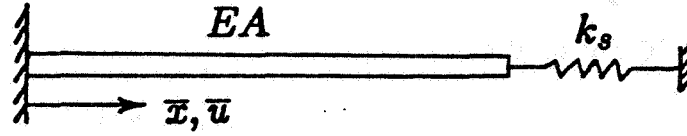


Fig. 7. A cantilevered axial rod with a spring restraint boundary condition

and Eqs. (5.6–5.8). Boundary conditions for the rod are

$$\bar{u}(0) = 0 \quad F_u(1) = -\bar{k}_s \bar{u}(1), \quad (5.26)$$

where

$$\bar{k}_s = \frac{k_s}{(EA)_R}. \quad (5.27)$$

As the nondimensional restraining spring stiffness \bar{k}_s varies from zero to infinity, the boundary conditions for the rod vary from cantilevered to clamped-clamped.

Solutions for this problem are obtained by the same approach as presented in Section 5.1.1. In fact, the only changes to be made are to the boundary condition solution in Eqs. (5.10–5.11) and to the \mathbf{H} matrix in Eq. (5.13). The boundary condition solution for the spring restrained end is given by

$$\mathbf{b}_n^T \{F_u\} = -\bar{k}_s \mathbf{b}_n^T \{u\} = -\lambda \mathbf{b}_n^T \mathbf{L}^T \bar{\mathbf{m}} \{u\} + k_F, \quad (5.28)$$

which yields the vector form

$$\mathbf{k}_F = \lambda \mathbf{B}_n \mathbf{L}^T \bar{\mathbf{m}} \{\bar{u}\} - \bar{k}_s \mathbf{B}_n \{\bar{u}\}. \quad (5.29)$$

From this result, one finds that the boundary condition matrix $\tilde{\mathbf{B}}$ is still given by Eq. (5.12), and the nonhomogeneous boundary condition matrix is now given by

$$\tilde{\mathbf{B}}_{nh} = \begin{bmatrix} 0 & \bar{k}_s \mathbf{B}_n \\ 0 & 0 \end{bmatrix}. \quad (5.30)$$

With the definition for \mathbf{H} in Eq. (4.11), the replacement for Eq. (5.13) is found to be

$$\mathbf{H} = \begin{bmatrix} \mathbf{I} & \bar{k}_s \mathbf{B}_n \\ -\mathbf{L}^* \tau & \mathbf{I} \end{bmatrix}. \quad (5.31)$$

If one now makes use of Eq. (4.27), along with Eqs. (5.14–5.15), the eigenvalue problem can be written as

$$[\mathbf{I}^* \mathbf{L}^* \tau \mathbf{L}_1^* \bar{m} - (1/\lambda) \mathbf{I}] \{\bar{u}\} = 0 \quad (5.32)$$

where

$$\mathbf{I}^* = [\mathbf{I} + \bar{k}_s \mathbf{L}^* \tau \mathbf{B}_n]^{-1}. \quad (5.33)$$

The eigenvalue problem in Eq. (5.32) applies to vibration of a nonuniform rod and can be solved for any value of restraining spring stiffness.

Although it might appear to be a formidable task, it is actually quite easy to analytically invert the expression in Eq. (5.33), and thus obtain a simpler form for the eigenvalue problem. The reason that Eq. (5.33) can be easily simplified is that \mathbf{B}_n contains unit terms only in the last row, and zeroes elsewhere. Thus, for all practical purposes, the second expression in the summation of Eq. (5.33) yields a vector. This allows easy inversion of the entire matrix when applying inversion by matrix partitioning. In general terms, one can write

$$[\mathbf{I} + \bar{k}_s \mathbf{L}^* \tau \mathbf{B}_n] = \begin{bmatrix} \mathbf{I} & \bar{z}_1 \\ 0 & e_2 \end{bmatrix} \quad (5.34)$$

where the matrix has been partitioned such that c_2 is a scalar and \vec{c}_1 is a vector. The inverse of Eq. (5.34) is

$$\mathbf{I}^* = \begin{bmatrix} \mathbf{I} & -\vec{c}_1/c_2 \\ 0 & 1/c_2 \end{bmatrix}. \quad (5.35)$$

This result can be conveniently written in the form

$$\mathbf{I}^* = [\mathbf{I} - v\bar{k}_s \mathbf{L}^T \tau \mathbf{B}_n] \quad (5.36)$$

where

$$v = \frac{1}{c_2} = \frac{1}{1 + \bar{k}_s \mathbf{b}_n^T \mathbf{L}^T \tau \vec{\mathbf{1}}}. \quad (5.37)$$

For the case of a uniform rod ($\tau = \bar{m} = 1$), the eigenvalue problem given by Eq. (5.32), in conjunction with Eq. (5.36), can be written as

$$[\mathbf{I}^* \mathbf{L} \mathbf{L}_1^* - (1/\lambda) \mathbf{I}] \{\vec{u}\} = 0 \quad (5.38)$$

where

$$\mathbf{I}^* = \left[\mathbf{I} - \frac{\bar{k}_s}{1 + \bar{k}_s} \mathbf{L} \mathbf{B}_n \right]. \quad (5.39)$$

Note that in obtaining Eq. (5.39) from Eq. (5.37) a special identity was used; namely,

$$\mathbf{b}_n^T \mathbf{L} \vec{\mathbf{1}} = 1. \quad (5.40)$$

This identity applies when the integrating matrix has been written for a normalized interval of unit length. It is well worth remembering this identity since it appears often in solving for various types of boundary conditions.

Exact eigenvalues for the uniform cantilevered rod with spring restraint are easily found by analytically solving the differential equations. It can be shown that

the eigenvalues are given by the roots of the transcendental equation

$$\bar{k}_s \tan \sqrt{\lambda} + \sqrt{\lambda} = 0, \quad (5.41)$$

and the corresponding axial mode shapes are obtained from

$$u(x) = C \sin \sqrt{\lambda} x. \quad (5.42)$$

For the exact solutions, as $\bar{k}_s \rightarrow 0$, $\sqrt{\lambda} \rightarrow n\pi/2$, with $n = 1, 3, 5, \dots, \infty$. This is the result for a purely cantilevered rod. On the other hand, as $\bar{k}_s \rightarrow \infty$, $\sqrt{\lambda} \rightarrow n\pi$, with $n = 0, 1, 2, \dots, \infty$, which is the solution for a rod clamped at both ends.

Presented in Table 5 for a uniform rod are nondimensional frequencies calculated from Eq. (5.38). Comparisons are made with the exact results of Eq. (5.41). The frequencies are presented for the first three modes and are calculated for several values of the restraint spring stiffness \bar{k}_s . These calculations make use of a Jacobi integrating matrix corresponding to six collocation points. The exact frequencies listed under $\bar{k}_s = 1 \times 10^6$ actually correspond to $\bar{k}_s = \infty$. This gives a valid comparison with the integrating matrix solutions since values of the spring stiffness larger than 1×10^6 produce no significant changes in the integrating matrix results when using single precision calculations.

5.1.4 Rods with Concentrated Mass

Another important example deals with the vibration of rods having concentrated mass points in addition to continuously distributed mass properties. The approach to solving problems with concentrated masses involves a simple extension of methods already presented for continuous parameter problems. This extension of the foregoing methods is presented in Appendix E, which discusses the treatment

of any type of concentrated loading. For the problem at hand, the point loads arise from concentrated masses.

The problem to be considered in this section is the axial vibration of a cantilevered rod with a tip mass. The method of solution will be that of Appendix E, but one should note that for this particular problem the mass provides a tip boundary condition that can also be handled with the approach given in the previous section. Since the solution turns out to be an extension of that presented in Section 5.1.1, the matrices defined in Eqs. (5.13–5.15) still apply. To account for the concentrated inertia loads, however, it is necessary to include from Eq. (E.11) the matrix

$$\mathbf{F}^+ = \begin{bmatrix} (\mathbf{B}_n - \mathbf{I})\mathbf{S} & 0 \\ 0 & -\mathbf{S} \end{bmatrix} = \begin{bmatrix} \mathbf{S}_1^* & 0 \\ 0 & -\mathbf{S} \end{bmatrix}. \quad (5.43)$$

Notice that this matrix is the same as \mathbf{F} in Eq. (5.15) with the summing matrix \mathbf{S} substituted for the integrating matrix. A second matrix that must be added is the matrix containing the concentrated mass terms specified at the collocation points. For the problem under consideration this matrix is

$$\mathbf{A}_{FD}^+ = \begin{bmatrix} 0 & & \\ & \ddots & \\ & & m_n^+ \end{bmatrix} = \bar{m}^+ \quad (5.44)$$

where $m_n^+ = m_n/m_R \ell$ is the tip mass nondimensionalized by the total mass of a reference rod (i.e., m_n is a total mass and m_R is a running mass). With the matrices defined in Eqs. (5.43–5.44), the eigenvalue problem given by Eq. (E.16) can be written as

$$[(\mathbf{L}^* \tau \mathbf{L}_1^* \bar{m} + \mathbf{L}^* \tau \mathbf{S}_1^* \bar{m}_n^+) - (1/\lambda)\mathbf{I}]\{\mathbf{u}\} = 0. \quad (5.45)$$

This eigenvalue problem is the extension of Eq. (5.18) to include point mass terms. For a uniform beam, Eq. (5.45) simplifies to

$$[(LL_1^* + LS_1^* m_n^+) - (1/\lambda)I]\{u\} = 0 \quad (5.46)$$

where it should be noted that the lumped tip mass will only affect terms in the last column of the matrix from which the eigenvalues are found.

Exact solutions for the eigenvalues of a similar Sturm-Liouville problem can be found in Section 5.9 of Meirovitch [42]. The transcendental equation for the eigenvalues is given by

$$\sqrt{\lambda} \tan \sqrt{\lambda} - 1/m_n^+ = 0. \quad (5.47)$$

Upon examining this equation, one finds that when $m_n \rightarrow 0$, then $\sqrt{\lambda} \rightarrow n\pi/2$, with $n = 1, 3, 5, \dots, \infty$. Similarly, as $m_n \rightarrow \infty$, $\sqrt{\lambda} \rightarrow n\pi$, with $n = 0, 1, 2, \dots, \infty$. In physical terms, as the tip mass tends to zero, the eigenvalue solution reduces to that for a simple cantilever rod. As the tip mass grows very large, the solution approaches that for a rod clamped at both ends.

Table 6 gives for a uniform rod the nondimensional frequencies calculated from Eq. (5.46). Comparisons are made with the exact results of Eq. (5.47). The frequencies are given for the first three modes and are calculated for several values of the tip mass ratio m_n^+ . Calculations are based on a Jacobi integrating matrix corresponding to six collocation points. The exact frequencies that are listed under $m_n^+ = 1 \times 10^8$ actually correspond to $m_n^+ = \infty$. This gives a valid comparison with the integrating matrix solutions since values of the tip mass ratio larger than 1×10^8 produce no further changes in the integrating matrix results when using single precision calculations.

5.2 Bending Vibration of Beams

Applications of the hybrid state vector approach are now examined for beam vibration problems. Since beam vibration analyses are so common in structural dynamics and aeroelasticity, it is useful to give them a separate treatment. The following problems demonstrate the application of hybrid state vector techniques to the lateral vibration of beams with various type of boundary conditions, including unrestrained beams possessing rigid body modes. Sample results are presented for uniform beams.

The differential equations that describe lateral vibration of isotropic beams are well known. Rather than rederiving the nondimensional state vector equations, they can be extracted from the anisotropic beam equations given in Section 2.3. After including inertia terms and neglecting transverse shear effects, the appropriate equations can be written as

$$\frac{d}{dx} \begin{Bmatrix} M \\ V \\ \gamma \\ w \end{Bmatrix} = \begin{bmatrix} 0 & 1 & 0 & 0 \\ 0 & 0 & 0 & 0 \\ EI & 0 & 0 & 0 \\ 0 & 0 & -1 & 0 \end{bmatrix} \begin{Bmatrix} M \\ V \\ \gamma \\ w \end{Bmatrix} - \lambda \begin{bmatrix} 0 & 0 & 0 & 0 \\ 0 & 0 & 0 & m \\ 0 & 0 & 0 & 0 \\ 0 & 0 & 0 & 0 \end{bmatrix} \begin{Bmatrix} M \\ V \\ \gamma \\ w \end{Bmatrix} \quad (5.48)$$

where

$$EI = \frac{(EI)_R}{EI}, \quad m = \frac{m}{m_R}, \quad (5.49)$$

and

$$\lambda = \frac{\omega^2 m_R \ell^4}{(EI)_R}. \quad (5.50)$$

Other nondimensional terms are as defined in Eq. (2.29) and Eq. (2.31), with c taken to have unit value for a beam.

Irrespective of boundary conditions, one can begin the solution of Eq. (5.48) by discretizing, multiplying through by the global integrating matrix, and adding the constant vector of integration. In a manner analogous to Eqs. (5.6-5.8), this result can be expanded into the set of equations

$$\{M\} = L\{V\} + k_m \quad (5.51)$$

$$\{V\} = -\lambda L^T m\{w\} + k_v \quad (5.52)$$

$$\{\gamma\} = L^T EI\{M\} + k_\gamma \quad (5.53)$$

$$\{w\} = -L\{\gamma\} + k_w. \quad (5.54)$$

Boundary conditions can be applied to these equations to solve for the constant vectors of integration.

The basic approach to be used in solving for the constants of integration of two-point boundary value problems is demonstrated in Section 5.1.1. Only the important aspects of boundary condition determination will be addressed in detail in the following problems. It is worth noting, however, that there is a recommended procedure to simplify the solution for boundary conditions. One should first apply any homogeneous or nonhomogeneous boundary conditions at the end $\bar{x} = 0$. It is assumed that this end is the starting point for the integrations performed by the integrating matrix. The second step is to apply boundary conditions at the point $\bar{x} = 1$ (assuming, of course, a normalized interval $\bar{x} = [0, 1]$). This second step often involves applying boundary conditions to state variables that were already used in the boundary conditions at $\bar{x} = 0$. When this occurs, one must express these variables in terms of the remaining unused variables to insure that all unknown constants are determined. An important requirement when solving for constants of integration is that the resulting boundary condition matrix \tilde{B} be block diagonal.

5.2.1 Cantilevered Beam

A cantilevered beam offers simple boundary conditions from which the constants of integration are readily determined from Eqs. (5.51-5.54). The boundary conditions to be satisfied are given by

$$\gamma(0) = 0, \quad \psi(0) = 0, \quad \bar{M}(1) = 0, \quad \bar{V}(1) = 0. \quad (5.55)$$

It is clear from the first two conditions that $k_\gamma = k_\psi = 0$. The boundary conditions at the free end of the beam yield

$$k_m = -B_n L \{V\} \quad (5.56)$$

$$k_v = \lambda B_n L \{w\}. \quad (5.57)$$

With these constants determined, one finds that

$$F = \begin{bmatrix} (B_n - I)L & 0 & 0 & 0 \\ 0 & (B_n - I)L & 0 & 0 \\ 0 & 0 & -L & 0 \\ 0 & 0 & 0 & -L \end{bmatrix} = \begin{bmatrix} L_1^* & 0 & 0 & 0 \\ 0 & L_1^* & 0 & 0 \\ 0 & 0 & -L & 0 \\ 0 & 0 & 0 & -L \end{bmatrix} \quad (5.58)$$

and as a result,

$$H = \begin{bmatrix} I & L_1^* & 0 & 0 \\ 0 & I & 0 & 0 \\ -L^* EI & 0 & I & 0 \\ 0 & 0 & L & I \end{bmatrix}. \quad (5.59)$$

From Eq. (4.25), one then obtains

$$T = \begin{bmatrix} L^* EI L_1^* & -L^* EI L_1^{*2} \\ -L^2 EI L_1^* & L^2 EI L_1^{*2} \end{bmatrix} \quad (5.60)$$

which, when substituted into Eq. (4.29), yields the eigenvalue problem

$$[\mathbf{L}^2 \cdot E\mathbf{I} \mathbf{L}_1^{*2} \cdot \mathbf{m} - (1/\lambda)\mathbf{I}]\{\mathbf{w}\} = 0. \quad (5.61)$$

This simplifies for a uniform beam since $E\mathbf{I}$ and \mathbf{m} are then identity matrices. It should be noted that the row and column of Eq. (5.61) corresponding to the constrained lateral displacement at the fixed end can be deleted before solving for the eigenvalues and eigenvectors.

Results are presented in Table 7 for the nondimensional frequencies of a uniform cantilevered beam. The numerically computed results are based on a Jacobi integrating matrix for five collocation intervals and are compared with exact results tabulated by Hunter [27]. One can also refer to Hunter for detailed Newton integrating matrix solutions of the cantilevered beam problem.

Mode shapes corresponding to the first three modes of the Jacobi solutions are given in Table 8. The accuracy of the higher modes can be improved further by adding rotary inertia and transverse shear terms to the analysis. The mode shapes in Table 8 were interpolated to the evenly spaced grid points with a Jacobi polynomial of the same order used in the integrating matrix solution. Some of the aspects of this type of interpolation are discussed in Section 5.1.1.

5.2.2 Simply Supported Beam

A simply supported beam requires boundary conditions to be applied to both moment and lateral displacement variables at both ends of the beam. The familiar boundary conditions for a simply supported beam are concisely stated as

$$\overline{M}(0) = 0, \quad w(0) = 0, \quad \overline{M}(1) = 0, \quad w(1) = 0. \quad (5.62)$$

The boundary conditions at $x = 0$ applied to Eqs. (5.51) and (5.54) yield immediately

$$K_m = K_w = 0. \quad (5.63)$$

To apply boundary conditions at $x = 1$, it is necessary to write expressions for \bar{M} and \bar{w} in terms of the other unknown constants appearing in Eqs. (5.52) and (5.53). These expressions are

$$\{\bar{M}\} = L(-\lambda L' \bar{m})\{\bar{w}\} + Lk_v \quad (5.64)$$

$$\{\bar{w}\} = -L(L' EI)\{\bar{M}\}w - Lk_\gamma. \quad (5.65)$$

After applying the boundary conditions at $x = 1$ and making use of the two identities $k_j = \bar{1}k_j$ and $b_n^T L \bar{1} = 1$, one obtains the results

$$\begin{aligned} k_v &= -B_n L(\lambda L' \bar{m})\{\bar{w}\} \\ k_\gamma &= -B_n L(L' EI)\{\bar{M}\}, \end{aligned} \quad (5.66)$$

which leads to

$$F = \begin{bmatrix} -L & 0 & 0 & 0 \\ 0 & (B_n L - I)L & 0 & 0 \\ 0 & 0 & (B_n L - I)L & 0 \\ 0 & 0 & 0 & -L \end{bmatrix} = \begin{bmatrix} -L & 0 & 0 & 0 \\ 0 & L_2^* & 0 & 0 \\ 0 & 0 & L_2^* & 0 \\ 0 & 0 & 0 & -L \end{bmatrix}. \quad (5.67)$$

From Eq. (5.67), one then obtains in the manner of Section 5.2.1 that

$$T = \begin{bmatrix} L_2^* EI L & -L_2^* EI L L_2^* \\ -L L_2^* EI L & L L_2^* EI L L_2^* \end{bmatrix} \quad (5.68)$$

from which follows the reduced eigenvalue problem

$$[L L_2^* EI L L_2^* \bar{m} - (1/\lambda)I]\{\bar{w}\} = 0. \quad (5.69)$$

Results are presented in Table 9 for the nondimensional frequencies of a uniform simply supported beam. The numerically computed results are based on Jacobi integrating matrices and are compared with exact results given in Ref. [45].

5.2.3 Hinged-Free Beam

The hinged-free beam considered in the following analysis is assumed to be simply supported at $x = 0$ and unrestrained at $x = 1$; this leads to a single rigid body mode in rotation. Boundary conditions for this beam are specified by

$$\bar{M}(0) = 0, \quad \bar{w}(0) = 0, \quad \bar{M}(1) = 0, \quad \bar{V}(1) = 0. \quad (5.70)$$

From the conditions at $x = 0$ it is easily found that

$$k_m = k_w = 0, \quad (5.71)$$

and at $x = 1$ one readily has

$$k_v = \lambda B_n L^* \bar{m} \{w\}. \quad (5.72)$$

To complete the solution for the remaining constant of integration, it is necessary to write an expression for \bar{M} in terms of k_γ . After substituting Eqs. (5.71–5.72) into Eqs. (5.51–5.54), this expression can be obtained in the form

$$\{\bar{M}\} = -\lambda L L_1^* \bar{m} L (L^* EI \{\bar{M}\} + k_\gamma). \quad (5.73)$$

From the boundary condition $\bar{M}(1) = 0$, one then obtains the result

$$k_\gamma = -c_\gamma B_n L L_1^* \bar{m} L (L^* EI) \{\bar{M}\} \quad (5.74)$$

where

$$c_\gamma = \frac{1}{b_n^T L L_1^* \bar{m} L \bar{1}}. \quad (5.75)$$

The foregoing solutions for the constants of integration lead to the expressions

$$F = \begin{bmatrix} -L & 0 & 0 & 0 \\ 0 & (B_n - I)L & 0 & 0 \\ 0 & 0 & (c_7 B_n L L_1^* \bar{m} L - I)L & 0 \\ 0 & 0 & 0 & -L \end{bmatrix} = \begin{bmatrix} -L & 0 & 0 & 0 \\ 0 & L_1^* & 0 & 0 \\ 0 & 0 & L_3^* & 0 \\ 0 & 0 & 0 & -L \end{bmatrix} \quad (5.76)$$

and

$$T = \begin{bmatrix} L_3^* E L & -L_3^* E L L_1^* \\ -L L_3^* E L & L L_3^* E L L_1^* \end{bmatrix}. \quad (5.77)$$

From Eq. (5.77) follows the reduced eigenvalue problem

$$[L L_3^* E L L_1^* \bar{m} - (1/\lambda)I]\{\bar{w}\} = 0. \quad (5.78)$$

Results are presented in Table 10 for the nondimensional frequencies of a uniform hinged-free beam. The numerically computed results are based on Jacobi integrating matrices and are compared with exact results obtained from the expression $\tan \beta - \tanh \beta = 0$, where $\sqrt{\lambda} = \beta^2$ is the nondimensional frequency.

Solutions for the eigenvalues of Eq. (5.78) can be obtained without having to apply constraint equations. Constraint equations do exist, however, in problems with rigid body modes. The presence of constraints in an eigenvalue problem will be evident from the existence of zero eigenvalues. With finite precision calculations, the zero eigenvalues are not guaranteed to be exactly zero for nonsymmetric eigenvalue problems like that in Eq. (5.78). In practice, these zero eigenvalues can appear as very small positive or negative quantities, and in some cases, complex quantities with very small real parts. The appearance of these parasitic eigenvalues is not an indication that a solution has gone astray; parasitic eigenvalues can simply be

neglected. In Eq. (5.78) the eigenvalues are related to reciprocals of the vibration frequency; therefore, the parasitic eigenvalues will equivalently manifest themselves as very high frequencies.

For problems with rigid body modes, conservation of linear and angular momentum provide the constraints that can eliminate associated zero eigenvalues. The constraint arising from linear momentum conservation is

$$\int_0^{\ell} \tilde{w} m \, dx = 0, \quad (5.79)$$

which, for free vibration, leads to the discrete constraint equation

$$\mathbf{b}_n^T \mathbf{L}\{wm\} = 0. \quad (5.80)$$

Similarly, the constraint given by angular momentum conservation is

$$\int_0^{\ell} \tilde{w} m x \, dx = 0, \quad (5.81)$$

which results in

$$\mathbf{b}_n^T \mathbf{L}\{wm x\} = 0. \quad (5.82)$$

These constraint equations can be used to reduce an eigenvalue problem as discussed in Appendix F.

5.2.4 Free-Free Beam

A free-free beam possessing rigid body translation and rotation modes presents a slightly more complicated solution for the constants of integration. Nonetheless, the procedure to be followed is similar to that used in previous problems. The

boundary conditions for the free-free beam are given by

$$\overline{M}(0) = 0, \quad V(0) = 0, \quad \overline{M}(1) = 0, \quad V(1) = 0. \quad (5.83)$$

The application of these boundary conditions to Eqs. (5.51–5.54) gives the constants of integration

$$\begin{aligned} k_m &= 0 \\ k_v &= 0 \\ k_w &= -c_w B_n L \cdot \overline{m}(-L) \{\gamma\} \\ k_\gamma &= -c_\gamma B_n L^2 \cdot \overline{m} L_4^* (L \cdot EI) \{\overline{M}\}, \end{aligned} \quad (5.84)$$

where

$$\begin{aligned} c_w &= \frac{1}{b_n^T L \cdot \overline{m} \mathbf{1}} \\ c_\gamma &= \frac{1}{b_n^T L^2 \cdot \overline{m} L_4^* \mathbf{1}} \end{aligned} \quad (5.85)$$

and

$$L_4^* = (c_w B_n L \cdot \overline{m} - I) L. \quad (5.86)$$

These results then lead to the expressions

$$F = \begin{bmatrix} -L & 0 & 0 & 0 \\ 0 & -L & 0 & 0 \\ 0 & 0 & (c_\gamma B_n L^2 \cdot \overline{m} L_4^* - I) L & 0 \\ 0 & 0 & 0 & (c_w B_n L \cdot \overline{m} - I) L \end{bmatrix} = \begin{bmatrix} -L & 0 & 0 & 0 \\ 0 & -L & 0 & 0 \\ 0 & 0 & L_5^* & 0 \\ 0 & 0 & 0 & L_4^* \end{bmatrix} \quad (5.87)$$

and

$$T = \begin{bmatrix} L_5^* \cdot EI L & L_5^* \cdot EI L^2 \\ L_4^* L_5^* \cdot EI L & L_4^* L_5^* \cdot EI L^2 \end{bmatrix}. \quad (5.88)$$

With the aid of Eq. (5.88), the reduced eigenvalue problem is given by

$$[\mathbf{L}_4^* \mathbf{L}_5^* E \mathbf{L}^2 - (1/\lambda) \mathbf{I}] \{w\} = 0. \quad (5.89)$$

For a uniform property beam the eigenvalue problem reduces to

$$[\mathbf{L}_2^* \mathbf{L}_5^* \mathbf{L}^2 - (1/\lambda) \mathbf{I}] \{w\} = 0 \quad (5.90)$$

where

$$\mathbf{L}_5^* = (c_\gamma \mathbf{B}_n \mathbf{L}^2 \mathbf{L}_2^* - \mathbf{I}) \mathbf{L} \quad (5.90)$$

and

$$c_\gamma = \frac{1}{\mathbf{b}_n^T \mathbf{L}^2 \mathbf{L}_2^* \mathbf{i}}. \quad (5.91)$$

Note that \mathbf{L}_2^* is the same as given in Section 5.2.2.

Table 11 gives the results for the nondimensional frequencies of a uniform free-free beam. The numerically computed results are based on Jacobi integrating matrices and are compared with exact results obtained from $(\cosh \beta) \cos \beta - 1 = 0$, where $\sqrt{\lambda} = \beta^2$ is the nondimensional frequency. If desired, constraint equations that reduce out the rigid body modes can be applied as discussed in the previous section.

5.3 Buckling of a Rotating Beam

In the following analysis, the state vector approach will be used to obtain solutions for buckling instabilities of the cantilevered, inward oriented rotating beam pictured in Fig. 8. Buckling is assumed to take place in the plane of rotation. Since this problem has been thoroughly examined by many investigators, results

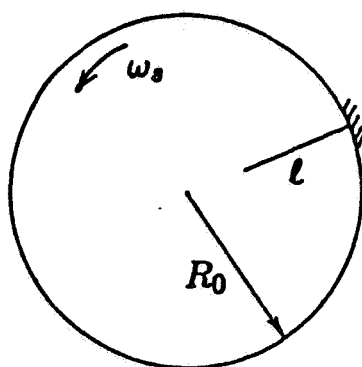


Fig. 8. Rotating beam geometry

are available with which to compare the integrating matrix solutions. This analysis demonstrates that solutions can be easily obtained for many problems involving aeroelasticity, buckling, or vibration of rotating machinery.

The state vector equations to be employed in the buckling analysis compare directly with the equations used by Steele and Barry [13]. Considering bending deformations in the plane of rotation, the nondimensional form of these equations is given by

$$\frac{d}{d\bar{x}} \begin{Bmatrix} \bar{M} \\ \bar{V} \\ \gamma \\ \bar{w} \end{Bmatrix} = \begin{bmatrix} 0 & 1 & 0 & 0 \\ 0 & 0 & 0 & 0 \\ EI & 0 & 0 & 0 \\ 0 & 0 & -1 & 0 \end{bmatrix} \begin{Bmatrix} \bar{M} \\ \bar{V} \\ \gamma \\ \bar{w} \end{Bmatrix} - \lambda_s \begin{bmatrix} 0 & 0 & -F_t & 0 \\ 0 & 0 & 0 & \bar{m} \\ 0 & 0 & 0 & 0 \\ 0 & 0 & 0 & 0 \end{bmatrix} \begin{Bmatrix} \bar{M} \\ \bar{V} \\ \gamma \\ \bar{w} \end{Bmatrix} \quad (5.92)$$

where the nondimensional tension parameter F_t is given as

$$F_t(\bar{x}) = (1/2) [(\alpha_s - 1)^2 - (\alpha_s - \bar{x})^2] \quad (5.93)$$

with

$$\alpha_s = R_0/l. \quad (5.94)$$

The nondimensional spin parameter λ_s is given by

$$\lambda_s = \frac{\omega_s^2 m_R \ell^4}{(EI)_R}. \quad (5.95)$$

Except for the displacement dependent load terms, these equations are very similar to those presented in Eq. (5.48). The solution to Eq. (5.92) is readily obtained by using the \mathbf{T} matrix presented in Eq. (5.60) for cantilever boundary conditions. The resulting buckling eigenvalue problem is given by

$$[\mathbf{T}\mathbf{A}_{FD} - (1/\lambda_s)\mathbf{I}]\begin{Bmatrix} \gamma \\ w \end{Bmatrix} = 0 \quad (5.96)$$

where

$$\mathbf{T}\mathbf{A}_{FD} = \begin{bmatrix} -L^2 EI L_1^* F_t & -L^2 EI L_1^{*2} \bar{m} \\ L^2 EI L_1^* F_t & L^2 EI L_1^{*2} \bar{m} \end{bmatrix}. \quad (5.97)$$

Results are given in Table 12 for the nondimensional critical buckling speed Ω of a uniform beam, where $\Omega = \alpha_s^2 \sqrt{\lambda_s}$. The buckling speeds, which are presented for varying values of the parameter α_s , are compared with numerical solutions given in Ref. [13]. These comparison solutions consist of results from an asymptotic iteration scheme as well as results from a high order Ritz finite element method due to Hodges [49]. Further elaboration on these critical buckling speed solutions is given by White, Kvaternik, and Kaza [31] and by Peters and Hodges [50].

5.4 Deflection of Beams

Static beam deflections and forces can be easily and accurately calculated with the hybrid state vector approach. The nondimensional state vector equations

describing lateral deflection of a beam under an applied loading p are

$$\frac{d}{dx} \begin{Bmatrix} M \\ V \\ \gamma \\ w \end{Bmatrix} = \begin{bmatrix} 0 & 1 & 0 & 0 \\ 0 & 0 & 0 & 0 \\ EI & 0 & 0 & 0 \\ 0 & 0 & -1 & 0 \end{bmatrix} \begin{Bmatrix} M \\ V \\ \gamma \\ w \end{Bmatrix} - \begin{Bmatrix} 0 \\ \bar{p} \\ 0 \\ 0 \end{Bmatrix} \quad (5.98)$$

where

$$\bar{p} = \frac{p\ell^3}{(EI)_R} \quad (5.99)$$

Solutions to Eq. (5.98) are given by Eqs. (4.23) and (4.24). If aerodynamic loads are not present, one must take $\lambda = 0$. Noting that $H_{FD} = 0$, then for cantilever boundary conditions the deflection and force solutions are given by

$$y_D = T \bar{a}_{r_F}, \quad (5.100)$$

$$y_F = H_{FF}^{-1} L_1^* \bar{a}_{r_F}. \quad (5.101)$$

By using the T matrix in Eq. (5.60), these solutions can be further refined to give

$$y_D = \begin{Bmatrix} \gamma \\ w \end{Bmatrix} = \begin{Bmatrix} -L^* EI L_1^{*2} \bar{p} \\ L^2 EI L_1^{*2} \bar{p} \end{Bmatrix} \quad (5.102)$$

and

$$y_F = \begin{Bmatrix} M \\ V \end{Bmatrix} = \begin{Bmatrix} -L_1^{*2} \bar{p} \\ L_1^* \bar{p} \end{Bmatrix}. \quad (5.103)$$

As an indicator of solution accuracy, one can easily verify with a sample calculation that a four interval Jacobi integrating matrix solution will provide the exact deflections for a uniform cantilevered beam having a constant load distribution.

It should be noted that matrix inversions are not required in solving for either forces or displacements. Deflection solutions similar to these are used to obtain static aeroelastic lift distributions in the next chapter.

Table 1

Nondimensional frequencies, $\lambda^{1/2}$, for the axial modes of a uniform cantilevered rod with N collocation intervals. ($\lambda = \omega^2 m_R \ell^2 / (EA)_R$)

N	Mode	% Error				
		Jacobi	Newton	Exact	Jacobi	Newton
2	1	1.582576	1.582576	1.570796	.749938	.749938
	2	7.582580	7.582580	4.712389	60.9073	60.9073
3	1	1.571009	1.569703	1.570796	.013560	-.069583
	2	4.962687	4.826099	4.712389	5.31149	2.41300
	3	15.39166	14.25626	7.853982	95.9727	81.5163
4	1	1.570799	1.570732	1.570796	.000191	-.004074
	2	4.735692	4.665351	4.712389	.494505	-.998177
	3	8.807365	8.070704	7.853982	12.1388	2.75939
	4	25.64255	21.64282	10.99557	133.208	96.8321
5	1	1.570797	1.570803	1.570796	.000064	.000446
	2	4.713869	4.706141	4.712389	.031407	-.132587
	3	8.011505	7.631141	7.853982	2.00564	-2.83730
	4	13.27345	11.23810	10.99557	20.7163	2.20567
	5	38.40523	29.57599	14.13717	171.661	109.207

Table 2

Axial vibration mode shapes, $\{\bar{u}\}$, for a uniform cantilevered rod (Numerical solutions obtained with five collocation intervals)

\bar{x}	0.0	0.2	0.4	0.6	0.8	1.0
Mode 1						
Jacobi	0.00000	0.30903	0.58779	0.80902	0.95107	1.00000
Newton	0.00000	0.30902	0.58779	0.80902	0.95106	1.00000
Exact	0.00000	0.30902	0.58779	0.80902	0.95106	1.00000
Mode 2						
Jacobi	0.00000	-.81474	-.94453	-.30816	0.58191	1.00000
Newton	0.00000	-.81516	-.95512	-.31182	0.59050	1.00000
Exact	0.00000	-.80902	-.95106	-.30902	0.58779	1.00000
Mode 3						
Jacobi	0.00000	0.91354	-.01155	-.87489	-.09662	1.00000
Newton	0.00000	0.98697	-.03503	-.95027	-.08023	1.00000
Exact	0.00000	1.00000	0.00000	-1.0000	0.00000	1.00000

Table 3

Nondimensional frequencies, $\lambda^{1/2}$, for the axial modes of a linearly tapered cantilevered rod with N collocation intervals. ($\beta_t = 0.5$; $\lambda = \omega^2 m_R \ell^2 / (EA)_R$)

N	Mode	Jacobi	Newton	Exact	% Error	
					Jacobi	Newton
2	1	1.613095	1.613095	1.652805	-2.40258	-2.40258
	2	11.15869	11.15869	3.627852	207.584	207.584
3	1	1.643238	1.665064	1.652805	-.578834	.741709
	2	3.587127	3.535655	3.627852	-1.12257	-2.54137
	3	22.39381	20.38371	5.807501	285.601	250.989
4	1	1.652913	1.649068	1.652805	.006534	-.226100
	2	3.580021	3.658788	3.627852	-1.31844	.852736
	3	6.040474	5.622661	5.807501	4.01159	-3.18278
	4	37.76820	30.95097	8.215935	359.694	276.719
5	1	1.652826	1.653185	1.652805	.001271	.022991
	2	3.633674	3.608995	3.627852	.160481	-.519784
	3	5.721657	5.887524	5.807501	-1.47816	1.37793
	4	9.001691	7.591113	8.215935	9.56381	-7.60500
	5	57.31683	42.52789	10.27790	457.671	313.780

Table 4

Nondimensional frequencies, $\lambda^{1/2}$, for the axial modes of a three segment cantilevered rod with discontinuous stiffness and mass. There are N collocation intervals per segment. ($\lambda = \omega^2 m_R \ell^2 / (EA)_R$; $\gamma = 10$, $\delta = 100$; Error based on six significant figures)

N	Mode	Jacobi	Newton	Exact	% Error	
					Jacobi	Newton
1	1	.8336431	.8336431	.8267091	.838747	.838747
	2	22.20007	22.20007	6.097328	264.095	264.095
	3	121.7023	121.7023	11.98907	915.105	915.105
2	1	.8267307	.8267298	.8267091	.002661	.002540
	2	6.729430	6.729422	6.097328	10.3668	10.3667
	3	19.03003	19.03001	11.98907	58.7275	58.7275
	4	41.08241	41.08287	17.57944	133.696	133.699
	5	85.56076	85.56099	19.46456	339.571	339.572
3	1	.8267099	.8267071	.8267091	.000121	-.000242
	2	6.139068	6.082418	6.097328	.684562	-.244533
	3	14.52343	13.85007	11.98907	21.1384	15.5224
	4	19.45551	19.33504	17.57944	10.6722	9.98669
	5	38.17844	37.79570	19.46456	96.1427	94.1766
4	1	.8267105	.8267104	.8267091	.000121	.000121
	2	6.099150	6.085790	6.097328	.029849	-.189263
	3	12.34547	11.82625	11.98907	2.97270	-1.35790
	4	18.83118	18.54741	17.57944	7.12083	5.50645
	5	25.28983	22.48436	19.46456	29.9271	15.5143
5	1	.8267107	.8267107	.8267091	.000242	.000242
	2	6.097375	6.097551	6.097328	.000820	.003608
	3	12.03000	11.86734	11.98907	.341143	-1.01592
	4	18.17894	17.10370	17.57944	3.41024	-2.70601
	5	20.28574	19.38240	19.46456	4.21843	-.422331

Table 5

Nondimensional frequencies, $\lambda^{1/2}$, for the axial modes of a uniform cantilevered rod with variable stiffness elastic restraint at the free end. Results were obtained with a Jacobi integrating matrix using six collocation points. ($\bar{k}_e = k/(EA)_R$; $\lambda = \omega^2 m_R \ell^2 / (EA)_R$)

Mode	$\bar{k}_e = 0.0$	$\bar{k}_e = 0.25$	$\bar{k}_e = 1.0E8$
1	1.57080	1.71551	3.14161
(exact)	(1.57080)	(1.71551)	(3.14159)
2	4.71387	4.76644	6.30594
(exact)	(4.71239)	(4.76481)	(6.28318)
3	8.01150	8.04779	10.1059
(exact)	(7.85398)	(7.88567)	(9.42478)

Table 6

Nondimensional frequencies, $\lambda^{1/2}$, for the axial modes of a uniform cantilevered rod with tip mass. Results were obtained with a Jacobi integrating matrix using six collocation points. ($\bar{m}_n^+ = m_n/m_R \ell$; $\lambda = \omega^2 m_R \ell^2 / (EA)_R$)

Mode	$\bar{m}_n^+ = 0.0$	$\bar{m}_n^+ = 0.25$	$\bar{m}_n^+ = 1.0E8$
1	1.57080	1.26770	0.00010
(exact)	(1.57080)	(1.26459)	(0.00000)
2	4.71387	3.98864	3.24838
(exact)	(4.71239)	(3.93517)	(3.14159)
3	8.01150	7.00118	6.52342
(exact)	(7.85398)	(6.81401)	(6.28319)

Table 7

Nondimensional bending frequencies, $\lambda^{1/2}$, of a uniform cantilever beam for a Jacobi integrating matrix solution using five collocation intervals. ($\lambda = \omega^2 m_R \ell^4 / (EI)_R$)

Mode	1	2	3	4	5
Calculated	3.516022	22.04884	64.15257	178.0921	1032.319
Exact	3.516015	22.03449	61.69721	120.9019	199.8595

Table 8

Lateral bending mode shapes, $\{w\}$, of a uniform cantilever beam (Jacobi integrating matrix solution using five collocation intervals)

Mode \ x	0.0	0.2	0.4	0.6	0.8	1.0
1	0.00000	0.06386	0.22990	0.46114	0.72547	1.00000
(exact)	(0.00000)	(0.06387)	(0.22989)	(0.46114)	(0.72548)	(1.00000)
2	0.00000	-.30660	-.68022	-.58537	0.06418	1.00000
(exact)	(0.00000)	(-.30106)	(-.68347)	(-.58948)	(0.07004)	(1.00000)
3	0.00000	0.60087	0.45954	-.40455	-.41063	1.00000
(exact)	(0.00000)	(0.60450)	(0.52593)	(-.47377)	(-.39488)	(1.00000)

Table 9

Nondimensional bending frequencies, $\lambda^{1/2}$, of a uniform, simply supported beam with N collocation intervals; ($\lambda = \omega^2 m_R \ell^4 / (EI)_R$)

<i>N</i>	Mode	Jacobi	Exact
2	1	12.00003	9.86960
3	1	10.00003	9.86960
	2	59.99989	39.4784
4	1	9.875132	9.86960
	2	41.99992	39.4784
	3	170.1317	88.8264
5	1	9.869781	9.86960
	2	39.76482	39.4784
	3	102.1309	88.8264
	4	380.2456	157.9137

Table 10

Nondimensional bending frequencies, $\lambda^{1/2}$, of a uniform, hinged-free beam with N collocation intervals; ($\lambda = \omega^2 m_R \ell^4 / (EI)_R$)

<i>N</i>	Mode	Jacobi	Exact
2	1	24.00014	15.41821
3	1	16.07796	15.41821
	2	105.5557	49.96487
4	1	15.46149	15.41821
	2	56.60144	49.96487
	3	295.1689	104.2477
5	1	15.42012	15.41821
	2	50.88158	49.96487
	3	131.8585	104.2477
	4	628.4688	178.2697

Table 11

Nondimensional bending frequencies, $\lambda^{1/2}$, of a uniform, free-free beam with N collocation intervals; ($\lambda = \omega^2 m_R \ell^4 / (EI)_R$)

N	Mode	Jacobi	Exact
3	1	24.49481	22.37332
4	1	22.61198	22.37332
	2	76.68076	61.68503
5	1	22.38678	22.37332
	2	64.21640	61.68503
	3	174.3449	120.9027

Table 12

Nondimensional buckling speeds, Ω , of a uniform, inward-oriented, rotating beam. Jacobi integrating matrix solutions with N collocation intervals. ($\Omega = \alpha_s^2 \sqrt{\lambda_s}$)

α_s	<u>WKB</u>	<u>Hodges</u>	<u>State Vector Method</u>			
	Direct Integration	Ritz FEM	$N = 5$	$N = 4$	$N = 3$	$N = 2$
.2	.35	.35	.35	.35	.35	.65
.5	1.13	1.13	1.13	1.13	1.13	1.19
1.0	2.96	2.99	2.99	2.99	2.99	3.05
1.5	5.35	5.38	5.38	5.38	5.38	5.46
2.0	8.27	8.19	8.19	8.19	8.19	8.30
3.0	14.91	14.87	14.87	14.87	14.89	15.05
4.0	22.70	22.77	22.77	22.77	22.81	23.03

Chapter 6

Divergence and Aeroelastic Lift of Composite Wings

STATIC AEROELASTIC BEHAVIOR, which includes both divergence instability and aeroelastic lift distribution, is an important consideration in the design of elastically flexible lifting surfaces. An innovative approach to aeroelastic design is provided by the concept of aeroelastic tailoring, which addresses the problem of designing a flexible lifting surface to take advantage of structural deformation. Essentially, one strives to control the deformation, and thus the load distribution, in a way that enhances aerodynamic performance. Because of their unique directional properties, advanced composite materials prove to be an important ingredient in many tailored designs.

Along with the increased design flexibility allowed by composite materials, there comes an additional complexity in the structural analysis. The hybrid state vector method discussed in previous chapters provides a simple, yet powerful tool for analyzing large aspect ratio composite lifting surfaces. The primary focus of this chapter is on applying the anisotropic beam equations developed in Section 2.3 to the static aeroelastic analysis of forward swept composite wings.

The potential benefits of aeroelastic tailoring applied to forward swept composite wings have been thoroughly examined by Weisshaar [4,5,51]. In order to

facilitate the verification of the hybrid state vector solutions, the problems considered in this chapter are similar in nature to those discussed by Weisshaar for uniform geometry wings. In the following analyses, aerodynamic loads will be calculated from modified strip theory aerodynamics.

6.1 Divergence of a Forward Swept Composite Wing

The cantilevered composite wing structure considered in the following analysis is identical to the lifting surface model presented in Fig. 1 of Chapter 2. The aeroelastic equations apply to aerodynamic sections taken normal to the swept structural reference axis. A detailed derivation of the differential equations for this plate-beam model, including important assumptions, is presented in Section 2.3. It should be noted that for static aeroelastic stability calculations, these equations are, in fact, perturbation equations, with the state vector containing perturbation quantities.

For the sake of simplifying the presentation, it is assumed that transverse shear terms can be neglected. Another important assumption to be used in the analysis is that the composite wing structure, which is modelled as an equivalent composite plate, can be considered as having the same properties as a midplane symmetric laminate. Primarily, this means that the \bar{B}_{ij}^* coupling compliances in Eq. (2.28) will be taken as zero.

For fixed wing problems, it is clear that no appreciable external spanwise loads exist. In the event that \bar{B}_{ij}^* coupling compliances are included in the analysis, there will be induced spanwise loads that arise from satisfying the fifth equation in Eq. (2.28). These coupling-induced spanwise loads can be directly calculated if one has solutions for the static spanwise midplane deformations u_0 . If solutions for u_0 are not readily available, the coupling-induced loads can be approximately determined

by assuming that the spanwise strains and strain gradients are negligible.

By following the solution procedure described in Chapter 4, the \mathbf{T} matrix corresponding to Eq. (2.28) can be easily determined for a cantilevered composite wing. When the \bar{B}_{ij}^* terms are assumed to be zero, this matrix can be written as

$$\mathbf{T} = \begin{bmatrix} L \bar{A}_{11}^* L_1^* & 0 & 0 & 0 \\ 0 & L \bar{D}_{11}^* L_1^* & -L \bar{D}_{11}^* L_1^{*2} & L \bar{D}_{13}^* L_1^* \\ 0 & -L^2 \bar{D}_{11}^* L_1^* & L^2 \bar{D}_{11}^* L_1^{*2} & -L^2 \bar{D}_{13}^* L_1^* \\ 0 & L \bar{D}_{13}^* L_1^* & -L \bar{D}_{13}^* L_1^{*2} & L \bar{D}_{33}^* L_1^* \end{bmatrix}. \quad (6.1)$$

A steady aerodynamics matrix based on strip theory can be extracted from the unsteady strip theory results in Appendix D by taking $s^* = 0$, $C(0) = 1.0$, and $R = 1.0$. The resulting aerodynamic matrix is given by

$$\mathbf{A}_{FD} = \begin{bmatrix} 0 & 0 & 0 & 0 \\ 0 & 0 & 0 & 0 \\ 0 & \lambda L_\gamma & 0 & \lambda L_\alpha \\ 0 & \lambda M_\gamma & 0 & \lambda M_\alpha \end{bmatrix} \quad (6.2)$$

where the terms in \mathbf{A}_{FD} are obtained from the corresponding terms of Eqs. (D.1–D.2) in Appendix D. For example, $\lambda L_\gamma = \lambda \hat{L}_\gamma(s^* = 0, \lambda)$, where λ is a nondimensional dynamic pressure parameter (see Appendix D). For large aspect ratio and moderate sweep angles, the terms in Eqs. (D.3–D.4) involving λL_γ and λM_γ are negligible.

Substituting Eqs. (6.1–6.2) into Eq. (4.29) leads to the divergence eigenvalue problem

$$\left[\begin{bmatrix} \mathbf{G}_{11} & \mathbf{G}_{12} \\ \mathbf{G}_{21} & \mathbf{G}_{22} \end{bmatrix} - \frac{1}{\lambda} \begin{bmatrix} \mathbf{I} & \mathbf{0} \\ \mathbf{0} & \mathbf{I} \end{bmatrix} \right] \begin{Bmatrix} \gamma \\ \alpha \end{Bmatrix} = 0, \quad (6.3)$$

where

$$\begin{aligned}
G_{11} &= -L^* \bar{D}_{11}^* L_1^{*2} L_\gamma + L^* \bar{D}_{13}^* L_1^* M_\gamma \\
G_{12} &= -L^* \bar{D}_{11}^* L_1^{*2} L_\alpha + L^* \bar{D}_{13}^* L_1^* M_\alpha \\
G_{21} &= -L^* \bar{D}_{13}^* L_1^{*2} L_\gamma + L^* \bar{D}_{33}^* L_1^* M_\gamma \\
G_{22} &= -L^* \bar{D}_{13}^* L_1^{*2} L_\alpha + L^* \bar{D}_{33}^* L_1^* M_\alpha.
\end{aligned} \tag{6.4}$$

Since the divergence problem being considered involves neither axial loading nor constitutive terms that couple axial deformations with other degrees of freedom, one might expect that the use of simple strip theory aerodynamics, as given above, should allow representation of the eigenvalue problem in Eq. (6.3) in terms of an effective angle of attack. This is indeed the situation.

In order to carry out the reduction to effective angle of attack, first note that because of the nature of the aerodynamic terms one can write

$$\begin{bmatrix} G_{11} & G_{12} \\ G_{21} & G_{22} \end{bmatrix} = \begin{bmatrix} -G_{12} & G_{12} \\ -G_{22} & G_{22} \end{bmatrix} \begin{bmatrix} \tan \Lambda & 0 \\ 0 & 1 \end{bmatrix}. \tag{6.5}$$

Second, note that a constraint equation involving the effective angle of attack α_e can be written as

$$\alpha_e = \alpha - \gamma \tan \Lambda. \tag{6.6}$$

This constraint equation expresses the fact that the effective angle of attack for a swept wing consists of the actual twist of the wing plus an induced angle of attack that arises from lateral bending. From this constraint equation, one can obtain the transformation

$$\begin{Bmatrix} \alpha_e \\ \alpha \end{Bmatrix} = U^{-1} \begin{Bmatrix} \gamma \\ \alpha \end{Bmatrix}, \tag{6.7}$$

Table 13

Geometric, aerodynamic, and structural parameters for a uniform composite wing

<u>ELASTIC MODULI:</u>	<u>WING PROPERTIES:</u>
$E_2/E_1 = 0.1$	$\ell/b_R = 6.67$
$G_{12}/E_1 = 0.0373$	$b_R = 1.0$
$\nu_{12} = 0.25$	$\bar{b} = 1.0$
	$a_0 = 2\pi$
	$a_c = 0.5$
	$\alpha = 0.34$

where

$$U^{-1} = \begin{bmatrix} -\tan \Lambda & I \\ 0 & I \end{bmatrix}. \quad (6.8)$$

By applying this transformation in the form of a similarity transformation to Eq. (6.3) while making use of Eq. (6.5), one obtains a reduced eigenvalue problem that can be written as

$$[G_{22} - (\tan \Lambda)G_{12}]\{\alpha_e\} = (1/\lambda)\{\alpha_e\}. \quad (6.9)$$

Details on the transformation process used in obtaining Eq. (6.9) are presented in Appendix F. Note that either a similarity transformation or a congruence transformation must be used since these transformations do not affect the eigenvalues.

In order to verify solutions given by Eq. (6.9), divergence eigenvalues were obtained for uniform, forward swept, composite wings with cantilever boundary conditions. Verification was established by comparing the trends of the results with analytical solutions given by Weisshaar [4]. The data used in the analysis are presented in Table 13, and are taken from a uniform, composite wing analyzed by Housner and Stein [52]. These data are also used in a composite wing flutter analysis presented in Chapter 7.

From the material parameters listed in Table 13, angle-ply laminate stiffnesses were calculated for a midplane symmetric composite plate by using the methods given in Appendix C. A special form of these calculations for angle-ply laminates is given in Section 4.4.4 of Jones [25]. Box beam type structures are easily analyzed by carrying out the analyses in terms of an equivalent composite plate. Divergence solutions were investigated for laminates having nondimensional stiffnesses equivalent to an angle-ply laminate with a given number of layers. Since the magnitudes of the composite laminate coupling terms vary with the number of layers, this allows investigation of the effects of coupling stiffness on divergence velocity. The maximum values of coupling are obtained for a laminate with a single layer (i.e., the same as multiple layers with all layers oriented in the same direction). Thus, a single layer angle-ply laminate provides a limiting case solution. As the number of layers increases, the coupling terms decrease and the laminate tends toward quasi-isotropic behavior.

Fig. 9 displays the variation of the nondimensional bending and torsion compliances for a single layer angle-ply laminate as the fiber orientation angle varies. Material properties were taken from Table 13. The orientation angle θ , positive as shown in Fig. C-2, is measured with respect to the laminate reference axis, which in the following problems will be assumed the same as the structural reference axis. For analyzing a composite wing, the structural reference axis is chosen as the mid-chord of the structural box, since the composite stiffness expressions are developed with respect to this axis. One should note that \bar{D}_{11}^* and \bar{D}_{33}^* are symmetric with respect to $\theta = 0$, whereas the coupling term \bar{D}_{13}^* is antisymmetric in θ . The compliances in Fig. 9 are nondimensionalized as shown in Eqs. (2.30) and (2.32), with the reference stiffness chosen to be D_{11} evaluated at $\theta = 0$.

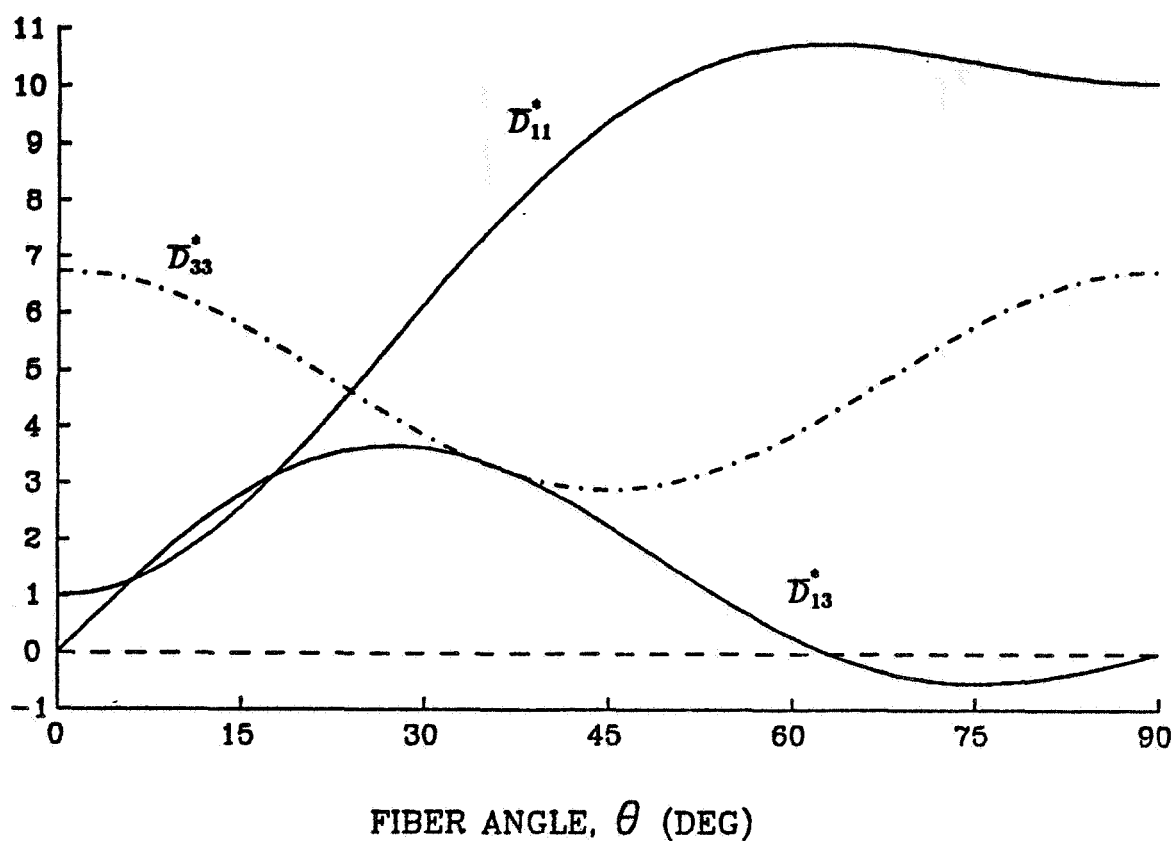


Fig. 9. Nondimensional compliances for a symmetric angle-ply laminate with a single layer

Presented in Fig. 10 are the nondimensional divergence velocities of a uniform, cantilevered, composite wing that is swept forward 30 degrees ($\Lambda = -30^\circ$). Data are taken from Table 13. The nondimensional divergence velocities are plotted as a function of the fiber orientation angle for the equivalent of a midplane symmetric angle-ply laminate. The reference divergence velocity for this figure is the velocity for a one layer laminate with $\theta = -90^\circ$. Three different curves are shown corresponding to coupling stiffnesses equivalent to laminates with one, five, and fifteen layers. As can be seen, the predicted divergence velocities dramatically increase for a range of fiber orientation angles greater than zero. These angles correspond to fibers that are oriented ahead of the structural reference axis. Some of the fiber orientation angles yield negative eigenvalues that give imaginary divergence velocities,

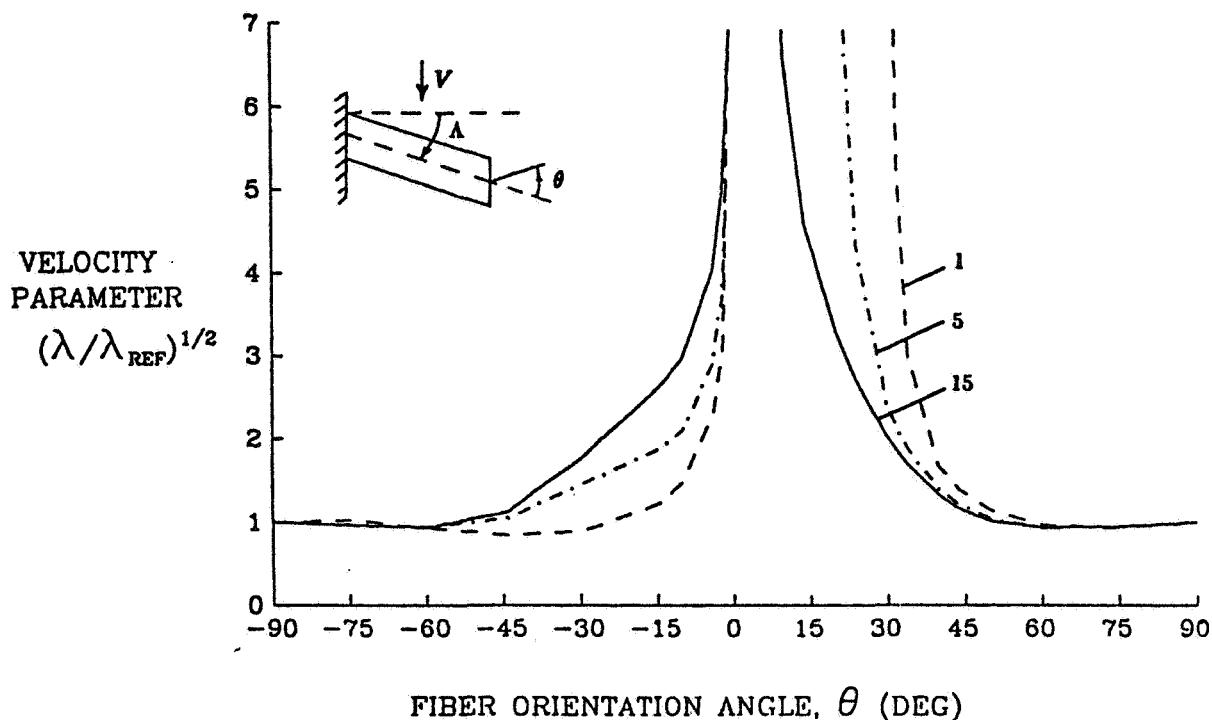


Fig. 10. Nondimensional divergence velocities of a uniform, cantilevered, composite wing—symmetric angle-ply with 1, 5, and 15 layers. ($\Lambda = -30^\circ$, $\lambda_{REF} = \lambda_{(\Lambda=-30^\circ, \theta=-90^\circ)}$)

indicating that divergence does not occur for these fiber angles. The largest range of infinite divergence velocities is exhibited by the single layer equivalent laminate, which possesses the largest value of bending-twist coupling. Although the bending-twist coupling is not the only factor determining the divergence velocity, it is clear that it has a dominant effect. The physical reason underlying the importance of the coupling stiffness is that it can give a lifting surface a washout property, meaning that bending of the surface, and resulting twist, act to alleviate the excessive buildup of aerodynamic loads.

Similar divergence velocity solutions are given in Fig. 11 for a wing that is swept forward 60 degrees ($\Lambda = -60^\circ$). Again, three curves are presented, each

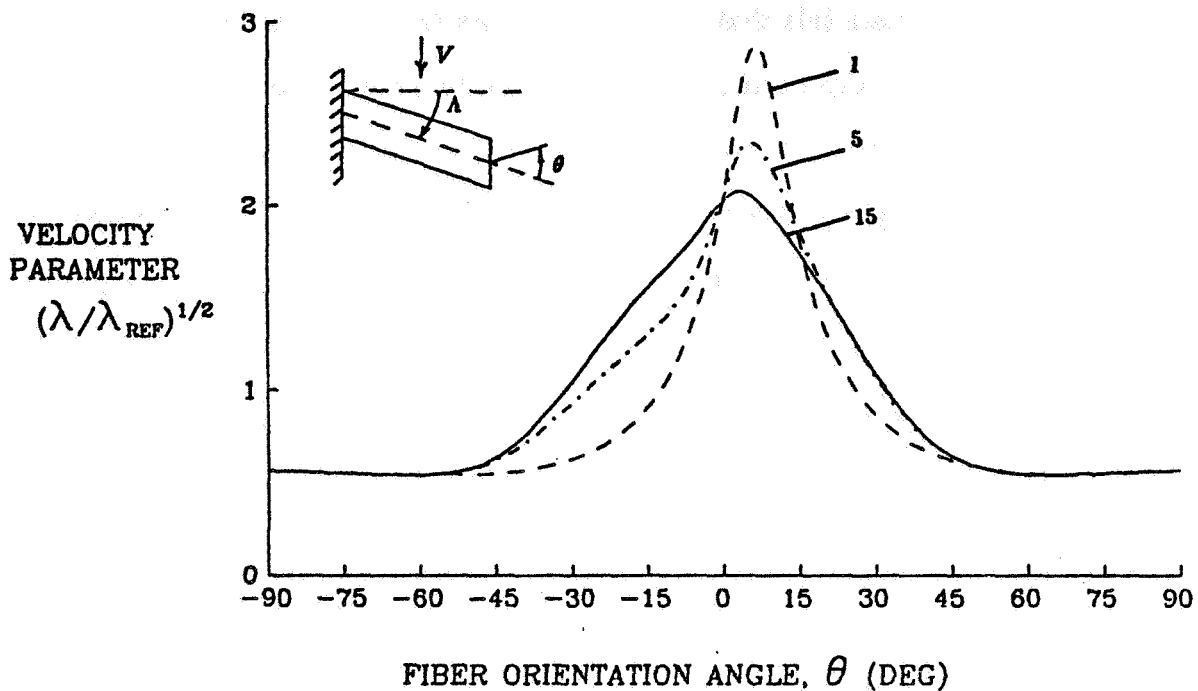


Fig. 11. Nondimensional divergence velocities of a uniform, cantilevered, composite wing—symmetric angle-ply with 1, 5, and 15 layers. ($\Lambda = -60^\circ$, $\lambda_{REF} = \lambda_{(\Lambda = -30^\circ, \theta = -90^\circ)}$)

corresponding to an equivalent angle-ply laminate with a specified number of layers. The reference velocity is the same as that in Fig. 10, which is the divergence velocity for a single layer laminate having a fiber orientation of $\theta = -90^\circ$ and a forward aerodynamic sweep of 30 degrees. For this example, no infinite divergence velocities are predicted since the coupling and bending stiffnesses are not large enough to completely override the aerodynamic loading. The maximum values of divergence velocity still occur at fiber orientation angles slightly ahead of the structural reference axis. An interesting point to note from Fig. 11 is that the result for a laminate with 15 layers, which has only a small amount of coupling stiffness, is nearly symmetric about $\theta = 0$. This indicates that the behavior of a

wing with 60 degrees of forward sweep is also strongly influenced by the bending stiffness. The bending stiffness is symmetric in θ and peaks at $\theta = 0$.

For composite materials that are different from the one on which Figs. 10 and 11 are based, one can expect the locations of the peaks in the divergence velocity to shift slightly. These shifts are possible because other composites may exhibit different ratios of coupling to bending stiffness. The basic trends demonstrated are expected to be valid, however, for any type of unidirectional laminated composite. The trends demonstrated in Figs. 10 and 11 are corroborated by the analytical results presented by Weisshaar [4].

6.2 Aeroelastic Lift of a Forward Swept Composite Wing

Of great interest in aeroelastic design is the equilibrium lift distribution of a flexible wing, especially since aerodynamic efficiency is strongly impacted by the lift distribution. The lift distribution of a flexible wing is also closely tied to maneuver performance as well as to divergence instabilities. That is, the combined bending and twisting of a loaded wing can act either to amplify or to attenuate the loading and the bending moments associated with disturbances about a nominal equilibrium lift condition.

Successful design of forward swept wings hinges upon the ability to "tailor" the lift distribution. Composite materials offer significant advantages in the design and construction of lifting surfaces that are tailored to maintain favorable deformation patterns, and therefore favorable lift distributions, over a range of flight conditions. The following analysis investigates solutions for symmetrical aeroelastic lift of forward swept, cantilevered wings. These wings can be described by the same composite plate-beam model employed in Section 6.1.

The approach adopted in solving for the lift distribution involves specifying

the pitch attitude (angle of attack) of the untwisted, rigid wing. This provides the initial load distribution from which the elastic deformation is determined. The total deformation of the wing is the sum of the rigid wing attitude plus the elastic deformation component. Correspondingly, the total lift distribution of the wing (assuming linear aerodynamics) is the sum of the rigid wing lift plus the elastic lift. A similar approach has been used by Diederich and Foss [3] to study the lift of metallic swept wings, and by Weisshaar [5] to examine the lift of composite wings. Further elaboration on solutions for aeroelastic lift distribution can be found in Chapter 8 of Bisplinghoff, Ashley, and Halfman [45].

Equations that provide the lift distribution solutions for the aforementioned composite plate-beam can be obtained by substituting Eqs. (6.1–6.2) into Eq. (4.26), resulting in

$$\begin{bmatrix} \mathbf{I} - \lambda \mathbf{G}_{11} & -\lambda \mathbf{G}_{12} \\ -\lambda \mathbf{G}_{21} & \mathbf{I} - \lambda \mathbf{G}_{22} \end{bmatrix} \begin{Bmatrix} \gamma \\ \alpha \end{Bmatrix} = \lambda \begin{bmatrix} \mathbf{G}_{11} & \mathbf{G}_{12} \\ \mathbf{G}_{21} & \mathbf{G}_{22} \end{bmatrix} \begin{Bmatrix} \gamma_r \\ \alpha_r \end{Bmatrix} \quad (6.10)$$

where the \mathbf{G} terms are given by Eq. (6.4). The attitude of the rigid wing is specified by γ_r and α_r . Similar to the reduction of the dependent variables in the divergence problem of Section 6.1, the linear system in Eq. (6.10) can be reduced to an effective angle of attack variable, α_e , since neither axial loading nor axial deformation coupling terms are present. By employing the same relationships and the same approach presented in Eqs. (6.5–6.8), Eq. (6.10) reduces to

$$[\mathbf{I} - \bar{\mathbf{G}}] \{\alpha_e\} = \bar{\mathbf{G}} \{\alpha_{er}\} \quad (6.11)$$

where

$$\bar{\mathbf{G}} = \lambda [\mathbf{G}_{22} - (\tan \Lambda) \mathbf{G}_{12}]. \quad (6.12)$$

To verify these results, lift distribution solutions have been obtained from Eq. (6.11) for a uniform, swept-forward composite wing. Material property data for the

analysis were taken from Table 13, and aerodynamic loads were calculated with the aid of simple strip theory aerodynamics. Results are displayed in Fig. 12 for the maximum and minimum values of normalized elastic lift distribution, C_{ℓ_e}/C_{ℓ_r} , as a function of the nondimensional spanwise coordinate \bar{x} . A symmetric angle-ply composite with a single layer has been assumed (i.e., all fibers are oriented in the same direction). Since the lift curve slope is assumed constant, the use of strip theory aerodynamics allows the lift distributions to be calculated as the ratio of elastic wing deflections (effective angle of attack) to rigid wing deflections. For solutions obtained in this manner, it is convenient to specify the rigid wing effective angle of attack as a unit value. Also specified prior to the solution of Eq. (6.11) is the nondimensional dynamic pressure parameter λ . The value for this parameter was arbitrarily picked to be one half of the divergence dynamic pressure parameter for a wing having 60 degrees of forward sweep and an angle-ply fiber orientation angle of $\theta = -90^\circ$.

For the wing used in the analysis, it is assumed that all fibers are oriented at an angle θ with respect to the structural reference axis. The results display for each constant wing sweep angle the fiber orientation angle that corresponds to either the maximum load amplification or attenuation that can be achieved by orienting the reinforcing fibers. Hence, these solutions are an indicator of the maximum amount of "tailoring" that can be achieved for a given configuration and material. The designs that fall below the dashed rigid wing reference line in the figure are referred to as load attenuating designs, while those above the reference line correspond to load amplifying designs. It is interesting to note that the maximum amount of lift attenuation, which also corresponds to maximum divergence speed, occurs when the fibers are oriented ahead of the structural reference axis. Those swept-forward wings whose lift distributions fall below the dashed rigid wing reference line are in fact displaying the load alleviating property of an isotropic swept-back wing.

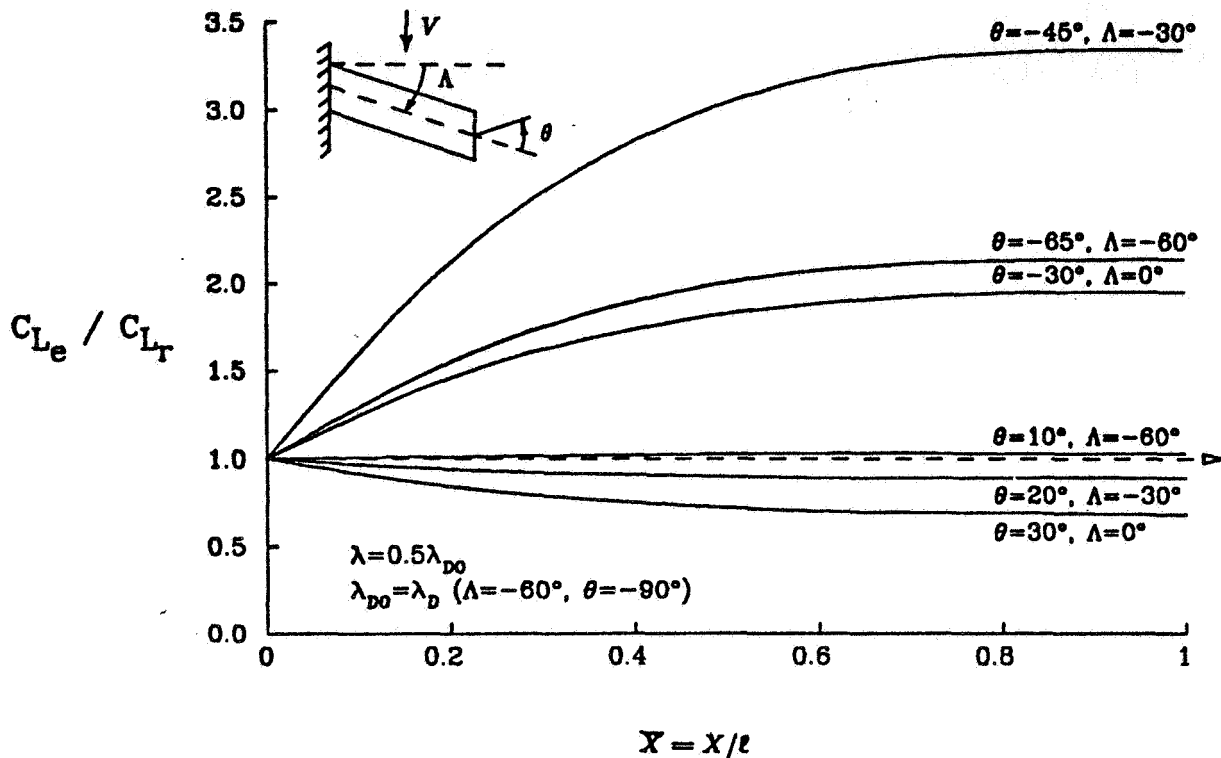


Fig. 12. Limiting elastic lift distributions for a uniform composite wing—symmetric angle-ply with a single layer

These results are verified by an analytical solution developed by Weisshaar [5] for normalized elastic lift distribution of uniform composite wings. A comparison of the analytical solutions with the approximate Jacobi integrating matrix solutions (based on five discretization intervals) shows a maximum deviation from the true lift distribution curves of less than one-tenth of one percent.

Another conclusion that comes from Fig. 12 is that the wing of this example, with 60 degrees of forward sweep, never completely reaches the load attenuating region. This corresponds to the fact that for $\Lambda = -60^\circ$, the wing will always possess a finite divergence velocity. For the other wing sweep angles given in the figure, there exists a fiber orientation angle for which the result is coincident with the rigid wing reference solution. Such designs are referred to as *aero-isoclinic* and have

neither a load attenuating nor load amplifying character.

Chapter 7

Flutter of Isotropic and Composite Wings

DYNAMIC AEROELASTIC BEHAVIOR will now be examined for both isotropic and composite wings having cantilever boundary conditions. The solutions to be pursued in the following problems will yield the airspeeds associated with flutter instabilities. For composite lifting surfaces, it will be shown that the fiber orientation angles have a very strong influence on the points of instability, as well as on the subcritical dynamic response. It should be pointed out that the following investigations are meant only to demonstrate the solution capabilities available with the hybrid state vector approach. A detailed investigation of various types of flutter phenomena is not attempted here since the scope of such a study falls outside the objectives of the present work.

In the sample flutter calculations to be presented, a single formulation of the flutter equations will be used that is appropriate for anisotropic structures; isotropic structures are simply considered as a subset of the anisotropic case. The approach used to obtain the subcritical dynamic response and the flutter points involves tracing out the complex roots loci of the matrix flutter equations. A description of this solution process will be presented in the course of the following analyses.

7.1 Flutter Equations

The general form of the flutter eigenvalue equation to be used was presented in Eq. (4.30). It appears as

$$\left[\mathbf{I} + \mathbf{T}[\mathbf{M}_{FD}s^{*2} + \mathbf{C}_{FD}s^* - \mathbf{Q}_{FD}(s^*, \lambda)] \right] \hat{\mathbf{y}}_D = 0 \quad (7.1)$$

where \mathbf{M}_{FD} is the discrete mass matrix for the lifting surface, \mathbf{C}_{FD} is a damping matrix, and \mathbf{Q}_{FD} is an unsteady aerodynamic matrix. Note that Eq. (7.1) is actually the Laplace transform with respect to time of the homogeneous, unsteady aeroelastic equations. It is assumed that the equations have been nondimensionalized such that s^* is a nondimensional, complex-valued, Laplace transform variable given by

$$s^* = s\ell^2 \sqrt{\frac{m_R}{(EI)_R}} \quad (7.2)$$

and $\hat{\mathbf{y}}_D$ is a nondimensional complex eigenvector. Also note that in the present application λ is a dimensionless dynamic pressure parameter whose definition is given in Appendix D.

Precise forms of the matrix terms in Eq. (7.1) are taken to correspond to the anisotropic plate-beam equations presented in Eq. (2.28). The unsteady aerodynamic matrix, which will be calculated from modified strip theory, is given in Appendix D. The \mathbf{T} matrix has already been presented in Eq. (6.1) for cantilever boundary conditions. It will also be assumed for convenience that the damping terms are zero for the following analyses. In nondimensional form, the mass matrix in Eq. (7.1) can be expressed as

$$\mathbf{M}_{FD} = \begin{bmatrix} 0 & 0 & 0 & 0 \\ 0 & 0 & 0 & 0 \\ 0 & 0 & \bar{m}_{ww} & \bar{m}_{w\alpha} \\ 0 & 0 & \bar{m}_{w\alpha} & \bar{m}_{\alpha\alpha} \end{bmatrix} \quad (7.3)$$

where

$$\begin{aligned} \bar{m}_{ww} &= \frac{m}{m_R}, \\ \bar{m}_{w\alpha} &= \bar{m} \left(\frac{b_R}{\ell} \right) \bar{\chi}_\alpha, \\ \bar{m}_{\alpha\alpha} &= \bar{m} \left(\frac{b_R}{\ell} \right)^2 \bar{r}_\alpha^2. \end{aligned} \tag{7.4}$$

The term $\bar{\chi}_\alpha$ represents a section mass static unbalance about the structural reference axis, and \bar{r}_α represents a section dimensionless radius of gyration.

Taking into consideration the zero columns in the mass and aerodynamic matrices, it is readily shown for the case of no damping that the flutter eigenvalue problem can be reduced to

$$\begin{bmatrix} (I + G_{22}) & G_{23} & G_{24} \\ G_{32} & (I + G_{33}) & G_{34} \\ G_{42} & G_{43} & (I + G_{44}) \end{bmatrix} \begin{Bmatrix} \gamma \\ \bar{w} \\ \alpha \end{Bmatrix} = 0, \tag{7.5}$$

where

$$G = T[M_{FD}s^{*2} - Q_{FD}(s^*, \lambda)]. \tag{7.6}$$

Even further, the first row and first column of Eq. (7.5) can be dropped if the lifting surface has no aerodynamic sweep. Eq. (7.5) can be numerically evaluated for the roots loci of the aeroelastic modes as a function of the dynamic pressure parameter λ , with instability being associated with complex roots s^* having positive real parts.

The procedure used in the present analyses to trace out the complex roots loci was based on a determinant iteration scheme. A determinant iteration method has the advantage of being simple to implement, and furthermore, it is not restricted to solving a particular form of the flutter equations. If desired, the determinant

method can easily solve the flutter equations when the unsteady aerodynamic terms are calculated directly from the Bessel function representation of the generalized Theodorsen function.

Since the roots of the flutter equation correspond to the zeroes of the determinant of the complex-valued matrix in Eq. (7.5), the determinant method simply searches for these zeroes. For a given dynamic pressure and a trial root, the determinant is numerically evaluated from the product of the diagonal terms of the triangular factor that is obtained by applying Gaussian elimination. Muller's method is used to iteratively search for the complex roots of the determinant.

A computer code for determinant iteration was developed directly from routines available in Chapters 2 and 3 of Conte and de Boor [38]. The resulting program worked remarkably well for tracing out the roots loci. Solutions could be started by specifying trial roots along the positive imaginary axis and letting the solutions converge to the free vibration eigenvalues. By incrementing the dynamic pressure and using the roots at the previous dynamic pressure point as iteration starting values, a specified number of branches of the complex roots loci could be simultaneously traced out. Any complex valued roots had their conjugates added to the function deflation in the Muller routine so that only the upper half-plane of the symmetric roots loci was extracted. Zero frequency static divergence roots could also be extracted with determinant iteration.

One point to be aware of is that small sized flutter equations (i.e., not too many degrees of freedom) will usually not encounter problems with determinant evaluation since the range of determinant values tends to be reasonable. For larger problems, one may find it necessary to employ scaled arithmetic in the determinant evaluation in order to prevent overflow or underflow during the computation. Another alternative is to keep the size of the flutter equations small by applying modal superposition to Eq. (7.5). As a result of standard superposition procedures, the flutter matrix

Table 14

Flutter velocities for an unswept, uniform,
isotropic wing

Solution	Description	Flutter Velocity km/hr
Ref. [53,54]	Exact Analysis	494
Ref. [52]	25 finite-difference points	483
State Vector	Jacobi I.M., 2 intervals	486
State Vector	Jacobi I.M., 3 intervals	494
State Vector	Jacobi I.M., 4 intervals	494

will be formed by premultiplying the matrix in Eq. (7.5) by the transpose of the modal matrix and postmultiplying it by the untransposed modal matrix.

7.2 Flutter of an Isotropic Wing

Flutter calculations using the state vector approach were verified through comparisons with analytical solutions presented by Goland [53] for an unswept, cantilevered, isotropic wing. (Corrections for Ref. [53] are given in Ref. [54].) The appropriate data for this problem were taken from Ref. 44. Table 14 gives a comparison of numerical flutter results from Eq. (7.5) with those of Goland and with a numerical solution of Housner and Stein [52]. The state vector solutions are based on Jacobi integrating matrices corresponding to two, three, and four collocation intervals, and unsteady aerodynamic calculations employ a rational approximation of the Theodorsen function due to R.T. Jones. Details on the unsteady aerodynamic strip theory can be found in Appendix D.

It is readily seen that the hybrid state vector solutions are quite accurate and converge rapidly to the exact solution as the number of collocation intervals increases. Similar solutions based on Newton integrating matrices also yield highly accurate results that are virtually identical with the Jacobi solutions. The flutter

Table 15

Inertia parameters for the uniform composite wing of Table 13

$\bar{\chi}_\alpha = 0.2$	$\bar{m}_{ww} = 1.0$
$\bar{r}_\alpha = 0.29$	$\bar{m}_{w\alpha} = 0.03$
$\mu = 8.0$	$\bar{m}_{\alpha\alpha} = 0.0065$

solutions for this particular problem depend heavily on the accuracies of the lower frequency coupled bending-torsion modes of free vibration. The high accuracy with which the flutter velocities are determined demonstrates the fact that the integrating matrix solutions contain precise information for these lower modes.

7.3 Flutter of a Composite Wing

Flutter solutions will now be obtained for an unswept, uniform composite wing. The wing geometric, aerodynamic, and structural data to be used in the flutter solutions can be found in Table 13 and Fig. 9 of Section 6.1. (Fig. 9 contains data for a single layer laminate only.) Inertia data are given in Table 15. This data corresponds to a wing that was analyzed by Housner and Stein [52]. The analysis to be given here, however, includes the effect of bending-twist coupling represented by the \bar{D}_{13}^* term. It is assumed that the composite layup is equivalent to a midplane symmetric angle-ply laminate, for which the effective coupling decreases with an increasing number of layers. As in the preceding section, the unsteady aerodynamic loads are calculated from the modified strip theory presented in Appendix D, and the Theodorsen function is calculated from the R.T. Jones rational approximation. No compressibility corrections are applied to the unsteady aerodynamic terms.

Plotted in Fig. 13 is the nondimensional flutter dynamic pressure parameter for the unswept, uniform composite wing as a function of the fiber orientation angle θ . The results are normalized by the flutter dynamic pressure at $\theta = -90^\circ$.

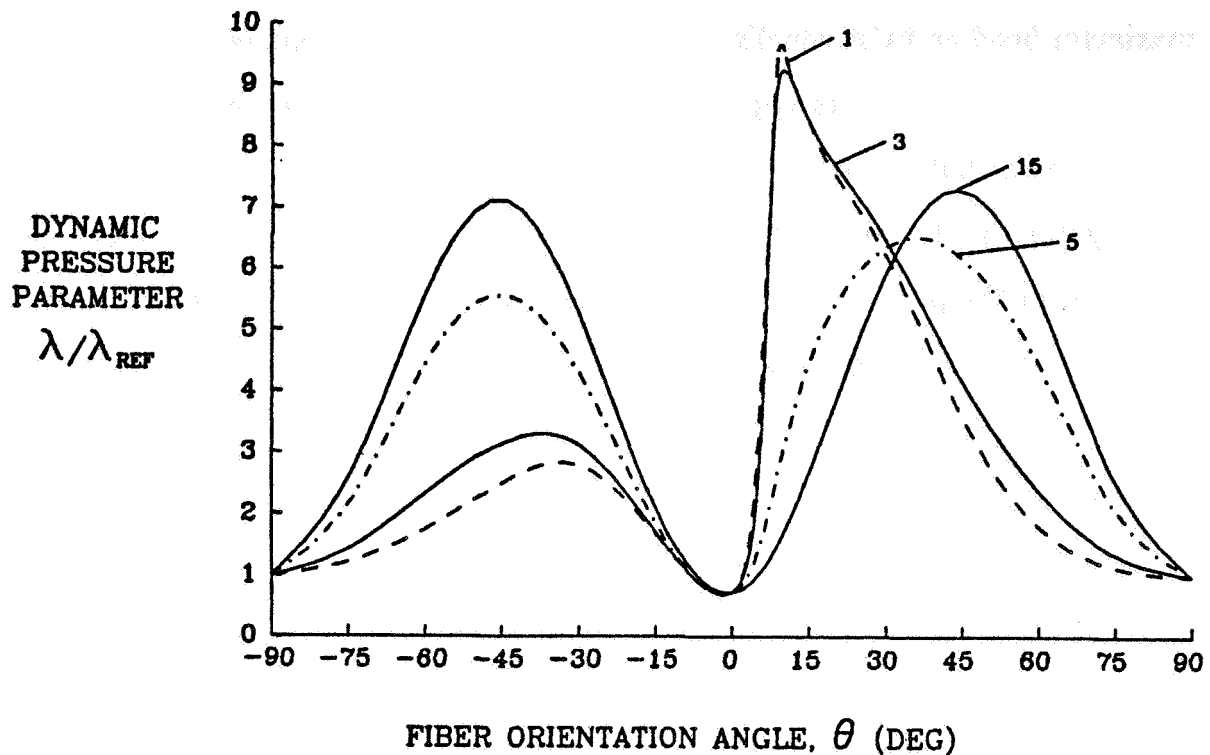


Fig. 13. Effect of fiber orientation on flutter dynamic pressure for an unswept, uniform composite wing—symmetric angle-ply laminate with 1, 3, 5, and 15 layers. ($\lambda_{REF} = \lambda_{(\theta=-90^\circ)}$)

Several curves are displayed corresponding to symmetric angle-ply laminates having 1, 3, 5, and 15 layers. The single layer equivalent laminate possesses the maximum amount of bending twist coupling, while the 15 layer equivalent possesses very little coupling and exhibits essentially quasi-isotropic behavior. It is apparent from Fig. 13 that in the limit of quasi-isotropic behavior, the flutter speed for the unswept wing follows the torsional stiffness variation, with a peak in the flutter dynamic pressure occurring at maximum torsional stiffness corresponding to $\theta = 45^\circ$. These nondimensional results for the 15 layer laminate compare very closely with the quasi-isotropic results given in Fig. 9 of Housner and Stein [52].

In contrast with the quasi-isotropic limit, the behavior of a single layer equivalent symmetric angle-ply laminate demonstrates a limiting case solution involving maximum bending-twist coupling. The asymmetry of the bending-twist coupling term about $\theta = 0^\circ$ is quite apparent from Fig. 13. The sharp peak and the rapid changes in the flutter dynamic pressure for this case are caused by the important participation of the coupling term in the solution. The rapid variation and the sharpness of the peak are quickly diminished when more layers are taken. Since practical composite layups tend more toward quasi-isotropic behavior, it is not anticipated that this single layer limiting case solution will necessarily be attained in practice.

The flutter curves presented in Fig. 13 were obtained directly from Eq. (7.5) by using the previously described root tracking scheme based on determinant iteration. Both Jacobi and Newton integrating matrices for two and three collocation intervals were employed in the flutter calculations. By using the two different interval sizes, the convergence of the flutter solutions as a function of the discretization level could be checked. For the composite wing flutter problem examined here, it was concluded that three intervals gave sufficient convergence, as it did for the case of isotropic wing flutter in Section 7.2. Because of the small number of discretization intervals needed, both the Jacobi and Newton integrating matrix solutions gave the same result. It should also be noted that since solutions were obtained directly from Eq. (7.5), modal superposition was not employed and the question of the number of modes used in the analysis does not arise. For flutter problems in which much more discretization is needed to adequately describe the structure, modal techniques can be applied to keep the flutter solutions within manageable proportions.

To obtain each flutter dynamic pressure, the complex roots loci ($s^* = \sigma^* + j\omega^*$) for that value of fiber orientation angle were traced out beginning with zero dynamic pressure and continuing until one of the branches had roots with positive real parts,

thus indicating a dynamic instability. Figs. 14 and 15 give typical examples of roots loci for two different sets of wing parameters. Fig. 14 gives the roots loci corresponding to the highest peak in the flutter dynamic pressure for the three layer laminate solution plotted in Fig. 13. This peak occurs at a fiber angle of $\theta = 10^\circ$. Fig. 15 gives the roots loci for a single layer equivalent laminate when the mass ratio is taken to be $\mu = 64$ and the fibers are oriented at $\theta = 45^\circ$. For both of these figures only the three lowest root branches are shown. These two figures are indicative of two different types of instability. The instability in Fig. 14 is approached rather slowly as dynamic pressure increases, whereas the instability shown in Fig. 15 is approached very rapidly with a small change in dynamic pressure and involves strong coupling between two of the wing modes.

By tracing each root branch starting with zero dynamic pressure, it was possible to avoid the program logic necessary to detect discontinuities in the flutter speed as θ varies. Such discontinuities were encountered by Housner and Stein [52] for certain values of the mass ratio parameter μ , but not for $\mu = 8$, which was used in obtaining Fig. 13. With the implementation of such detection logic, flutter solutions as a function of θ can be carried out by using the flutter dynamic pressure at an adjacent value of θ as a starting point for the next flutter solution.

The current investigation did not attempt to make a complete examination of the instabilities associated with composite wings. A more thorough study of the instability boundary must involve simultaneous consideration of divergence and flutter and should include the effects of rigid body modes. As indicated by Weisshaar [51], the stability boundary of cantilevered, forward swept composite wings will be determined for a wide range of fiber angles by the low divergence velocities associated with those fiber orientations. Also indicated in Ref. [51] are various changes in the mode of flutter instability as the fiber orientation changes. The presence of these different modes of instability as the wing parameters vary

is worthy of further investigation. It is felt that the solution methods presented here will provide a convenient tool for conducting further research on instability phenomena of composite lifting surfaces.

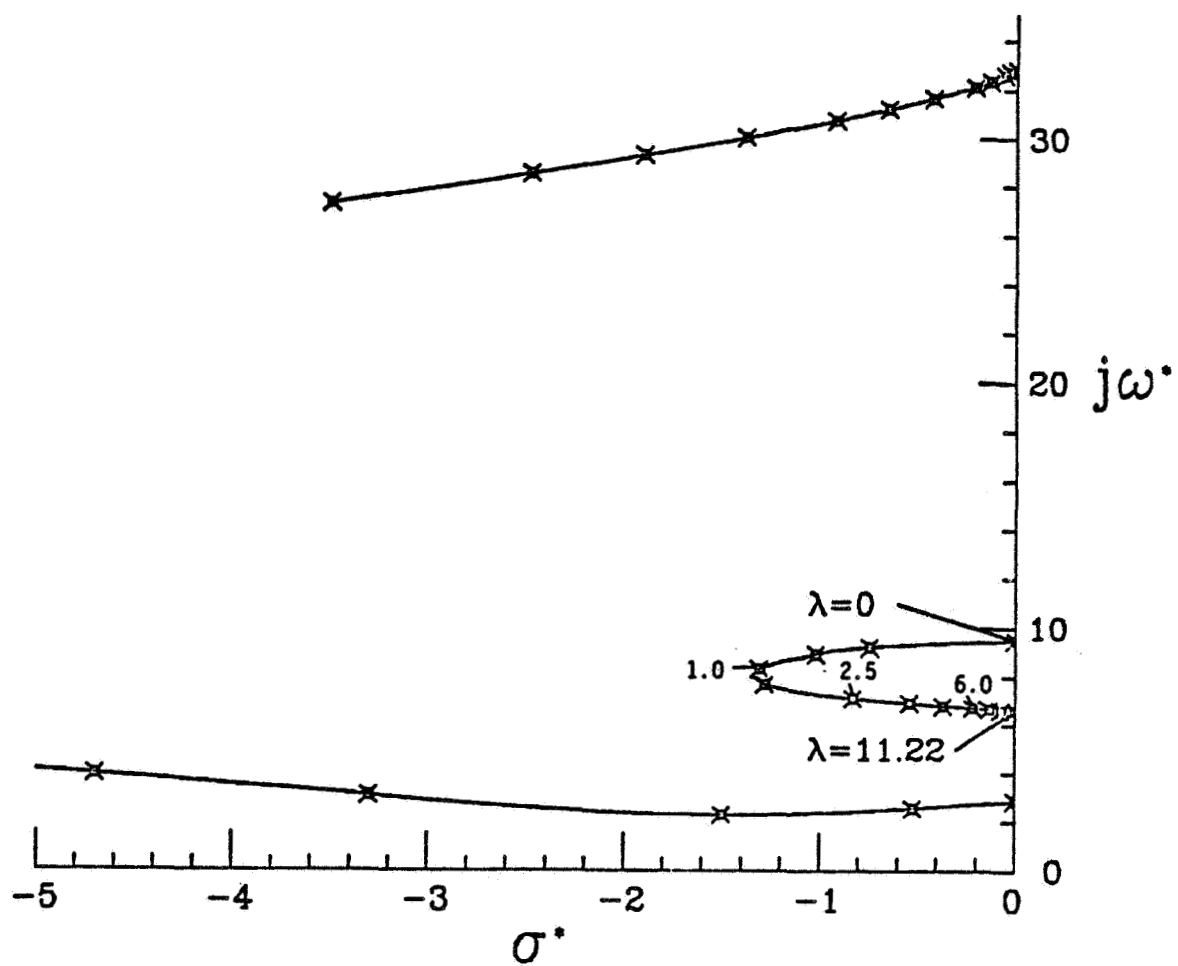


Fig. 14. Roots loci of aeroelastic modes for a uniform composite wing. (Three layer laminate; $\mu = 10$; $\theta = 10^\circ$)

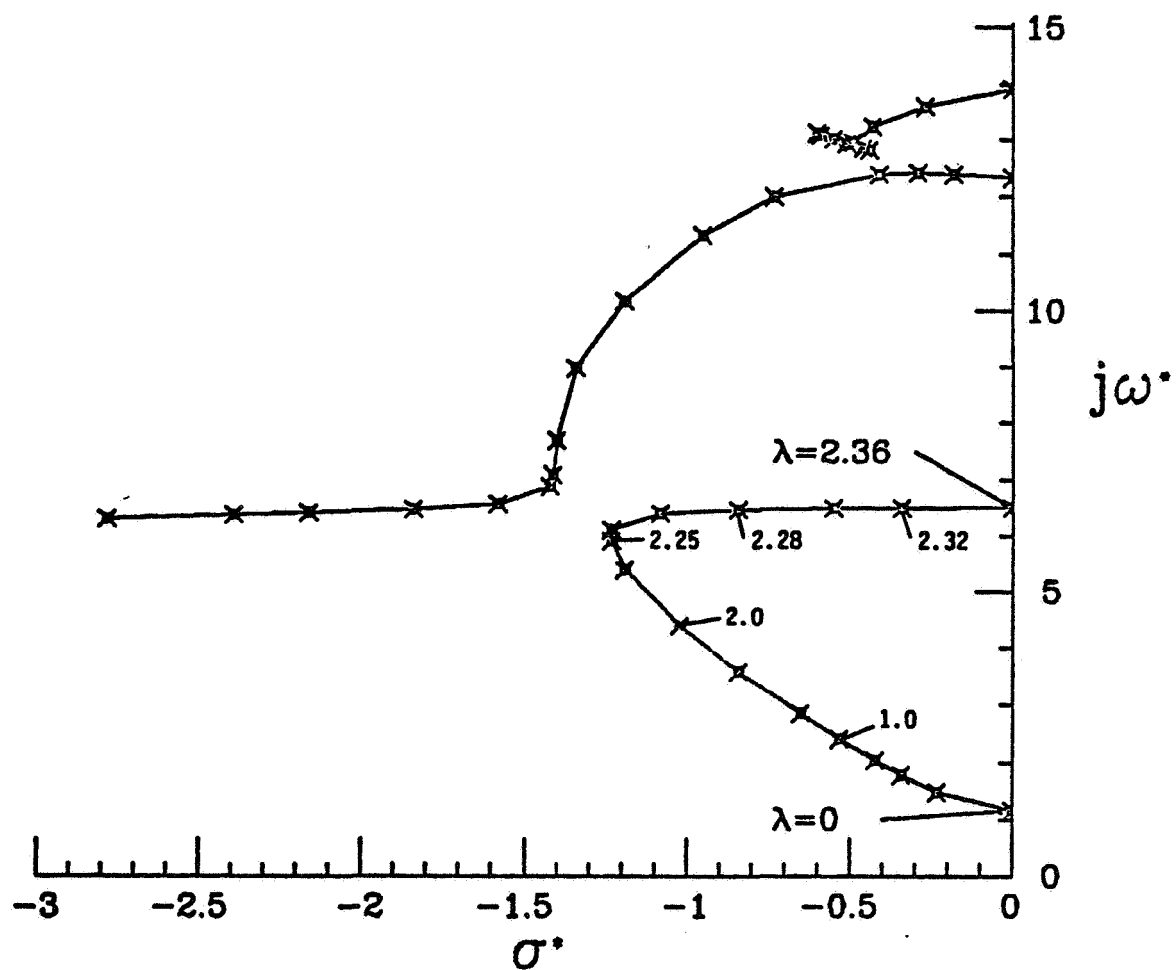


Fig. 15. Roots loci of aeroelastic modes for a uniform composite wing. (Single layer laminate; $\mu = 64$; $\theta = 45^\circ$)

Chapter 8

Summary and Recommendations

THE PREVIOUS CHAPTERS describe a hybrid state vector method for solving the differential equations arising in structural dynamics and aeroelasticity. The method proves to be very versatile and can be applied to the solution of any form of ordinary differential equation.

Solutions can be obtained in a consistent fashion for any size problem by working with the state vector form of the differential equations. An integrating matrix method is used to discretize the differential equations, yielding standard linear matrix equations from which one obtains the desired solutions. It is also shown that for simple problems, the integrating matrix can be applied directly to other forms of the differential equations.

It is demonstrated that a convenient form of the state vector equations can be obtained from a variational formulation of the structural equilibrium equations. The equations given by this formulation have properties that are useful for numerical calculations. For structural problems, the state vector equations can be partitioned corresponding to generalized force and displacement variables. By applying matrix partitioning techniques, the solution state vector can be reduced to the displacement state variables only. This reduction process can often be carried out analytically to yield expressions for the direct calculation of the terms in the reduced matrix

equations. For problems in which it might not be convenient to carry out analytical reductions of the equations, the calculations can be performed numerically.

As demonstrated in Chapters 5, 6, and 7, the hybrid state vector method is applicable to a variety of problems and boundary conditions. Results for these problems indicate that high accuracy is easily achievable. By employing high order polynomial approximations, the integrating matrix solutions are capable of providing sufficient accuracy with minimal discretization. The matrix operations required by this solution procedure are straight forward, easily programmable, and allow for efficient problem solution.

A theory of integrating matrices is presented and a calculation procedure is developed for maximum precision integrating matrices that are based on orthogonal polynomials. Discussions are given for several types of integrating matrices and some of their properties. Much flexibility is available in the types of integrating matrices that can be derived and used for special applications. Each type of integrating matrix has its own unique properties that make it more or less applicable to a particular situation. For the problems examined in this work, the integrating matrices based on Jacobi polynomials have proven to have good convergence properties and are capable of very high accuracy solutions. Newton based integrating matrices, which are convenient for applications requiring evenly spaced grid points, also provide very good accuracies. The convergence of solutions based on Newton matrices, however, tends to be oscillatory in character unless the number of grid points is somewhat larger than the minimum number of points required by a given order of approximating polynomial. Tabulations are presented in Appendix B for both Newton and Jacobi integrating matrices.

Additional work needs to be devoted toward extending the theory of hybrid state vector solutions to two and three dimensional problems. It should prove to be convenient in the development of multidimensional integrating matrices to

introduce the familiar concept of multidimensional shape functions. This concept is routinely employed in finite element analyses. For irregular shaped regions, it is anticipated that a transformation to a simpler domain will be useful in performing the integrations. That is, integrating matrices are more easily developed for these simpler domains. Again, this concept is very much similar to practices currently in use for isoparametric finite element solutions. It is also possible to extend the present method to two dimensional problems by applying separation of variables, thus allowing reduction of the partial differential equations to ordinary differential equations. For multidimensional problems in general, it should prove worthwhile to investigate the use of integration methods that are especially suited to multidimensional integration.

Other types of integrating matrices should be investigated for special types of problems. For instance, semi-infinite boundary value problems should easily yield to numerical solution by integrating matrix. In this connection, it would be worthwhile to examine the prospect of developing integrating matrices from the orthogonal polynomials that are normally used for quadratures on semi-infinite domains.

Further studies are also warranted for applications of the hybrid state vector method to nonlinear problems. For materially nonlinear structures in particular, it appears that the Reissner variational formulation (written in terms of the hybrid state vector) may offer important advantages for numerical solution by integrating matrices and is deserving of a more thorough investigation. In the presence of nonlinearities, the hybrid state vector formulation, in conjunction with integrating matrices, provides a very convenient method for obtaining a compact set of nonlinear algebraic equations that describe the solution of the nonlinear problem.

Finally, there are many questions yet to be answered concerning the flutter of composite wings. Some of the more important questions are mentioned in Chapter 7. The present examination does not attempt to address all of these problems, but

rather forms the foundation for further parameter studies of wing flutter. Most certainly, the answers to some of these problems will be very useful in preliminary aeroelastic design.

Appendix A

Weighting Matrices and Shape Functions for Jacobi Polynomials

The following presents a summary of the calculation procedures for Jacobi integrating matrices. Jacobi integrating matrices are developed from Lagrange interpolating polynomials that can be written in terms of the normalized Jacobi polynomials $p_n^{(1,1)}(x)$. Included in this formulation is a detailed description of the integration methods required to calculate the Jacobi weighting matrices. In addition, the interpolating polynomials are presented in the form of shape functions (basis functions). Discussions on shape functions can be found in Zienkiewicz [55] and Gallagher [56].

First, a distinction must be made between the notation in Chapter 3 and the notation appearing in this appendix. In Chapter 3, n denotes the number of subintervals in the interval of integration, with $n + 1$ being the total number of grid points on the interval. In this appendix, however, n refers to the number of grid points in the *interior* of the interval of integration (i.e., excluding end points). This notational change prevents undesirable complication of subscripts and limits and allows the use of an accepted notation for Jacobi polynomials. Since the notational change is confined entirely to the calculations in this appendix, no confusion should arise. It should be noted that whenever n is used as a subscript in a polynomial, it denotes the degree of the polynomial; however, the degree is the same as the number of interior grid points.

All of the integrations and interpolations will be written for the normalized

interval $[-1, 1]$, and the subscript k will designate the quadrature points on this interval. The quadrature points x_k are fixed grid point locations that are determined by the zeroes of the appropriate Jacobi polynomial. These quadrature points are the same as the abscissas for Lobatto integration, which can be found, for instance, on page 920 of Abramowitz and Stegun [40]. Appendix B lists these abscissas for each Jacobi integrating matrix. Note too, that a distinction will be made between the unnormalized Jacobi polynomials $P_n^{(1,1)}(x)$ and the normalized polynomials $p_n^{(1,1)}(x)$. These polynomials are a special case of the general Jacobi polynomial

$$p_n^{(\alpha,\beta)}(x) = \sqrt{\delta_n} P_n^{(\alpha,\beta)}(x) \quad (\text{A.1})$$

where the normalizing factor δ_n is

$$\delta_n = \frac{(\alpha + \beta + 2n + 1)n! \Gamma(\alpha + \beta + n + 1)}{2^{\alpha+\beta+1} \Gamma(\alpha + n + 1) \Gamma(\beta + n + 1)}. \quad (\text{A.2})$$

For $\alpha = \beta = 1$, the normalizing factor can be reduced to

$$\delta_n = \frac{(2n + 3)(n + 2)}{8(n + 1)}. \quad (\text{A.3})$$

Some more preliminaries on Jacobi polynomials are necessary before discussing shape functions and integrating matrices. First, the Jacobi polynomials $P_n^{(1,1)}(x)$ can be calculated recursively via the formula

$$P_n^{(1,1)}(x) = (n + 1)r_0(x) \quad (\text{A.4})$$

with

$$r_{m-1}(x) = 1 + \frac{(n + 1 - m)(n + 2 + m)}{2m(m + 1)}(x - 1)r_m(x). \quad (\text{A.5})$$

The recursive calculation is repeated for $m = n, n-1, \dots, 2, 1$, beginning with $r_n(x) = 1$. By means of Eqs. (A.4–A.5) one can show that

$$P_0^{(1,1)}(x) = 1 \quad (\text{A.6})$$

and

$$P_n^{(1,1)}(1) = (n+1). \quad (\text{A.7})$$

Using identities listed on page 777 of Abramowitz and Stegun [40], one also finds that

$$P_n^{(1,1)}(-1) = (-1)^n P_n^{(1,1)}(1) = (-1)^n (n+1), \quad (\text{A.8})$$

and from the differential relations given on page 783 of Ref. [40], a useful derivative term is expressible in the form

$$P_n^{(1,1)'}(x_k) = \frac{n+1}{1-x_k^2} P_{n-1}^{(1,1)}(x_k). \quad (\text{A.9})$$

From the recursion relations given in Eqs. (A.4–A.5), the following series expansion of $P_n^{(1,1)}(x)$ was developed for use in integrations:

$$P_n^{(1,1)}(x) = (n+1) \left[1 + \sum_{m=1}^n c_m^n (x-1)^m \right] \quad (\text{A.10})$$

where

$$c_m^n = \prod_{k=1}^m \left(\frac{(n+1-k)(n+2+k)}{2k(k+1)} \right). \quad (\text{A.11})$$

Note that the summation on the right-hand side of Eq. (A.10) vanishes whenever $n < 1$. One final definition that's needed in the following discussion is the definition for the leading coefficient of an orthonormal polynomial. For the normalized Jacobi

polynomials with $\alpha = \beta = 1$, the leading coefficient, a_n (i.e., the coefficient of the highest order term x^n) can be expressed as

$$a_n = \sqrt{\delta_n} \frac{(2n+2)!}{2^n n! (n+2)!} \quad (A.12)$$

Turning now to interpolation, it is assumed that a sufficiently smooth function $f(x)$ can be reasonably approximated by a Lagrange interpolating polynomial. If the end points of the interval $[-1, 1]$ are included in the interpolation, then an approximation to $f(x)$ can be expressed as

$$f(x) \approx \sum_{k=1}^n \frac{p_n^{(1,1)}(x)(x^2-1)}{(x-x_k)p_n^{(1,1)'}(x_k)(x_k^2-1)} f(x_k) + \sum_{j=1}^2 \frac{p_n^{(1,1)}(x)(x^2-1)}{(x-d_j)p_n^{(1,1)}(d_j)(2d_j)} f(d_j) \quad (A.13)$$

where the end points of the interval are $d_1 = -1$ and $d_2 = 1$. This particular form of the Lagrange interpolating polynomial is convenient for use with orthogonal functions.

The interpolation given by Eq. (A.13) can be equivalently written in terms of shape functions, $\mathcal{N}(x)$, as

$$f(x) \approx [\mathcal{N}_{-1}(x) \ \mathcal{N}_k(x) \ \mathcal{N}_{+1}(x)] \{f\} \quad (A.14)$$

where

$$\{f\} = \{f(-1) \ f(x_k) \ f(+1)\}^T. \quad (A.15)$$

If interpolation is to be performed for multiple points, then the left hand side of Eq. (A.14) becomes a column vector and the shape function terms are written in the form of a rectangular matrix rather than a row matrix.

The shape functions, which provide a convenient way of expressing Eq. (A.13), can be simplified by applying Eqs. (A.6–A.8). As a result of this simplification, the

end point shape functions appear as

$$\mathcal{N}_{-1}(x) = \frac{(-1)^{n+1}}{2(n+1)}(x-1)P_n^{(1,1)}(x) \quad (\text{A.16})$$

and

$$\mathcal{N}_{+1}(x) = \frac{1}{2(n+1)}(x+1)P_n^{(1,1)}(x). \quad (\text{A.17})$$

For internal points x_k on the interval $[-1, 1]$ the shape functions are

$$\mathcal{N}_k(x) = \frac{p_n^{(1,1)}(x)\vartheta(x)}{(x-x_k)p_n^{(1,1)'}(x_k)(x_k^2-1)} \quad (\text{A.18})$$

where the weighting function $\vartheta(x) = x^2 - 1$. This weighting function is the same as mentioned in Section 3.1. Note too, that the prime in the denominator of Eq. (A.18) indicates differentiation with respect to x . To facilitate further manipulation of the shape functions, the superscript $(1, 1)$ will be dropped in the remainder of this appendix. That is, $p_n^{(1,1)}(x)$ and $P_n^{(1,1)}(x)$ will now be referred to simply as $p_n(x)$ and $P_n(x)$.

Unfortunately, Eq. (A.18) is very inconvenient for numerical calculations. The Christoffel-Darboux identity, however, proves useful in reducing the interior point shape functions to a much more desirable form (see, for example, Krylov [39], p. 103). By using the fact that $P_n(x_k) = 0$ when evaluated at its zero points, x_k , a useful form of the Christoffel-Darboux identity can be written as

$$\sum_{s=0}^{n-1} p_s(x)p_s(x_k) = \frac{-a_n}{a_{n+1}} \frac{p_n(x)p_{n+1}(x_k)}{x-x_k}. \quad (\text{A.19})$$

If Eq. (A.19) is first multiplied through by $\vartheta(x) = x^2 - 1$, then some rearranging gives

$$\frac{p_n(x)\vartheta(x)}{x-x_k} = \frac{a_n B_k(x)}{a_{n-1} P_{n-1}(x_k)}, \quad (\text{A.20})$$

where

$$B_k(x) = \sum_{s=0}^{n-1} \delta_s P_s(x_k) \vartheta(x) P_s(x). \quad (\text{A.21})$$

To write Eq. (A.20) in its present form, use was made of the standard recurrence relation for orthonormal polynomials, which allows one to obtain the equality

$$\frac{-a_{n+1}}{a_n P_{n+1}(x_k)} = \frac{a_n}{a_{n-1} P_{n-1}(x_k)}. \quad (\text{A.22})$$

By substituting Eq. (A.20) into Eq. (A.18), one finally obtains a convenient form for the shape functions

$$N_k(x) = \frac{-8B_k(x)}{(n+1)(n+2)(P_{n-1}(x_k))^2} \quad (\text{A.23})$$

where Eq. (A.3), Eq. (A.9), and Eq. (A.12) have been employed to arrive at Eq. (A.23). The final form of the shape functions are represented by Eq. (A.16), Eq. (A.17), and Eq. (A.23). With the aid of the recursion relations given by Eqs. (A.4–A.5), the shape functions, used in conjunction with Eq. (A.14), provide a convenient way of numerically performing interpolations. These interpolation expressions also provide the foundation for calculation of the Jacobi weighting matrices.

It is useful to note that the interpolations can be carried out in matrix notation after defining a matrix of shape function values. For example, if one chooses a number of fixed points $x = x_j$, ($j = 1, \dots, t$) at which to interpolate, then the $t \times n$ matrix $[N_{j,k}]$, for the interior point shape functions, is given by

$$[N_{j,k}] = [N_k(x_j)] = \frac{-8}{(n+1)(n+2)} [B_{j,k}] [P_{n-1}^2(x_k)]^{-1} \quad (\text{A.24})$$

where the $t \times n$ matrix $[B_{j,k}]$ is written as

$$[B_{j,k}] = [\mathcal{R}_{j,s}] [\delta_s P_{s,k}]. \quad (\text{A.25})$$

The matrix product on the right-hand side of Eq. (A.25) performs the same summation as the right-hand side of Eq. (A.21). $[R_{j,s}]$ is a $t \times n$ matrix given by

$$[R_{j,s}] = [(x_j^2 - 1)P_s(x_j)] \quad (A.26)$$

and $[\delta_s P_{s,k}]$ is an $n \times n$ matrix calculated as

$$[\delta_s P_{s,k}] = [\delta_s P_s(x_k)]. \quad (A.27)$$

In addition to $[N_{j,k}]$, the following column vectors arise from evaluating the end point shape functions via Eqs. (A.16–A.17):

$$\{N_{-j}\} = \{N_{-1}(x_j)\}, \quad (A.28)$$

$$\{N_{+j}\} = \{N_{+1}(x_j)\}. \quad (A.29)$$

Finally, by collecting Eqs. (A.24), (A.28), and (A.29), one obtains the complete shape function matrix in the form

$$N = [\{N_{-j}\} \mid [N_{j,k}] \mid \{N_{+j}\}]. \quad (A.30)$$

This matrix of shape function values can now be used for function interpolation in the manner indicated by Eq. (A.14).

Having obtained expressions for the interpolation of $f(x)$, the next step is to calculate the weighting matrices from these approximations. But first, a convenient notation must be agreed upon for the subintervals over which the integrations will be performed. In Section 3.1, it was convenient to label subintervals by grid points. That is, a particular subinterval was referred to by $[x_i, x_{i+1}]$, where the subscripts i and $i+1$ designated the two consecutive grid points on that subinterval. In discussing

the integrations required for Jacobi weighting matrices, however, it will greatly simplify the notation to refer to the same subinterval by $[x_j, x_{j+}]$ ($j = 1, \dots, n+1$), where j denotes a particular interval rather than a grid point.

The elements in a Jacobi weighting matrix can be determined by integrating the approximate expression for $f(x)$ given in Eq. (A.14). These integrations, which will be carried out over subintervals, are written in the general form

$$\int_{x_j}^{x_{j+}} f(x) dx = \int_{x_j}^{x_{j+}} g(x) \vartheta(x) dx. \quad (\text{A.31})$$

As mentioned in Chapter 3, a maximum precision quadrature will result only if $g(x)$ is orthogonal to $\vartheta(x)$ over the total interval of integration. The total interval of integration here is the normalized interval $[-1, 1]$. Since the weighting function that arises during interpolation is $\vartheta(x) = x^2 - 1$, the Jacobi polynomials are the proper choice for the orthogonal function.

Equation (A.14) is now substituted into Eq. (A.31). When the shape function definitions in Eq. (A.16), (A.17), and (A.23) are taken into account, one can define the integrals

$$D_{-j} = \int_{x_j}^{x_{j+}} N_{-1}(x) dx = \frac{(-1)^{n+1}}{2(n+1)} \int_{x_j}^{x_{j+}} (x-1) P_n(x) dx \quad (\text{A.32})$$

and

$$D_{+j} = \int_{x_j}^{x_{j+}} N_{+1}(x) dx = \frac{1}{2(n+1)} \int_{x_j}^{x_{j+}} (x+1) P_n(x) dx \quad (\text{A.33})$$

and finally,

$$C_{j,k} = \int_{x_j}^{x_{j+}} N_k(x) dx = \frac{-8}{(n+1)(n+2)(P_{n-1}(x_k))^2} \int_{x_j}^{x_{j+}} B_k(x) dx. \quad (\text{A.34})$$

In order to isolate the integral portion of the terms in Eqs. (A.32–A.33), it is convenient to rewrite these equations as

$$D_{-j} = \frac{(-1)^{n+1}}{2(n+1)} Q_{-j} \quad (\text{A.35})$$

and

$$D_{+j} = \frac{1}{2(n+1)} Q_{+j} \quad (\text{A.36})$$

where

$$Q_{-j} = \int_{x_j}^{x_{j+}} (x-1) P_n(x) dx \quad (\text{A.37})$$

and

$$Q_{+j} = \int_{x_j}^{x_{j+}} (x+1) P_n(x) dx. \quad (\text{A.38})$$

With the aid of Eq. (A.21), it is possible to recast Eq. (A.34) in a similar manner to obtain

$$C_{j,k} = \frac{-8B_{j,k}^*}{(n+1)(n+2)(P_{n-1}(x_k))^2} \quad (\text{A.39})$$

where

$$B_{j,k}^* = \sum_{s=0}^{n-1} \delta_s P_s(x_k) R_{j,s}^* \quad (\text{A.40})$$

and

$$R_{j,s}^* = \int_{x_j}^{x_{j+}} (x^2-1) P_s(x) dx. \quad (\text{A.41})$$

The next step in calculating the weighting matrices requires the development of expressions for the integrals in Eqs. (A.37), (A.38), and (A.41). Appropriate expressions for these integrals are derived with the help of Eqs. (A.10–A.11), which will allow term by term integration. Therefore, substitution of Eq. (A.10) for $P_n(x)$ in Eq. (A.37) yields the integration

$$Q_{-j} = (n+1) \left[\int_{x_j}^{x_{j+}} (x-1) dx + \sum_{m=1}^n c_m^n \int_{x_j}^{x_{j+}} (x-1)^{m+1} dx \right]. \quad (\text{A.42})$$

Carrying out this integration provides the result

$$\mathcal{Q}_{-j} = (n+1) \left[\frac{1}{2}(x_{j+}^2 - x_j^2) - (x_{j+} - x_j) + \sum_{m=1}^n e_m^n \left\{ \frac{1}{m+2} [(x_{j+} - 1)^{m+2} - (x_j - 1)^{m+2}] \right\} \right] \quad (\text{A.43})$$

A similar operation applied to Eq. (A.38) yields the integrals

$$\mathcal{Q}_{+j} = (n+1) \left[\int_{x_j}^{x_{j+}} (x+1) dx + \sum_{m=1}^n e_m^n \int_{x_j}^{x_{j+}} [(x-1)^m + x(x-1)^m] dx \right] \quad (\text{A.44})$$

with the final result of the integration being

$$\begin{aligned} \mathcal{Q}_{+j} = (n+1) \left[\frac{1}{2}(x_{j+}^2 - x_j^2) + (x_{j+} - x_j) + \sum_{m=1}^n e_m^n \left\{ \frac{2}{m+1} [(x_{j+} - 1)^{m+1} - (x_j - 1)^{m+1}] \right. \right. \\ \left. \left. + \frac{1}{m+2} [(x_{j+} - 1)^{m+2} - (x_j - 1)^{m+2}] \right\} \right] \quad (\text{A.45}) \end{aligned}$$

Proceeding with a similar approach for Eq. (A.41) gives

$$\mathcal{R}_{j,s}^* = (n+1) \left[\int_{x_j}^{x_{j+}} (x^2 - 1) dx + \sum_{m=1}^s e_m^s \int_{x_j}^{x_{j+}} [(x-1)^{m+1} + x(x-1)^{m+1}] dx \right] \quad (\text{A.46})$$

for which the integrated result is

$$\begin{aligned} \mathcal{R}_{j,s}^* = (s+1) \left[\frac{1}{3}(x_{j+}^3 - x_j^3) - (x_{j+} - x_j) + \sum_{m=1}^s e_m^s \left\{ \frac{2}{m+2} [(x_{j+} - 1)^{m+2} - (x_j - 1)^{m+2}] \right. \right. \\ \left. \left. + \frac{1}{m+3} [(x_{j+} - 1)^{m+3} - (x_j - 1)^{m+3}] \right\} \right] \quad (\text{A.47}) \end{aligned}$$

It is important to note that $0 \leq s \leq n-1$ as required by Eq. (A.21); however, the summation appearing on the right-hand side of Eq. (A.47) vanishes whenever $s < 1$.

The Jacobi weighting matrices can now be constructed from the values for \mathcal{D}_{-j} , \mathcal{D}_{+j} , and $\mathcal{C}_{j,k}$. Numerical calculation of these values makes use of Eqs. (A.35–A.36)

and Eqs. (A.39–A.40) in conjunction with Eqs. (A.43), (A.45), and (A.47). Note that D_{-j} and D_{+j} actually form column vectors with a dimension equal to the number of discretization subintervals. Similarly, the elements $C_{j,k}$ form a rectangular matrix with a row dimension equal to the number of discretization subintervals and a column dimension equal to the number of internal grid points, where the number of internal grid points is one less than the number of subintervals. Analogous to Eqs. (A.24–A.25), one finds that the matrix $[C_{j,k}]$ can be computed from

$$[C_{j,k}] = \frac{-8}{(n+1)(n+2)} [B_{j,k}^*] [P_{n-1}^2(x_k)]^{-1} \quad (\text{A.48})$$

where the $(n+1) \times n$ matrix $[B_{j,k}^*]$ is

$$[B_{j,k}^*] = [\mathcal{R}_{j,s}^*] [\delta_s P_{s,k}]. \quad (\text{A.49})$$

The second matrix on the right of Eq. (A.49) is the same as Eq. (A.27). And finally, with these definitions, the Jacobi weighting matrix is constructed in the form

$$\mathcal{W}_{n+1} = \begin{bmatrix} 0 & \cdots & 0 \\ \{D_{-j}\} & [C_{j,k}] & \{D_{+j}\} \end{bmatrix} \quad (\text{A.50})$$

where, as mentioned in Section 3.1, the first row contains only zeroes. Considering the definition of n in this appendix, the dimension of \mathcal{W}_{n+1} is $(n+2) \times (n+2)$.

Appendix B

Tables of Integrating Matrices

The integrating matrix L was defined by Eq. (3.11) as

$$L = S\mathcal{W}_n.$$

This definition applies to all of the integrating matrices given in this appendix.

Jacobi Integrating Matrices

The following Jacobi weighting matrices are for the normalized interval $[-1, 1]$, and can be transformed to the interval $[0, 1]$ by multiplying by the factor $1/2$. The coordinate values x , which denote grid points on $[-1, 1]$, are listed above the horizontal bar in each matrix. Equivalent grid points t on $[0, 1]$ are given by the linear transformation $t = 0.5(1 + x)$. For the Jacobi weighting matrices, the subscript n refers to the number of discretization intervals, with the integration being exact for all polynomials of degree $\leq 2n - 1$.

$$\mathcal{W}_2 = \begin{array}{c} \begin{array}{ccc} \hline -1.00000000 & .00000000 & 1.00000000 \\ .00000000 & .00000000 & .00000000 \\ .41666667 & .66666666 & -.08333333 \\ -.08333333 & .66666666 & .41666667 \end{array} \end{array} \quad (B.1)$$

$$\mathcal{W}_3 = \begin{array}{c} \begin{array}{cccc} \hline -1.00000000 & -.44721360 & .44721360 & 1.00000000 \\ .00000000 & .00000000 & .00000000 & .00000000 \\ .22060113 & .37939886 & -.06781473 & .02060113 \\ -.07453560 & .52174919 & .52174919 & -.07453560 \\ .02060113 & -.06781473 & .37939886 & .22060113 \end{array} \end{array} \quad (B.2)$$

$$w_4 = \begin{bmatrix} -1.00000000 & -.65465367 & .00000000 & .65465367 & 1.00000000 \\ .00000000 & .00000000 & .00000000 & .00000000 & .00000000 \\ .13545686 & .23948954 & -.04347144 & .02127165 & -.00740028 \\ -.05420686 & .36687883 & .39902700 & -.08319557 & .02615028 \\ .02615028 & -.08319557 & .39902700 & .36687883 & -.05420686 \\ -.00740028 & .02127165 & -.04347144 & .23948954 & .13545686 \end{bmatrix} \quad (B.3)$$

$$w_5 = \begin{bmatrix} -1.00000000 & -.76505532 & -.28523152 & .28523152 & .76505532 & 1.00000000 \\ .00000000 & .00000000 & .00000000 & .00000000 & .00000000 & .00000000 \\ .09135961 & .16373565 & -.02974921 & .01525535 & -.00894356 & .00328685 \\ -.03954284 & .26394600 & .29767068 & -.06326350 & .03255895 & -.01154547 \\ .02310851 & -.07282206 & .33494505 & .33494505 & -.07282206 & .02310851 \\ -.01154547 & .03255895 & -.06326350 & .29767068 & .26394600 & -.03954284 \\ .00328685 & -.00894356 & .01525535 & -.02974921 & .16373565 & .09135961 \end{bmatrix} \quad (B.4)$$

$$w_6 = \begin{bmatrix} -1.00000000 & -.83022390 & -.46884879 & .00000000 & .46884879 & .83022390 & 1.00000000 \\ .00000000 & .00000000 & .00000000 & .00000000 & .00000000 & .00000000 & .00000000 \\ .06569253 & .11864577 & -.02153719 & .01119518 & -.00697786 & .00443419 & -.00167654 \\ -.02968808 & .19675645 & .22624682 & -.04815170 & .02613302 & -.01579792 & .00587650 \\ .01905508 & -.05982575 & .27026169 & .28076604 & -.06238108 & .03261326 & -.01164044 \\ -.01164044 & .03261326 & -.06238108 & .28076604 & .27026169 & -.05982575 & .01905508 \\ .00587650 & -.01579792 & .02613302 & -.04815170 & .22624682 & .19675645 & -.02968808 \\ -.00167654 & .00443419 & -.00697786 & .01119518 & -.02153719 & .11864577 & .06569253 \end{bmatrix} \quad (B.5)$$

$$w_7 = \begin{bmatrix} -1.00000000 & -.87174015 & -.59170018 & -.20929922 & .20929922 & .59170018 & .87174015 & 1.00000000 \\ .00000000 & .00000000 & .00000000 & .00000000 & .00000000 & .00000000 & .00000000 & .00000000 \\ .04947503 & .08978532 & -.01628154 & .00850816 & -.00540841 & .00369077 & -.00245244 & .00094295 \\ -.02295759 & .15151413 & .17627681 & -.03746983 & .02067231 & -.01335611 & .00866234 & -.00330210 \\ .01555127 & -.04873911 & .21808803 & .23145357 & -.05153854 & .02849936 & -.01742762 & .00651400 \\ -.01050927 & .02936159 & -.05579463 & .24624152 & .24624152 & -.05579463 & .02936159 & -.01050927 \\ .00651400 & -.01742762 & .02849936 & -.05153854 & .23145357 & .21808803 & -.04873911 & .01555127 \\ -.00330210 & .00866234 & -.01335611 & .02067231 & -.03746983 & .17627681 & .15151413 & -.02295759 \\ .00094295 & -.00245244 & .00369077 & -.00540841 & .00850816 & -.01628154 & .08978532 & .04947503 \end{bmatrix} \quad (B.6)$$

$$w_8 = \begin{bmatrix} -1.00000000 & -.89975800 & -.67718628 & -.36311746 & .00000000 & .36311746 & .67718628 & .89975800 & 1.00000000 \\ .00000000 & .00000000 & .00000000 & .00000000 & .00000000 & .00000000 & .00000000 & .00000000 & .00000000 \\ .03858768 & .07025101 & -.01272820 & .00666755 & -.00427369 & .00298860 & -.00214812 & .00146755 & -.00057039 \\ -.01821952 & .11992193 & .14059219 & -.02983902 & .01657357 & -.01095025 & .00765877 & -.00516256 & .00199655 \\ .01277058 & -.03998597 & .17790013 & .19134243 & -.04256122 & .02396286 & -.01570330 & .01027426 & -.00393093 \\ -.00915870 & .02555263 & -.04839968 & .21134521 & .21602098 & -.04908886 & .02736692 & -.01682355 & .00630252 \\ .00630252 & -.01682355 & .02736692 & -.04908886 & .21602098 & .21134521 & -.04839968 & .02555263 & -.00915870 \\ -.00393093 & .01027426 & -.01570330 & .02396286 & -.04256122 & .19134243 & .17790013 & -.03998597 & .01277058 \\ .00199655 & -.00516256 & .00765877 & -.01095025 & .01657357 & -.02983902 & .14059219 & .11992193 & -.01821952 \\ -.00057039 & .00146755 & -.00214812 & .00298860 & -.00427369 & .00666755 & -.01272820 & .07025101 & .03858768 \end{bmatrix} \quad (B.7)$$

$\mathcal{W}_9 =$

-1.00000000	-.91953391	-.73877386	-.47792495	-.16527896	.16527896	.47792495	.73877386	.91953391	1.00000000
.00000000	.00000000	.00000000	.00000000	.00000000	.00000000	.00000000	.00000000	.00000000	.00000000
.03093030	.05643594	-.01021815	.00535941	-.00344925	.00243838	-.00180282	.00133952	-.00003228	.00036504
-.01478117	.00711306	.11445424	-.02425882	.01351771	-.00901930	.00647953	-.00474040	.00327262	-.00127744
.01060291	-.03317994	.14707011	.15961048	-.03544673	.02011031	-.01349794	.00954557	-.00647836	.00251255
-.00790229	.02203034	-.04165330	.18070787	.18731172	-.04253068	.02416459	-.01504323	.01047691	-.00401595
.00578828	-.01543233	.02503502	-.04471961	.19460760	.19460760	-.04471961	.02503502	-.01543233	.00578828
-.00401595	.01047691	-.01594323	.02416459	-.04253068	.18731172	.18070787	-.04165330	.02203034	-.00790229
.00251255	-.00647836	.00954557	-.01349794	.02011031	-.03544673	.15961048	.14707011	-.03317994	.01060291
-.00127744	.00327262	-.00474040	.00647953	-.00901930	.01351771	-.02425882	.11445424	.00711306	-.01478117
.00036504	-.00003228	.00133952	-.00180282	.00243838	-.00344925	.00535941	-.01021815	.05643594	.03093030

(B.8)

Newton Integrating Matrices

The following weighting matrices are repeated from Ref. [27]. For the Newton weighting matrices, the subscript n denotes the degree of the assumed polynomial upon which the integrating matrix is based. The parameter h is the step size.

$$\mathcal{W}_1 = \frac{h}{2} \begin{bmatrix} 0 & 0 & 0 & \dots & 0 \\ 1 & 1 & 0 & \dots & 0 \\ 0 & 1 & 1 & \dots & 0 \\ \vdots & & \ddots & & \vdots \\ 0 & \dots & 0 & 1 & 1 \end{bmatrix} \quad (B.9)$$

$$\mathcal{W}_2 = \frac{h}{12} \begin{bmatrix} 0 & 0 & 0 & 0 & \dots & 0 \\ 5 & 8 & -1 & 0 & \dots & 0 \\ 0 & 5 & 8 & -1 & \dots & 0 \\ \vdots & & \ddots & & & \vdots \\ 0 & \dots & 5 & 8 & -1 & 0 \\ 0 & \dots & 0 & 5 & 8 & -1 \\ 0 & \dots & 0 & -1 & 8 & 5 \end{bmatrix} \quad (B.10)$$

$$\mathcal{W}_3 = \frac{h}{24} \begin{bmatrix} 0 & 0 & 0 & 0 & 0 & \dots & 0 \\ 9 & 19 & -5 & 1 & 0 & \dots & 0 \\ -1 & 13 & 13 & -1 & 0 & \dots & 0 \\ 0 & -1 & 13 & 13 & -1 & \dots & 0 \\ \vdots & & \ddots & & & & \vdots \\ 0 & \dots & -1 & 13 & 13 & -1 & 0 \\ 0 & \dots & 0 & -1 & 13 & 13 & -1 \\ 0 & \dots & 0 & 1 & -5 & 19 & 9 \end{bmatrix} \quad (B.11)$$

$$w_4 = \frac{h}{720} \begin{bmatrix} 0 & 0 & 0 & 0 & 0 & 0 & & \dots & 0 \\ 251 & 646 & -264 & 106 & -19 & 0 & & \dots & 0 \\ -19 & 346 & 456 & -74 & 11 & 0 & & \dots & 0 \\ 0 & -19 & 346 & 456 & -74 & 11 & & \dots & 0 \\ \vdots & & & & & & \ddots & & \vdots \\ 0 & \dots & & & -19 & 346 & 456 & -74 & 11 & 0 \\ 0 & \dots & & & 0 & -19 & 346 & 456 & -74 & 11 \\ 0 & \dots & & & 0 & 11 & -74 & 456 & 346 & -19 \\ 0 & \dots & & & 0 & -19 & 106 & -264 & 646 & 251 \end{bmatrix} \quad (B.12)$$

$$w_5 = \frac{h}{1440} \begin{bmatrix} 0 & 0 & 0 & 0 & 0 & 0 & 0 & & \dots & 0 \\ 475 & 1427 & -798 & 482 & -173 & 27 & 0 & & \dots & 0 \\ -27 & 637 & 1022 & -258 & 77 & -11 & 0 & & \dots & 0 \\ 11 & -93 & 802 & 802 & -93 & 11 & 0 & & \dots & 0 \\ 0 & 11 & -93 & 802 & 802 & -93 & 11 & & \dots & 0 \\ \vdots & & & & & & & \ddots & & \vdots \\ 0 & \dots & & & 11 & -93 & 802 & 802 & -93 & 11 & 0 \\ 0 & \dots & & & 0 & 11 & -93 & 802 & 802 & -93 & 11 \\ 0 & \dots & & & 0 & -11 & 77 & -258 & 1022 & 637 & -27 \\ 0 & \dots & & & 0 & 27 & -173 & 482 & -798 & 1427 & 475 \end{bmatrix} \quad (B.13)$$

$$W_6 = \frac{h}{60480} \begin{bmatrix} 0 & 0 & 0 & 0 & 0 & 0 & 0 & 0 & 0 & \dots & 0 \\ 19087 & 65112 & -46461 & 37504 & -20211 & 6312 & -863 & 0 & & \dots & 0 \\ -863 & 25128 & 46989 & -16256 & 7299 & -2088 & 271 & 0 & & \dots & 0 \\ 271 & -2760 & 30819 & 37504 & -6771 & 1608 & -191 & 0 & & \dots & 0 \\ 0 & 271 & -2760 & 30819 & 37504 & -6771 & 1608 & -191 & & \dots & 0 \\ \vdots & & & & & & & & & & \vdots \\ 0 & \dots & & 271 & -2760 & 30819 & 37504 & -6771 & 1608 & -191 & 0 \\ 0 & \dots & & 0 & 271 & -2760 & 30819 & 37504 & -6771 & 1608 & -191 \\ 0 & \dots & & 0 & -191 & 1608 & -6771 & 37504 & 30819 & -2760 & 271 \\ 0 & \dots & & 0 & 271 & -2088 & 7299 & -16256 & 46989 & 25128 & -863 \\ 0 & \dots & & 0 & -863 & 6312 & -20211 & 37504 & -46461 & 65112 & 19087 \end{bmatrix}$$

(B.14)

$$W_7 = \frac{h}{120960} \begin{bmatrix} 0 & 0 & 0 & 0 & 0 & 0 & 0 & 0 & 0 & 0 & \dots & 0 \\ 36799 & 139849 & -121797 & 123133 & -88547 & 41499 & -11351 & 1375 & 0 & \dots & 0 \\ -1375 & 47799 & 101349 & -44797 & 26883 & -11547 & 2999 & -351 & 0 & \dots & 0 \\ 351 & -4183 & 57627 & 81693 & -20227 & 7227 & -1719 & 191 & 0 & \dots & 0 \\ -191 & 1879 & -9531 & 68323 & 68323 & -9531 & 1879 & -191 & 0 & \dots & 0 \\ 0 & -191 & 1879 & -9531 & 68323 & 68323 & -9531 & 1879 & -191 & \dots & 0 \\ \vdots & & & & & & & & & & \vdots \\ 0 & \dots & -191 & 1879 & -9531 & 68323 & 68323 & -9531 & 1879 & -191 & 0 \\ 0 & \dots & 0 & -191 & 1879 & -9531 & 68323 & 68323 & -9531 & 1879 & -191 \\ 0 & \dots & 0 & 191 & -1719 & 7227 & -20227 & 81693 & 57627 & -4183 & 351 \\ 0 & \dots & 0 & -351 & 2999 & -11547 & 26883 & -44797 & 101349 & 47799 & -1375 \\ 0 & \dots & 0 & 1375 & -11351 & 41499 & -88547 & 123133 & -121797 & 139849 & 36799 \end{bmatrix}$$

(B.15)

A Sample Gauss-Legendre Integrating Matrix

The Gauss-Legendre integrating matrix presented here is an example of an integrating matrix that does not use end point nodes. Obviously, such matrices cannot be used for intervals where boundary conditions must be applied at the end points; instead, their intended use is for interior integration regions. As pointed out in Section 3.2, the merging process, which forms *global* weighting matrices from the summation of *local* weighting matrices, allows one to combine weighting matrices with and without endpoint nodes.

Gauss-Legendre integrating matrices, which are based upon Legendre polynomials, are related to Gauss-Legendre quadrature. These matrices are also a close relative of the Jacobi integrating matrices since Legendre polynomials prove to be a special case of the more general Jacobi polynomials with $\alpha = \beta = 0$. In fact, the general calculation procedure in Appendix A for Jacobi weighting matrices, when adapted to Legendre polynomials, can be used for the Gauss-Legendre weighting matrices. Note, however, that the Gauss-Legendre matrices, because of the lack of end points, are rectangular rather than square. To make the Gauss-Legendre matrices "conform" to other matrices with end points, the first and last columns of the matrix are "padded" with zeroes as shown in the example below; this padding allows the definition of consistent merging rules as noted in Section 3.2.

The weighting matrix below, with two internal grid points, is for the normalized interval $[-1, 1]$; it can be transformed to $[0, 1]$ by multiplying by the factor $1/2$. Similar to the Jacobi matrices, the coordinate values x , which denote grid points on $[-1, 1]$, are listed above the horizontal bar in the matrix. The grid points t on $[0, 1]$ can be obtained with the linear transformation $t = 0.5(1 + x)$. The subscript n refers to the number of discretization intervals, with the integration being exact for all polynomials of degree $\leq 2n - 3$.

$$W_3 = \begin{bmatrix} \begin{array}{cc} -.57735027 & .57735027 \end{array} \\ \begin{array}{cccc} .00000000 & .00000000 & .00000000 & .00000000 \\ .00000000 & -.07735027 & .50000000 & .00000000 \\ .00000000 & .57735027 & .57735027 & .00000000 \\ .00000000 & .50000000 & -.07735027 & .00000000 \end{array} \end{bmatrix} \quad (B.2)$$

Appendix C

Composite Laminate Constitutive Equations

The behavior of multi-ply laminated composites and composite skin box-beams can be predicted by developing relationships in the laminate axes between the applied loads and the resulting deflections. To develop such relationships, one begins with the stress-strain behavior of a single lamina of an orthotropic material. The lamina behavior is subsequently transformed from principal axes of the lamina to the reference axes for the multi-ply laminate. By then applying the assumptions of thin plate theory, expressions are developed from the properties of the constituent laminae relating force and moment resultants acting on the plate to midplane strains and plate curvatures. These expressions are the laminate constitutive equations. The following is intended only as a brief description of the process for obtaining the constitutive equations. More detailed presentations of these developments are given by Jones [25] and Ashton, Halpin, and Petit [57].

Assuming a state of plane stress, the simplified stress-strain relationships for a lamina of orthotropic material can be written as

$$\begin{Bmatrix} \sigma_1 \\ \sigma_2 \\ \tau_{12} \end{Bmatrix}_k = \begin{bmatrix} Q_{11} & Q_{12} & 0 \\ Q_{12} & Q_{22} & 0 \\ 0 & 0 & Q_{66} \end{bmatrix}_k \begin{Bmatrix} \epsilon_1 \\ \epsilon_2 \\ \gamma_{12} \end{Bmatrix}_k \quad (C.1)$$

where

$$\begin{aligned}
Q_{11} &= \frac{E_1}{1 - \nu_{12}\nu_{21}} \\
Q_{12} &= \frac{\nu_{12}E_2}{1 - \nu_{12}\nu_{21}} = \frac{\nu_{21}E_1}{1 - \nu_{12}\nu_{21}} \\
Q_{22} &= \frac{E_2}{1 - \nu_{12}\nu_{21}} \\
Q_{66} &= G_{12},
\end{aligned} \tag{C.2}$$

and the subscript k denotes the k th layer in the laminate. The terms Q_{ij} , which are referred to as reduced stiffnesses, are defined in the lamina principle axes (see Fig. C-1).

If θ is defined as the angle between the x -axis and the 1-axis (see Fig. C-2), then a transformation of both stress and strain components in Eq. (C.1) leads to the following stress-strain equations for the lamina in the laminate axis system:

$$\begin{Bmatrix} \sigma_x \\ \sigma_y \\ \tau_{xy} \end{Bmatrix}_k = \begin{bmatrix} \bar{Q}_{11} & \bar{Q}_{12} & \bar{Q}_{16} \\ \bar{Q}_{12} & \bar{Q}_{22} & \bar{Q}_{26} \\ \bar{Q}_{16} & \bar{Q}_{26} & \bar{Q}_{66} \end{bmatrix}_k \begin{Bmatrix} \epsilon_x \\ \epsilon_y \\ \gamma_{xy} \end{Bmatrix}_k \tag{C.3}$$

where the \bar{Q}_{ij} are the transformed reduced stiffnesses, which have the definitions

$$\begin{aligned}
\bar{Q}_{11} &= Q_{11} \cos^4 \theta + 2(Q_{12} + 2Q_{66}) \sin^2 \theta \cos^2 \theta + Q_{22} \sin^4 \theta \\
\bar{Q}_{12} &= (Q_{11} + Q_{22} - 4Q_{66}) \sin^2 \theta \cos^2 \theta + Q_{12}(\sin^4 \theta + \cos^4 \theta) \\
\bar{Q}_{22} &= Q_{11} \sin^4 \theta + 2(Q_{12} + 2Q_{66}) \sin^2 \theta \cos^2 \theta + Q_{22} \cos^4 \theta \\
\bar{Q}_{16} &= (Q_{11} - Q_{12} - 2Q_{66}) \sin \theta \cos^3 \theta + (Q_{12} - Q_{22} + 2Q_{66}) \sin^3 \theta \cos \theta \\
\bar{Q}_{26} &= (Q_{11} - Q_{12} - 2Q_{66}) \sin^3 \theta \cos \theta + (Q_{12} - Q_{22} + 2Q_{66}) \sin \theta \cos^3 \theta \\
\bar{Q}_{66} &= (Q_{11} + Q_{22} - 2Q_{12} - 2Q_{66}) \sin^2 \theta \cos^2 \theta + Q_{66}(\sin^4 \theta + \cos^4 \theta).
\end{aligned} \tag{C.4}$$

A convenient form exists for calculating the transformed reduced stiffnesses in terms of stiffness invariants. This invariant form, which was first developed by Tsai

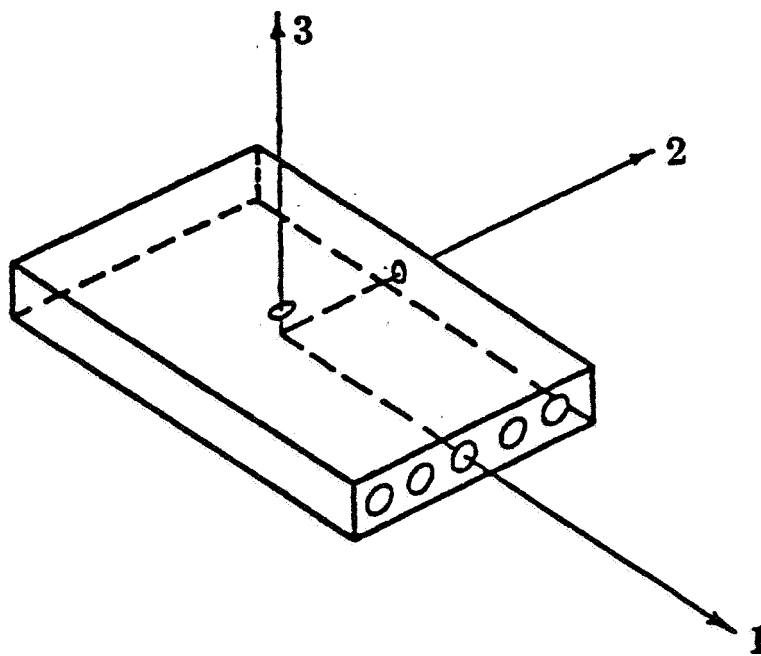


Fig. C-1. Lamina axis system (1,2,3)

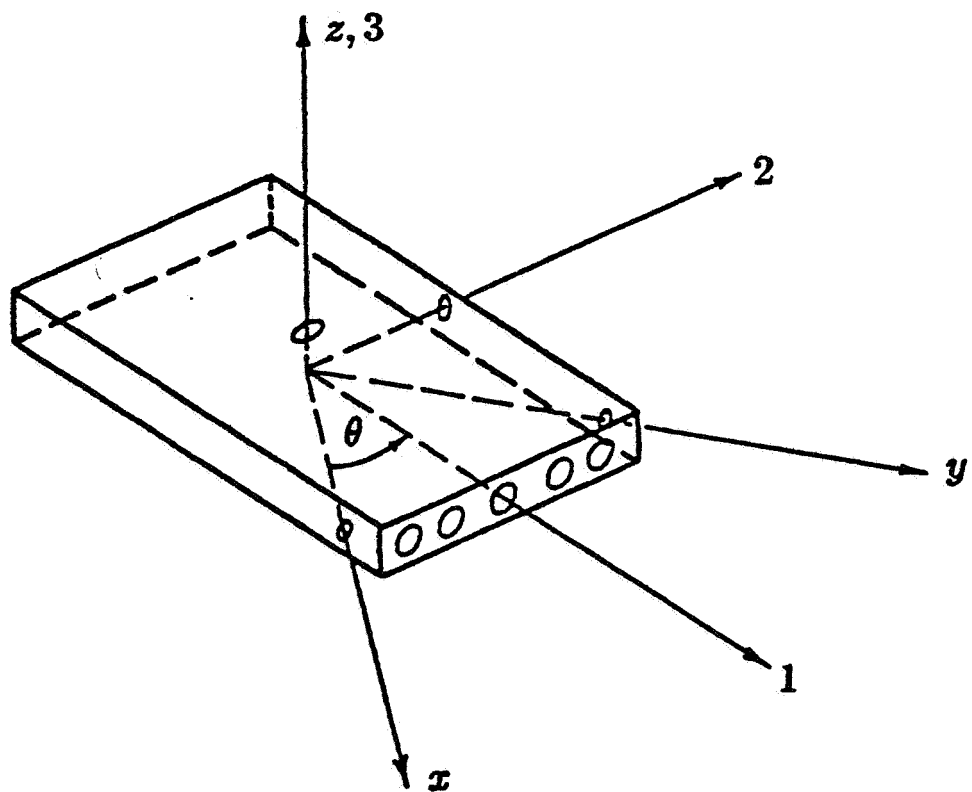


Fig. C-2. Laminate axis system (x, y, z)

and Pagano [58], is written as

$$\begin{aligned}
\bar{Q}_{11} &= U_1 + U_2 \cos 2\theta + U_3 \cos 4\theta \\
\bar{Q}_{12} &= U_4 + U_3 \cos 4\theta \\
\bar{Q}_{22} &= U_1 - U_2 \cos 2\theta + U_3 \cos 4\theta \\
\bar{Q}_{16} &= \frac{1}{2}U_2 \sin 2\theta + U_3 \sin 4\theta \\
\bar{Q}_{26} &= \frac{1}{2}U_2 \sin 2\theta - U_3 \sin 4\theta \\
\bar{Q}_{66} &= U_5 - U_3 \cos 4\theta
\end{aligned} \tag{C.5}$$

where the stiffness invariants are

$$\begin{aligned}
U_1 &= \frac{1}{8}(3Q_{11} + 3Q_{22} + 2Q_{12} + 4Q_{66}) \\
U_2 &= \frac{1}{2}(Q_{11} - Q_{22}) \\
U_3 &= \frac{1}{8}(Q_{11} + Q_{22} - 2Q_{12} - 4Q_{66}) \\
U_4 &= \frac{1}{8}(Q_{11} + Q_{22} + 6Q_{12} - 4Q_{66}) \\
U_5 &= \frac{1}{8}(Q_{11} + Q_{22} - 2Q_{12} + 4Q_{66}).
\end{aligned} \tag{C.6}$$

With the foregoing knowledge of the behavior of a single layer, classical lamination theory for thin plates can now be used to determine the behavior of the laminate, or laminated box-beam. Classical lamination theory embodies a collection of stress and deformation assumptions which constitute the familiar Kirchhoff hypothesis for plates. Under these assumptions, the strains for any point in the laminate can be written in terms of geometrical midplane displacements u_0 , v_0 , and

w_0 as

$$\begin{aligned}\epsilon_x &= \frac{\partial u_0}{\partial x} - z \frac{\partial^2 w_0}{\partial x^2}, \\ \epsilon_y &= \frac{\partial v_0}{\partial y} - z \frac{\partial^2 w_0}{\partial y^2}, \\ \gamma_{xy} &= \frac{\partial u_0}{\partial y} + \frac{\partial v_0}{\partial x} - 2z \frac{\partial^2 w_0}{\partial x \partial y}.\end{aligned}\tag{C.7}$$

Furthermore, the laminate strains given by Eq. (C.7) are equivalently expressed in terms of the midplane strains and plate curvatures as

$$\begin{Bmatrix} \epsilon_x \\ \epsilon_y \\ \gamma_{xy} \end{Bmatrix} = \begin{Bmatrix} \epsilon_x^0 \\ \epsilon_y^0 \\ \gamma_{xy}^0 \end{Bmatrix} + z \begin{Bmatrix} \kappa_x \\ \kappa_y \\ \kappa_{xy} \end{Bmatrix}.\tag{C.8}$$

If we now define the vectors

$$\begin{aligned}\sigma &= \{\sigma_x \quad \sigma_y \quad \tau_{xy}\}^T, \\ \epsilon^0 &= \{\epsilon_x^0 \quad \epsilon_y^0 \quad \gamma_{xy}^0\}^T, \\ \kappa &= \{\kappa_x \quad \kappa_y \quad \kappa_{xy}\}^T,\end{aligned}\tag{C.9}$$

then, with the aid of Eq. (C.8), the k th layer stress-strain relationships in Eq. (C.3) can be expressed in the form

$$\sigma_k = [\bar{Q}]_k \epsilon^0 + z [\bar{Q}]_k \kappa.\tag{C.10}$$

Force and moment resultants offer a convenient way of expressing the relationships between internal and external loads of a laminated plate. With this in mind, it is convenient to make use of a force resultant vector \mathbf{n} and a moment resultant

vector \mathfrak{m} which appear as

$$\mathfrak{n} = \{N_x \quad N_y \quad N_{xy}\}^T, \quad \mathfrak{m} = \{M_x \quad M_y \quad M_{xy}\}^T. \quad (C.11)$$

By assuming that the plate (or box-beam) has total thickness t and a number of layers NL , the force and moment resultants (i.e., force and moment per unit width) are defined by integrating the stresses in each lamina over the thickness, that is,

$$\begin{Bmatrix} \mathfrak{n} \\ \mathfrak{m} \end{Bmatrix} = \int_{-t/2}^{t/2} \begin{Bmatrix} \sigma_k \\ \sigma_k z \end{Bmatrix} dz = \sum_{k=1}^{NL} \int_{z_{k-1}}^{z_k} \begin{Bmatrix} \sigma_k \\ \sigma_k z \end{Bmatrix} dz. \quad (C.12)$$

By substituting Eq. (C.10) into Eq. (C.12) and noting that $[\bar{Q}]$, ϵ^0 , and κ are not functions of z , one obtains the force and moment resultant expressions

$$\mathfrak{n} = \sum_{k=1}^{NL} [\bar{Q}]_k \left\{ \epsilon^0 \int_{z_{k-1}}^{z_k} dz + \kappa \int_{z_{k-1}}^{z_k} z dz \right\} \quad (C.13)$$

and

$$\mathfrak{m} = \sum_{k=1}^{NL} [\bar{Q}]_k \left\{ \epsilon^0 \int_{z_{k-1}}^{z_k} z dz + \kappa \int_{z_{k-1}}^{z_k} z^2 dz \right\}. \quad (C.14)$$

After carrying out the integrations, Eqs. (C.13–C.14) can be written as

$$\begin{Bmatrix} N_x \\ N_y \\ N_{xy} \\ M_x \\ M_y \\ M_{xy} \end{Bmatrix} = \begin{bmatrix} A_{11} & A_{12} & A_{16} & B_{11} & B_{12} & B_{16} \\ A_{12} & A_{22} & A_{26} & B_{12} & B_{22} & B_{26} \\ A_{16} & A_{26} & A_{66} & B_{16} & B_{26} & B_{66} \\ B_{11} & B_{12} & B_{16} & D_{11} & D_{12} & D_{16} \\ B_{12} & B_{22} & B_{26} & D_{12} & D_{22} & D_{26} \\ B_{16} & B_{26} & B_{66} & D_{16} & D_{26} & D_{66} \end{bmatrix} \begin{Bmatrix} \epsilon_x^0 \\ \epsilon_y^0 \\ \gamma_{xy}^0 \\ \kappa_x \\ \kappa_y \\ \kappa_{xy} \end{Bmatrix} \quad (C.15)$$

where

$$\begin{aligned}
A_{ij} &= \sum_{k=1}^{NL} (\bar{Q}_{ij})_k (z_k - z_{k-1}) \\
B_{ij} &= \frac{1}{2} \sum_{k=1}^{NL} (\bar{Q}_{ij})_k (z_k^2 - z_{k-1}^2) \\
D_{ij} &= \frac{1}{3} \sum_{k=1}^{NL} (\bar{Q}_{ij})_k (z_k^3 - z_{k-1}^3)
\end{aligned} \tag{C.16}$$

In Eqs. (C.15) and (C.16), the A_{ij} are extensional stiffnesses, the B_{ij} are coupling stiffnesses, and the D_{ij} are bending stiffnesses. For those laminates with layers arranged symmetrically about the geometric midplane of the plate, the B_{ij} terms will be zero.

The integrating matrix approach requires knowledge of the compliance terms rather than the stiffness terms. The compliance terms are obtained by simply inverting the (6×6) matrix of stiffness terms appearing in Eq. (C.15). In symbolic form, the composite compliance relationship can be written as

$$\begin{Bmatrix} \epsilon^0 \\ \kappa \end{Bmatrix} = \begin{bmatrix} \mathbf{A}^* & \mathbf{B}^* \\ \mathbf{B}^* & \mathbf{D}^* \end{bmatrix} \begin{Bmatrix} \mathbf{n} \\ \mathbf{m} \end{Bmatrix}. \tag{C.17}$$

In Eq. (C.17), the subscripts of the terms in the (3×3) submatrices will be designated by $i, j = 1, 2, 3$, rather than $i, j = 1, 2, 6$.

Appendix D

Modified Strip Theory Aerodynamics

The following nondimensional unsteady aerodynamic loads have evolved from the modified strip theory developed by Yates [59,60]. These Laplace transformed aerodynamic loads, which are valid for arbitrary motion, are made applicable to the Laplace domain by inclusion of either a generalized Theodorsen's function or an appropriate rational approximation as discussed by Edwards [61-63]. The loads presented here are intended for use with the Laplace transformed flutter equations (cf., Eqs. (2.21) and (4.30)), and correspond to those load terms required by Eq. (2.28). The nondimensionalization of the aerodynamic loads is the same as that indicated for the p 's in Eq. (2.31).

As in the theory presented by Yates, these aerodynamics employ a variable section lift-curve slope $a_0(x)$ instead of 2π , a variable section aerodynamic center $a_c(x)$ instead of -0.5 (the quarter-chord), and a variable section structural reference axis location $a(x)$. The Theodorsen function can be modified by a factor which accounts for compressibility effects on the magnitude of the lift and pitching moment. For more details on the modifications accompanying a particular planform and Mach number, see the above references by Yates. It should be noted that for incompressible flow over untapered wings having a lift-curve slope of 2π and an aerodynamic center at the quarter-chord, the aerodynamics given here reduce to the elementary strip theory used by Barmby, Cunningham, and Garrick [64].

The nondimensional Laplace transformed aerodynamic loads providing lift and pitching moment per unit span can be conveniently calculated with the aid of an

aerodynamic influence matrix $\mathbf{Q}_{FD}(s^*, \lambda)$. The terms appearing in \mathbf{Q}_{FD} are given by

$$\begin{aligned}
\hat{L}_w(s^*, \lambda) &= \frac{\ell}{b_R} \left\{ -\pi \beta^2 s^{*2} - \text{RC}(\bar{s}) a_0 \sqrt{\lambda} \beta s^* \right\} \\
\hat{L}_\alpha(s^*, \lambda) &= b \left\{ \pi a \beta^2 s^{*2} - \pi \sqrt{\lambda} \beta s^* - \text{RC}(\bar{s}) a_0 (a_d - a) \sqrt{\lambda} \beta s^* - \text{RC}(\bar{s}) a_0 \lambda \right\} \\
\hat{L}_\gamma(s^*, \lambda) &= b \left\{ \pi \sqrt{\lambda} \beta s^* + \text{RC}(\bar{s}) a_0 \lambda \right\} \tan \Lambda \\
\hat{L}_r(s^*, \lambda) &= b^2 \frac{b_R}{\ell} \left\{ \pi a \sqrt{\lambda} \beta s^* - \text{RC}(\bar{s}) a_0 (a_d - a) \lambda \right\} \tan \Lambda \\
\hat{M}_w(s^*, \lambda) &= b \left\{ \pi a \beta^2 s^{*2} + \text{RC}(\bar{s}) a_0 (a - a_c) \sqrt{\lambda} \beta s^* \right\} \\
\hat{M}_\alpha(s^*, \lambda) &= b^2 \frac{b_R}{\ell} \left\{ -\pi \left(\frac{1}{8} + a^2 \right) \beta^2 s^{*2} - \pi (a_d - a) \sqrt{\lambda} \beta s^* + \text{RC}(\bar{s}) a_0 (a - a_c) (a_d - a) \sqrt{\lambda} \beta s^* \right. \\
&\quad \left. + \text{RC}(\bar{s}) a_0 (a - a_c) \lambda \right\} \\
\hat{M}_\gamma(s^*, \lambda) &= b^2 \frac{b_R}{\ell} \left\{ -\pi a \sqrt{\lambda} \beta s^* - \text{RC}(\bar{s}) a_0 (a - a_c) \lambda \right\} \tan \Lambda \\
\hat{M}_r(s^*, \lambda) &= b^3 \left(\frac{b_R}{\ell} \right)^2 \left\{ -\pi \left(\frac{1}{8} + a^2 \right) \sqrt{\lambda} \beta s^* + \text{RC}(\bar{s}) a_0 (a - a_c) (a_d - a) \lambda \right\} \tan \Lambda.
\end{aligned} \tag{D.1}$$

From the terms in Eq. (D.1), the aerodynamic matrix $\mathbf{Q}_{FD}(s^*, \lambda)$ is constructed in the form

$$\mathbf{Q}_{FD}(s^*, \lambda) = \begin{bmatrix} 0 & 0 & 0 & 0 \\ 0 & 0 & 0 & 0 \\ 0 & \hat{L}_\gamma & \hat{L}_w & \hat{L}_{\alpha,r} \\ 0 & \hat{M}_\gamma & \hat{M}_w & \hat{M}_{\alpha,r} \end{bmatrix} \tag{D.2}$$

where

$$\hat{L}_{\alpha,r} = \hat{L}_\alpha + \hat{L}_r D \tag{D.3}$$

and

$$\hat{M}_{\alpha, \tau} = \hat{M}_{\alpha} + \hat{M}_{\tau} D, \quad (D.4)$$

with D being a differentiating matrix. (Note that the subscript τ is used as a reference to the variable, $\tau = \frac{\partial \alpha}{\partial x}$.) For moderate angles of wing aerodynamic sweep and large aspect ratio, the last term on the right-hand side of Eqs. (D.3-D.4) is negligible compared to the remaining term.

The following definitions apply to the foregoing equations, in which λ is a dimensionless dynamic pressure parameter and s^* is a dimensionless Laplace variable:

$$\begin{aligned} s^* &= s \ell^2 \sqrt{\frac{m_R}{(EI)_R}} \\ \bar{s} &= \frac{s b}{V^*} = \frac{\beta s^*}{\sqrt{\lambda}} \\ \lambda &= \frac{\rho b_R \ell^3 V^{*2}}{(EI)_R} \\ V^* &= V \cos \Lambda \\ \mu &= \frac{m_R}{\pi \rho b_R^2} \\ \beta &= \bar{b} \sqrt{\frac{b_R}{\pi \mu \ell}} \\ \bar{b} &= \frac{b}{b_R}. \end{aligned} \quad (D.5)$$

The aerodynamic downwash point a_d is calculated from

$$a_d = \frac{a_0}{2\pi} + a_c. \quad (D.6)$$

A convenient rational approximation to the Theodorsen function, attributed to

R.T. Jones, is given by

$$C(\bar{x}) = \frac{0.5\bar{x}^2 + 0.2808\bar{x} + 0.01365}{\bar{x}^2 + 0.3455\bar{x} + 0.01365} . \quad (D.7)$$

As discussed in Yates [59], for higher Mach numbers M , $C(\bar{x})$ can be empirically corrected for compressibility effects by scaling by a factor $R(\bar{x}, M)$, which is determined from a ratio of the magnitudes of compressible and incompressible circulation functions.

Appendix E

Solutions for Problems with Concentrated Loads

Concentrated loads present a special type of discontinuity that can be treated with the help of delta functions. To include the possibility of delta functions in the integrating matrix approach, it is first necessary to extend the developments of Section 3.1 for the integrating matrices of continuous integrands. Once delta functions have been included in the formulation of integrating matrices, the solution methods presented in Chapter 4 can be expanded to accommodate concentrated loads.

Instead of considering a simple continuous function $f(x)$, as was done in Section 3.1, it is now necessary to consider a function of the form

$$\bar{f}(x) = f(x) + p_i^+ \delta(x - x_i) \quad (E.1)$$

where p_i^+ gives the magnitude of the delta function (concentrated load) at the point $x = x_i$. Taking the integral of Eq. (E.1) over the subinterval $[x_i, x_{i+1}]$, with the delta function located at x_{i+1} , yields

$$\begin{aligned} \int_{x_i}^{x_{i+1}} \bar{f}(x) dx &= \int_{x_i}^{x_{i+1}} f(x) dx + p_{i+1}^+ \int_{x_i}^{x_{i+1}} \delta(x - x_{i+1}) dx \\ &= \int_{x_i}^{x_{i+1}} f(x) dx + p_{i+1}^+ . \end{aligned} \quad (E.2)$$

By using the definitions for $\{\bar{f}\}$ and $\{f\}$ given in Eqs. (3.5) and (3.6) and including

the definition of the column vector

$$\{p^+\} = (p_0^+, p_1^+, \dots, p_N^+)^T, \quad (E.3)$$

one can express the set of all integrals given by Eq. (E.2) as

$$\{\mathcal{F}\} = \mathcal{W}_n\{f\} + \{p^+\}. \quad (E.4)$$

This result is analogous to Eq. (3.7); note, however, that the first term in $\{\mathcal{F}\}$ is zero only if p_0^+ is zero. As in Section 3.1, Eq. (E.4) can be premultiplied by the summing matrix \mathcal{S} to yield the integrating matrix relationship

$$\{\mathcal{F}\} = \mathcal{L}\{f\} + \mathcal{S}\{p^+\} \quad (E.5)$$

where the integrating matrix \mathcal{L} is the same as defined in Eq. (3.11). Thus, from Eq. (E.5) it is clear that the "integrating matrix" for delta functions is simply the summing matrix \mathcal{S} .

The foregoing results can be applied to solving problems as discussed in Section 4.1. Consider, for example, the discretized equations given in Eq. (4.2). After including the concentrated loads, the equation can be written in the form

$$\tilde{y}' = \tilde{Z}\tilde{y} - \lambda(\tilde{A} + \tilde{A}^+\delta(x - x_i)) - (\tilde{s}_r + \tilde{s}_r^+\delta(x - x_i)). \quad (E.6)$$

Applying the integrating matrices then yields

$$\tilde{y} = \tilde{L}(\tilde{Z}\tilde{y} - \lambda\tilde{A}\tilde{y} - \tilde{s}_r) - \tilde{S}(\lambda\tilde{A}^+\tilde{y} + \tilde{s}_r^+) + \tilde{k}. \quad (E.7)$$

This result compares with that of Eq. (4.3). Note that the global summing matrix \tilde{S} will be composed of diagonal blocks of dimension $(N+1) \times (N+1)$, which corresponds to \tilde{L} in Eq. (4.4).

If one now solves for $\tilde{\mathbf{k}}$, the equivalent of Eq. (4.9) is obtained. Thus,

$$\tilde{\mathbf{k}} = -\tilde{\mathbf{B}}[\tilde{\mathbf{L}}(\tilde{\mathbf{Z}}\tilde{\mathbf{y}} - \lambda\tilde{\mathbf{A}}\tilde{\mathbf{y}} - \tilde{\mathbf{a}}_r) - \tilde{\mathbf{S}}(\lambda\tilde{\mathbf{A}}^+\tilde{\mathbf{y}} + \tilde{\mathbf{a}}_r^+)] - \tilde{\mathbf{B}}_{nh}\tilde{\mathbf{y}}. \quad (E.8)$$

After substituting Eq. (E.8) into Eq. (E.7), grouping similar terms, and then rearranging, one has the result

$$[\mathbf{H} - \lambda(\mathbf{F}\tilde{\mathbf{A}} + \mathbf{F}^+\tilde{\mathbf{A}}^+)]\tilde{\mathbf{y}} = \mathbf{f} \quad (E.9)$$

where

$$\mathbf{H} = \mathbf{I} + \tilde{\mathbf{B}}_{nh} + \mathbf{F}\tilde{\mathbf{Z}} \quad (E.10)$$

$$\mathbf{F} = [\tilde{\mathbf{B}} - \mathbf{I}]\tilde{\mathbf{L}}, \quad \mathbf{F}^+ = [\tilde{\mathbf{B}} - \mathbf{I}]\tilde{\mathbf{S}} \quad (E.11)$$

$$\mathbf{f} = \mathbf{F}\tilde{\mathbf{a}}_r + \mathbf{F}^+\tilde{\mathbf{a}}_r^+. \quad (E.12)$$

It is clear that these equations are simply an extension of Eqs. (4.10–4.13).

Carrying the analysis one step further, the reduced nonhomogeneous linear system in Eq. (4.26), for $\mathbf{H}_{FD} = 0$, appears as

$$[\mathbf{I} - \lambda(\mathbf{T}\mathbf{A}_{FD} + \mathbf{T}^+\mathbf{A}_{FD}^+)]\tilde{\mathbf{y}}_D = \mathbf{T}\tilde{\mathbf{a}}_{rF} + \mathbf{T}^+\tilde{\mathbf{a}}_{rF}^+ \quad (E.13)$$

where

$$\mathbf{T} = -\mathbf{H}_{DD}^{-1}\mathbf{H}_{DF}\mathbf{H}_{FF}^{-1}\mathbf{F}_{FF} \quad (E.14)$$

and

$$\mathbf{T}^+ = -\mathbf{H}_{DD}^{-1}\mathbf{H}_{DF}\mathbf{H}_{FF}^{-1}\mathbf{F}_{FF}^+. \quad (E.15)$$

Similarly, the reduced eigenvalue problem can be written as

$$[(\mathbf{T}\mathbf{A}_{FD} + \mathbf{T}^+\mathbf{A}_{FD}^+) - (1/\lambda)\mathbf{I}]\tilde{\mathbf{y}}_D = 0. \quad (E.16)$$

Appendix F

Constraint Equations

Auxiliary constraint equations can be used in specific instances to reduce the degrees of freedom required for a numerical solution. To carry out reductions on matrix equations, it is convenient to think in terms of partitioned matrices, where the variables to be eliminated are placed in a partition of the solution vector, and all matrices appearing in the matrix equation are partitioned accordingly. The constraint equations are then used to obtain a transformation of variables

$$\mathbf{y} = \mathbf{U}\mathbf{y}^* \quad (F.1)$$

where \mathbf{y} is a vector containing the original variables, \mathbf{y}^* is a vector of transformed variables, and \mathbf{U} is a transformation matrix. It is assumed initially that \mathbf{U} is a square matrix that possesses an inverse, but as noted below, one can make use of other types of transformations that are characterized by rectangular transformation matrices.

Consider first a partitioned system of linear equations

$$\begin{bmatrix} \mathbf{G}_{11} & \mathbf{G}_{12} \\ \mathbf{G}_{21} & \mathbf{G}_{22} \end{bmatrix} \begin{Bmatrix} \mathbf{y}_1 \\ \mathbf{y}_2 \end{Bmatrix} = \begin{Bmatrix} \mathbf{f}_1 \\ \mathbf{f}_2 \end{Bmatrix}. \quad (F.2)$$

Equation (F.1) can be substituted into Eq. (F.2), and the resulting matrix equation premultiplied by \mathbf{U}^{-1} . If \mathbf{U} does in fact represent an elimination of variables, then \mathbf{G} will be transformed by this similarity transformation into a block triangular form

such that

$$\begin{bmatrix} \mathbf{G}'_{11} & \mathbf{0} \\ \mathbf{G}'_{21} & \mathbf{I} \end{bmatrix} \begin{Bmatrix} \mathbf{y}_1^* \\ \mathbf{y}_2^* \end{Bmatrix} = \begin{Bmatrix} \mathbf{f}_1^* \\ \mathbf{f}_2^* \end{Bmatrix} \quad (F.3)$$

where \mathbf{y}_2^* contains the eliminated variables and $\mathbf{f}^* = \mathbf{U}^{-1}\mathbf{f}$. The reduced linear system is obtained directly from Eq. (F.3) as

$$\mathbf{G}'_{11}\mathbf{y}_1^* = \mathbf{f}_1^*. \quad (F.4)$$

An identical approach can be followed for the eigenvalue problem given by

$$\begin{bmatrix} \mathbf{G}_{11} & \mathbf{G}_{12} \\ \mathbf{G}_{21} & \mathbf{G}_{22} \end{bmatrix} \begin{Bmatrix} \mathbf{y}_1 \\ \mathbf{y}_2 \end{Bmatrix} = \lambda \begin{Bmatrix} \mathbf{y}_1 \\ \mathbf{y}_2 \end{Bmatrix}. \quad (F.5)$$

The similarity transformation in this situation yields the equations

$$\begin{bmatrix} \mathbf{G}'_{11} & \mathbf{0} \\ \mathbf{G}'_{21} & \mathbf{0} \end{bmatrix} \begin{Bmatrix} \mathbf{y}_1^* \\ \mathbf{y}_2^* \end{Bmatrix} = \lambda \begin{Bmatrix} \mathbf{y}_1^* \\ \mathbf{y}_2^* \end{Bmatrix} \quad (F.6)$$

from which the reduced eigenvalue problem is

$$[\mathbf{G}'_{11} - \lambda\mathbf{I}]\mathbf{y}_1^* = \mathbf{0}. \quad (F.7)$$

For those problems for which \mathbf{U} is a square, invertible matrix, the foregoing reduction process is carried out as presented. On the other hand, it is also possible to use a transformation that involves a rectangular transformation matrix. In this situation, the above procedure requires a congruence transformation rather than a similarity transformation. To convert the resulting eigenvalue problem to standard form requires the inversion of the matrix product $\mathbf{U}^T\mathbf{U}$. Unless this product results in a diagonal matrix, or otherwise has some special form, the best numerical approach makes use of singular value decomposition and the pseudoinverse. Discussions on this subject can be found in Strang [65] and Atkinson [66].

Appendix G

Calculation of Transition and Influence Matrices

Integrating matrices offer a convenient method for numerically calculating transition matrix solutions of two-point boundary problems. For structural solutions, the transition matrix can also be applied to the development of stiffness influence matrices. In formulating eigenvalue problems, the direct integrating matrix approach presented in Chapter 4 is to be preferred for its simplicity and numerical efficiency. Nevertheless, it is possible to use the transition matrix concept to advantage in certain types of numerical calculations. A detailed description of transition (also known as transfer or transmission) matrix methods in structural mechanics is presented by Pestel and Leckie [67]. A brief, but useful account of the method can also be found in Chapter 10 of McGuire and Gallagher [20]. In addition, the reader can refer to Chapter 7 of Boyce and DiPrima [68] for a general review of fundamental matrices and the role they play in the solution of linear differential equations. For useful applications and properties of transition matrices, one should consult Appendix A4 of Bryson and Ho [21] and Chapter 9 of Kailath [69].

The calculation of a transition matrix begins with the integrated version of the homogeneous state vector equations. These equations can be obtained from Eq. (4.3) by dropping the nonhomogeneous term $\tilde{L}\tilde{a}_r$, thus yielding

$$\dot{\tilde{y}} = \tilde{L}\tilde{Z}\tilde{y} - \lambda\tilde{L}\tilde{A}\tilde{y} + \tilde{k}. \quad (G.1)$$

It will be assumed that the ordering of the components of the global state vector is

the same as that used in the derivations presented in Section 4.1. As will be recalled, the global state vector is arranged such that it can be partitioned into generalized force and generalized displacement subsets, and the discrete set of values for a particular variable are grouped together. (An alternate ordering scheme that can be used for transition matrix derivation involves consecutively placing each local state vector into the global state vector. This ordering scheme, however, requires one to use a modified definition of the global integrating matrix. The modified integrating matrix is obtained by expanding each element of \mathbf{L} into a diagonal submatrix, with the element value repeated in each of the diagonal terms of the submatrix.)

As the next step in calculating the transition matrix, choose the constant of integration to be equal to the local state vector at the end point $x = 0$. This means that the global constant vector of integration can be written as

$$\tilde{\mathbf{k}} = \mathbf{E}\mathbf{y}_0 = \begin{bmatrix} \mathbf{E}_{FF} & \mathbf{E}_{FD} \\ \mathbf{E}_{DF} & \mathbf{E}_{DD} \end{bmatrix} \begin{Bmatrix} \mathbf{y}_{F0} \\ \mathbf{y}_{D0} \end{Bmatrix} \quad (G.2)$$

where \mathbf{E} will be termed a selection matrix since it selects the component of the local state vector to be placed in each component of $\tilde{\mathbf{k}}$. \mathbf{E} consists primarily of zeroes, but has appropriately placed unit terms. For clarity, it is worth noting that if NS is the number of state variables and $(N + 1)$ is the number of grid points, then the dimension of \mathbf{y}_0 will be NS and the dimensions of \mathbf{E} will be $NS(N + 1) \times NS$.

If one now combines Eq. (G.1) with Eq. (G.2) the result is

$$\mathbf{H}\tilde{\mathbf{y}} = \mathbf{E}\mathbf{y}_0 = \tilde{\mathbf{k}} \quad (G.3)$$

where

$$\mathbf{H} = \mathbf{I} - \tilde{\mathbf{L}}\tilde{\mathbf{Z}} + \lambda\tilde{\mathbf{L}}\tilde{\mathbf{A}}. \quad (G.4)$$

The corresponding partitioned form of Eq. (G.3) appears as

$$\begin{bmatrix} \mathbf{H}_{FF} & \mathbf{H}_{FD} \\ \mathbf{H}_{DF} & \mathbf{H}_{DD} \end{bmatrix} \begin{Bmatrix} \tilde{\mathbf{y}}_F \\ \tilde{\mathbf{y}}_D \end{Bmatrix} = \begin{bmatrix} \mathbf{E}_{FF} & \mathbf{E}_{FD} \\ \mathbf{E}_{DF} & \mathbf{E}_{DD} \end{bmatrix} \begin{Bmatrix} \mathbf{y}_{F0} \\ \mathbf{y}_{D0} \end{Bmatrix}. \quad (G.5)$$

In a straight forward manner, Eq. (G.5) can be solved by partitions, which yields

$$\begin{Bmatrix} \tilde{y}_F \\ \tilde{y}_D \end{Bmatrix} = \begin{bmatrix} T_{FF} & T_{FD} \\ T_{DF} & T_{DD} \end{bmatrix} \begin{Bmatrix} y_{F0} \\ y_{D0} \end{Bmatrix} \quad (G.6)$$

where

$$\begin{aligned} T_{FF} &= H_{FF}^{-1} [E_{FF} - H_{FD} T_{DF}] \\ T_{FD} &= H_{FF}^{-1} [E_{FD} - H_{FD} T_{DD}] \\ T_{DF} &= [H_{DD} - H_{DF} H_{FF}^{-1} H_{FD}]^{-1} [E_{DF} - H_{DF} H_{FF}^{-1} E_{FF}] \\ T_{DD} &= [H_{DD} - H_{DF} H_{FF}^{-1} H_{FD}]^{-1} [E_{DD} - H_{DF} H_{FF}^{-1} E_{FD}]. \end{aligned} \quad (G.7)$$

By definition, the transition (transfer) matrix transforms the state vector at one point into the state vector at another point. Considering the transition matrix between the state vector at $x = 0$ and the state vector at the i th grid point, one can write the general transition matrix relationship as

$$\begin{Bmatrix} y_{Fi} \\ y_{Di} \end{Bmatrix} = \begin{bmatrix} \Phi_{FFi} & \Phi_{FDi} \\ \Phi_{DFi} & \Phi_{DDi} \end{bmatrix} \begin{Bmatrix} y_{F0} \\ y_{D0} \end{Bmatrix}. \quad (G.8)$$

At the same time, it is possible to write another expression for the local state vector appearing on the left-hand side of Eq. (G.8). This expression, which makes use of another selection matrix, Γ_i , transforms the global state vector into the local vector at the i th point. The expression is written as

$$\begin{Bmatrix} y_{Fi} \\ y_{Di} \end{Bmatrix} = \begin{bmatrix} \Gamma_i & 0 \\ 0 & \Gamma_i \end{bmatrix} \begin{Bmatrix} \tilde{y}_F \\ \tilde{y}_D \end{Bmatrix}. \quad (G.9)$$

By substituting the result for the global state vector from Eq. (G.6) into Eq. (G.9), and then comparing with Eq. (G.8), one finds that the transition matrix for the i th grid point is given by

$$\Phi_i = \begin{bmatrix} \Gamma_i T_{FF} & \Gamma_i T_{FD} \\ \Gamma_i T_{DF} & \Gamma_i T_{DD} \end{bmatrix}. \quad (G.10)$$

This equation, in conjunction with Eq. (G.7), provides a method for calculating the transition matrix.

The foregoing results for transition matrices can be applied in calculating a stiffness influence matrix. For the influence matrix calculation, the load terms multiplied by λ in Eq. (G.1) are set to zero; for certain problems this can mean that H_{FD} in Eqs. (G.5) and (G.7) will be zero. The strategy in developing a stiffness influence matrix from a transition matrix is to obtain a force-displacement relationship between degrees of freedom at each end of the normalized interval $[0, 1]$. By definition, the matrix that relates the force degrees of freedom to the displacement degrees of freedom will be the influence matrix.

By making use of Eq. (G.8), and taking into account the properties of a normalized transition matrix, one can write the expression

$$\begin{Bmatrix} y_D(0) \\ y_D(1) \end{Bmatrix} = \begin{bmatrix} \Phi_{DF}(0) & \Phi_{DD}(0) \\ \Phi_{DF}(1) & \Phi_{DD}(1) \end{bmatrix} \begin{Bmatrix} y_{F0} \\ y_{D0} \end{Bmatrix} = \begin{bmatrix} 0 & I \\ \Phi_{DF}(1) & \Phi_{DD}(1) \end{bmatrix} \begin{Bmatrix} y_{F0} \\ y_{D0} \end{Bmatrix}. \quad (G.11)$$

Solving for the constant vector on the far right-hand side of Eq. (G.11) gives

$$\begin{Bmatrix} y_{F0} \\ y_{D0} \end{Bmatrix} = \begin{bmatrix} -\Phi_{DF}^{-1}(1)\Phi_{DD}(1) & \Phi_{DF}^{-1}(1) \\ I & 0 \end{bmatrix} \begin{Bmatrix} y_D(0) \\ y_D(1) \end{Bmatrix}. \quad (G.12)$$

Similar to Eq. (G.11), an expression can be written for the forces at the endpoints. This expression appears as

$$\begin{Bmatrix} y_F(0) \\ -y_F(1) \end{Bmatrix} = \begin{bmatrix} \Phi_{FF}(0) & \Phi_{FD}(0) \\ -\Phi_{FF}(1) & -\Phi_{FD}(1) \end{bmatrix} \begin{Bmatrix} y_{F0} \\ y_{D0} \end{Bmatrix} = \begin{bmatrix} I & 0 \\ -\Phi_{FF}(1) & -\Phi_{FD}(1) \end{bmatrix} \begin{Bmatrix} y_{F0} \\ y_{D0} \end{Bmatrix}. \quad (G.13)$$

Substituting the constant vector from Eq. (G.12) into Eq. (G.13) yields

$$\begin{Bmatrix} y_F(0) \\ -y_F(1) \end{Bmatrix} = \begin{bmatrix} K'_{00} & K'_{01} \\ K'_{10} & K'_{11} \end{bmatrix} \begin{Bmatrix} y_D(0) \\ y_D(1) \end{Bmatrix} \quad (G.14)$$

where the stiffness influence matrix \mathbf{K}' is given by

$$\mathbf{K}' = \begin{bmatrix} -\Phi_{DF}^{-1}(1)\Phi_{DD}(1) & \Phi_{DF}^{-1}(1) \\ \Phi_{FF}(1)\Phi_{DF}^{-1}(1)\Phi_{DD}(1) - \Phi_{FD}(1) & -\Phi_{FF}(1)\Phi_{DF}^{-1}(1) \end{bmatrix}. \quad (G.15)$$

Provided that certain conditions are met by the transition matrix, it can be shown that \mathbf{K}' is a symmetric matrix. To demonstrate this fact requires knowledge of the transition matrix for the adjoint system of homogeneous differential equations, where the adjoint equations are obtained by substituting $-\mathbf{Z}^T$ for \mathbf{Z} in Eq. (G.1). The transition matrices of the original and adjoint systems share the identity

$$\Phi_A^T \Phi = \mathbf{I}. \quad (G.16)$$

where Φ_A is the transition matrix for the adjoint system. Normally, one would obtain Φ_A by solving the adjoint differential equations, but for symplectic systems (see Section 2.1) the adjoint transition matrix can be obtained directly from the original transition matrix through the relationship

$$\Phi_A^T = \Phi^{-1} = \mathbf{J}^T \Phi^T \mathbf{J} \quad (G.17)$$

where \mathbf{J} is as defined in Chapter 2 (see Bryson and Ho [21], p.157). With the aid of this relationship, it can be shown that if the numerically calculated transition matrices satisfy Eq. (G.16), then $\mathbf{K}' - \mathbf{K}'^T = 0$, which shows that \mathbf{K}' is symmetric. It should be noted, however, that sample numerical calculations seem to indicate that the discretization level determines how accurately the numerically calculated transition matrices match the identity in Eq. (G.16). The satisfaction of Eq. (G.16) possibly might serve as an indicator of sufficient discretization, but at the present time this has not been verified and thus remains an object for further study.

A final item to be noted about transition matrix solutions is that calculations for nonhomogeneous linear problems can be simplified considerably if they are symplectic. That is, by making use of integrating matrices and by applying the relationship in Eq. (G.17), one finds that the usual variation of parameters solution for the state vector equations can be written in a conveniently calculable form.

References

- [1] Gimmestad, D., "An Aeroelastic Optimization Procedure for Composite High Aspect Ratio Wings," AIAA/ASME/ASCE/AHS 20th Structures, Structural Dynamics, and Materials Conf., Vol. I, St. Louis, Mo., April 1979, pp. 79-86.
- [2] Diederich, F.W., and Budiansky, B., "Divergence of Swept Wings," NACA TN 1680, August 1948.
- [3] Diederich, F.W., and Foss, K.A., "Charts and Approximate Formulas for the Estimation of Aeroelastic Effects on the Loading of Swept and Unswept Wings," NACA TN 2608, February 1952.
- [4] Weisshaar, T.A., "Aeroelastic Stability and Performance Characteristics of Aircraft with Advanced Composite Sweptforward Wing Structures," AFFDL-TR-78-116, September 1978.
- [5] Weisshaar, T.A., "Forward Swept Wing Static Aeroelasticity," AFFDL-TR-79-3087, June 1979.
- [6] Lehman, L.L., "A Hybrid State Vector Approach to Aeroelastic Analysis with Application to Composite Lifting Surfaces," AIAA/ASME/ASCE/AHS 22nd Structures, Structural Dynamics and Materials Conference, Vol. II, Atlanta, Ga., April 1981, pp. 821-831.
- [7] Noor, A.K., Stephens, W.B., and Fulton, R.E., "An Improved Numerical Process for Solution of Solid Mechanics Problems," *Computers and Structures*, Vol. 3, 1973, pp. 1397-1437.
- [8] Noor, A.K., and Stephens, W.B., "Mixed Finite-Difference Scheme for Free-Vibration Analysis of Noncircular Cylinders," NASA TN D-7107, February 1973.
- [9] Noor, A.K., and Stephens, W.B., "Comparison of Finite-Difference Schemes for Analysis of Shells of Revolution," NASA TN D-7337, December 1973.
- [10] Stroud, R.C., and Mayers, J., "Dynamic Response of Rapidly Heated Plate Elements," *AIAA Journal*, Vol. 9, No. 1, January 1971, pp. 76-83.
- [11] Steele, C.R., "Asymptotic Solutions Without Special Functions for Steep and Shallow Shells," *Mechanics Today*, Vol. 5, 1980, pp. 483-494.
- [12] Steele, C.R., Ranjan, G.V., and Pulliam, T.H., "Computer Analysis of Shells of Revolution Using Asymptotic Results," AIAA/ASME/ASCE/AHS 20th Structures, Structural Dynamics and Materials Conf., Vol. I, St. Louis, Mo., April 1979, pp. 162-170.
- [13] Steele, C.R. and Barry, K.E., "Asymptotic Integration Methods Applied to Rotating Beams," *Journal of Applied Mechanics*, Vol. 47, No. 4, December 1980, pp. 884-890.

- [14] Nemat-Nasser, S., "General Variational Methods for Waves in Elastic Composites," *Journal of Elasticity*, Vol. 2, No. 2, June 1972, pp. 73-90.
- [15] Nemat-Nasser, S., "On Variational Methods in Finite and Incremental Elastic Deformation Problems With Discontinuous Fields," *Quarterly of Applied Mathematics*, July 1972, pp. 143-156.
- [16] Reissner, E., "Variational Methods and Boundary Conditions in Shell Theory," *Studies in Optimization, Proceedings of the Symposium on Optimization*, Vol. 1, Society for Industrial and Applied Mathematics, Philadelphia, Pa., 1970, pp. 78-94.
- [17] Reissner, E., "On a Variational Theorem in Elasticity," *Journal of Mathematics and Physics*, Vol. 29, 1950, pp. 27-52.
- [18] Nimmer, R.P., and Mayers, J., "Limit Point Buckling Loads of Axially Compressed, Circular Cylindrical Shells—The Effect of Nonlinear Material Behavior," *Journal of Applied Mechanics*, Vol. 46, No. 2, June 1979, pp. 386-392.
- [19] Anderson, R.E., and Mayers, J., "Effects of Nonlinear Material Behavior on Postbuckling Stiffness of Laminated Composite Plates," AIAA Paper No. 79-1806, August 1979.
- [20] McGuire, W., and Gallagher, R.H., *Matrix Structural Analysis*, Wiley, New York, 1979, pp. 362-369.
- [21] Bryson, A.E., and Ho, Y.-C., *Applied Optimal Control*, Hemisphere Publishing Corp., Washington, D.C., 1975.
- [22] Love, A.E.H., *A Treatise on the Mathematical Theory of Elasticity*, 4th. ed., Dover, New York, 1944, pp. 381-398.
- [23] Ojalvo, I.U., and Newman, M., "Buckling of Naturally Curved and Twisted Beams," *ASCE Journal of the Engineering Mechanics Division*, Vol. 94, No. EM5, October 1968, pp. 1067-1087.
- [24] Nitzsche, F., "Aeroelastic Analysis of a Troposkien-Type Wind Turbine Blade," *Proceedings of the International Colloquium on Wind Energy*, Brighton U.K., August 1981, pp. 255-260.
- [25] Jones, R.M., *Mechanics of Composite Materials*, McGraw-Hill, New York, 1975.
- [26] Vakhitov, M.B., "Integrating Matrices as a Means of Numerical Solution of Differential Equations in Structural Mechanics," *Izvestiya VUZ. Aviatcionnaya Tekhnika*, Vol. 9, No. 3, 1966, pp. 50-61 (English: *Soviet Aeronautics*, Vol. 9, No. 3, 1966, pp. 27-33).
- [27] Hunter, W.F., "Integrating-Matrix Method for Determining the Natural Vibration Characteristics of Propeller Blades," NASA TN D-6064, December 1970.
- [28] Spector, J., "Integral Series Solution for Uncoupled Vibrations of Nonuniform Bars," Master of Applied Mechanics Thesis, University of Virginia, May 1952, pp. 77-80.

- [29] White, W.F., Jr., and Malatino, R.E., "A Numerical Method for Determining the Natural Vibration Characteristics of Rotating Nonuniform Cantilever Blades," NASA TM X-72751, October 1975.
- [30] Kvaternik, R.G., White, W.F., Jr., and Kaza, K.R.V., "Nonlinear Flap-Lag-Axial Equations of a Rotating Beam with Arbitrary Precone Angle," AIAA Paper No. 78-491, AIAA/ASME 19th Structures, Structural Dynamics and Materials Conf., Bethesda, Md., April 1978, pp. 214-227.
- [31] White, W.F., Jr., Kvaternik, R.G., and Kaza, K.R.V., "Buckling of Rotating Beams," *International Journal of Mechanical Sciences*, Vol. 21, 1979, pp. 739-745.
- [32] Vakhitov, M.B., and Grankin, Y.G., "Bending Calculation of Axisymmetric Circular Plates of Variable Stiffness," *Izvestiya VUZ. Aviatsionnaya Tekhnika*, Vol. 16, No. 4, 1973, pp. 35-41 (English: *Soviet Aeronautics*, Vol. 16, No. 4, 1973, pp. 26-30).
- [33] Levashov, P.D., "Determination of the Deflections and Stresses in a Low-Aspect-Ratio Wing by the Displacement Method," *Izvestiya VUZ. Aviatsionnaya Tekhnika*, Vol. 16, No. 2, 1973, pp. 34-39 (English: *Soviet Aeronautics*, Vol. 16, No. 2, 1973, pp. 27-31).
- [34] Levashov, P.D., "Numerical Solution for Determining Deflections and Stresses in a Monolithic Wing by the Generalized Ritz Method," *Izvestiya VUZ. Aviatsionnaya Tekhnika*, Vol. 16, No. 4, 1973, pp. 42-48 (English: *Soviet Aeronautics*, Vol. 16, No. 3, 1973, pp. 31-35).
- [35] Levashov, P.D., "Influence of Differentiation and Integration Matrix Structure on Stiffness Matrix Accuracy," *Izvestiya VUZ. Aviatsionnaya Tekhnika*, Vol. 20, No. 4, 1977, pp. 126-128 (English: *Soviet Aeronautics*, Vol. 20, No. 4, 1977, pp. 101-103).
- [36] Lakin, W.D., "Integrating Matrices for Arbitrarily Spaced Grid Points," NASA CR-159172, November 1979.
- [37] Schneider, H., and Reddy, P.B., "Spline Method for Nonlinear Optimal Thrust Vector Controls for Atmospheric Interceptor Guidance," *AIAA Journal*, Vol. 15, No. 4, April 1977, pp. 449-450.
- [38] Conte, S.D., and de Boor, C., *Elementary Numerical Analysis, An Algorithmic Approach*, 2nd ed., McGraw-Hill, New York, 1972.
- [39] Krylov, V.I., *Approximate Calculation of Integrals*, (translated by A.H. Stroud), MacMillan, New York, 1962.
- [40] Abramowitz, M., and Stegun, I.A. (ed.), *Handbook of Mathematical Functions*, Dover, New York, 1965.
- [41] Collatz, L., *The Numerical Treatment of Differential Equations*, Springer-Verlag, Berlin, 1960.
- [42] Meirovitch, L., *Analytical Methods in Vibrations*, MacMillan, New York, 1967, pp. 156-160.

- [43] Przemieniecki, J.S., *Theory of Matrix Structural Analysis*, McGraw-Hill, New York, 1968.
- [44] Smith, B.T., et al., *Matrix Eigensystem Routines: EISPACK Guide*, Springer-Verlag, New York, 1974.
- [45] Bisplinghoff, R.L., Ashley, H., and Halfman, R.L., *Aeroelasticity*, Addison-Wesley, Reading, Mass., 1955.
- [46] Hildebrand, F.B., and Reissner, E., "The Influence of the Aerodynamic Span Effect on the Magnitude of the Torsional Divergence Velocity and on the Shape of the Corresponding Deflection Mode," N.A.C.A. T.N. 926, February, 1944.
- [47] Hodges, D.H., "Direct Solutions for Sturm-Liouville Systems with Discontinuous Coefficients," *AIAA Journal*, Vol. 17, No. 8, August 1979, pp. 924-926.
- [48] Hodges, D.H., personal communication, May 1981.
- [49] Hodges, D.H., and Rutkowski, M.J., "Free-Vibration Analysis of Rotating Beams by a Variable-Order Finite-Element Method," *AIAA/ASME/ASCE/AHS 22nd Structures, Structural Dynamics and Materials Conference*, Vol. 2, Atlanta, Ga., April 1981, pp. 444-453.
- [50] Peters, D.A., and Hodges, D.H., "In-Plane Vibration and Buckling of a Rotating Beam Clamped Off the Axis of Rotation," *Journal of Applied Mechanics*, Vol. 102, No. 2, June 1980, pp. 398-402.
- [51] Weisshaar, T.A., "The Influence of Aeroelasticity on Swept Composite Wings," AFWAL-TR-80-3137, Vol. 1, November 1980.
- [52] Housner, J.M., and Stein, M., "Flutter Analysis of Swept-wing Subsonic Aircraft with Parameter Studies of Composite Wings," NASA TN D-7539, September 1974.
- [53] Goland, M., "The Flutter of a Uniform Cantilever Wing," *Journal of Applied Mechanics*, Vol. 12, No. 4, December 1945, pp. A-197-A-208.
- [54] Goland, M., and Luke, Y.L., "The Flutter of a Uniform Wing with Tip Weights," *Journal of Applied Mechanics*, Vol. 15, No. 1, March 1948, pp. 13-20.
- [55] Zienkiewicz, O.C., *The Finite Element Method*, 3rd. ed., McGraw-Hill, London, 1977.
- [56] Gallagher, R. H., *Finite Element Analysis Fundamentals*, Prentice-Hall, Englewood Cliffs, New Jersey, 1975.
- [57] Ashton, J.E., Halpin, J.C., and Petit, P.H., *Primer on Composite Materials: Analysis*, Technomic, Stamford, Conn., 1969.
- [58] Tsai, S.W., Halpin, J.C., and Pagano, N.J., *Composite Materials Workshop*, Technomic, Stamford, Conn., 1968, pp. 233-253.
- [59] Yates, E.C., Jr., "Calculation of Flutter Characteristics for Finite-Span Swept or Unswept Wings at Subsonic or Supersonic Speeds by a Modified Strip Analysis," NACA RM L57L10, 1958.

- [60] Yates, E.C., Jr., "Flutter and Unsteady Lift Theory. Performance and Dynamics of Aerospace Vehicles," NASA SP-258, 1971, pp. 289-374.
- [61] Edwards, J.W., "Unsteady Aerodynamic Modeling and Active Aeroelastic Control," SUDAAR 504, Stanford University, February 1977.
- [62] Edwards, J.W., Ashley, H., and Breakwell, J.V., "Unsteady Aerodynamic Modeling for Arbitrary Motions," AIAA Paper No. 77-451, March 1977.
- [63] Edwards, J.W., "Applications of Laplace Transform Methods to Airfoil Motion and Stability Calculations," AIAA/ASME/ASCE/AHS 20th Structures, Structural Dynamics and Materials Conf., Vol. II, St. Louis, Mo., April 1979, pp. 465-481.
- [64] Barmby, J.G., Cunningham, H.J., and Garrick, I.E., "Study of Effects of Sweep on the Flutter of Cantilever Wings," NACA Report 1014, 1951.
- [65] Strang, G., *Linear Algebra and its Applications*, Academic Press, New York, 1976, pp. 130-137.
- [66] Atkinson, K.E., *An Introduction to Numerical Analysis*, Wiley, New York, 1978, pp. 408-410.
- [67] Péstel, E.C., and Leckie, F.A., *Matrix Methods in Elastomechanics*, McGraw-Hill, New York, 1963.
- [68] Boyce, W.E., and DiPrima, R.C., *Elementary Differential Equations and Boundary Value Problems*, 2nd. ed., Wiley, New York, 1969.
- [69] Kailath, T., *Linear Systems*, Prentice-Hall, Englewood Cliffs, New Jersey, 1980.

D₃
STARTS
2N
P.C-1

UNSTEADY AERODYNAMIC PROPULSION

A DISSERTATION

SUBMITTED TO THE DEPARTMENT OF AERONAUTICS AND ASTRONAUTICS

AND THE COMMITTEE ON GRADUATE STUDIES

OF STANFORD UNIVERSITY

IN PARTIAL FULFILLMENT OF THE REQUIREMENTS

FOR THE DEGREE OF

DOCTOR OF PHILOSOPHY

By

James K. Nathman

October 1981

I certify that I have read this thesis and that in my opinion it is fully adequate, in scope and quality, as a dissertation for the degree of Doctor of Philosophy.

(Holt Ashley - Adviser)

I certify that I have read this thesis and that in my opinion it is fully adequate, in scope and quality, as a dissertation for the degree of Doctor of Philosophy.

(Brian Cantwell)

I certify that I have read this thesis and that in my opinion it is fully adequate, in scope and quality, as a dissertation for the degree of Doctor of Philosophy.

(Daniel B. DeBra)

Approved for the University Committee
on Graduate Studies:

Dean of Graduate Studies & Research

ACKNOWLEDGEMENTS

I wish to give credit to those without whom the experiment would be impossible. They are:

Dick Van Patten for his advice and design of electronics.

John Gill for assembling and maintaining the electronics.

Russ Hacker for his advice on mechanical design.

Gerry Pauley for electron-beam welding the spar and fittings.

Keith Horrocks of E G & G Instruments for the loan of his demonstrator 5204 Lock-In Analyzer.

My thanks are given to Daniel DeBra for the loan of a major part of the apparatus and his advice on the conduct of the experiment. And finally, this project would not have been completed without the infinite patience of my adviser, Holt Ashley.

↓ This Research was supported by the Air Force Office of Scientific Research under Contract Nos. AFOSR 74-2712A, AFOSR 77-3263 and AFOSR 79-0061.

ABSTRACT

Theoretical and experimental results are presented from an investigation into the thrust of oscillating airfoils. The voluminous previous work is reviewed and some new conclusions are drawn. First, that oscillatory camber can be an important part of natural flight. Second, that under optimum propulsive conditions, a simple relationship between thrust and efficiency exists.

The theory of Timman is expanded to predict the thrust of a thin, two-dimensional airfoil oscillating in a wind tunnel. Also, a lifting-surface method is developed to model a thick wing in a wind tunnel. The full Bernoulli equation is used in incompressible, inviscid flow to accurately calculate the suction, including the second harmonic force which is analogous to the leading-edge suction of thin-airfoil theory.

An experimental apparatus consisting of an airfoil with an internal force balance, which is pitched and plunged in a low-speed tunnel, is used to measure the lift, moment and drag during oscillatory motion. The experimental data compares very well with theory for simple pitch motion. Data for pure plunge and combined motions are also presented.

CONTENTS

ACKNOWLEDGEMENTS	iv
ABSTRACT	v

<u>Chapter</u>	<u>page</u>
I. INTRODUCTION	1
Preface	1
Thesis Outline	2
Summary of Contributions	2
II. HISTORICAL OVERVIEW	5
Introduction	5
Historical Developments	6
Theory of Two-Dimensional Oscillating Wings	10
Rigid Airfoils	10
Flexible Airfoils	18
Experimental Validation	20
Application to Propulsion in Natural Flight	23
Surge Motion	25
Effect of Amplitude	25
Optimization	28
Thickness and Profile Shape	33
Viscous Drag	34
Leading-edge Suction Restraints	34
Three-Dimensional Effects	35
Interference	39
III. CALCULATION OF AERODYNAMIC FORCES ON AN AIRFOIL OSCILLATING IN A WIND TUNNEL	43
Analytic Thin-Airfoil Theory	43
Normal Force and Moment	43
Leading-edge Suction	50
Numerical Panel Method	53
Airfoil Geometry	57
Computation of Coefficients	60
Doublet Integral	60
Source Coefficients	61
Source Strengths	62
Steady Flow	62
Unsteady Flow	63
Wake Contribution	64

Pressures	66
Viscous Effects	73
Including Wind Tunnel Walls	75
IV. MEASUREMENT OF AERODYNAMIC FORCES ON AN AIRFOIL OSCILLATING IN A WIND TUNNEL	77
Introduction	77
Experimental Apparatus	78
Wind Tunnel	78
Suspension	79
Wing and Internal Balance	83
Airfoil Balance Calibration	92
Wing Control	100
Signal Acquisition	102
Tares	106
Wind Tunnel Corrections	109
Measured Results and Comparison with Theory	110
Static Tests	110
Simple Pitch Oscillatory Results	116
Simple Pitch with Mean Angle of Attack	122
Simple Plunge	125
Combined Pitch and Plunge Motion	129
Measurement Errors	133
Discussion	134
V. SUMMARY AND RECOMMENDATIONS	137
Summary	137
Recommendations	138
APPENDIX A	141
APPENDIX B	145
APPENDIX C	153
APPENDIX D	161
APPENDIX E	175
REFERENCES	183

LIST OF TABLES

<u>Table</u>	<u>page</u>
1. Series Values for $H/b = 2$	49
2. Wing Parameters	91
3. Balance Calibration Matrix	95
4. Filter Characteristics	106

LIST OF FIGURES

<u>Figure</u>	<u>page</u>
1. The Model of Miturich Powered by a Rotating Mass.	7
2. Fitz Patrick's Ornithopter Design.	9
3. Airfoil Reference System.	11
4. Airloads on an Airfoil Oscillating in Free Air.	16
5. Comparison of Results of Obye and Theory of Garrick.	22
6. Effect of Oscillatory Camber on the Propulsion of a Thin Airfoil.	24
7. The Effect of Amplitude on Mean Thrust.	27
8. Optimal Motion of a 2-D Airfoil for Propulsion from Wu [17]. . .	29
9. Maximum Thrust of a 2-D Airfoil from Wu [17].	30
10. Low-Frequency Relationship between Efficiency and Thrust of a 2-D Airfoil.	31
11. Effect of Aspect Ratio on Oscillatory Thrust predicted by RH0IV. .	36
12. Effect of Spanwise Differences in Amplitude on Mean Thrust from Tuck [52].	38
13. Constructive Interference between an Oscillating and a Stationary Airfoil from Bosch [59].	41
14. Conformal Transformation of Timman [16].	44
15. Geometry of Circular-Arc Panel.	59
16. Approximate Representation of NACA 0015 Profile.	59
17. Convergence of Steady Potential-Flow Drag Predicted by Panel Method.	70
18. Oscillatory Lift Predicted by Panel Method.	71
19. Second Harmonic Suction Predicted by Panel Method.	72

20.	Wind Tunnel Representation in Panel Code.	76
21.	Comparison of Force Convention and Tunnel Axis System.	80
22.	Four-Bar Pitch Suspension and Actuator.	81
23.	Detail of Flexpivot Pitch Joint.	81
24.	Arrangement of Plunge Suspension System.	82
25.	Internal Construction of Wing.	84
26.	Sketches of the Normal and Chordwise Balance Suspension.	86
27.	Airfoil Mounted in Wind Tunnel.	89
28.	Dimensions of Wing.	90
29.	Calibration of Airfoil Balance.	93
30.	Axis System of Balance.	97
31.	Schematic of Suspension Actuator Control.	101
32.	Flow Chart of Data Reduction.	103
33.	Experimental Electronic Equipment.	105
34.	One-Hz Bandwidth Noise Spectra of Sensor Outputs, $q=0.9''$ water.	107
35.	Static Lift of Airfoil with and without Boundary-Layer Trip.	111
36.	Static Moment of Airfoil with and without Boundary-Layer Trip.	111
37.	Static Drag of Airfoil with and without Boundary-Layer Trip.	112
38.	Static Lift of Airfoil with attached Endplates.	114
39.	Static Moment of Airfoil with attached Endplates.	114
40.	Static Drag of Airfoil with attached Endplates.	115
41.	Oscillatory Lift Slope in Simple Pitch versus Reduced Frequency.	118
42.	Oscillatory Moment about Pitch Axis in Simple Pitch versus Reduced Frequency.	119
43.	Mean Suction per Degree in Simple Pitch versus Reduced Frequency.	120
44.	Mean Drag per Degree in Simple Pitch versus Reduced Frequency.	120

45.	Second Harmonic Suction in Simple Pitch versus Reduced Frequency.	121
46.	First Harmonic Suction versus Mean Angle of Attack in Simple Pitch.	124
47.	Lift per Unit Plunge versus Reduced Frequency.	126
48.	Moment per Unit Plunge versus Reduced Frequency.	127
49.	Change in Thrust per Unit Plunge versus Reduced Frequency. . .	128
50.	Normal Force in Combined Motion versus Pitch/Plunge Phase. . .	130
51.	Moment about Pitch Axis versus Pitch/Plunge Phase.	131
52.	Change in Suction in Combined Motion versus Pitch/Plunge Phase.	132
53.	Change in Drag in Combined Motion versus Pitch/Plunge Phase. .	132

NOTATION

ENGLISH SYMBOLS

a	Position of pitch axis
a_n	Fourier coefficient of acceleration potential
a_0, a_1	Generalized airfoil displacements of Timman
A	Flow Domain
A	Wing Area
b	Semichord length
c	Chord length
cn	Jacobian elliptic function
C	Theodorsen function
C	Euler's constant, 0.577215...
C'	Theodorsen function in wind tunnel
C_d	Nondimensional drag per unit span, D/qA
C_l	Nondimensional lift per unit span, L/qA
C_m	Nondimensional moment about mid-chord, M/qAc
C_{ma}	Moment coefficient about the pitch axis
C_n	Nondimensional normal force per unit span, N/qA
C_p	Pressure coefficient, $(p-p_\infty)/q$
C_s	Nondimensional suction per unit span, S/qA
C_t	Nondimensional thrust per unit span, T/qA
C_w	Nondimensional power per unit span, W/qAU
dn	Jacobian elliptic function
D	Drag

D	Doublet influence coefficient
f	Acceleration potential
F _a	Applied force
F _m	Measured Force
F _n	Normal component of force
F _s	Suction component of force
G	Green's function*
h	Nondimensional plunge displacement of airfoil at pitch axis
h ₁ (x)	Nondimensional transverse displacement of airfoil
H	Tunnel half height
i	$\sqrt{-1}$
k	Reduced frequency, $\omega b/U$
k _c	Minimum frequency for thrust loading
k*	Tunnel height modulus
k'	Complementary modulus
K	Complete elliptic integral of first kind of modulus k*
K'	Complete elliptic integral of first kind of modulus k'
L	Lift
L _x	Rolling moment (about X axis)
M _a	Pitching moment about x=a
n	Normal to airfoil surface
N	Force normal to airfoil chord
N _y	Yawing moment (about Y axis)
p	Static pressure
q	Dynamic pressure, $\frac{1}{2}\rho U^2$
q	Name of Jacobian elliptic function
r	Distance between points

r_a, r_s, r'	Position vectors
R	Radius of curvature of panel
R_1	Distance to center of curvature of panel
R'	Ratio of R to R_1
s	Arc length
s	Suction direction
s	Semispan
s_n, s_n'	Wall correction series
sn	Jacobian elliptic function
S	Suction force
S	Flow boundary
S	Source influence coefficient
t	Nondimensional time, $\tau U/b$
T	Thrust
U	Freestream velocity
v_n	Normalwash velocity
V	Velocity vector
V_b	Nondimensional velocity of body
w	Downwash velocity
W	Power
W	Wake influence coefficient
x	Nondimensional coordinate, X/b
X	Wind tunnel centered coordinate, positive downstream
y	Nondimensional coordinate, Y/b
Y	Wind tunnel centered coordinate
z	Complex coordinate, $x+iy$
Z	Wind-tunnel centered coordinate, positive down

$Z(\xi)$ Jacobi Zeta function

GREEK SYMBOLS

α angle of attack

α_n Generalized airfoil displacement of Timman

β Deviation of load cell axis from normal to suction axis

β_n Fourier Coefficients of airfoil displacement of Wu

β_n Generalized airfoil displacements of Timman

γ Euler's constant, 1.781...

γ Angular size of panel

γ_n Fourier coefficients of airfoil slope

γ_n Wall correction parameter

Γ Circulation strength

δ Misalignment of internal balance from the chord

δ Wall correction parameter

ϵ Wall correction parameter

ζ Complex coordinate of transformed domain, $\xi+i\sigma$

η Efficiency

θ Substitute coordinate of airfoil

θ Feathering parameter

θ Angular coordinate of panel

λ Wall correction parameter

ξ Transformed x coordinate

ρ Air density

σ Transformed y coordinate

σ Tangential coordinate of panel

τ Dimensional time

ϕ	Nondimensional perturbation velocity potential
Φ	Dimensional perturbation velocity potential
ψ	Transformed x coordinate
ω	Dimensional frequency
ω_i	Ratio of downwash to span

SUBSCRIPTS

a	Applied
b	Body
c	Center of curvature
h	Plunge dependent
l	Lower surface
m	Measured
max	Maximum
mean	Mean value
n	Component normal to chord
n	Derivative normal to surface
osc	Oscillatory
s	Suction component
te	Trailing edge
w	Wake
x	X component
y	Y component
α	Pitch dependent
α'	Pitch velocity dependent
0	Mean value
1	First harmonic amplitude

2	Second harmonic amplitude
0,1,2...	Fourier coefficient
∞	Conditions at infinity

SUPERSCRIPTS

0	Static value
t	Time dependent
\wedge	Unit vector

OPERATORS

\bullet	Vector dot product
\perp	Vector cross product
∇	Gradient
()	Time derivative
Re	Real part of
*	Complex conjugate
O()	Order of
	Modulus

ABBREVIATIONS

DVM	Digital voltmeter
LVDT	Linear Variable Differential Transformer
rms	Root mean square
Re	Reynolds Number
2-D	Two Dimensional
AR	Aspect ratio

Chapter I

INTRODUCTION

1.1 PREFACE

People were already flying across the Atlantic before it was possible to analyze the flight of the birds which gave us our inspiration to fly. Now, with the success of the man-powered Gossamer Albatross we have reached the point at which we can bring together many separate theories to analyze natural flight.

Past work has included:

1. 2-D rigid wings in sinusoidal transverse motion.
2. Wings with oscillating camber.
3. Rigid wings in longitudinal motion.
4. 3-D wings in transverse motion.
5. Effects of large amplitude motion.
6. Boundary-layer drag analysis.
7. Leading-edge suction restraints.
8. Interference between multiple wings.

This past work is reviewed in the first chapter of this dissertation.

Predicting the thrust of a wing in unsteady motion is not only a prerequisite for ornithopters; but also, as the references indicate, it is vital to the design of vertical-axis wind turbines, helicopter rotors in forward flight and aircraft with slender, nonplanar wings.

The objectives of this research were to summarize and simplify the body of reports on oscillating wings, apply them to the case of an airfoil in a wind tunnel, and measure the actual forces experienced by such an airfoil.

1.2 THESIS OUTLINE

In the next chapter a review of work on the thrust of oscillating wings is presented, with particular emphasis on two-dimensional theory.

Chapter III details the calculation of the lift, moment and thrust for an airfoil oscillating in a wind tunnel. Both an analytic theory, which is exact for a thin airfoil in incompressible flow, and a numerical computational procedure for thick wings are included.

Chapter IV describes the apparatus designed for measuring the aerodynamic forces in Stanford's low-speed wind tunnel. Results for pitch, plunge and combined motion are reported and compared to the developed theories.

A summary and recommendations for future research are given in Chapter V.

1.3 SUMMARY OF CONTRIBUTIONS

A) The thrust of an airfoil operating optimally below the critical frequency is shown to have a parabolic dependency on the efficiency.

This behavior has been found to be true of wings, also, but has not yet been recognized in its general form. This relation makes it easy to estimate the optimum propulsive performance for an oscillating wing.

B) Wu's theory for the thrust of a 2-D airfoil was used to investigate the effect of variable camber. A bird-like camber shape was chosen and added to a rigid airfoil moving in a natural manner. In the right proportion, the camber increases the thrust by 50 percent while the efficiency remains unchanged. Moreover, the leading-edge suction was drastically reduced, another advantage over the rigid airfoil.

C) Timman's theory for the lift and moment on a wing in a wind tunnel was modified to predict thrust. This was done by extracting the leading-edge pressure singularity from Timman's pressure distribution and inferring the suction from this.

D) A thick-airfoil panel method has also been used to predict the drag of the airfoil in the wind tunnel. Comparisons between the prediction of these theories and the experiment are made.

E) A 2-D wing was designed, constructed and instrumented to measure the axial and normal forces as the airfoil is pitched and plunged in Stanford's low-speed wind tunnel.

F) Measurements of the aerodynamic forces during simple pitch and pure plunge at three reduced frequencies are presented. The results

from combined pitch and plunge motion with six various pitch/plunge phases are also included. Excellent agreement is found for most cases, particularly simple pitch oscillations.

Chapter II

HISTORICAL OVERVIEW

2.1 INTRODUCTION

A complete review of oscillating wings, like a mirage, appears to recede with the coming of familiarity in the subject. There will always be an excluded paper or overlooked book which bears some relation to flapping flight. Further, a proper abstract of the information in the 2000 references collected by Fitz Patrick [1] would not only be inappropriate for this thesis but would also be self-defeating by its intimidating size. The review given here is therefore necessarily arbitrary and incomplete. The papers included in this review are, firstly, pertinent to the other work in this thesis. Secondly, they treat the fundamental problems of flapping flight, and finally, they illuminate the troubled evolution of a technology which often appears on the verge of maturity.

A relevant review of unsteady aerodynamics is given by McCroskey [2]. For indepth collections the reader is referred to Swimming and Flying in Nature [3] and Biofluidynamics [4].

2.2 HISTORICAL DEVELOPMENTS

Persistent attempts at sustained flight in aircraft propelled by oscillating wings have been made since the early days of aviation and have continued to this day. In 1867, Otto Lilienthal [5] conducted tests on a full scale machine whose wings were made of multiple slats which 'feathered' on the upstroke and closed to form a solid wing on the downstroke, but this was much too inefficient for flight.

Before the Wrights' development of propeller theory and efficient propellers, the means of propulsion of an aircraft was a point of argument. In 1904, Samuelson [6] asked

Which of the two systems, exclusively coming into question for human flight, offers the greater probability of a future development? Is it the sailing-flight by screw propulsion in the manner of W. Kress, Prof. S.P. Langley, W. and O. Wright brothers &c. or is it the bird-like flight, performed as far as I know, till now only by myself...?

and based on his own experimental evidence, answered

...I do not intend to dispute a possible success of the screw sailing-flyer.
But I say this: the sailing flight has narrow limits; the rowing flight the infinite possibilities.

Since then the "infinite possibilities" have been investigated by an innumerable multitude with narrow success.

Patrick [1] mentions some 2000 references and 500 inventions pertinent to oscillating wings, including no less than twenty model or full scale aircraft, some of which are illustrated in his paper. Vasil'yev [7,8] mentions a number of Soviet inventors who often flew their models in competition culminating in All-Union contests in 1950 and 1951. As

an example, Figure 1 presents the elegantly simple propulsion scheme of Miturich. This is a motor whose shaft is parallel to the span and which rotates an unbalanced mass. In reaction to this the airplane oscillates up and down to produce thrust. This idea was recently again forwarded by Wolf [9] and Smith [10] to propel ultra-light man-carrying aircraft, except this time it is the pilot who is the vibrating mass!

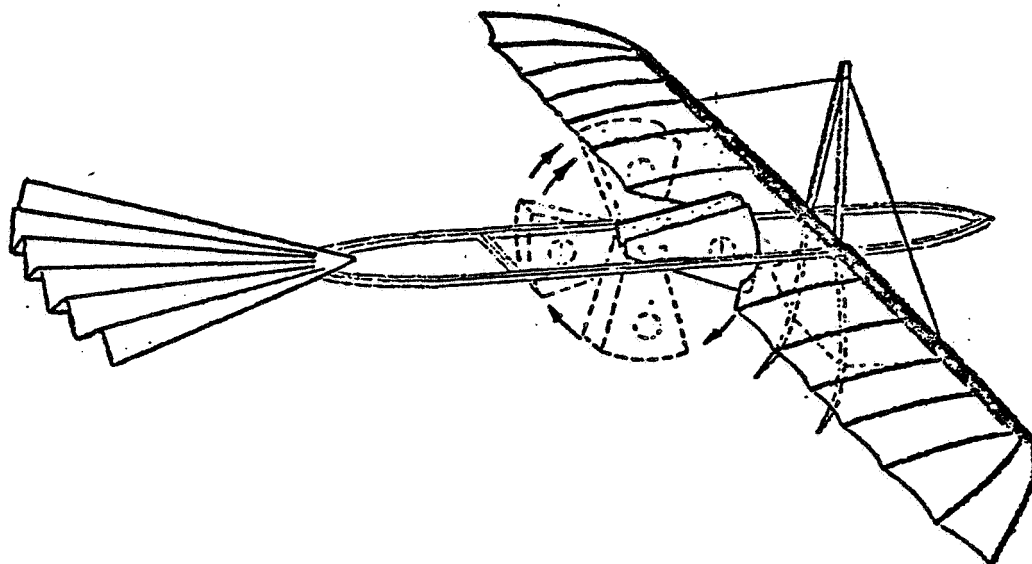


Figure 1: The Model of Miturich Powered by a Rotating Mass.

The meeting of the Experimental Aircraft Association at Oshkosh is the gathering point for present-day inventors interested in ornithopters. Among them are P.H. Spencer of Santa Monica, who has flown gas-driven models. Another is J.L.G. Fitz Patrick of Staten Island Community College who has designed and built several prototypes of piloted ornithopters. These vehicles are intended to test the unique empirical

theory developed by Patrick [11]. This theory is based on much personal observation of flying and swimming creatures, and, in fact, the patented [12] flapping mechanism of the wings is a "bird-bat analog" with the names of the parts taken from bird physiology. A physical description of Patrick's ornithopter is presented in Figure 2. Captive tests have so far met expected thrust levels, but no free flights have been made.

The work of Patrick is typical of the attempts to overcome the severe limitations of aerodynamic theory which has sound mathematical basis, limitations which are often violated in natural flight [13]. This review will next concern itself with the progress that orthodox aerodynamic theory has made in the area of oscillating wing propulsion.

MARK V ORNITHOPTER

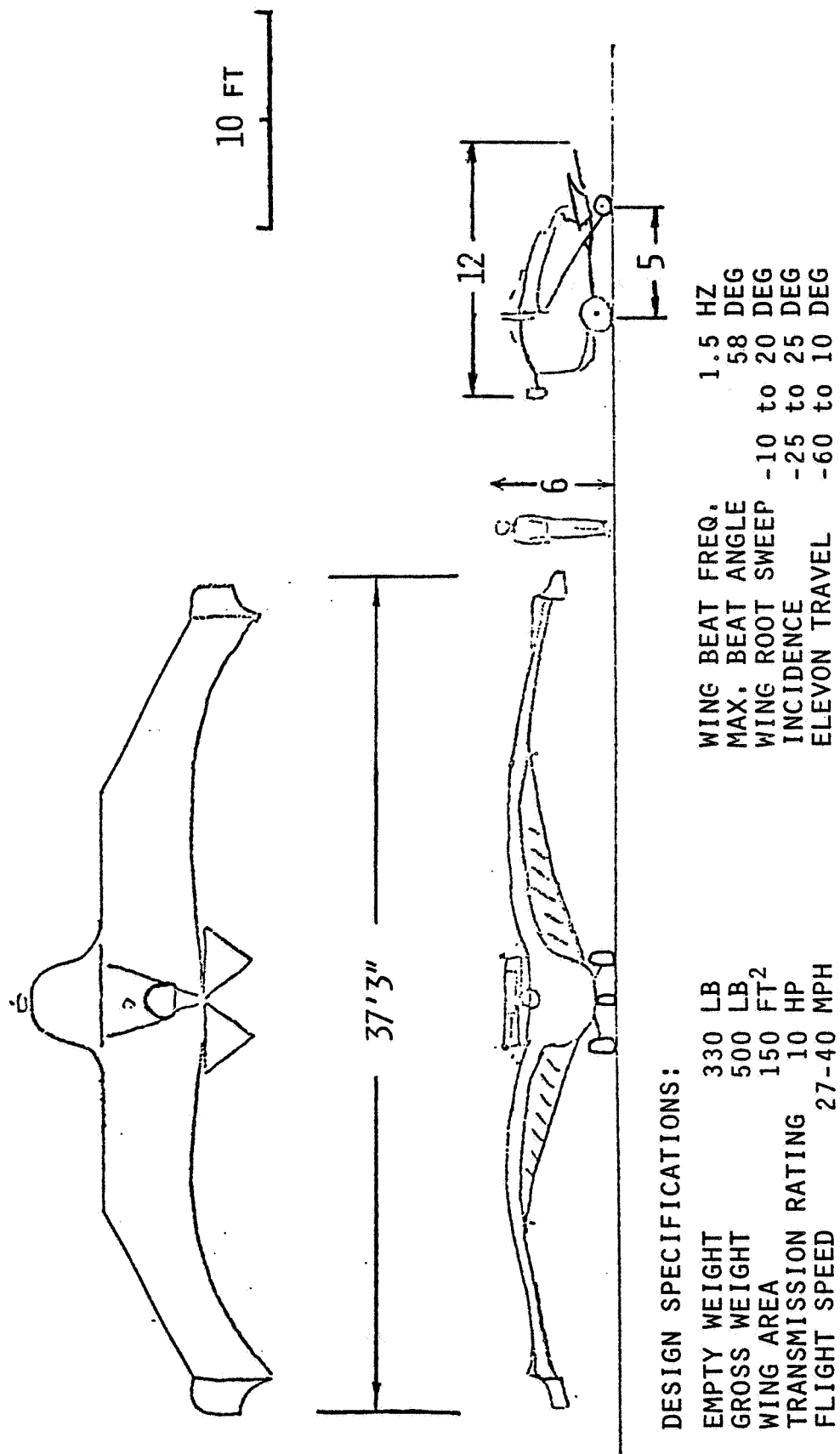


Figure 2: Fitz Patrick's Ornithopter Design.

2.3 THEORY OF TWO-DIMENSIONAL OSCILLATING WINGS

2.3.1 Rigid Airfoils

Consider an airfoil which oscillates transversely in a constant free-stream. The flow is assumed to be describable by a velocity potential and to remain attached to the thin airfoil as it flows from the leading edge to the trailing edge where the Kutta condition is enforced. As shown in Figure 3, the plunge displacement of the airfoil is measured at a point a semichords behind the midchord. Let us define this displacement as the real part of hbe^{ikt} , and the pitch displacement as the real part of αe^{ikt} so that h and α are nondimensional amplitudes, which may be complex to include a phase angle. In complex notation (see Appendix A), the normal force and moment coefficients, as found by Theodorsen [14], are:

$$C_n = \pi(ik\alpha - k^2h + ak^2\alpha) + 2\pi C\{\alpha + ikh + ik(\frac{1}{2} - a)\alpha\} \quad (2.1)$$

$$C_{ma} = \frac{1}{8}\pi\{-k^2ah - ik(\frac{1}{2} - a)\alpha + k^2(\frac{1}{8} + a^2)\alpha\} + \pi(a + \frac{1}{2})C\{ikh + \alpha + ik(\frac{1}{2} - a)\alpha\}. \quad (2.2)$$

Garrick [15] in 1936 found the suction coefficient to be:

$$C_s = \frac{1}{2}\pi[4C^2\{\alpha + ikh + ik(\frac{1}{2} - a)\alpha\}^2 - k^2\alpha^2 - 2ikaC\{\alpha + ikh + ik(\frac{1}{2} - a)\alpha\}]. \quad (2.3)$$

In terms of these coefficients, the thrust coefficient is

$$C_t = C_s - \alpha C_n. \quad (2.4)$$

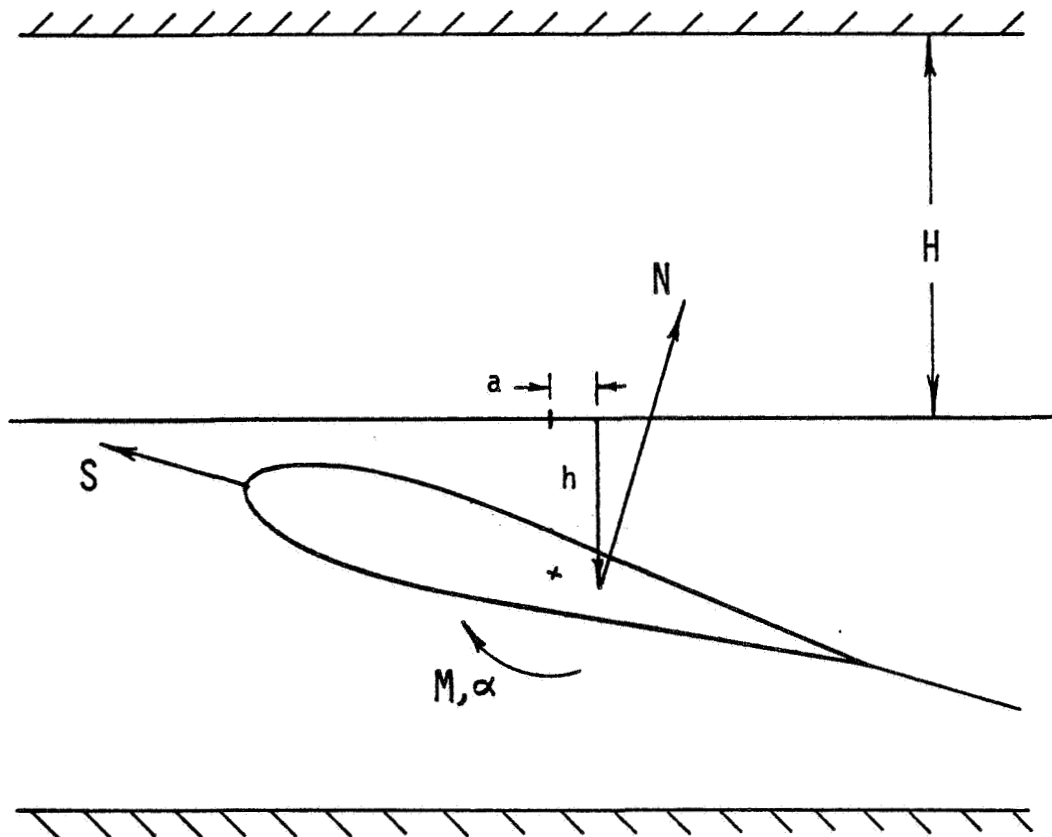


Figure 3: Airfoil Reference System.

To provide a simpler notation that will allow easy comparison with later results, the form of Timman [16] is used. Let:

$$C_n = C_{nh} h + (C_{n\alpha}' - \frac{i}{k} C_{nh}) \alpha \quad (2.5)$$

$$C_m = C_{mh} h + (C_{m\alpha}' - \frac{i}{k} C_{mh}) \alpha \quad (2.6)$$

$$\sqrt{C_s} = \sqrt{C_{sh}} h + (\sqrt{C_{s\alpha}'} - \frac{i}{k} \sqrt{C_{sh}}) \alpha \quad (2.7)$$

where we now measure h and C_m at the midchord, that is, $a=0$.

Comparing (2.1-2.3) with (2.5-2.7) leads to:

$$C_{nh} = -k^2 \pi + ik2\pi C \quad (2.8)$$

$$C_{n\alpha}' = ik\pi C \quad (2.9)$$

$$C_{mh} = ik \frac{\pi}{2} C \quad (2.10)$$

$$C_{m\alpha}' = k^2 \frac{\pi}{16} - ik \frac{\pi}{4} (1-C) \quad (2.11)$$

$$\sqrt{C_{sh}} = \frac{1}{\sqrt{2\pi}} ik 2\pi C \quad (2.12)$$

$$\sqrt{C_{s\alpha}'} = \frac{1}{\sqrt{2\pi}} ik \pi (C-1). \quad (2.13)$$

The major point to note is that the thrust is dependent on the square of the motion amplitudes. If the ratio α/h is kept constant then doubling the flapping amplitude at fixed frequency will quadruple the

thrust. By originating the term thrust loading, $(C_{t0}/\pi h^2)$, Wu [17] introduces a measure of the thrust which is independent of amplitude. This quadratic behavior results in a mean thrust when the instantaneous thrust is averaged over each cycle. The average thrust is

$$C_{t0} = \frac{1}{2} \text{Re} \left\{ \sqrt{C_s} \sqrt{C_s^*} - C_n \alpha^* \right\}. \quad (2.14)$$

(The star indicates the conjugate.)

The average non-dimensional power required to drive the oscillation is

$$C_{w0} = \text{Re} \left\{ \frac{ik}{2} (C_n^* h - C_m^* \alpha) \right\}. \quad (2.15)$$

We can relate the efficiency of thrust production as

$$\eta = C_{t0}/C_{w0}, \quad (2.16)$$

which is independent of amplitude and meaningful only for a positive thrust.

To include the effect of mean angle of attack one superposes the solution,

$$\sqrt{C_{s\text{mean}}} = \sqrt{2\pi} \alpha_0 \quad (2.17)$$

to (2.7). The suction will then be

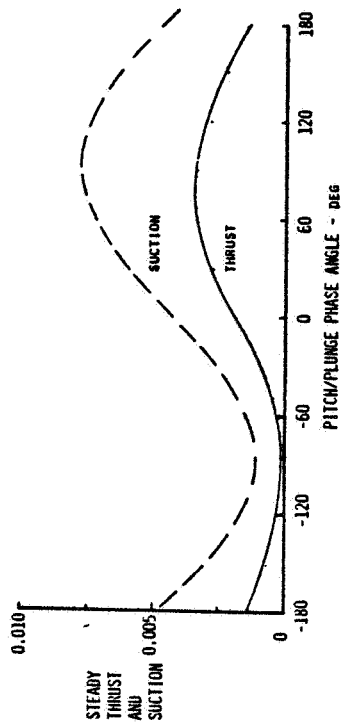
$$\begin{aligned}
C_s &= \left[\sqrt{C_{sosc}} e^{ikt} + \sqrt{C_{smean}} \right]^2 \\
&= \frac{1}{2} \sqrt{C_{sosc}} \sqrt{C_{sosc}^*} + \frac{1}{2} C_{sosc} e^{2ikt} \\
&\quad + 2 \sqrt{C_{sosc}} \sqrt{C_{smean}} e^{ikt} + C_{smean}
\end{aligned}
\tag{2.18}$$

where the time dependence has been included in (2.18) to indicate that a mean angle of attack leaves the second harmonic suction unchanged, while adding a mean suction. The mean drag is unaltered because the added mean suction is cancelled out by the mean drag component of the normal force. An important consequence of a mean angle of attack is the first harmonic term, which is a coupling between the unsteady and steady forces. Lift and pitching moments due to a steady angle of attack are added to the oscillatory forces due to airfoil motion.

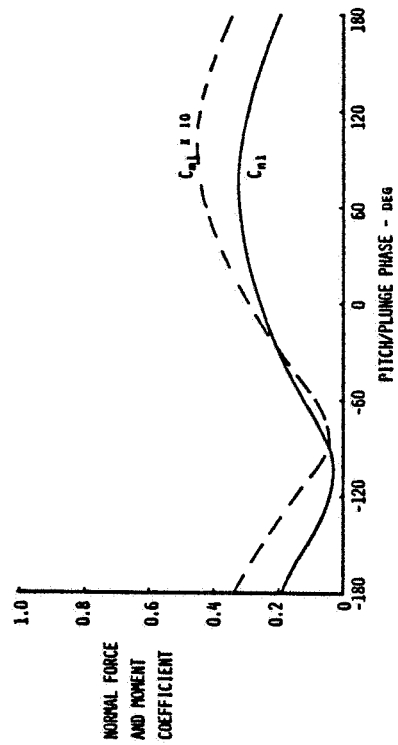
Garrick and others have provided values of the average thrust during heaving and pitching. But some of the interesting and necessary quantities from a design standpoint are the amplitudes of the oscillatory forces. Figure 4 shows values of mean thrust and suction (Fig. 4a), normal force and moment amplitudes (Fig. 4b), normal force and moment phase angles (Fig. 4c), suction and thrust amplitudes (Fig. 4d), second harmonic suction and thrust phase angles (Fig. 4e) and finally the efficiency (Fig. 4f) for an airfoil heaving 0.108 semichords and pitching 2 degrees as measured at -0.30 b. The reduced frequency is 0.395. The horizontal axis in all the figures is the phase angle by which pitching leads heaving. For a wing with a 24 cm chord at a flight velocity of, say, 14 m/s these parameters correspond to a flapping amplitude of 1.3

cm at a frequency of 7.5 Hz. The maximum thrust produced is 0.09 N per meter of span. For the experimental wing of Chapter IV this is only 0.04 N. Under less than maximum conditions the thrust is much less.

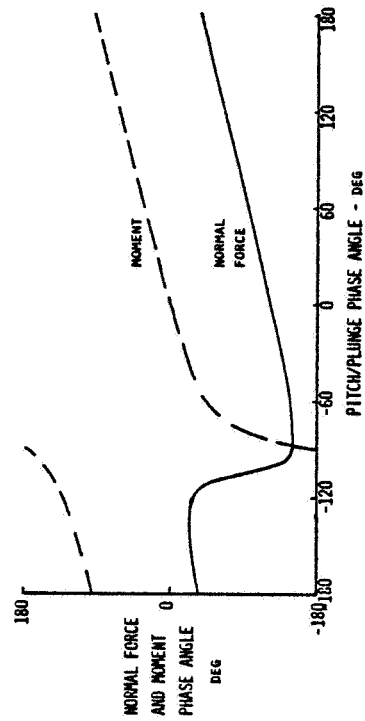
$h = 0.108$
 $\alpha = 2 \text{ deg}$
 $k = 0.395$
 $a = -0.3$



(a)



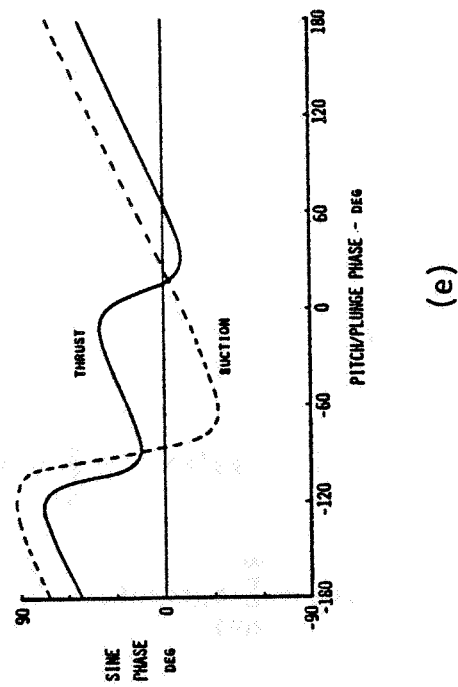
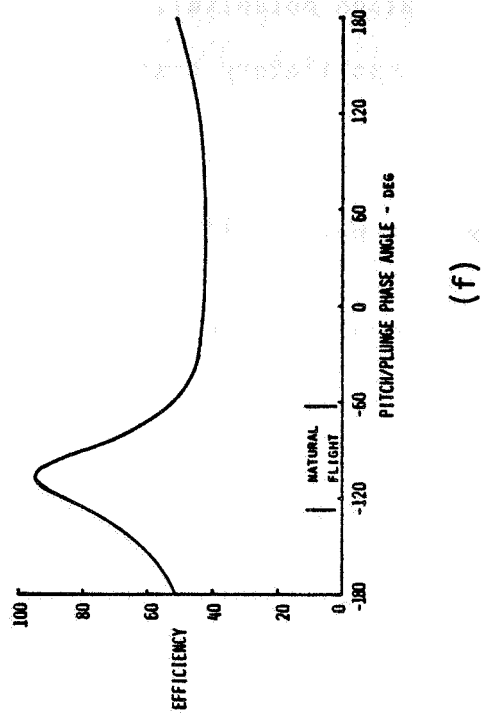
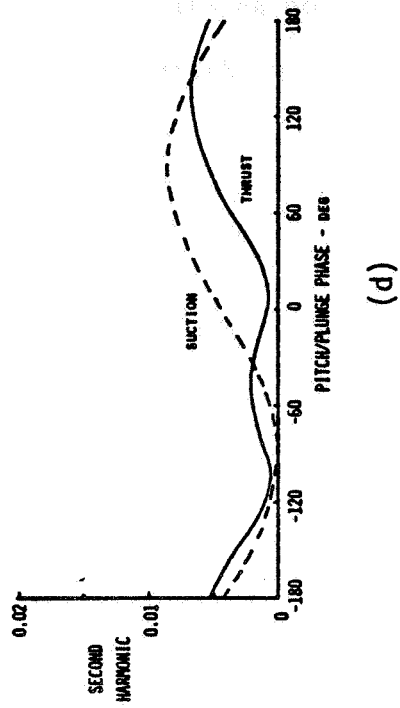
(b)



(c)

Figure 4: Airloads on an Airfoil Oscillating in Free Air.

$h = 0.108$
 $\alpha = 2 \text{ deg}$
 $k = 0.395$
 $a = -0.3$



Airloads on an Airfoil Oscillating in Free Air

2.3.2 Flexible Airfoils

Wu [18] went beyond Garrick and allowed oscillatory camber. Wu uses the acceleration potential, f , to find the forces on an airfoil undergoing general oscillatory transverse motion. Let the displacement of the airfoil be

$$h(x,t) = h_1(x) e^{ikt}. \quad (2.19)$$

The Fourier expansions of the displacement and the slope are:

$$h_1(x) = \frac{1}{2}\beta_0 + \sum_{n=1}^{\infty} \beta_n \cos n\theta \quad (2.20)$$

$$\frac{\partial h_1}{\partial x} = \frac{1}{2}\gamma_0 + \sum_{n=1}^{\infty} \gamma_n \cos n\theta \quad (2.21)$$

where $x = \cos\theta$.

Thus, for tangent flow the velocity of the fluid normal to the chord is

$$v_n(x,t) = -U[\frac{1}{2}\lambda_0 + \sum_{n=1}^{\infty} \lambda_n \cos n\theta] \quad (2.22)$$

$$\text{where } \lambda_n = -(\gamma_n + ik\beta_n). \quad (2.23)$$

Now on the airfoil the real and imaginary components of the acceleration potential are:

$$\Delta C_p = \text{Re}\{f\} = \frac{1}{2}a_0 \tan \frac{1}{2}\theta + \sum_{n=1}^{\infty} a_n \sin n\theta \quad (2.24)$$

$$\text{Im}\{f\} = \frac{1}{2}a_0 + \sum_{n=1}^{\infty} a_n \cos n\theta. \quad (2.25)$$

Relating the acceleration potential and the normalwash through the linearized Bernoulli equation leads to:

$$a_0 = (\lambda_0 + \lambda_1) C(k) - \lambda_1 \quad (2.26)$$

$$a_n = \lambda_n + ik \frac{\lambda_{n-1} - \lambda_{n+1}}{2n}. \quad (2.27)$$

Integrating the pressure over the airfoil produces the normal force and moment:

$$C_n = 2\pi(a_0 + a_1) \quad (2.28)$$

$$C_m = \frac{1}{2}\pi(a_0 - a_2). \quad (2.29)$$

The leading-edge suction is

$$\sqrt{C_s} = i\sqrt{\pi} a_0. \quad (2.30)$$

Finally, the thrust, including the leading-edge suction, is

$$C_t = \frac{\pi}{4} \left[a_0^2 + a_0(\gamma_0 - \gamma_1) - \gamma_0\gamma_1 + k^2(\beta_0\beta_1) - ik \sum_{n=1}^{\infty} n\beta_n^2 \right]. \quad (2.31)$$

The instantaneous power to drive the motion is

$$W = - \int_{-1}^1 \text{Re}\{\Delta p\} \text{Re} \left\{ U \frac{\partial h}{\partial t} \right\} dx. \quad (2.32)$$

To calculate the efficiency, we need only the average power coefficient, which is

$$\begin{aligned}
C_{M0} &= -\frac{1}{2} \int_{-1}^1 \operatorname{Re} \left\{ -ikh^* \Delta C_p \right\} dx \\
&= \frac{1}{2} \operatorname{Re} \int_0^\pi ik \left[\frac{1}{2} \beta_0^* + \sum_{n=1}^{\infty} \beta_n^* \cos n\theta \right] \left[\frac{1}{2} a_0 \tan \frac{1}{2} \theta + \sum_{n=1}^{\infty} a_n \sin n\theta \right] \sin \theta d\theta. \quad (2.33)
\end{aligned}$$

Performing the integration leaves

$$C_{M0} = \frac{\pi k}{4} \operatorname{Re} \left\{ -i \beta_0^* (a_0 + a_1) + \sum_{n=1}^{\infty} \beta_n^* (-a_{n-1} + a_{n+1}) \right\}. \quad (2.34)$$

The efficiency is again expressed by (2.16). The implications of a steady angle of attack or camber on drag are the same as those discussed under rigid airfoils. Mean lift and moment is produced only by steady angle of attack or camber.

McCroskey [19], while not stating the forces explicitly, contributes by clearly expressing the pressure distribution on an airfoil in unsteady motion.

2.3.3 Experimental Validation

A number of experiments on oscillating airfoils have been reported (see the bibliography to Ref. 20). The majority have been designed to measure the oscillatory lift and moment, and only recent experiments have been devoted to measuring the thrust [21-31]. A relatively extensive set of lift and moment measurements was made by Halfman [32]. His results indicate good agreement with theory except for a decrease in

amplitude at low reduced frequency typical of static measurements of lift. This discrepancy is attributed to the lack of thickness and boundary-layer effects in the model.

The oscillatory drag of an airfoil has been measured in connection with the dynamic stall of helicopter blades, for example by Philippe and Sagner [21]. Favier et. al. [22, 23] report sketchy results for an airfoil at large mean angle of attack and performing oscillatory translation at an arbitrary angle to the freestream. Kunz [24] used a stationary airfoil and a fluctuating free stream. Hien [25] measured the drag of an airfoil undergoing large amplitude pitching typical of a vertical axis wind turbine.

The thrust of a plunging and pitching airfoil has been measured by Scherer [26] and Obye [27], who validated Garrick's theory in the wind tunnel at low reduced frequency ($k < 0.1$) and large amplitude, Figure 5. Siekmann [28] and Kelly [29] also present some data, including tests with oscillatory camber, for a thin plate in a water tunnel. Archer et. al. [30] and Fejtek and Nehera [31] have measured the thrust of a finite flapping wing.

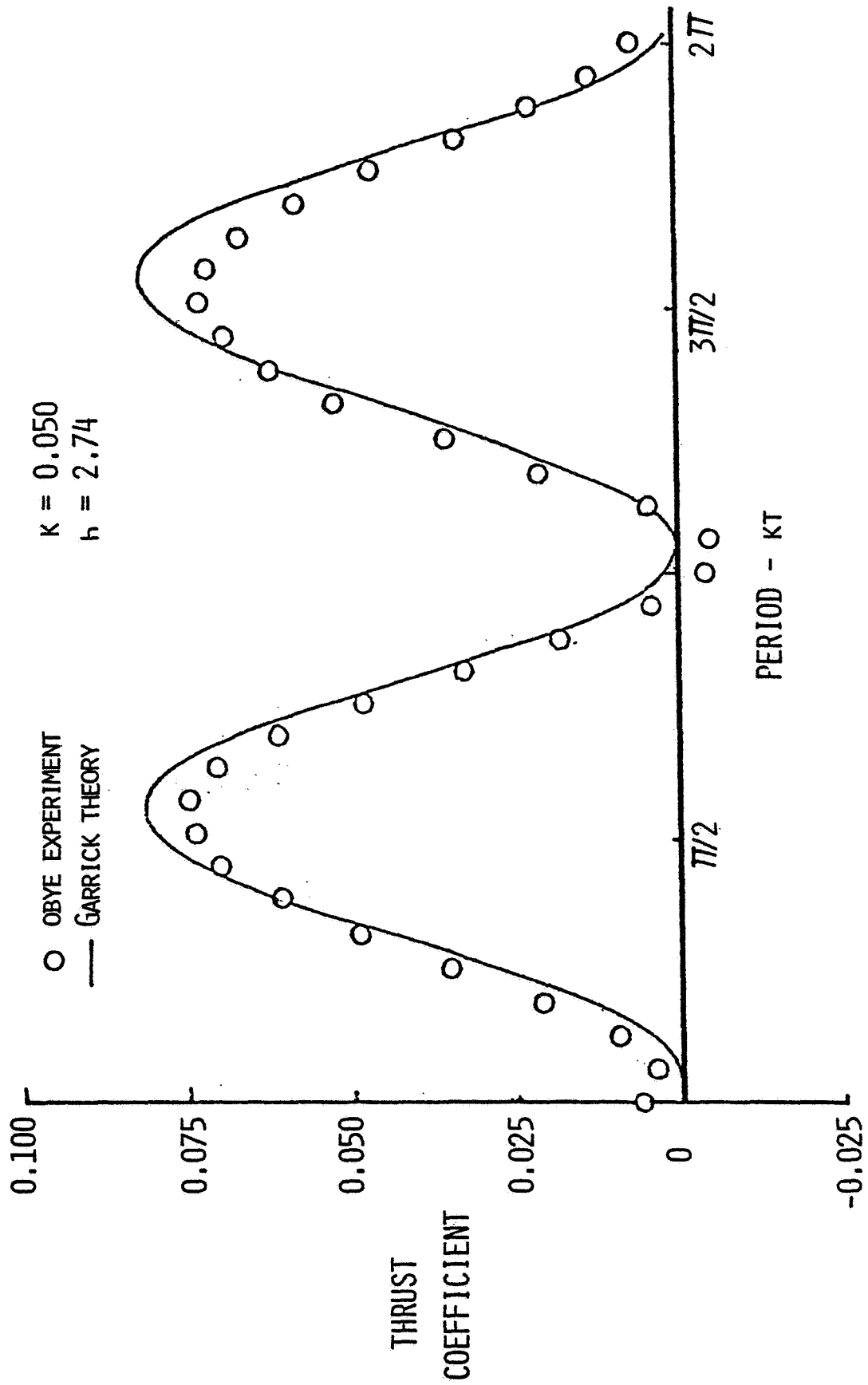


Figure 5: Comparison of Results of Obye and Theory of Garrick.

2.3.4 Application to Propulsion in Natural Flight

The theory of oscillating wings applies directly to the forward flight of birds [33] and insects [34]. It is also appropriate for the carangiform mode of propulsion of fish with lunate tails, which is characterized by large amplitude tail motion but the body forming less than one-half a sine wave, (see Ref. 35). Under these conditions, surging is minimal and the theory of Garrick or Wu is appropriate. In animal propulsion it is observed that α lags h by approximately 90 degrees, which tends to minimize the instantaneous angle of attack. (Lighthill [4] finds it convenient to assume this phase angle implicitly and make slight adjustments by altering the pitch axis position. He also introduces the feathering parameter $\theta = \alpha/hk$). At this phase angle the thrust loading is near minimum, but birds and fish rightly prefer to flap their wings and tails with this phase angle because the efficiency is markedly higher in this region (Fig. 4f). In fact, it is near 95 percent. To compensate for the relatively small thrust loading, animals operate with large amplitudes. Further, you will note that the leading-edge suction is a minimum in the natural flight region (Fig. 4d). As Lighthill [36] observes, it is doubtful that the values of suction predicted by Garrick or Wu are obtained. Thus, propulsive motion depending mostly on leading-edge suction will deviate the most from theory.

During our study, Wu's analysis was coded to provide quantitative predictions of thrust and lift. When bird flight was simulated by adding oscillatory camber, Figure 6, to an airfoil operating in the

EFFECT OF CAMBER



$$\kappa = 0.395$$

	WITHOUT CAMBER	WITH CAMBER
C_{T0} :	0.0077	0.0113
η :	86.7%	85.3%
β_0 :	0.894 i0.0	0.894 i0.0
β_1 :	0.0 -i0.145	0.0 -i0.145
β_2 :	0.0 i0.0	0.0 i0.010
β_3 :	0.0 i0.0	0.0 i0.002

Figure 6: Effect of Oscillatory Camber on the Propulsion of a Thin Airfoil.

natural flight region, it was noted that the mean thrust could be significantly affected. Small amounts of camber can increase the thrust by 50 percent while maintaining the same efficiency. Also, the leading-edge suction is almost eliminated, further suggesting the desirability of camber. Alternatively, the efficiency could be raised, but only slightly since it is very close to 100 percent. Additionally, it was recognized that oscillatory camber could be used to tailor the pressure distribution of the airfoil to prevent separation under certain operating conditions, although this has not been validated.

2.3.5 Surge Motion

James [37] has looked at yet another motion employed in natural flight - surging, the motion of an airfoil parallel to the freestream. While not including the interesting case of a pitching airfoil, he does show that surging and flapping increase the mean lift of an airfoil at constant angle of attack. Although the efficiency of thrust production is below 80 percent, this is offset by the fact that, since mean lift is increased, some of the power calculated to produce thrust is being used to sustain flight. Thus, comparing efficiencies to those of Garrick or Wu is pessimistic, because those motions do not affect average lift.

2.3.6 Effect of Amplitude

As was noted in describing Garrick's theory, derived assuming small oscillations, the thrust is dependent on the square of the amplitude. The obvious question is then what happens as the oscillation grows in

amplitude? Chopra [38] calculated the thrust of an aspect ratio 8 wing oscillating with flapping amplitudes of 2, 3, and 4 semichords and pitching about its trailing edge such that $\theta(=\tan\alpha/hk)=0.6$. After replotting his figure to keep the pitch/plunge ratio, α/h , constant, we produce Figure 7. This indicates that the thrust loading increases very slightly with amplitude. Of course, a linearly flapping wing where the amplitude is greatest at the tip may show more losses at higher amplitudes.

At large amplitudes, the flapping velocity begins to contribute appreciably to the dynamic pressure and wake curvature is significant; then the parameter $k_z=kh$ becomes important in describing the flow as noted by Oshima [39]. Katz and Weihs [40] have also studied large-amplitude motion. Unfortunately, they state no conclusion as to whether including large amplitude effects increases or decreases the quadratic trend. Lorell and Bennett [41] found an analytic expression for the lift in large amplitude motion. Depending on the phase between pitching, plunging and surging, the oscillatory lift can either be substantially increased or reduced.

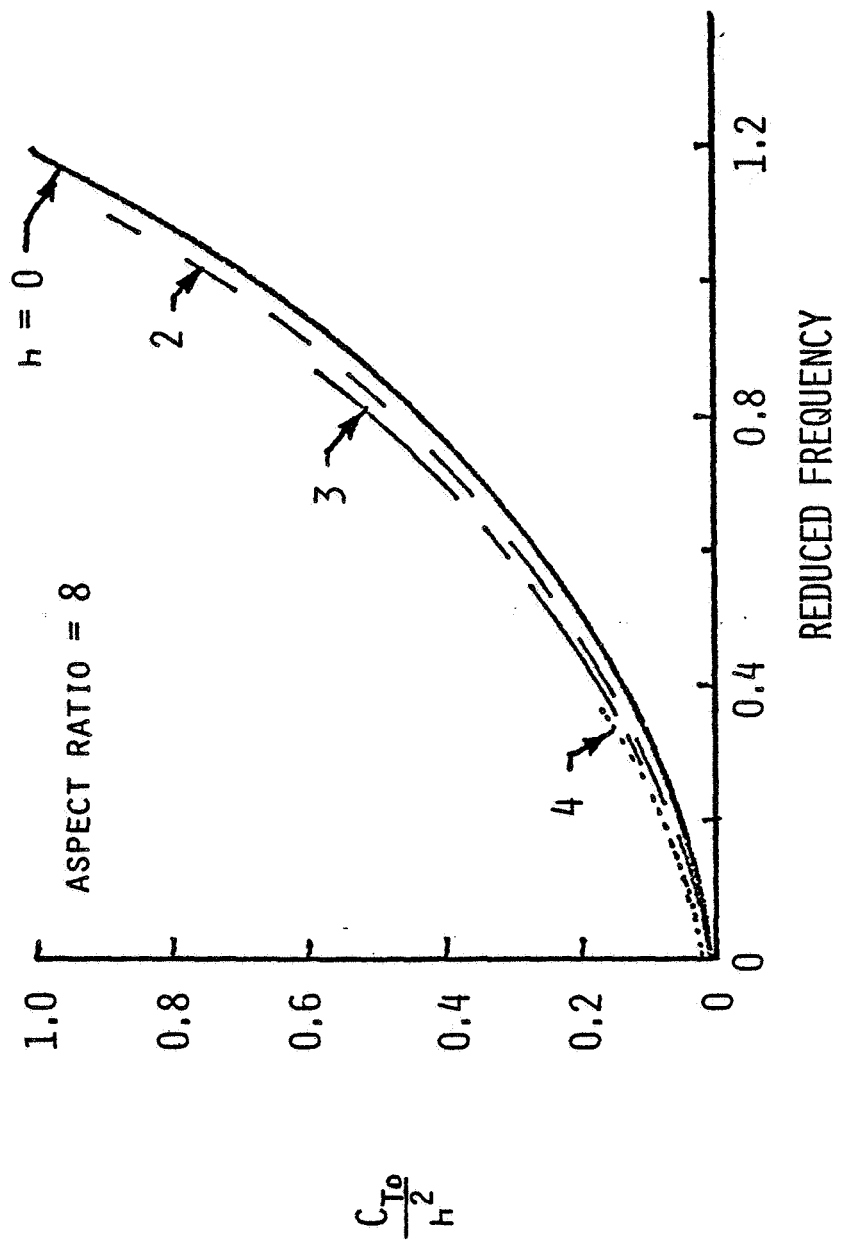


Figure 7: The Effect of Amplitude on Mean Thrust.

2.3.7 Optimization

Wu [17] has studied the optimum motion of airfoils and slender bodies. For the two-dimensional rigid airfoil which is flapping and pitching, Wu finds the motion which gives the maximum efficiency for a given thrust loading, $C_{t0}/\pi h^2$, Figure 8. For frequencies below $k=1.781$, there is a maximum thrust loading, see Figure 9. Above this frequency, it is possible to produce thrust without flapping; the thrust loading is limited only by pitch amplitude.

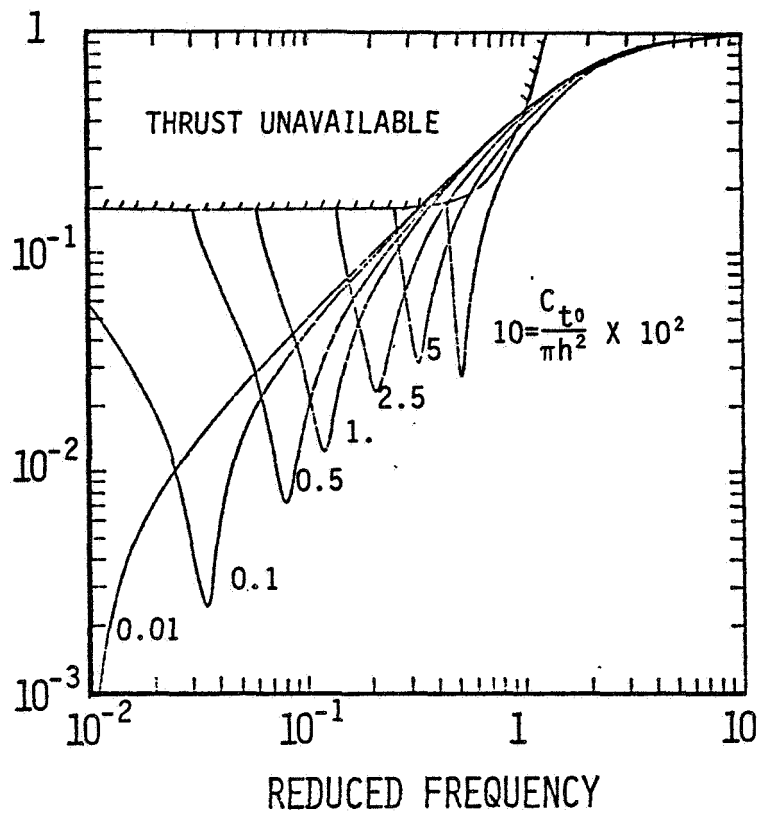
Wu concludes in Reference 17 by saying that, for the rigid airfoil in particular, one can approach arbitrarily close to unit efficiency as the thrust loading goes to zero. For the case of general motion, there is an infinite set of motions which will allow this.

It is interesting that for k less than approximately 1, which is of greatest interest in natural flight, one can make a very simple link between the thrust loading and optimum efficiency. At any frequency below $k=1$, a plot of the thrust loading as a function of efficiency turns out to be a parabola, Figure 10. The form is

$$\frac{C_{t0}}{\pi h^2} = \left[1 - (1-2\eta)^2 \right] \left(\frac{C_{t0}}{\pi h^2} \right)_{\max}, \quad (2.35)$$

where $(C_{t0}/\pi h^2)_{\max}$ is given in Figure 9.

PITCH/PLUNGE RATIO
 $\frac{\text{RADIANS}}{4 \text{ CHORD}}$



PITCH/PLUNGE PHASE
 DEGREES

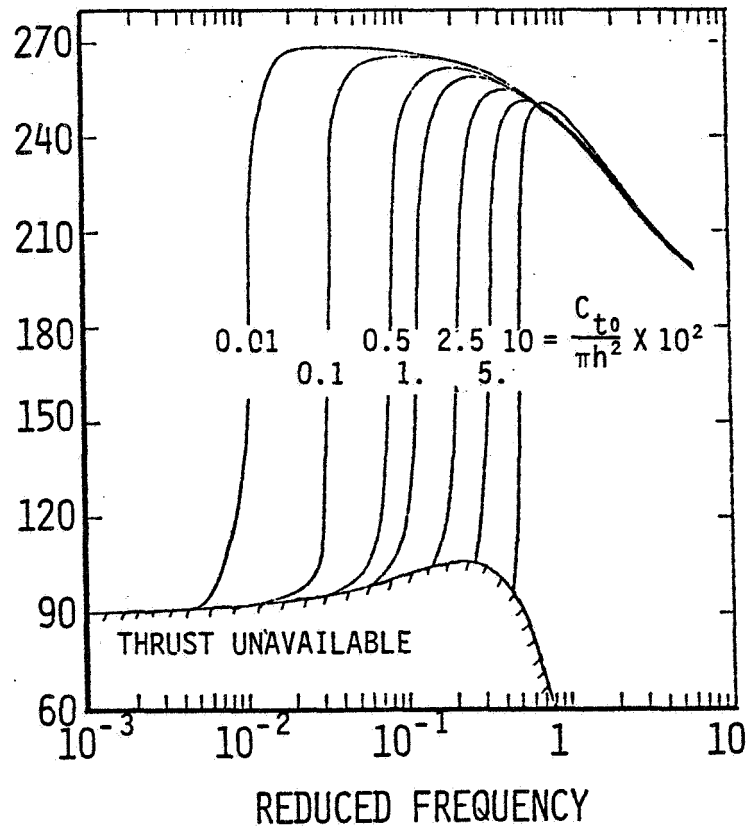


Figure 8: Optimal Motion of a 2-D Airfoil for Propulsion from Wu [17].

MAXIMUM MEAN THRUST

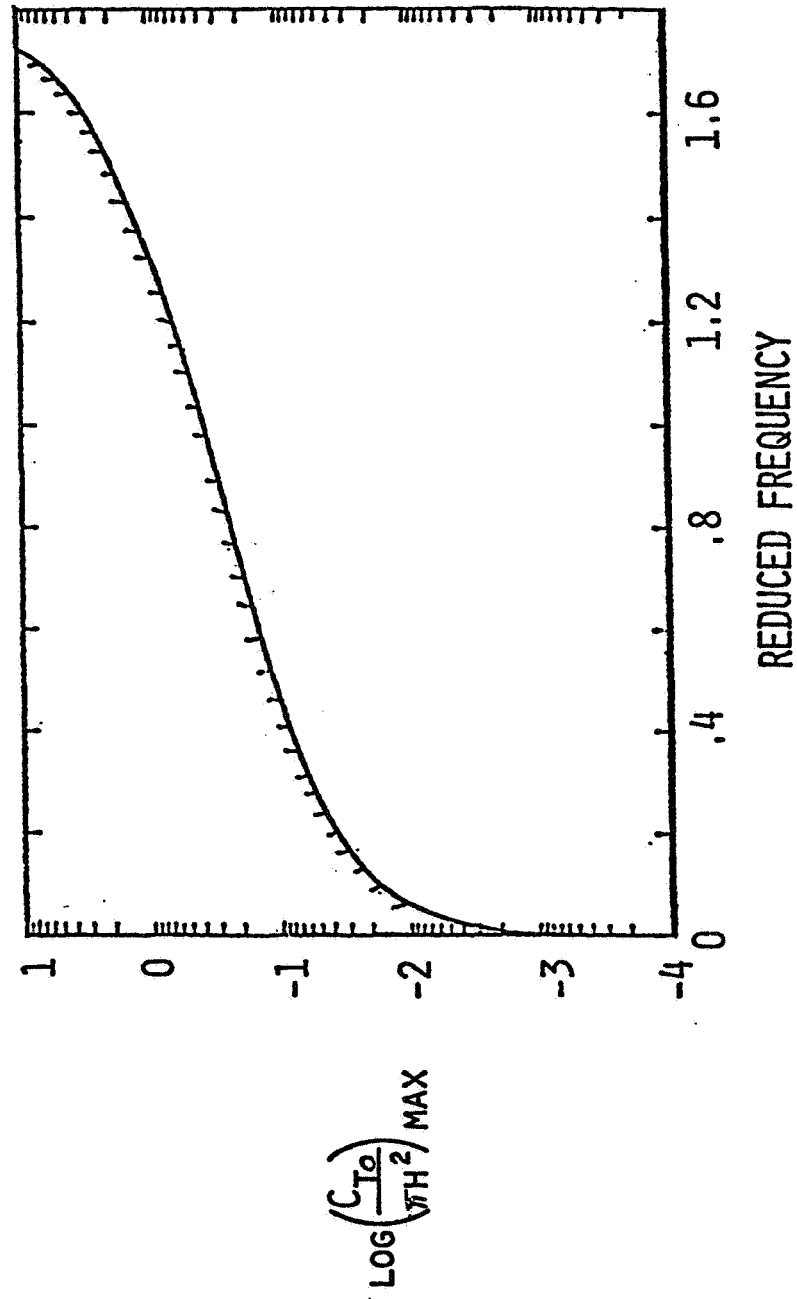


Figure 9: Maximum Thrust of a 2-D Airfoil from Wu [17].

OPTIMAL THRUST vs. EFFICIENCY

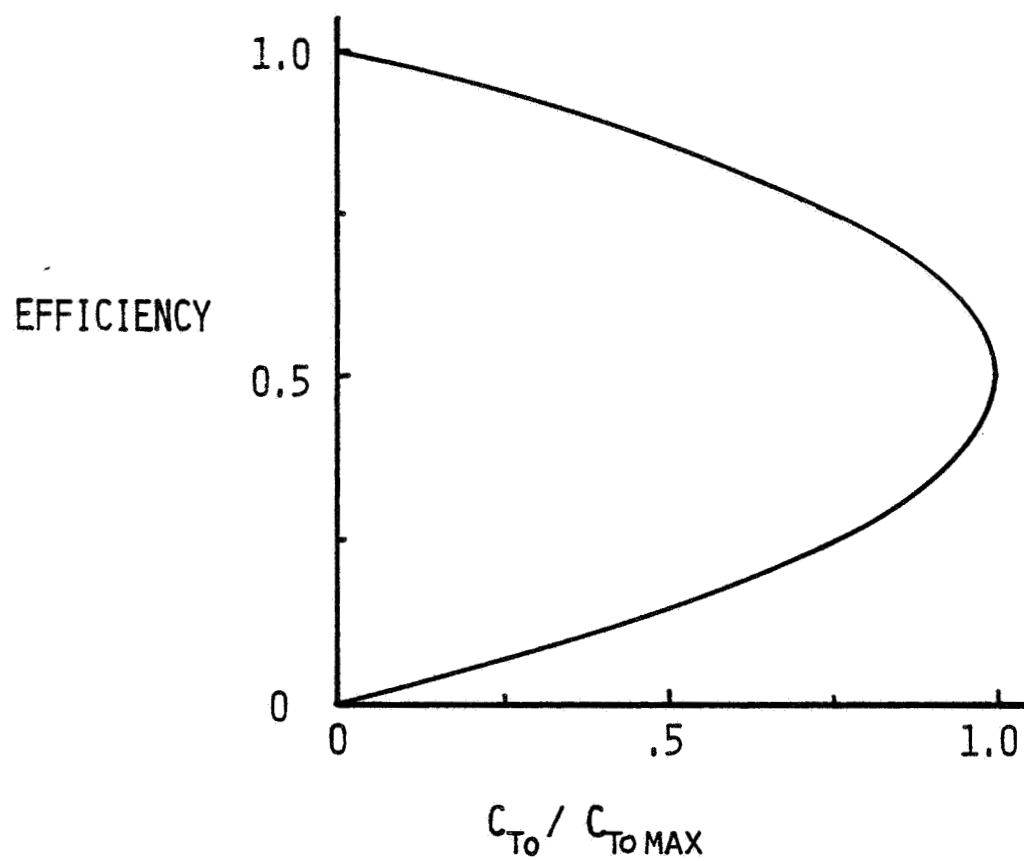


Figure 10: Low-Frequency Relationship between Efficiency and Thrust of a 2-D Airfoil.

This form can be derived starting with Wu's equations for the optimum efficiency as a function of reduced frequency and the minimum reduced frequency (k_c) at which a given thrust loading is possible:

$$\eta_{\max} = \frac{1}{2} \left[1 - \frac{k}{2\pi} \ln \frac{2}{\gamma k} + \left(\frac{k-k_c}{k} \right)^{\frac{1}{2}} \left(1 - \frac{\pi+4}{4} k \ln \frac{2}{\gamma k} \right) \right] \quad (2.36)$$

$$k_c = 2\pi \frac{C_{to}}{\pi h^2} \left[1 + \frac{C_{to}}{\pi h^2} \left[\left(2 - \frac{1}{\pi} \right) \ln \frac{2h^2}{\gamma C_{to}} + \frac{\pi}{2} \right] \right] \quad (2.37)$$

(γ is Euler's constant, 1.781...)

So for small k :

$$\eta_{\max} = \frac{1}{2} \left(1 + \left(\frac{k-k_c}{k} \right)^{\frac{1}{2}} \right) \quad (2.38)$$

$$k_c = 2\pi \frac{C_{to}}{\pi h^2} \quad (2.39)$$

We may interchange dependent and independent variables and write

$$\left(\frac{C_{to}}{\pi h^2} \right)_{\max} = \frac{k}{2\pi} \quad (2.40)$$

So

$$\eta_{\max} = \frac{1}{2} \left(1 + \left[1 - \frac{C_{to}/\pi h^2}{(C_{to}/\pi h^2)_{\max}} \right]^{\frac{1}{2}} \right), \quad (2.41)$$

from which the final form is apparent. Interestingly, according to Wu the lower bound is the minimum efficiency at which a given thrust can be produced. This type of curve appears to apply to three-dimensional

wings, see Ref. 42 or Ref. 43, provided the maximum loading coefficient is adjusted accordingly. Figure 10 permits a very rapid estimation of the maximum thrust available and efficiency if one knows the operating frequency and amplitude.

2.3.8 Thickness and Profile Shape

Woods [44] is one of the few investigators to explicitly derive the drag of a thick oscillating airfoil from an analytic theory. Unfortunately, he neglects all second-order quantities, thus throwing away the mean and second harmonic drag. He is left with only the added mass due to surging. Since his approach is so general, including surging as well as thickness, plunging and pitching, retracing his steps appears as a promising research topic. Of course, since he uses a potential theory, it does not include boundary-layer drag.

No known numerical studies of unsteady drag versus profile shape have been done. However, many airfoil shapes found in nature have been examined in the course of physiology. For examples, see References 45 and 46. The thin wing sections of birds are probably a consequence of their low Reynolds number flight and requirement for minimum weight. Only in some very large or fast swimming fish do we find appreciable thickness. This thickness may be required for reasons of strength and from the dependence of carangiform propulsion on leading-edge suction, for which a rounded leading edge which resists boundary-layer separation is necessary.

2.3.9 Viscous Drag

Kottapalli and Pierce [47] and Archer et.al. [30] have attempted to include the effect of profile drag in calculating the thrust. Kottapalli used a finite-difference boundary-layer calculation imbedded in a thin-airfoil potential solution with thickness corrections. Besides finding that the viscous drag of an airfoil is markedly changed while the airfoil oscillates, they also conclude that the phase relationship between flapping and pitching is important. They also state that the oscillatory drag varied linearly with amplitude.

Archer used a quasi-steady drag theory to show that linearly flapping wings produce no net thrust if the maximum tip flapping velocity is less than approximately one third the forward flight speed. Although Kottapalli describes Archer's theory as inadequate, this conclusion would indicate that very high angular velocities are required for fast forward flight.

2.3.10 Leading-edge Suction Restraints

An often-mentioned restriction on the thrust of oscillating airfoils is leading-edge separation, or equivalently, the maximum possible leading-edge suction. A crude estimate of this is obtained by using the static stall value for the airfoil. A more accurate calculation of this limit is facilitated by Beddoes' [48] leading-edge velocity criterion for dynamic stall. This is a simple criterion which can be calculated from unsteady potential flow. The peak velocity at the leading edge and

the 'idealized adverse gradient parameter' are compared against a locus of maximum peak velocity and pressure gradient found experimentally by Evans and Mort [49]. Although limited to Mach numbers below 0.3, Beddoes finds good agreement for the onset of dynamic stall is obtained under a wide range of conditions. The quantitative effect on drag of dynamic stall is of intense interest to helicopter research [21-23].

2.4 THREE-DIMENSIONAL EFFECTS

The effects of three-dimensional aerodynamics are, for convenience, grouped under three categories: Aspect Ratio, Non-uniform Motion and Planform Effects.

Chopra [38,50] has done extensive work on the propulsion of wings with aspect ratios of 4, 6 and 8. He has found that the thrust and efficiency decrease, compared to two-dimensional flow, with decreasing aspect ratio. The difference is not extreme, and the dependence of these quantities on the reduced frequency and phase angle is nearly the same as for 2-D flow. To corroborate these conclusions, RHQIV, the very accurate lifting surface code of Rowe et al. [51], was obtained from the Boeing Commercial Airplane Company. Rectangular wings with aspect ratios of 3, 10 and 25 were analyzed for thrust while in pure plunging motion. The results, presented in Figure 11, show that an aspect ratio 10 wing produces at least 80 percent of the thrust of an infinite aspect-ratio wing. Just as important, to the experimental results in Chapter IV, is that the phase shift of the unsteady thrust, compared to 2-D values, is less than 5 degrees for the same wing.

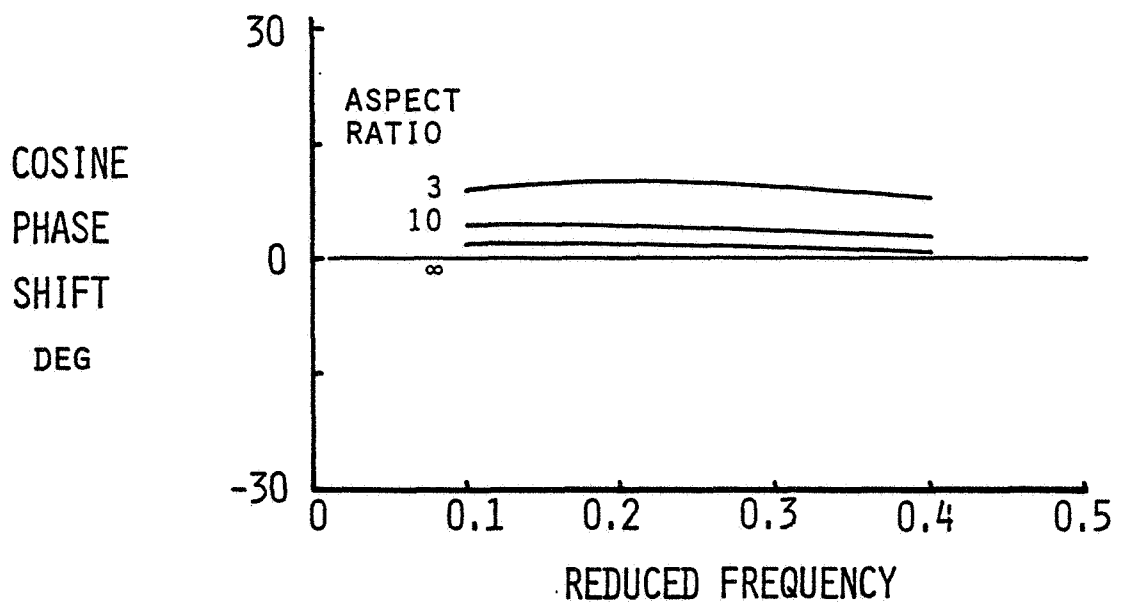
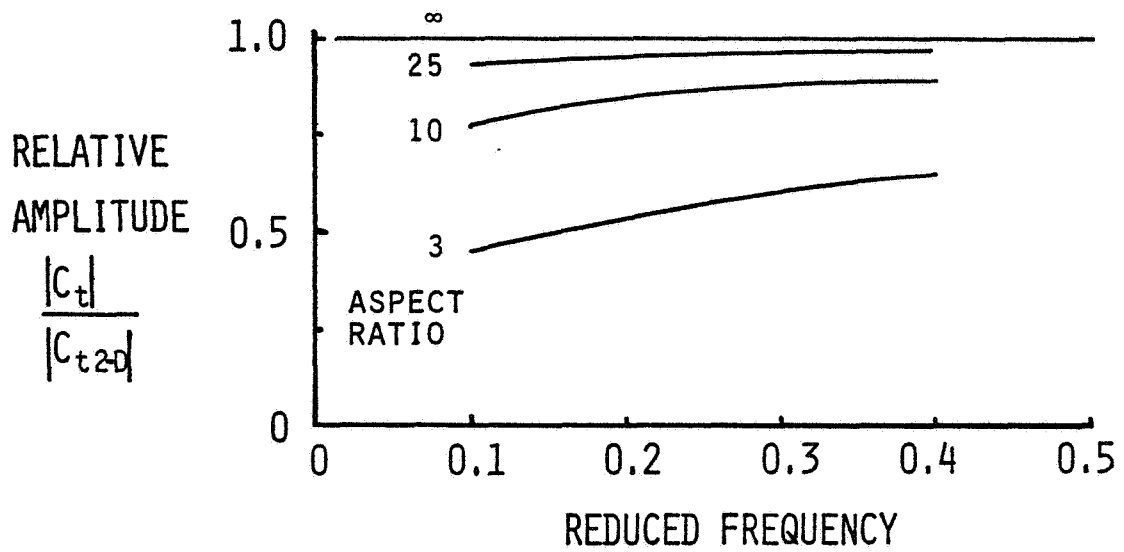


Figure 11: Effect of Aspect Ratio on Oscillatory Thrust predicted by RHOIV.

Tuck [52] studied the thrust and efficiency of infinite aspect-ratio, plunging wings with spanwise variations in the motion. As shown in Figure 12, the most efficient mode of propulsion for a plunging wing has a constant amplitude along the span. This would indicate that the carangiform motion of a fish tail has an inherent advantage over the linear flapping of a bird's wing. This fact also tends to rule out propulsion by exciting any of the higher elastic modes of a wing.

Chopra and Kambe [53] and Bennett [54] have analyzed wings of different planforms in an attempt to find a preferred shape. Chopra was interested in constant-amplitude flapping and pitching, i.e. carangiform motion, while Bennett looked at linear variations of amplitude (birds). Chopra finds that small amounts of sweepback increase the efficiency and decrease the dependence upon leading-edge suction. Untapered wings can also produce more thrust at a given frequency. Bennett found that elliptic planforms are preferred for bird flight, although this conclusion has been modified somewhat by Jones [43]. Lan [55] finds that the efficiency of a rectangular planform is much more sensitive to phase variations than a swept wing.

Jones [43] has found the optimum loading for a linearly flapping wing. The circulation as a function of span distance, Z , is:

$$\Gamma = \frac{4}{\pi} \omega_i \left[\sqrt{1 - (Z/s)^2} + (Z/s)^2 \cosh^{-1}(s/|Z|) \right] \quad (2.42)$$

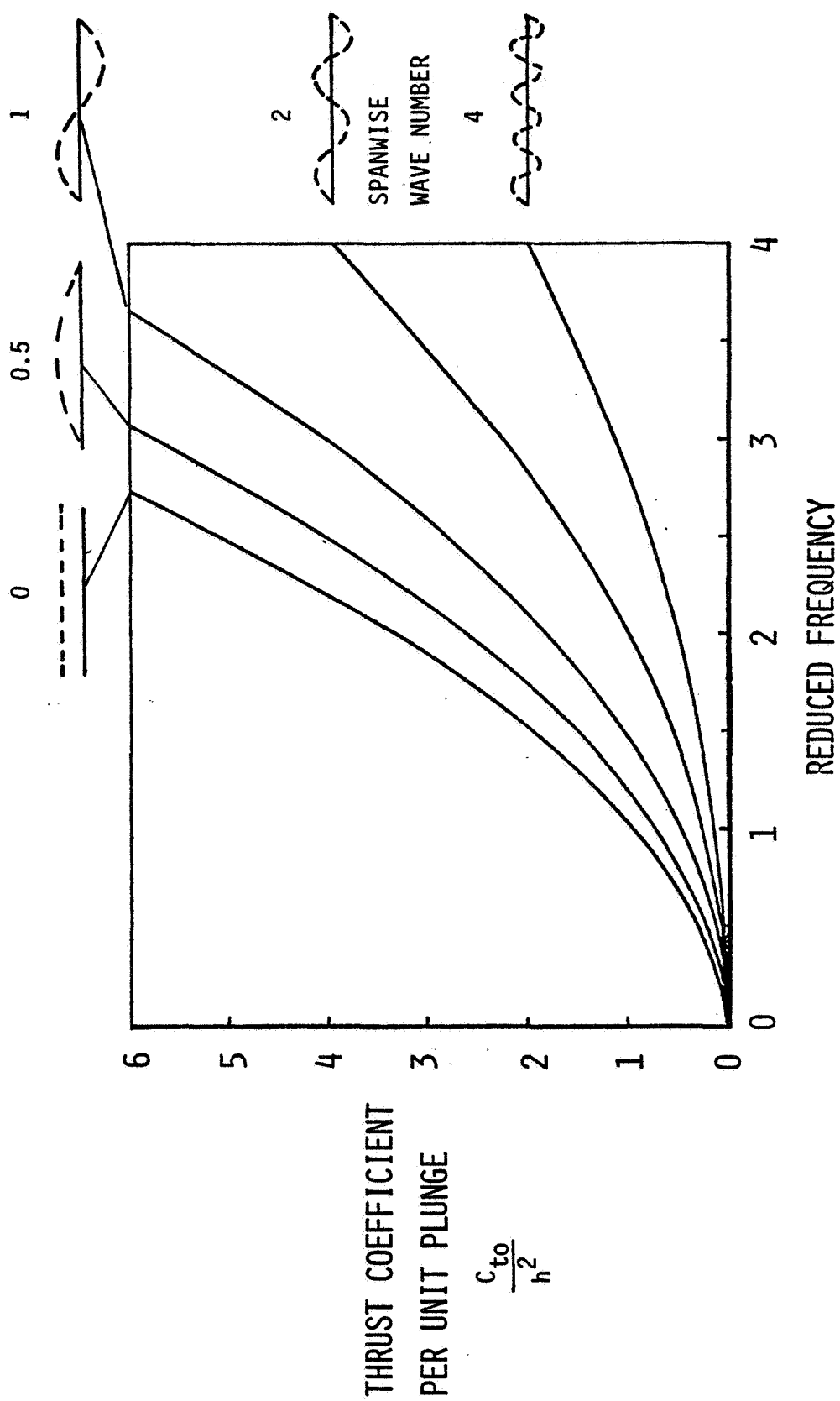


Figure 12: Effect of Spanwise Differences in Amplitude on Mean Thrust from Tuck [52].

where s is the semispan and ω_i is a constant of proportionality between the downwash, w , and the span ($w=\omega_i Z$). This loading is shown to be better than an elliptic loading in minimizing the drag for a specified wing root bending moment. Jones' result is obtained by employing a lifting line, or vortex, theory without regard to the mechanics of the wing motion. Several other investigators have successfully used this approach [42, 56, 57].

Jones concludes that for a linearly flapping wing, the downwash should vary linearly along the span. More generally, "minimum energy loss (maximum efficiency) occurs when the wake moves so as to satisfy the boundary condition of an impermeable surface having the shape of the wing trace and executing a similar motion." Maximum efficiency also corresponds to constant efficiency along the span.

2.5 INTERFERENCE

So far we have discussed only isolated oscillating airfoils. Sparenburg and Wiersma [58] and Bosch [59] have examined the thrust of tandem 2-D airfoils. Bosch calculates the thrust efficiency for various values of the spacing between the airfoils and the operating frequency. He gives calculations for only one of the wings oscillating. The most interesting case, Figure 13, involves the stationary airfoil with its leading edge one chord length behind the trailing edge of the oscillating airfoil. Bosch's results show that the efficiency can remain very close to 100 percent for all frequencies. This is possible because the

rear stationary airfoil uses the wake energy expended by the upstream oscillating airfoil to produce thrust in a manner similar to that described by Wu [60].

Lan [55], using a unique "quasi-vortex lattice method", surpasses Bosch by investigating finite tandem wings with both wings moving. He finds that, unlike an isolated airfoil, "maximum thrust can be generated with maximum efficiency if the hindwing flaps in advance of the forewing by 135 to 180 degrees", with a gap between the wings of one-half chord. This is one explanation for the tandem arrangement of wings on many insects, most notably the dragonfly.

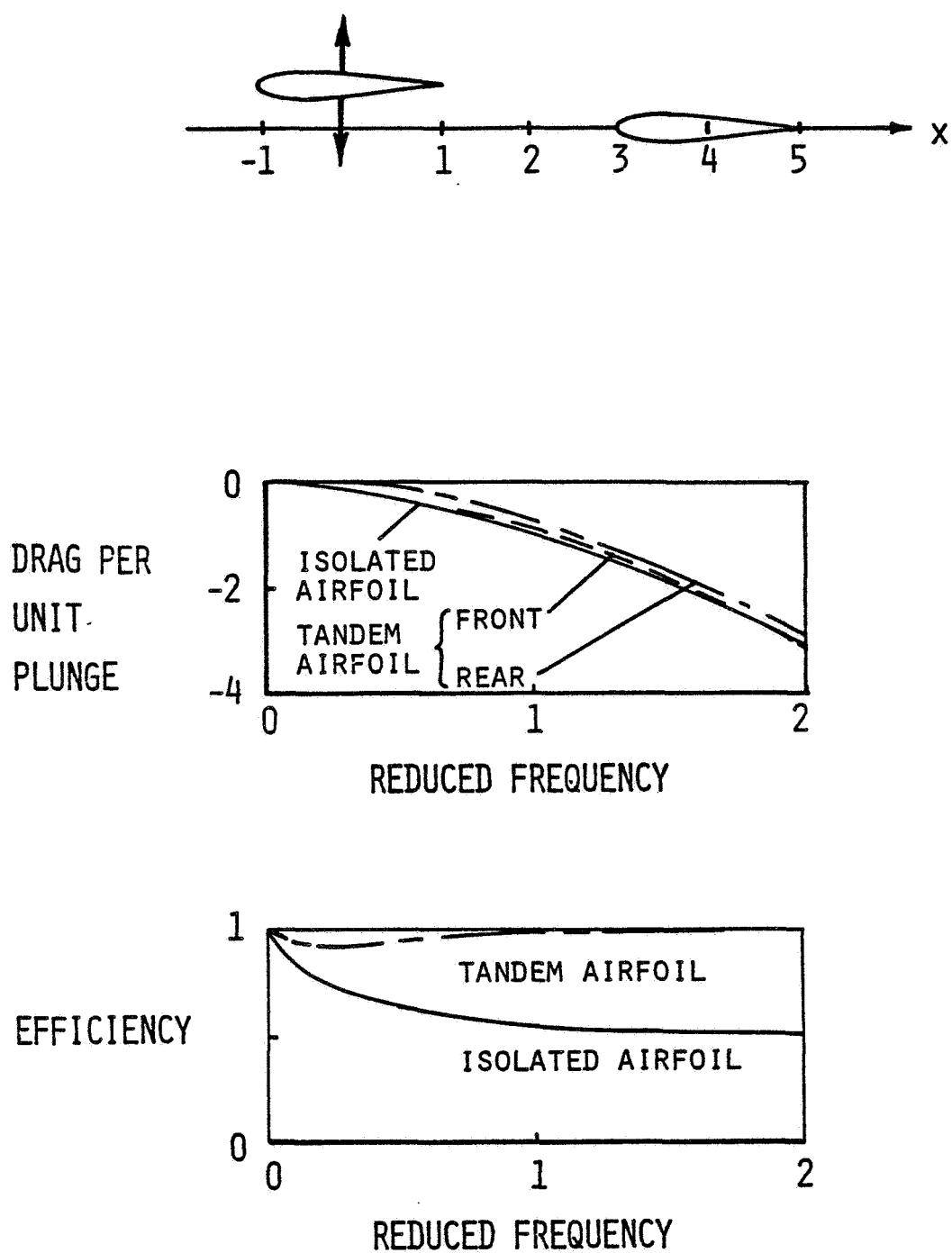


Figure 13: Constructive Interference between an Oscillating and a Stationary Airfoil from Bosch [59].

Chapter III

CALCULATION OF AERODYNAMIC FORCES ON AN AIRFOIL OSCILLATING IN A WIND TUNNEL

3.1 ANALYTIC THIN-AIRFOIL THEORY

3.1.1 Normal Force and Moment

Timman [16] has determined exactly the effect of the wind tunnel walls on a thin airfoil oscillating infinitesimally. The reader may find his paper difficult to follow, in which case the theses by Rock [61] and especially Stoltz [61] are recommended as sources of further detail. Timman maps the region in the complex z -plane which is bounded by the airfoil and the wind-tunnel walls into a rectangle in the ζ -plane through the implicit conformal transformation

$$\operatorname{cn}(\zeta, k^*) = \frac{\sinh \frac{\pi z}{2H}}{\sinh \frac{\pi b}{2H}}, \quad (3.1)$$

where:

$$z = x + iy \quad (3.2)$$

$$\zeta = \xi + i\sigma = \frac{2K\psi}{\pi} + i\sigma \quad (3.3)$$

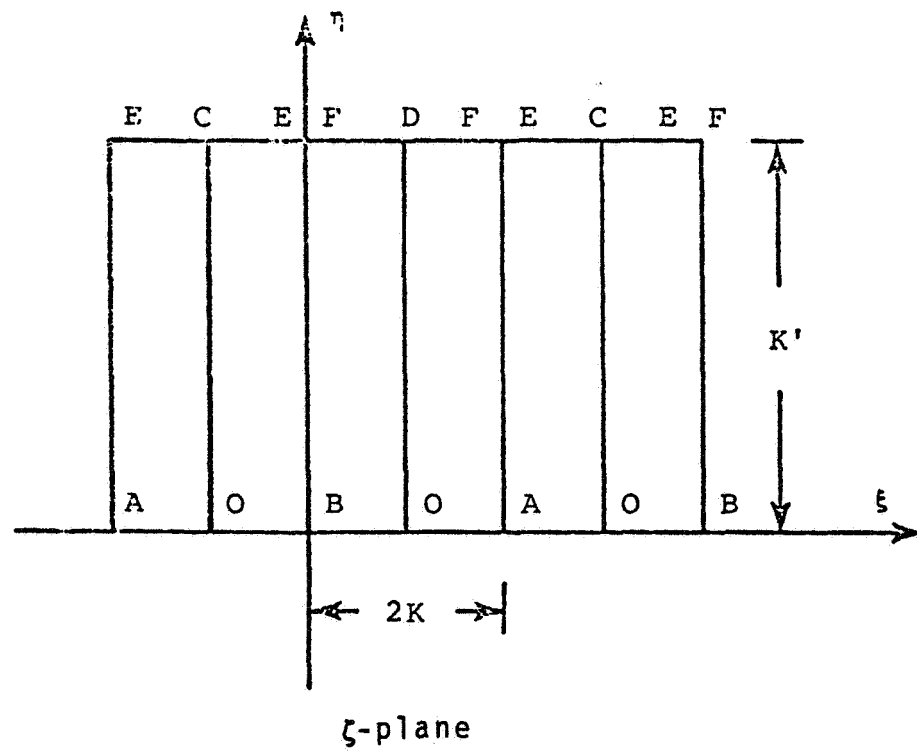
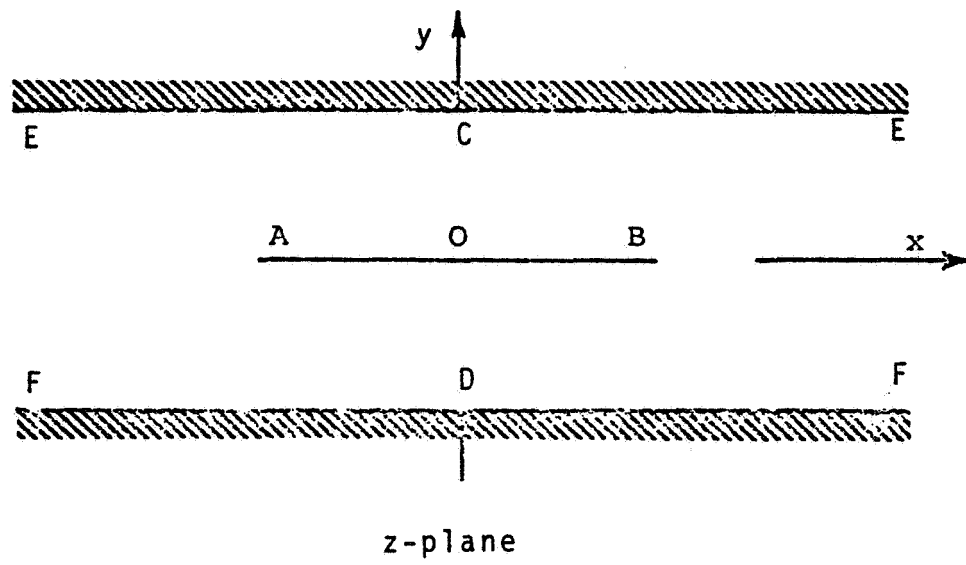


Figure 14: Conformal Transformation of Timman [16].

$$k^* = \tanh \frac{\pi b}{2H} \quad (3.4)$$

K is the complete elliptic integral
of the first kind of modulus k^* .

cn is the Jacobian elliptic function.

This transformation, illustrated in Figure 14, reduces the problem to one which he can solve for the disturbance velocity potential subject to the boundary condition

$$\frac{1}{U} \frac{\partial \phi}{\partial n} = v_n(x) e^{ikt} \quad y=0, -1 \leq x \leq 1. \quad (3.5)$$

The normalwash, $v_n(x)$, is a known function derived from the motion of the airfoil.

From the potential, the pressure distribution round the airfoil, found through the Bernoulli equation, is

$$\Delta C_p = e^{ikt}.$$

$$\left[\frac{4}{K} \left\{ a_0 C' - a_1 (1 - C') \right\} \sum_{n=1}^{\infty} (-1)^{n+1} \frac{1+q^n}{1-q^n} \sin(n\psi) \right. \\ \left. + \frac{8}{\pi} \sum_{n=1}^{\infty} \left\{ \alpha_n + \frac{ik}{n} \beta_n \right\} \frac{1+q^n}{1-q^n} \sin(n\psi) \right] \quad (3.6)$$

where:

$$q = \exp \left(\frac{-\pi K'}{K} \right) \quad (3.7)$$

K' is the complete elliptic integral
of the first kind of modulus k' .

$$k' = \sqrt{1-k^2} \quad (3.8)$$

$$a_0 = \int_0^{2K} v_n(\xi) d\xi \quad (3.9)$$

$$a_1 = \int_0^{2K} v_n(\xi) (cn\xi dn\xi + Z(\xi) sn\xi) d\xi \quad (3.10)$$

$$\alpha_n = \int_0^{\pi} v_n(\psi) \cos n\psi d\psi \quad (3.11)$$

$$\beta_n = \frac{4k*KH}{\pi^2 b} \int_0^{\pi} v_n(\psi) \sin(n\psi) \operatorname{sn}\left(\frac{2K\psi}{\pi}\right) d\psi \quad (3.12)$$

$Z(\xi)$ is Jacobi's Zeta function

C' is the Theodorsen function in the wind tunnel.

In pure plunge:

$$a_0 = ik \ 2K \quad (3.13)$$

$$a_1 = 0 \quad (3.14)$$

$$\alpha_n = 0 \quad (3.15)$$

$$\beta_{2n+1} = ik \frac{H}{b} \sqrt{q} \frac{q^n}{1-q^{2n+1}} \quad \left. \vphantom{\beta_{2n+1}} \right\} n=0,1,2,\dots \quad (3.16)$$

$$\beta_{2n} = 0 \quad (3.17)$$

In pure pitch about the midchord:

$$a_0 = 0 \quad (3.18)$$

$$a_1 = ik \frac{H}{b} \frac{\pi^2}{K^2 k^*} s_3 \quad (3.19)$$

$$a_{2n+1} = ik \frac{H}{b} \sqrt{q} \frac{q^n}{(2n+1)(1-q^{2n+1})} \quad (3.20)$$

$$a_{2n} = 0 \quad (3.21)$$

$$\beta_{2n} = ik \frac{16}{\pi} \left(\frac{H}{b} \right)^2 \gamma_n q^n \quad (3.22)$$

$$\beta_{2n+1} = 0 \quad (3.23)$$

} n=0, 1, 2, ...

Finally, the lift and moment about midchord may be found by integrating the pressure distribution over the airfoil. For the simple plunge and pitch motion of a rigid airfoil, the results are:

$$C_{nh} = -k^2 \frac{64}{\pi} \left(\frac{H}{b} \right)^2 q s_2 + ik \frac{16}{b} \sqrt{q} C' s_1 \quad (3.24)$$

$$C_{na'} = ik \frac{64}{\pi} \left(\frac{H}{b} \right)^2 (q s_2 - (1-C') s_3) \quad (3.25)$$

$$C_{mh} = ik \frac{32}{\pi} \left(\frac{H}{b} \right)^2 C' s_3 \quad (3.26)$$

$$C_{ma'} = k^2 \frac{256}{\pi^3} \left(\frac{H}{b} \right)^4 s_6 - ik \frac{128}{K^2 k^*} \left(\frac{H}{b} \right)^3 (1-C')^2 s_3 \quad (3.27)$$

where:

$$s_1 = \sum_{n=0}^{\infty} q^n \frac{1+q^{2n+1}}{(1-q^{2n+1})^2} \quad (3.28)$$

$$s_2 = \sum_{n=0}^{\infty} \frac{q^{2n}}{2n+1} \frac{1+q^{2n+1}}{(1-q^{2n+1})^3} \quad (3.29)$$

$$s_3 = \sum_{n=1}^{\infty} \gamma_n q^n \frac{1+q^{2n}}{1-q^{2n}} \quad (3.30)$$

$$s_6 = \sum_{n=1}^{\infty} \frac{\gamma_n q^{2n}}{n} \frac{1+q^{2n}}{1-q^{2n}} \quad (3.31)$$

$$\gamma_n = n \sum_{m=0}^{n-1} \frac{1}{(2m+1)(2n-2m-1)(1-q^{2m+1})(1-q^{2n-2m-1})} \\ + n \sum_{m=0}^{\infty} \frac{q^{2m+1}}{(2m+1)(2n+2m+1)(1-q^{2m+1})(1-q^{2n+2m+1})} \quad (3.32)$$

To compare with Garrick's free-air results, the following substitutions are made:

$$s_3' = s_3/q \quad (3.33)$$

$$s_6' = s_6/q^2 \quad (3.34)$$

$$\lambda = \frac{8H}{\pi b} \sqrt{q}. \quad (3.35)$$

It should be noted that these new parameters all approach 1 as the tunnel height becomes infinite. The aerodynamic derivatives can then be written:

$$C_{nh} = -k^2 \pi \lambda^2 s_2 + ik 2\pi C' \lambda s_1 \quad (3.36)$$

$$C_{n\alpha'} = ik \pi \lambda^2 (C' s_3' + s_2 - s_3') \quad (3.37)$$

$$C_{mh} = ik \frac{\pi}{2} C' \lambda^2 s_3' \quad (3.38)$$

$$C_{m\alpha'} = k^2 \frac{\pi}{16} \lambda^4 s_6' - ik \frac{\pi}{4} (1-C') \lambda^3 \frac{s_3'^2}{s_1}. \quad (3.39)$$

When comparing (3.36-3.39) to (2.8-2.11) it is easy to see that in free air (3.36-3.39) revert to (2.8-2.11), because all the extra symbols tend toward 1 while C' becomes C as the tunnel height increases. The values of series s_1 through s_6 are tabulated in Table 1 for the experimental height to chord ratio, H/b , of 2.

TABLE 1
Series Values for $H/b = 2$

s_1	:	1.148
s_2	:	1.153
s_3'	:	1.141
s_6'	:	1.187

In the wind tunnel the branch cut of the Theodorsen function disintegrates into a set of poles and zeros on the negative real axis. The density of the singularities becomes more sparse as the tunnel height is decreased. For small ratios of H/b , the rational approximation of Rock [61] is accurate. In particular, for $H/b=2$,

$$C'(ik) = \frac{ik + 0.538}{2ik + 0.538} \quad (3.40)$$

3.1.2 Leading-edge Suction

The leading-edge suction in the wind tunnel, as in free air, is due to the presence of a singular pressure at the nose. Bearing this in mind, Timman's equation for the pressure is written

$$\Delta C_p = e^{ikt} \frac{4}{\pi} (a_0 C' - a_1 (1 - C')) \frac{1 - \operatorname{cn} \xi \operatorname{dn} \xi}{\operatorname{sn} \xi} + \text{nonsingular terms} \quad (3.41)$$

Now recall, from Reference 63,

$$\sqrt{C_s} = \lim_{x \rightarrow -1} \left\{ \frac{\sqrt{\pi(x+1)}}{4} \Delta C_p \right\}. \quad (3.42)$$

Also, from Timman's transformation,

$$x = -\frac{2H}{\pi b} \tanh^{-1} \left(-k * \frac{\operatorname{cn} \xi}{\operatorname{dn} \xi} \right), \quad (3.43)$$

where use has been made of (4.6.22) of Reference 64. It follows that

$$\begin{aligned} \sqrt{C_s} &= e^{ikt} \frac{1}{\sqrt{\pi}} (a_0 C' - a_1 (1 - C')) \cdot \\ &\lim_{\xi \rightarrow 2K} \left\{ \left[1 - \frac{2H}{\pi b} \tanh^{-1} \left(-k * \frac{\operatorname{cn} \xi}{\operatorname{dn} \xi} \right) \right]^{\frac{1}{2}} \frac{1 - \operatorname{cn} \xi \operatorname{dn} \xi}{\operatorname{sn} \xi} \right\}. \end{aligned} \quad (3.44)$$

Let $\xi' = 2K - \xi$, then in the limit as $x \rightarrow -1$ ($\xi' \rightarrow 0$):

$$\operatorname{cn} \xi = -1 + \frac{1}{2} \xi'^2 \quad (3.45)$$

$$\operatorname{sn} \xi = \xi' \quad (3.46)$$

$$\operatorname{dn} \xi = 1 - \frac{1}{2} (k * \xi')^2 \quad (3.47)$$

$$\tanh^{-1} \left(-k^* \frac{cn\xi}{dn\xi} \right) = \frac{\pi b}{2H} - \tanh^{-1} \left(\frac{1}{2} k^* \xi'^2 \right) \quad (3.48)$$

$$1 - cn\xi dn\xi = 2 \quad (3.49)$$

Then

$$\sqrt{C_s} = e^{ikt} \frac{2}{\sqrt{\pi}} (a_0 C' - a_1 (1 - C')) \lim_{\xi' \rightarrow 0} \left[\frac{2H}{\pi b} \frac{\tanh^{-1} \left(\frac{1}{2} k^* \xi'^2 \right)}{\xi'^2} \right]^{\frac{1}{2}} \quad (3.50)$$

which, taking into account the behavior of \tanh^{-1} , is

$$\sqrt{C_s} = e^{ikt} \frac{2}{\sqrt{\pi}} (a_0 C' - a_1 (1 - C')) \left(\frac{H}{b} \frac{k^*}{\pi} \right)^{\frac{1}{2}} \quad (3.51)$$

Substituting the parameters,

$$\delta = \left[\frac{k^*}{4\sqrt{q}} \right]^{\frac{1}{2}}, \quad (3.52)$$

$$\epsilon = \frac{2K}{\pi}, \quad (3.53)$$

(where, again, δ and ϵ go to unity as the tunnel height becomes infinite), allows the suction to be put in Timman's form with:

$$\sqrt{C_{sh}} = \frac{1}{\sqrt{2\pi}} i k \pi C' \sqrt{\lambda} \epsilon \delta \quad (3.54)$$

$$\sqrt{C_{sa'}} = \frac{1}{\sqrt{2\pi}} i k \pi (C' - 1) \sqrt{\lambda^3} \delta \frac{s_3'}{s_1} \quad (3.55)$$

The similarity with (2.12) and (2.13) is apparent. Equations (3.54) and (3.55) are believed to be original with the author.

Since in steady, potential flow the drag is zero, the leading-edge suction must equal the normal force multiplied by the angle of attack. This leads to the relation

$$\frac{\kappa^2 k^*}{\pi^2} = \sqrt{q} s_1 \quad (3.56)$$

or

$$s_1 = \frac{\kappa^2 k^*}{\pi^2 \sqrt{q}}, \quad (3.57)$$

which is a closed form for s_1 . One consequence of this relation, (which the author has proved to be true to $O(q^{20})$ by expanding each side), is that Rock's parameter, β , is then exactly unity and many of his and Timman's equations simplify to those presented here.

The remarks about the effects of mean angle of attack on an airfoil in free air are also applicable to the airfoil in the wind tunnel if the substitution

$$\sqrt{C_{s\text{mean}}} = \sqrt{2\pi} \sqrt{\lambda} \epsilon \delta \alpha_0 \quad (3.58)$$

is made.

It will be seen in Chapter IV, when the theories are compared to experiment, that the tunnel walls increase both the normal force and the suction.

3.2 NUMERICAL PANEL METHOD

The panel method used here for computing the aerodynamic coefficients is based on the Green's function method of deriving the governing equation. Morino [65] has developed one such formulation capable of handling finite wings in compressible flow. However, in order to compute accurately the suction of an airfoil in a wind tunnel, a more suitable formulation is appropriate.

In using the Green's function method, one begins with the problem statement in terms of the perturbation velocity potential,

$$\nabla^2 \phi(r_a) = 0 \quad (3.59)$$

$$\frac{\partial \phi}{\partial n}(r_s) = \left[-\hat{i} + \frac{V_b(r_s)}{U} \right] \cdot \hat{n}(r_s) \quad (3.60)$$

r_a is some point in the flow, A

r_s is a point on the boundary, S

V_b is the velocity of the boundary

\hat{n} is the normal on the boundary directed into the flow.

Now, Green's Identity is [66]:

$$\begin{aligned} \iiint_A \left[\phi(r_a) \nabla^2 G(r_a, r') - G(r_a, r') \nabla^2 \phi(r_a) \right] dA \\ = \int_S \left[G(r_s, r') \frac{\partial \phi}{\partial n}(r_s) - \phi(r_s) \frac{\partial G}{\partial n}(r_s, r') \right] dS \end{aligned} \quad (3.61)$$

where G is a well-behaved function. In particular, let it be a Green's function, that is, a solution of:

$$\nabla^2 G(r, r') = \delta(|r - r'|) \equiv \text{delta function} \quad (3.62)$$

We have considerable latitude in choosing $G(r, r')$, and a great simplification would be possible if we could find G such that its normal derivative on the boundary is zero. However, this is not easily done.

Instead, we choose the simple form

$$G(r, r') = \frac{1}{2\pi} \ln|r - r'| = \frac{1}{4\pi} \ln(r - r')^2. \quad (3.63)$$

Then (3.61) transforms into

$$\phi(r') = \int_S \left[\frac{\ln(r_s - r')^2}{4\pi} \frac{\partial \phi}{\partial n} - \frac{\phi(r_s)}{4\pi} \frac{\partial \ln(r_s - r')^2}{\partial n} \right] dS. \quad (3.64)$$

We now let r' approach the surface point r_{si} :

$$4\pi\phi(r_{si}) + \int_S \phi(r_s) \frac{\partial \ln(r_s - r_{si})^2}{\partial n} dS = \int_S \frac{\partial \phi}{\partial n}(r_s) \ln(r_s - r_{si})^2 dS. \quad (3.65)$$

This is the governing equation relating the potential on the surface $\phi(r_s)$ to the boundary condition on the surface, $\partial\phi/\partial n$. It may be noted that $\partial \ln r^2 / \partial n$ is the potential of a 2-D doublet oriented along the surface normal, while $\ln r^2$ is the potential of a 2-D source. Thus, the perturbation flow arises from a distribution of sources and doublets on the boundary surface. Before proceeding with the solution we make the following observations.

First, we may divide the general problem into two, which may be called the steady and unsteady solutions. In either case, the field equation is the same, but for steady flow the boundary condition is

$$\frac{\partial \phi^0}{\partial n} = -\hat{i} \cdot \hat{n}^0. \quad (3.66)$$

While for unsteady flow it is

$$\frac{\partial \phi^t}{\partial n} = -\hat{i} \cdot \hat{n}^t + \frac{V_b}{U} \cdot \hat{n}^0. \quad (3.67)$$

where

$$\hat{n} = \hat{n}^0(r_s) + \hat{n}^t(r_s, t). \quad (3.68)$$

The steady and unsteady potentials may be found independently, but, as will be shown later, the pressures and therefore forces on the airfoil are dependent on the coupled solution.

Second, in dealing with the unsteady solution the possibility that the influence coefficients change as a result of the changing geometry is ignored, that is, the motion of the airfoil is assumed small. Then the unsteady potential for oscillatory motion is linearly dependent on the amplitude of oscillation, and the aerodynamic derivatives may be calculated by replacing the doublets and sources with their derivatives. For example, the derivative source strength in pure pitch is

$$\frac{\partial}{\partial \alpha} \left(\frac{\partial \phi^t}{\partial n} \right) = \frac{\partial}{\partial \alpha} \left[-\hat{i} \cdot \hat{n}^t + \frac{V_b}{U} \cdot \hat{n}^0 \right] \quad (3.69)$$

from which the derivative pressures and forces are found. It will be shown later that these forces are not strictly oscillatory of the same frequency as the motion, but have a significant second harmonic analogous to the leading-edge suction of thin-airfoil theory.

To solve the governing equation numerically, one assumes the distribution of the doublet strength is described by an equation with unknown coefficients and satisfies the governing equation at as many collocation points as there are unknown coefficients. In this case we assume that, in the neighborhood of the point r_{s0} , the distributions can be described by the first three terms of the Taylor series:

$$\phi(r_s) = \phi_0(r_{s0}) + \phi_1(r_{s0})\sigma + \phi_2(r_{s0})\sigma^2 \quad (3.70)$$

$$\frac{\partial \phi}{\partial n}(r_s) = \phi_{n0}(r_{s0}) + \phi_{n1}(r_{s0})\sigma + \phi_{n2}(r_{s0})\sigma^2 \quad (3.71)$$

$$\sigma = s(r_s) - s(r_{s0}). \quad (3.72)$$

Thus, quadratic variations of the strengths are assumed. Summing over all the panels, S_j , implies

$$\begin{aligned} 4\pi\phi(r_{si}) + \sum_j \int_{S_j} [\phi_0 + \phi_1\sigma + \phi_2\sigma^2]_j \frac{\partial \ln(r_s - r_{si})^2}{\partial n} dS \\ = \sum_j \int_{S_j} [\phi_{n0} + \phi_{n1}\sigma + \phi_{n2}\sigma^2]_j \ln(r_s - r_{si})^2 dS. \end{aligned} \quad (3.73)$$

The position of the collocation points are chosen to be at the center of the panel and a distance σ_c on either side of the center. The three

collocation points provide three equations for determining the unknown potential coefficients. When the 'doublet' integrals, D , and 'source' integrals, S , are evaluated, this may be put into matrix form:

$$\begin{bmatrix} D_{11}^0 + 4\pi & D_{11}^1 - 4\pi\sigma_c & D_{11}^2 + 4\pi\sigma_c^2 & D_{12}^0 & \dots \\ D_{21}^0 + 4\pi & D_{21}^1 & D_{21}^2 & D_{22}^0 & \dots \\ D_{31}^0 + 4\pi & D_{31}^1 + 4\pi\sigma_c & D_{31}^2 + 4\pi\sigma_c^2 & D_{32}^0 & \dots \\ D_{41}^0 & D_{41}^1 & D_{41}^2 & D_{42}^0 + 4\pi & \dots \\ \dots & \dots & \dots & \dots & \dots \end{bmatrix} \begin{Bmatrix} \phi_{01} \\ \phi_{11} \\ \phi_{21} \\ \phi_{02} \\ \dots \end{Bmatrix}$$

$$= \begin{Bmatrix} \sum_j (S_{1j}^0 \phi_{n0j} + S_{1j}^1 \phi_{n1j} + S_{1j}^2 \phi_{n2j}) \\ \sum_j (S_{2j}^0 \phi_{n0j} + S_{2j}^1 \phi_{n1j} + S_{2j}^2 \phi_{n2j}) \\ \sum_j (S_{3j}^0 \phi_{n0j} + S_{3j}^1 \phi_{n1j} + S_{3j}^2 \phi_{n2j}) \\ \sum_j (S_{4j}^0 \phi_{n0j} + S_{4j}^1 \phi_{n1j} + S_{4j}^2 \phi_{n2j}) \\ \dots \end{Bmatrix} \quad (3.74)$$

3.2.1 Airfoil Geometry

To evaluate each element it is necessary to know the geometry of each panel. It should be noted that a certain consistency between the geometry and assumed singularity distribution is desired, for an unbalanced effort invested in either is wasted. For example, replacing a smooth airfoil by straight line segments will produce a pressure distribution which will have singularities at each sharp corner. Here each panel is assumed to be an arc of a circle with the various parameters shown in Figure 15. As the airfoil is divided into more panels, the discontinuity in slope at each boundary tends quickly to zero. For a practical

geometry, 32 panels, one can see in Figure 16 that the approximate representation is indistinguishable from the real airfoil. The only deviation is at the trailing edge, which has been sharpened from the finite thickness edge of the real profile. Assuming circular arc panels leads to the simple relations:

$$r^2 = (r_s - r_{s1})^2 = R^2 + R_1^2 - 2RR_1\cos(\beta+\theta) \quad (3.75)$$

$$\sigma = \theta R \quad (3.76)$$

So the doublet integral is of the form

$$\begin{aligned} D_{ij}^n &= \int_{S_j} \sigma^n \frac{\partial \ln r^2}{\partial n} dS \\ &= \int_{-\gamma_j}^{\gamma_j} (\theta R)^n \frac{2R - 2R_1\cos(\beta+\theta)}{R^2 + R_1^2 - 2RR_1\cos(\beta+\theta)} R d\theta \\ &= \int_{-\gamma_j}^{\gamma_j} (\theta R)^n d\theta + \int_{-\gamma_j}^{\gamma_j} (\theta R)^n \frac{R' - 1/R'}{R' + 1/R' - 2\cos(\beta+\theta)} d\theta \end{aligned} \quad (3.77)$$

where

$$R' = R/R_1 \quad (3.78)$$

The source integral is

$$S_{ij}^n = \int_{S_j} \sigma^n \ln r^2 dS = \int_{-\gamma_j}^{\gamma_j} (\theta R)^n \ln(R^2 + R_1^2 - 2RR_1\cos(\beta+\theta)) R d\theta \quad (3.79)$$

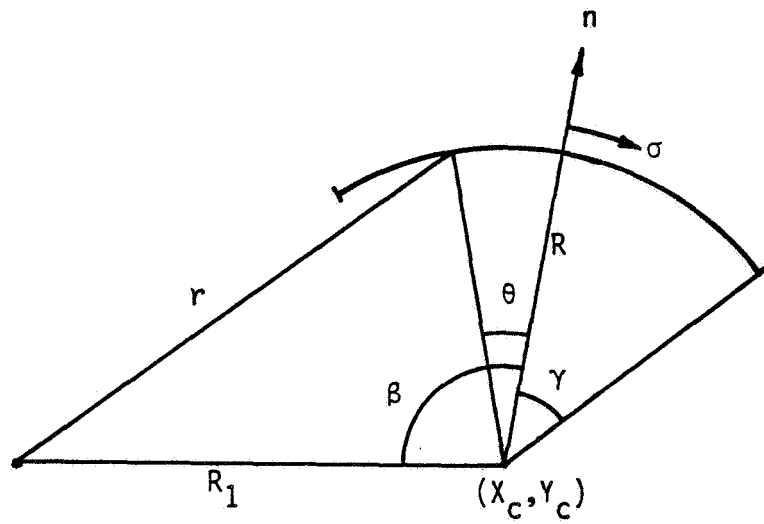


Figure 15: Geometry of Circular-Arc Panel.

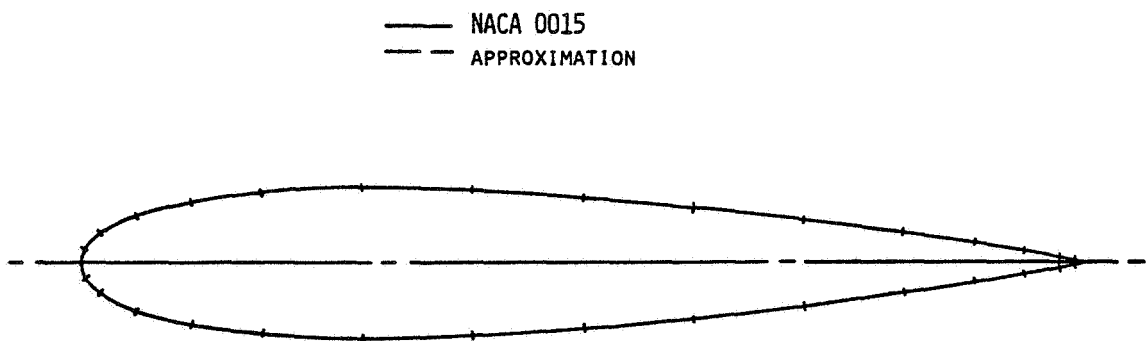


Figure 16: Approximate Representation of NACA 0015 Profile.

3.2.2 Computation of Coefficients

The computation of each of the doublet and source influence coefficients is dependent upon the juxtaposition of the collocation points with respect to the panel and the panel geometry. Firstly, if the panel subtends less than 0.02 radian then it is treated as being flat, in which case the integrals are greatly simplified. If the panel's curvature must be included then either a close field ($|\beta| < 3/2 \gamma$) or a far field computation is done. The close field computation is necessary to include properly the singularity in the integrand as the collocation point approaches a panel end. Finally, two more pathological cases may arise. One is $\sin\beta=0$, the other is $R' = 0$. The full derivation of each case will not be given here, but some of the details will now be sketched.

3.2.2.1 Doublet Integral

The doublet integral for $n=0$ can be evaluated in closed form (Ref. 67, Eq. 342) as

$$D^0 = 2\gamma \pm 2 \left[\tan^{-1} \left\{ \frac{b+(a-c)\tan\frac{1}{2}\theta}{|R'-1/R'|} \right\} \right]_{-\gamma}^{\gamma} \quad (3.80)$$

where

$$a = R' + 1/R' \quad (3.81)$$

$$b = 2 \sin\beta \quad (3.82)$$

$$c = -2 \cos \beta . \quad (3.83)$$

The choice of sign in (3.80) is dependent on the sign of $(R'-1/R')$. For the higher integrals the far field approximation,

$$\sin \theta \approx \theta \quad (3.84)$$

$$\cos \theta \approx 1 - \frac{1}{2}\theta^2 \quad (3.85)$$

is used. While for the near field we use

$$\sin(\beta+\theta) \approx \beta+\theta \quad (3.86)$$

$$\cos(\beta+\theta) \approx 1 - \frac{(\beta+\theta)^2}{2}. \quad (3.87)$$

The integrals are then evaluated using Eq. 2.175 of Reference 68.

3.2.2.2 Source Coefficients

The source integral is first partially integrated

$$S^n = \frac{(\theta R)^{n+1}}{n+1} \ln[(R^2+R_1^2-2RR_1\cos(\beta+\theta))] \Big|_{-\gamma}^{\gamma} \quad (3.88)$$

$$- \int_{-\gamma}^{\gamma} \frac{(\theta R)^{n+1}}{n+1} \frac{2RR_1\sin(\beta+\theta)}{R^2+R_1^2-2RR_1\cos(\beta+\theta)} d\theta$$

The same approximations to the integral in (3.88) are then used as were applied to the doublet integral.

3.2.3 Source Strengths

3.2.3.1 Steady Flow

From the boundary condition,

$$\frac{\partial \phi}{\partial n} = -\hat{i} \cdot \hat{n}^0 = \phi_{n0} + \theta R \phi_{n1} + (\theta R)^2 \phi_{n2}. \quad (3.89)$$

Expanding \hat{n} about $\theta=0$, one obtains

$$\hat{n}^0 = \hat{n}_0 + \frac{\partial \hat{n}}{\partial \theta R} \theta R + \frac{1}{2} \frac{\partial^2 \hat{n}}{\partial^2 \theta R} (\theta R)^2 \quad (3.90)$$

where

$$\hat{n}_0 = \hat{n}(\theta=0) = n_{0x} \hat{i} + n_{0y} \hat{j} \quad (3.91)$$

$$\frac{\partial \hat{n}}{\partial \theta R} = \frac{1}{R} (n_{0y} \hat{i} - n_{0x} \hat{j}) \quad (3.92)$$

$$\frac{\partial^2 \hat{n}}{\partial^2 \theta R} = -\frac{1}{R^2} (n_{0x} \hat{i} + n_{0y} \hat{j}). \quad (3.93)$$

This leads to

$$\phi_{n0} = -n_{0x} \quad (3.94)$$

$$\phi_{n1} = -\frac{n_{0y}}{R} \quad (3.95)$$

$$\phi_{n2} = \frac{n_{0x}}{2R^2}. \quad (3.96)$$

3.2.3.2 Unsteady Flow

The unsteady condition is

$$\frac{\partial \phi^t}{\partial n} = -\hat{i} \cdot \hat{n}^t + \frac{V_b}{U} \cdot \hat{n}^0 \quad (3.97)$$

which ignores second order variations in the normal. For a rigid airfoil plunging with velocity h and pitching with angular velocity $-\dot{\alpha}$ about midchord,

$$\hat{n}^t = (n_{0y}\hat{i} - n_{0x}\hat{j}) \alpha \quad (3.98)$$

$$V_b = -\dot{h}\hat{j} + (-\dot{\alpha}\hat{k}) \perp r \quad (3.99)$$

$$= -\dot{h}\hat{j} + (-\dot{\alpha}\hat{k}) \perp (x\hat{i} + y\hat{j})$$

where the symbol, \perp , is used for the vector cross product. Let:

$$x = x_c + R(n_{0x} + n_{0y}\theta - \frac{1}{2}n_{0x}\theta^2) \quad (3.100)$$

$$y = y_c + R(n_{0y} - n_{0x}\theta - \frac{1}{2}n_{0y}\theta^2) \quad (3.101)$$

This leads to

$$\begin{aligned} V_b \cdot \hat{n}^0 = & -\dot{h}n_{0y} + \dot{\alpha}(n_{0x}y_c - n_{0y}x_c) \\ & + \frac{1}{R} [\dot{h}n_{0x} + \dot{\alpha}(n_{0x}x_c + n_{0y}y_c)] \theta R \\ & + \frac{1}{2R^2} [\dot{h}n_{0y} + \dot{\alpha}(n_{0y}x_c - n_{0x}y_c)] (\theta R)^2 \end{aligned} \quad (3.102)$$

From which the values of the unsteady source strengths are apparent. Notice that, for steady and unsteady flow, the boundary condition follows a cyclic pattern,

$$\phi_{n2} = - \frac{\phi_{n0}}{2R^2}. \quad (3.103)$$

3.2.4 Wake Contribution

Since we are dealing with a lifting problem it is necessary to include a wake. For steady flow this is simple, if we first make the assumption that the wake will lie along a straight line parallel to the x axis. The wake in reality leaves the trailing edge along a line within the angle formed by the upper and lower surfaces. However, the assumption is still usable. The Kutta condition is enforced implicitly when we designate the trailing edge as the point from which the wake emanates. The steady wake has a constant strength equal to the difference between the potentials on the upper and lower surface.

$$\Delta\phi^0_w(x) = \phi^0_u(1) - \phi^0_l(1) = \Delta\phi^0_{te} \quad (3.104)$$

The influence of the steady wake is then the same as a constant-strength, flat panel.

For an oscillating airfoil the strength of the wake is assumed to be sinusoidal in time and with distance downstream, that is,

$$\Delta\phi^t_w(x) = \Delta\phi^t_{te} e^{ik(t-x+1)}. \quad (3.105)$$

The doublet influence of the wake at $t=0$ is then

$$W_i = \int_{\text{wake}} e^{-ik(x-x_{te})/b} \frac{\partial \ln(r_s - r_{si})^2}{\partial n} dx. \quad (3.106)$$

Again we assume the wake is parallel to the x axis, so that

$$(r_s - r_{si})^2 = (x_s - x_{si})^2 + (y_s - y_{si})^2 \quad (3.107)$$

$$\frac{\partial}{\partial n} = \frac{\partial}{\partial y_s}. \quad (3.108)$$

Letting

$$x' = x_s - x_{si} \quad (3.109)$$

$$\Delta y = y_s - y_{si} \quad (3.110)$$

$$\Delta x = x_{te} - x_{si} \quad (3.111)$$

implies

$$W_i = 2 \Delta y e^{ik\Delta x} \int_{\Delta x}^{\infty} \frac{e^{-ikx'}}{x'^2 + \Delta y^2} dx'. \quad (3.112)$$

To evaluate the integral we remove the possible singularities;

$$\begin{aligned} \int_{\Delta x}^{\infty} \frac{e^{-ikx'}}{x'^2 + \Delta y^2} dx' &= \int_0^{\infty} \frac{e^{-ikx'}}{x'^2 + \Delta y^2} dx' - \int_0^{\Delta x} \frac{1 - ikx'}{x'^2 + \Delta y^2} dx' \\ &\quad - \int_0^{\Delta x} \frac{(\cos kx' - 1) - ik(\sin kx' - kx')}{x'^2 + \Delta y^2} dx'. \end{aligned} \quad (3.113)$$

The first two integrals are evaluated to yield

$$\begin{aligned}
 W_i = e^{\frac{ik\Delta x}{|\Delta y|}} & \left[\pi e^{-k|\Delta y|} + i2\sinh k|\Delta y| \left\{ c + \ln k|\Delta y| + 2 \sum_{j=2,2}^{\infty} \frac{(k|\Delta y|)^j}{jj!} \right\} \right. \\
 & - i4\cosh k|\Delta y| \sum_{j=1,2}^{\infty} \frac{(k|\Delta y|)^j}{jj!} - 2\tan^{-1} \frac{\Delta x}{|\Delta y|} + ik|\Delta y| \ln \frac{\Delta x^2 + \Delta y^2}{\Delta y^2} \\
 & \left. - 2|\Delta y| \int_0^{\Delta x} \frac{(\cos kx' - 1) - i(\sin kx' - kx')}{x'^2 + \Delta y^2} dx' \right] \quad (3.114)
 \end{aligned}$$

where $c = 0.577215\dots$. The remaining integral is evaluated numerically to calculate the wake influence.

3.2.5 Pressures

Since the value of the drag in steady flow depends upon the pressure near the stagnation points, the complete Bernoulli equation is used.

That is,

$$\frac{v^2}{2} + \frac{p}{\rho} + \frac{\partial \Phi}{\partial \tau} = \frac{U^2}{2} + \frac{p_{\infty}}{\rho} \quad (3.115)$$

This is manipulated to express the pressure coefficient,

$$\frac{p - p_{\infty}}{\frac{1}{2}\rho U^2} \equiv C_p = 1 - \left(\frac{v}{U} \right)^2 - \frac{2}{U^2} \frac{\partial \Phi}{\partial \tau} \quad (3.116)$$

Now,

$$V/U = \hat{i} + \nabla\phi \quad (3.117)$$

$$\frac{\partial\phi}{\partial t} = \phi' bU \quad (3.118)$$

$$\tau = t' b/U. \quad (3.119)$$

So,

$$\begin{aligned} C_p &= 1 - |\hat{i} + \nabla\phi|^2 - 2 \frac{\partial\phi}{\partial t} \\ &= -2(\hat{i} \cdot \nabla\phi) - |\nabla\phi|^2 - 2 \frac{\partial\phi}{\partial t} \end{aligned} \quad (3.120)$$

In sinusoidal motion,

$$\phi(r_s, t) = \phi^0(r_s) + \phi^t(r_s) e^{ikt} \quad (3.121)$$

and

$$V_b = V_b(r_s) e^{ikt}. \quad (3.122)$$

Then, for a point on the airfoil surface,

$$\frac{\partial\phi}{\partial t} = ik\phi^t - V_b \cdot \nabla\phi \quad (3.123)$$

and

$$\begin{aligned} C_p &= -2 \left(\hat{i} \cdot (\nabla\phi^0 + \nabla\phi^t e^{ikt}) + \frac{|\nabla\phi^0 + \nabla\phi^t e^{ikt}|^2}{2} \right. \\ &\quad \left. + ik\phi^t e^{ikt} - V_b \cdot \nabla\phi^0 e^{ikt} - V_b e^{ikt} \cdot \nabla\phi^t e^{ikt} \right) \end{aligned} \quad (3.124)$$

$$\begin{aligned}
C_p = & - \left[2\hat{i} \cdot \nabla \phi^0 + |\nabla \phi^0|^2 + \frac{1}{2} \nabla \phi^t \cdot \nabla \phi^{t*} - v_b \cdot \nabla \phi^{t*} \right] \\
& - 2 \left[i k \phi^t + \hat{i} \cdot \nabla \phi^t + \nabla \phi^0 \cdot \nabla \phi^t - v_b \cdot \nabla \phi^0 \right] e^{i k t} \\
& - 2 \left[\frac{1}{2} |\nabla \phi^t|^2 - \frac{1}{2} v_b \cdot \nabla \phi^t \right] e^{2 i k t} .
\end{aligned} \tag{3.125}$$

This form shows the steady-flow pressure, the first harmonic pressure including the coupling between the steady and unsteady flows, and the second harmonic pressure. For a thin airfoil, the second harmonic pressure is equal on top and bottom surfaces, and no second harmonic force results except that due to the singular pressure at the leading edge. However, in calculating the drag of a thick wing, the second harmonic pressure does not integrate to zero. In fact, it is solely responsible for the thrust of an airfoil in pure plunge oscillation. It should be noted that a second harmonic pressure also arises from a second harmonic variation in the potential, which is ignored in (3.97).

To actually calculate the pressure we write

$$\nabla \phi = \frac{\partial \phi}{\partial n} \hat{n} + \frac{\partial \phi}{\partial \sigma} \sigma \tag{3.126}$$

where \hat{n} and σ are the normal and tangential directions, respectively. The normal derivative is known from the boundary condition, whereas from the Taylor's expansion

$$\frac{\partial \phi}{\partial \sigma} = \phi_1 + 2\phi_2 \sigma. \tag{3.127}$$

Since the doublet strength was assumed to be quadratic, the pressure distribution consistent with that distribution is linear. By using the potential distribution in adjacent panels, other approximations to the pressure distribution can be made.

The lift, moment and drag are found by integrating the pressure over each panel, including the curvature of the panel.

By way of demonstrating the accuracy of the developed program, Figure 17 presents the convergence of the steady drag towards zero as the number of panels is increased. Figure 18 presents the oscillatory lift amplitude and phase in pure plunge versus reduced frequency. Figure 19 shows the oscillatory suction and phase. The amplitude comparison with thin airfoil theory shows the expected increase due to thickness, while the phase is only slightly changed. These results were obtained with only 18 panels on the airfoil. With this minimal paneling, a 3 second run time is achieved on Stanford's IBM 3033, which means that costs can be kept below \$1 a run.

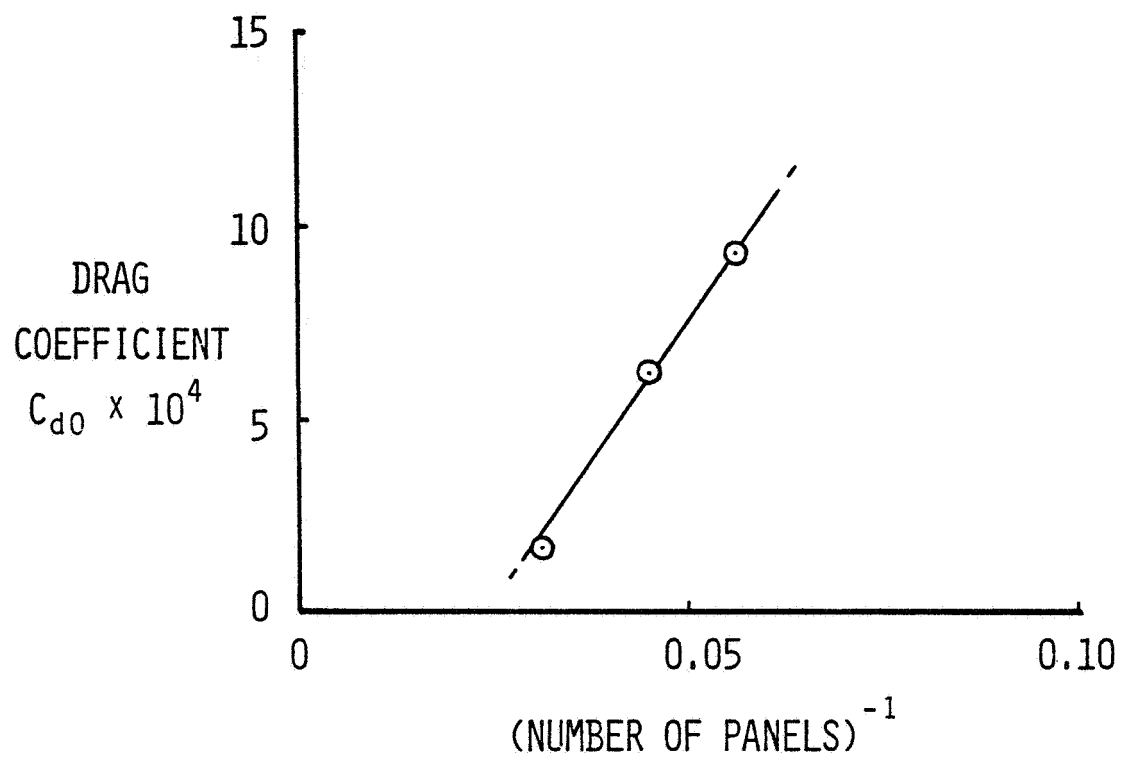


Figure 17: Convergence of Steady Potential-Flow Drag Predicted by Panel Method.

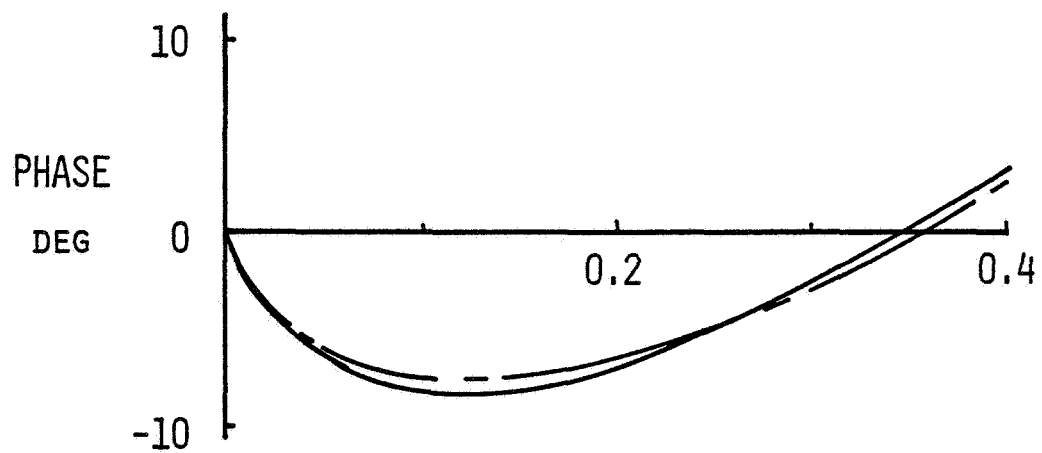
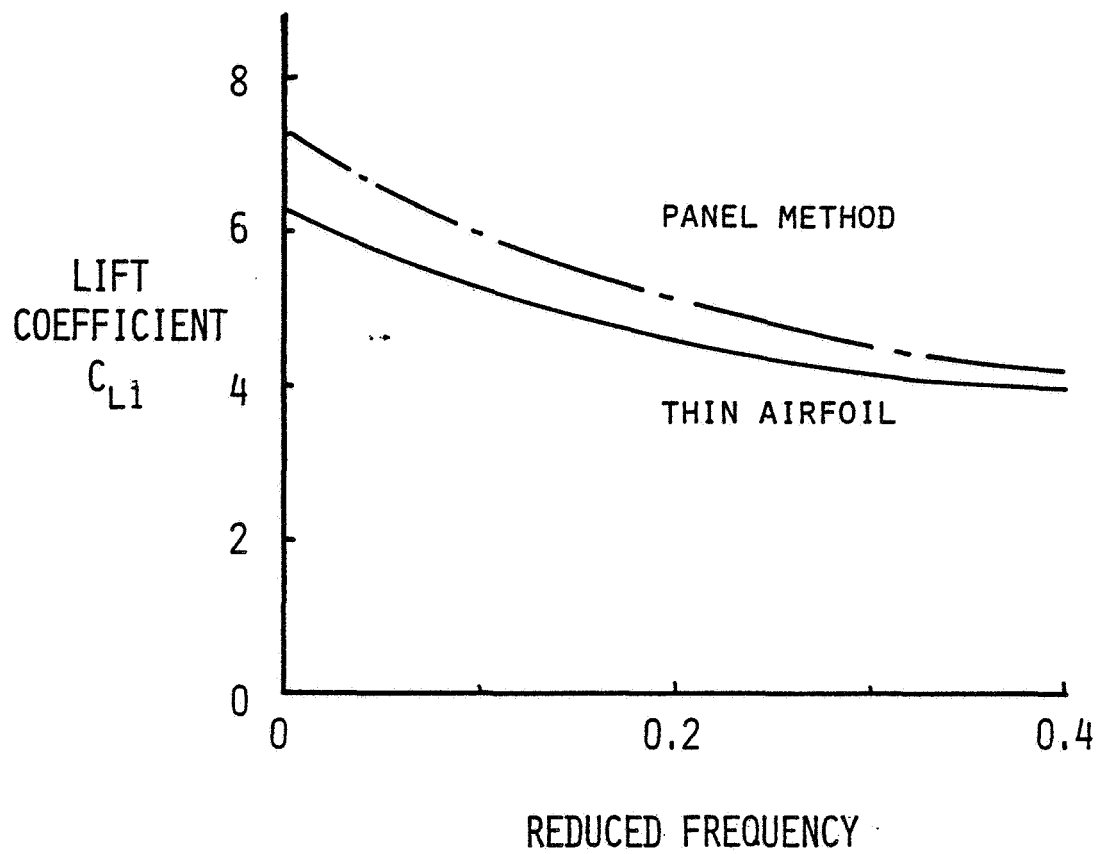


Figure 18: Oscillatory Lift Predicted by Panel Method.

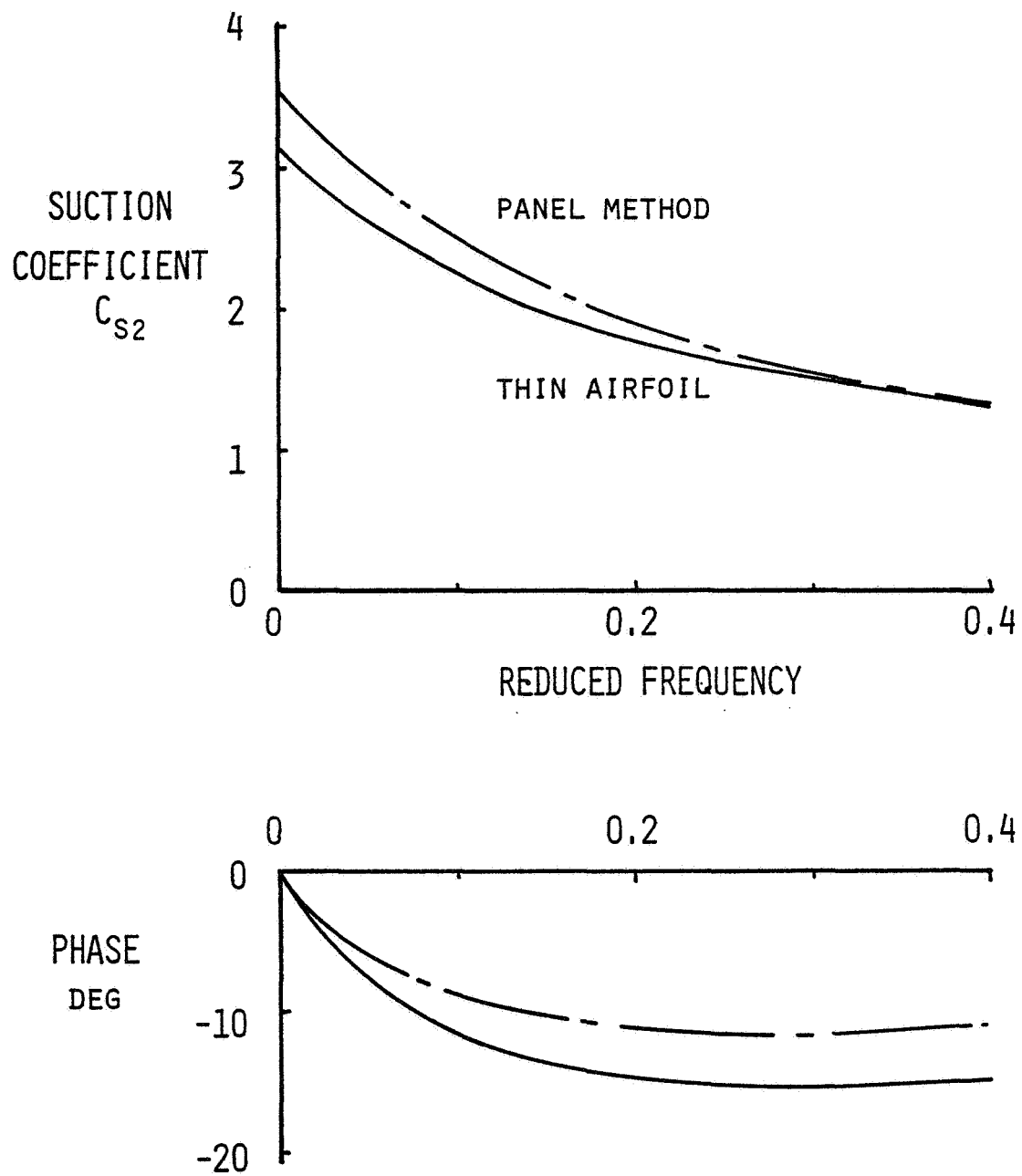


Figure 19: Second Harmonic Suction Predicted by Panel Method.

3.2.6 Viscous Effects

Viscous effects can be included in the panel method by calculating the characteristics of the boundary-layer surrounding the airfoil. This has been done before in steady flow [69] and unsteady flow [cf. 70]. This approach is most successful when the boundary-layer calculations include unsteady terms and the external flow properties are dependent upon the boundary layer characteristics, that is, the two calculations are coupled.

Boundary-layer drag can be divided into two constituents. The first is the skin friction on the airfoil proportional to the viscosity and the velocity gradient at the surface. The second is the pressure drag which arises because the drag component of the integrated pressure is no longer zero. The thickness of the boundary-layer modifies the profile shape and decreases the pressures on the aft portion of the airfoil. In steady flow over unstalled airfoils, the ratio of pressure drag to total boundary-layer drag is approximately the thickness to chord ratio of the profile [71]. If the potential and boundary-layer flows are not coupled, only an approximation to the skin friction can be obtained. This is the case with the results of Kottapalli and Pierce [47].

The finite difference scheme of Dwyer [72] has been selected for boundary-layer calculations by Kottapalli and Pierce [47] and McCroskey [70]. McCroskey gives a good description of the solution for an

oscillating airfoil using this scheme, provided the velocities due to angle of attack, camber and thickness are given. For an airfoil with a turbulent boundary layer, the computation took up to 7½ minutes on an IBM 360/67.

In order to reduce costs, the use of an integral boundary-layer method was pursued. For the present research, a steady flow, integral method for boundary-layer calculations was available through the NASA Ames Research Center. This was the code developed by McNally [73] that calculates laminar characteristics using the approach of Cohen and Reshotko [74] and turbulent characteristics based on Sasman and Cresci [75]. Transition can be calculated or specified to occur at one spot.

The envisioned procedure in steady flow is to calculate the potential flow about the profile. Using that external flow calculate the boundary-layer displacement thickness. Add the displacement thickness to the coordinates of the airfoil and use that shape as input to the potential solution. This iteration can be continued until convergence. The skin friction is then included along with the final external pressure distribution to calculate the forces on the airfoil. This procedure results in a finite-thickness wake. Unfortunately, the variation of the potential along the wake must now also be included. To avoid iteration on this quantity, a constant potential was assumed.

For the experimental airfoil at zero angle of attack and a Reynolds number of 0.3 million, the drag coefficient due to skin friction was

0.010. However the computed pressure drag was nil. This problem has been traced to the formulation of the finite thickness wake which was acting like a jet to propel the airfoil and hence give no pressure drag. Until this is corrected, the calculation of drag versus angle of attack appears unwarranted. Nor has the panel method been coupled with the boundary layer in unsteady calculations.

In unsteady flow, for moderate reduced frequencies, a quasi-static calculation neglecting the unsteady terms and using the instantaneous pressure distribution appears to be quite accurate [76, 77]. This is possible because at low reduced frequencies, $(k[x+1] < 0.3)$, the phase of the shear stress lags the external velocity by less than 45 deg for a laminar boundary layer [78] and less than 10 deg for a turbulent layer [79]. It should be mentioned that boundary-layer compliance [80] is ignored.

3.2.7 Including Wind Tunnel Walls

Having progressed this far, the representation of the wing in the wind tunnel is straightforward. The upper and lower walls are replaced with doublet panels exactly as the wing was, as shown in Figure 20. The walls upstream of the wing are truncated while wake panels are included to model the downstream section walls. For the results reported here, the tunnel was truncated four semichords upstream. Additionally, since the tunnel wall is far from the wing, only constant strength doublet panels were used on the wall.

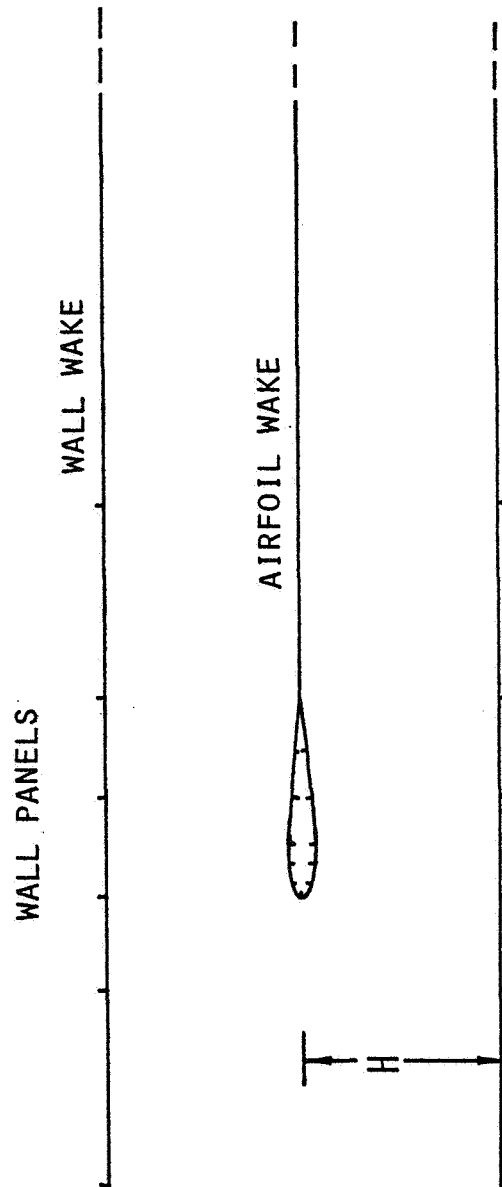


Figure 20: Wind Tunnel Representation in Panel Code.

Chapter IV

MEASUREMENT OF AERODYNAMIC FORCES ON AN AIRFOIL OSCILLATING IN A WIND TUNNEL

4.1 INTRODUCTION

At the time the author began research at Stanford two other students had nearly completed their work. Bill Boyd had examined theoretically the effect of chordwise forces on wing flutter [81]. Steve Rock under Professor Daniel DeBra had measured experimentally the flutter speed of a two-dimensional wing [61]. Professor DeBra graciously offered to loan Rock's apparatus to me upon the suggestion that I would use it to measure the chordwise forces on an airfoil during oscillatory motion.

Rock's apparatus was a 2-D wing section mounted on an elastic suspension that allowed the airfoil to pitch and plunge. The airfoil could be excited by two actuators, a pitch torquer motor and a plunge motor. After studying the different ways to measure the aerodynamic forces with this apparatus, (the suspension actuator inputs, an external balance in the suspension, and/or an internal balance within the airfoil), we perceived that a balance within a new airfoil was the least expensive option that might succeed.

The design of that airfoil, the apparatus to oscillate it and the measurement of the aerodynamic forces will now be described.

4.2 EXPERIMENTAL APPARATUS

4.2.1 Wind Tunnel

The experiment was conducted in Stanford's low-speed wind tunnel. This is a closed-circuit tunnel, which operates at speeds from 18 to 60 m/s. Airspeed is controlled by a constant-speed, 16-blade fan turning at 1150 rpm (19.2 Hz). Mean turbulence level in the test section is reported to be about 0.1% [62].

The test section is a constant cross-section duct 0.457 m square and 0.91 m long. The floor is steel plate, whereas the walls and top are clear plastic. The test section is supported by four legs with castors on their ends, which allow it to be removed from the tunnel circuit. A 10 mm breather between the test section and diffuser keeps the static pressure inside near atmospheric.

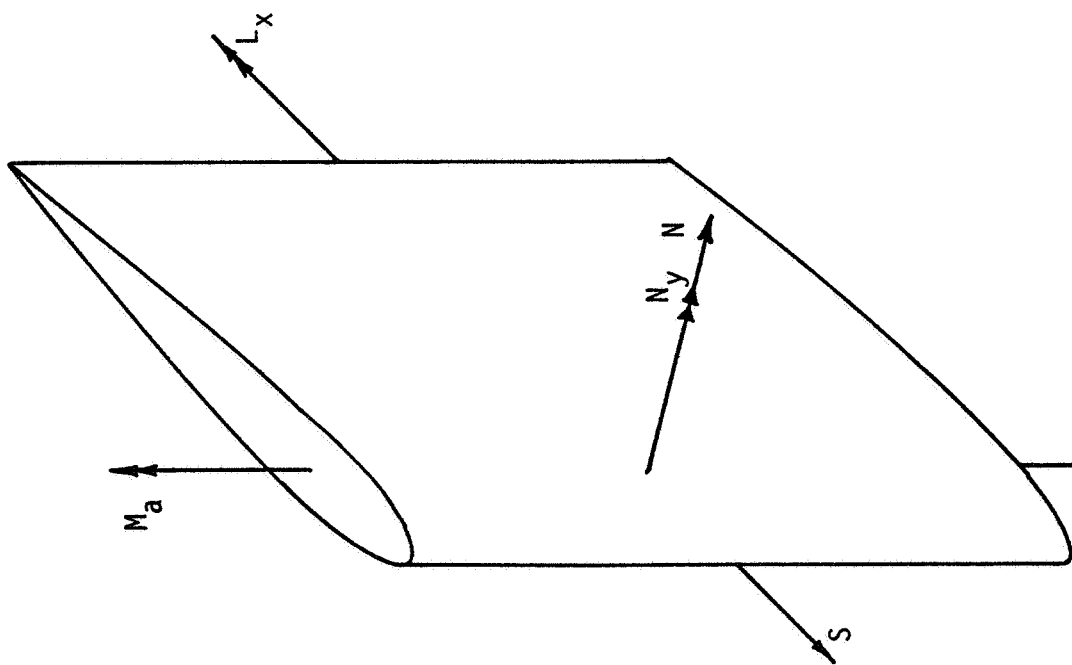
The dynamic pressure is measured with a United Sensors PDC-8-KL pitot-static tube mounted one and a half chord lengths in front of the airfoil. The pitot-static tube is connected to an oil-filled manometer that is read directly in inches of water. The reading is accurate to about 0.02 inches of water.

4.2.2 Suspension

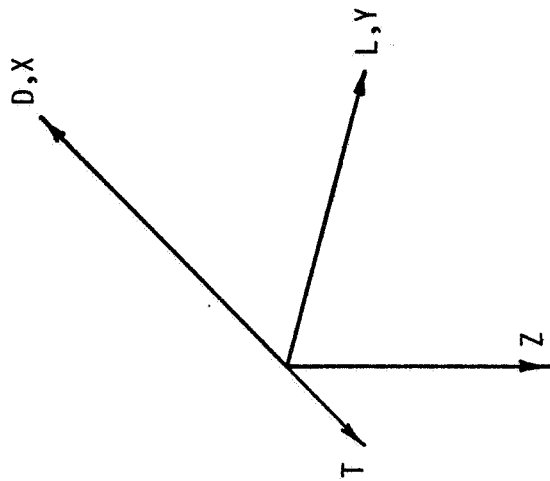
The suspension was inherited from Rock [61] without modification except for replacement of the pitch flexures and wing. All suspension components are located outside of the wind tunnel. The wing is suspended with its span parallel to the vertical to reduce gravity effects. Unfortunately, the standard correspondence between the airloads (defined by the airfoil axes) and the tunnel axes (X, Y, Z) is not retained. The force convention is diagrammed in Figure 21.

The wing is pitched about an axis 35%-chord behind its leading edge by an Aeroflex brushless motor operating through a four-bar linkage below the test section, Figure 22. All motion at the pivots is accomplished elastically through Bendix Flexpivots, Figure 23, with a combined spring rate of 212 in.-lb/rad (24. N-m/rad). The uncoupled pitch frequency is 10.4 Hz. The pitch motion is limited to ± 2.5 deg and is measured by a Kearfott R235 1A Synchro Resolver located on the top crossbeam.

Plunge actuation is by a linear motor of the type found in computer disc drives. The coil is attached to a vertical beam connecting the two crossbeams. Adjustable stops on the crossbeams limit the plunge motion up to the maximum displacement of ± 10 mm allowed by four folded-cantilever flexures, Figure 24. The plunge natural frequency is 7.5 Hz with a spring rate of 10.5 kN/m. The displacement is measured by a Schaevitz 500 HR Linear Variable Differential Transformer (LVDT). The characteristics of the pitch and plunge sensors are given in Appendix B.



AXIS FIXED TO AIRFOIL



AXIS FIXED TO WIND TUNNEL

Figure 21: Comparison of Force Convention and Tunnel Axis System.

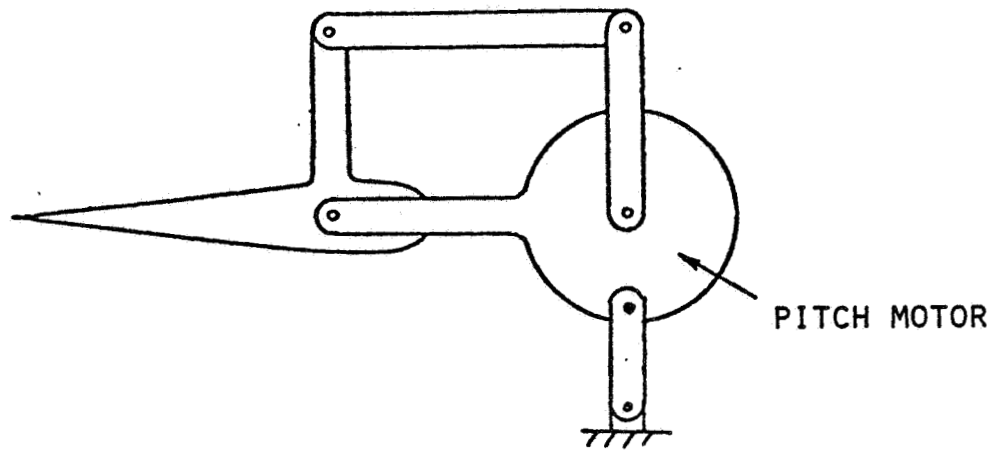


Figure 22: Four-Bar Pitch Suspension and Actuator.

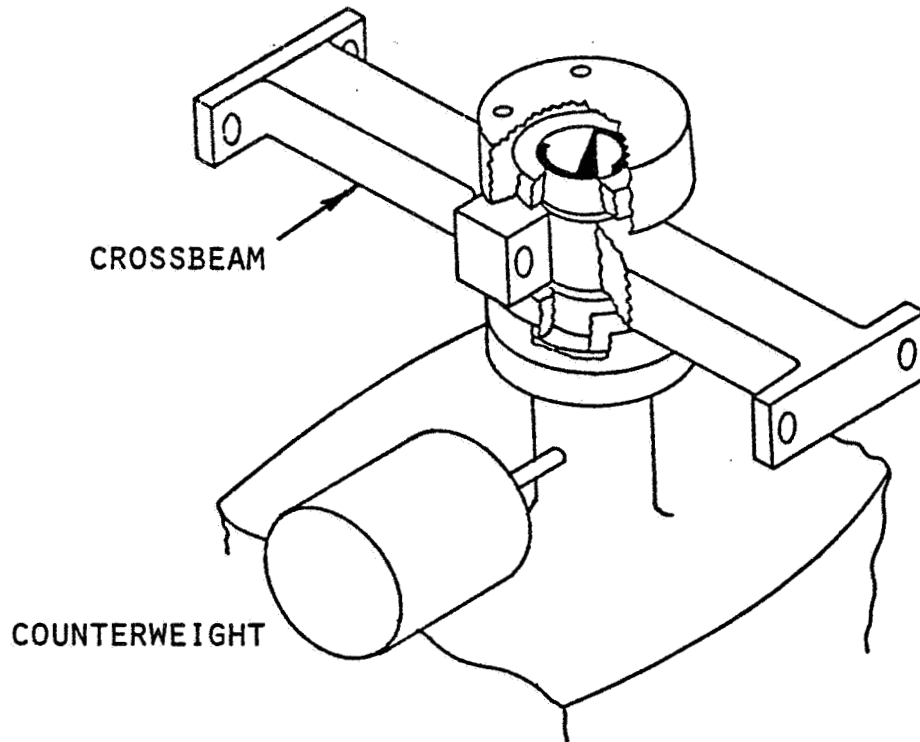


Figure 23: Detail of Flexpivot Pitch Joint.

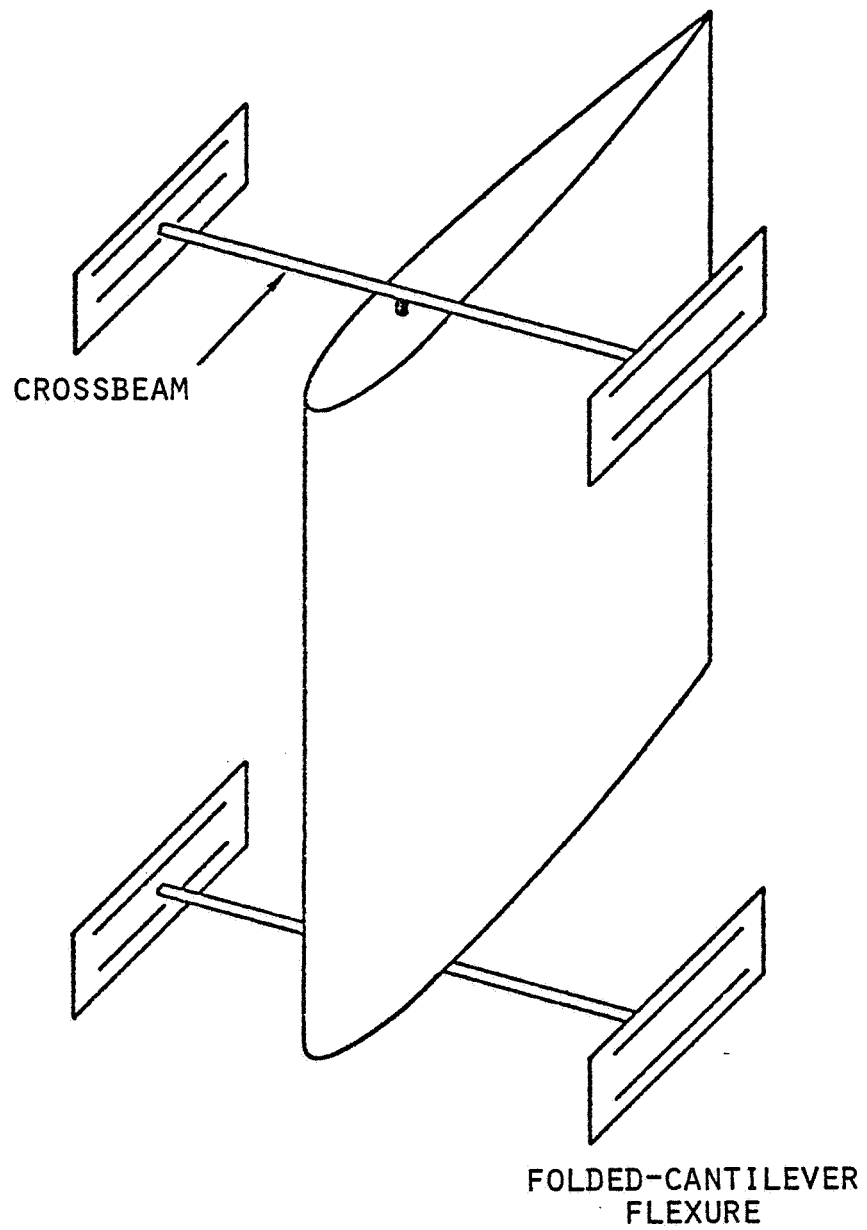


Figure 24: Arrangement of Plunge Suspension System.

The advantages of this type of suspension are: it is linear, (to within 2% over ± 6 mm), it has low damping (0.5% critical), and most importantly for this application, it is quiet. That is, except for spurious suction signals due to fore and aft excursions during plunge motion there is little noise in the output of the airfoil balance, due to motion of the wing, other than the inertia forces.

The suspension system is permanently attached to the portable test section. When installed in the tunnel, the test section is placed on foam blocks imbedded in sand to reduce vibration. Further, it is not bolted to the inlet or diffuser, which conduct fan noise. The inlet section gap is sealed by foam rubber. The response of the test section to airfoil pitching is negligible, but 67 kg must be added to the test section so that during plunge tests its transverse reaction is less than 5% of the motion of the airfoil. Axial tilting of the section is less than one milliradian. The plunge motion is measured relative to inertial space by mounting the LVDT case in an isolation frame separate from the test section.

4.2.3 Wing and Internal Balance

The central structure of the wing, Figure 25, consists of a spar and two end fittings, which fasten to the flexpivots on the upper and lower crossbeams of the suspension. Near the connection with the suspension and external to the wind tunnel, adjustable counterweights project forward from each end fitting. The counterweights place the center of gravity of the wing at the pitch axis, thus providing an acceptably high

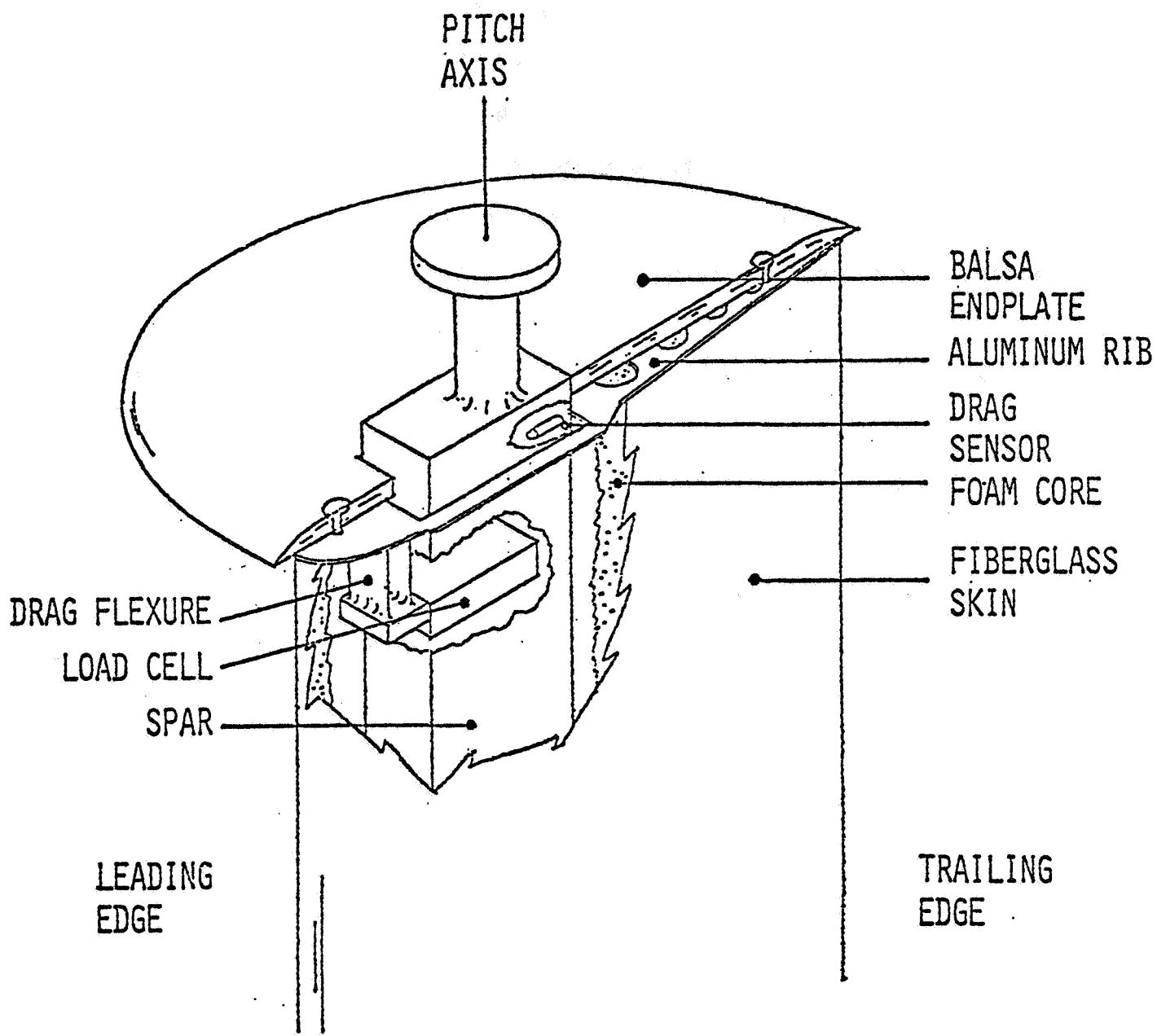


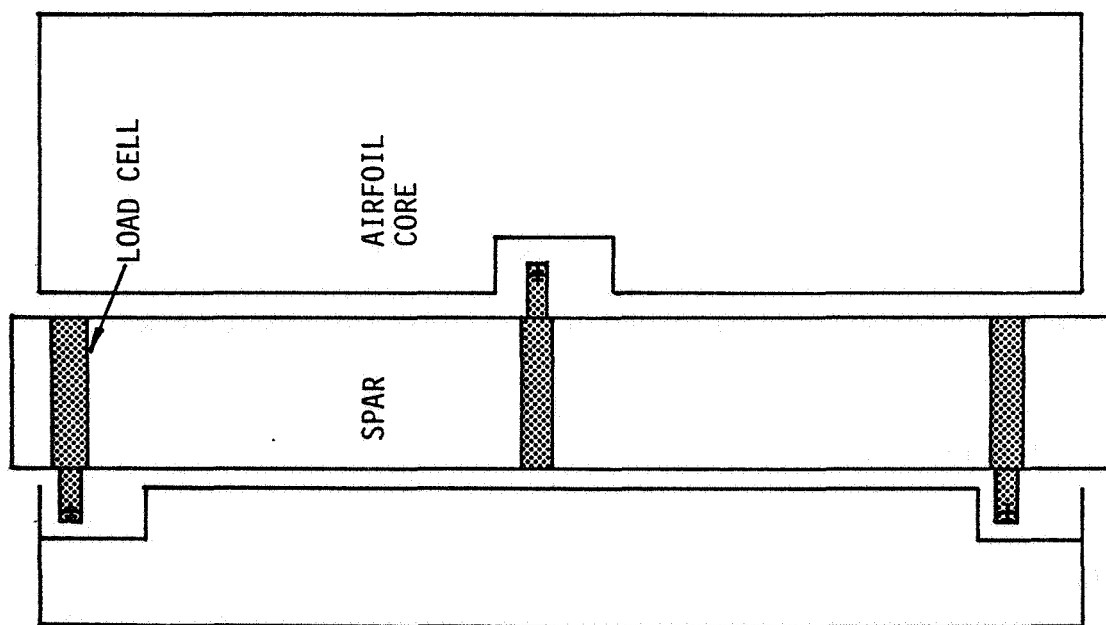
Figure 25: Internal Construction of Wing.

flutter speed (40 m/sec) and minimum coupling between the pitch and plunge motion for simple controllability. The neck of the endfitting passes through the wind tunnel wall and fastens to the spar.

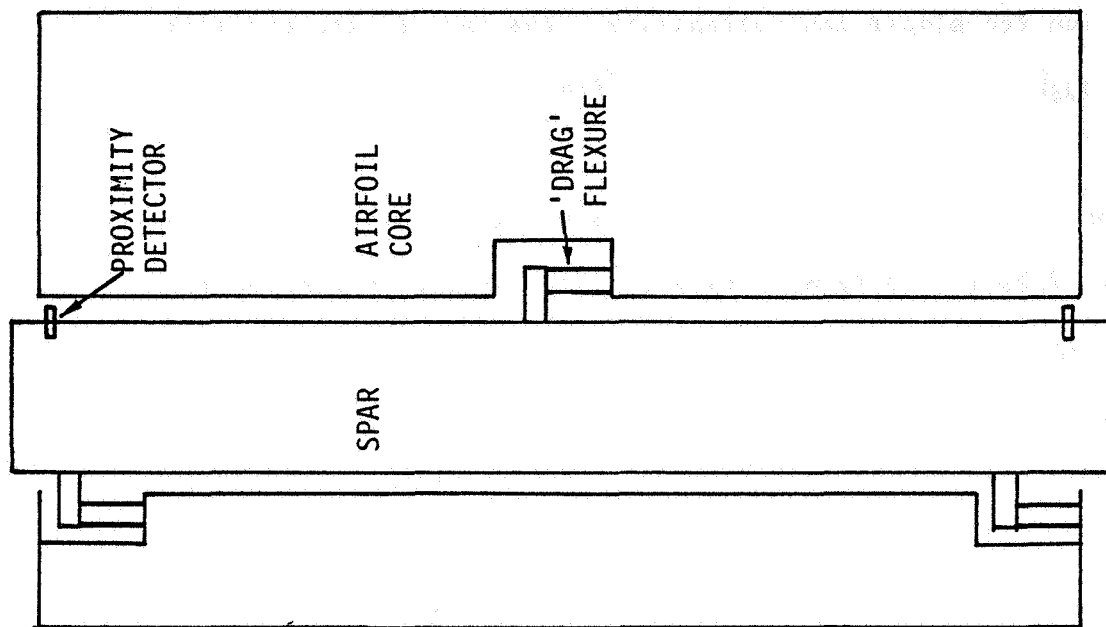
The spar is made of 0.040 in. aluminum sheet, electron-beam welded into a box 17.75 in. (0.45 m) long with a rectangular cross-section. Inside the spar are three Celesco Transducer Products MB101 load cells. Two project forward of the spar at each end of the wing and one to the rear in the center of the wing. The load cells are most sensitive to forces normal to the airfoil chord. The intent of this design was to produce as close to a statically-determinant three-point suspension as possible, while eliminating any hysteresis from pinned joints. The normal force suspension is diagrammed in Figure 26a.

Connecting the load cells to the airfoil itself are parallelogram shaped flexures. The flexures permit the airfoil to displace chordwise in response to suction loads, but are stiff in other directions. This chordwise displacement is measured by two Kaman Measuring Systems KD-2300-.5SU proximity detectors, ('drag sensor' in Figure 25), located in the spar, adjacent to targets on each of the airfoil ribs. Each flexure has a measured spring rate of 49 lb/in. (8600 N/m) for a total spring rate of 147 lb/in. (25.8 kN/m). The chordwise suspension is diagrammed in Figure 26b.

More information on the balance sensors is provided in Appendix B.



a)



b)

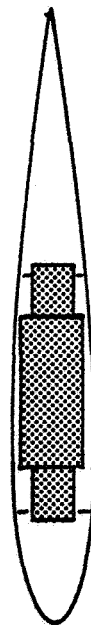
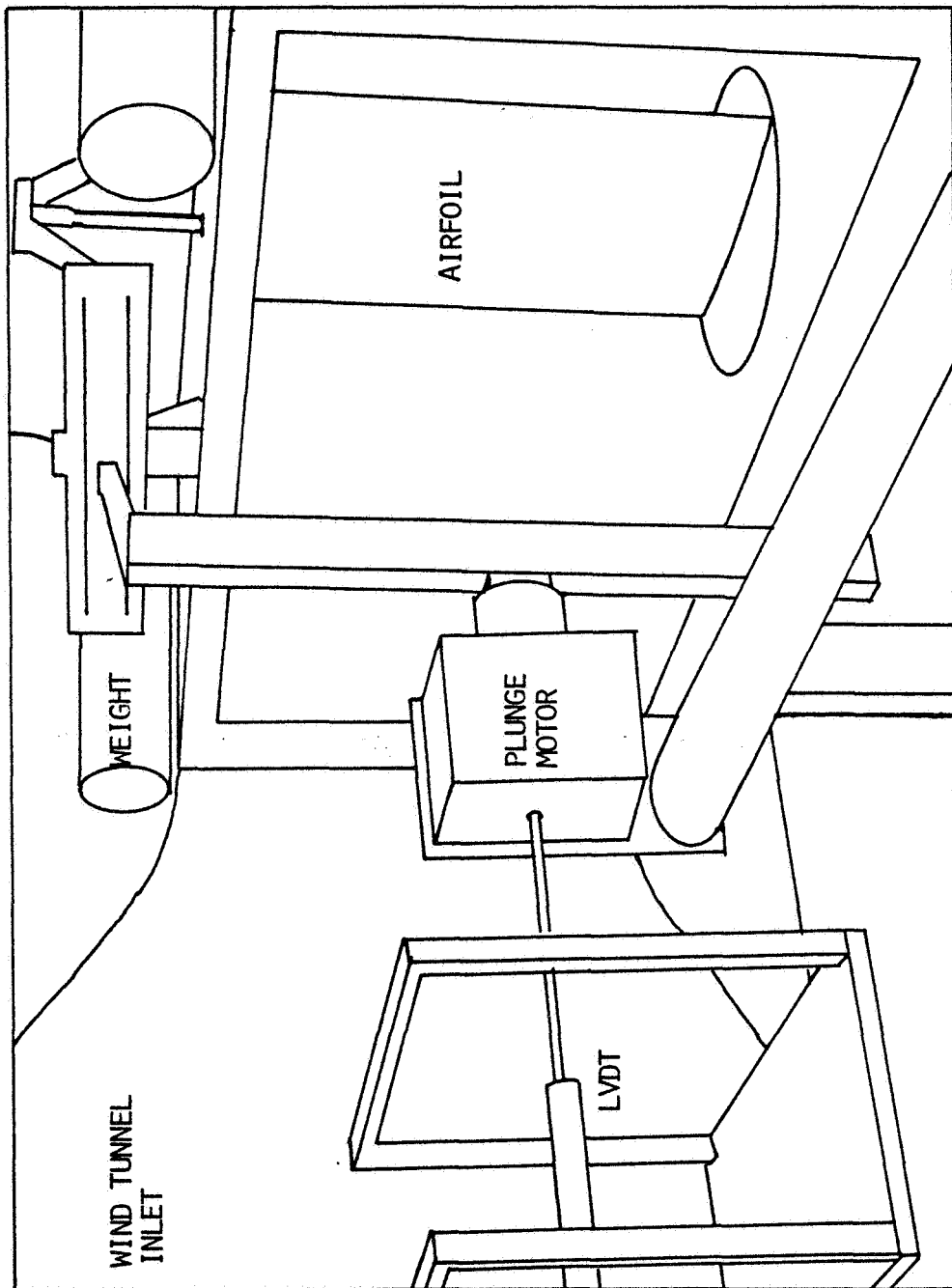


Figure 26: Sketches of the Normal and Chordwise Balance Suspension.

The airfoil is made from a single block of styrene foam which has been cut to form by a hot wire and covered with epoxy/fiberglass-cloth skin. It is then hollowed out to accept the spar and flexures. The forward flexures are screwed to aluminum ribs glued to the core and skin. The rear flexure is in an enclosure which is epoxied to the skin. Finally, laminated-balsa endplates are attached to the end of the wing. For the majority of tests they were mounted on the airfoil ribs, but later the endplates were attached to the spar, with a gap of 0.7 mm between the endplate and airfoil. A clay fillet on the endplate helped to seal the gap. In the first configuration the flow was comparatively free of gap losses. The second configuration provided data free of the inertial and aerodynamic loads on the endplates.

The airfoil is an NACA 0015 profile with a chord of 238 mm and a span of 417 mm. This corresponds to a tunnel height to chord ratio (H/b) of slightly less than 2. A glass-bead boundary-layer transition strip was applied at 10% of the chord in accordance with instructions in Reference 82 for ensuring transition to turbulent flow. The airfoil weighs 595 gm with endplates and 454 gm without. The circular endplates have a diameter of 254 mm and are centered on the midchord of the airfoil, following the guidelines of Reference 83. They are 7 mm thick except near the edge, which tapers to a 30 degree sharp angle. A photograph of the airfoil being tested is shown in Figure 27. Other pertinent physical parameters of the wing and airfoil are presented in Figure 28 and Table 2.



Key to Figure 27.

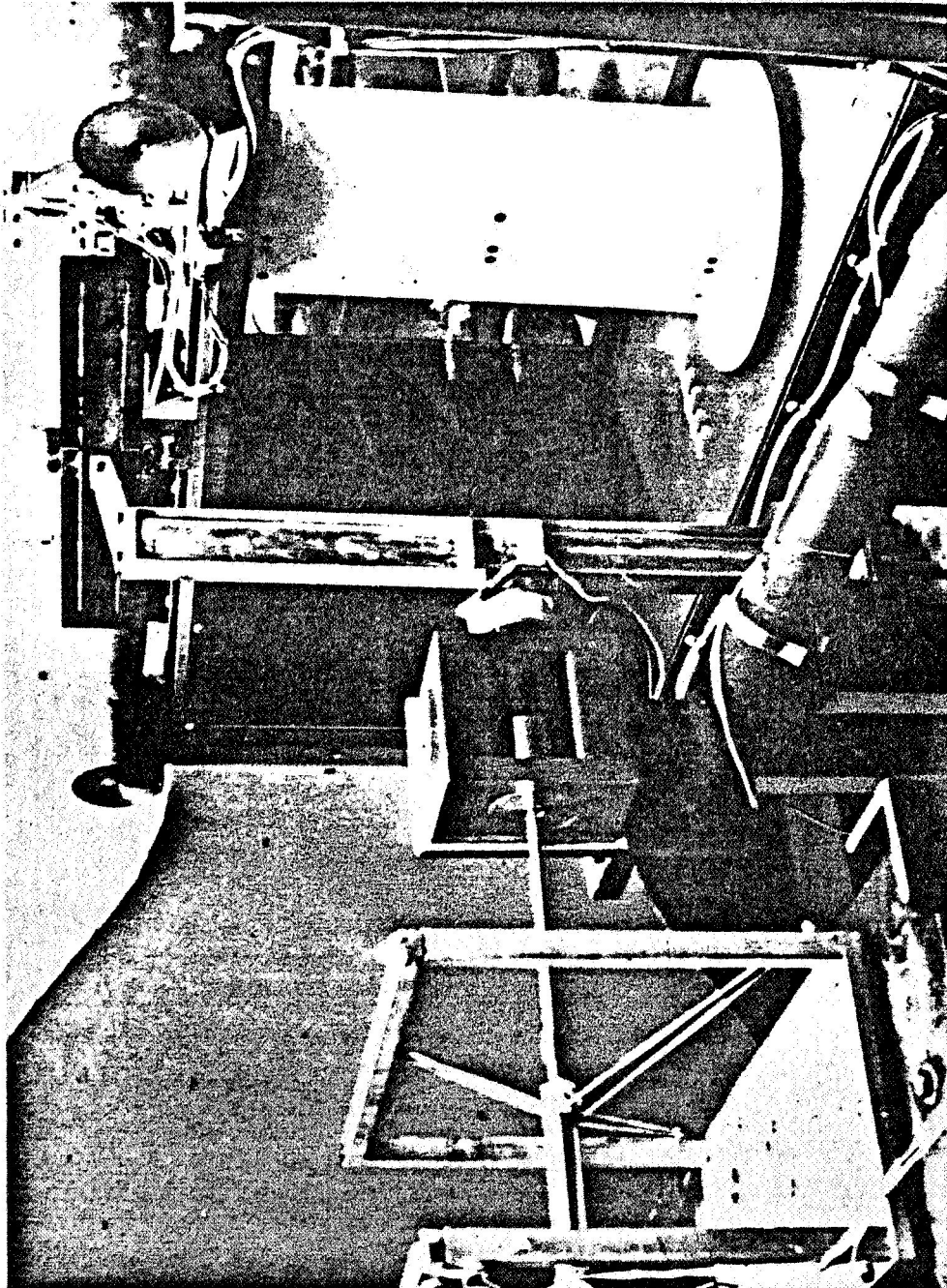


Figure 27: Airfoil Mounted in Wind Tunnel.

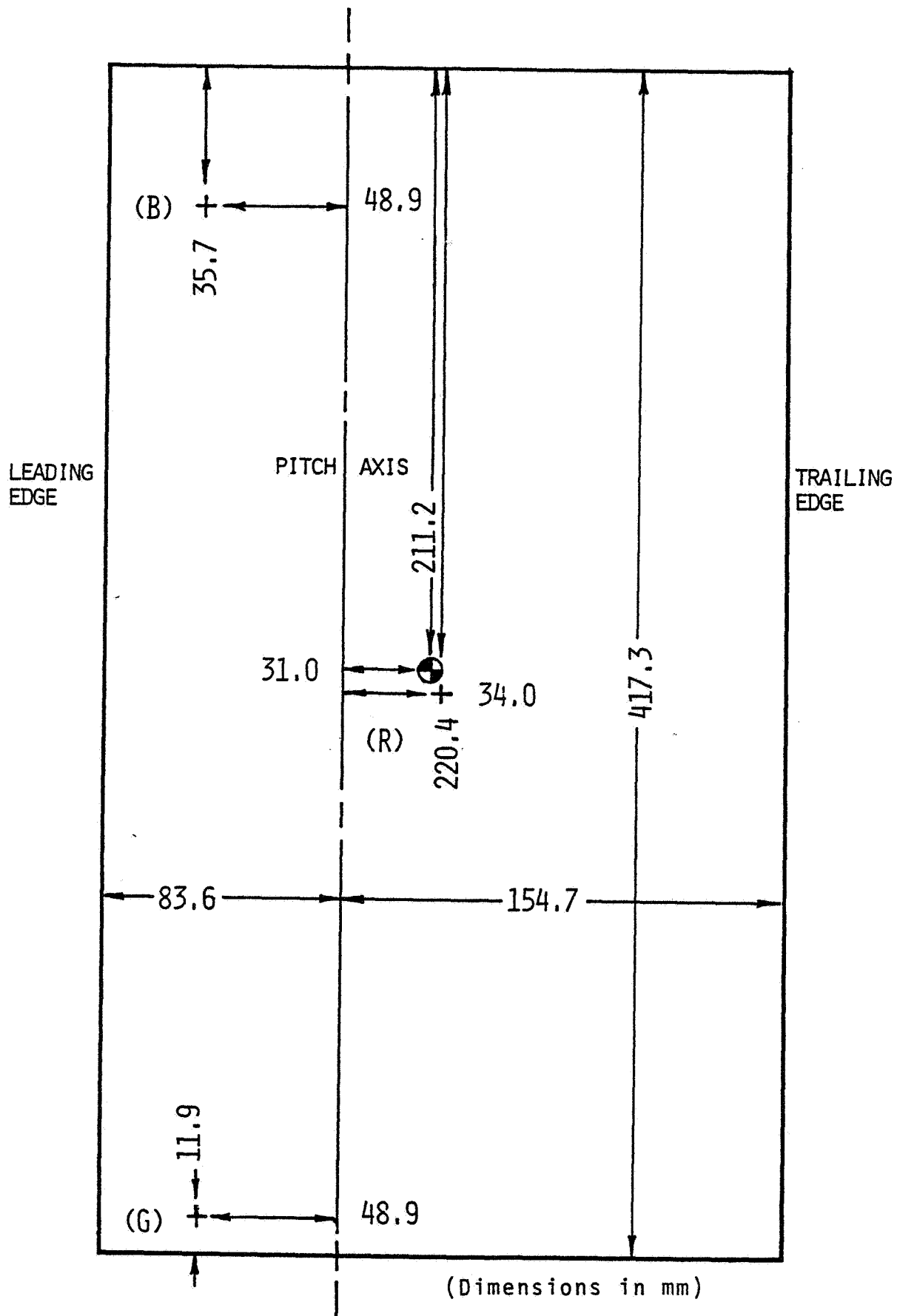


Figure 28: Dimensions of Wing.

TABLE 2
Wing Parameters
(Endplates on Airfoil)

Item	Value	Accuracy
Balance supported weight	0.595 kg	±0.2%
Chord	0.238 m	±0.2%
Span	0.417 m	±0.2%
Area	0.0992 m ²	±0.3%
H/b	1.92	±1.0%
Pitch axis	35.0% chord	±0.5% c
Center of gravity	48.1% chord	±0.5% c
Suction balance frequency	31.0 Hz	±3.0%
Operating frequency	7.5 Hz	±1.0%

Before proceeding further, it should be noted that a reference to the airfoil means that part of the structure whose loads are being monitored (the foam core, skin, ribs and sometimes endplates); whereas the wing means the entire structure which pitches and plunges, i.e. the airfoil and the spar, counterweights and sometimes suspension. Also, a color coding system is used to differentiate between the sensors. With the wing suspended vertically, the uppermost sensors are the blue load cell (B) and proximity detector (Bd), the center load cell is red (R) and the lower sensors are the green load cell (G) and proximity detector (Gd).

4.3 AIRFOIL BALANCE CALIBRATION

The expected ranges of the suction, normal force and moment encountered by the wing were:

S: -3.0 to 2.5 N

N: -15.0 to 15.0 N

M_a: -0.4 to 0.4 N-m

Experience in the tunnel showed that, at no time, did a positive suction force occur.

The airfoil balance was calibrated in the test section, Figure 29. The acrylic sides were removed and solid 0.015 in. steel wires were attached to the airfoil leading and trailing edges with strapping tape. The wires were led horizontally over bell cranks to pans which held the weights. The bell cranks consisted of two lengths of balsa wood at right angles to each other with a knife edge at their junction. The knife edge was placed into an angle at the side or end of the test section. The wires were guided through the slots of flat-head screws tapped into the ends of the wood. The bell cranks were made in various lengths as needed.

The load fixtures were used in pairs, Figure 29, one exerting a force opposite to the other. To calibrate the output with respect to any force, both pans of a pair were loaded with slightly more than the maximum negative load desired, so that little net force on the wing was present. Weights were then added to one pan, representing positive load. After returning to zero, weight was removed from the same pan,

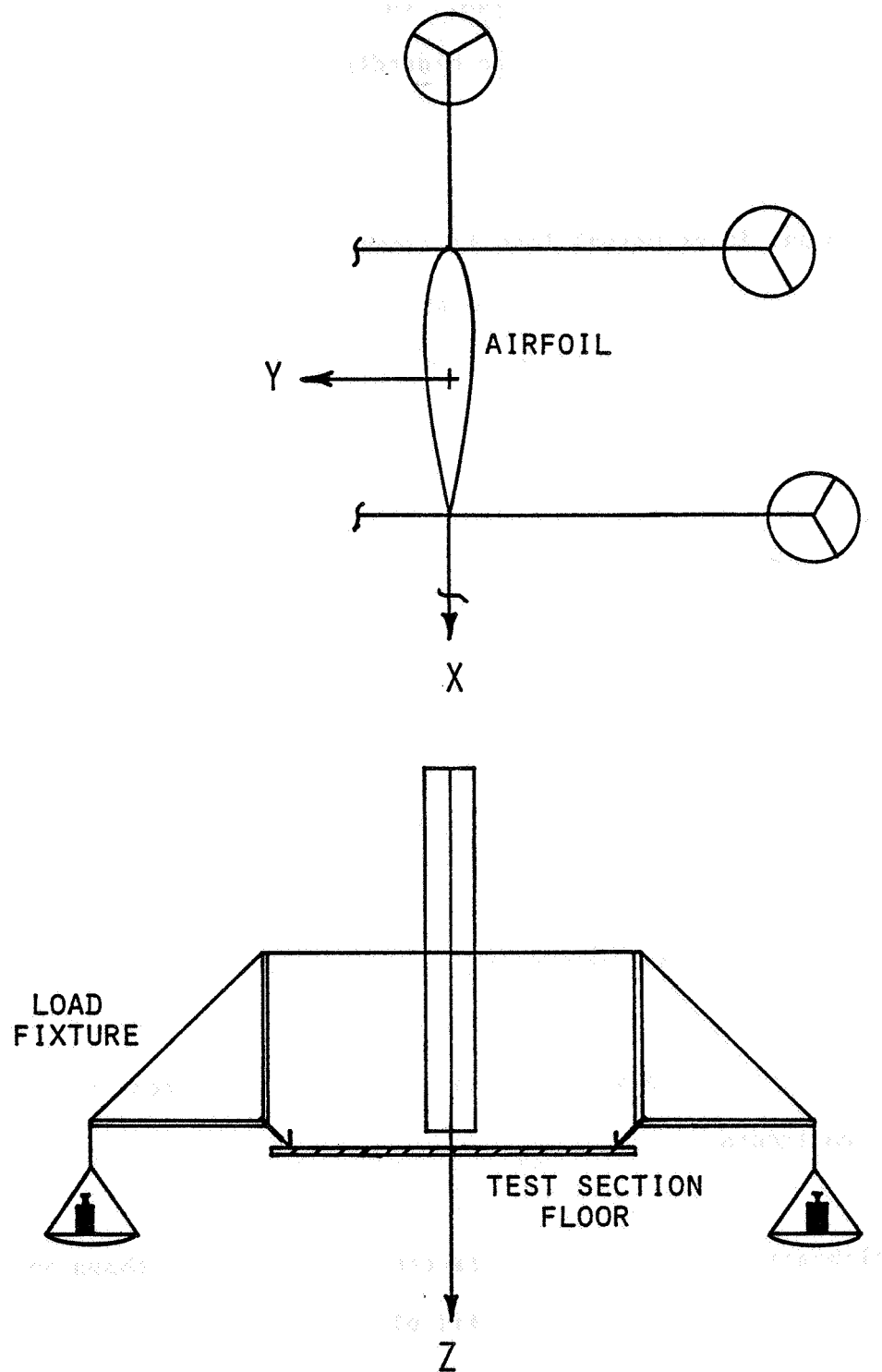


Figure 29: Calibration of Airfoil Balance.

representing negative load, until the pan was almost empty. The applied force was returned to zero by adding weight to the pan until it again equaled the weight in the other pan. This procedure ensures that an exactly negative force is produced regardless of any misalignment between the two fixtures.

Two drag and three normal load fixtures were used to calibrate the balance outputs. Most of the calibration points involved a combination of forces. Two normal loads and one drag load were the maximum simultaneous number. Usually a drag sequence (from zero to plus maximum through zero to minus maximum back to zero) was recorded with no normal load. Then the normal loads were increased to a high lift or high moment condition and another drag sequence recorded.

The data were recorded on an eight channel digital tape recorder using 12-bit words. At each calibration point at least 16 samples were taken at 100 msec intervals. If no large variations were present in the sample, a simple average was used. The few samples with sizable variations were inspected, and individual decisions were made as to their useability. Because of the word size, a significant amount of the non-linearity present in the proximity sensor output was expected to be from quantization errors.

The calibration matrix from the second calibration is shown in Table 3. This matrix is a least squares fit of 290 data points.

TABLE 3					
Balance Calibration Matrix					
	F_s (N/V)	F_n (N/V)	M (mN-m/V)	L_x (mN-m/V)	N_y (mN-m/V)
Gd:	-3.582	-0.470	-79.1	-36.6	-1614.
Bd:	-1.631	0.235	38.3	16.6	864.
G :	-0.005	1.519	135.4	-305.1	-2.
R :	0.003	1.529	-62.7	-1.6	0.
B :	-0.001	1.527	138.0	296.0	4.

This matrix relates the sensor outputs, (δG_d , δB_d , etc.), to the measured forces (F_s , F_n , etc.), by the equation,

$$[\delta G_d \ \delta B_d \ \delta G \ \delta R \ \delta B] C = [F_s \ F_n \ M \ L_x \ N_y] \quad (4.1)$$

where C is the calibration matrix.

Before assembling the wing, the gains of the load cells were at the same level, while the outputs of the proximity sensors were at a ratio of two to one. This fact is reflected in the almost equal matrix elements for the load cells in the normal force column and the two to one ratio of the proximity detector outputs in the suction column. A satisfactory symmetry in the load cell outputs appears in the pitching moment (M) and rolling moment (L_x) columns.

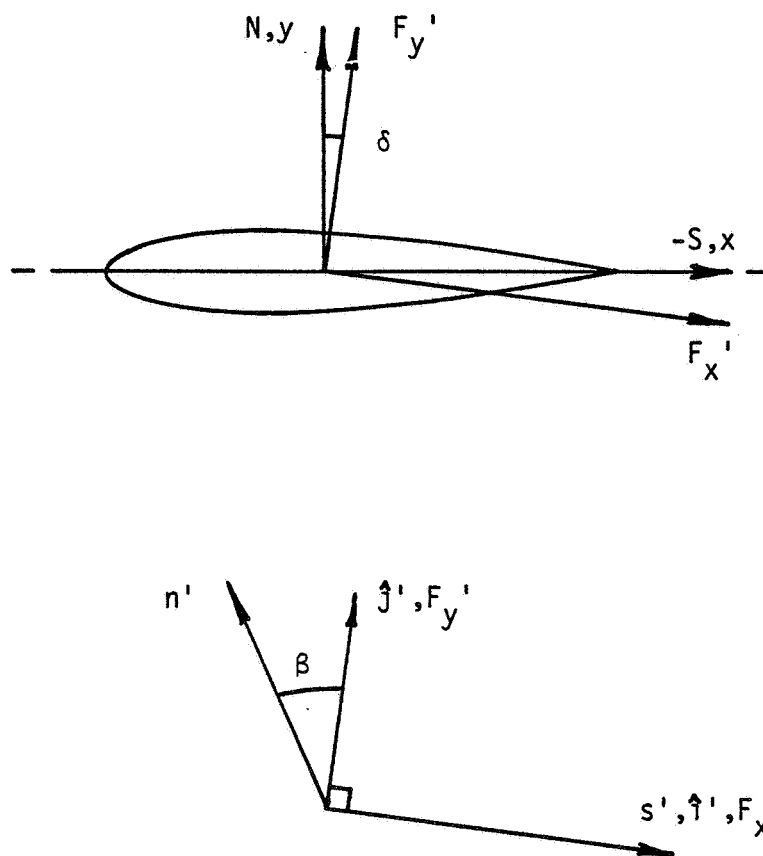
The cross-talk between the outputs is very small, as evidenced by the load cell elements in the suction column. The drag elements in the F_n and M columns are due to a screw type of misalignment in which the

airfoil tends to yaw about the Y axis in response to a normal force. Since the proximity detector outputs are nearly in phase and in the ratio two to one, their contribution or cross-talk to F_n , M and L_x are equal to the first row plus twice the second row. Inspection shows this summed contribution is very small.

The possibility that a pitching moment would distort the balance and produce a suction signal by rotating the suction axis into the direction of the applied normal force was also explored. This spurious signal would be proportional to the product of the normal force and the moment about the elastic axis of the balance. By curve-fitting the data to this variable, it was apparent that, under the worst conditions, a negligible signal was produced during the tests.

Another task in calibrating the airfoil balance is to establish the orientation of the sensitive axes of the balance. The procedure to do this begins by assuming arbitrary alignments between the lines of maximum sensor output and the chord, as shown in Figure 30. Before calibrating, the load fixtures which apply normal loads are adjusted until adding fifty percent of the maximum load produces no output at the proximity detectors. Because the applied suction loads are much smaller than the normal loads, it is sufficient to align the suction load fixtures with the chord.

If (s', n') are unit vectors along the sensitive axes of the proximity detectors and load cells, respectively, and (s, n) are their reciprocal base vectors (see Ref. 84), then the applied load is



s' : Most-sensitive axis of proximity detectors
 n' : Most-sensitive axis of load cells

Figure 30: Axis System of Balance.

$$F_a = F_{x'} \hat{i}' + F_{y'} \hat{j}'. \quad (4.2)$$

Let us pick (\hat{i}', \hat{j}') so that \hat{i}' is parallel to s' , so:

$$s' = \hat{i}' \quad (4.3)$$

$$n' = -\sin\beta \hat{i}' + \cos\beta \hat{j}'. \quad (4.4)$$

The load applied as described above may also be written as

$$F_a = (F \cdot s') \hat{i}' + (F \cdot n') \hat{j}'. \quad (4.5)$$

In terms of the reciprocal base vectors the measured load is:

$$F_m = F_s s + F_n n. \quad (4.6)$$

$$F_m = (F \cdot s') s + (F \cdot n') n. \quad (4.7)$$

The reciprocal base vectors are

$$n = \frac{\hat{j}'}{\cos\beta} \quad (4.8)$$

and

$$s = \hat{i}' + \tan\beta \hat{j}'. \quad (4.9)$$

Since the loads, (4.2) and (4.7), are equal

$$\begin{Bmatrix} F_{x'} \\ F_{y'} \end{Bmatrix} = \begin{bmatrix} 1 & 0 \\ \tan\beta & 1 \end{bmatrix} \begin{Bmatrix} F \cdot s' \\ F \cdot n' \end{Bmatrix}. \quad (4.10)$$

Now to find the suction and normal forces we must transform from the sensitive axes to the airfoil axes, as follows:

$$\begin{aligned} \begin{Bmatrix} -S \\ N \end{Bmatrix} &= \begin{bmatrix} \cos\delta & \sin\delta \\ -\sin\delta & \cos\delta \end{bmatrix} \begin{Bmatrix} F_{x'} \\ F_{y'} \end{Bmatrix} \\ &= \begin{bmatrix} \cos\delta & \sin\delta \\ -\sin\delta & \cos\delta \end{bmatrix} \begin{bmatrix} 1 & 0 \\ \tan\beta & 1 \end{bmatrix} \begin{Bmatrix} F_s \\ F_n \end{Bmatrix} \end{aligned} \quad (4.11)$$

Considering that δ and β are less than 0.01 radian (actually δ is 0.4 deg) and F_s/qA is less than 0.1, then for the present accuracy requirements

$$\begin{Bmatrix} -S \\ N \end{Bmatrix} = \begin{bmatrix} 1 & \sin\delta \\ 0 & 1 \end{bmatrix} \begin{Bmatrix} F_s \\ F_n \end{Bmatrix} \quad (4.12)$$

The measurement of delta will be considered later.

The nonlinearities and the standard deviations [85] of the calibration points are:

	Nonlinearity	Std. Dev.
Suction Force	0.4%	0.4%
Normal Force	0.8%	0.2%
Pitching Moment	1.5%	0.6%

Because of the 12-bit word size, quantization contributes approximately 0.1% nonlinearity and 0.1% deviation to the suction measurements. The repeatability of three calibrations was excellent; the drag calculated by each agreed within 0.5%.

4.4 WING CONTROL

Wing control is entirely open loop. As shown in Figure 31, a signal generator provides a sine wave at 7.5 Hz. This signal is conditioned by an Electronic Associates TR48-1 analog computer into two signals of the necessary phase and amplitude and fed to the actuator current amplifiers to drive the wing as desired. It was originally desired to drive the wing at plunge amplitudes as high as 10 mm. However, above 6 mm contact between the plunge actuator coil and core often occurs and introduces higher harmonics. So the plunge tests were conducted below amplitudes of 6 mm. The second harmonic content of the displacements were spot checked and were never found to exceed 1 percent of the first harmonic during any test.

The drive frequency corresponds with the natural frequency of the plunge system because the plunge actuator could not drive the wing at large enough displacements away from resonance. No phase instability was noticed. To vary the reduced frequency, the speed of the wind tunnel was changed. The minimum speed (maximum k) possible was 19 m/sec ($k=0.3$). The maximum speed was limited by the controllability of the model as it neared its flutter speed of 40 m/sec. The Reynolds number range was 0.3 to 0.6 million. This, of course, introduces Reynolds number effects in the data. To minimize these effects, boundary-layer turbulence is artificially induced by glass beads on the airfoil.

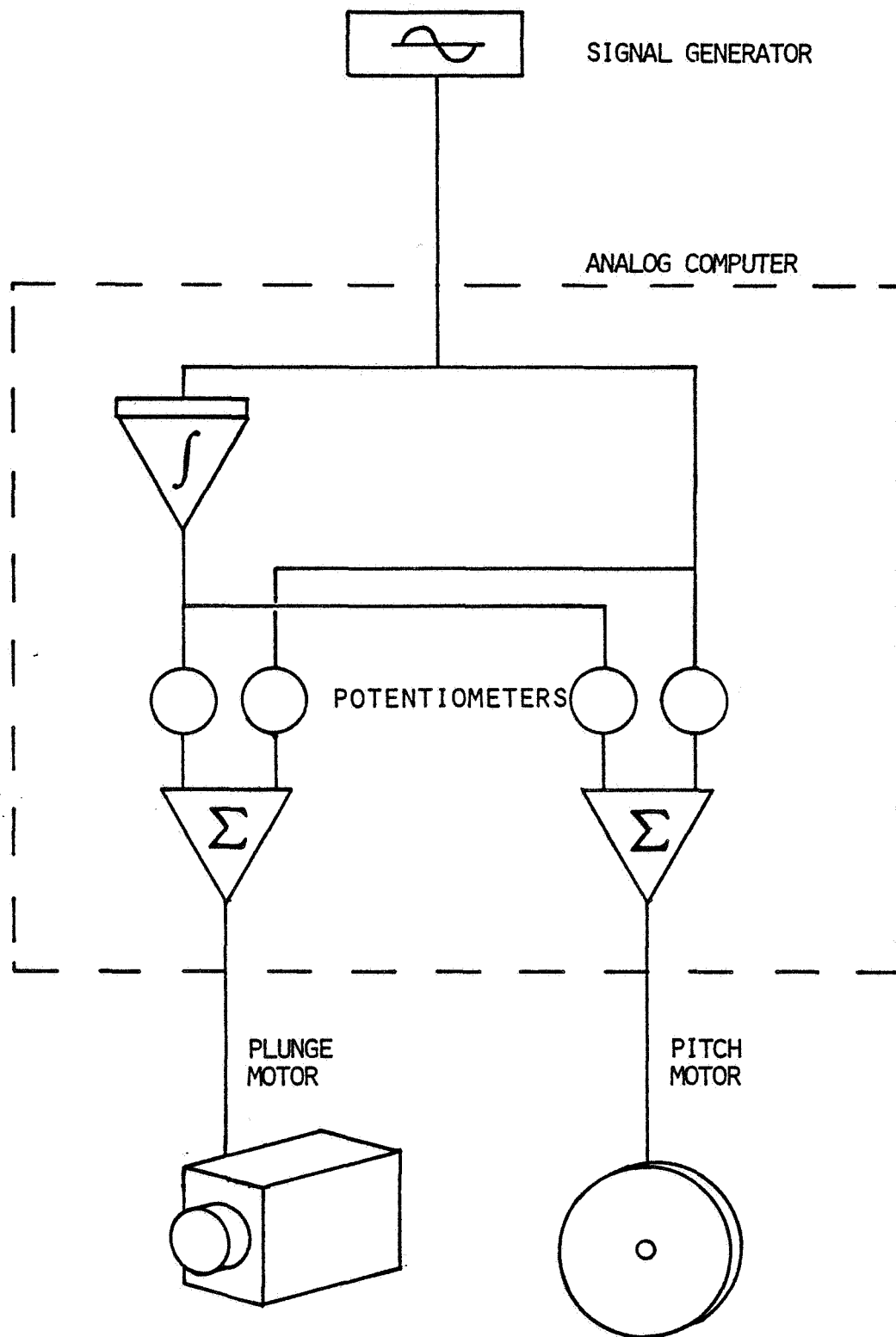


Figure 31: Schematic of Suspension Actuator Control.

4.5 SIGNAL ACQUISITION

As shown in Figure 32, the sensor outputs were routed through low-pass filters. The load cell outputs were also routed through the analog computer, for reasons described in the Tares section. The signals were then analyzed by a Princeton Applied Research Model 5204 Lock-in Analyzer. The Model 5204 consists of two phase-sensitive detectors, synchronized by the sine-wave generator, which detect the in-phase and quadrature components of an analog signal. The fundamental harmonic of the output from each sensor was recorded and, in the case of the proximity detectors, the second harmonic output was also measured. For mean values, the sensor outputs were connected to a very low-pass filter.

The signals are corrected for the presence of the filters, including the mechanical filtering which occurs because the ratio of the suction-force frequency (15 Hz) to the suction-balance frequency (35 Hz) is significant. Physical characteristics of the filters in the network are described in Table 4. A photograph of the experimental electronics is presented in Figure 33.

DATA ACQUISITION

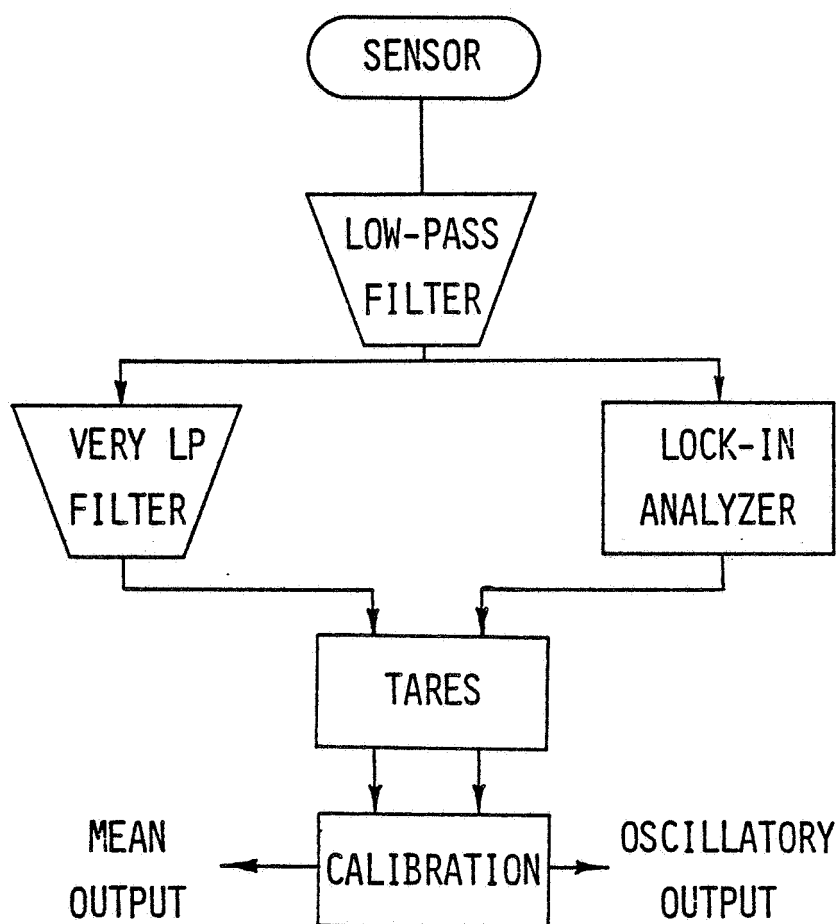
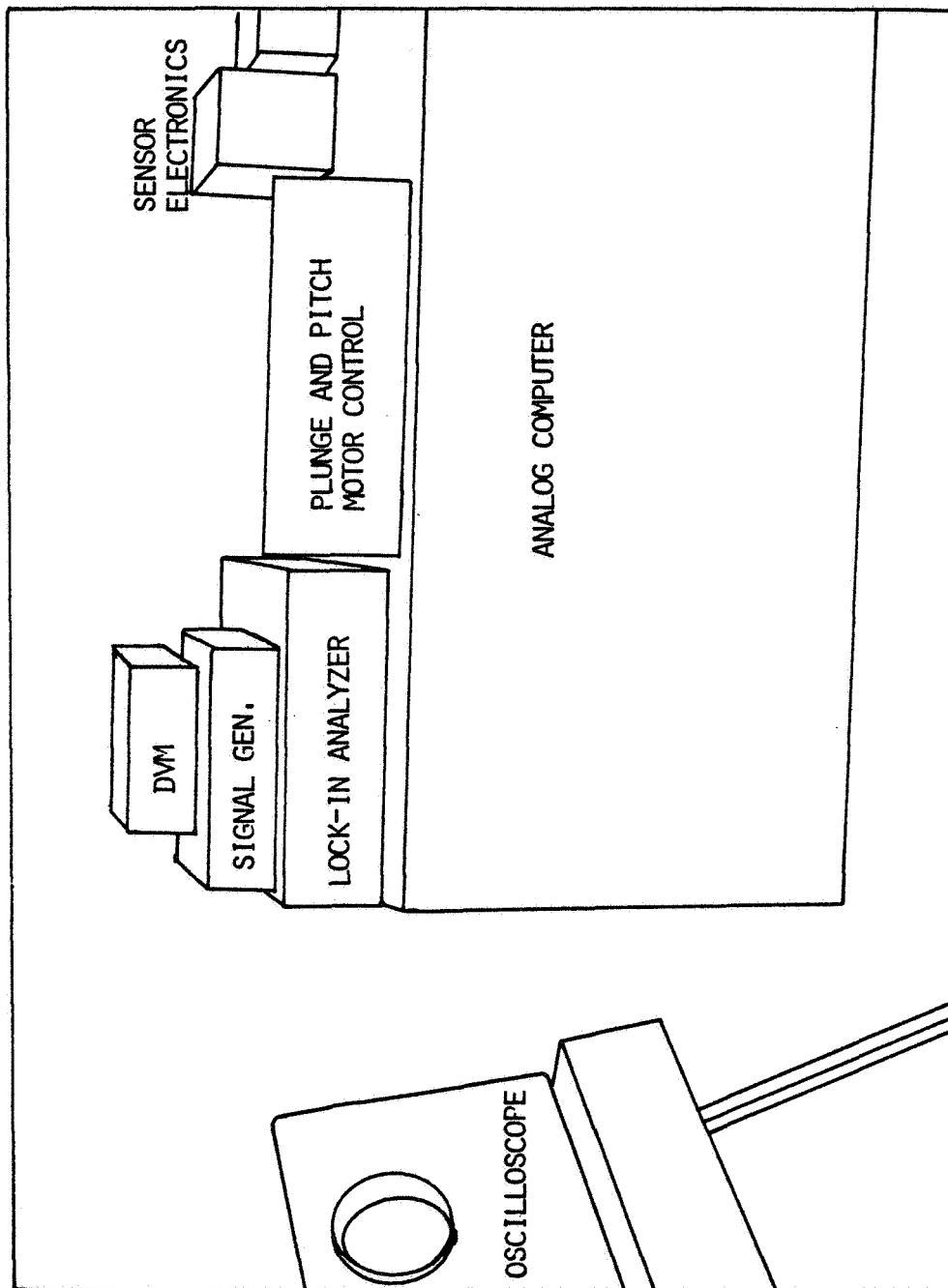


Figure 32: Flow Chart of Data Reduction.



Key to Figure 33.

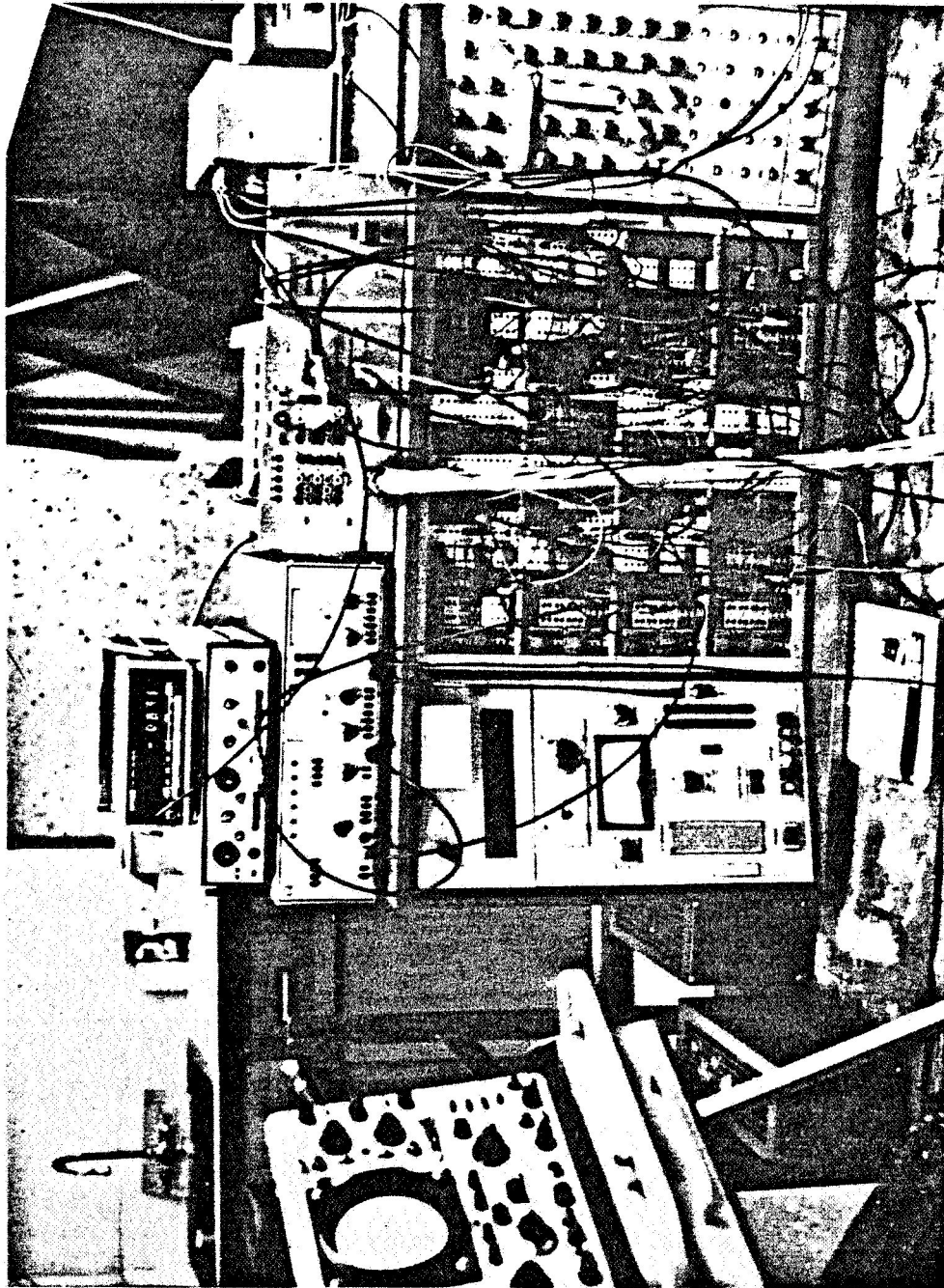


Figure 33: Experimental Electronic Equipment.

TABLE 4

Filter Characteristics

(A) Three-pole Butterworth

Channel	Cutoff Frequency (Hz)	Measured Amplitude Ratio/Phase (deg) at	
		7.5 Hz	15 Hz
a	160	0.999 -5.4	- -
b	160	1.000 -5.4	- -
gd	100	0.997 -8.7	0.998 -16.9
bd	100	0.993 -8.7	0.995 -17.0
g	100	0.999 -8.7	- -
n	100	0.999 -8.8	- -
B	100	0.995 -8.7	- -

Accuracy: Amplitude Ratio ~ 0.2%; Phase ~ 0.2 deg

4.6 TARES

The raw analyzed signals are due to aerodynamic forces, inertia forces, elastic tares and noise.

Figure 34 shows the 1-Hz bandwidth noise spectra for the outputs of

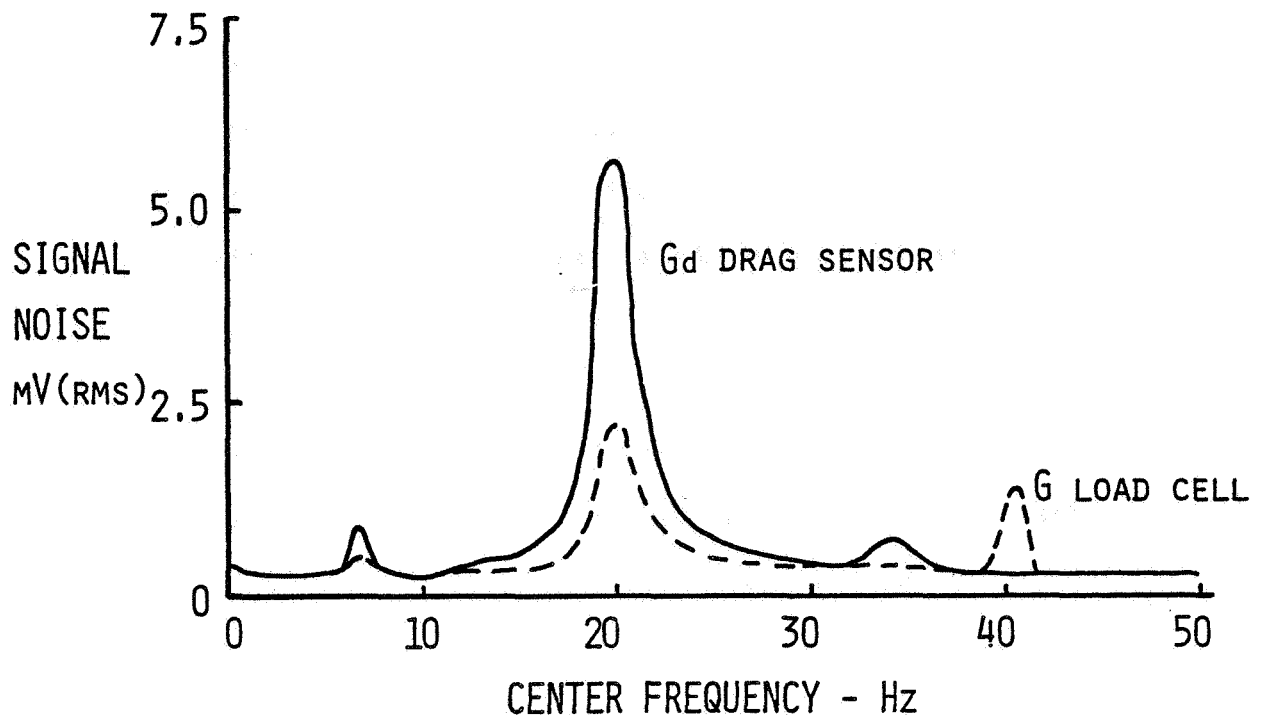


Figure 34: One-Hz Bandwidth Noise Spectra of Sensor Outputs, $q=0.9''$ water.

the G load cell and the Gd proximity detector. The airfoil configuration is with the endplates on the spar and the tunnel operating at a dynamic pressure of 0.9 inches of water. The largest peak (19.5 Hz) is at the fundamental fan frequency. Other peaks that show up are the plunge natural frequency (7.5 Hz), the suction-balance frequency (35 Hz) and the wing differential plunge frequency (41 Hz). Except for the unavoidable plunge resonance, the frequencies at which the data are collected, 7.5 and 15 Hz, are quiet. The noise in the analyzed signal is negligible because the effective bandwidth of the 5204 Analyzer can be made as low as 0.01 Hz.

Signals due to inertia forces are obvious in the case of the load cells but appear also in the suction sensors' output. The latter result

from a nonzero pitch angle coupled with plunge acceleration or centripetal acceleration of the offset airfoil c.g. during pitch motions. The inertia tares were easily measured by oscillating the wing in still air. The mass due to the air surrounding the oscillating wing was eliminated by purging the test section with Helium until the signals stabilized. The added mass in pure Helium is 10% of that in air. Assuming that at least 90% of the air was replaced by Helium, the measured added mass in plunge was 28 ± 7 gm, compared to a calculated value of 24 gm. The measured and calculated masses of the wing of 595 gm agreed within 1 percent. It is also significant that the phase angles indicate very little aerodynamic damping. Graphs of the pitch and plunge tares for the airfoil with endplates are shown in Appendix C.

Subtracting the inertia tares from the signals before analyzing them was first attempted by adding signals proportional to the displacement by means of the analog computer. As long as the displacement is sinusoidal and at the reference frequency, this is similar to the inertia subtraction used by Hien [25]. However, the inertia tares were found to be quite linear, and the analyzer was capable of detecting the aerodynamic signals in the presence of the inertia signals. Therefore, upon considering the nonlinearities added by the extra signals, this method of tare subtraction was abandoned. The airfoil balance was recalibrated with the load-cell outputs routed through the analog computer and this arrangement was kept. The calibration obtained this way was consistent with the earlier calibration when due consideration is given to the gains in the analog computer.

The elastic tares result when the torque required to pitch the airfoil twists the spar and produces apparent forces. These are small (<5% of output) but significant. Graphs of the elastic tares are also included in Appendix C.

4.7 WIND TUNNEL CORRECTIONS

The purpose of wind-tunnel corrections, as they are ordinarily applied, is to infer free flight experience from wind-tunnel data. That is not a requirement for the present research. Instead, the purpose of Timman's work and the panel method theory is to predict the forces on the airfoil while it is in the tunnel.

The three corrections suggested by Reference 86 that should be applied to wind-tunnel data are: buoyancy, blockage and streamline curvature.

Buoyancy is produced from a gradient in the static pressure along the test section and streamline 'squeezing', which tend to suck the airfoil downstream. This gradient was not measured, but from Reference 86 it can be estimated that buoyancy adds a mean drag coefficient of 0.002.

Blockage refers to the forces on the airfoil due to the increased speed of the flow as it moves around anything of finite thickness, either the airfoil or its wake. Together, solid and wake blocking increase the effective velocity round the airfoil by about 2%. In the case of the panel method without boundary layer, the solid blocking is

included and so would wake blocking if a boundary layer were modeled. Since the airfoil boundary conditions in unsteady flow are a function of the uncorrected frequency, it is more appropriate to include blockage in the theory. However, the theoretical results shown from thin-airfoil theory do not account for either solid or wake blockage. This is easy to correct, however, since it only entails a 4 percent increase in the force amplitudes.

The effect of streamline curvature is predicted by the analytic and numerical theories, therefore no adjustments were made to the data. Statically, streamline curvature leads to a 10 percent reduction in the lift-curve slope found in the tunnel. There remains the effect of the side walls and the finite span of the model. It is assumed that the combination of endplates and sidewalls ensures a two-dimensional flow.

4.8 MEASURED RESULTS AND COMPARISON WITH THEORY

4.8.1 Static Tests

In order to estimate flow smoothness, tufts were attached to the airfoil, endplates and walls. The reaction of the tufts indicated very smooth flow over the airfoil, including the airfoil/endplate joint, throughout the pitch range of the suspension. Some turbulence was noted between the walls and the endplates due to flow around the endfittings.

Figures 35, 36 and 37 show the static lift, moment and drag for the

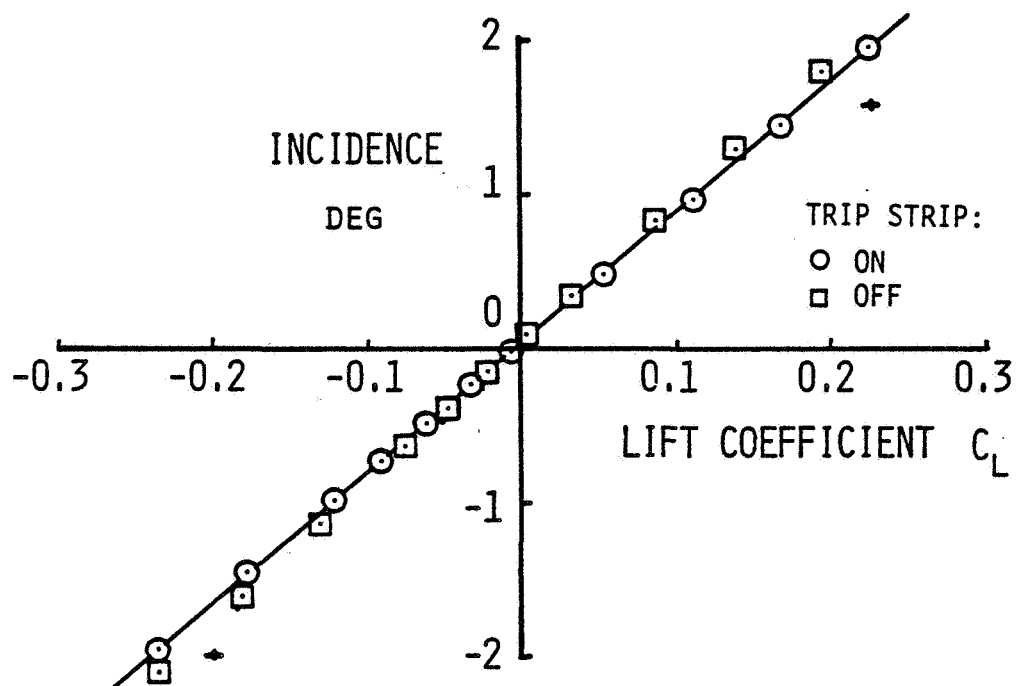


Figure 35: Static Lift of Airfoil with and without Boundary-Layer Trip.

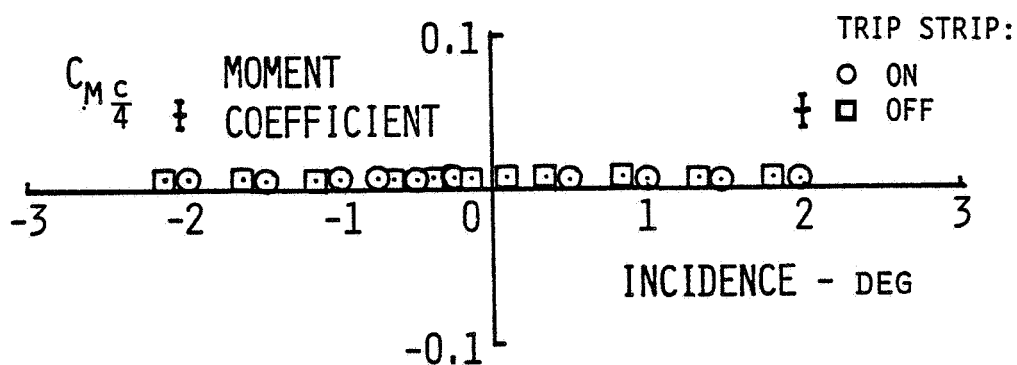


Figure 36: Static Moment of Airfoil with and without Boundary-Layer Trip.

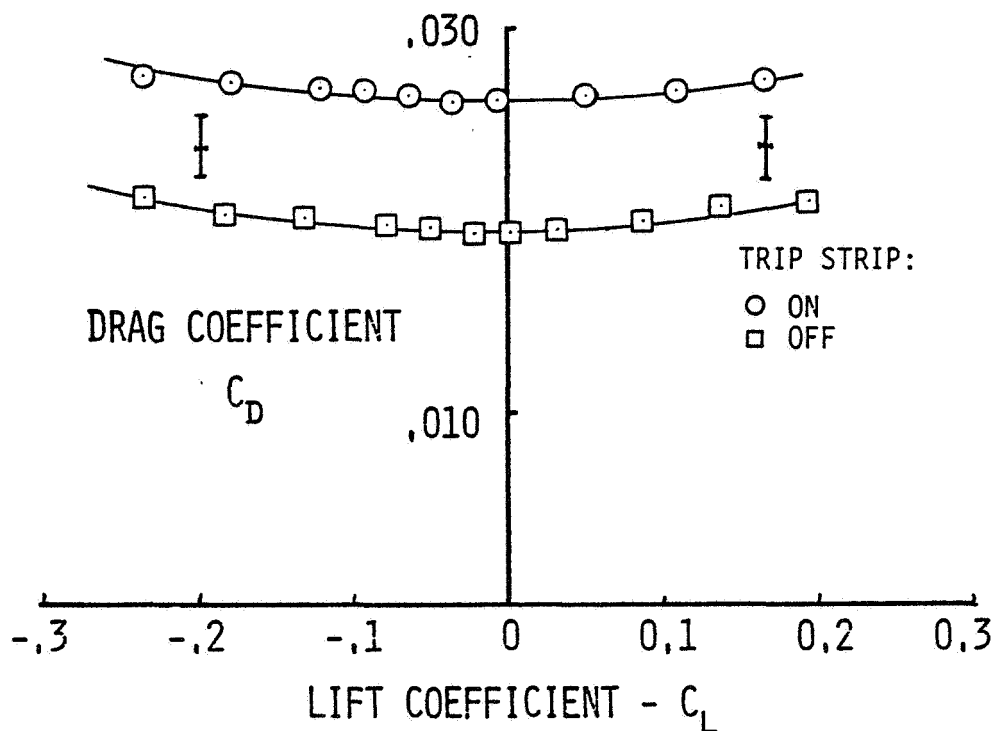


Figure 37: Static Drag of Airfoil with and without Boundary-Layer Trip.

airfoil with and without boundary-layer trip and with the endplates attached to the spar. The Reynolds number is 0.33 million. The incidence angle is the output of the pitch sensor, which was set to zero with the airfoil coarsely aligned with the section centerline.

The lift slope for the airfoil with boundary-layer trip, Figure 35, is 0.118 per degree, quite close to the 0.120 per degree found with the endplates on the wing. However, there is a noticeable drop in slope for the airfoil without boundary-layer trip, which is quite possibly a reflection of the low Reynolds number [86].

Figure 36 shows the expected very low, almost-constant moment about the quarter chord.

Before calculating the drag, the balance orientation angle δ must be determined. The criterion for selecting δ is that the correct δ produces a symmetric drag curve. Since δ is a fixed physical parameter, one value should suffice for all conditions. On this basis a delta of 0.4 degrees produces the curves shown in Figure 37. With the airfoil isolated from the endplates, the typical parabolic section drag curve is seen. As expected, the drag of the airfoil without the boundary-layer trip is less than with the trip. The size of the drop indicates that the difference is due not only to the lessened skin friction and pressure drag of the untripped boundary layer but also the absence of the drag of the glass beads. The minimum drag of 0.019, while the same as found by Hien [25] in a similar test, still appears high as if affected by a poor seal at the endplates.

Figures 38, 39 and 40 show steady-flow measurements of the lift, moment and drag for the airfoil and endplates with the boundary-layer trip applied. The three Reynolds numbers correspond to the speeds used to obtain the three reduced frequencies in the oscillatory tests.

The lift coefficients in Figure 38 show good repeatability among the tests, and the lift curve slope is 0.120 per degree (6.88 per rad). Again, these data are not corrected for wall effects. If, to compare to other experiments, we apply blockage and streamline curvature corrections to the static lift curve slope, the uncorrected value of 0.120 is decreased 10 percent for streamline curvature and 4 percent because of blockage. The corrected lift slope of 0.104 per degree compares very

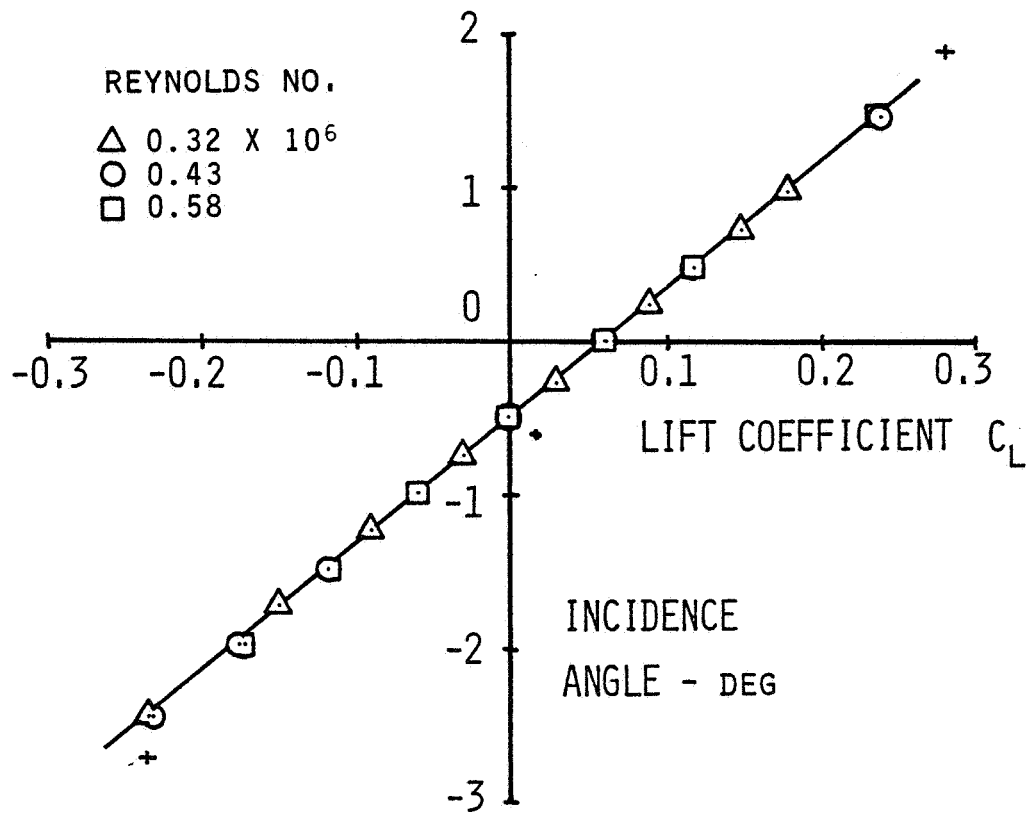


Figure 38: Static Lift of Airfoil with attached Endplates.

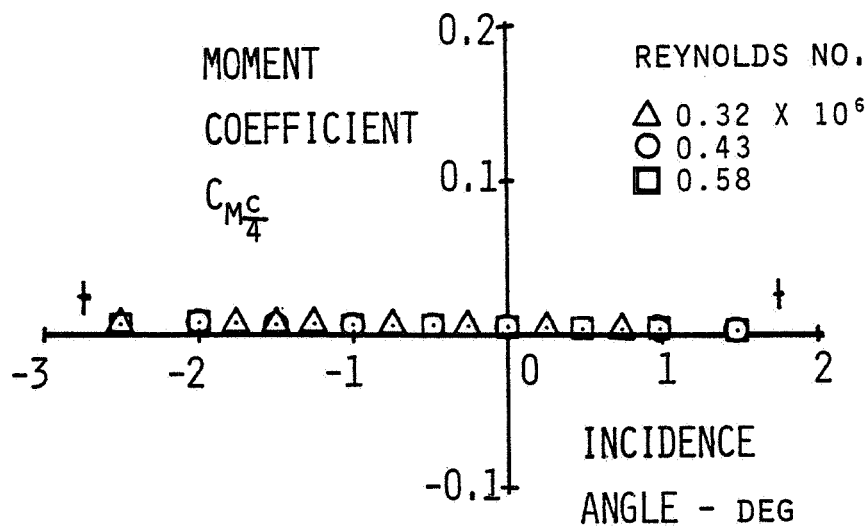


Figure 39: Static Moment of Airfoil with attached Endplates.

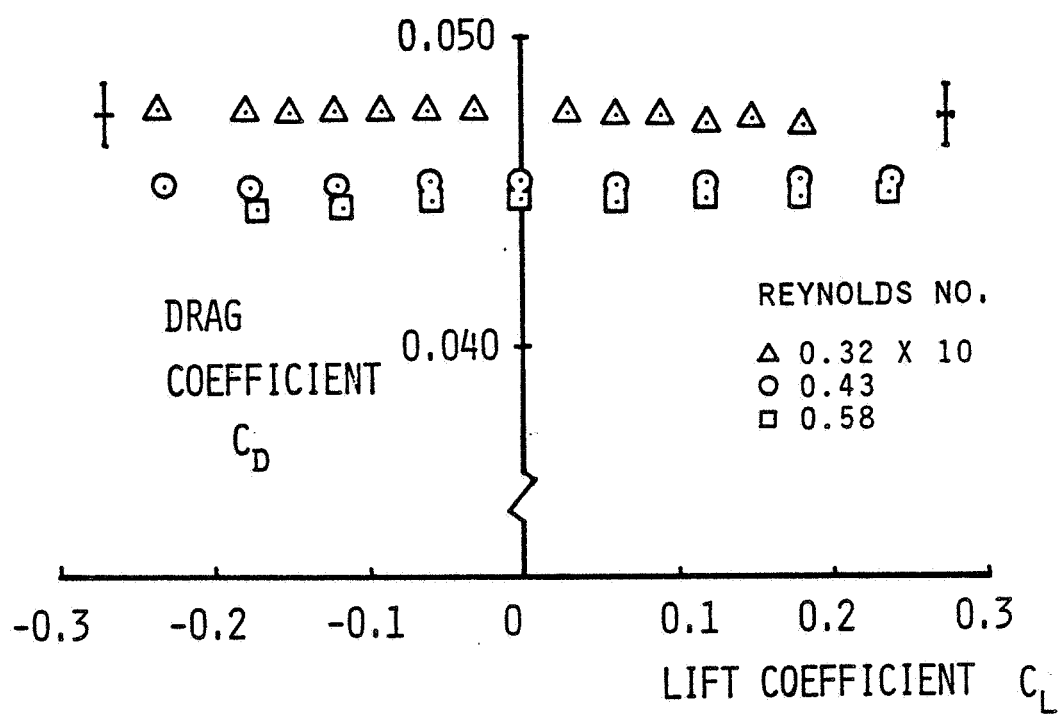


Figure 40: Static Drag of Airfoil with attached Endplates.

well with other measured values of slightly more than 0.10 per degree [87].

The moment curve of Figure 39 is almost exactly the same as for the airfoil without endplates, Figure 36.

It can be seen in Figure 40 that the addition of the endplates increases the drag to very high levels and masks the characteristics normally seen in an airfoil. The data do show the expected decrease in drag with Reynolds number.

4.8.2 Simple Pitch Oscillatory Results

When the airfoil is pitched about an axis other than midchord, more than one mode of displacement, as defined by Timman [16] or Wu [18], is involved. This is a matter of definition theoretically, but, in practice, the pitch suspension is superior to the plunge suspension, for reasons mentioned in the Tares section. It is therefore desirable to perform many tests without using the plunge suspension. The tests in this section were made with the plunge degree of freedom locked by using the stops on the crossbeams.

The data in the simple pitch tests were taken at four different amplitudes ($\alpha_1 = 0.5, 1.0, 1.5,$ and 2.0 degrees) about the angle of zero lift (incidence = -0.5 degrees) and three reduced frequencies ($k = 0.16, 0.22, 0.29$). The data at the different amplitudes are given in Appendix D. Since the trends with amplitude were as expected, (linear for lift

and moment; quadratic for suction and drag), the forces per unit amplitude are presented in Figures 41-45. For comparison, the airloads predicted by potential flow are also drawn. The dashed line represents the forces in free air; the solid line is Timman's theory, which includes wall effects. The third, broken curve is the result of the panel method without boundary layer. The expected errors at each reduced frequency are shown as small crosses.

The lift data, Figure 41, agree very well with thin-airfoil theory corrected for wall effects, much better than with the uncorrected theory. The panel method differs considerably in phase. There is no significant difference between the data measured with the endplates on the spar or on the airfoil.

The moment amplitude is also predicted well by Timman's theory. On the other hand the experimental phase is about 10 degrees above the predicted values, Figure 42.

Without viscous effects included, the theories cannot predict the static drag or suction. Here the theories are used to estimate the difference between the mean suction or drag during oscillation and the static values. The change in mean suction, ΔC_{s0} , predicted by Timman's theory is again much closer to the measured values than the theory without wall effects, although there is not as much actual variation with frequency in the data as in the theory, Figure 43. One important reason that the trends with frequency of the data are not as expected is that Reynolds number effects are also involved.

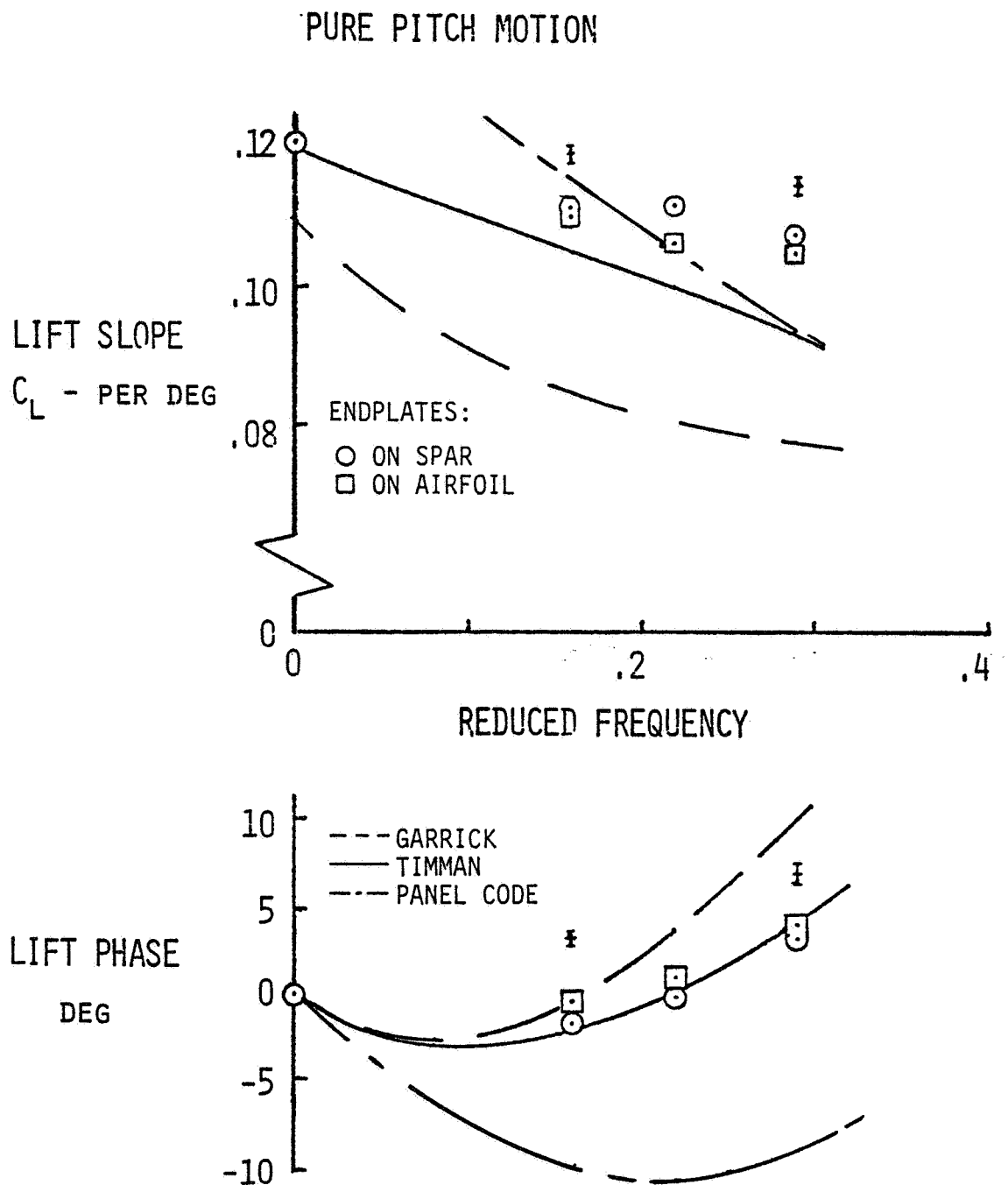


Figure 41: Oscillatory Lift Slope in Simple Pitch versus Reduced Frequency.

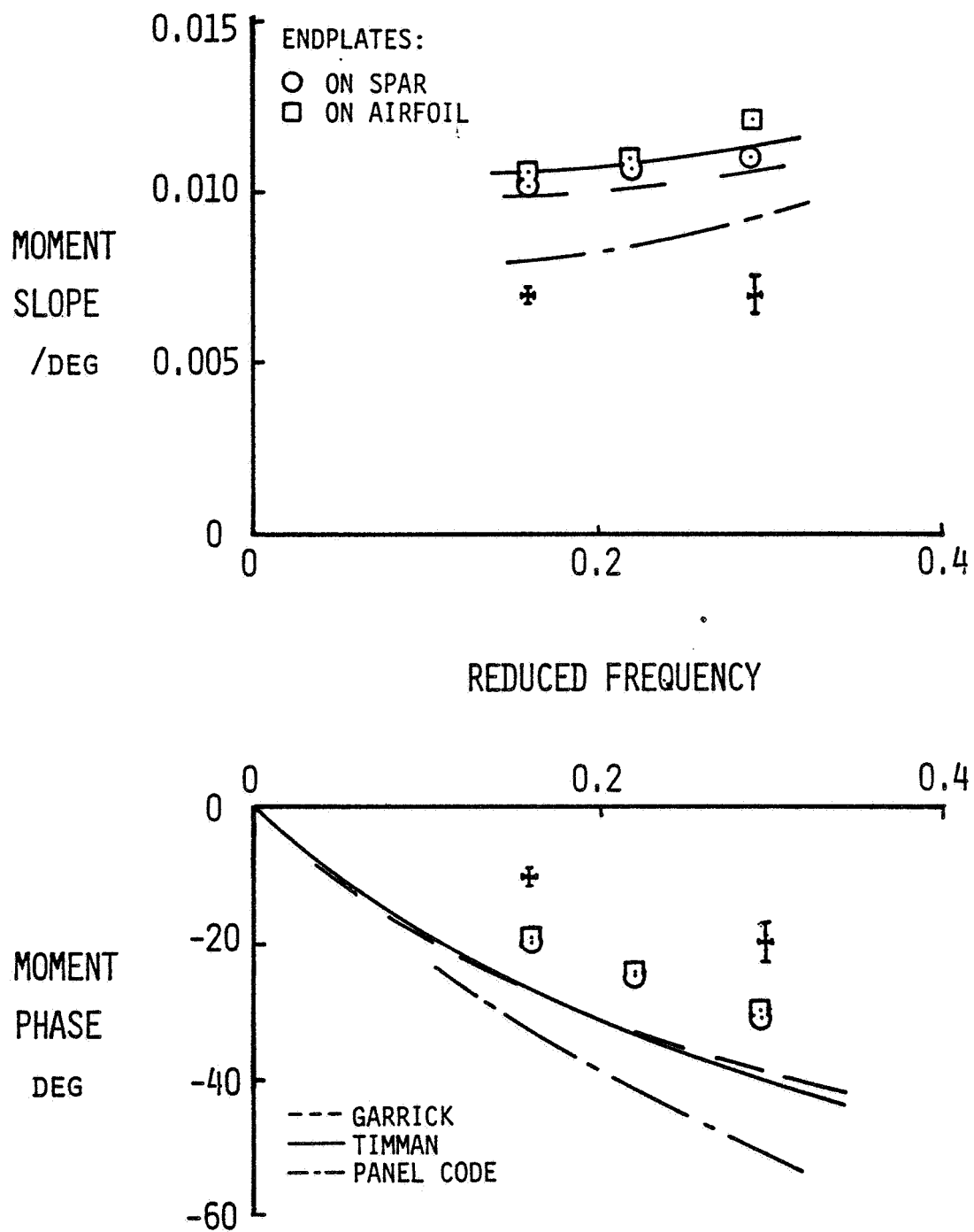


Figure 42: Oscillatory Moment about Pitch Axis in Simple Pitch versus Reduced Frequency.

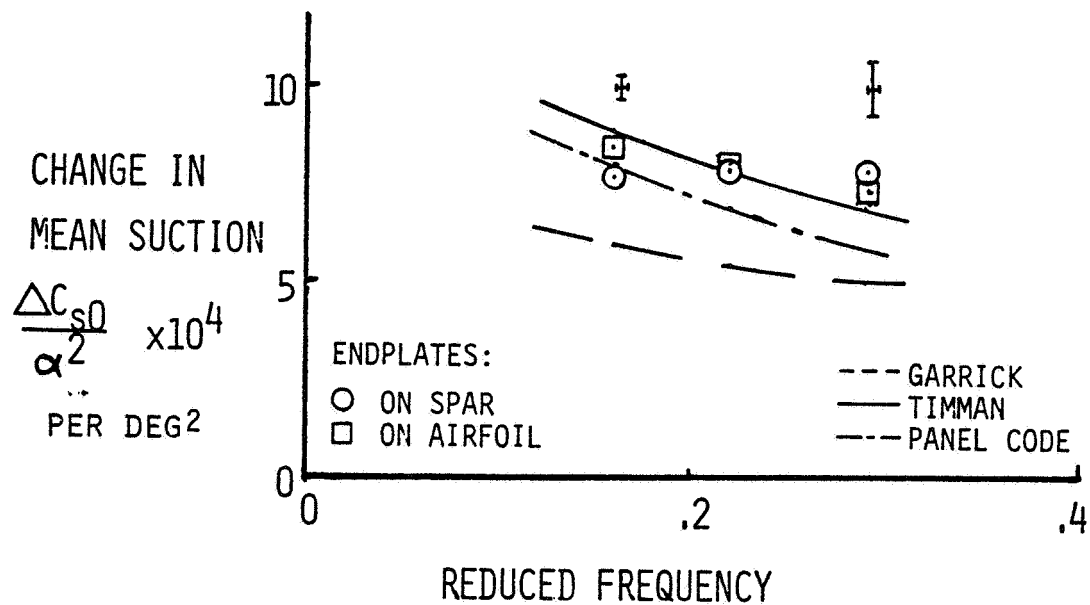


Figure 43: Mean Suction per Degree in Simple Pitch versus Reduced Frequency.

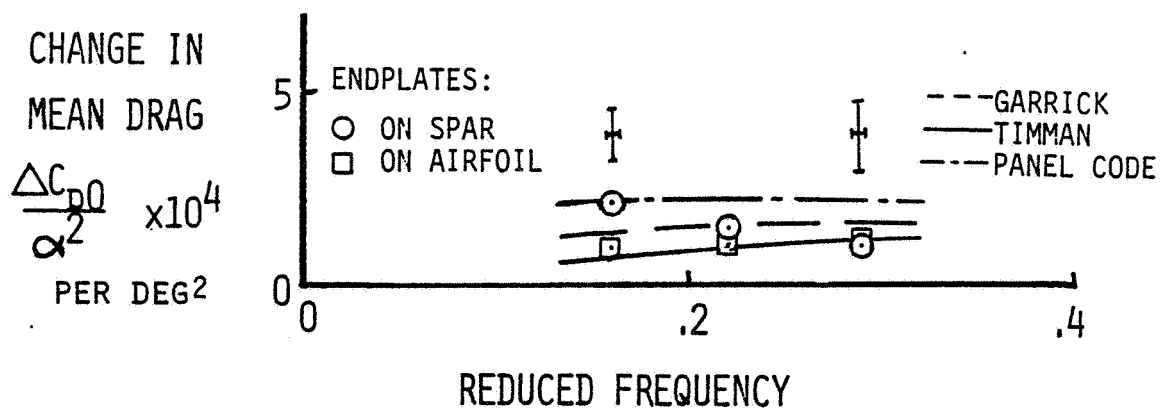


Figure 44: Mean Drag per Degree in Simple Pitch versus Reduced Frequency.

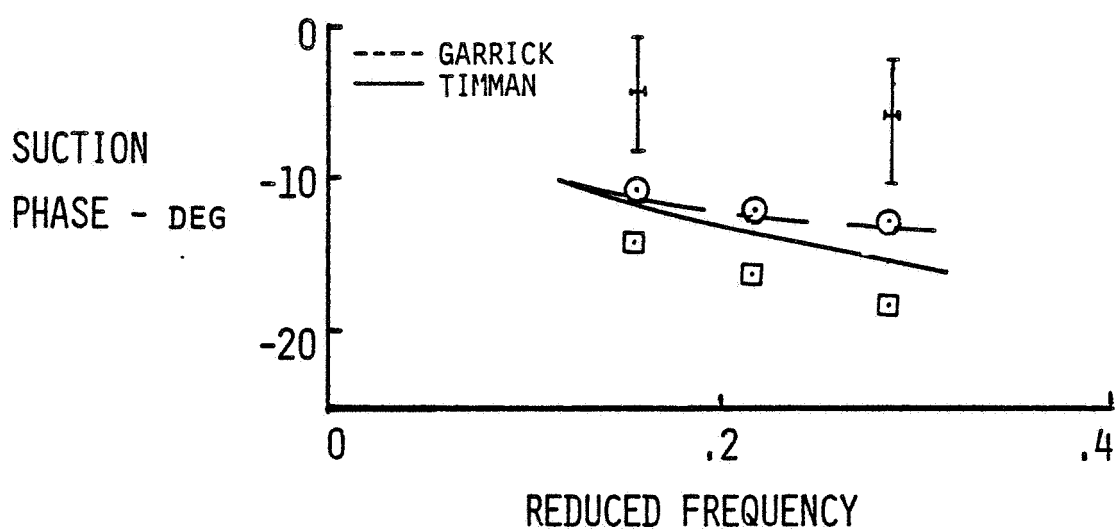
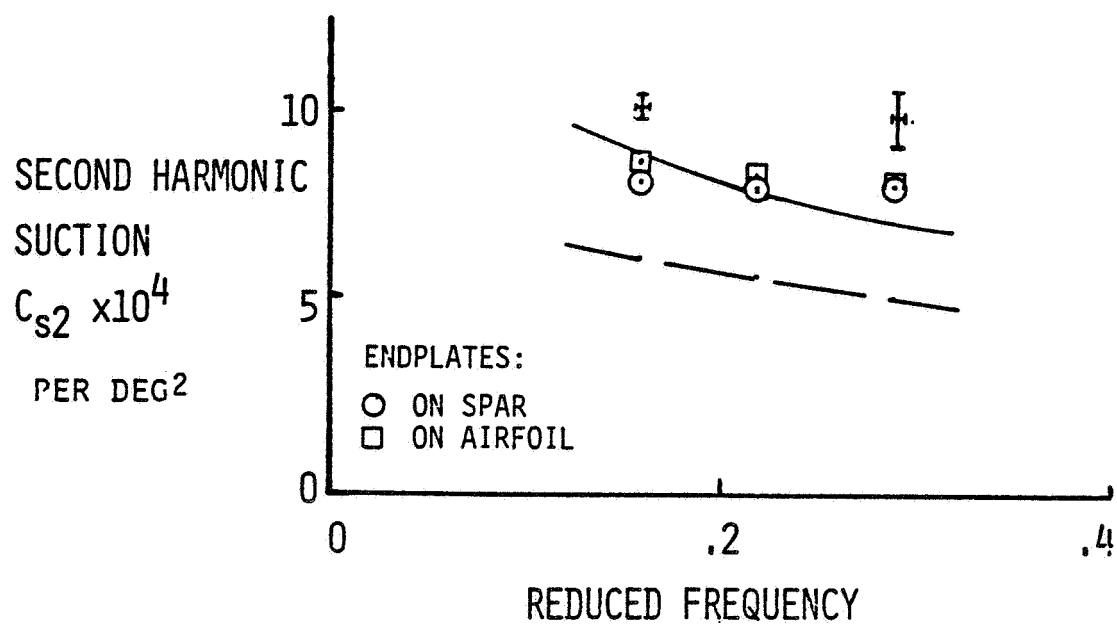


Figure 45: Second Harmonic Suction in Simple Pitch versus Reduced Frequency.

The change in mean drag, ΔC_{D0} , inferred by the components of the normal force and suction falls in the region of both thin-airfoil theories, Figure 44. The resolution of the data is not quite good enough to allow comment on the merit of either. The panel method appears to underpredict the suction and therefore overpredict ΔC_{D0} .

One of the singular successes of the pitch tests was the measurement of the second harmonic suction, Figure 45. Both the amplitude and phase agree well with corrected thin-airfoil theory. Furthermore, it is to be noted that this amplitude is experimentally close to the mean value of suction as predicted, despite the fact that viscous effects might be expected to decrease the mean suction. The fact that the phase of the second harmonic suction differs from the phase of the normal force signifies that the suction force is not just a rectified normal force, that is, the aerodynamic force vector is definitely tilting back and forth as the airfoil pitches. No second harmonic suction prediction by the panel method is shown. It is considerably different from thin airfoil theory. One can conjecture that it is necessary to include second-order variations in the potential to accurately calculate the second harmonic suction.

4.8.3 Simple Pitch with Mean Angle of Attack

In general, an oscillating wing will not be operating with zero mean lift. Theoretically, the only effect of a steady angle of attack will be the appearance of a mean lift and a first harmonic suction and drag. To test this, the wing was oscillated in simple pitch at four different

mean angles of attack, -1.0 , -0.5 , 0.5 and 1.0 degrees. The reduced frequency was 0.22 and the pitch amplitude was 1 degree in all cases.

As shown in Figure 46, the measured first harmonic suction is linear in mean angle of attack, as expected. The measured slope is 0.0037 per degree, compared to thin-airfoil prediction of 0.0034 in free air and 0.0036 in the wind tunnel. Again the corrected theory proves more accurate. The phase is predicted well by either theory. There was no change in the oscillatory lift and moment or second harmonic suction. Incidentally, the incidence at which the fundamental suction goes to zero (-0.55 degrees) correlates very well with the incidence of zero lift (-0.50 degrees).

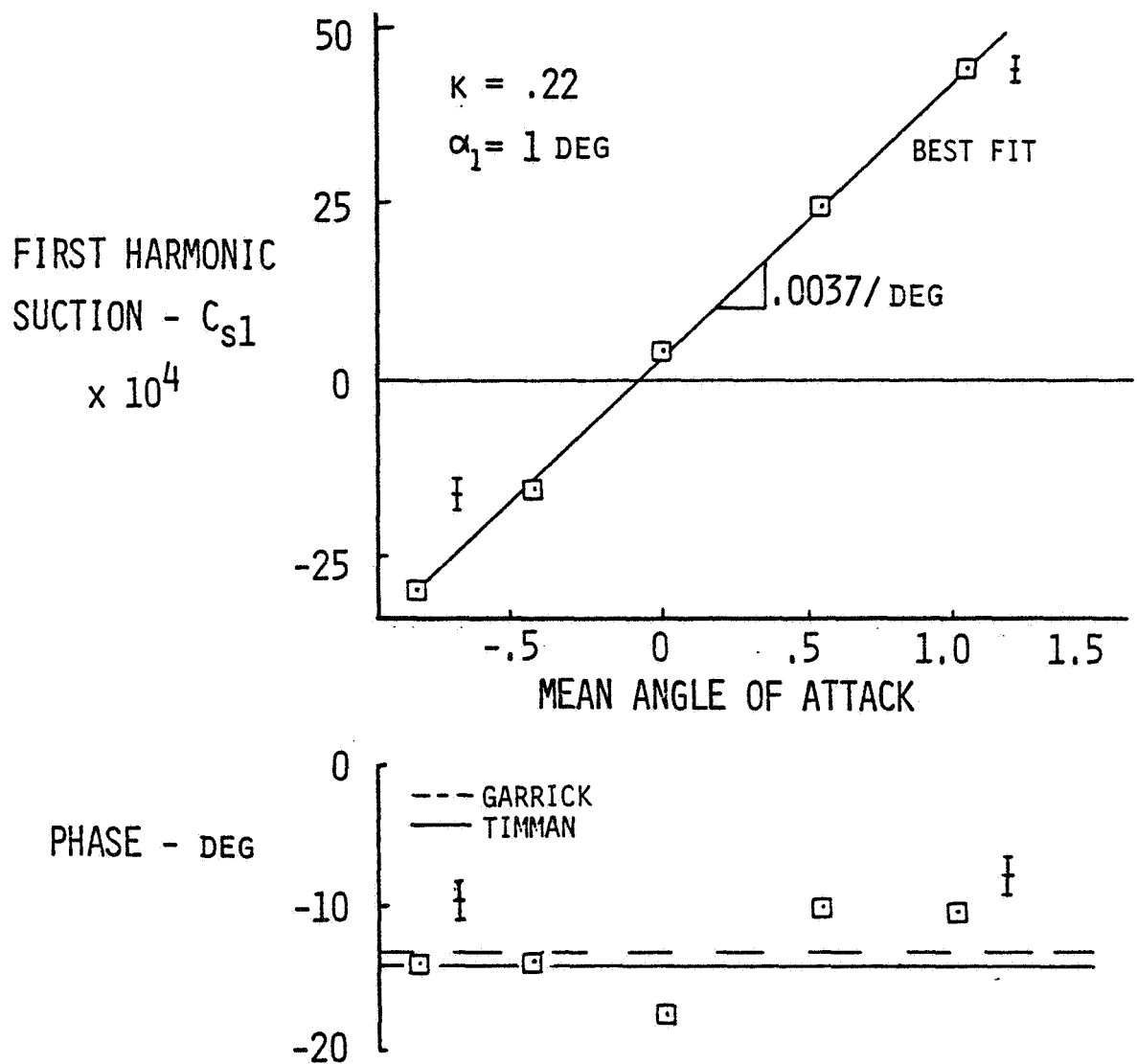


Figure 46: First Harmonic Suction versus Mean Angle of Attack in Simple Pitch.

4.8.4 Simple Plunge

As for simple pitch, the wing was oscillated at four different amplitudes ($h = 0.013, 0.026, 0.039, 0.052$ semichords) for the same values of reduced frequency (0.16, 0.22, 0.29). The mean angle of attack was zero. The measured data are in Appendix E and the values for unit amplitude are presented in Figures 47, 48 and 49.

The measured lift, Figure 47, is predicted well by the corrected thin-airfoil theory, both in amplitude and phase. The panel method's amplitude is close; but the phase is too large.

The amplitude of the moment is also a good comparison, Figure 48. The thin-airfoil theories and the panel method are close to each other. As in the simple pitch case, the phase agreement is not good. The actual phase remains very close to the static value of 90 degrees, while the prediction has a strong frequency dependence. No systematic source is known for an error as large as the 20 deg discrepancy between theory and experiment. The largest deviation is predicted to be 10 deg at $k=0.29$, and the data from each test (Figs. E.4-E.6) have no more than this scatter. It is also noteworthy that the results of the two airfoil configurations do not differ markedly.

The measured ΔC_{d0} , which is the negative of ΔC_{s0} in pure plunge, varies significantly between the two airfoil configurations, Figure 49.

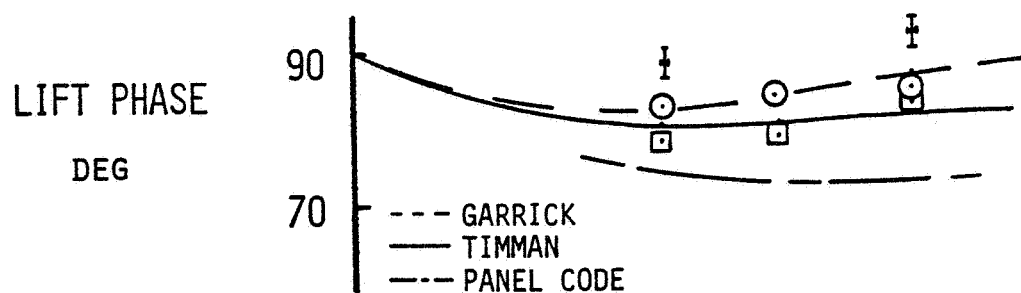
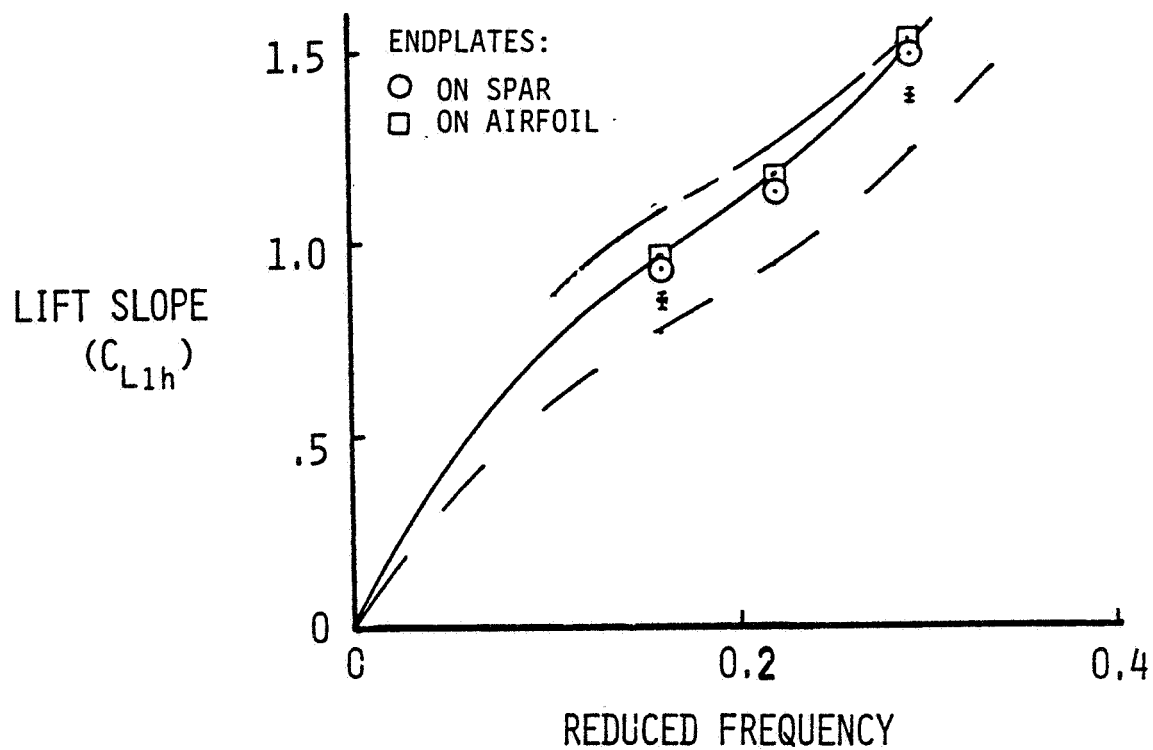


Figure 47: Lift per Unit Plunge versus Reduced Frequency.

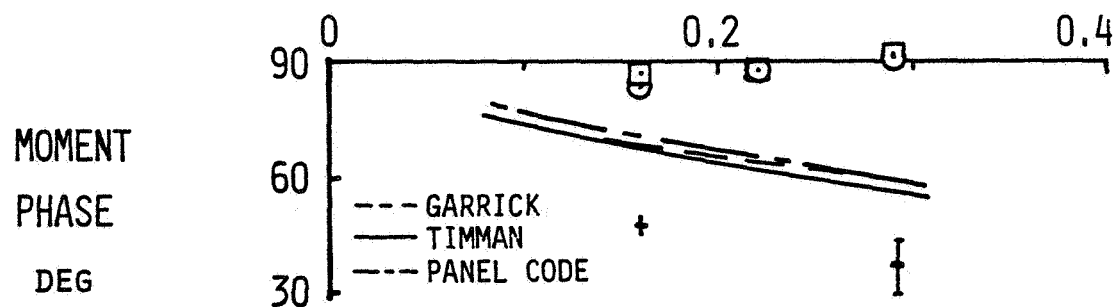
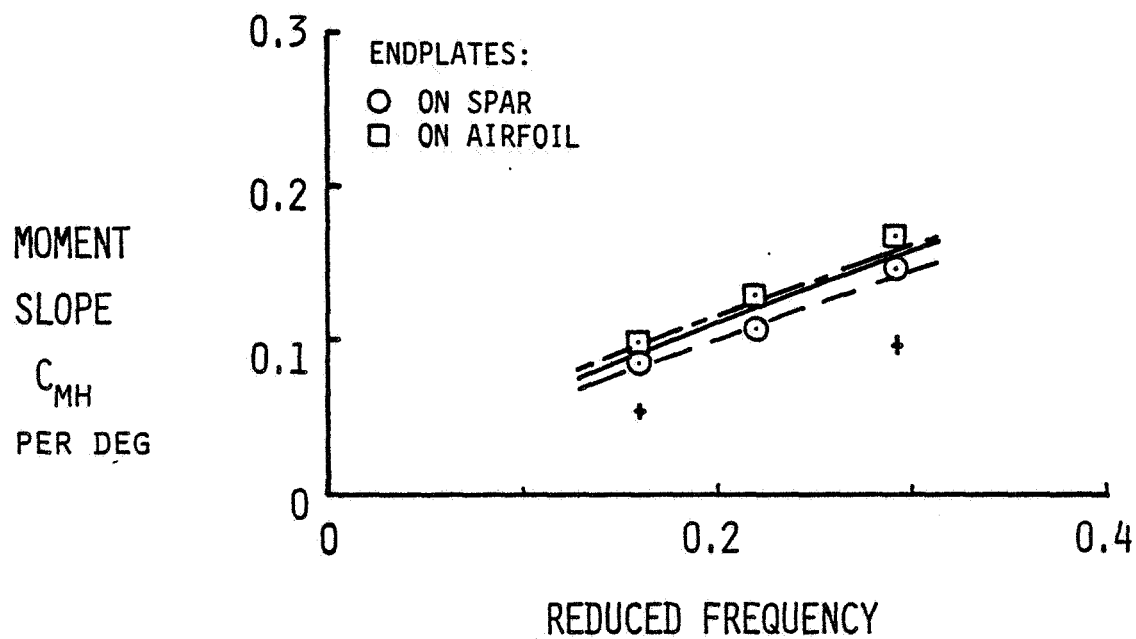


Figure 48: Moment per Unit Plunge versus Reduced Frequency.

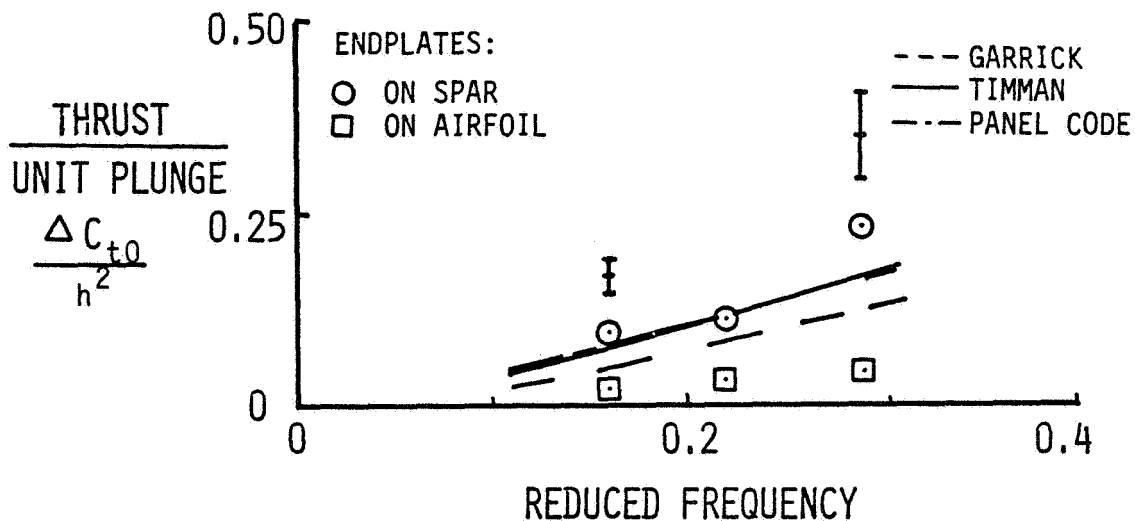


Figure 49: Change in Thrust per Unit Plunge versus Reduced Frequency.

With the endplates attached to the airfoil, little thrust is produced. However, when the endplates are not attached to the airfoil a thrust equal to or exceeding the prediction is measured. This is the only dynamic test which showed any significant change between endplate configurations. Again, the panel method and Timman's theory agree.

No measured data for the second harmonic suction in pure plunge is presented. As was mentioned, misalignment in the plunge suspension imparts signals to the suction sensors which, although apparently not random, (see Appendix C), are large enough that uncertainty in the tares swamps the expected signal. No confidence can be held in the results and so none are presented.

4.8.5 Combined Pitch and Plunge Motion

As a final test, measurements were made of the airloads on an airfoil which is pitching and plunging with various phase angles between the two motions. The motion, intended to be representative of a propulsive wing, was a plunge amplitude of 0.040 semichords and a pitch amplitude of 0.7 degrees at a reduced frequency of 0.22. Six different phase angles were chosen: 0, 90, 180, 270, 225, and 315 degrees. The last two were chosen to investigate better the natural flight region near 270 (~90) degrees.

The lift, moment, and changes in suction and drag are plotted against the phase angle between the displacement and pitch in Figures 50-53. The solid curve represents the prediction of Timman. The predictions are exact at each experimental phase angle, but, since some experimental deviation occurred from the desired pitch and plunge amplitudes, the curves are approximate between data points.

The measured data follow the predicted lift and phase well, Figure 50, except for an apparently erroneous data point at 235 degrees. The moment data, Figure 51 is ambiguous. The data at 0, 90, and 315 degrees follow the prediction, while the points at 180 and 270 are much higher than predicted. The phases at these two points also differ from the theory. The large scale of Figure 51 makes the phase comparison between theory and experiment appear good, but actually the discrepancy is 10 to 20 deg, the same as in the pure plunge case.

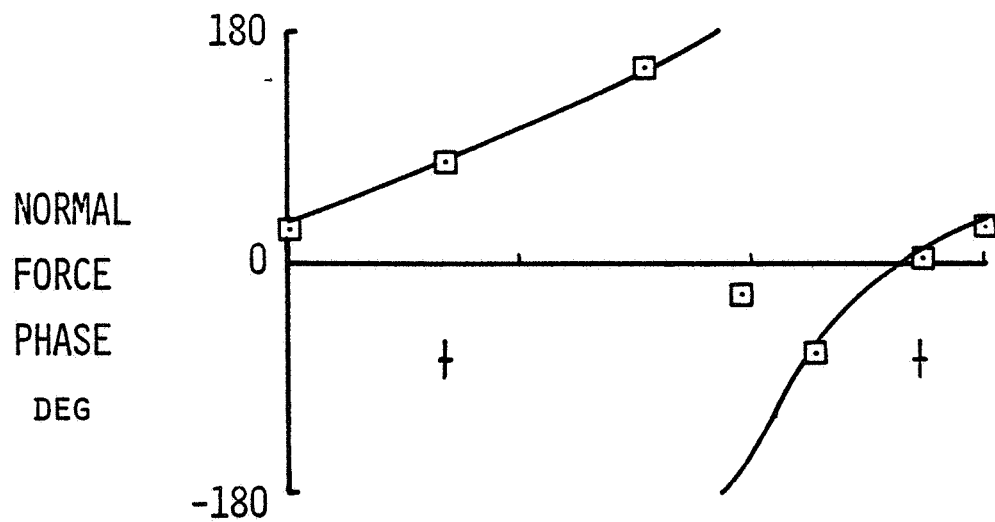
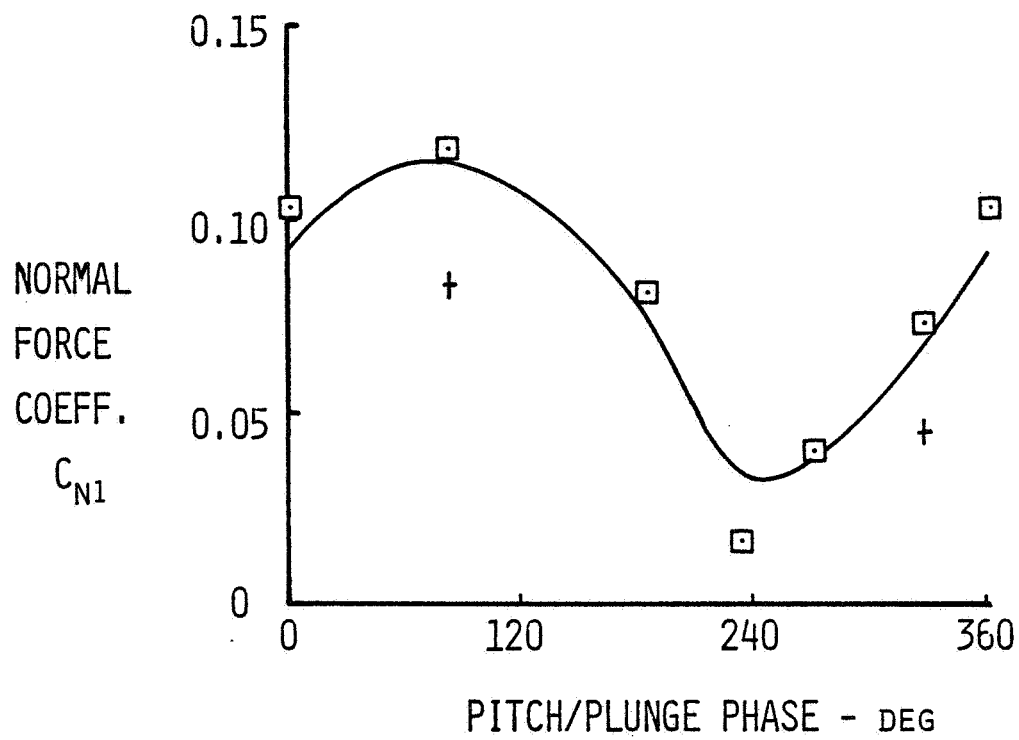


Figure 50: Normal Force in Combined Motion versus Pitch/Plunge Phase.

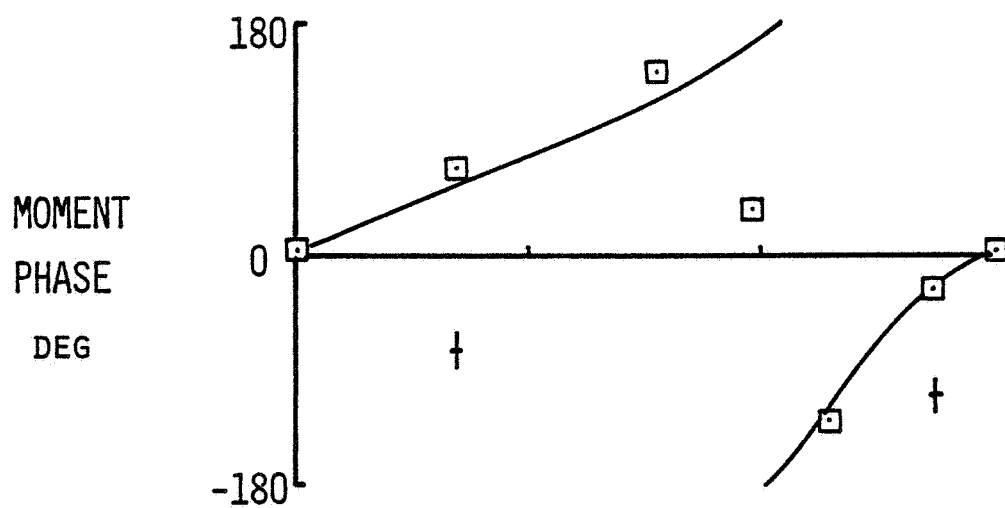
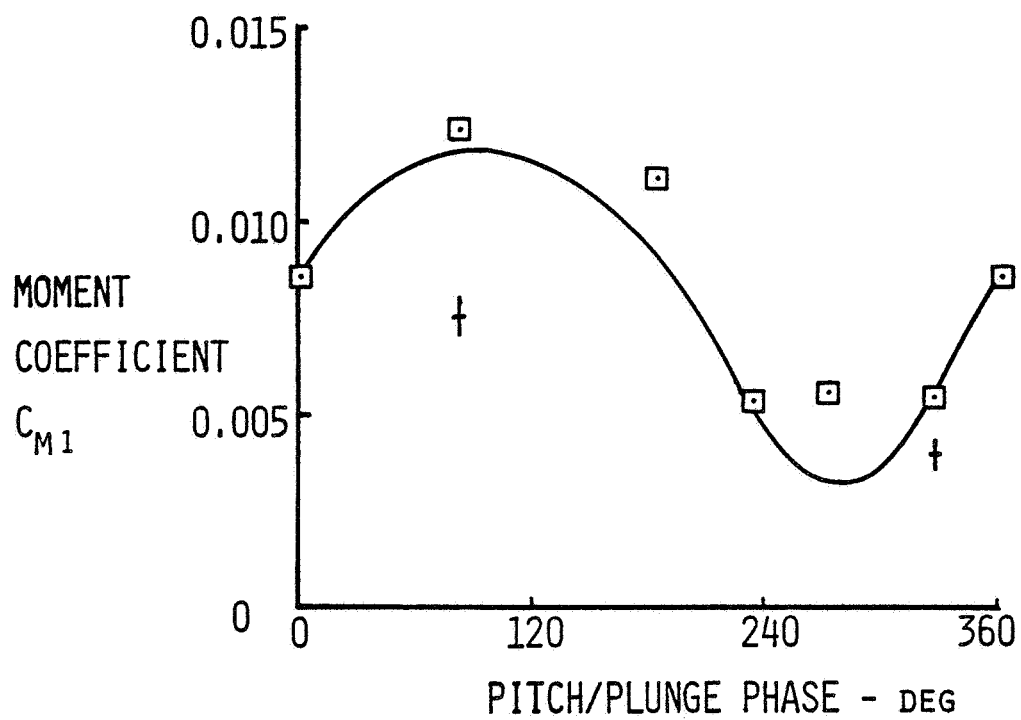


Figure 51: Moment about Pitch Axis versus Pitch/Plunge Phase.

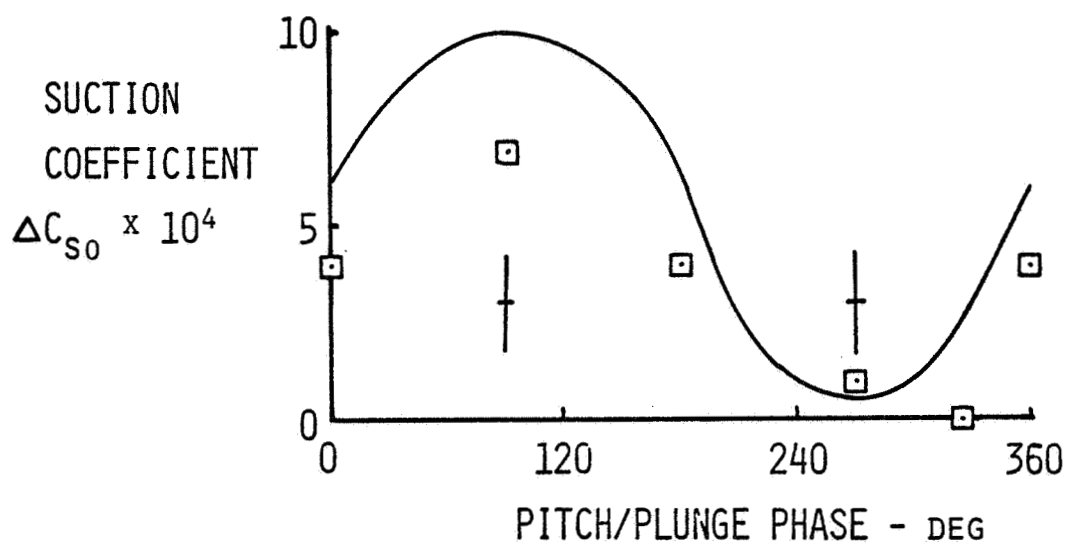


Figure 52: Change in Suction in Combined Motion versus Pitch/Plunge Phase.

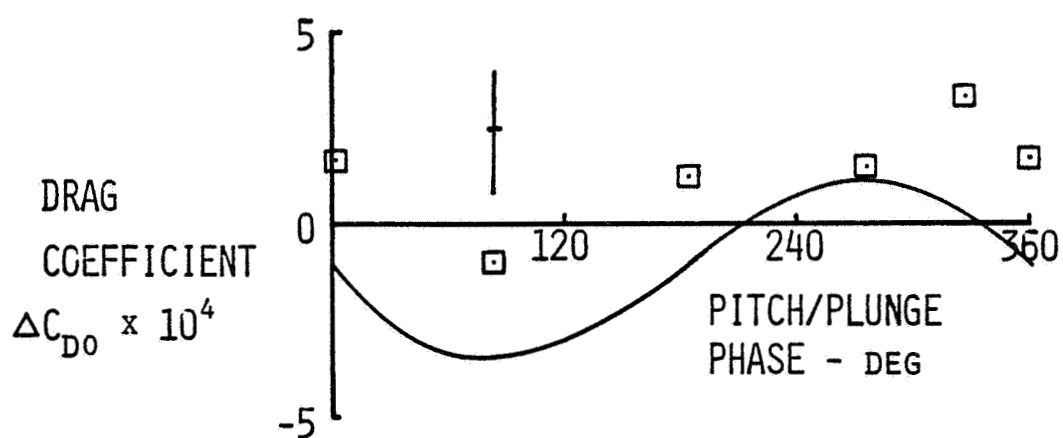


Figure 53: Change in Drag in Combined Motion versus Pitch/Plunge Phase.

The suction data, which are recorded separately from the normal force data, are shown in Figure 52. Overall, the measured suction is much less than predicted. This leads to measured increases in drag at all but one point, Figure 53.

4.9 MEASUREMENT ERRORS

An analysis of the error sources for each of the results was made using the accuracies mentioned for the values of dynamic pressure, calibration nonlinearity, etc. Each source was assumed to be independent of the other so that the square root of the sum of the squares of each separate error would be a good approximation to the standard deviation of the final error. These expected deviations are included in each of the figures by a Maltese-cross type of symbol.

In the suction measurements the expected error appears to be pessimistic, see Figure 45. This may be caused by an overly large calibration nonlinearity due to temperature drift of the balance. To explain, the suction sensors were not well temperature compensated, and the zero drifts as ambient temperature changes. Over one oscillation cycle, (1/7.5 sec), this drift is negligible and below the passband of the lock-in analyzer, but during a long calibration this drift produces a nonlinearity which would not be present if the balance could be calibrated quickly. By measuring the change in mean suction when stationary and immediately afterward while moving, the effect of this drift is minimized.

4.10 DISCUSSION

The experimental program succeeded in measuring the unsteady chord-wise airloads on an oscillating airfoil at reduced frequencies above that of Obye [27].

The pitch data show a very convincing consistency. The lift agrees in amplitude and phase with corrected thin-airfoil theory. The moment agrees in amplitude but shows about 10 degrees more advance than theory or the results of Halfman [32]. Very good agreement is obtained for the values of the mean, first and second harmonic suction. These data support the common origin of the mean and second harmonic suction predicted in potential theory. This finding also agrees with the results of Obye [27].

It should be reiterated that some Reynolds-number effects appear when the data are plotted versus reduced frequency. The extent of these effects is difficult to estimate in the absence of independent variations of k and Re .

Except for the moment phase, the data in plunge also agree with theory. The two endplate configurations produce two distinct trends in the mean drag curve, the more doubtful one, (the one in which the drag of the endplates is also being measured), is further from the theory.

It would be easy to speculate that the effects of a boundary layer are responsible for the poor prediction of the moment phase in pure

plunge. However, the experimental moment phases do not match those found by Halfman [32]. The error analysis indicates that the reported phases are correct for this experiment. It seems likely, therefore, that the low Reynolds numbers of this experiment, resulting in some separation, produce misleading moment phases.

Drag measurements in plunge constitute the only case in which the model configuration produces significant changes in the data. This is a vital point. Putting the endplates on the spar instead of the airfoil reduces the plunge tares by 25 percent and the pitch tares by 30 percent. The inertia forces can be as high as 75 percent of the output of the sensors. If these had been measured incorrectly, large changes in the aerodynamic coefficients would result. On the other hand, oscillatory flow over the endplates should produce some variation in their drag.

Measurement of the second harmonic force during plunge motion was found impractical. First, the useable amplitude was sixty percent of original estimates, and secondly, the second harmonic signals due to unintentional fore-and-aft airfoil motion were much larger than the expected signal. Both of these problems were due to misalignment of the plunge suspension, a problem that is not easily corrected.

The theory most successful in predicting the forces is the thin-airfoil theory corrected for wind tunnel walls. Increasing the theory 4 percent to include blockage further improves the comparison, (see, for

example, Figure 41). Garrick's theory neglects the important wall effects, while the panel method includes second order effects such as thickness and solid blockage corrections, but inconsistently does not include viscous effects. When a boundary layer is successfully incorporated in the panel method, it may prove capable of predicting the steady as well as the oscillatory drag.

The experimental data do support the conclusion that oscillating pressures are responsible for the chordwise forces on an oscillating airfoil, as well as a large part of the drag forces. Viscous effects show up mainly in the static drag component, (which was subtracted from all unsteady data before comparison with theory), and the change in mean drag.

Chapter V
SUMMARY AND RECOMMENDATIONS

5.1 SUMMARY

A review of the present state of aerodynamic theories concerning oscillating wings in incompressible flow has been given. From among these, two were selected to calculate the forces on a 2-D airfoil pitching and plunging in a low-speed wind tunnel.

Timman's analytic theory was completed by deriving the leading-edge suction force. If blockage corrections are also made, this theory predicts best the characteristics of the measured airloads. Using the full Bernoulli equation, the presence of second harmonic pressures due to first-order changes in potential was revealed. These pressures lead to a second-harmonic force analogous to the leading-edge suction of thin airfoil theory. Because this theory predicts the mean chordwise force much better than the second-harmonic force, it is conjectured that it is necessary to include the second-order variations in potential. To be consistent with the inclusion of thickness effects, the characteristics of a boundary layer should also be included.

An airfoil model to measure the unsteady aerodynamic forces was successfully designed, constructed and tested. Excellent agreement between theory and experiment in simple motions was found for all airloads

except the pitching moment phase. This indicates that the theoretical model should include a boundary layer and further tests be conducted at higher Reynolds numbers than present.

The success of Timman's [16] theory indicates that viscosity does not play a primary role in generating the unsteady measured forces.

5.2 RECOMMENDATIONS

The author considers the following to be the next logical steps in pursuing this line of research:

1. Continue the improvement of the panel code. Firstly, the second-order variation in potential is required to calculate the second harmonic force. Secondly, the ability of the program to handle surge motion should be checked. Finally the panel code should be coupled with a method for predicting the effects of the unsteady boundary layer.
2. Since a parallel analytic theory was found so helpful, retrace Woods' analysis [42] and derive the unsteady suction force from his theory for a thick airfoil with surge motion.
3. Use the existing apparatus to repeat and expand upon the present experiments. Since the pitch tests were so successful, they should be expanded by running at a greater range of frequencies than was thought possible originally. The pitch suspension can also be used to separate frequency and Reynolds Number effects.

Combined motion measurements were limited; more phase angles and motions should be simulated. The discrepancy between the moment phase and theory and the data of Halfman should be investigated.

4. Improve the experimental apparatus by aligning the plunge suspension and adding accelerometers to the airfoil. By carefully aligning the plunge suspension, the tares may be reduced to the point where the signals due to aerodynamic forces are measurable. If complexity and cost are not as vital as in the original design, then accelerometers on the airfoil would be worthwhile. They would independently provide a measure of the inertia forces while the airfoil is oscillating.
5. Other improvements to the apparatus that would be worthwhile would include:
 - A) A quick way to calibrate the balance, thus minimizing drift effects and allowing more calibrations.
 - B) A computer available during experiments to reduce data immediately after a test.
 - C) The use of a synchronous demodulation technique, suggested by Dan Debra, that involves slowly modulating the amplitude of the oscillation in order to generate a sinusoidal mean suction which can be detected by a Lock-In Analyzer.
6. Using the panel method and Woods' theory investigate more fully the effect of surging. This plays an important part in natural flight along with the performance of vertical-axis wind turbines and helicopter rotors.

APPENDIX A

Complex Notation

Most readers of this dissertation will be familiar with describing an oscillatory quantity as being the real part (or the imaginary part) of a complex quantity, for example

$$\text{plunge displacement} = \text{Re} \left\{ h e^{ikt} \right\}. \quad (\text{A.1})$$

The fact that h is complex infers that there is a phase shift of the plunge displacement at $t=0$. For convenience, (A.1) is usually written

$$\text{plunge displacement} = h, \quad (\text{A.2})$$

and 'Real part of' and e^{ikt} is understood.

If the plunge displacement is multiplied by a real or imaginary number, as in

$$\dot{h} = ik h, \quad (\text{A.3})$$

it is still correct to interpret this as

$$\text{plunge velocity} = \text{Re} \left\{ ik h e^{ikt} \right\}. \quad (\text{A.4})$$

But if an oscillatory quantity, \dot{h} , is multiplied by another oscillatory quantity, C_n , to obtain the power in pure plunge oscillation, the product might be written

$$C_w = C_n \dot{h}. \quad (A.5)$$

It would be incorrect to interpret this as

$$\text{Power} = \text{Re} \left\{ C_n e^{ikt} \dot{h} e^{ikt} \right\}. \quad (A.6)$$

Rather it is

$$\text{Power} = \text{Re} \left\{ C_n e^{ikt} \right\} \text{Re} \left\{ \dot{h} e^{ikt} \right\} \quad (A.7)$$

which when everything is written out and regrouped can be written

$$\begin{aligned} \text{Power} &= \frac{1}{2} \text{Re} \left\{ C_n^* \dot{h} \right\} + \frac{1}{2} \text{Re} \left\{ C_n \dot{h} e^{2ikt} \right\} \\ &= \frac{1}{2} \text{Re} \left\{ C_n \dot{h}^* \right\} + \frac{1}{2} \text{Re} \left\{ C_n \dot{h} e^{2ikt} \right\}. \end{aligned} \quad (5.18)$$

This illustrates that the product of two oscillatory quantities of the same frequency is a constant and a double frequency term. As long as we keep the correct interpretation in mind, though, it is still more convenient to use the form of (A.5). This has been done in the text.

This form is also particularly convenient in computation to take advantage of the complex capability of FORTRAN. The more general theory of Wu [18] was programmed in complex arithmetic in half the steps required for a real arithmetic version of Garrick's simpler theory [15]. The reader may compare the condensation in the text, for example Eqs.

(2.31-2.34), to Wu's original paper and decide for themselves which is preferable.

In describing the phase relationship between the second-harmonic power and displacement, the ambiguity which arises due to the dissimilar frequencies of the two signals must be resolved. To illustrate how this is done in the text, the power can be written

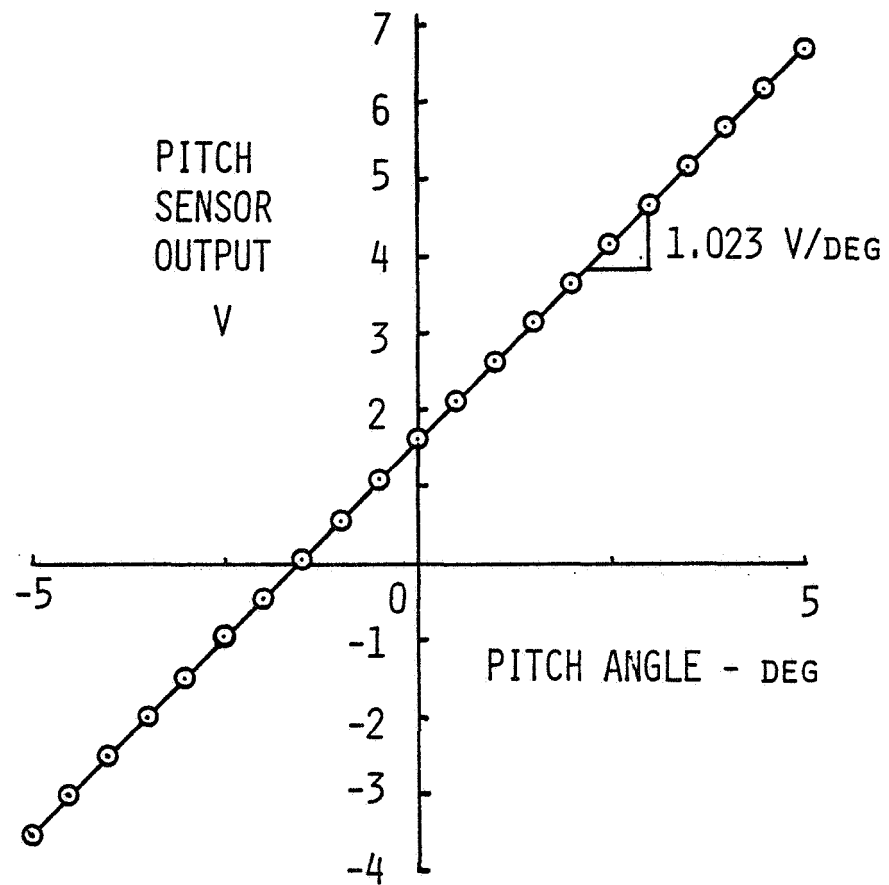
$$\text{Power} = C_{w0} + C_{w2} e^{2(ikt + \phi_w)} \quad (5.19)$$

where C_{w0} and C_{w2} are real amplitudes. ϕ_w describes the phase lead of the power. The reader should be aware that this phase is always between -90 and 90 degrees, and is referred to here as the cosine phase shift, since the real part of the complex quantity was used. If one uses the imaginary part, as Garrick [15] did, the phase is shifted by 45 degrees and is referred to as the sine phase angle.

APPENDIX B

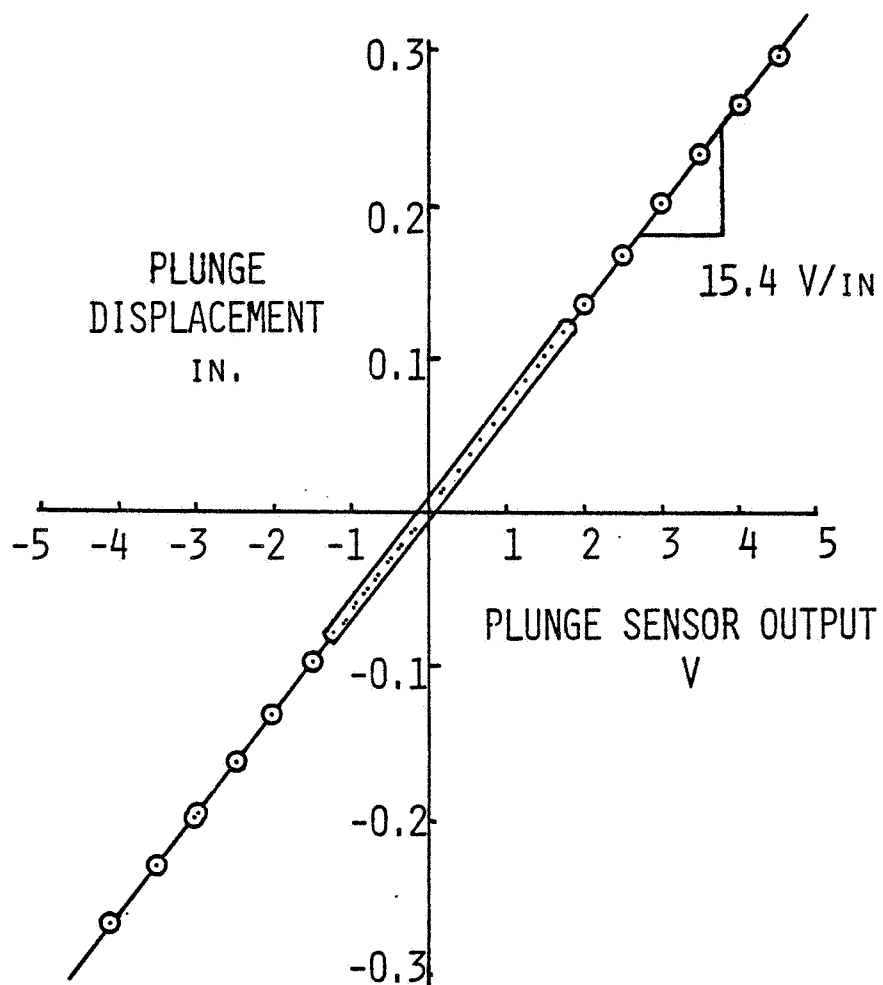
Sensor Characteristics

Figures B.1 and B.2 present the calibration data for the pitch and plunge displacement sensors. They are followed by the manufacturer's descriptions of the balance sensors.



Nonlinearity: 0.3% over the range ± 3 deg.

Figure B.1: Calibration Characteristics of Pitch Sensor.



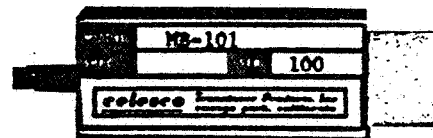
Nonlinearity: 0.2% over the range ± 6 mm.

Figure B.2: Calibration Characteristics of Plunge Sensor.

MB101 MICRO BEAM LOAD CELL

FEATURES:

- LOW COST
- EXCELLENT ACCURACY
- SMALL SIZE
- RUGGED CONSTRUCTION



DESCRIPTION

The Micro-Beam Load Cell is designed to provide all the advantages of a beam for low range force measurements.

This combination of high output, low deflection and ruggedized construction provides for excellent accuracy.

A wide choice of ranges and low unit cost make this controlled environment load cell ideal for OEM scale manufacturers.

SPECIFICATIONS

Non-Linearity (Terminal Method): $\pm .05\%$ F.S. Ten. or Comp.
Hysteresis (Unidirectional): $.03\%$ full scale.
Sensitivity Series 20: 2MV/V at rated capacity.
Sensitivity Series 30: 3MV/V at rated capacity.
Accuracy of Full Scale Output: 0.10% Ten. or Comp.
Zero Balance: $\pm 1.0\%$ Full Scale.
Input & Output Resistance 350 Std.: $\pm 1.0\%$ ohms tolerance.
Temperature Effect on Zero Balance: $\pm 0.0008\%$ of full scale/ $^{\circ}\text{F}$.
Temperature Effect on Output: $\pm 0.0008\%$ of full scale/ $^{\circ}\text{F}$.
Temperature Range, Compensated: $+30^{\circ}$ to $+130^{\circ}$ Fahrenheit.
Temperature Range, Safe: -65° to $+275^{\circ}$ Fahrenheit.
Excitation Voltage Recommended: 10 Volts, DC or AC.
Max.: 18 Volts, DC or AC.

Overload Rating:

3 MV/V 150% Rated capacity (min.)
2 MV/V 300% Rated capacity (min.)

Side Load Effects:

1° off axis $< 0.10\%$ full scale
3° off axis $< 0.30\%$ full scale

Deflection: $< .002$ in. full scale.

Creep, 20 minutes at full load: $< 0.3\%$ full scale.

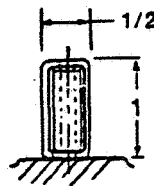
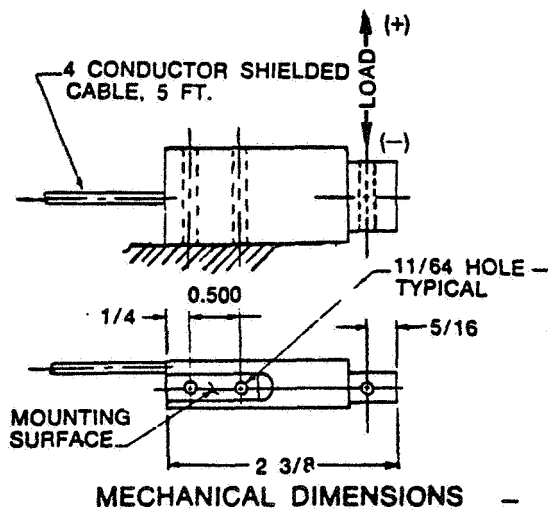
STANDARD RANGES (Pounds)*

Uni-Directional	Bi-Directional
0 - 2.5	± 2.5
0 - 5.0	± 5.0
0 - 7.5	± 7.5
0 - 10.0	± 10.0
0 - 15.0	± 15.0
0 - 20.0	± 20.0
0 - 25.0	± 25.0

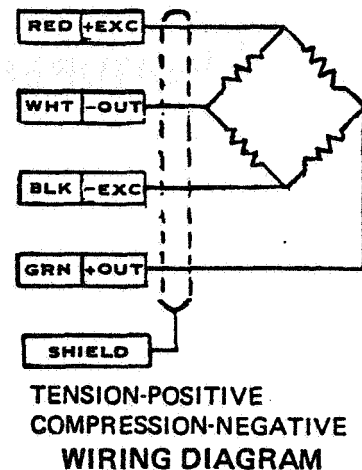
*Divide by 2.204 to obtain range in Kilograms.



MB101 MICRO BEAM LOAD CELL



MOUNTING INSTRUCTIONS
Fasten securely to flat rigid surface with two 8-32 x 1 1/4 screws.



NOTES:

1. Special Ranges and configurations available on special order.
2. Normal Delivery: up to 10 units, four (4) weeks from date of purchase order.
3. All standard cells are supplied with 10 feet of cable.
4. Celesco Transducer Products certifies that all load cells are tested and inspected and found to meet published specifications at time of shipment.
5. Celesco Transducer Products further certifies that its calibration measurements are traceable to NBS.
6. Prices are subject to change without notice.

Terms and Conditions:

1. Please place your order with our local representative or with the factory direct.
2. Terms: Net 30 days, FOB Canoga Park, Ca.
3. Warranty: Celesco Transducer Products Standard Warrantee is applicable to the low range Micro-Beam Load Cell products.

Ordering Information:

MODEL NUMBER MB101 - 3 - 2Kg - XXX
 SENSITIVITY MV/V _____
 RANGE Lb or Kg _____
 SPECIAL _____



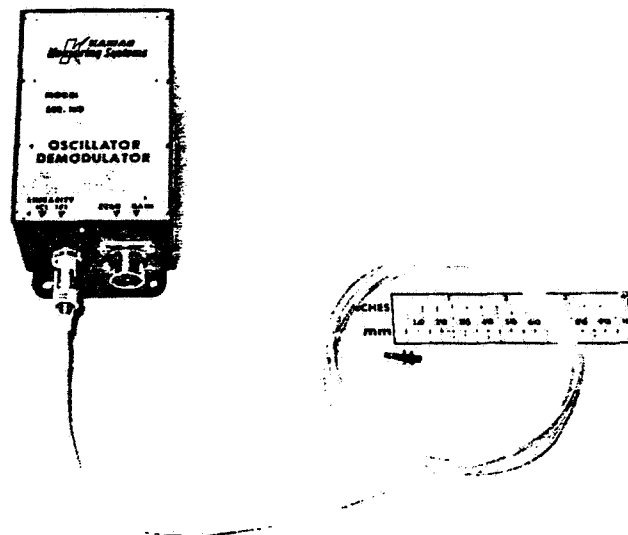
Celesco Transducer Products, inc.
division of Transducers Controls Corporation

DISPLACEMENT MEASURING SYSTEM

MODELS KD-2300-.5SU & KD-2300-.5SUM

FEATURES

- SMALL SENSOR DIAMETER — 2mm (0.080 inches)
- MICROINCH RESOLUTION
- EXCELLENT THERMAL STABILITY
- NON-CONTACTING Eddy Current Operating Principle
- LINEARITY Within ± 1.25 microns (± 50 microinches)
- UP TO 50 kHz FREQUENCY RESPONSE



DESCRIPTION

KAMAN'S MULTI-VIT (MULTI-purpose Variable Impedance Transducer) Displacement Measuring System is a non-contacting proximity measuring system consisting of sensor, cabling, and signal conditioning electronics. The output voltage of the system is proportional to the distance between the face of the sensor and any metallic (conductive) target. The displacement measuring range of up to 0.5 mm (20 mils) features linearity within ± 1.25 microns (± 50 microinches, see Figure 1), repeatability and resolution better than 0.25 microns (10 microinches).

OPERATING PRINCIPLE*

The measuring system utilizes a principal of impedance variation which is caused by eddy currents induced in the conductive target material. The electromagnetic coupling between the coil and the target is dependent upon their common separation distance. In the functional system, a bridge circuit is used in a manner such that the temperature effects are essentially cancelled.

The cabling is used to transmit the signal to and from the sensor. The associated signal conditioning consists of an oscillator, amplifiers, and a demodulator that provides an analog output signal directly proportional to displacement.

*Patent Pending

TYPICAL APPLICATIONS

Applications include displacement (proximity) measurements of shafts, disks, plates, foils, or other ferrous and non-ferrous metallic objects. Oily, dirty, or humid environments between the sensor and target will not affect the system accuracy.

The 2 mm diameter sensor permits non-contacting measurement at points never before possible. Additionally, the excellent accuracy and thermal stability permit the ultimate in precision displacement measurement. The KD-2300-.5SU is designed for use with nonmagnetic targets and KD-2300-.5SUM with magnetic targets.

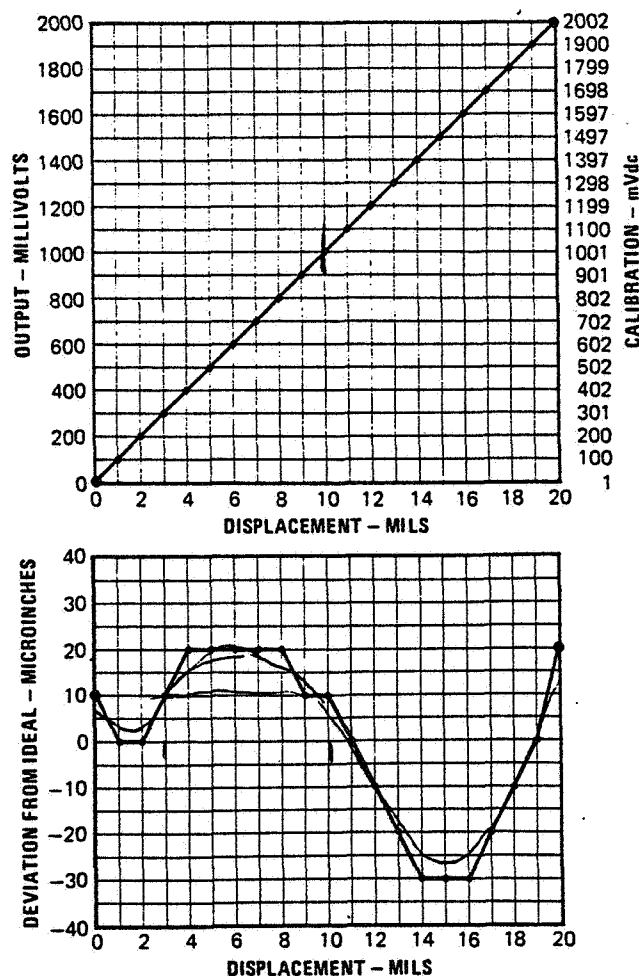


Figure 1 Linearity

One mil offset between KD - 2300 - .5SU sensor face and 304 SS target. Output voltage adjusted to 2 volts full scale.

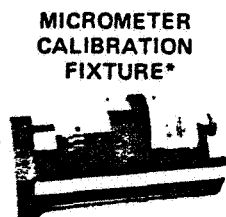
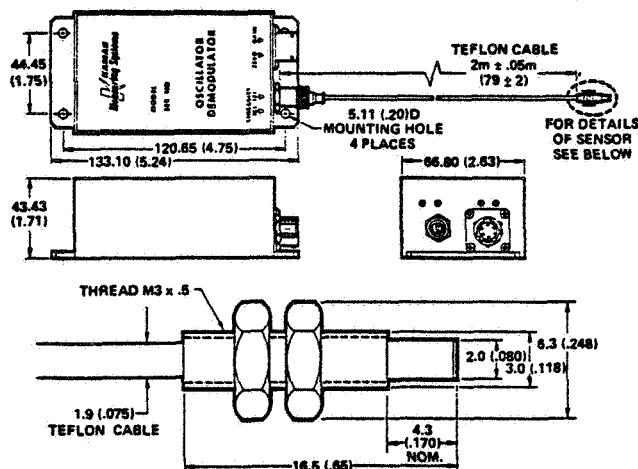
SPECIFICATIONS*

	METRIC UNITS	ENGLISH UNITS
SYSTEM PERFORMANCE Displacement Range [Offset ≤ 0.05 mm (2 mils)] Linearity (see Figure 1) Repeatability Resolution (static) Hysteresis Sensitivity Frequency Response @ 1 Volt Output Output Voltage, Analog Factory Calibration Field Adjustable Output Current Output Impedance	0.5 mm Within ± 1.25 microns Better than 0.25 microns Better than 0.25 microns None 4 mV/micron (adjustable to > 8 mV/micron) Zero to 50 kHz (-3 dB point) 0 – 1 Vdc From -5.5 to $+6.5$ Vdc or in direct engineering units 15 mA maximum 5 ohms maximum	0.020 inches Within ± 50 microinches Better than 10 microinches Better than 10 microinches None 100 mV/mil (adjustable to > 200 mV/mil) Zero to 50 kHz (-3 dB point) 0 – 1 Vdc From -5.5 to $+6.5$ Vdc or in direct engineering units 15 mA maximum 5 ohms maximum
TEMPERATURE Thermal Sensitivity Shift Sensor Operating Temperature Range Sensor and Cable (excluding connector) Electronics Storage Temperature Sensor and Cable (excluding connector) Electronics	Less than 0.23 microns/ $^{\circ}\text{C}$ -55°C to 150°C 0°C to 55°C -55°C to 150°C -55°C to 105°C	Less than 5 microinches/ $^{\circ}\text{F}$ -67°F to 300°F 32°F to 132°F -67°F to 300°F -67°F to 220°F
POWER SUPPLY REQUIREMENTS** Voltage Voltage Regulation Current	Plus and Minus 12 Vdc $\pm \frac{1}{2}$ Vdc 70 mA	Plus and Minus 12 Vdc $\pm \frac{1}{2}$ Vdc 70 mA

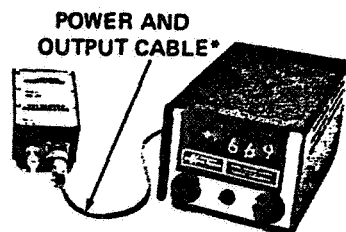
* Values are typical (unless noted) and based upon 300 Series Stainless Steel nonmagnetic or ASME 4130 magnetic targets.
** See options for Kaman Power Supply.

SYSTEM CONFIGURATIONS

DIMENSIONS ARE MAXIMUM IN MILLIMETERS (INCHES)



**MICROMETER
CALIBRATION
FIXTURE***



**POWER AND
OUTPUT CABLE***

KD-2300-.5SU

P-3100
POWER SUPPLY*

Figure 2 Calibration and Measuring System

* Recommended optional accessories.

OPTIONS

Thermal Sensitivity compensation calibration at specified displacement over any 56C degrees (100F degrees) maximum band between -55°C and 150°C (-67°F and 300°F) for sensor and cable.

† Power Supply P-3000 or P-3100 with digital readout, to provide regulated + and - 12Vdc output for up to 6 systems. Standard input voltage is 115 Vac. If 230 Vac is required add suffix A (e.g. P-3000A). Specification sheets are available.

† Power and output cable: 10 feet (part no. 850657-010).

† Micrometer Calibration Fixture:

English - part number 850854 - 001

Metric - part number 850854 - 002

† Recommended accessories for ease of system calibration and use. (see Figure 2).

ORDERING INFORMATION

Specify by model number and the desired options. Model number KD-2300-.5SU is for nonmagnetic targets and KD-2300-.5SUM is for magnetic targets. If two or more sensors are to be mounted within 4 mm (0.160 inches) of each other, synchronization of the electronics is suggested.

All specifications are subject to change without notice.

KAMAN SCIENCES CORPORATION
A KAMAN COMPANY

1500 Garden of the Gods Rd • Tel. (303) 599-1500 • Telex 452412
Mailing Address: P. O. Box 7463 • Colorado Springs, Colorado 80933

Printed in the U.S.A.

APPENDIX C

Tares

The following figures are the outputs of the sensors with the wind off. The endplates are on the airfoil. In order, they are the elastic tares (Figure C.1), pitch tares (Figures C.2-C.4), and plunge tares (Figures C.5-C.6). There were no mean outputs from the balance sensors due to pure plunge.

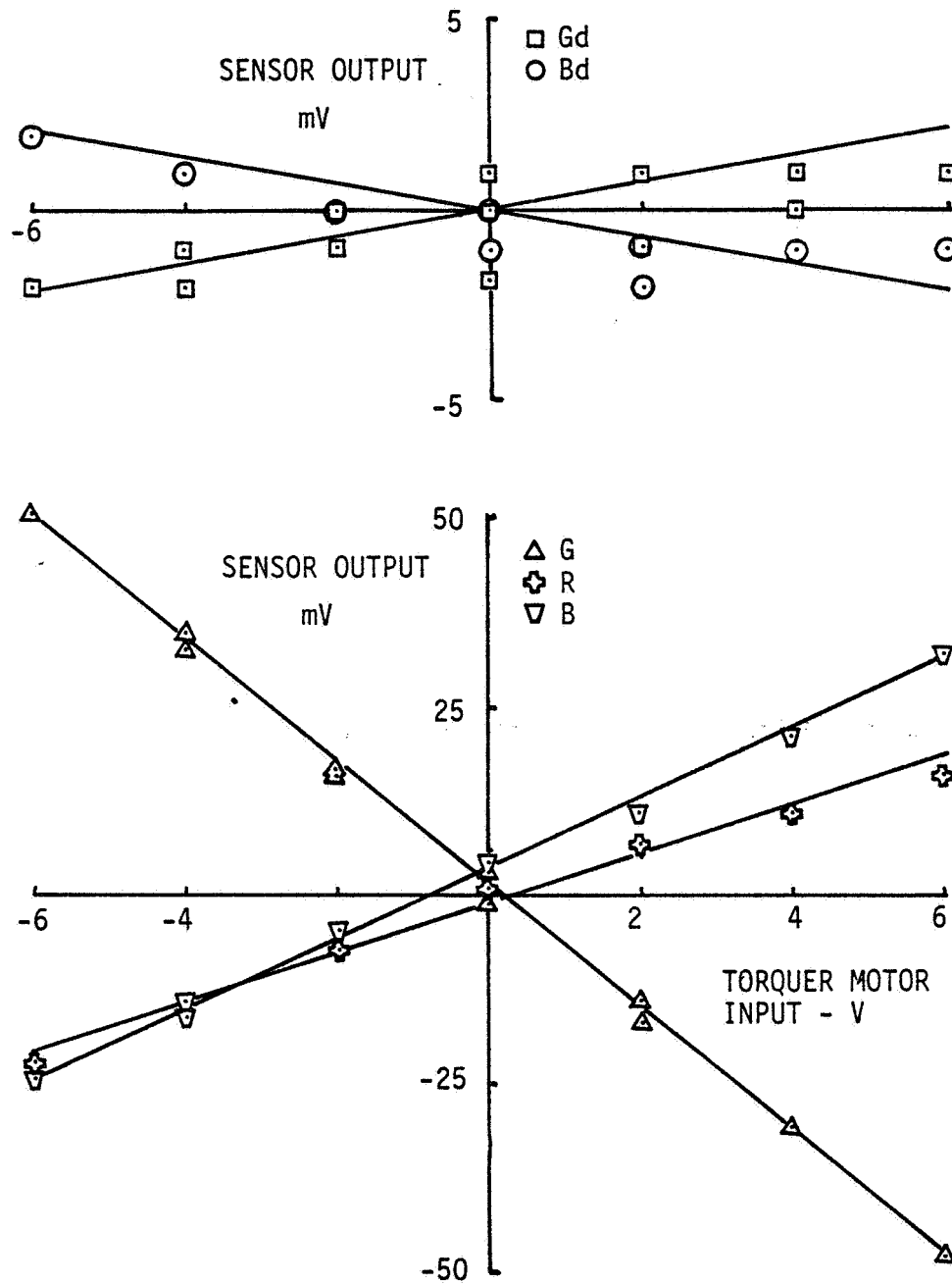


Figure C.1: Sensor Outputs due to Pitch Motor Torque.

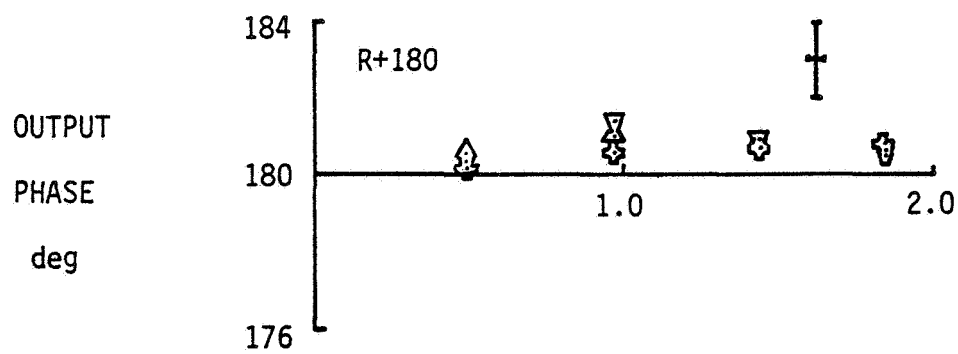
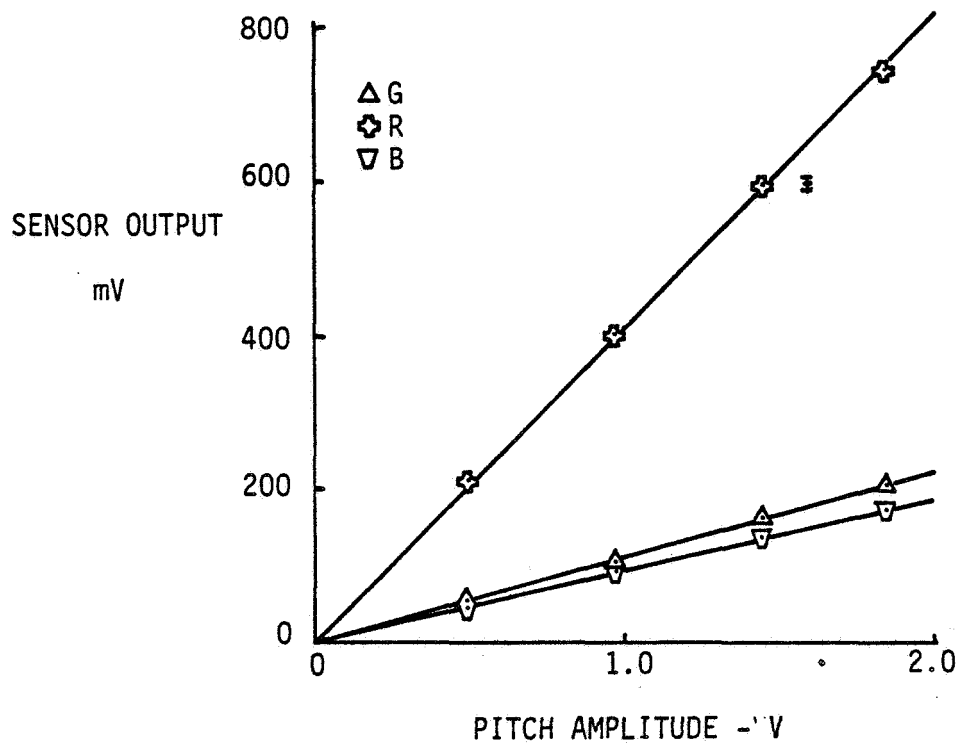


Figure C.2: Load-Cell Tares in Simple Pitch.

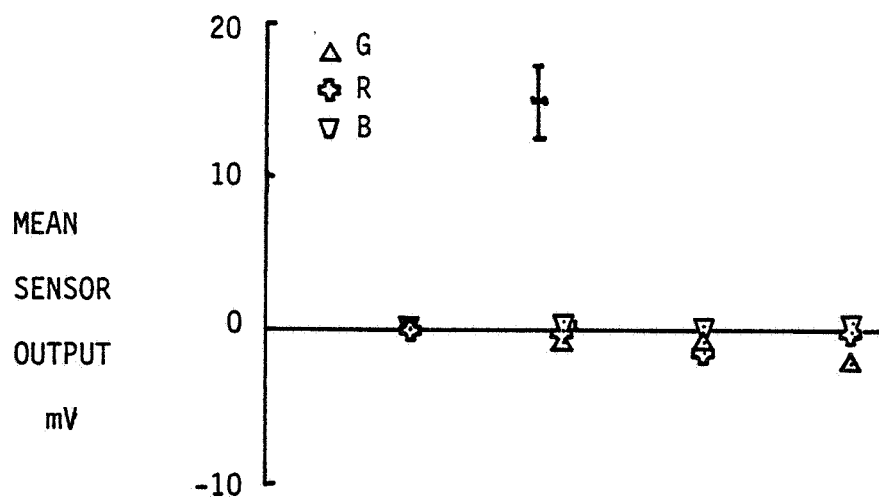
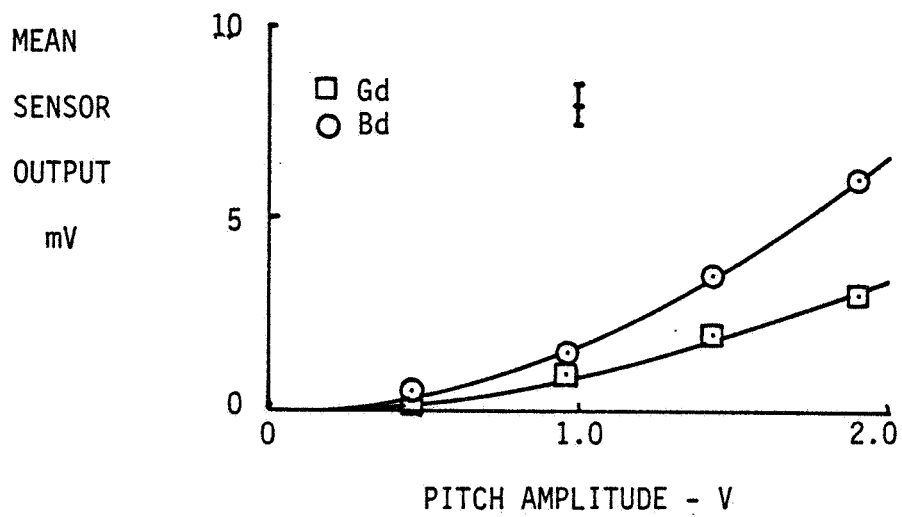


Figure C.3: Sensor Mean Output Tares in Simple Pitch.

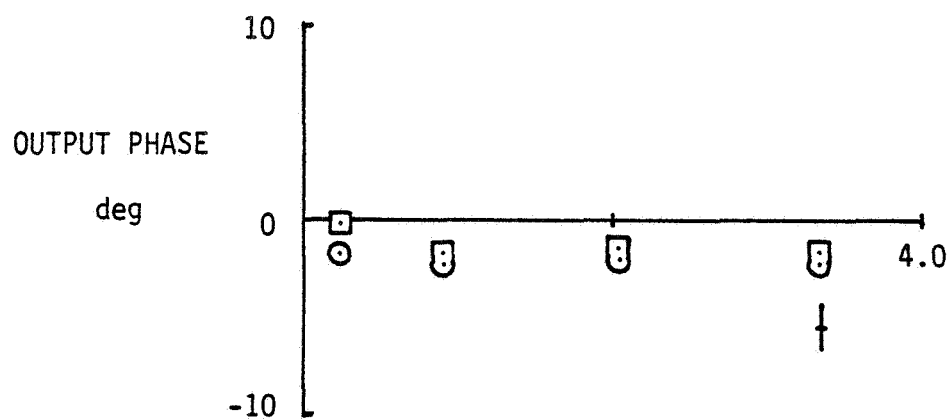
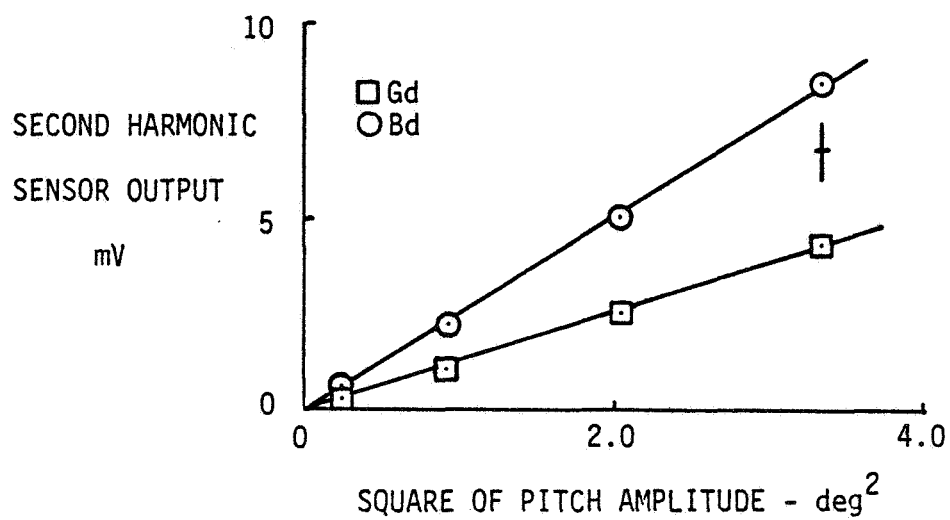


Figure C.4: Sensor Second-Harmonic Output Tares in Simple Pitch.

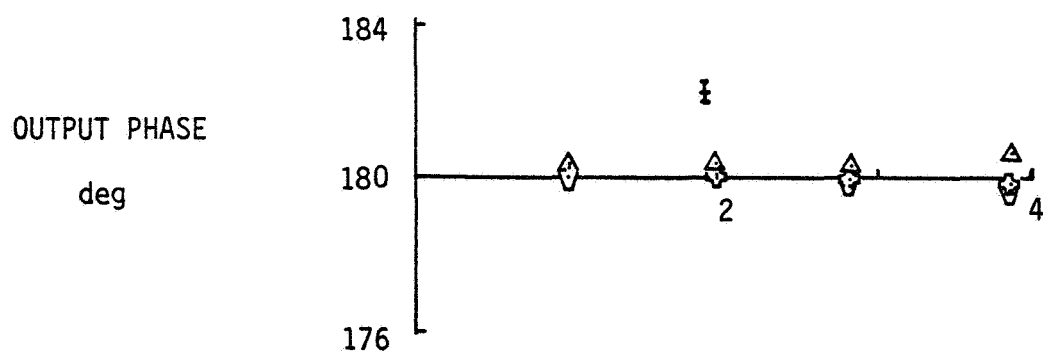
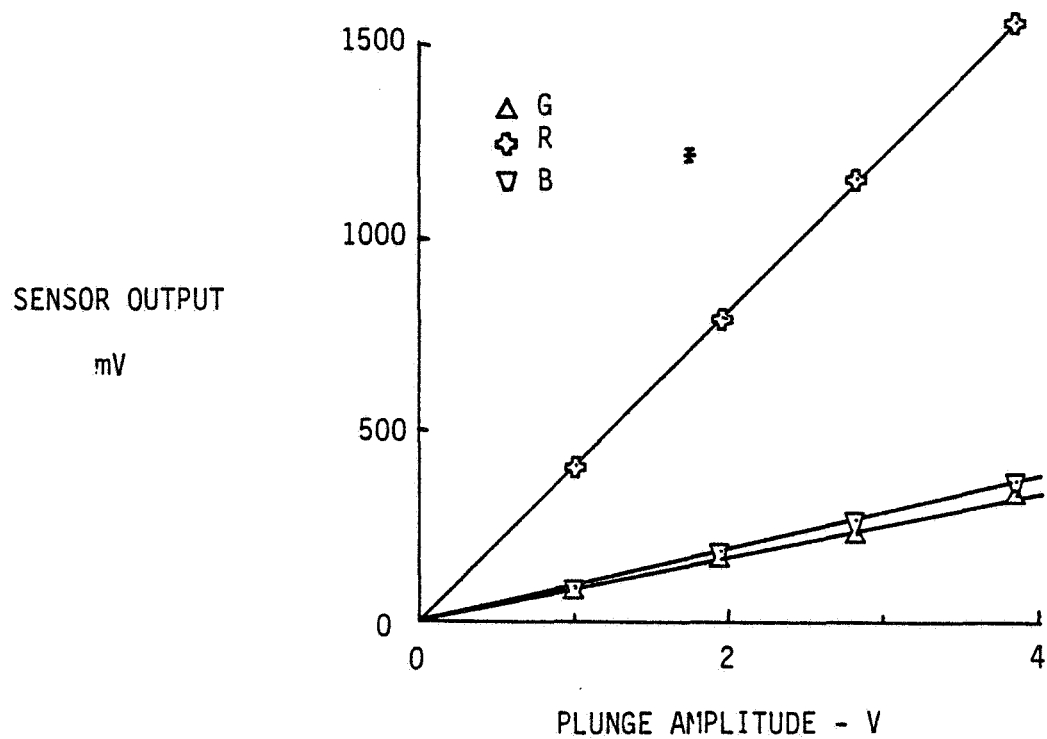


Figure C.5: Load-Cell Tares in Pure Plunge.

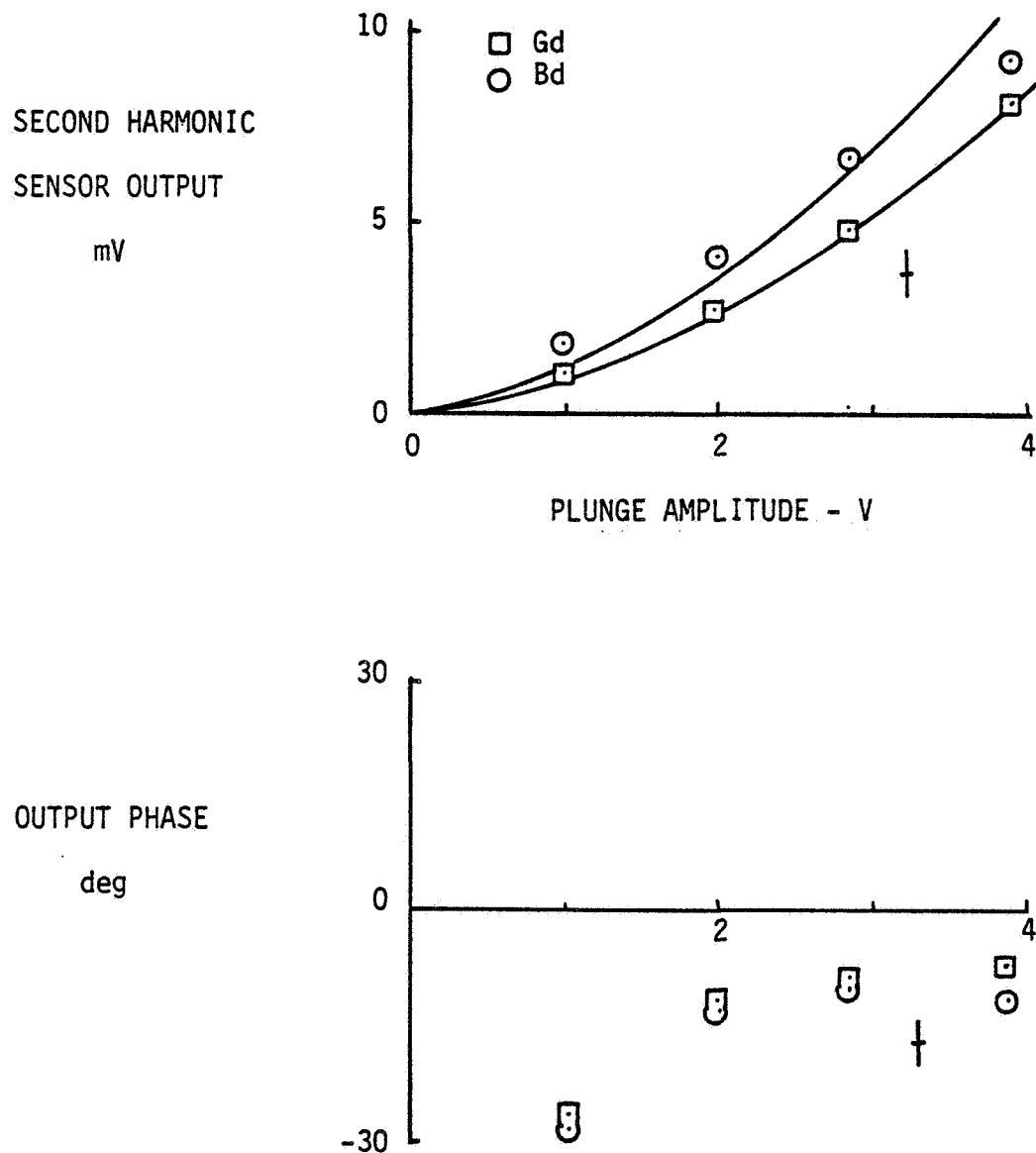


Figure C.6: Sensor Second-Harmonic Output Tares in Pure Plunge.

APPENDIX D

Simple Pitch Data

Figures D.1-D.3 show the variation of the normal force with respect to the amplitude of pitch oscillation at three reduced frequencies. Figures D.4-D.6 show the pitching moment. The changes in mean suction and drag are presented in Figures D.7-D.9. Finally, the second harmonic suction is shown in Figures D.10-D.12. For comparison the potential theory corrected for wall effects is drawn as a solid line.

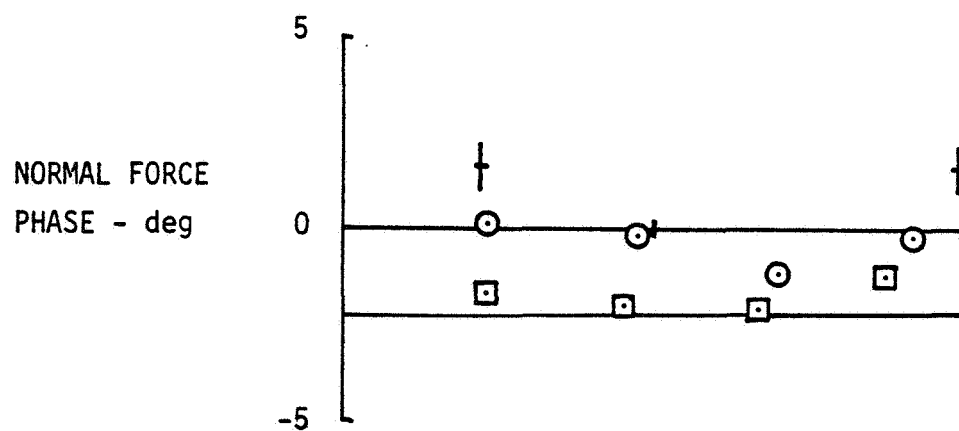
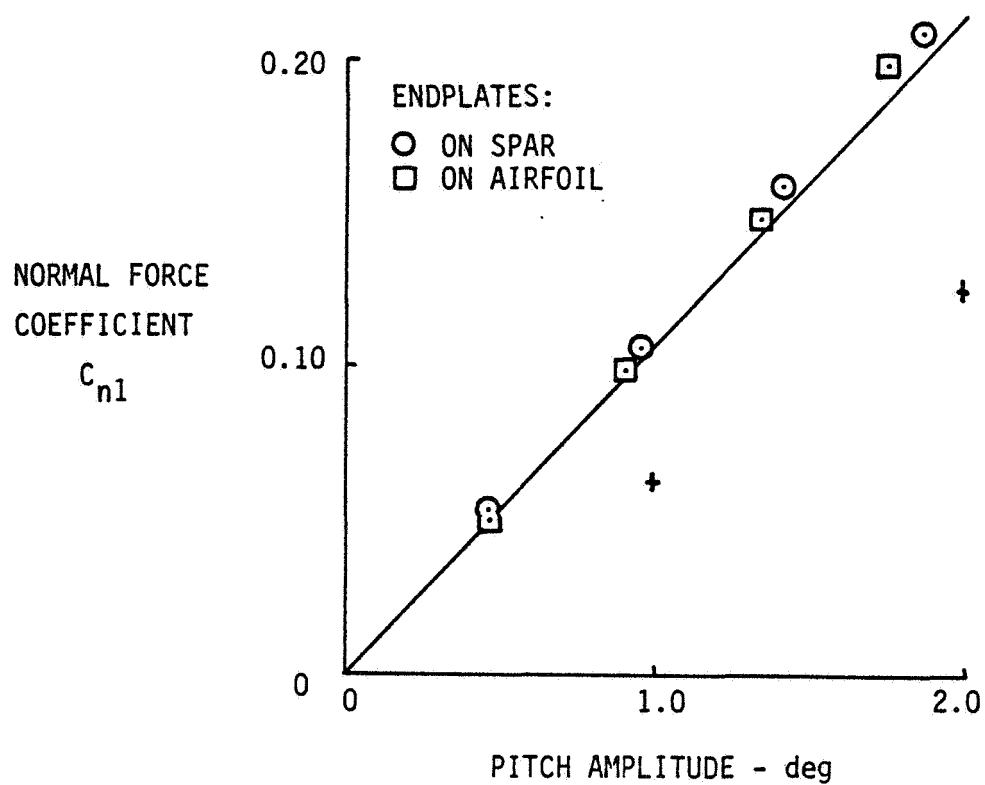


Figure D.1: Normal Force in Simple Pitch, $k=0.16$.

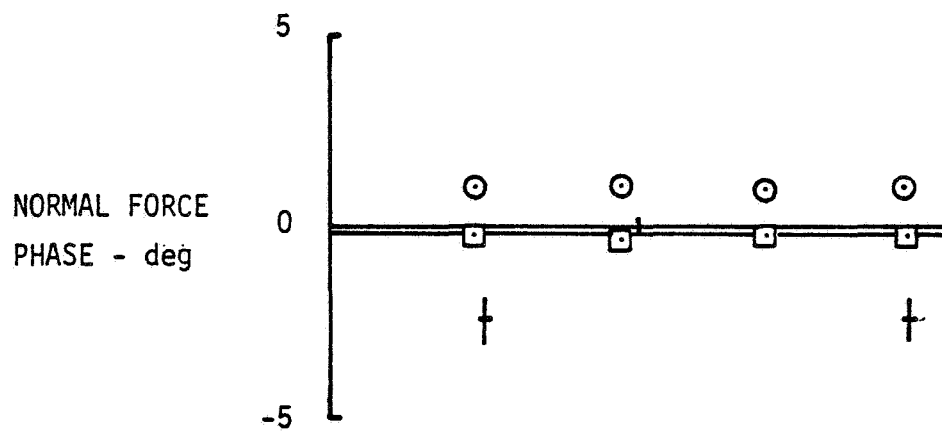
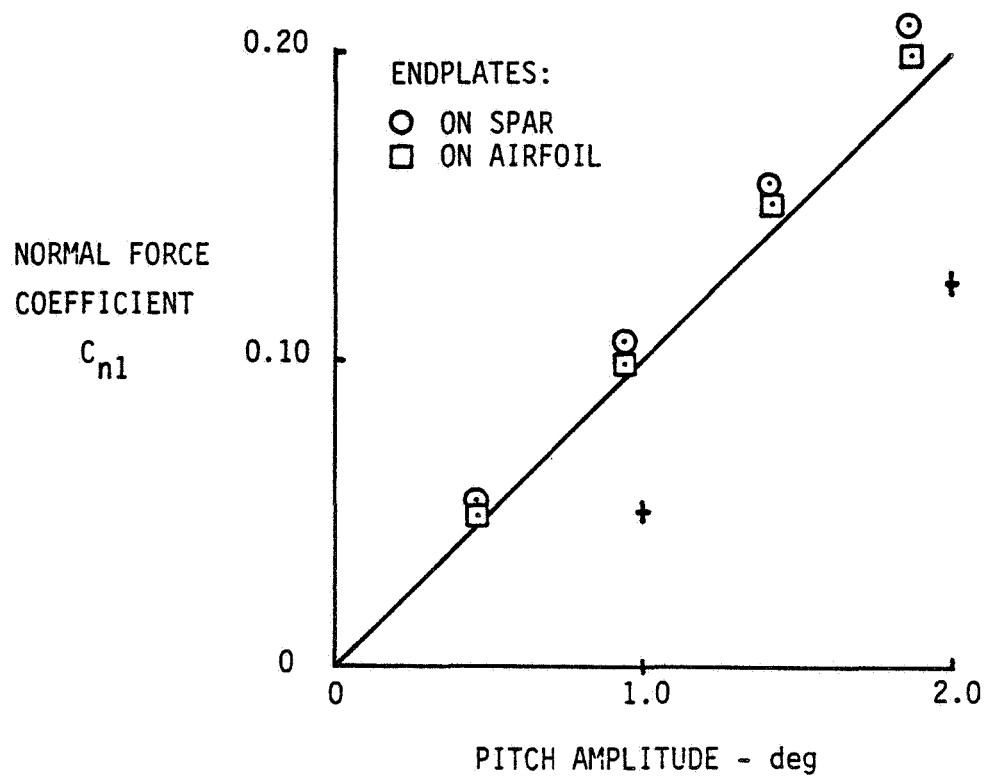


Figure D.2: Normal Force in Simple Pitch, $k=0.22$.

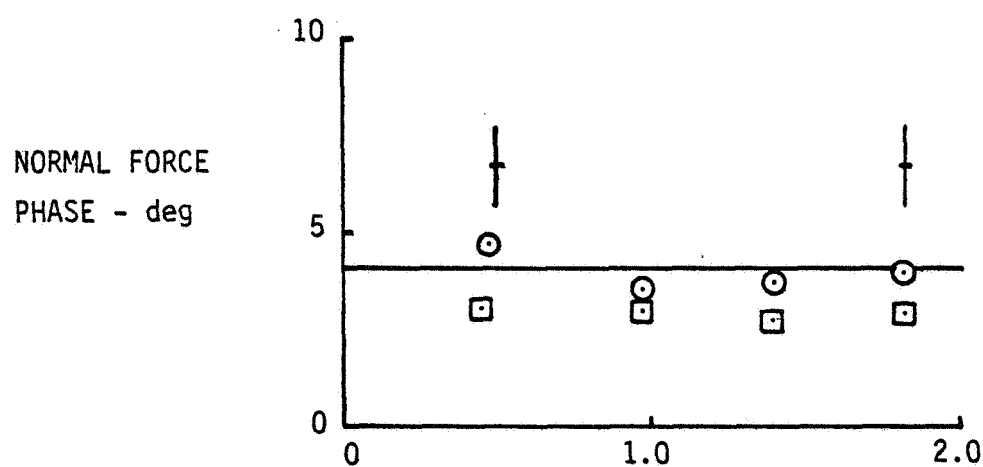
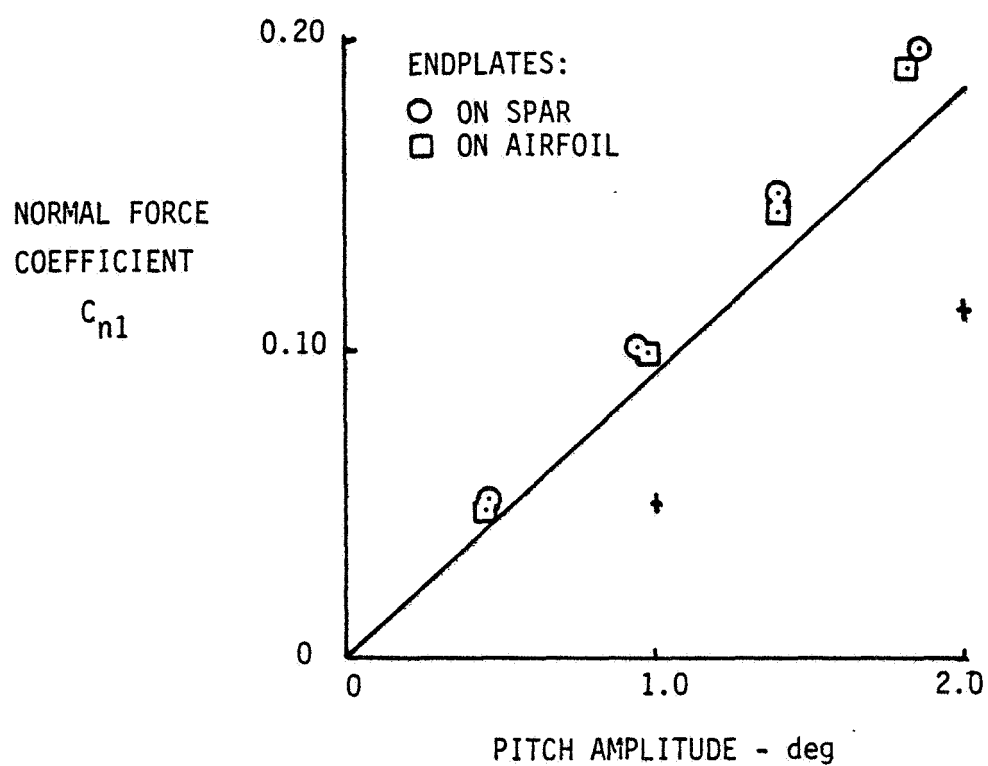


Figure D.3: Normal Force in Simple Pitch, $k=0.29$.

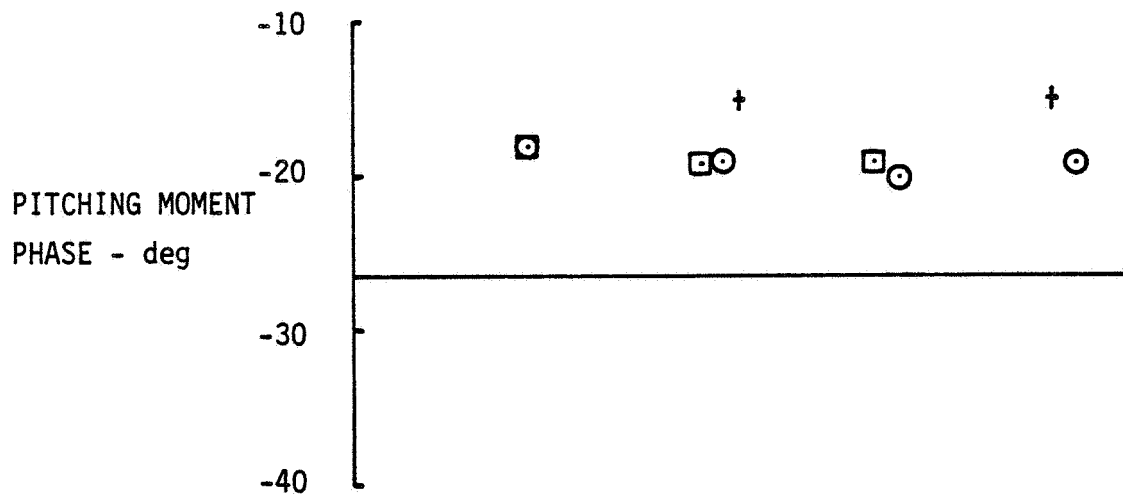
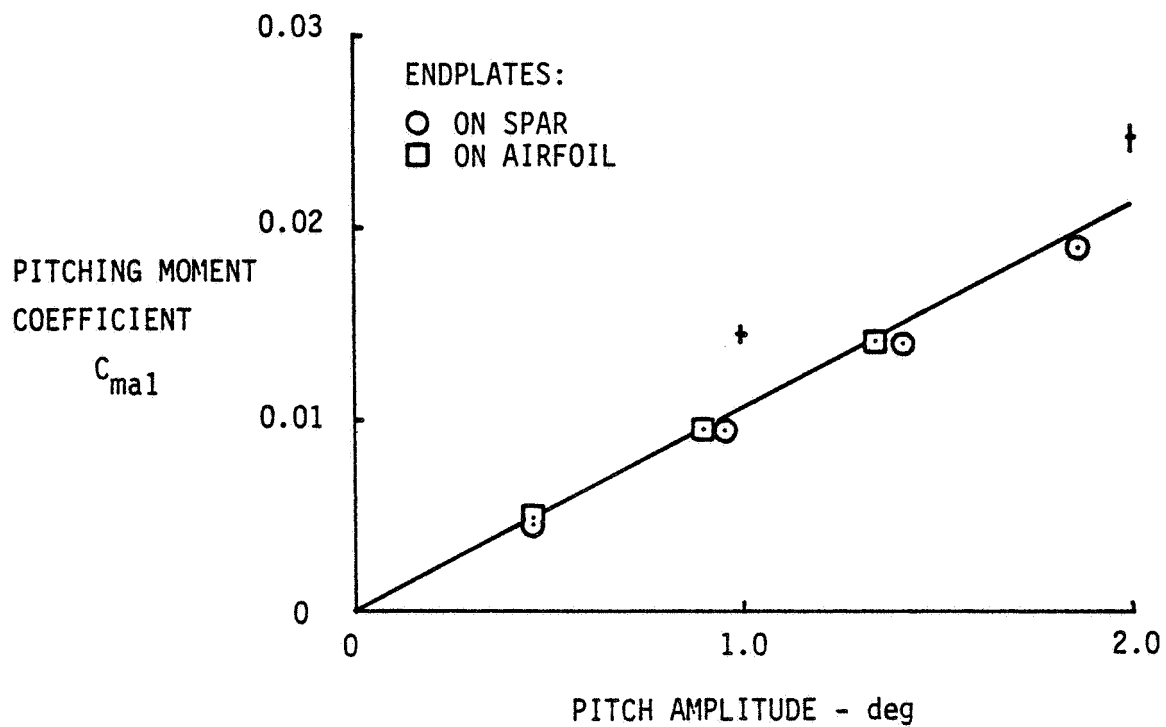


Figure D.4: Pitching Moment in Simple Pitch, $k=0.16$.

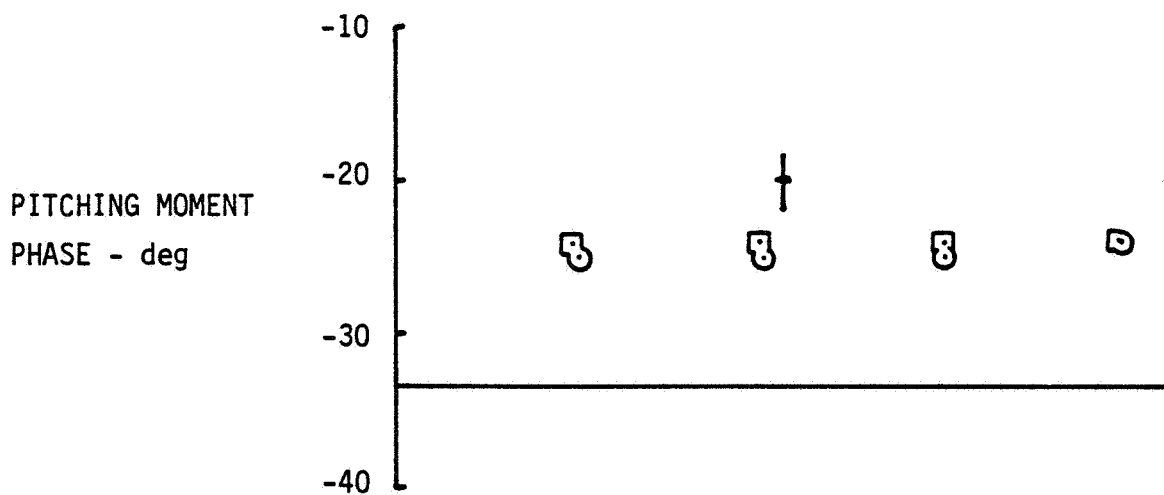
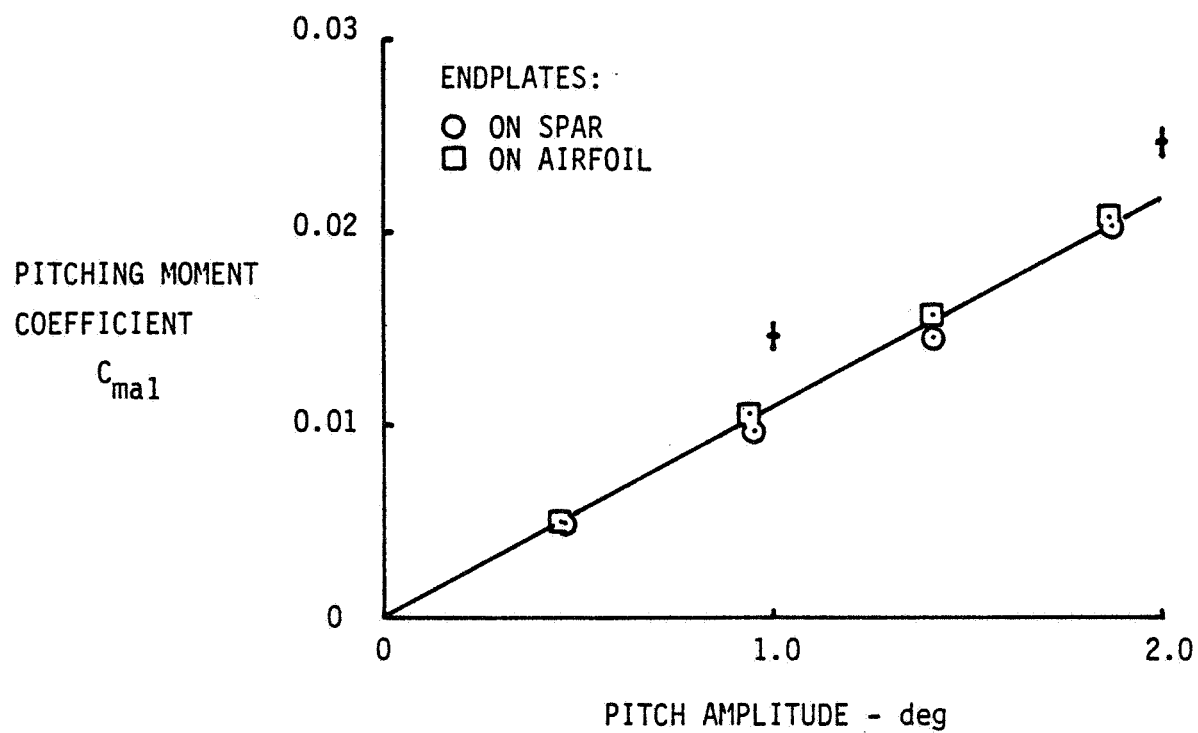


Figure D.5: Pitching Moment in Simple Pitch, $k=0.22$.

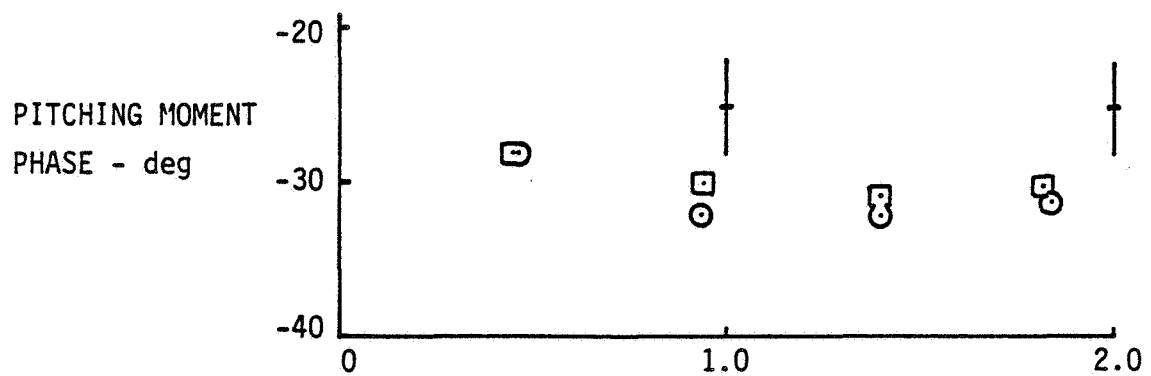
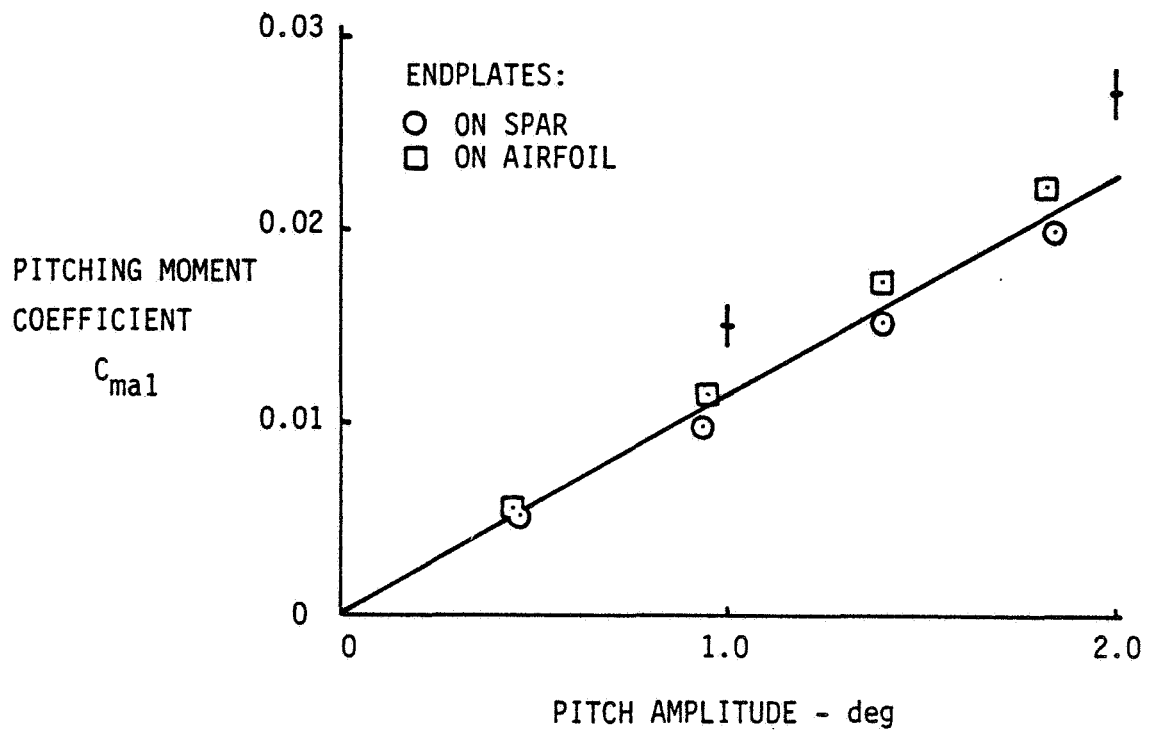


Figure D.6: Pitching Moment in Simple Pitch, $k=0.29$.

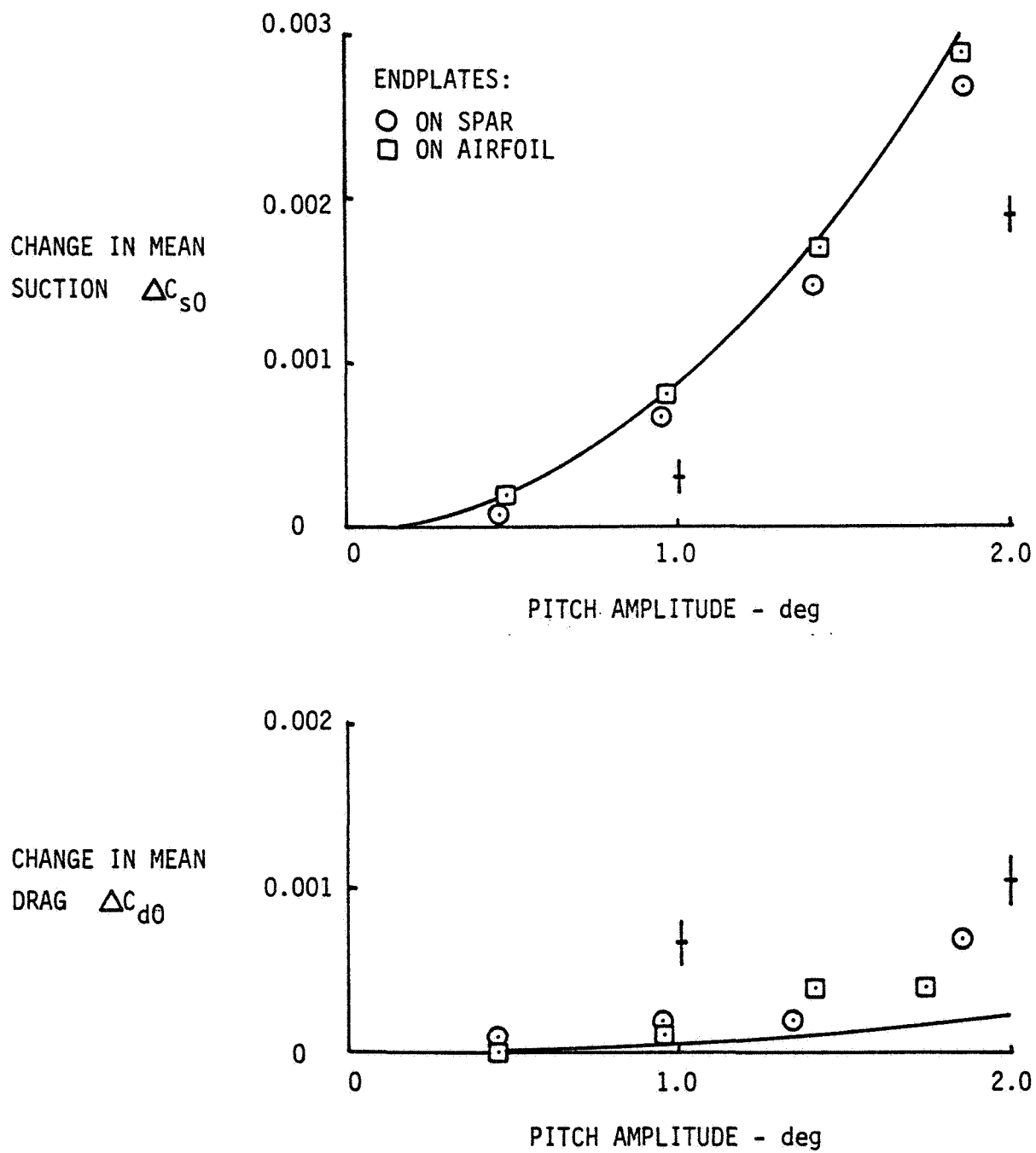


Figure D.7: Change in Mean Suction and Drag in Simple Pitch, $k=0.16$.

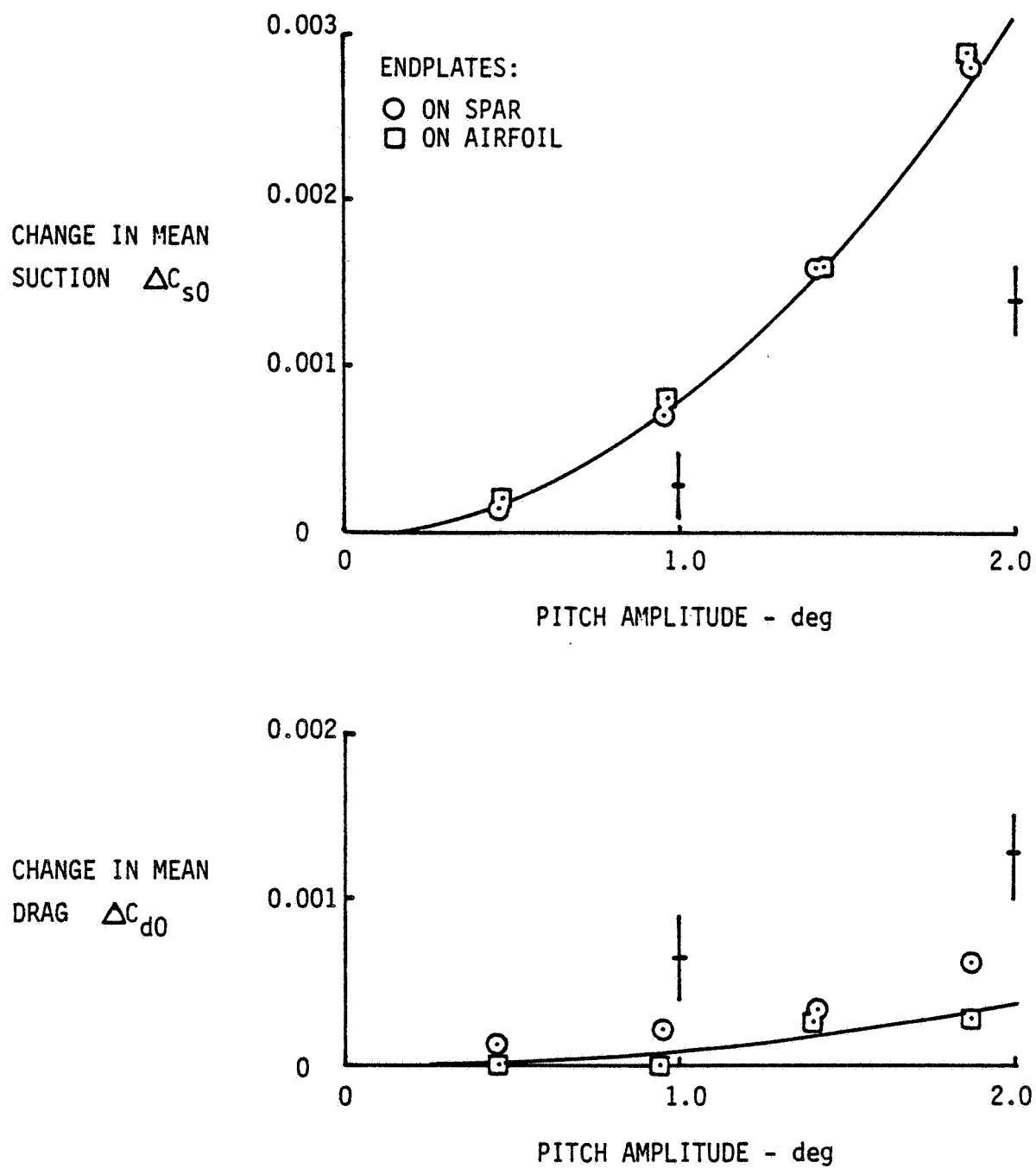


Figure D.8: Change in Mean Suction and Drag in Simple Pitch, $k=0.22$.

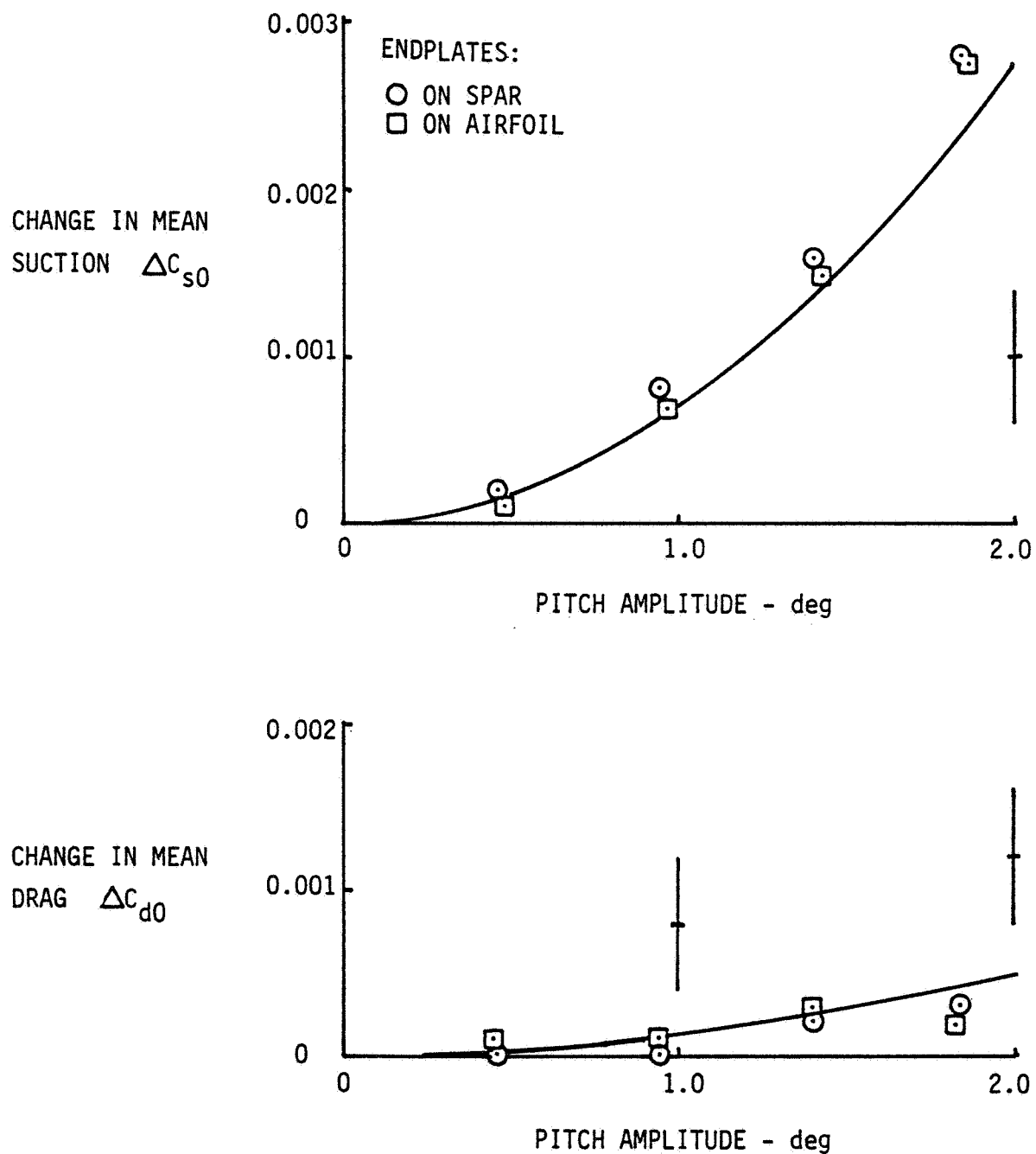


Figure D.9: Change in Mean Suction and Drag in Simple Pitch, $k=0.29$.

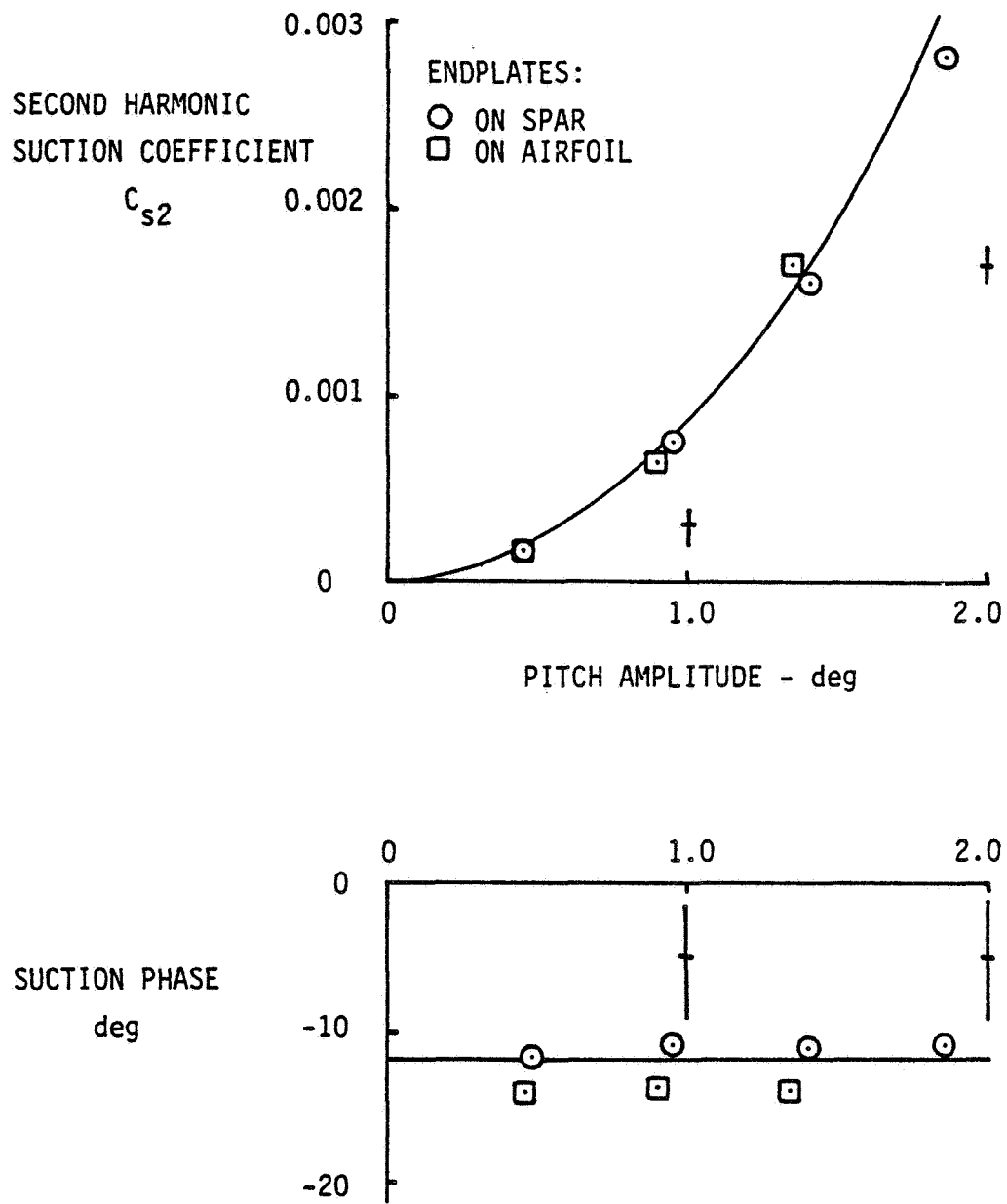


Figure D.10: Second Harmonic Suction in Simple Pitch, $k=0.16$.

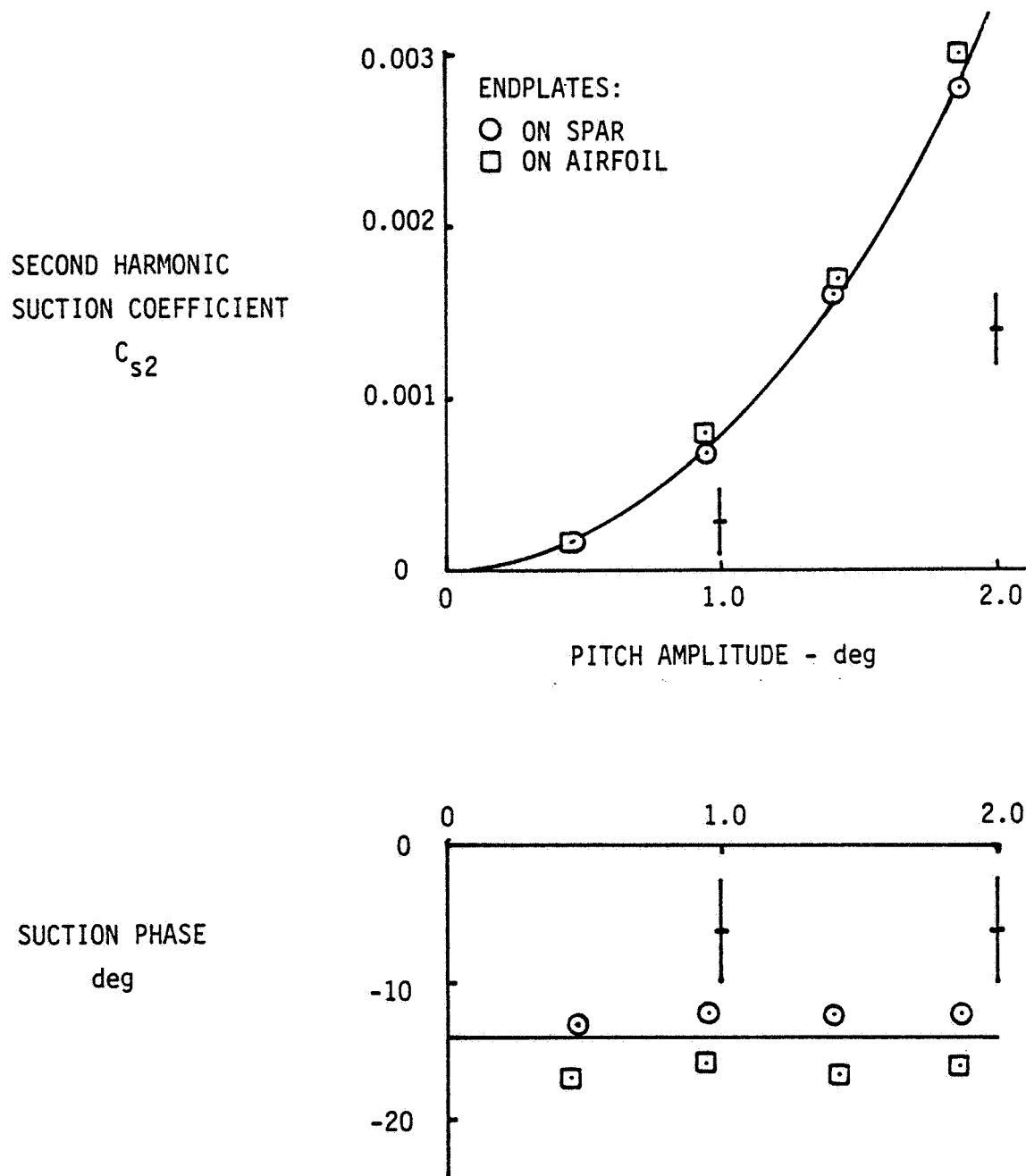


Figure D.11: Second Harmonic Suction in Simple Pitch, $k=0.22$.

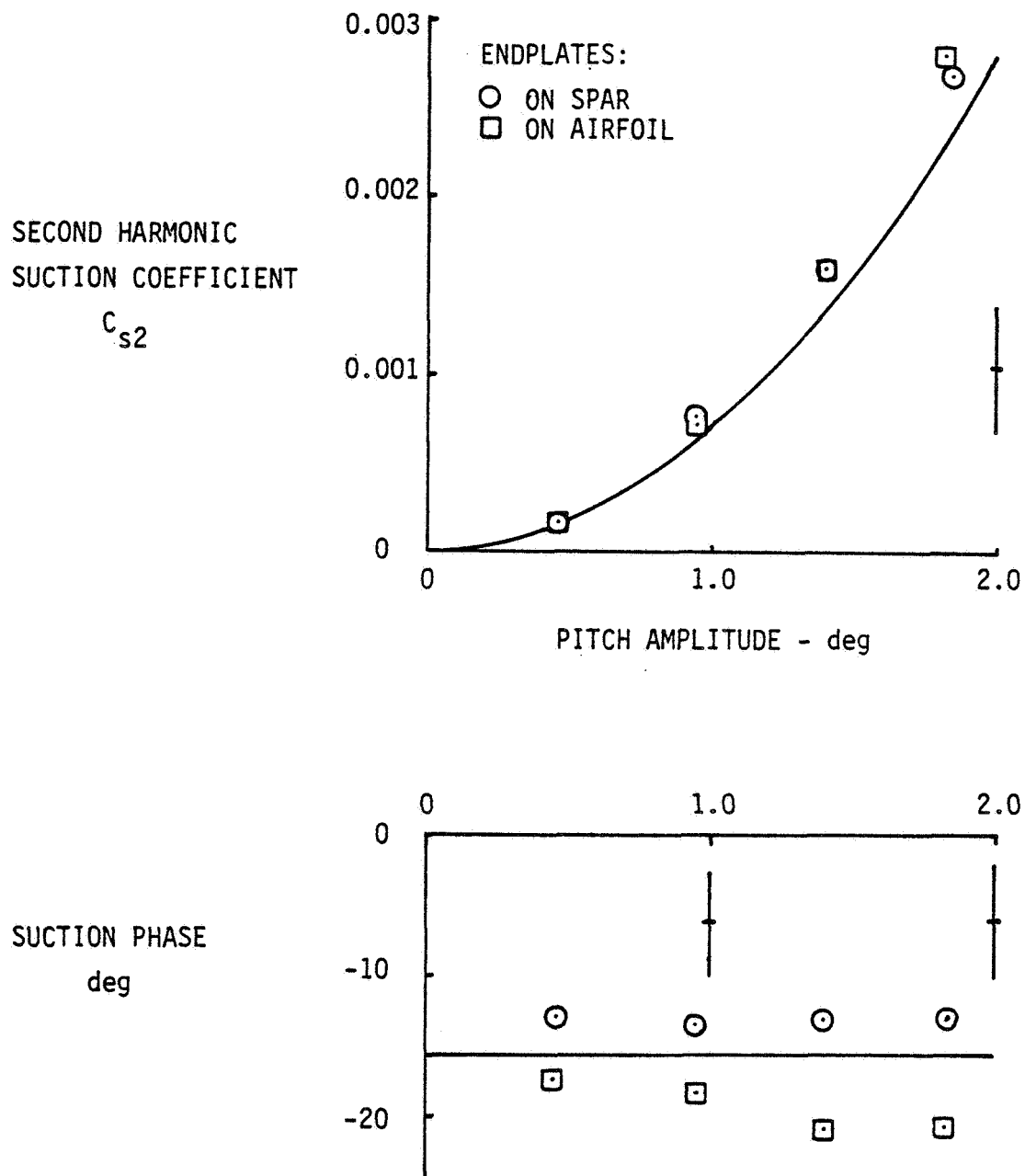


Figure D.12: Second Harmonic Suction in Simple Pitch, $k=0.29$.

APPENDIX E

Simple Plunge Data

Figures E.1-E.3 show the variation of the lift with respect to the amplitude of plunge oscillation at the three reduced frequencies. Following that is the pitching moment (E.4-E.6) and the change in mean drag (E.7-E.9). For comparison the potential theory corrected for wall effects is drawn as a solid line.

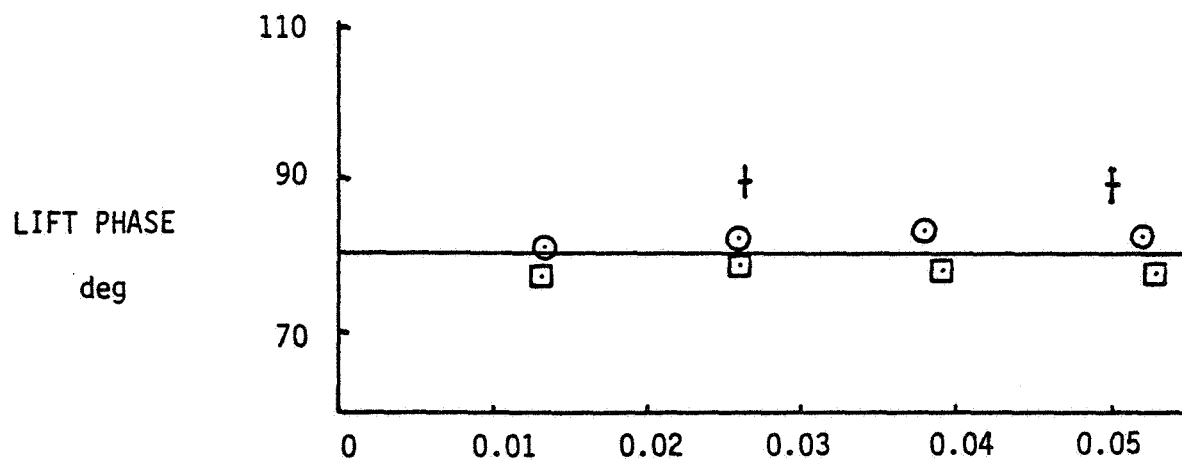
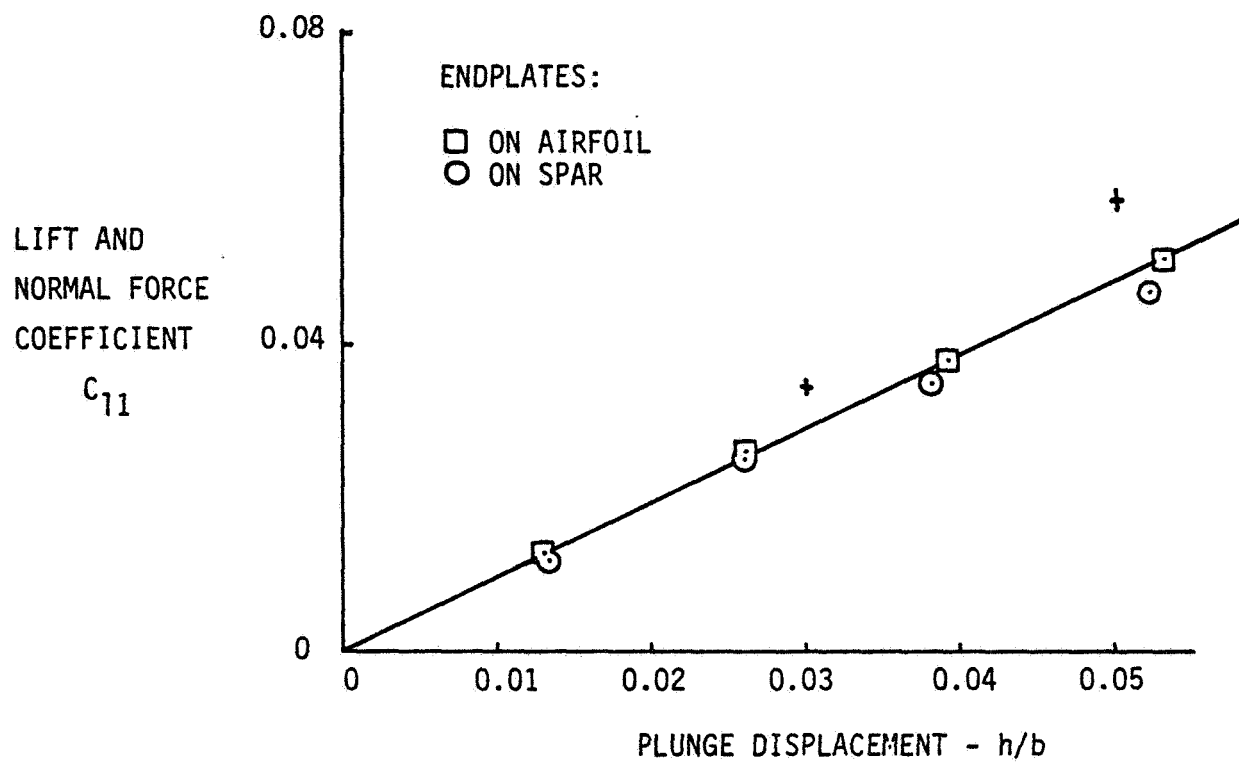


Figure E.1: Lift in Pure Plunge, $k=0.16$.

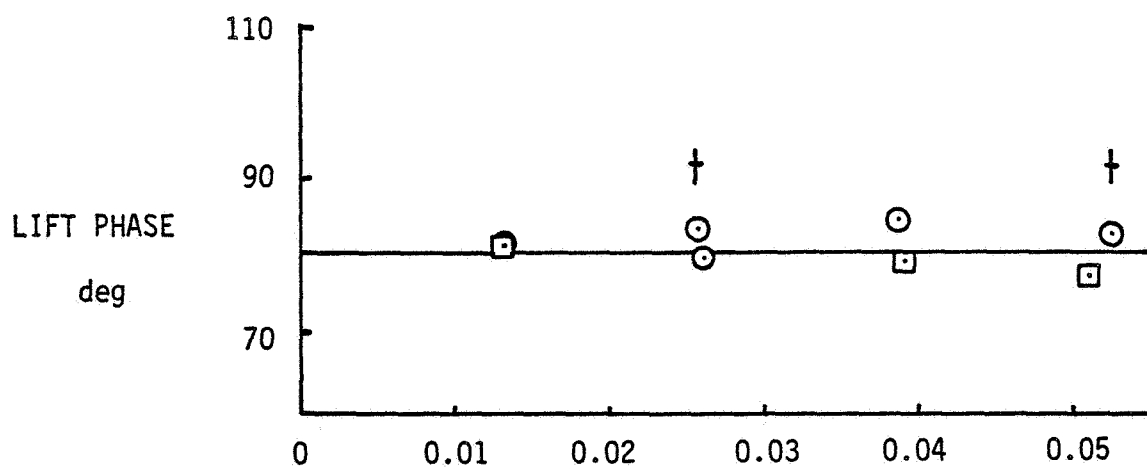
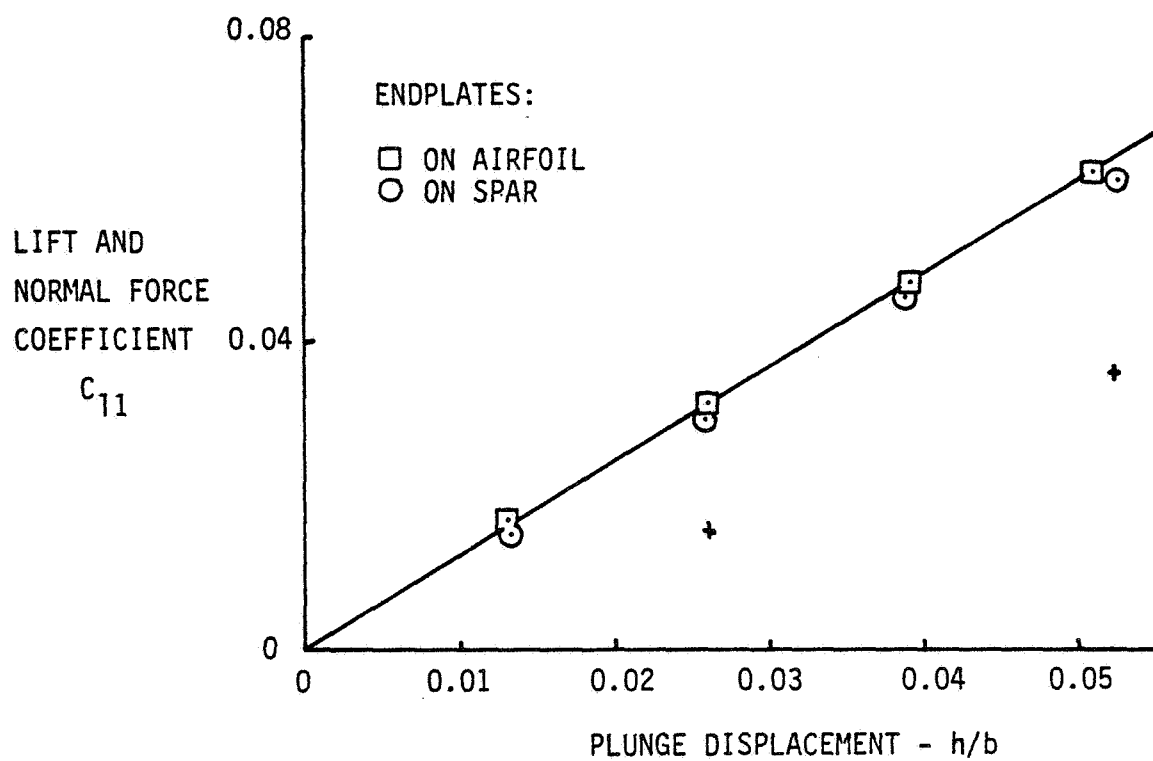


Figure E.2: Lift in Pure Plunge, $k=0.22$.

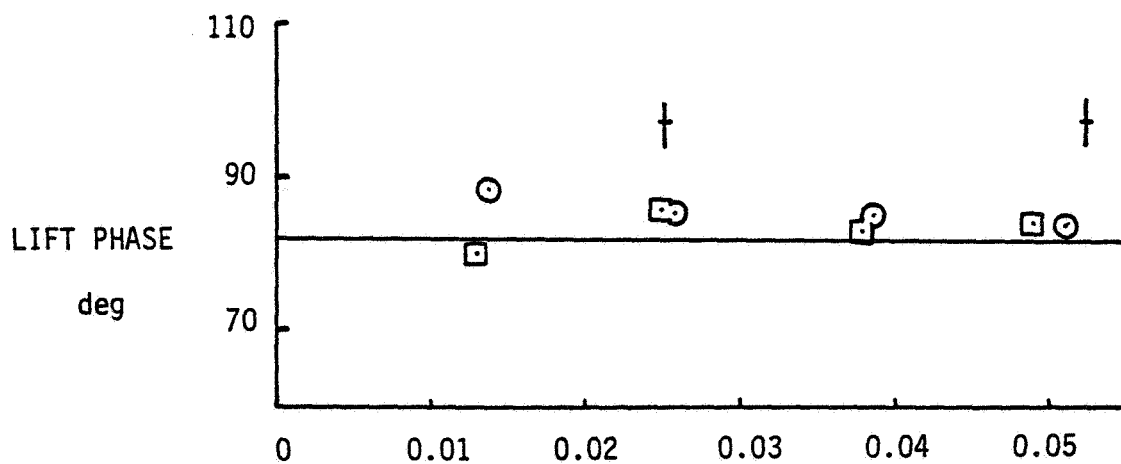
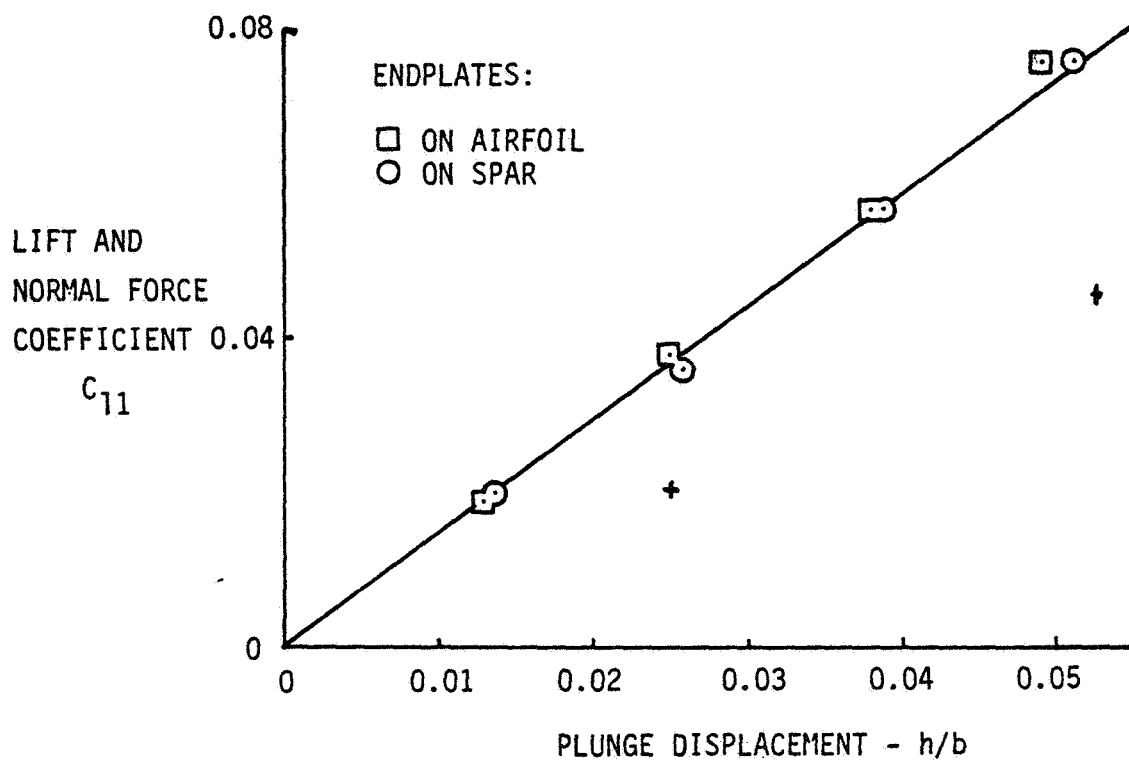


Figure E.3: Lift in Pure Plunge, $k=0.29$.

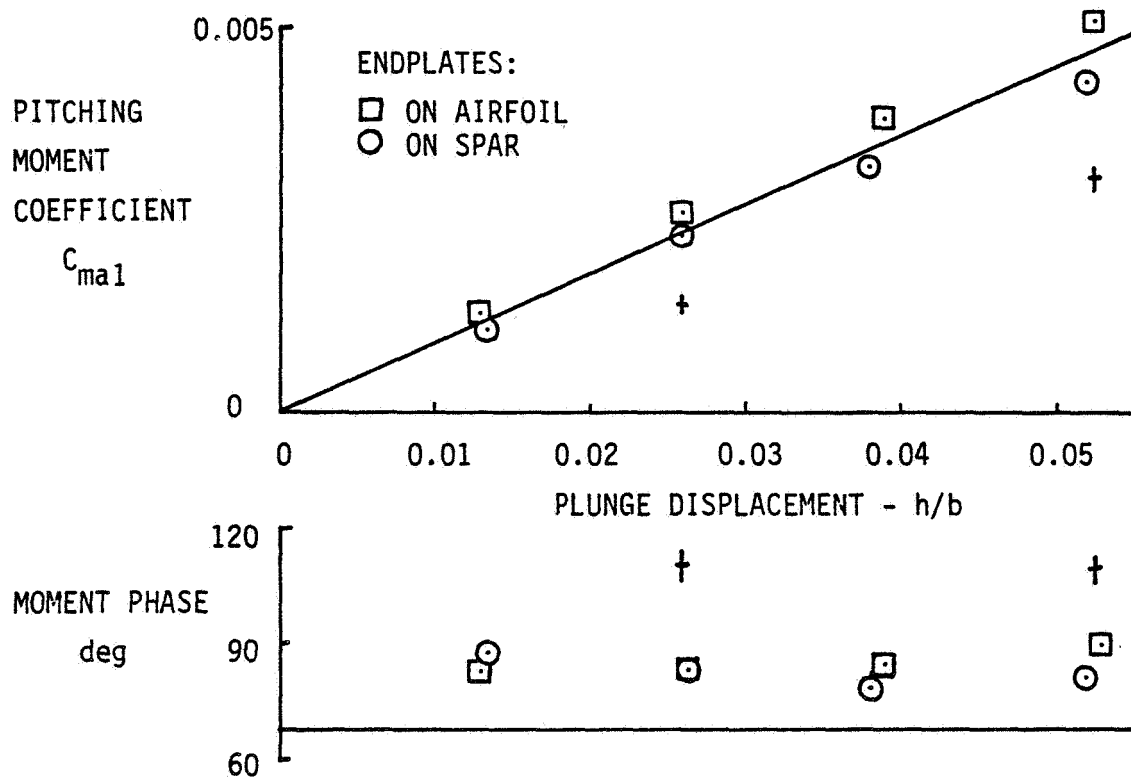


Figure E.4: Pitching Moment in Pure Plunge, $k=0.16$.

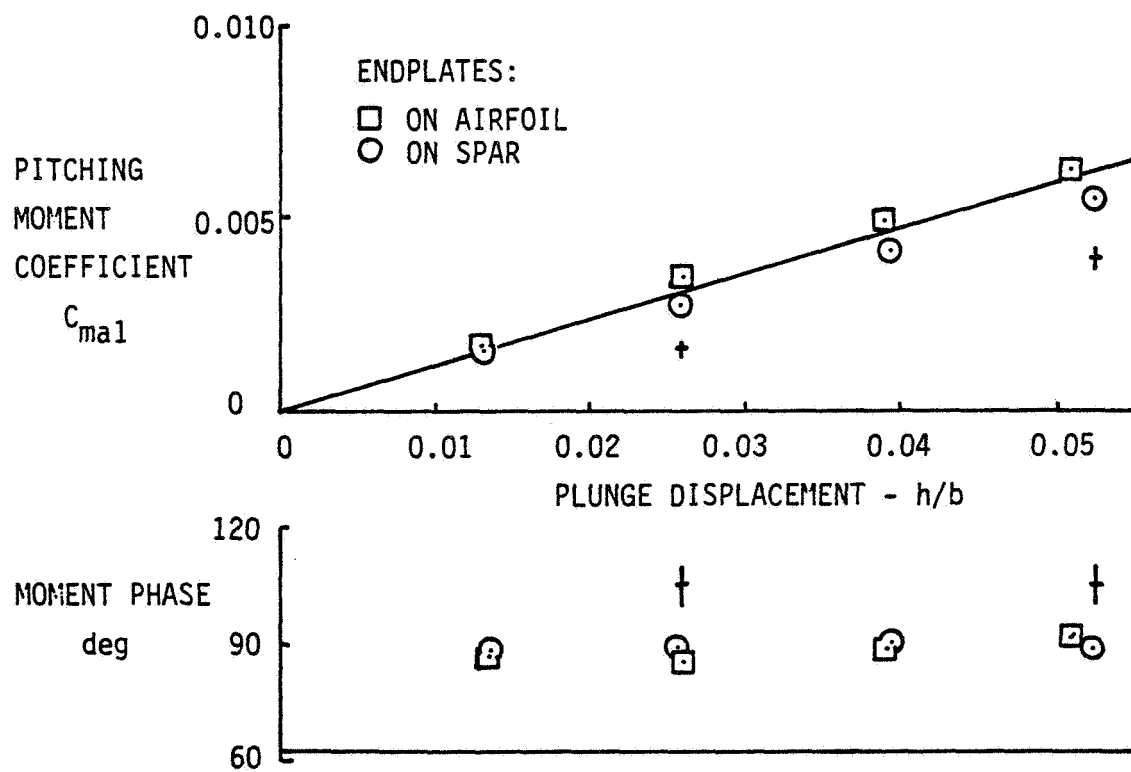


Figure E.5: Pitching Moment in Pure Plunge, $k=0.22$.

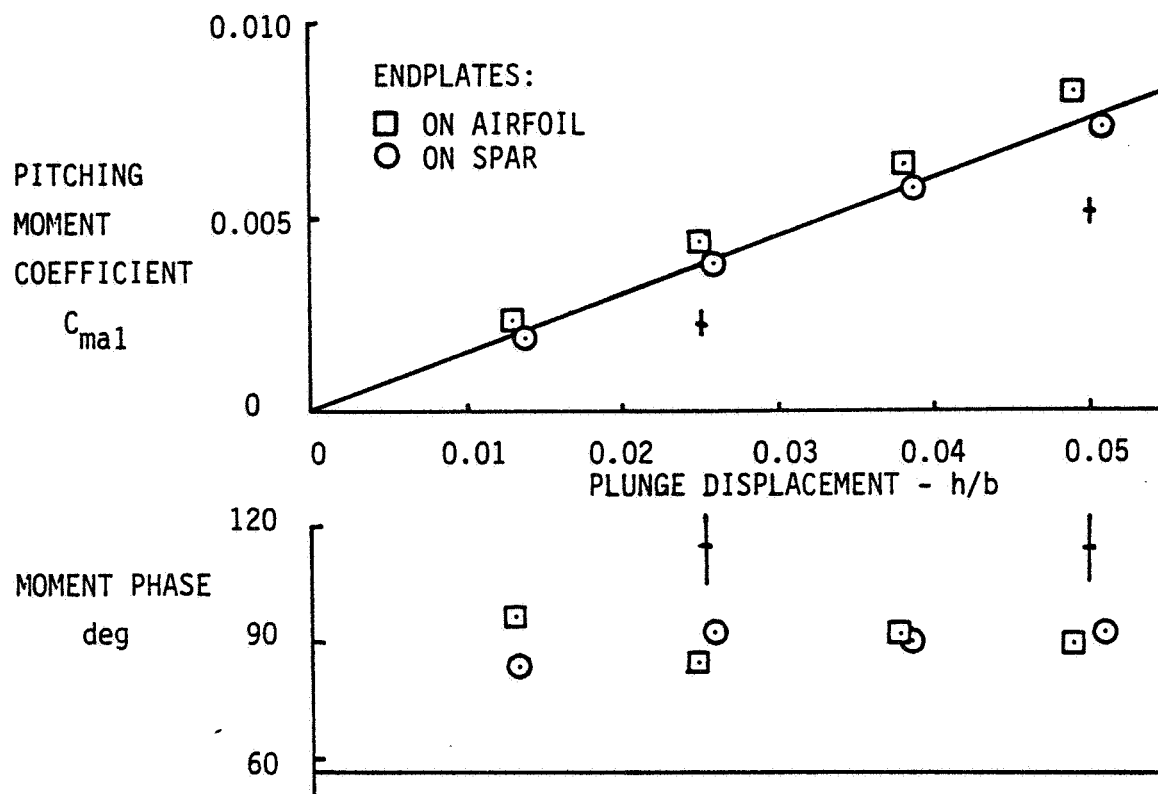


Figure E.6: Pitching Moment in Pure Plunge, $k=0.29$.

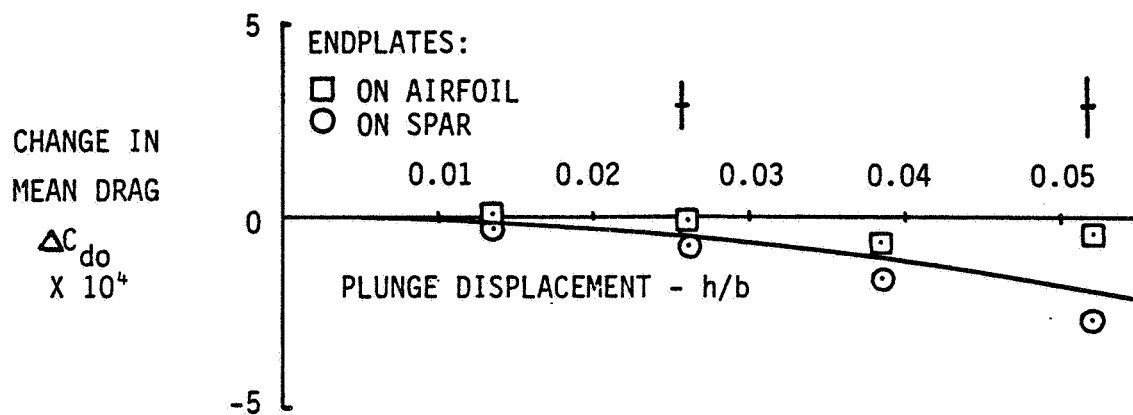


Figure E.7: Drag in Pure Plunge, $k=0.16$.

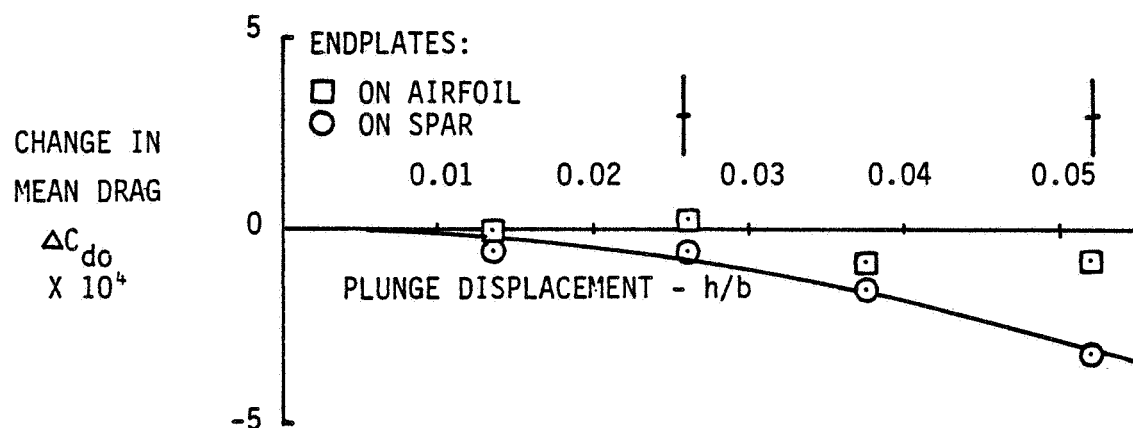


Figure E.8: Drag in Pure Plunge, $k=0.22$.

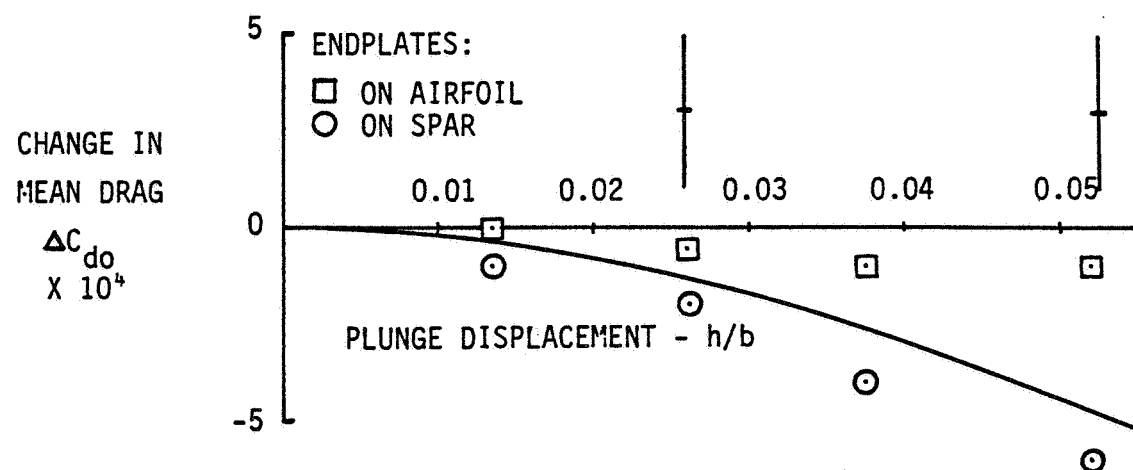


Figure E.9: Drag in Pure Plunge, $k=0.29$.

REFERENCES

1. Patrick, J.L.G.F., "Natural Flight and Related Aeronautics", Paper No. FF-7, Institute of Aeronautical Sciences, New York, 1952.
2. McCroskey, W.J., "Some Current Research in Unsteady Fluid Dynamics", ASME Winter Meeting, New York, 8 December 1976.
3. Swimming and Flying in Nature, ed. by Wu, Brokaw and Brennan, Plenum Press, New York, 1975.
4. Lighthill, M.J., Mathematical Biofluidynamics, SIAM, Philadelphia, 1975.
5. Lilienthal, O., Birdflight as the Basis of Aviation, Longmans, Green & Co., New York, 1911.
6. Samuelson, A., Flight-Velocity, Boysen & Maasch, Hamburg, 1906.
7. Vasil'yev, G.S., "Principles of Flight of Models with Flapping Wings", Moscow 1953, (AD 107 173).
8. Vasil'yev, G.S., "Models with Flapping Wings", Izdatel'stvo Dosaaf, Moscow 1960, (NTIS IT 66-62401).
9. Wolf, J. "The Technological Prospects for Oscillating Wing Propulsion of Ultralight Gliders", Proc. Second Int'l. Symp. on the Technology and Science of Low-speed and Motorless Flight, Cambridge, MA, 11-15 Sept. 1974, p.173.
10. Smith, G., "Pseudo-ornithopter Propulsion", First International Symposium on the Technology and Science of Low-Speed and Motorless Flight, Boston, MA, October 1972.
11. Patrick, J.L.G.F., "Design and Construction of a Full Scale Ornithopter", Staten Island Community College, 1960.
12. Patrick, J.L.G.F., U.S. Patent 2,783,955, March 5, 1957.
13. Weis-Fogh, T., "Unusual Mechanisms for the Generation of Lift in Flying Animals", Scientific American, November 1975.
14. Theodorsen, T., "General Theory of Aerodynamic Instability and the Mechanism of Flutter", NACA Report 496, 1935.

15. Garrick, I.E., "Propulsion of a Flapping and Oscillating Airfoil", NACA Report 557, 1936.
16. Timman, R., "The Aerodynamic Forces on an Oscillating Airfoil between Two Walls", J. Applied Scientific Research, Vol. A3, 1951, pp. 31-57.
17. Wu, T.Y., "Hydrodynamics of Swimming Propulsion Parts 1, 2 and 3", J. Fluid Mechanics, Vol. 46, Part 1 (1971), pp. 337-355, Part 3 (1971), pp. 521-544, Part 3 (1971), pp. 545-568.
18. Wu, T.Y., "Swimming of a Waving Plate", J. Fluid Mechanics, Vol. 10, Part 3 (1961), pp. 321-344.
19. McCroskey, W.J., "Inviscid Flowfield of an Unsteady Airfoil", AIAA J., Vol. 11, No. 8, August 1973, pp. 1130-1137.
20. Fung, Y.C., The Theory of Aeroelasticity, Dover, New York, 1969.
21. Philippe, J.J., and Sagner, J., "Calcul et Mesure des Forces Aerodynamiques sur un Profil Oscillant avec et sans Decrochage", AGARD Conference Proceedings No. 111 on Aerodynamics of Rotary Wings, Paper 11, Sept. 1972.
22. Maresca, C., Favier, D., and Rebont, J., "Experiments on an Aerofoil at high Angle of Incidence in Longitudinal Oscillations", J. Fluid Mechanics, Vol. 92, Part 4 (1979), pp. 671-690.
23. Favier, D., Rebont, J., and Maresca, C., "Large Amplitude Fluctuations of Velocity and Incidence on an Oscillating Airfoil", AIAA J., Vol. 17, No. 11, Nov. 1979, pp. 1265-1266.
24. Kunz, D.L., "Unsteady Drag and Dynamic Stall as Simulated in a Varying Freestream", Georgia Institute of Technology School of Aerospace Engineering Ph.D. Thesis, March 1976.
25. Hien, L.K., "Measurements on an Oscillating Aerofoil with Applications to Wind Energy Conversion", University of Auckland Department of Mechanical Engineering Ph. D. Thesis, Private Bag, Auckland, New Zealand, March 1980.
26. Scherer, J.O., "Experimental and Theoretical Investigation of Large Amplitude Oscillating Foil Propulsion Systems", Hydronautics, Inc., Tech. Report No. 662-1, 1968.
27. Obye, R.C., "Experimental Measurement of Lift and Thrust on an Airfoil Undergoing Large Amplitude Motion", Mississippi State University Dept. of Aerophysics and Aerospace Engr., M.S. Thesis, State College, MS, Dec. 1972.
28. Siekmann, J., "Theoretical Studies of Sea Animal Locomotion, Part 1", and "... Part 2", Ingenieur-Archiv, Vol. 31, 1962, p. 214, and Vol. 32, 1963, p. 40.

29. Kelly, H.R., "Fish Propulsion Hydrodynamics", Developments in Mechanics, Vol. 1, Plenum Press, New York. 1961.
30. Archer, R.D., Sapuppo, J., and Betteridge, D.S., "Propulsion Characteristics of Flapping Wings", Aeronautical Journal, Vol. 83, No. 825, Sept. 1979.
31. Fejtek, I., Nehera, J., "Experimental Study of Flapping Wing Lift and Propulsion", Aeronautical Journal, Vol. 84, No. 829, Jan. 1980, pp. 28-33.
32. Halfman, R.L., "Experimental Aerodynamic Derivatives of a Sinusoidally Oscillating Airfoil in Two Dimensional Flow", NACA Report 1108, 1952.
33. Walker, C., "The Flapping Flight of Birds", Journal of the Royal Aeronautical Society Vol. 31, 1927, pp. 337-342.
34. Osborne, M.F.M., "Aerodynamics of Flapping Flight with Application to Insects", Journal of Experimental Biology, Vol. 28, 1951, pp. 221-245.
35. Breder, C.M., "The Locomotion of Fishes", Zoologica, Vol. IV, No. 5, Sept. 28, 1926, pp. 159-296.
36. Lighthill, M.J., "Aquatic Animal Propulsion of High Hydromechanical Efficiency", J. Fluid Mech. (1970), Vol. 44, part 2, pp. 265-301.
37. James, E.C., "A Note on Flapping Flight with Surging", Swimming and Flying in Nature, Vol. 2, Plenum Press, New York, 1975, pp. 919-937.
38. Chopra, M.G., "Large-Amplitude Lunate-Tail Theory of Fish Locomotion", J. Fluid Mechanics, Vol. 74, Part 1 (1976), pp. 161-182.
39. Oshima, K., "Flow Pattern Around an Oscillating Airfoil", Computational Fluid Dynamics Seminar, Ames Research Center, 1 Oct. 1979.
40. Katz, J., and Weihs, D., "Hydrodynamic Propulsion by Large Amplitude Oscillation of an Airfoil with Chordwise Flexibility", J. Fluid Mechanics, Vol. 88, Part 3 (1978), pp. 485-497.
41. Lorell, W. and Bennett, L., "Lift in Large Order Unsteady Oscillating Two Dimensional Flow", New York University School of Engineering and Science, Research Division, Tech. Report 1426.02, March 1969.
42. Betteridge, D.S., and Archer, R.D., "A study of the Mechanics of Flapping Wings", Aeronautical Quarterly, Vol. 25, Part 2, May 1974, pp. 129-142.

43. Jones, R.T., "Wing Flapping with Minimum Energy", NASA TM 81174, Jan. 1980.
44. Woods, L.C., "The Lift and Moment Acting on a Thick Aerofoil in Unsteady Motion", Philosophical Transactions of the Royal Society, London, A 247, 1954, p. 131.
45. Oehme, H. and Kitzler, U., "Abteilung fur allgemeine zoologie und physiologie der tiere", Zoologische Jahrbucher, Vol. 79, No. 3, 1975, pp. 402-424, (NASA TT F-16901).
46. Lang, T.G., "Hydrodynamic Analysis of Dolphin Fin Profiles", Nature, Vol. 209, March 12, 1966.
47. Kottapalli, S.B.R., and Pierce, G.A., "Drag on an Oscillating Airfoil in a Fluctuating Free Stream", Nonsteady Fluid Dynamics, Winter Annual Meeting of ASME, San Francisco, CA, 10-15 December 1978.
48. Beddoes, T.S., "Onset of Leading-Edge Separation Effects under Dynamic Conditions and Low Mach Number", Proceedings, Thirty-Fourth Annual National Meeting of the American Helicopter Society, May 1978.
49. Evans, W.T., and Mort, K.W., "Analysis of Computed Flow Parameters for a Set of Sudden Stalls in Low Speed Two-Dimensional Flow", NASA TND-85, 1959.
50. Chopra, M.G., "Hydromechanics of Lunate-Tail Swimming Propulsion", J. Fluid Mechanics, Vol. 64, Part 2 (1974), pp. 375-391.
51. Rowe, W., Redman, M.C., Ehlers, F.E. and Sebastian, J.D., "Prediction of Unsteady Aerodynamic Loadings caused by Leading-Edge and Trailing Edge Control Surface Motions in Subsonic Compressible Flow - Analysis and Results", NASA CR 2543, Aug. 1975.
52. Tuck, E.O., "The Effect of Span-wise Variations in Amplitude on the Thrust-Generating Performance of a Flapping Thin Wing", Swimming and Flying in Nature, Vol. 2, Plenum Press, New York, 1975, pp. 953-973.
53. Chopra, M.G., Kambe, T., "Hydromechanics of Lunate-Tail Swimming Propulsion, Part 2", J. Fluid Mechanics, Vol. 79, Part 1 (1977), pp. 49-69.
54. Bennett, A.G., "A Preliminary Study of Ornithopter Aerodynamics", University of Illinois Dept. of Aeronautical and Astronautical Engineering, Ph. D. Thesis, Urbana, IL, 1970.
55. Lan, C.E., "The Unsteady Quasi-Vortex-Lattice Method with Application to Animal Propulsion", J. Fluid Mechanics, Vol. 93, Part 4 (1979), pp. 747-763.

56. Rayner, J.M., "A Vortex Theory of Animal Flight. Part 1" and "... Part 2", J. Fluid Mechanics, Vol. 91, Part 4 (1979), pp. 697-730 and pp. 731-763.
57. Weihs, D., "Semi-Infinite Vortex Trails, and Their Relation to Oscillating Airfoils", J. Fluid Mechanics, Vol. 54, Part 4 (1972), pp. 679-690.
58. Sparenberg, J.A., Wiersma, A.K., "On the Efficiency Increasing Interaction of Thrust Producing Lifting Surfaces", Swimming and Flying in Nature, Vol. 2, Plenum Press, New York, 1975, p. 891-917.
59. Bosch, H., "Interfering Airfoils in Two-Dimensional Unsteady Incompressible Flow", AGARD CP-227, Fluids Dynamics Panel Conference, Ottawa, Canada, 26-28 Sept. 1977.
60. Wu, T.Y., "Extraction of Flow Energy By a Wing Oscillating in Waves", J. of Ship Research, Vol 14, No. 1 (1972), pp. 66-78.
61. Rock, S.M., "Transient Motion of an Airfoil: An Experimental Investigation in a Small Subsonic Wind Tunnel", SUDAAR 513, Department of Aeronautics and Astronautics, Stanford University, 1978.
62. Stoltz, P.M., "Unsteady Aeroelastic Modeling and Trailing-Edge Flap Control of an Experimental Wing in a Two-Dimensional Wind Tunnel", Stanford University Department of Aeronautics and Astronautics, SUDAAR 527, 1981.
63. Von Karman, T., and Burgers, J.M., General Aerodynamic Theory - Perfect Fluids, (Volume II of Aerodynamic Theory, Div. E, W.F. Durand ed.), Julius Springer, Berlin, 1935.
64. Handbook of Mathematical Functions, ed. by M. Abramowitz and I. Stegun, Dover, New York, 1970.
65. Morino, L., "Steady, Oscillatory, and Unsteady Subsonic and Supersonic Aerodynamics - Volume I", NASA CR 159130, January 1980.
66. Kaplan W., Advanced Calculus, Addison-Wesley, Menlo Park, 1973.
67. Standard Mathematical Tables, 22nd Edition, CRC Press, Cleveland, 1974.
68. Gradshteyn, I.S., and Ryzhik, I.M., Table of Integrals, Series and Products, Academic Press, New York, 1965.
69. Dutt, H.N., and Sreekanth, A.K., "Theoretical Method for the Analysis of Airfoils in Viscous Flows", J. of Aircraft, Vol. 17, Sept. 1980, pp. 700-702.

70. McCroskey, W.J., and Philippe, J.J., "Unsteady Viscous Flow on Oscillating Airfoils", AIAA J. Vol. 13, No. 1, Jan 1975, pp. 71-79.
71. Duncan, W.J., Thom, A.S., and Young, A.D., Mechanics of Fluids, American Elsevier Publishing, New York, 1970.
72. Dwyer, H.A., "Calculation of Unsteady and Three-Dimensional Boundary Layer Flows", AIAA J., Vol. 11, No. 6, June 1973, pp. 773-774.
73. McNally, W.D. "Fortran Program for Calculating Compressible Laminar and Turbulent Boundary Layers in Arbitrary Pressure Gradients", NASA TN D-5681, May 1970.
74. Cohen, C., and Reshotko, E., "The Compressible Laminar Boundary Layer with Heat Transfer and Arbitrary Pressure Gradient", NACA TR 1294, 1956.
75. Sasman, P.K., and Cresci, R.J., "Compressible Turbulent Boundary Layers with Pressure Gradient and Heat Transfer", AIAA J., Vol. 4, No. 1, Jan 1966, pp. 19-25.
76. "Boundary Layer Effects on Unsteady Airloads", AGARD CP-296, Sept. 1980.
77. Triebstein, H. "Instationäre Druckverteilungsmessungen an Flügel-Außenlastkombinationen in inkompressibler Strömung", Deutsche Luft- und Raumfahrt Forschungsbericht, DLR-FB 77-12, 1977.
78. Patel, M.H., "On Laminar Boundary Layers in Oscillating Flow", Proceedings of the Royal Society of London, Series A, Vol. 347, No. 1648, Dec. 1975, pp. 99-123.
79. Telionis, D.P., and Tsahalis, D.T., "Unsteady Turbulent Boundary Layers and Separation", AIAA Journal, Vol. 14, No. 4, April 1976, pp. 468-474.
80. Landahl, M.T., and Ashley, H., "Thickness and Boundary Layer Effects", Part I, Chapter 9, AGARD Manual on Aeroelasticity, March 1969.
81. Boyd, W.N., "Effect of Chordwise Forces and Deformations and Deformations Due to Steady Lift on Wing Flutter", Ph.D. Dissertation, Stanford University Dept. of Aeronautics and Astronautics, November 1977.
82. Braslow, A.L., Knox, E.C., "Simplified Method for Determination of Critical Height of Distributed Roughness Particles for Boundary-Layer Transition at Mach No.s from 0 to 5", NACA TN 4363, Sept. 1958.

83. Riley, D.R., "Wind-Tunnel Investigation and Analysis of the Effects of End Plates on the Aerodynamic Characteristics of an Unswept Wing", NACA TN 2440, Aug. 1951.
84. Gibbs, J.W., Vector Analysis, C. Scribner's Sons, New York, 1902.
85. "Load Cell Terminology and Test Procedure Redommendation", Scale Manufacturer's Association, Washington, D.C., 1977.
86. Pope, A., Wind-Tunnel Testing, Second Edition, John Wiley & Sons, New York, 1960.
87. Abbott, I.H., and Von Doenhoff, A.E., Theory of Wing Sections, Dover, New York, 1959.